



BİNGÖL
ÜNİVERSİTESİ

e-ISSN 2149-6366

Cilt 13, Sayı 1, Mart 2024

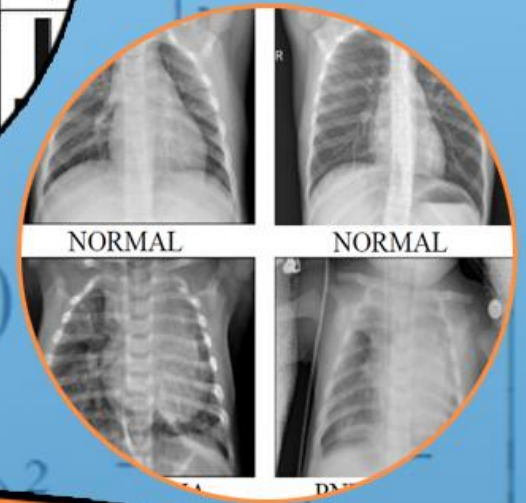
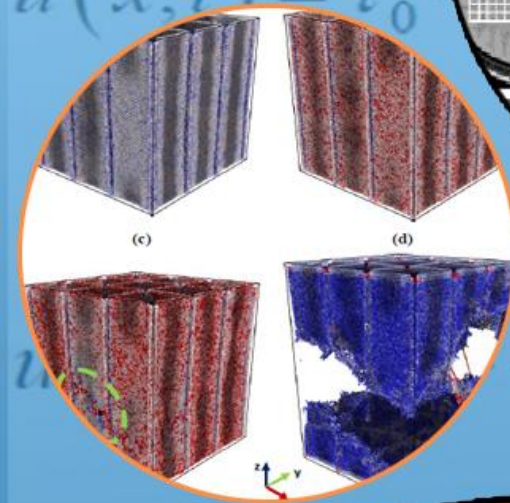
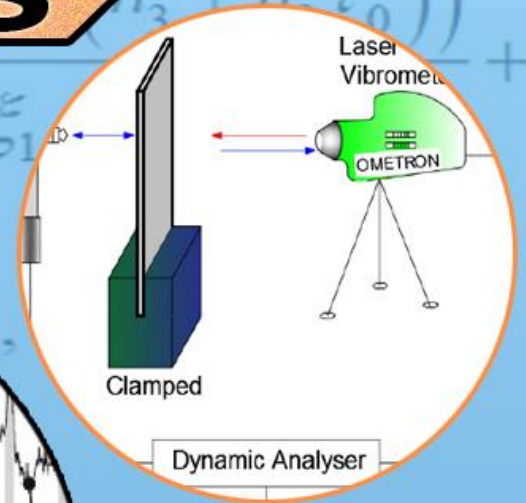
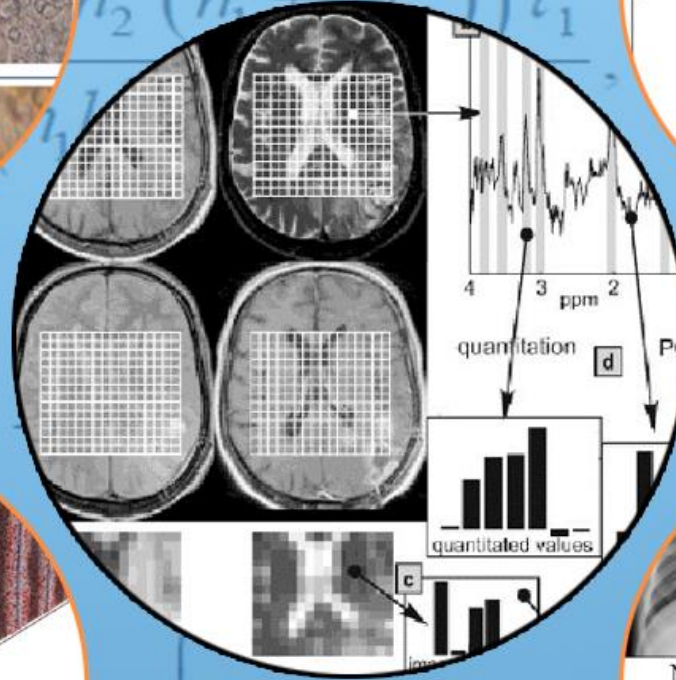
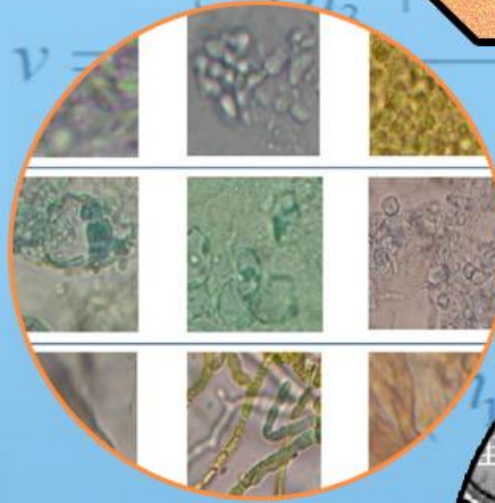
Volume 13, Issue 1, March 2024

TDFD

TÜRK DOĞA ve FEN DERGİSİ

TURKISH JOURNAL OF NATURE AND SCIENCE

TJNS



www.dergipark.gov.tr/tdfd

Bingöl Üniversitesi Fen Bilimleri Enstitüsü tarafından
yayımlanmaktadır.

Published by Bingöl University Institute of Science

ULAKBİM

TRDİZİN

TÜRK DOĞA VE FEN DERGİSİ

Amaç

Türk Doğa ve Fen Dergisi, Dergipark tarafından yayınlanan Bingöl Üniversitesi Fen Bilimleri Enstitüsüne ait ulusal ve hakemli bir dergidir. Türk Doğa ve Fen Dergisi, Türkiye ve dünyanın her yerinden gelen doğa ve fen bilimlerinin her alanında özgün, yayımlanmamış, yayımlanmak üzere başka yere gönderilmemiş makale, derleme ve sempozyum değerlendirmesi gibi çalışmaların bilim alemine sunulması amacıyla kurulmuştur.

Kapsam

Türk Doğa ve Fen Dergisinde Mühendislik, Ziraat, Veterinerlik, Fen ve Doğa Bilimleri alanlarından olmak üzere Türkçe ve İngilizce hazırlanmış orijinal makale, derleme ve sempozyum değerlendirmesi gibi çalışmalar yayımlanır. Türk Doğa ve Fen Dergisi sadece online sistemde yayımlanmakta olup ayrıca kağıt baskısı bulunmamaktadır.

Merhaba...

Türk Doğa ve Fen Dergisi, Dergipark tarafından yayımlanmakta olup Bingöl Üniversitesi Fen Bilimleri Enstitüsüne aittir. Bahar ve güz dönemi olmak üzere yılda iki defa çıkarılan ulusal hakemli bir dergi olarak ilk sayısını 2012 bahar döneminde yayımlamıştır. Türk Doğa ve Fen Dergisi, Türkiye ve dünyanın her yerinden gelen doğa ve fen bilimlerinin her alanında özgün, yayımlanmamış, yayımlanmak üzere başka yere gönderilmemiş makale, derleme ve sempozyum değerlendirmesi gibi çalışmaların bilim alemine sunulması amacıyla kurulmuştur. İlk sayısından bugüne kesintisiz olarak faaliyetlerini sürdürmektedir.

Türk Doğa ve Fen Dergisi sadece online sistemde yayımlanmakta olup ayrıca kağıt baskısı bulunmamaktadır. Dergimize gelen her çalışma öncelikle Turnitin intihal programında taranmaktadır. Dergimizde editörlerin, hakemlerin ve yazarların, uluslararası yayım etik kurallarına uyması ve makalelerin yazım kurallarına uyumlu olması zorunluluğu vardır.

Yazarlar yayımlanmak üzere dergimize gönderdikleri çalışmalarını ile ilgili telif haklarını zorunlu olarak Bingöl Üniversitesi Türk Doğa ve Fen Dergisi'ne devretmiş sayılırlar. Yazarlardan herhangi bir ücret talep edilmemektedir. Yazarların değerlendirmeleri, dergimizin resmi görüşü olarak kabul edilemez. Çalışmaların her türlü sorumluluğu yazarlarına aittir. Araştırma ürünleri için etik kurul raporu gerekli ise, çalışma üzerinde bu raporun alınmış olduğu belirtilmeli ve kurul raporu sisteme kaydedilmelidir. Araştırma ile ilgili intihal, atıf manipülasyonu, sahte veri uydurma vb. suistimallerin tespit edilmesi halinde yayım ve etik ilkelerine göre davranılır. Bu durumda çalışmanın yayımlanmasını önlemek, yayımdan kaldırmak ya da başka işlemler yapmak için gerekli işlemler takip edilmektedir.

Dergimizde, kaynak gösteriminde uluslararası Vancouver sistemine geçilmiştir. Ayrıca dergimiz, Creative Commons ile lisanslanmak suretiyle dergimizde yayımlanan makalelerin paylaşımı, kaynak gösterimi ve yayımlanmasında dergi ve yazar haklarını korumaya almıştır. 2018 yılı güz döneminden itibaren makaleler, uluslararası yazar kimlik numarası ORCID No'su ile yayımlanmaktadır.

Dergi ekibi, dergimizin ulusal ve uluslararası indekslerce taranan bir dergi olması yönünde çalışmalarını titizlikle sürdürmektedir. Dergimize gösterilen ilgi bu yönde bizleri teşvik etmeye devam edecektir.

Bingöl Üniversitesi Fen Bilimleri Enstitüsü tarafından yayımlanmaktadır

EDİTÖRLER (YAYIN) KURULU

BAŞEDİTÖR

Doç. Dr. Ekrem DARENDELİOĞLU

Bingöl Üniversitesi, Fen-Edebiyat Fakültesi, Moleküler Biyoloji ve Genetik
Bölümü

E-Mail: edarendelioglu@bingol.edu.tr

EDİTÖR YARDIMCILARI

Doç. Dr. Adnan AYNA

Bingöl Üniversitesi, Fen-Edebiyat Fakültesi, Kimya Bölümü

E-Mail: aayna@bingol.edu.tr

Dr. Öğr. Üyesi Mücahit ÇALIŞAN

Bingöl Üniversitesi, Mühendislik-Mimarlık Fakültesi, Bilgisayar Mühendisliği

E-Mail: mcalisan@bingol.edu.tr

EDİTÖRLER

Fen ve Doğa Bilimleri

Doç. Dr. İkram ORAK

Bingöl Üniversitesi, Sağlık Hizmetleri Meslek Yüksekokulu, Tıbbi Hizmetler ve
Teknikler

E-Mail: iorak@bingol.edu.tr

Prof. Dr. Selami SELVİ

Balıkesir Üniversitesi, Altınoluk Meslek Yüksekokulu, Bitkisel ve Hayvansal
Üretim Bölümü

E-Mail: sselvi2000@yahoo.com

Prof. Dr. Refik KESKİN

Sakarya Üniversitesi, Fen-Edebiyat Fakültesi, Matematik Bölümü

E-Mail: rkeskin@sakarya.edu.tr

Prof. Dr. Halim ÖZDEMİR

Sakarya Üniversitesi, Fen-Edebiyat Fakültesi, Matematik Bölümü

E-Mail: hozdemir@sakarya.edu.tr

Prof. Dr. Zafer ŞİAR

Bingöl Üniversitesi, Fen-Edebiyat Fakültesi, Matematik Bölümü
E-Mail: zsiar@bingol.edu.tr

Prof. Dr. Uğur ÇAKILCIOĞLU

Munzur Üniversitesi, Pertek Sakine Genç Meslek Yüksekokulu, Bitki Morfolojisi
ve Anatomisi Bölümü
E-Mail: ucakilcioglu@yahoo.com

Doç. Dr. Kamuran DİLSİZ

Bingöl Üniversitesi, Fen-Edebiyat Fakültesi, Fizik Bölümü
E-Mail: kdilsiz@bingol.edu.tr

Doç. Dr. Şükran KONCA

Bakırçay Üniversitesi, Mühendislik ve Mimarlık Fakültesi, Temel Bilimler,
Matematik Bölümü
E-Mail: sukran.konca@bakircay.edu.tr

Doç. Dr. İdris YAZGAN

Kastamonu Üniversitesi, Fen Edebiyat Fakültesi, Biyoloji
E-Mail: idrisyazgan@gmail.com

Doç. Dr. Abdulcabbar YAVUZ

Gaziantep Üniversitesi, Mühendislik Fakültesi, Metalurji ve Malzeme Mühendisliği
E-Mail: ayavuz@gantep.edu.tr

Doç. Dr. Bünyamin ALIM

Bayburt Üniversitesi, Teknik Bilimler Meslek Yüksekokulu, Elektrik ve Enerji
Bölümü
E-Mail: balim@bayburt.edu.tr

Dr. Öğr. Üyesi Mustafa Şükrü KURT

Erzurum Teknik Üniversitesi, Fen Fakültesi, Temel Bilimler
E-Mail: mustafa.kurt@erzurum.edu.tr

Dr. Öğr. Üyesi Sinan SAĞIR

Karamanoğlu Mehmetbey Üniversitesi, Fizik
E-Mail: sinansagir@kmu.edu.tr / sinan.sagir@cern.ch

Doç. Dr. Murat AYDEMİR

Erzurum Teknik Üniversitesi, Fen Fakültesi, Temel Bilimler

E-Mail: murat.aydemir@erzurum.edu.tr

Mühendislik Bilimleri

Doç. Dr. Özgür ÖZGÜN

Bingöl Üniversitesi, Sağlık Bilimleri Fakültesi, İş Sağlığı ve Güvenliği Bölümü

E-Mail: oozgun@bingol.edu.tr

Prof. Dr. Figen KOREL

İzmir Yüksek Teknoloji Enstitüsü, Gıda Mühendisliği Bölümü

E-Mail: figenkorel@iyte.edu.tr

Prof. Dr. Kubilay ASLANTAŞ

Afyon Kocatepe Üniversitesi, Teknoloji Fakültesi, Makine Mühendisliği Bölümü

E-Mail: aslantas@aku.edu.tr

Prof. Dr. Hamit Özkan GÜLSOY

Marmara Üniversitesi, Teknoloji Fakültesi, Metalurji ve Malzeme Mühendisliği
Bölümü

E-Mail: ogulsoy@marmara.edu.tr

Prof. Dr. Ali Adnan HAYALOĞLU

İnönü Üniversitesi, Mühendislik Fakültesi, Gıda Mühendisliği Bölümü

E-Mail: adnan.hayaloglu@inonu.edu.tr

Prof. Dr. Barbara SAWICKA

University of Life Sciences in Lublin, Department of Plant Production Technology
and Commodities Sciences

E-Mail: barbara.sawicka@gmail.com

Prof. Dr. İbrahim GÜNEŞ

Giresun Üniversitesi, Mühendislik Fakültesi, İnşaat Mühendisliği Bölümü

E-Mail: ibrahim.gunes@giresun.edu.tr

Doç. Dr. Sırma YEĞİN

Ege Üniversitesi, Mühendislik Fakültesi, Gıda Mühendisliği Bölümü
E-Mail: sirma.yegin@ege.edu.tr

Doç. Dr. Hasan OĞUL

Sinop Üniversitesi, Mimarlık ve Mühendislik Fakültesi, Nükleer Enerji
Mühendisliği
E-Mail: hogul@sinop.edu.tr

Doç. Dr. Murat YILMAZTEKİN

İnönü Üniversitesi, Mühendislik Fakültesi, Gıda Mühendisliği Bölümü
E-Mail: murat.yilmaztekin@inonu.edu.tr

Doç. Dr. Ferhat AYDIN

Sakarya Uygulamalı Bilimler Üniversitesi, Teknoloji Fakültesi, İnşaat
Mühendisliği Bölümü
E-Mail: ferhata@subu.edu.tr

Dr. Öğr. Üyesi Nurullah DEMİR

Bingöl Üniversitesi, Mühendislik ve Mimarlık Fakültesi, Gıda Mühendisliği
Bölümü
E-Mail: ndemir@bingol.edu.tr

Dr. Öğr. Üyesi Ahmet GÜNER

Bingöl Üniversitesi, Mühendislik ve Mimarlık Fakültesi, Elektrik ve Elektronik
Mühendisliği Bölümü
E-Mail: aguner@bingol.edu.tr

Dr. Öğr. Üyesi Tahir AKGÜL

Sakarya Uygulamalı Bilimler Üniversitesi, Teknoloji Fakültesi, İnşaat
Mühendisliği Bölümü
E-Mail: tahirakgul@subu.edu.tr

Dr. Erhan Sulejmani

University of Tetova, Faculty of Food Technology and Nutrition
E-Mail: erhan.sulejmani@unite.edu.mk

Dr. Hacène Medjoudj

Larbi Ben M'Hidi University of Oum El Bouaghi, Food Science Department
E-Mail: medjoudjh@yahoo.com

Dr. Avinash Lakshmikanthan

Nitte Meenakshi Institute of Technology, Department of Mechanical Engineering,
Karnataka, India
E-Mail: avinash.laks01@gmail.com

Dr. Manjunath Patel GC

PES Institute of Technology and Management, Department of Mechanical
Engineering, Karnataka, India
E-Mail: manju09mpm05@gmail.com

Sağlık Bilimleri

Doç. Dr. Aydın Şükrü BENGÜ

Bingöl Üniversitesi, Sağlık Hizmetleri Meslek Yüksekokulu, Tıbbi Hizmetler ve
Teknikler
E-Mail: abengu@bingol.edu.tr

Dr. Öğr. Üyesi Dilhun Keriman ARSERİM UÇAR

Bingöl Üniversitesi, Sağlık Bilimleri Fakültesi, Beslenme ve Diyetetik Bölümü
E-Mail: dkucar@bingol.edu.tr

Dr. Öğr. Üyesi Abdullah TUNÇ

Bingöl Üniversitesi, Sağlık Bilimleri Fakültesi, İş Sağlığı ve Güvenliği Bölümü
E-Mail: atunc@bingol.edu.tr

Dr. Öğr. Üyesi Ramazan GÜNDOĞDU

Bingöl Üniversitesi, Sağlık Hizmetleri Meslek Yüksekokulu, Eczane Hizmetleri
E-Mail: rgundogdu@bingol.edu.tr

Dr. Alexander HERGOVICH

UCL Cancer Institute, Faculty of Medical Sciences, Department of Cancer Biology,
UCL, London, UK
E-Mail: a.hergovich@uc.ac.uk

Dr. Valenti GOMEZ

UCL Cancer Institute, Faculty of Medical Sciences, Department of Oncology,
UCL, London, UK

E-Mail: valentin.gomez@ucl.ac.uk

Veterinerlik Bilimleri

Doç. Dr. Cüneyt ÇAĞLAYAN

Bilecik Şeyh Edebali Üniversitesi, Tıp Fakültesi, Temel Tıp Bilimleri Bölümü,
Tıbbi Biyokimya Anabilim Dalı

E-Mail: cuneyt.caglayan@bilecik.edu.tr

Prof. Dr. Fatih Mehmet KANDEMİR

Atatürk Üniversitesi, Veteriner Fakültesi, Veteriner Hekimliği Temel Bilimler

E-Mail: fmehmet.kandemir@atauni.edu.tr

Doç. Dr. Akın KIRBAŞ

Bozok Üniversitesi, Veteriner Fakültesi, Klinik Bilimler Bölümü

E-Mail: akindahiliye55@yahoo.com

Doç. Dr. Emrah Hicazi AKSU

Atatürk Üniversitesi, Veteriner Fakültesi, Klinik Bilimler Bölümü

E-Mail: emrahaksu@atauni.edu.tr

Ziraat Bilimleri

Dr. Öğr. Üyesi Zeynep DUMANOĞLU

Bingöl Üniversitesi, Ziraat Fakültesi, Biyosistem Mühendisliği Bölümü

E-Mail: zdumanoglu@bingol.edu.tr

Prof. Dr. Kağan KÖKTEN

Bingöl Üniversitesi, Ziraat Fakültesi, Tarla Bitkileri Bölümü

E-Mail: kahafe1974@yahoo.com

Prof. Dr. Mustafa SÜR MEN

Adnan Menderes Üniversitesi, Ziraat Fakültesi, Tarla Bitkileri Bölümü

E-Mail: mustafa.surmen@adu.edu.tr

Prof. Dr. Banu YÜCEL

Ege Üniversitesi, Ziraat Fakültesi, Hayvan Yetiştirme Anabilim Dalı, Zootekni
Bölümü

E-Mail: banu.yucel@ege.edu.tr

Doç. Dr. Hakan İNCİ

Bingöl Üniversitesi, Ziraat Fakültesi, Zootekni Bölümü

E-Mail: hinci@bingol.edu.tr

TEKNİK EDİTÖRLER

Dr. Nimetullah KORKUT

Bingöl Üniversitesi, BİNUZEM, Bilgisayar Teknolojileri

E-Mail: nkorkut@bingol.edu.tr

Öğr. Gör. MEHMET VURAL

Bingöl Üniversitesi, Genç Meslek Yüksek Okulu, Bilgisayar Teknolojileri

E-Mail: mvural@bingol.edu.tr









DİL EDİTÖRÜ

Öğr. Gör. Dr. Ahmet KESMEZ










Bingöl Üniversitesi, Yabancı Diller Yüksekokulu, İngilizce Bölümü







E-Mail: akesmez@bingol.edu.tr










İÇİNDEKİLER/CONTENTS












<p>Genetic Diversity of <i>Cucumber mosaic virus</i> in Cucumber Plants Grown in Diyarbakır Province</p> <p>Abdullah GÜLLER¹ , Serap DEMİREL^{2*} , Mustafa USTA³ , Gülüstan KORKMAZ³ </p> <p>¹ Bingöl University, Agriculture Faculty, Plant Protection Department, Bingöl, Türkiye ² Van Yüzüncü Yıl University, Science Faculty, Molecular Biology and Genetic Department, Van, Türkiye ³ Van Yüzüncü Yıl Üniversitesi, Agriculture Faculty, Plant Protection Department, Van, Türkiye</p> <p>Abdullah GÜLLER ORCID No: 0000-0003-3887-4208 Serap DEMİREL ORCID No: 0000-0002-1877-0797 Mustafa USTA ORCID No: 0000-0002-3940-2774 Gülüstan KORKMAZ No: 0000-0002-9032-5823</p> <p>*Serap DEMİREL: serap_comart@hotmail.com</p> <p>(Received: 16.03.2023, Accepted: 19.12.2023, Online Publication: 26.03.2024)</p>	<p>1</p>
<p><i>Celtis australis</i> Exhibits Cytotoxic Effects by Inducing DNA Damage in Human Ovarian Cancer Cells</p> <p>Gülsüm Nur FİDAN¹ , Sevilay GÜNAY² , Yavuz ERDEN^{1*} </p> <p>¹ Bartın University, Science Faculty, Molecular Biology and Genetics Department, Bartın, Türkiye ² Gazi University, Medicine Faculty, Biophysics Department, Ankara, Türkiye</p> <p>Gülsüm Nur FİDAN ORCID No: 0009-0001-4474-0962 Sevilay GÜNAY ORCID No: 0000-0002-0130-5629 Yavuz ERDEN ORCID No: 0000-0002-2807-6096</p> <p>*Corresponding author: yerden@bartin.edu.tr</p> <p>(Received: 23.08.2023, Accepted: 25.12.2023, Online Publication: 26.03.2024)</p>	<p>7</p>
<p>Experimental Study to Determine the Backscattering, Asymmetry, and Tailing Factors for Some Elements in the Atomic Number Range of $4 \leq Z \leq 48$ at 59.54 keV Using the Gamma Backscattering Method</p> <p>Zeynep UZUNOĞLU^{1*} </p> <p>¹ Ağrı İbrahim Çeçen University, Patnos Vocational School, Department of Medical Services and Techniques, Opticianry Program, Ağrı, Türkiye</p> <p>Zeynep UZUNOĞLU ORCID No: 0000-0003-1997-1870</p> <p>*Corresponding author: zuzunoglu@agri.edu.tr</p> <p>(Received: 8.09.2023, Accepted: 6.01.2024, Online Publication: 26.03.2024)</p>	<p>12</p>





<p>Experimental Study to Determine the Backscattering, Asymmetry, and Tailing Factors for Some Elements in the Atomic Number Range of $4 \leq Z \leq 48$ at 59.54 keV Using the Gamma Backscattering Method</p> <p>Zeynep UZUNOĞLU^{1*} </p> <p>¹ Ağrı İbrahim Çeçen University, Patnos Vocational School, Department of Medical Services and Techniques, Opticianry Program, Ağrı, Türkiye Zeynep UZUNOĞLU ORCID No: 0000-0003-1997-1870</p> <p><i>*Corresponding author: zuzunoglu@agri.edu.tr</i></p> <p>(Received: 8.09.2023, Accepted: 6.01.2024, Online Publication: 26.03.2024)</p>	<p>19</p>
<p>Deceptive Patch Solutions for Protecting Industrial Control Systems Based on Discovered Vulnerabilities</p> <p>Özlem BATUR DİNLER^{1*} </p> <p>¹ Siirt University, Engineering Faculty, Computer Engineering Department, Siirt, Türkiye Özlem BATUR DİNLER ORCID No: 0000-0002-2955-6761</p> <p><i>*Corresponding author: o.b.dinler@siirt.edu.tr</i></p> <p>(Received: 30.03.2023, Accepted: 15.01.2024, Online Publication: 26.03.2024)</p>	<p>26</p>
<p>Investigation of Fourier Transform Infrared (FT-IR) Spectroscopy and Chemometric Analysis Method as an Alternative Method in the Diagnosis of Prostate Cancer</p> <p>Yılmaz ŞAHİN^{1*} </p> <p>¹ Atatürk University, Vocational School of Health Services, Department of Therapy and Rehabilitation, Erzurum, Turkey Yılmaz ŞAHİN ORCID No: 0000-0003-2998-8879 <i>*Corresponding author: yilmazsahin86@gmail.com</i></p> <p>(Received: 21.11.2023, Accepted: 17.01.2024, Online Publication: 26.03.2024)</p>	<p>35</p>
<p>Green Supplier Assessment with Fuzzy Expert System Approach</p> <p>Çağatay TEKE^{1*} </p> <p>¹ Bayburt University, Engineering Faculty, Industrial Engineering Department, Bayburt, Türkiye Çağatay TEKE ORCID No: 0000-0002-6975-8544</p> <p><i>*Corresponding author: cagatayteke@bayburt.edu.tr</i></p> <p>(Received: 28.08.2023, Accepted: 23.01.2024, Online Publication: 26.03.2024)</p>	<p>40</p>











<p>Investigation of the Effects of PFKFB3 Small Molecule Inhibitor KAN0438757 on Cell Migration and Expression Level of N-cadherin Protein in Glioblastoma Cell Lines</p> <p>Seher SARUHAN¹  , Deniz ÖZDEMİR¹  Remziye SAFA¹  , Can Ali AĞCA^{1*} </p> <p>¹Bingöl University, Faculty of Arts and Sciences, Department of Molecular Biology and Genetics, Bingöl, Türkiye</p> <p>Seher SARUHAN ORCID No: 0000-0003-1641-8519 Deniz ÖZDEMİR ORCID No: 0000-0001-7659-742X Remziye SAFA ORCID No: 0009-0002- 0392-3196 Can Ali AĞCA ORCID No: 0000-0002-0244-3767</p> <p><i>*Corresponding author: c.aliagca@gmail.com</i></p> <p>(Received: 02.11.2023, Accepted: 10.02.2024, Online Publication: 26.03.2024)</p>	<p>47</p>
<p>Detection of Pneumonia Using A Hybrid Approach Consisting of MobileNetV2 and Squeeze-and-Excitation Network</p> <p>Hüseyin FIRAT¹  , Hüseyin ÜZEN² </p> <p>¹ Dicle University, Faculty of Engineering, Department of Computer Engineering, Diyarbakır, Türkiye ² Bingöl University, Faculty of Engineering-Architecture, Department of Computer Engineering, Bingöl, Türkiye</p> <p>Hüseyin FIRAT ORCID No: 0000-0002-1257-8518 Hüseyin ÜZEN ORCID No: 0000-0002-0998-2130</p> <p><i>*Corresponding author: huseyin.firat@dicle.edu.tr</i></p> <p>(Received: 19.09.2023, Accepted: 10.02.2024, Online Publication: 26.03.2024)</p>	<p>54</p>
<p>Purification, Characterization of Glutathion Reductase Enzyme From Sheep Spleen Tissue and Investigation of the Effects of Some Antibiotics on Enzyme Activity</p> <p>Çiğdem ÇOBAN¹  , Yusuf TEMEL²  , Mehmet ÇİFTÇİ³ </p> <p>¹ Bingöl University, Solhan Health Services Vocational School, Bingöl, Türkiye ² Bingöl University, Solhan Health Services Vocational School, Bingöl, Türkiye ³ Bingöl University, Faculty of Veterinary, Bingöl, Türkiye</p> <p>Çiğdem ÇOBAN ORCID No: 0000-0003-1141-544X Yusuf TEMEL ORCID No: 0000-0001-8148-3718 Mehmet ÇİFTÇİ ORCID No: 0000-0002-1748-3729</p> <p><i>*Corresponding author: mciftci@bingol.edu.tr</i></p> <p>(Received: 27.07.2023, Accepted: 20.02.2024, Online Publication: 26.03.2024)</p>	<p>62</p>

<p>An Investigation on the Use of Clustering Algorithms for Data Preprocessing in Breast Cancer Diagnosis</p> <p>Ali ŞENOL^{1*} , Mahmut KAYA² </p> <p>¹ Tarsus University, Engineering Faculty, Department of Computer Engineering, Mersin, Türkiye</p> <p>² Fırat University, Engineering Faculty, Department of Artificial Intelligence and Data Engineering, Elazığ, Türkiye</p> <p>Ali ŞENOL ORCID No: 0000-0003-0364-2837 Mahmut KAYA ORCID No: 0000-0002-7846-1769</p> <p><i>*Corresponding author: alisenol@tarsus.edu.tr</i></p> <p>(Received: 21.09.2023, Accepted: 26.02.2024, Online Publication: 26.03.2024)</p>	<p>70</p>
<p>Protective Effect of Royal Jelly on Some Hematologic Parameters Against Sodium Arsenite Toxicity: A Study in Rats</p> <p>Enes KAYA^{1*} , Halil ŞİMŞEK² </p> <p>¹ Bingöl University, Bee and Natural Products R&D and P&D Application and Research Center, Bingöl, Türkiye</p> <p>² Bingöl University, Vocational School of Health Services, Department of Medical Services and Techniques, Bingöl, Türkiye</p> <p>Enes KAYA ORCID No: 0000-0003-3973-168X Halil ŞİMŞEK ORCID No: 0000-0002-9637-1265</p> <p><i>*Corresponding author: eneskaya@bingol.edu.tr</i></p> <p>(Received: 10.10.2023, Accepted: 29.02.2024, Online Publication: 26.03.2024)</p>	<p>78</p>
<p>PSO Training Neural Network MPPT with CUK Converter Topology for Stand-Alone PV Systems Under Varying Load and Climatic Conditions</p> <p>Mehmet YILMAZ¹ , M. Fatih ÇORAPSIZ^{1*} </p> <p>¹ Ataturk University, Engineering Faculty, Electrical-Electronics Engineering, Erzurum, Türkiye</p> <p>Mehmet YILMAZ ORCID No: 0000-0001-7624-4245 M. Fatih ÇORAPSIZ ORCID No: 0000-0001-5692-8367</p> <p><i>*Corresponding author: corapsiz@atauni.edu.tr</i></p> <p>(Received: 22.01.2024, Accepted: 01.03.2024, Online Publication: 26.03.2024)</p>	<p>88</p>

<p>The Effect of Cadmium and Lead Exposure on the Development and Physical Structure of Quinoa (<i>Chenopodium quinoa</i> Willd.)</p> <p>Zeynep GÜL^{1*} , Abdullah YAZICI² , Özlem ÇAKIR³ </p> <p>¹ Atatürk Üniversitesi, Bitkisel Üretim ve Uygulama Merkezi, Erzurum, Türkiye ² Atatürk Üniversitesi, Ziraat Fakültesi, Tarla Bitkileri Bölümü, Erzurum, Türkiye ³ Bayburt Üniversitesi, Mühendislik Fakültesi, Gıda Mühendisliği Bölümü, Bayburt, Türkiye</p> <p>Zeynep GÜL ORCID No: 0000-0003-2961-1473 Abdullah YAZICI ORCID No: 0000-0003-0362-2799 Özlem ÇAKIR ORCID No: 0000-0002-5080-7721</p> <p><i>*Corresponding author: zdumlu@atauni.edu.tr</i></p> <p>(Received: 06.10.2023, Accepted: 07.03.2024, Online Publication: 26.03.2024)</p>	<p>98</p>
<p>Screening Some Advanced Upland Cotton (<i>Gossypium Hirsutum</i> L.) Genotypes Tolerance Under Water Deficit Stress</p> <p>Sadettin ÇELİK^{1*} </p> <p>¹University of Bingol, Genç vocational school, Department of Forestry, 12500, Genç, Bingol/ Turkey</p> <p>Sadettin ÇELİK ORCID No: 0000-0002-8396-4627 <i>*Corresponding author: sadettincelik@bingol.edu.tr</i></p> <p>(Received: 07.11.2023, Accepted: 07.03.2024, Online Publication: 26.03.2024)</p>	<p>104</p>
<p>Isolation, Identification and Molecular Characterization of Lactic Acid Bacteria from Raw Milk Samples Collected from Erzurum Region</p> <p>Selcan DOĞAN¹ , Gulsah ADIGUZEL^{1*} </p> <p>¹Ataturk University, Faculty of Veterinary Science, Department of Food Science and Technology, Erzurum, Türkiye Selcan DOĞAN ORCID No: 0000-0001-6196-7950 Gulsah ADIGUZEL ORCID No: 0000-0003-1207-6742</p> <p><i>*Corresponding author: gulsah@atauni.edu.tr</i></p> <p>(Received: 24.01.2024, Accepted: 11.03.2024, Online Publication: 26.03.2024)</p>	<p>111</p>
<p>Ergonomics in Beekeeping Activities</p> <p>Özgür ÖZGÜN^{1*} , Timuçin ÇİNKİLİÇ¹ , İsa AK¹ </p> <p>¹ Bingöl University, Health Sciences Faculty, Occupational Health and Safety Department, 12000, Bingöl, Türkiye Özgür ÖZGÜN ORCID No: 0000-0003-3816-6746 Timuçin ÇİNKİLİÇ ORCID No: 0009-0006-1812-9680 İsa AK ORCID No: 0009-0009-6862-4526</p> <p><i>*Corresponding author: oozgun@bingol.edu.tr</i></p> <p>(Received: 15.12.2023, Accepted: 11.03.2024, Online Publication: 26.03.2024)</p>	<p>118</p>

<p>Partially Purification and Biochemical Characterization of Phytase Enzyme from <i>Lactobacillus brevis</i> Isolated from Fresh Kashar Cheese</p> <p>Neslihan DİKBAŞ^{1*} , Şeyma ALIM¹ , Sümeyra UÇAR¹ , Sevda UÇAR² , Ayşe Gül KASAPOĞLU³ , Esmâ YİĞİDER¹ </p> <p>¹ Ataturk University, Agricultural Faculty, Department of Agricultural Biotechnology, Erzurum, Türkiye ² Sivas Science and Technology University, Faculty of Agricultural Sciences and Technology Department of Herbal Production and Technologies, Sivas, Türkiye ³ Erzurum Technical University, Faculty of Science, Department of Molecular Biology and Genetics, Erzurum, Türkiye</p> <p>Neslihan DİKBAŞ ORCID No: 0000-0001-9096-2761 Şeyma ALIM ORCID No: 0000-0001-6684-7974 Sümeyra UÇAR ORCID No: 0000-0002-7629-0206 Sevda UÇAR ORCID No: 0000-0002-3612-457X Ayşe Gül KASAPOĞLU ORCID No: 0000-0002-6447-4921 Esmâ YİĞİDER ORCID No: 0000-0002-6896-0193</p> <p><i>*Corresponding author: neslidikbas@atauni.edu.tr</i></p> <p>(Received: 21.02.2024, Accepted: 15.03.2024, Online Publication: 26.03.2024)</p>	<p>123</p>
<p>Vibration Response of Thermoplastic Veil Interleaved Carbon Fiber Reinforced Epoxy Composites</p> <p>Yavuz Selim TARİH^{1*} , Volkan ACAR² , Ömer GÜNDOĞDU² , Adem YAR³ </p> <p>¹ Vocational College of Technical Sciences, Bingöl University, Bingöl/Türkiye ² Department of Mechanical Engineering, Atatürk University, Erzurum/Türkiye ³ Department of Mechanical Engineering, Bingöl University, Bingöl/Türkiye</p> <p>Yavuz Selim TARİH ORCID No: 0000-0002-8267-7706 Volkan ACAR ORCID No: 0000-0001-7412-301X Ömer GÜNDOĞDU ORCID No: 0000-0003-2656-4181 Adem YAR ORCID No: 0000-0002-1432-9590</p> <p><i>*Corresponding author: ystarih@bingol.edu.tr</i></p> <p>(Received: 8.12.2023, Accepted: 17.03.2024, Online Publication: 26.03.2024)</p>	<p>128</p>
<p>Investigation of Mechanical Properties of Graphene-CNT Reinforced Nickel Metal Matrix Nanocomposite Structure</p> <p>Ünal DEĞİRMENCI^{1*} </p> <p>¹ Bingöl University, Department of Machinery and Metal Technologies, Bingöl, Türkiye</p> <p>Ünal DEĞİRMENCI ORCID No: 0000-0003-1480-2488</p> <p><i>*Corresponding author: udegirmenci@bingol.edu.tr</i></p> <p>(Received: 16.02.2024, Accepted: 17.03.2024, Online Publication: 26.03.2024)</p>	<p>133</p>

<p>Developing a Regression Model for Predicting the Seismic Input Energy of RC Buildings Using 6 February 2023 Kahramanmaraş Earthquake</p> <p>Bilal BALUN^{1*} </p> <p>¹ Bingöl University, Centre for Energy the Environment and Natural Disasters and Department of Architecture, Bingöl, Türkiye Bilal BALUN ORCID No: 0000-0003-0906-4484</p> <p><i>*Corresponding author: bbalun@bingol.edu.tr</i></p> <p>(Received: 18.09.2023, Accepted: 19.03.2024, Online Publication: 26.03.2024)</p>	<p>142</p>
<p>Classification of Microscopic Fungi Images Using Vision Transformers for Enhanced Detection of Fungal Infections</p> <p>Abdurrahman GUMUS^{1*} </p> <p>¹ Izmir Institute of Technology, Faculty of Engineering, Electrical-Electronics Engineering, Izmir, Türkiye Abdurrahman GUMUS ORCID No: 0000-0003-2993-5769</p> <p><i>*Corresponding author: abdurrahmangumus@iyte.edu.tr</i></p> <p>(Received: 24.02.2024, Accepted: 19.03.2024, Online Publication: 26.03.2024)</p>	<p>152</p>
<p>Use of New Natural Dyes Extracted from Different Sections of <i>Salvia urica</i> in Dye-Sensitized Solar Cells</p> <p>Fehmi ASLAN^{1*} , Halil İbrahim YAMAÇ² </p> <p>¹ MTU University, Yeşilyurt MYO, Department of Motor Vehicles and Transportation Technologies, Malatya, Türkiye ² Fırat University, Technologies Faculty, Department of Mechatronics Engineering, Elazığ, Türkiye Fehmi ASLAN ORCID No: 0000-0002-5304-0503 Halil İbrahim YAMAÇ ORCID No: 0000-0002-4628-0971</p> <p><i>*Corresponding author: fehmi.aslan@ozal.edu.tr</i></p> <p>(Received: 5.01.2024, Accepted: 21.03.2024, Online Publication: 26.03.2024)</p>	<p>161</p>

<p style="text-align: center;">Dyadic Maximal Function Maps the Weighted Hardy Space $H^1(w)$ to the Weighted $L^1(w)$ Space</p> <p style="text-align: center;">Sakin DEMIR^{1*} </p> <p style="text-align: center;">¹ Agri Ibrahim Cecen University, Faculty of Education, Department of Basic Education, Ağrı, Türkiye Sakin DEMIR ORCID No: 0000-0002-8019-6917</p> <p style="text-align: center;"><i>*Corresponding author: sakin.demir@gmail.com</i></p> <p style="text-align: center;"><small>(Received: 09.01.2024, Accepted: 20.03.2024, Online Publication: 26.03.2024)</small></p>	172
<p style="text-align: center;">Possible Health Problems Caused by Bee Products and Uncontrolled Use</p> <p style="text-align: center;">Gıyasettin BAYDAŞ^{1*} , F. Tutku AKSOY² , Zeynep GÜNGÖRDÜ DALAR³ , Merve Nur AKSAKAL⁴ , İpek ÇORUHLU⁵ , Sara ÇIBİK² , Elif Sena ÖZCAN⁶ , Öykü TOPTAŞ³ , Zümra KUL¹ </p> <p style="text-align: center;">¹Altınbaş University, Faculty of Medicine, Department of Medical Physiology, İstanbul, Türkiye ²Altınbaş University, Faculty of Medicine, Department of Medical Biochemistry, İstanbul, Türkiye ³Altınbaş University, Faculty of Medicine, Department of Medical Microbiology, İstanbul, Türkiye ⁴Altınbaş University, Faculty of Medicine, Department of Medical Biology, İstanbul, Türkiye ⁵Altınbaş University, Faculty of Medicine, Department of Histology&Embryology, İstanbul, Türkiye ⁶Altınbaş University, Faculty of Medicine, Department of Anatomy, İstanbul, Türkiye</p> <p style="text-align: center;">Gıyasettin BAYDAŞ ORCID No: 0000-0002-9206-3177 F. Tutku AKSOY ORCID No: 0000-0001-6402-0666 Zeynep GÜNGÖRDÜ DALAR ORCID No: 0000-0003-2177-4235 Merve Nur AKSAKAL ORCID No: 0000-0001-5624-0140 İpek ÇORUHLU ORCID No: 0000-0003-3925-0413 Sara ÇIBİK ORCID No: 0000-0003-0100-3409 Elif Sena ÖZCAN ORCID NO: 0000-0002-4410-7622 Öykü TOPTAŞ ORCID NO: 0000-0002-0342-535X Zümra KUL ORCID NO: 0000-0002-6317-5639</p> <p style="text-align: center;"><i>*Corresponding author; baydas@hotmail.com</i></p> <p style="text-align: center;"><small>(Received: 1.02.2024, Accepted: 11.03.2024, Online Publication: 26.03.2024)</small></p>	176

Genetic Diversity of *Cucumber mosaic virus* in Cucumber Plants Grown in Diyarbakır Province

Abdullah GÜLLER¹ , Serap DEMİREL^{2*} , Mustafa USTA³ , Gülüstan KORKMAZ³ 

¹ Bingöl University, Agriculture Faculty, Plant Protection Department, Bingöl, Türkiye

² Van Yüzüncü Yıl University, Science Faculty, Molecular Biology and Genetic Department, Van, Türkiye

³ Van Yüzüncü Yıl Üniversitesi, Agriculture Faculty, Plant Protection Department, Van, Türkiye

Abdullah GÜLLER ORCID No: 0000-0003-3887-4208

Serap DEMİREL ORCID No: 0000-0002-1877-0797

Mustafa USTA ORCID No: 0000-0002-3940-2774

Gülüstan KORKMAZ No: 0000-0002-9032-5823

*Serap DEMİREL: serap_comart@hotmail.com

(Received: 16.03.2023, Accepted: 19.12.2023, Online Publication: 26.03.2024)

Keywords

Coat protein,
RT-PCR,
Cloning

Abstract: The cucumber plant (*Cucumis sativus* L.) is an important cultivated plant produced worldwide. *Cucumber mosaic virus* (CMV), one of the common viral diseases, causes economic losses by reducing the yield and quality of the cucumber plant. In the observations performed in Diyarbakır in September 2021, cucumber plants showing virus-like symptoms such as mosaic, irregular yellowish spots, and deformity on the leaves were observed. Symptomatic and non-symptomatic samples were collected and subjected to a reverse transcription polymerase chain reaction (RT-PCR) using CMV-specific primers, and the produced DNA bands were visualized on an agarose gel. CMV infection was detected in seven of the 15 samples. Bacterial cloning and sequencing of a randomly selected specimen determined that the CMV partial coat protein gene was 593 bp long and was registered in the NCBI database with the accession number MW962979.1. According to the phylogenetic tree performed with different isolates of CMV, Diyarbakır CMV isolate clustered with CMV isolates from Australia, Israel, Spain, Hungary, Japan, and Korea forming Subgroup IA. The presence of CMV and group/subgroup diagnosis in cucumber plants grown in the Diyarbakır region were confirmed molecularly for the first time by this study.

1

Diyarbakır İlinde Yetiştirilen Hıyar Bitkilerinde Hıyar Mozayik Virüsü'nün Genetik Çeşitliliği

Anahtar Kelimeler

Kılıf proteini,
RT-PCR,
Klonlama

Öz: Hıyar bitkisi (*Cucumis sativus* L.) dünya çapında üretilen önemli bir kültür bitkisidir. Yaygın viral hastalıklarından biri olan Hıyar mozayik virüsü (*Cucumber mosaic virus*, CMV) hıyar bitkisinde verim ile birlikte kaliteyi düşürerek ekonomik kayıplara neden olmaktadır. Diyarbakır ilinde 2021 yılı Eylül ayında yapılan gözlemlerde, yapraklarda mozaik, düzensiz sarımsı lekeler ve deformite gibi virüs benzeri belirtiler gösteren hıyar bitkileri gözlenmiştir. Simptom gösteren ve göstermeyen örnekler toplanarak CMV spesifik primerler kullanılarak ters transkriptaz polimeraz zincir reaksiyonu (RT-PZR)'na tabi tutulmuş ve üretilen DNA bantları agaroz jelde görüntülenmiştir. CMV enfeksiyonu 15 örnekten yedisinde belirlenmiştir. Rastgele seçilen bir örneğin bakteriyel klonlanması ve dizilenmesi sonucunda, CMV kısmi kılıf proteini geninin 593 bp uzunluğunda olduğu belirlenmiş ve NCBI veri tabanına MW962979.1 erişim numarası ile kaydedilmiştir. CMV'nin farklı izolatlarıyla gerçekleştirilen filogenetik ağaca göre, Diyarbakır CMV izolatı Subgrup IA grubunu oluşturan Avustralya, İsrail, İspanya, Macaristan, Japonya ve Kore'ye ait CMV izolatları ile kümelendirilmiştir. Diyarbakır bölgesinde yetiştirilen hıyar bitkilerinde CMV'nin varlığı ve grup/subgrup teşhisi ilk defa bu çalışma ile doğrulanmıştır.

1. INTRODUCTION

Cucumber mosaic virus (CMV), responsible for significant agricultural losses in many cultivated plants worldwide, is probably one of the viruses with the largest host range among plant viruses. CMV firstly described in 1916 by Doolittle in Michigan and by Jagger in New York is a disease of cucurbits. CMV has a high degree of diversity and a large number of isolates due to differing biological and molecular properties [1, 2]. CMV, a type of member of the Cucumovirus genus, has a wide host range with 1241 species in 101 plant families consist of monocotyledon and dicotyledonous plants. In addition, the virus's host range includes a large number of wild species that are important for its year-round survival, as well as plants from all kinds of cultures such as food and feed products, ornamental plants [3].

CMV virions are icosahedral particles having a diameter of 29 nm and include 18% RNA and a single capsid protein (CP) with 180 subunits. CMV genome having single-stranded positive-sense RNA consists of three pieces named as RNA1, RNA2 and RNA3 in decreasing order of size. RNA1, which is monocistronic, encodes protein 1a. This fragment includes an admitted methyltransferase domain at its N-terminal portion and also a helicase domain at its C-terminal portion. RNA2 encodes the huge 2a protein containing the GDD motif typical responsible for an RNA-dependent RNA polymerase (RdRp), as well as the small 2b protein expressed from an open reading frame 2b (ORF2b). 2b protein is a suppressor of RNA silencing. RNA3 encodes the coat (CP) and the movement proteins (MP) has a bicistronic structure. The first ORF of each bicistronic RNA is expressed from genomic RNA, but the second ORFs are expressed from RNA4 and RNA4A [4]. CMV divided into two groups as group I and II according to their serological relationships and genetic diversity by Palukaitis et al. [5]. CMV causes typical mosaic symptoms on melon and cucumber leaves, stunting and reduced fruit yield. Symptoms on fruits are usually seen in the form of spots or mosaics. Adult plants of some cucumber cultivars may show rapid and complete wilting a few days after CMV infection. In pumpkin, the symptoms of CMV are very severe, including mosaic, yellow spots and leaf rot. Infected plants often deform fruit, drastically reducing fruit retention, or even stopping [7]. The existence of CMV has been reported in many countries in the world and has been detected in many regions and plants in Türkiye [8, 9, 10, 11, 12].

Recently, the research in the world shown that CMV subgroup I divided into two subgroups (Ia and Ib) with the analysis of non-protein coding regions at the 5' end and the CP gene [6]. Previous studies have shown the presence of CMV infections in various hosts in Turkey, as described by several researchers [29, 32, 36, 37, 38]. A few studies have shown that subgroup IA isolates are frequently observed in molecular investigations carried with CMV [34, 39, 40]. Moreover, Group II and subgroup IB have been seen in Turkey in recent years [33]. Although CMV infection has been reported in cucumber

growing regions in our country, the genetic diversity of these isolates remains unknown.

Turkey stands out as one of the leading nations worldwide in the production of vegetables from the *Cucurbitaceae* family, with Diyarbakır playing a significant role in this contribution [31]. Cucurbits are susceptible to a wide variety of viral infections, which may result in considerable productivity reductions in these crops [18]. The objective of this study is to identify CMV in the cucumber plant and to investigate its genetic diversity in the cucumber growing areas of Diyarbakır, which is located in the Eastern Anatolia region of Türkiye. It has also been investigated the phylogenetic relationships of Diyarbakır isolate using other worldwide CMV isolates from the gene bank for determine the genetic diversity.

2. MATERIAL AND METHOD

2.1. Virus Isolates and Total RNA Extraction

In 2021, fresh leaves were collected from 5 CMV-suspicious and 10 healthy-looking plants out of a total of 15 plants in the five fields where cucumbers were grown Çınar town of Diyarbakır. Total RNA isolation was performed by using method described by Foissac et al. [13]. The RNA samples obtained were stored at -80°C for testing.

2.2. cDNA Synthesis and PCR

The cDNA synthesis was performed by using RNAs obtained from the previous step. Gene-specific oligonucleotide designed for CP was used in cDNA synthesis. cDNA synthesis was carried out in two steps. In the first step, 12 µl of the reaction mixture (2 µl RNA, 1 µl dNTP, 8 µl RNase-free water and 1 µl reverse primer were incubated at 65°C for 5 minutes and then was kept on ice for 5 minutes. In the second step, a mixture of components of 1 µl RNase-free water, 4 µl 5X RT buffer, 1 µl reverse transcriptase and 2 µl 0.1 M DTT was incubated at 42°C for 45 minutes and then at 70°C for 15 minutes, respectively. cDNAs in a total volume of 20 µl were stored at -80°C until use. Specific forward and reverse primers were used to obtain the coat protein gene of CMV (Table 1). 25 µl RT-PCR reaction volume contains 3 µl cDNA, 15.6 µl nuclease-free water, 0.5 µl dNTP, 0.4 µl DreamTaq DNA polymerase (Thermo Scientific), 1.5 µl MgCl₂, 2.5 µl 10X Taq buffer, 0.5 µl forward and reverse primer. RT-PCR reactions were performed with the following conditions: initial denaturation 1 cycle at 94°C for 2 min, 36 cycles of 94°C for 30 s, 52°C for 30 s, and 72°C for 45 and final extension of 1 cycle at 72°C for 10 min. The standard marker (1 kb, Thermo Scientific) (5 µl) and obtained reaction products (15 µl) were run on an agarose gel (1.5%) including 1×TAE Buffer and EtBr (1%) for 45 minutes at 85 volts and visualized under UV light. In order to strengthen the accuracy of PCR tests, CMV [14] isolate obtained from previous studies was used as a positive control and asymptomatic cucumber samples were used as negative controls.

Table 1: Primer information that is used for the CMV CP gene

Primer name	Primer sequence	Position	Product size (bp)	Ref.
Forward primer	5'GCCACCAAAAATAGACCG3'	1484–1502		[35]
Reverse primer	5'ATTCGCTGGCGTGGATTCT3'	2057–2076	593	[35]

2.3. Sequencing analysis, BLAST and Phylogenetic construction

RT-PCR amplified DNA was purified with the Gene Jet " (Cat. No. K0691, Thermo) in accordance with the manufacturer's instructions. Purified products were cloned into the prokaryotic cloning vector (pGEM T-Easy, Promega) and transferred to *E. coli* by electro transformation method. Recombinant plasmids including CMV coat protein in bacteria were purified with Miniprep Kit (Thermo GeneJet Plasmid, Cat. No. K0503,) and DNA fragment of CMV coat protein sequenced by next generation sequencing (NGS) (Sentebiolab/Ankara/Türkiye) [41]. The resulting sequence has been registered in the NCBI database.

A phylogenetic tree was generated with the CMV coat protein sequence belong to Diyarbakir isolate, 25 different sequences from different hosts and countries (including CMV IA, CMV IB and CMV II group) on the NCBI website. Pairwise identity of CMV isolates used in the present study calculated with Sequence Demarcation Tool Version 1.2 (SDTv1.2). The phylogenetic dendrogram was created with the Neighbor-Joining method (NJM) using CLC Main Workbench 6.7.1 software with 100 replications. Tomato aspermia virus, accession number EF153735, was assigned as outgroup in order to promote better branching of the tree.

3. RESULTS

As a result of the field studies carried out in the province of Diyarbakir in the Eastern Anatolia region, symptoms caused by viruses and virus-like factors such as mosaic and blistering, yellowish spots and abnormal leaves were observed on the leaves from the cucumber production areas. The total of 15 cucumber leaves in this study were collected and RT-PCR tests applied to the collected samples yielded DNA bands of approximately 593 bp in 7 samples, confirming the presence of CMV (Figure 1). According to the PCR test results, the percentage of infection was calculated as 46.6.

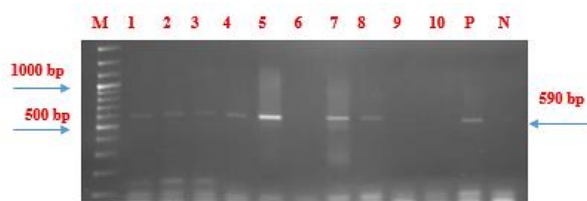


Figure 1. Agarose gel electrophoresis image of RT-PCR products obtained using CP specific primers for cucumber samples collected from Diyarbakir province. M: Marker, P: Positive control, N: Negative control

After the RT-PCR result, bacterial cloning of a CMV isolate from 7 samples that gave positive results among the plants tested in Diyarbakir province was performed and its nucleotide sequence was revealed. The resulting partial coat protein nucleotide sequence was named Diyarbakir D4 and registered in the gene bank with the accession number MW962979.1 as shown in figure 2.

BLAST analysis was performed to determine the nucleotide similarity ratio of the obtained sequence from the current study. According to the comparison based on other CMV isolates worldwide, the similarity rate of Diyarbakir D4-CMV isolate was found to be between 96.63% and 99.49% at the nucleotide level (Figure 3). Based on the sequence of 593 nucleotides, we also investigated the phylogenetic relationships of Diyarbakir D4-CMV isolate with other isolates and to which group it belongs. While constructing the tree, 25 different DNA sequences selected from Group I (A and B) and Group II from different gene sources were used (Table 2).

```
GCCACCAAAAATAGACCGTGGGTCTTATACGGTAAAAGTTGTACTACCTGATTGATCAGTACGGGA
ATATGATAAGAAAGCTGTTTCGCGCATTCAAATTCGAGTTAATCCITGCGCAAAITTGATCTACCG
TGTGGGTGACAGTCCGTAAGTTCCTGCCTCCTCGACTTATCCGTTGCCCATTTCTGCTATGTTT
GCGGACGGAGCCTCACCGTACTGGTTTTCAGTATGCCGTCATCTGGAATCCAAGCCAACAACAA
ACTGTTGATGATCTTTCGGCGATGCGCGCTGATATAGGTGACATGAGAAAGTACCGCGTCTCTGT
GATTCAAAAGACGATGCGCTGAGACGGACGAGCTAGTACTCATGTTGACATCGAGCCCAAC
GCATCCACGCTGGAGTCTCCAGTCTGATTCGGTGTTCAGAAATCCCTCCGATCTCTGT
GGCGGAGCTGAGTTGGCAGTCTGCTATAAAGTCTGAGTCACTAAACGTTTTTACGGTGA
CGGTTGTCATCCAGCTTACGGCTAAAATGGTCACTGCGGAGAAATCCACGCGCAGCAGAT
```

Figure 2. Partial coat protein nucleotide sequence (593 bp) obtained by cloning of CMV isolate (MW962979.1) obtained from Diyarbakir province

Table 2. Gene bank information relating to the genes used in the investigation of phylogenetic relationships of Diyarbakir D4 isolate

No	Country	Accession number	Plant source	Gene source	Virus types noted in NCBI
1	Australia	U22821	-	Complete	Group I and II
2	Israel	U66094	<i>Cucurbita pepo</i>	Complete	-
3	Spain	AM183119	Tomatoes	Complete	Group IB
4	Hungary	AJ517802	<i>Raphanus sativus</i>	Genomic RNA	-
5	Japan	D28487	<i>Lycopersicon esculentum</i>	Complete	Subgroup I
6	Korea	L36251	-	Complete	-
7	Korea	AF013291	-	Complete	-
8	India	AF281864	<i>Datura innoxia</i>	Complete	-
9	Thailand	AJ810259	Chili pepper	CP	-
10	China	KJ746022	<i>Nicotiana tabacum</i>	CP	-
11	Türkiye	KY474380	Kidney bean	CP	-
12	Türkiye	MW962980	<i>Cucumis melo</i>	CP	-
13	Türkiye	MT361015	<i>Cucumis melo</i>	CP	-
14	Türkiye	MT361015	<i>Cucumis melo</i>	CP	-
15	Japan	AB042294	-	Complete	-
16	USA	U31220	Musa	Complete	-
17	China	AF268598	Banana	Complete	-
18	-	M21464	-	Complete	-
19	India	AJ585086	Lilium	Genomic RNA	-
20	USA	AF127976	-	Complete	-

21	India	HE583224	<i>Nicotiana glutinosa</i>	Genomic RNA	-
22	-	L15336	-	Complete	-
23	Japan	AB006813	-	Complete	-
24	Netherlands	AJ304397	<i>Alstroemeria</i>	CP	-

CP: Coat protein

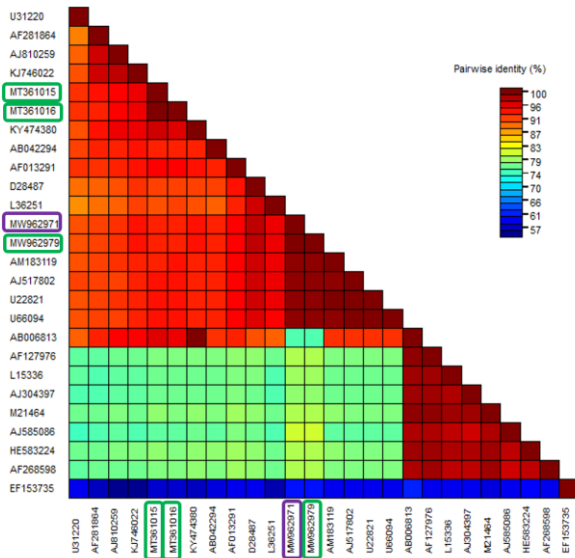


Figure 3. Similarity matrix created by using nucleotide sequences of CP genes of Diyarbakır D4 isolate and world CMV isolates

Based on sequence similarity ratios, the results are consistent with the phylogenetic tree constructed with the same sequences. According to the phylogenetic tree formed by the neighbor-joining method, 3 groups were formed, namely Group I (A and B) and Group II. According to the phylogeny, it was determined that the CMV D4 isolate clustered with the isolates of Subgroup IA (Figure 4).

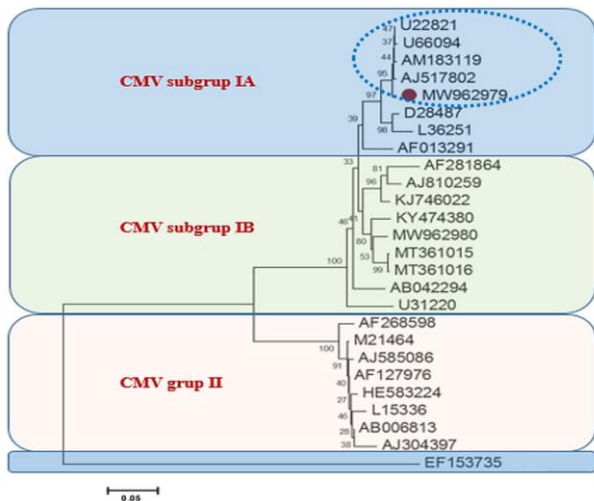


Figure 4. Phylogenetic dendrogram of CP gene sequences of CMV isolates. Diyarbakır D4-CMV isolate is shown in red (MW962979)

CMV isolates from Australia, Israel, Spain, Hungary, Japan and Korea were also included in the cluster (Subgroup IA) in which Diyarbakır isolate accession number MW962979 is located. In addition, as result of the isolate obtained from the cucumber showed a closer phylogenetic relationship with the CMV isolates isolated

from Australia, Israel, Spain and Hungary. Different clustering of Japanese and Korean isolates with other isolates in subgroup IA by tree supports this information. On the other hand, although they share almost the same geography, the Diyarbakır cucumber isolate and the melon plant isolates with accession numbers MW962980, MT361015 and MT361015, also reported from Türkiye, were in different groups. On the other hand, although they share almost the same geography, the Diyarbakır cucumber isolate and the melon plant isolates (MW962980, MT361015 and MT361015) reported from Türkiye, clustered in different groups. Also, it can be concluded that plant species as based on Table 2 is not important in phylogenetically separating CMV groups.

4. DISCUSSION AND CONCLUSION

Cucurbits are an important host of many viral pathogens. The viruses can cause %50 to 100% damage depending on the plant species, vector density, virus strain and environmental conditions. Mixed infection of these viruses with other viruses has the potential to cause epidemics in vegetable growing areas around the world [15, 16]. CMV is prevalent in mostly all continents, including Europe, Asia, North America, Africa, and Australia [17]. CMV is also widespread in agriculture in Türkiye and constitutes a wide viral study area. The presence of CMV has been reported in many cultivated and wild plants such as tobacco, beans, spinach, peppers, tomatoes, cucumbers olives and *Polygala myrtifolia* [18, 19, 20, 21, 22, 23, 24]. Virus and virus-like symptom symptoms, including mosaic and blistering, yellowish spots, and abnormal leaves, were noted on cucumber leaves harvested from in this study. These symptoms are in agreement with those reported in other studies in the literature [25, 26].

CMV has been reported nationally in different geographies and in different hosts in Türkiye. The 113 tomato leaves in total with virus and virus-like symptoms from production areas in the Marmara region were tested with the DAS-ELISA test (Double-antibody sandwich enzyme linked immuno sorbent assay) by Karanfil [27]. The infection rate was founded 30.08% in the samples collected. In a similar study conducted in the same region (Çanakkale, Bursa and Bilecik), the presence of CMV with the DAS-ELISA test was determined in 67 of 77 samples belong to different plant species and the infection rate was reported as 87% [22]. A research conducted in the Western Mediterranean area revealed that 53 out of 138 tomato samples, accounting for 38.40% of the total, were found to be infected with CMV [28].

In the surveys carried out in Bingöl province in 2019, melon leaf samples with mosaic patterns in different shades of green and vein bands and leaf deformations were collected and analyzed with PCR to detect the presence of CMV and Watermelon mosaic virus (WMV). As a result of RT-PCR performed using primer sets specific to the coat protein (CP) gene, it was determined that the partial coat protein gene length contained 657 bp [29]. Furthermore, two separate research have shown the existence of CMV isolate in the region of Diyarbakır. [30,

31]. In the study carried out by Öztürk [30] in the fields of watermelon cultivation, leaf curling, chlorotic mottling, mosaic formations, thinning and fruit deformations were detected in plants and tested with DAS-ELISA tests against various cucurbit viral agents. In the study, 53 of 60 leaf samples infected with one or more viruses. While Zucchini yellow mosaic virus (ZYMV) had the most infection, the lowest infection rate was found in CMV. In the other study carried out in Diyarbakır, a total of 547 samples, including 34 cucumbers, 176 zucchini, 142 watermelons and 195 melons, were collected and tested by applying the DAS-ELISA method against 7 cucurbit viruses. As a result of the analysis, CMV pathogen was reported with an infection rate of 18.28% in 100 of 547 samples [31]. The result of previous studies regarding molecular characterization of CMV illustrated that CMV isolates of Türkiye are generally 80-100% similar to the world isolates [32, 33]. In this regard, the results provided from this study are consistent with those from previous studies.

Geographical conditions have been suggested as a potential influence on phylogenetic groupings. However, it has been shown that the geographical origins of CMV do not have a significant impact on its phylogenetic grouping. It has been suggested that isolates from the immediate region are distributed in different phylogenetic groups [34]. In spite of the fact that a great number of research on CMV have been conducted in our country, the fact that the majority of these studies were conducted using the ELISA test results in uncertainty about the differentiated groups and subgroups of CMV isolates. The subgroup IA CMV isolates are present in different plants in Türkiye [27, 33]. Moreover, the availability of subgroup IB and II isolates has been stated in different studies.

In the present study, the phylogenetic relationships of CMV and its infection in cucumber plants obtained from Diyarbakır province were revealed. Moreover, this study is the first report in Diyarbakır province where this isolate is included in Subgroup IA. In addition, the registration of the CP partial gene sequence of the cucumber CMV isolate to GenBank for the first time is among the original outputs of the study. Although the infection rate was calculated as 46.6 according to the collected samples, it is recommended to test the samples with the PCR test, which is more sensitive than the DAS-ELISA test by using more samples for the current rate. In addition to the partial coat protein, the complete gene of coat protein of belong to CMV Diyarbakır D4 isolate should be amplified and molecular characterization should be made.

REFERENCES

- [1] Doolittle SP. A new infectious mosaic disease of cucumber. *Phytopathology*. 1916; 6(2):145-147.
- [2] Adams IP, Glover RH, Monger WA, Mumford R, Jackeviciene E, Navalinskiene M, Samuitiene M, Boonham N. Next-generation sequencing and metagenomic analysis: A universal diagnostic tool in plant virology. *Molecular Plant Pathology*. 2009; 10(4):537-545.
- [3] Edwardson JR, Christie RG. Cucumoviruses. In: Edwardson JR, Christie RG, editors. *CRC handbook of viruses infecting Legumes*. CRC Press: Boca Raton; 1991. p. 293-319.
- [4] Jacquemond M. *Cucumber mosaic virus*. *Advances in Virus Research*. 2012; 84:439-504.
- [5] Palukaitis P, Roossinck MJ, Dietzgen RG, Francki RI. *Cucumber mosaic virus*. *Advances in Virus Research*. 1992; 41:281-348.
- [6] Roossinck MJ, Zhang L, Hellwald KH. Rearrangements in the 5' nontranslated region and phylogenetic analyses of *Cucumber mosaic virus* RNA 3 indicate radial evolution of three subgroups. *Journal of Virology*. 1999; 73(8):6752-6758.
- [7] Lecoq, H., and Desbiez, C. Virus of cucurbit crops in the Mediterranean Region: an ever-changing picture. In: Loebenstein G, Lecoq H, editors. *Viruses and Virus Diseases of Vegetables in the Mediterranean Basin*. *Virus Research*; 2012. p. 67-126.
- [8] Mijatovic M, Zdravkovic J, Markovic Z, Obradovic A. Disease intensity of some tomato viruses in Serbia. *Acta Physiologiae Plantarum*. 2000; 22(3):332-335.
- [9] Arlı-Sökmen M, Mennan H, Şevik MA, Ecevit O. Occurrence of Viruses in Field grown Pepper Crops and Some of Their Reservoir Weed Hosts in Samsun, Turkey. *Phytoparasitica*. 2005; 33:347-358.
- [10] Çağlar BK. Characterization of melon (CMV-K), tomato (CMV-D), pepper (CMV-B) isolates of *Cucumber mosaic virus* (CMV) by biological, serological, molecular methods and effect of satellite-RNAs on virus. Adana: Çukurova University, 2006.
- [11] Berniak H, Kaminska M, Malinowski T. *Cucumber mosaic virus* groups IA and II are represented among isolates from naturally infected lilies. *European Journal of Plant Pathology*. 2010; 127:305-309.
- [12] Temfack D, Dély C, Chofong G, Mbuli A, Gentil I, Ouboum F, et al. Detection of *Cucumber mosaic virus* on *Solanum lycopersicum* L. and *Capsicum annum* L. in Western region of Cameroon. *Journal of Agriculture and Food Research*. 2022; 8:100294.
- [13] Foissac X, Svanella-Dumas L, Dulucq MJ, Candresse T, Gentil P. Polyvalent detection of fruit tree tricho, capillo and foveaviruses by nested RT-PCR using degenerated and inosine containing primers (PDO RT-PCR). *Acta Hort*. 2001; 550:37-43.
- [14] Günay A. The investigation of some tobacco viruses in tobacco fields of Adıyaman by multiplex RT-PCR method and the molecular characterization of some virus isolates. Van: Van Yüzüncü Yıl University; 2019.
- [15] Raccab B. Detection of virus diseases by advanced techniques and control. *Epidemiology and control of cucurbit viruses in Israel*. 1. Israeli-Turkish Workshop. Turkey: Adana; 1999. p. 45-46.
- [16] Kaya A, Erkan S. Detection and incidence of viruses in cucurbits grown in Izmir, Aydın, Manisa and Balıkesir provinces. *Plant Protection Bulletin*. 2011; 51(4):387-405.

- [17] Palukaitis P, Garcia-Arenal F. *Cucumber mosaic virus* [Internet], Description of Plant Viruses, 2003: No; 400 [cited 2023 February 20]. Available from: <https://www.dpvweb.net/dpv/showdpv/?dpvno=400>
- [18] Gümüş M, Erkan S, Tok S. Studies on determination of virus diseases in the seeds of some Cucurbitaceous species. *Ege Üniversitesi Ziraat Fakültesi Dergisi*. 2004; 41(1):49-56.
- [19] Çulal Kılıç H, Yardımcı N. *Cucumber mosaic virus* in Bean Growing Areas of Çine Plain, Burdur, Turkey. *Mehmet Akif Ersoy Üniversitesi Fen Bilimleri Enstitüsü Dergisi*. 2012; 3(2):12-15.
- [20] Ergün M, Semih E, Paylan İC. *Cucumber mosaic virus* in globe artichoke in Turkey. *Canadian Journal of Plant Pathology*. 2013; 35(4):514-517.
- [21] Erkan S, Gümüş M, Paylan İC, Duman İ, Ergün M. The determination of viral agents in certain cold-season vegetables in İzmir province and its around. *Ege Üniversitesi Ziraat Fakültesi Dergisi*. 2013; 50(3):311-322.
- [22] Uzunoğulları N, Gümüş M. Detection of *Cucumber mosaic virus* (CMV) causing natural infection on some cultured plants in Marmara Region. *Trakya University Journal of Natural Sciences*. 2015; 16(1):9-15.
- [23] Gökdağ S, Karanfil A, Korkmaz S. Çanakkale ili ıspanak alanlarındaki Şalgam mozaik virüsü ve Hıyar mozaik virüsü varlığının belirlenmesi. *Bahçe*. 2016; özel sayı (cilt II):166-170.
- [24] Güngör M, Uzunbacak H, Kutluk-Yılmaz ND, Şevik MA. Determination of viruses causing infection in spinach fields in Samsun province. *Anadolu Journal of Agricultural Sciences*. 2017; 32(2):164-168.
- [25] Katul L, Makkouk KM. Occurrence and serological relatedness of five cucurbit potyviruses in Lebanon and Syria. *Phytopathologia Mediterranea*. 1987; 26(1):36-42.
- [26] Tobias I, Szabo B, Salanki K, Sari L, Kuhlmann H, Palkovics L. Seed borne transmission of Zucchini yellow mosaic virus and *Cucumber mosaic virus* in Styrian Hulless group of Cucurbita pepo. *Proceedings of the IX EUCARPA Meeting of Genetics and Plant Breeding of Cucurbitaceae*. France: Avignon; 2008. p. 189-197.
- [27] Karanfil A. Prevalence and molecular characterization of *Cucumber mosaic virus* isolates infecting tomato plants in Marmara region of Turkey. *Plant Protection Bulletin*. 2021; 61(4):19-25.
- [28] Yardımcı N, Eryigit H. Identification of *Cucumber mosaic virus* in tomato (*Lycopersicon esculentum*) growing areas in the north-west Mediterranean region of Turkey. *New Zealand Journal of Crop and Horticultural Science*. 2006; 34(2):173-175.
- [29] Güller A, Usta M. Occurrence of Cucumber mosaic cucumovirus and Watermelon mosaic potyvirus on Melon exhibiting viral symptoms in Bingöl province of Turkey and their phylogenetic affinities. *Türk Tarım ve Doğa Bilimleri Dergisi*. 2020;7(4):948-958.
- [30] Öztürk S. Survey on the virus diseases of watermelon in Diyarbakır and districts. Adana: Çukurova University; 2000.
- [31] Budak E. Determination and incidence of viruses in cucurbits grown in Diyarbakır and its districts. Şanlıurfa: Harran University; 2015.
- [32] Güneş N, Gümüş M. Detection and characterization of tomato spotted wilt virus and *Cucumber mosaic virus* on pepper growing areas in Antalya. *Journal of Agricultural Sciences*. 2019;25(3):259-271.
- [33] Karanfil A, Korkmaz S. Detection and molecular characterization based on coat protein gene of *Cucumber mosaic virus* (CMV) from cowpea production fields of Çanakkale province in Turkey. *Plant Protection Bulletin*. 2017; 57(3):293-304.
- [34] Ohshima K, Matsumoto K, Yasaka R, Nishiyama M, Soejima K, Korkmaz S, et al. Temporal analysis of reassortment and molecular evolution of *Cucumber mosaic virus*: Extra clues from its segmented genome. *Virology*. 2016; 487:188-197.
- [35] Chen S, Gu H, Wang X, Chen J, Zhu W. Multiplex RT-PCR detection of *Cucumber mosaic virus* subgroups and Tobamoviruses infecting Tomato using 18S rRNA as an internal control. *Acta Biochim Biophys Sin*. 2011; 43(6), 465-471.
- [36] Balsak SC, Kardeş H, Buzkan N. First report of *Cucumber mosaic virus* in cyclamen (*Cyclamen* spp.) in Turkey. *Journal of Plant Pathology*, 2021; 103 (1), 361-362.
- [37] Kurtoğlu A, Korkmaz S. Determination and molecular characterization of *Cucumber mosaic virus* (CMV) infection on spinach production fields of Çanakkale province, Turkey. *The Journal of Turkish Phytopathology*, 2018; 47 (2), 43-51.
- [38] Özdemir S, Erilmez S. First report of Alfalfa mosaic virus and *Cucumber mosaic virus* in pepino in Turkey. *Journal of Plant Pathology*, 2012; 94 (4), 91.
- [39] Çağlar BK. Characterization of melon (CMV-K), tomato (CMV-D), pepper (CMV-B) isolates of *Cucumber mosaic virus* (CMV) by biological, serological, molecular methods and effect of satellite-RNAs on virus. Çukurova University, PhD Thesis, 2006; 89 p., Adana.
- [40] Ergün M, Erkan S, Paylan İC. *Cucumber mosaic virus* in globe artichoke in Turkey. *Canadian Journal of Plant Pathology*, 2013; 35 (4), 514-517.
- [41] Korkmaz G, Mustafa U, Demirel S. Potato virus S (PVS)-Bitlis izolatinın kılıf proteininin in silico karakterizasyonu ve konak proteini ile Docking analizi. *Journal of Agriculture*, 2022; 5(1), 57-67.

***Celtis australis* Exhibits Cytotoxic Effects by Inducing DNA Damage in Human Ovarian Cancer Cells**

Gülsüm Nur FİDAN¹ , Sevilay GÜNAY² , Yavuz ERDEN^{1*} 

¹ Bartın University, Science Faculty, Molecular Biology and Genetics Department, Bartın, Türkiye

² Gazi University, Medicine Faculty, Biophysics Department, Ankara, Türkiye

Gülsüm Nur FİDAN ORCID No: 0009-0001-4474-0962

Sevilay GÜNAY ORCID No: 0000-0002-0130-5629

Yavuz ERDEN ORCID No: 0000-0002-2807-6096

*Corresponding author: yerden@bartin.edu.tr

(Received: 23.08.2023, Accepted: 25.12.2023, Online Publication: 26.03.2024)

Keywords

Ovarian cancer,
Celtis australis,
Cytotoxicity,
DNA damage

Abstract: Native to the Mediterranean and southwest Asia, *Celtis australis* is used in folk medicine to treatment of many diseases such as peptic ulcer, diarrhea, dysentery, pain, and colic. However, there are very few studies on the effects of this species on cancer. We report for the first time the cytotoxic and genotoxic properties of *C. australis* on the human ovarian cancer cell line A2780. In the study, *C. australis* extract prepared in ethanol/phosphate buffer was applied to A2780 cells. The change in viability level in A2780 cells after treatment was determined by MTT assay and DNA damage was determined by single-cell gel electrophoresis (Comet) analysis. Our results showed that plant extract application at doses above 200 µg/mL significantly decreased A2780 cell viability ($p<0.05$). The IC₅₀ value for A2780 cells of *C. australis* was determined as 251.43 µg/mL. Comet analysis results revealed that 50 µg/mL and above dose applications increased the level of DNA damage ($p<0.05$). These results suggest that *C. australis* mediates cell death by inducing DNA damage in A2780 cancer cells.

7

***Celtis australis* İnsan Over Kanseri Hücrelerinde DNA Hasarını İndükleyerek Sitotoksik Etki Sergiler**

Anahtar Kelimeler

Over kanseri,
Celtis australis,
Sitotoksosite,
DNA hasarı

Öz: Akdeniz ve güneybatı Asya'ya özgü olan *Celtis australis*, halk tıbbında yaprak ve meyveleri peptik ülser, ishal, dizanteride, ağrı ve kolik gibi birçok hastalığın tedavisinde kullanılmaktadır. Buna karşın bu türün kanser üzerine etkilerini konu edinen oldukça az sayıda çalışma vardır. Bu çalışmada *C. australis*'in insan over kanseri hücre serisi A2780 üzerine sitotoksik ve genotoksik özelliklerini ilk defa rapor ediyoruz. Çalışmada *C. australis*'in etanol/fosfat tamponu içerisinde hazırlanan özütü A2780 hücrelerine uygulandı. Uygulama sonrası A2780 hücrelerinde canlılık düzeyi değişimi MTT analiziyle, DNA hasarı ise tek hücre jel elektroforezi (Comet) analiziyle belirlendi. Sonuçlarımız 200 µg/mL üzeri dozlarda bitki özütü uygulamasının A2780 hücre canlılığını anlamlı düzeyde azalttığını gösterdi ($p<0.05$). *C. australis*'in A2780 hücreleri için IC₅₀ değeri 251,43 µg/mL olarak belirlendi. Comet analiz sonuçları 50 µg/mL ve üzeri doz uygulamalarının DNA hasar düzeyini arttırdığını ortaya koydu ($p<0.05$). Bu sonuçlar *C. australis*'in A2780 kanser hücrelerinde DNA hasarını indükleyerek hücre ölümüne aracılık ettiğini göstermektedir.

1. INTRODUCTION

Cancer is an important public health problem that negatively affects human health and quality of life and is increasing day by day. It is characterized by abnormal growth of cells in any tissue of the body as a result of genetic alteration and spread to different regions [1].

Ovarian cancer is the eighth leading cause of cancer-related death in women worldwide. It is the fifth most common cause of cancer-related death in women in Australia, North America and Western Europe [2]. In Turkey, ovarian cancer is women's the 7th most common cancer type [3]. According to World Health Organization data, 295,414 people were diagnosed with

ovarian cancer in 2018 and 184,799 people died from ovarian cancer that year [4].

Medicinal plants, which have been used for therapeutic purposes from the past to the present, have been instrumental in the discovery and development of many drugs in modern pharmacy [5, 6]. *Celtis australis*, also known as the hedgehog in our country, grows wild in temperate Mediterranean regions (e.g. southern Europe, northern Africa) and Southeast Asia. It has been reported that *C. australis* is an important source of fiber, protein, vitamins and also important bioactive compounds such as lutein, β -carotene, zeaxanthin and tocopherols in fruit samples [7]. It also contains rare flavonoids (such as flavone O-glycosides and flavone C-glycosides) and important metabolites such as tannins and saponins [8, 9]. Due to these, it is reported to exhibit strong antimicrobial and antioxidant effects [7]. Moreover, considering the cytotoxic effects of these compounds, it can be assumed that the extract prepared from the fruits and leaves of *C. australis* may have cytotoxic potential.

A few number of studies report the cytotoxic effect of *Celtis* species against cancer cells. It has been reported that a new flavonoid C-Glycoside isolated from *C. australis* and *C. occidentalis* leaves exhibits strong antioxidant effects and cytotoxic effects on different cancer cell lines [10]. Acquaviva *et al.* have shown that the extract obtained from *C. aetnensis* caused cell damage and inhibited viability by interfering with the oxidant/antioxidant cell balance in Caco-2 human colon carcinoma cells [11]. In addition, local people in South Africa use the sun-dried bark and roots of *C. africana* in the treatment of cancer [12, 13]. However, most other studies have focused on content analysis of these genres. This study aimed to elucidate the *in vitro* effects of *C. australis* on ovarian cancer, an important malignancy in women. In this context, the cytotoxic activity and genotoxic effect of *C. australis* extract against A2780 cell lines were evaluated.

2. MATERIAL AND METHOD

2.1. Preparation of Plant Extract

Ripe fruits of *C. australis* were extracted in 80% ethanol/phosphate buffer at a ratio of 1:10 (g/mL). The solvent of the extract was evaporated in a rotary evaporator (Buchi R100, Switzerland) and the total volume was made up to 10 mL with phosphate buffer. The stock solution was sterilized by filtration through a 0.22 μ m filter and stored at 4°C for the duration of the experiment.

2.2. Cell Culture Studies

Human ovarian cancer cell line A2780 was used in the study. Cells were cultured in RPMI-1640 medium (10% FBS, 1% penicillin-streptomycin solution, 1% non-essential amino acid solution). Cell flasks were maintained at 37°C (Thermo Forma II CO₂ Incubator, USA) with 5% CO₂ throughout the experimental process. Confluent cells were removed with

trypsin/EDTA solution and cell counting was performed. 96-well plates were used for cytotoxic assays. Approximately 15,000 cells were seeded in each well. The next day, the medium in the well was aspirated and a new medium was added. The treatment groups were treated with different doses (50-600 μ g/mL) of the prepared plant extract for 24 hours. At the end of the period, cell viability levels in the groups were determined by MTT assays [14]. The absorbance values obtained from the wells were ratioed to the control absorbance value and percent viability values were calculated.

2.3. Genotoxicity Analysis

In the study, DNA damage effects of plant extract were determined by single-cell gel electrophoresis (Comet) analysis [15]. For analysis, cells were seeded in 6-well plates. Cells were treated with 50, 100, and 200 μ g/mL doses of the plant extract for 24 hours. The collected cell samples were then washed with phosphate buffer and resuspended. Approximately 10,000 cells were mixed with low-melting agarose and this mixture was dropped onto agarose-coated slides and coverslips were closed. The preparations were kept at 4°C for 10-15 minutes and the coverslips were separated. The slides were then kept in lysis solution for 1 hour and placed in a horizontal gel electrophoresis tank. Samples were run at 25 volts (maximum 300 mA) for 25 minutes. After electrophoresis, the slides were washed 3 times for 5 minutes with a neutralization buffer. Finally, ethidium bromide solution was added to the slides and DNA damage images were recorded under a Zeiss Axio Scope.A1 fluorescence microscope. Analyses were performed using Tritex Comet Score software. This program analyzes images using the background of the image taken as a reference and uses pixel changes/intensity to determine the level of DNA damage. Tail length (tail length; TL), tail moment (tail moment; TM), tail intensity (tail intensity; TI), and %DNA tail ratio (%DNA tail) parameters were determined for at least 100 random cells from each group.

2.4. Statistical Analysis

Sigma Plot 12 package program was used in the analysis. The normal distribution of the analyzed variables was examined by the Shapiro-Wilk test before comparisons were made between groups. Kruskal Wallis H test was used to determine the differences between groups and Dunn's test was used for multiple comparisons. Statistically, $p < 0.05$ was considered statistically significant. After MTT assays, the IC₅₀ of the plant extract for A2780 cells was calculated using AAT Bioquest IC₅₀ Calculator [16].

3. RESULTS

3.1. Cell Viability Level

The viability change in the A2780 cell line treated with different concentrations of *C. australis* plant extract is

shown in Figure 1. 24 hours after treatment, *C. australis* 400 and 600 $\mu\text{g/mL}$ doses significantly reduced cell viability compared to the control group ($p < 0.05$). Furthermore, the IC₅₀ value on *C. australis* A2780 cells was determined as 251.43 $\mu\text{g/mL}$.

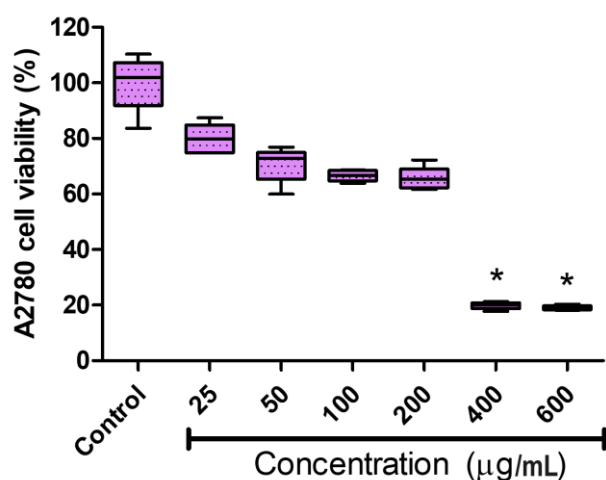


Figure 1. Viability change (%) in A2780 cell line 24 hours after plant extract treatment. Box plots are expressed as median (min.–max.). * $p < 0.05$ compared to control.

3.2. Impact on DNA Damage

After MTT analysis, doses with at least 70% viability were applied to the cells for Comet analysis. The results of Comet analysis after the treatments are summarized in the Table 1. Accordingly, %DNA tail and TI parameters determined after the treatments were higher in the treatment groups compared to the control group ($p < 0.05$). On the other hand, no difference was observed between the groups in the other two parameters (TL and TM). These results indicate that the plant extract causes DNA damage and decreases cell viability. Microscope images of the study are presented in Figure 2.

Table 1. Comet analysis results

	%DNA tail	TL	TI	TM
Control	4.03 (2.83 - 5.03)	1.00 (0.00 - 2.00)	30405.00 (21320.00 - 37024.00)	0.01 (0.00 - 0.06)
50 $\mu\text{g/mL}$	4.61 (3.12 - 9.01)*	0.00 (0.00 - 3.00)	34439.00 (22192.50 - 84088.00)*	0.00 (0.00 - 0.13)
100 $\mu\text{g/mL}$	10.89 (3.84 - 43.72)*	0.00 (0.00 - 8.75)	99552.50 (25614.25 - 510185.75)*	0.00 (0.00 - 1.33)
200 $\mu\text{g/mL}$	11.11 (3.58 - 88.37)*	1.00 (0.00 - 48.50)	75139.00 (30188.50 - 705810.00)*	0.02 (0.00 - 31.43)

Values expressed as median (25% - 75%). * $p < 0.05$ compared to the control group.

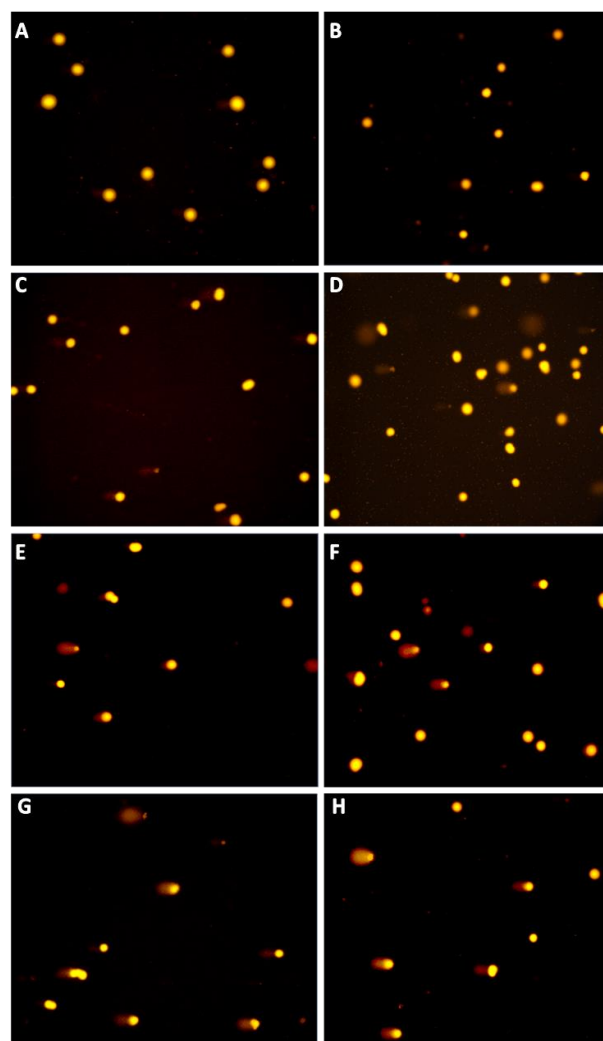


Figure 2. DNA damage image after plant extract application to A2780 cell line. (A,B: control group, C,D: 50 $\mu\text{g/mL}$, E,F: 100 $\mu\text{g/mL}$ and G,H: 200 $\mu\text{g/mL}$ plant extract treated groups. X100).

4. DISCUSSION AND CONCLUSION

Recent developments have led to the realization that free radical-induced lipid peroxidation and DNA damage are associated with major health problems such as cancer and aging. Plant-derived antioxidants are reported to be effective in protecting against these processes [17-19]. *C. australis* has various uses in folk medicine. Studies have shown that this species is a rich source of phytochemicals such as phenolic compounds, flavonoids and minerals [20, 21]. Most of the studies on *C. australis* have focused on revealing the phytochemical composition of the plant and determining its antioxidant activity. In this study, we present the first findings showing the cytotoxic and genotoxic effects of *C. australis* species on ovarian cancer A2780 cells.

Few studies have focused on the effects of *C. australis* on cancer cells. El-Alfy *et al.* evaluated the cytotoxic effects of ethanol and aqueous extracts of *C. australis* and *C. occidentalis* plants on human hepatocellular carcinoma (HEP-G2), leukemia carcinoma (CCRF-CEM), colon adenocarcinoma (COLO 205), ovarian adenocarcinoma (NIH: OVCAR-3) and gastric carcinoma (NCI-N87) cell lines. The results showed that COLO 205, HEP-G2 and NCI-N87 cell lines were the

cancer types most affected by the viability change after treatments. ED50 values for *C. australis* ovarian adenocarcinoma cells were reported as 77.65 ± 0.52 $\mu\text{g/mL}$ (ethanolic extract) and 72.77 ± 0.48 $\mu\text{g/mL}$ (aqueous extract) [10]. Some studies on other *Celtis* species support the cytotoxic activity of *C. australis*. Acquaviva *et al.* reported that *C. aetnensis* extract applied at doses of 5 $\mu\text{g/mL}$ and above-induced apoptosis in Caco-2 cells and decreased cell viability. In addition, while an increase in reactive oxygen level was observed in cell lines after plant extract application, a decrease in HO-1 protein expression, which mediates cell survival, was detected [22]. In another study, the cytotoxic effect of two new triterpene ester isolates from *C. philippinensis* on Lu1 (human lung cancer), Col2 (human colon cancer), KB (human oral epidermoid carcinoma) and LNCaP (hormone-dependent human prostate cancer) was investigated. The results of the study revealed that these compounds exhibited significant cytotoxic effects in cell lines with ED50 values generally in the range of 5-15 $\mu\text{g/mL}$ [23].

This study provides evidence that *C. australis* extract, which is considered a valuable medicinal plant species, exhibits strong cytotoxic and genotoxic effects against ovarian cancer cell line. Our results showed that *C. australis* extract significantly decreased cell viability in A2780 cells at doses above 200 $\mu\text{g/mL}$ and caused DNA damage from 50 $\mu\text{g/mL}$. These results show that *C. australis* extract causes cell death by inducing DNA damage in A2780 cells. Our study supports the growing data in this field showing the anti-cancer effect of *Celtis* species. We can say that this species, which is widely used in traditional medicine practices, reveals these effects through the secondary metabolites it contains. In light of the study's findings, further investigation into the use of this plant is necessary as a supplementary natural product for cancer treatment and prevention in both *in vitro* molecular study and *in vivo* animal models.

Acknowledgement

This study was supported by The Scientific and Technological Research Council of Türkiye (TÜBİTAK) 2209-A University Students Research Projects Support Program (Project No: 1919B012111685).

REFERENCES

- [1] Jiramongkol Y, Lam EW. FOXO transcription factor family in cancer and metastasis. *Cancer Metastasis Rev.* 2020;39(3):681-709.
- [2] Wild C, Weiderpass E, Stewart B. World cancer report. International agency for research on cancer: WHO; 2020.
- [3] Kara F, Keskinlik B. Türkiye kanser istatistikleri 2017 Ankara: T.C. Sağlık Bakanlığı Halk Sağlığı Genel Müdürlüğü; 2021 [updated 17.11.2021. Available from: https://hsgm.saglik.gov.tr/depo/birimler/kanser-db/istatistik/Turkiye_Kanser_Istatistikleri_2017.pdf
- [4] Bray F, Ferlay J, Soerjomataram I, Siegel RL, Torre LA, Jemal A. Global cancer statistics 2018: GLOBOCAN estimates of incidence and mortality worldwide for 36 cancers in 185 countries. *CA Cancer J Clin.* 2018;68(6):394-424.
- [5] Romero-Sandoval EA, Fincham JE, Kolano AL, Sharpe BN, Alvarado-Vazquez PA. Cannabis for chronic pain: Challenges and considerations. *Pharmacotherapy.* 2018;38(6):651-62.
- [6] Shaito A, Thuan DTB, Phu HT, Nguyen THD, Hasan H, Halabi S, Abdelhady S, Nasrallah GK, Eid AH, Pintus G. Herbal medicine for cardiovascular diseases: Efficacy, mechanisms, and safety. *Front Pharmacol.* 2020;11:422.
- [7] Ota A, Visnjevec AM, Vidrih R, Prgomet Z, Necemer M, Hribar J, Cimerman NG, Mozina SS, Bucar-Miklavcic M, Ulrih NP. Nutritional, antioxidative, and antimicrobial analysis of the Mediterranean hackberry (*Celtis australis* L.). *Food Sci Nutr.* 2017;5(1):160-70.
- [8] Spitaler R, Gurschler S, Ellmerer E, Schubert B, Sgarbossa M, Zidorn C. Flavonoids from *Celtis australis* (Cannabaceae). *Biochem Syst Ecol.* 2009;37(2):120-1.
- [9] Zehrmann N, Zidorn C, Ganzera M. Analysis of rare flavonoid C-glycosides in *Celtis australis* L. by micellar electrokinetic chromatography. *J Pharm Biomed Anal.* 2010;51(5):1165-8.
- [10] El-Alfy TS, El-Gohary HM, Sokkar NM, Hosny M, Al-Mahdy DA. A new flavonoid C-glycoside from *Celtis australis* L. and *Celtis occidentalis* L. leaves and potential antioxidant and cytotoxic activities. *Sci Pharm.* 2011;79(4):963-75.
- [11] Acquaviva R, Sorrenti V, Santangelo R, Cardile V, Tomasello B, Malfa G, Vanella L, Amodeo A, Genovese C, Mastrojeni S, Pugliese M, Ragusa M, Di Giacomo C. Effects of an extract of *Celtis aetnensis* (Tornab.) Strobl twigs on human colon cancer cell cultures. *Oncol Rep.* 2016;36(4):2298-304.
- [12] Krief S, Hladik CM, Haxaire C. Ethnomedicinal and bioactive properties of plants ingested by wild chimpanzees in Uganda. *J Ethnopharmacol.* 2005;101(1-3):1-15.
- [13] Koduru S, Grierson DS, Afolayan AJ. Ethnobotanical information of medicinal plants used for treatment of cancer in the Eastern Cape Province, South Africa. *Curr Sci.* 2007;92(7):906-8.
- [14] Mosmann T. Rapid colorimetric assay for cellular growth and survival: application to proliferation and cytotoxicity assays. *J Immunol Methods.* 1983;65(1-2):55-63.
- [15] Singh NP, McCoy MT, Tice RR, Schneider EL. A simple technique for quantitation of low levels of DNA damage in individual cells. *Exp Cell Res.* 1988;175(1):184-91.
- [16] Bioquest A. "Quest Graph™ IC50 Calculator." AAT Bioquest, Inc. 2021 [updated 14.04.2021. Available from: <https://www.aatbio.com/tools/ic50-calculator>.
- [17] Shen CY, Jiang JG, Yang L, Wang DW, Zhu W. Anti-ageing active ingredients from herbs and

nutraceuticals used in traditional Chinese medicine: pharmacological mechanisms and implications for drug discovery. *Br J Pharmacol.* 2017;174(11):1395-425.

- [18] Dhanjal DS, Bhardwaj S, Sharma R, Bhardwaj K, Kumar D, Chopra C, Nepovimova E, Singh R, Kuca K. Plant fortification of the diet for anti-ageing effects: A review. *Nutrients.* 2020;12(10):3008.
- [19] Shin SA, Moon SY, Kim WY, Paek SM, Park HH, Lee CS. Structure-based classification and anti-cancer effects of plant metabolites. *Int J Mol Sci.* 2018;19(9):2651.
- [20] Safari F, Hassanpour H, Alijanpour A. Evaluation of hackberry (*Celtis australis* L.) fruits as sources of bioactive compounds. *Sci Rep.* 2023;13(1):12233.
- [21] Badoni R, Semwal DK, Rawat U, Rawat M. Chemical constituents from fruits and stem bark of *Celtis australis* L. *Helvetica Chimica Acta.* 2011;94:464-73.
- [22] Acquaviva R, Sorrenti V, Santangelo R, Cardile V, Tomasello B, Malfa G, Vanella L, Amodeo A, Genovese C, Mastrojeni S. Effects of an extract of *Celtis aetnensis* (Tornab.) Strobl twigs on human colon cancer cell cultures. *Oncol Rep.* 2016;36(4):2298-304.
- [23] Hwang BY, Chai H-B, Kardono LBS, Riswan S, Farnsworth NR, Cordell GA, Pezzuto JM, Douglas Kinghorn A. Cytotoxic triterpenes from the twigs of *Celtis philippinensis*. *Phytochemistry.* 2003;62(2):197-201.

Experimental Study to Determine the Backscattering, Asymmetry, and Tailing Factors for Some Elements in the Atomic Number Range of $4 \leq Z \leq 48$ at 59.54 keV Using the Gamma Backscattering Method

Zeynep UZUNOĞLU^{1*} 

¹ Ağrı İbrahim Çeçen University, Patnos Vocational School, Department of Medical Services and Techniques, Opticianry Program, Ağrı, Türkiye
 Zeynep UZUNOĞLU ORCID No: 0000-0003-1997-1870

*Corresponding author: zuzunoglu@agri.edu.tr

(Received: 8.09.2023, Accepted: 6.01.2024, Online Publication: 26.03.2024)

Keywords

Backscattering,
 Backscattering factor,
 Asymmetry factor,
 Tailing factor,
 HPGe detector

Abstract: This experimental study has been carried out by using gamma backscattering method which is a non-destructive method. Some elements which are in the atomic number range of $4 \leq Z \leq 48$ have been used as backscatterer samples to investigate the variation of backscattering factor, asymmetry factor, and tailing factor with atomic number. These samples were irradiated by γ -rays of 59.54 keV energy emitted from a 10 μ Ci ²⁴¹Am point radioactive source. To count the backscattered photons from samples, a high purity germanium detector (HPGe) with a resolution of 182 eV at 5.9 keV and active area of 200 mm² was used. It was concluded that the coherent to backscattering ratio, asymmetry factor, and tailing factor increased with increasing atomic number, but the count rate and backscattering factor decreased.

12

Gama Geri Saçılma Yöntemini Kullanarak 59.54 keV'de $4 \leq Z \leq 48$ Atom Numarası Aralığındaki Bazı Elementler İçin Geri Saçılma, Asimetri ve Kuyruklanma Faktörlerini Belirlemeye Yönelik Deneysel Çalışma

Anahtar Kelimeler

Geri saçılma,
 Geri saçılma faktörü,
 Asimetri faktörü,
 Kuyruklanma faktörü,
 HPGe dedektör

Öz: Bu deneysel çalışma, tahribatsız bir yöntem olan gama geri saçılma yöntemi kullanılarak gerçekleştirilmiştir. Geri saçılma faktörü, asimetri faktörü ve kuyruklanma faktörünün atom numarasına göre değişimini araştırmak için, geri saçıcı numuneler olarak $4 \leq Z \leq 48$ atom numarası aralığındaki bazı elementler kullanılmıştır. Bu numuneler, 10 μ Ci ²⁴¹Am radyoaktif nokta kaynaktan yayılan 59.54 keV enerjili γ -ışınları ile ışınlanmıştır. Numunelerden geri saçılan fotonları saymak için, 5.9 keV'de 182 eV çözünürlüğe ve 200 mm² aktif alana sahip yüksek saflıkta germanyum dedektörü (HPGe) kullanıldı. Koherent/geri saçılma oranı, asimetri faktörü ve kuyruklanma faktörünün artan atom numarası ile arttığı, ancak sayma hızı ve geri saçılma faktörünün azaldığı sonucuna varıldı.

1. INTRODUCTION

Backscattering (i.e., backscatter) is defined as the reflection of radiation or particles back to the direction from which they came. Backscattering has many important application areas as astronomy, radar systems (especially weather radar), radiation dosimetry, fiber optics, photography, X-ray imaging, neutron or X-ray spectroscopy, and medical ultrasonography. The gamma backscattering method is a non-destructive method. This method can be used to determine physical parameters as thickness (or saturation thickness), density, and shape of backscattering samples (or materials). When the material used as target are irradiated by gamma photons, the

gamma photons are backscattered from the interior of the target and then these gamma photons backscattered backwards are detected using a detector in this method.

There are many studies with regard gamma backscattering in the literature. Because the backscattering method is very useful, it is used to determine parameters such as effective atomic number, saturation thickness, and albedo factor for a material. Udagani [1] studied experimentally gamma backscattering and saturation thickness for granite and glass using ¹³⁷Cs radioactive source and NaI(Tl) detector at 180° scattering angle. Then, Udagani [2] investigated gamma ray backscattering for water, kerosene, petrol, and admixture of kerosene and petrol.

He concluded that the gamma backscattering technique is very useful and sensitive analytical technique for performing quantitative analysis of samples. Almayahi [3] measured the backscattering factor of gamma rays for pure concretes of different thicknesses using gamma energies in range of 0.088 MeV to 1.253 MeV and a NaI(Tl) scintillation detector. He concluded that the backscattering factor increased with increasing target thickness and gamma photon energy. However, he observed that the backscattering factor remains constant at a certain thickness value called the saturation thickness. Singh et al. [4] measured effective atomic number of composite materials at 662 keV using gamma backscattering technique. They investigated the effect of target thickness on intensity distribution of gamma photons. These gamma photons are multiply backscattered from targets. They found that intensity of multiply backscattering increased with increasing target thickness and finally saturated. Also, Singh et al. [5] determined the effective atomic number of biomedical samples the same technique. Kiran et al. [6] carried out an experimental study to determine effective atomic number of composite materials by Compton scattering. Then, Kiran et al. [7] calculated the effective atomic number of some construction materials for gamma photons scattered in backward direction of 90° to incident photon and detected the backscattered gamma photons by a NaI(Tl) detector. Uzunoğlu et al. [8] investigated experimentally the multiple scattered fraction as a function of target thickness for HgO and PbO at a scattering angle of 168° , and incident gamma photon energy of 59.54 keV. Backscattered photons were collected using a HPGe semiconductor detector in their study. Ravindraswami et al. [9] studied experimentally selected polymers by multiple scattering of gamma rays of 662 keV energy and detected the backscattered photons by a NaI(Tl) detector. In their study, the detector was placed at an angle of 90° to the incident gamma photons. They compared their experimental results with the results obtained from Monte Carlo N-particle simulation code. Sharma et al. [10] investigated effective atomic numbers for binary alloys as PbSn, PbZn and ZnSn at 662 keV using gamma backscattering technique. They compared their experimental results with the theoretical ones which were obtained from WinXCom, and observed that there is a good agreement between theoretical and experimental results. Wirawan et al. [11] performed simulations using Monte Carlo GEANT4 toolkit for analyzing the gamma backscattering of different flaw types and their orientations. Sabharwal et al. [12] measured albedo factors for targets of different atomic numbers and various target thicknesses using backscattered gamma photons of 279, 320, 511 and 662 keV. They detected the backscattered gamma photons by an NaI(Tl) scintillation detector and found that the energy albedos decreased with the increase in the atomic number of the target and incident gamma photon energy. Naji et al. [13] examined the effect of backscattering gamma radiation on X-ray image contrast. Qutub MAZ. [14] investigated the photon backscattering for various stainless-steel thicknesses. He carried out this work using the FLUKA code for Monte Carlo simulations in the 0.25- 20 MeV energy range.

Özdemir et al. [15] determined asymmetry factor and energy shifts of the K_β and K_α peaks for the transition metals by using a Si(Li) detector at temperatures between 40 and 400 °C. Gotmar et al. [16] explored the peak tailing in linear chromatography. They mentioned that peak tailing reduces often considerably the resolution between analytes and causes band interference. In addition, they presented that it prevents an accurate interpretation of UV spectra. Also, peak tailing reduces the accuracy of quantitative results. Therefore, the tailing (or fronting) of the peak has an undesirable effect, which is a problem in XRF peak analysis as well as in chromatography. Wahab et al. [17] carried out detection and quantitation of fronting, tailing. In addition, they investigated the effects of tailing and fronting on asymmetry measurements.

Parameters such as peak height, area, and resolution are very important for peak shape analysis. Gaussian function is used to assess problems in a peak such as tailing (or fronting), shouldering, or splitting. The Gaussian function, which is widely used, enables qualitative and quantitative assessment of individual contributions to the overall peak distortion. But this situation is rarely noticed and it is never quantified. Therefore, the signal to noise ratio should be determined for XRF analysis and this ratio should be high.

In this experimental study, peak asymmetry has been used as a way to quantify the contributions of fronting and tailing to non-Gaussian peaks with gamma backscattering method. The variation of count rate, backscattering factor, coherent to backscattering ratio, asymmetry factor (A_s) and tailing factor (TF) with atomic number were investigated using backscattered peaks of some elements which are in $4 \leq Z \leq 48$ atomic number range.

2. MATERIAL AND METHODS

2.1. Experimental Setup and Acquisition System

In this work, some elements which are in the atomic number range of $4 \leq Z \leq 48$ were used as samples for gamma backscattering method. These elements in the form of foil were Be, Cu, Nb and Cd. The masses of these samples were 0.47877, 0.16778, 0.27006 and 0.57235, respectively. These samples were irradiated with gamma rays of 59.54 keV energy emitted from ^{241}Am point radioactive source which has an activity of 10 μCi . High-Purity Germanium (HPGe) detector, which has a DSG planar high purity germanium crystal with an active diameter of 16 mm, was used to detect gamma photons backscattered. In addition, this detector has an active area of 200 mm^2 , sensitive depth (i.e., active thickness) of 10 mm, Be window thickness of 0.12 mm, distance from window (i.e., distance between Ge crystal and Be window) of 5 mm, and a resolution of 182 eV at 5.9 keV. A bias voltage of -1500 V was applied to the detector.

The time used as the data acquisition time was 18000 s for each measurement. The channel was set to 4096 for the multichannel analyzer. To ensure optimum detector performance specified by the manufacturers, the time constant of the amplifier was set to 6 μs . MAESTRO, which is a computer program, was used to govern and

control the operating parameters of the system. The Origin 7.5 software program was used to analyze the pulse height spectra acquired with and without the backscattered target.

The experimental setup of the present measurements for backscattering method is shown in Figure 1. According to Figure 1, the distance between the point radioactive source and the HPGe detector is 1.9 cm. Also, the distance between the point radioactive source and sample is 1 mm. The centers of the HPGe detector, radioactive point source, and target are on the same axis. The backscattering angle was 180° . HPGe detectors should always be kept at low temperatures such as liquid nitrogen temperature, which is -196°C . For this, detector crystal is placed in a dewar containing liquid nitrogen.

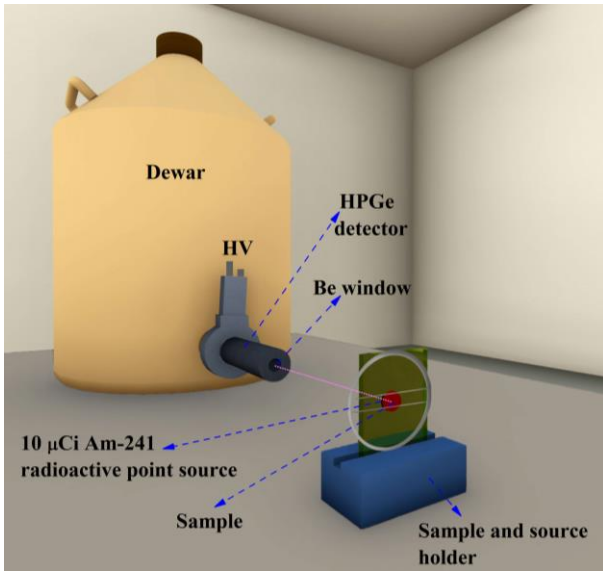


Figure 1. Experimental setup of the present measurements for backscattering method

2.2. Calculation Method of Backscattering, Asymmetry and Tailing Factors

The gamma backscattering method, which is dependent on the sample property, is based on the Compton scattering effect. Compton scattering is the scattering of a high-energy photon from an electron, which is generally considered to be at rest and free, or from a bound electron whose binding energy is small compared to the energy of the incident photon. Compton scattering is dominant for light (or low atomic number) elements. The backscattered gamma rays are those scattered through a large angle ($> 120^\circ$) by the shielding or target. Compton scattering energy (or backscattering energy) varies with angle. When angle approaches 180° , the maximum energy to sample is transferred. In this study, the backscattering angle is 180° as seen from Figure 1. The energy dependence of backscattered gamma photons as a function of angle is given by the following formula:

$$E_s = \frac{E_i}{[1 + (E_i/m_0c^2)(1 - \cos \theta)]} \quad (1)$$

where E_i , E_s , m_0 , c and θ are the energy of incident photon, the energy of scattered (or backscattered) photon, the rest mass of the electron, the speed of light, and the

scattering (or backscattering) angle, respectively. In this equation, m_0c^2 is the rest mass energy of an electron and its value is 511 keV.

The backscattering factor depends on some variables. These are thickness of the backing material, kinetic energy of particle, and atomic number of the backing material. To understand the effect of backscattering, a source backscattering factor (F_b) must be calculated [3, 18]. It can be defined by the following equation:

$$F_b = \frac{N_b}{N_i} \times 100\% \quad (2)$$

where N_b and N_i are number of photons counted with source backing, and number of photons counted without source backing, respectively.

An ideal peak has a sharp symmetrical shape on a flat baseline such as a Gaussian peak. However, a peak can deviate from this ideal form for different reasons. These are that the peak can be asymmetrical, flatten and broader, or the baseline can rise.

Asymmetry factor (A_s) describes how symmetrical a peak is, as the name indicates. In addition, it also indicates whether a peak has either fronting or tailing. Namely, the asymmetry factor is a way of measuring peak tailing (or fronting). It is related to the distances from the center of the peak to either side of the peak (i.e, right or left of peak). Asymmetry factor is calculated by the following equation [17]:

$$A_s = (bc/ca)_{10\%} \quad (3)$$

where bc is the distance from the centre line of the peak, which is a perpendicular line drawn from maximum point of the peak, to the left back slope of the peak measured at 10% of peak height. Also, ca is the distance from the centre line of the peak to the right front slope of peak measured at 10% of peak height. All A_s measurements were made for 10% of the maximum peak height. The value of A_s is equal to 1 for exactly symmetrical peaks. If the value of A_s is less than 1, fronting is observed at the peak. On the contrary, if A_s is greater than 1, tailing is observed at the peak.

Peak fronting occurs when the first half is broader than the second half, and the second half is narrower in an asymmetric peak. The inverse of peak fronting is called as peak tailing. Such a peak is asymmetrical and also second half is broader than the front half of peak. Peak tailing is calculated by the following equation [17]:

$$TF = (ab/2ac)_{5\%} \quad (4)$$

where ab is defined as the distance from the right front slope of the peak to the left back slope. Also, ac is the distance from the centre line of the peak to the right front slope. All TF measurements were made for 5% of the maximum peak height.

3. RESULTS AND DISCUSSION

For this study, the experimental measurements were performed by using gamma backscattering method at scattering angle of 180° as seen from Figure 1. Be, Cu, Nb, and Cd which are in the atomic number range of $4 \leq Z \leq 48$ and in the form of foil were used as samples. These samples were irradiated by γ -rays of 59.54 keV energy emitted from ^{241}Am point radioactive source, which has an activity of $10 \mu\text{Ci}$. Gamma photons backscattered from these samples were counted using an HPGc detector. Then, the spectra were obtained for with and without backscattering (or backscatterer) sample. The typical backscattering spectra obtained with and without a Be sample were shown in Figure 2. The value of energy for backscattered peak was calculated by using Equation 1. For this study, the energy of the backscattered peak was defined as 48.287 keV.

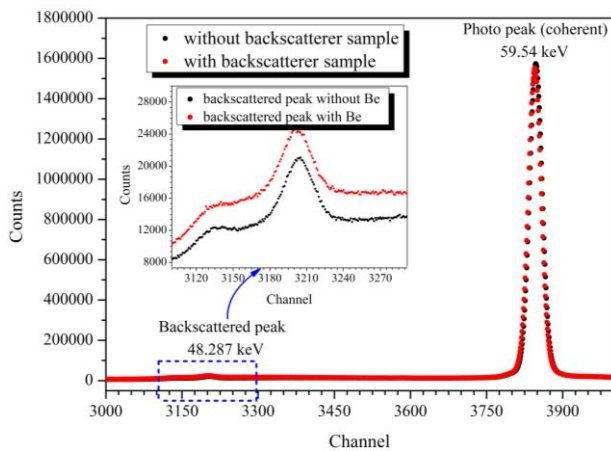


Figure 2. Typical backscattering spectra obtained with and without a Be sample

To define the peak area under the backscattering peak, 'subtract baseline' mode was first used in the peak analyzer of Origin 7.5 program. The baseline subtraction is used to estimate and eliminate background noise. Signals with intensity lower than a threshold value are considered to be noise. So, these undesirable background signals must be removed of peak or spectrum. Because of the shifts away from a Gaussian peak (that is, because it is a peak that cannot be fitted to the gaussian function), it is necessary to select the correct peak regions. Region of interest (ROI) was defined between the start and stop

channels of peak to determine the net peak areas under these backscattering peaks [1]. Then, the area under the backscatter peak was calculated by summing the counts corresponding to each channel in this region. For this total area of peak in the ROI region, the counts were integrated by Origin 7.5 program. The representation for ROI analysis under the backscattering peak on a typical spectrum obtained from Be was shown in Figure 3.

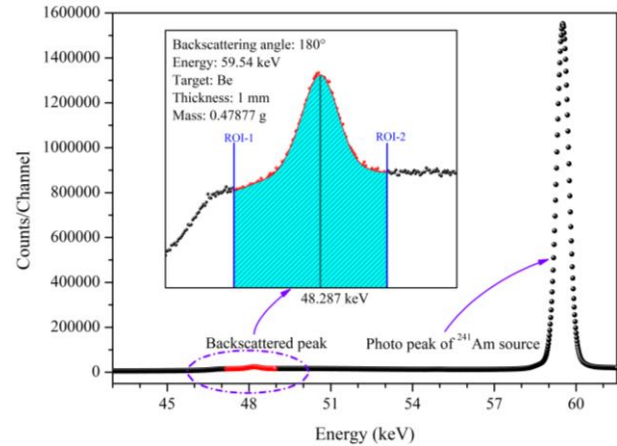


Figure 3. Representation for ROI analysis under the backscattering peak on a typical spectrum obtained from Be

As seen from Figure 3, ROI-1 is the start point and ROI-2 is the stop point of the ROI region of the backscattering peak. The values of counts under ROI, count rate, backscattering factor (F_b) (which is calculated using Equation 2), and coherent to backscattering intensity ratio (Coherent/BS) were given in Table 1. Also, the variations of these parameters dealing with backscattering with various atomic numbers were shown in Figure 4.

When the Table 1 and Figure 4 are examined, it is seen that the counts under ROI, the count rate, and backscattering factor decrease with increasing atomic number, but the coherent to backscattering intensity ratio increases. The experimentally measured values of these parameters were fitted to the second-degree polynomial curves. The fit functions and the correlation coefficients obtained for these fit functions are also given in Figure 4. It is seen that these correlation coefficients are quite high from Figure 4.

Table 1. The values of measured parameters dealing with backscattering for various atomic number

Elements	Z	Counts Under ROI	Count Rate	F_b	Coherent/BS
Be	4	285531	15.863	1.092	170.709
Cu	29	269578	14.977	1.031	180.352
Nb	41	257113	14.284	0.984	188.297
Cd	48	234241	13.013	0.911	203.211

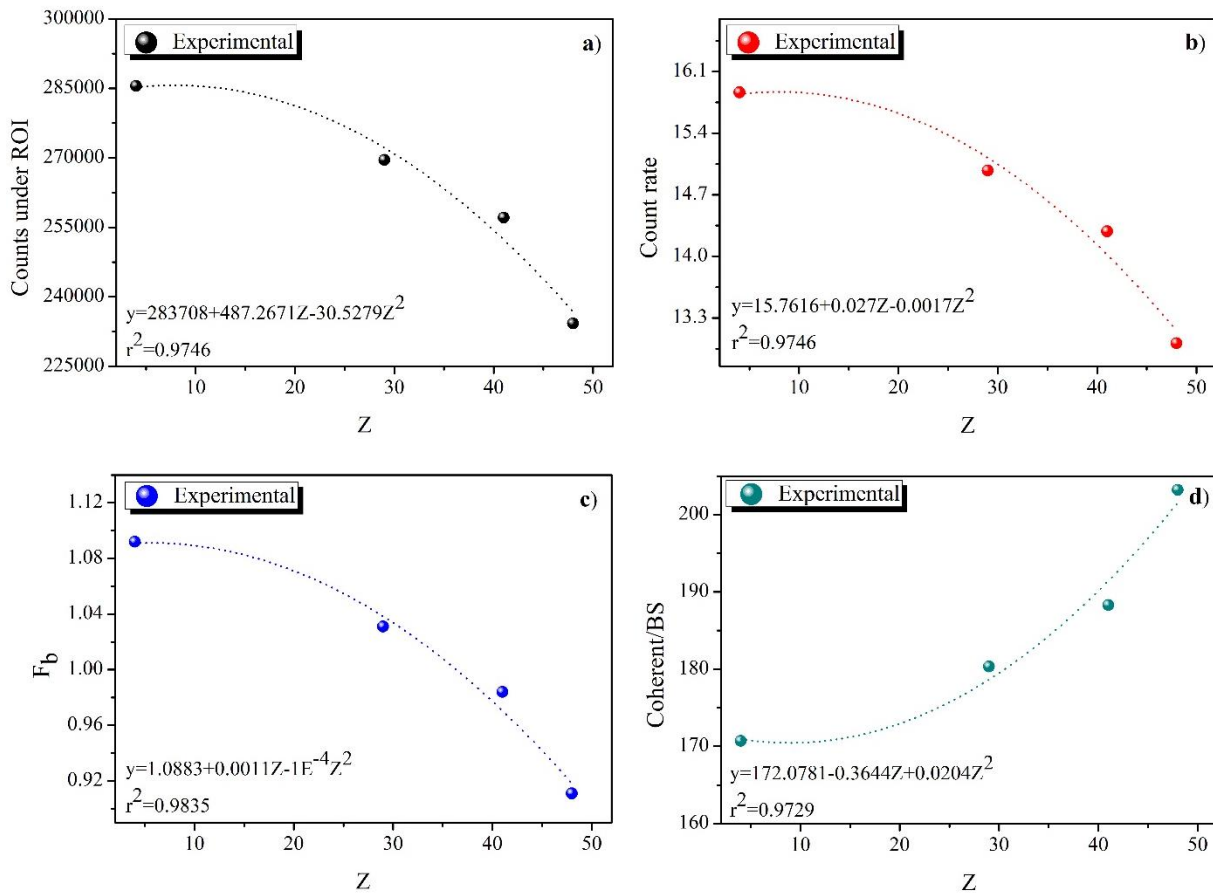


Figure 4. Variation of a) counts under ROI, b) count rate, c) backscattering factor (F_b), and d) coherent to backscattering (Coherent/BS) intensity ratio as a function of atomic number (Z)

As a result of the interaction of high-energy rays with target, either complete absorption or scattering occurs for each interaction. When electromagnetic radiation is sent on any material, photons can interact with bonded atomic electrons, free electrons, the nucleus or the Coulomb field of electrons, nucleons or the whole nucleus, or they can pass without any interaction. Interactions with energies up to 10 MeV often result in any of the events such as photoelectricity, Compton or pair production [19]. However, cross sections can be used to determine what kind of the interactions occur when a photon of 59.54 keV energy interacts with the material. For this study, the coherent, incoherent

(Compton or backscattering), photoelectric cross sections for 59.54 keV energy, and their contributions to total photon interaction (%) were calculated using WinXCOM program. Then, these results were given in Table 2. According to Table 2, there is a relationship such as Compton>coherent>photoelectric between scattering and photoelectric effects of the elements with low atomic number. Conversely, it is obvious that there is a relationship such as photoelectric>coherent>Compton for elements with large atomic numbers.

Table 2. The cross sections obtained for 59.54 keV energy using WinXCOM program and their contributions to total photon interaction (%)

Z	Cross Sections (cm^2g^{-1})			The contributions to total photon interaction (%)		
	Coherent	Incoherent	Photoelectric	Coherent	Incoherent	Photoelectric
4	0.005	0.143	0.001	3.339	95.948	0.713
29	0.109	0.131	1.385	6.727	8.081	85.193
41	0.184	0.122	3.812	4.468	2.955	92.576
48	0.229	0.115	5.759	3.757	1.887	94.357

When photons are sent onto the target, these photons not only lose energy as they pass through the target, but also scatter at very small angles along their path. Single scattering occurs if there is only one scattering in a target, and multiple scattering can occur if there are more than once scatterings in a target. Photons scattered from a target that undergo re-scattering from neighboring atoms in target cause to multiple scattering

[8]. The parameters such as photon energy, scattering angles, source and detector collimation, sample thickness, and density must be taken into account for the experimental determination of multiple scattering. In Compton scattering or backscattering, the incoming photon undergoes to multiple scattering in the sample before it leaves the sample. The multiple scatterings of photons occur as a hump on the left slope of the

Compton (or backscattering) peak. This hump is shown in Figure 5 for Be. Because the hump is on the left slope of the peak, peak fronting occurs, not tailing. The peaks, which have such a hump, are not perfect like the Gaussian peak, so they are not symmetrical. It is known that tailing or fronting is most clearly seen close to the baseline. A representation for measurement of peak tailing factor and asymmetry factor is given in Figure 5.

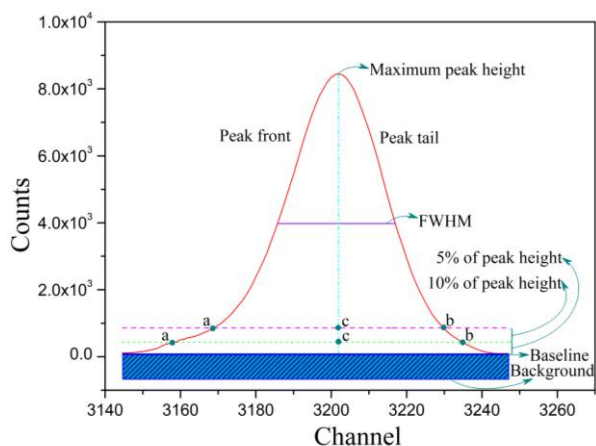


Figure 5. Representation and measurement of peak tailing factor and asymmetry factor

Table 3. The channel numbers of backscattering peak maximum for elements of various atomic numbers, the values of their asymmetry factors (A_s) and tailing factors (TF)

Z	Channel Peak Max.	A_s	A	B	TF	A	B
4	3201	0.763	38	29	0.924	46	39
29	3198	0.875	32	28	0.944	45	40
41	3195	0.897	29	26	0.950	40	36
48	3194	0.926	27	25	0.953	32	29

4. CONCLUSION

The experiments were carried out using gamma backscattering method in this study. The variation of count rate, backscattering factor, coherent to backscattering ratio, asymmetry factor (A_s) and tailing factor (TF) with atomic number were investigated for some elements which are in $4 \leq Z \leq 48$ atomic number range. It is concluded that the count rate, and backscattering factor decrease with increasing atomic number, but the coherent to backscattering intensity ratio increases. Then, the variation of the interaction cross sections (the coherent, incoherent (Compton or backscattering), photoelectric) with atomic number and their contributions to total photon interaction (%) were defined for 59.54 keV energy using WinXCOM. Finally, how the asymmetry factor and peak tailing change with atomic number was investigated for asymmetric backscattering peaks. It was seen that the photoelectric absorption increases as the atomic number increases, the multiple scattering will decrease and therefore the peak tailing will also decrease. So, the contributions of multiple scattering on backscattering peak were quantified. Because the backscattering method is nondestructive method, it can be used for qualitative and quantitative analysis of compounds, alloys, and composite materials.

Asymmetry factors were calculated using Equation 3 at 10% of peak height. Also, tailing factors were calculated using Equation 4 at 5% of peak height. The channel to which the maximum peak height corresponds, asymmetry factor and tailing factor are given in Table 3. In addition, the number of channels to the left and right of backscattering peak is defined as A and B, respectively. The values of A and B are also given in Table 3 for both asymmetry factor and tailing factor. Thus, the amount of tailing at the backscattering peak was determined for various atomic numbers. When the Table 3 is examined, it can be concluded that A is bigger than B and there is a tailing on the left slope of backscattering peak. That is, there is peak fronting for a backscattering peak, which in this case TF is lower than 1. Also, it was found that the values of asymmetry factor and tailing factor approach 1 with increasing atomic number. Because, as the asymmetry factor is closer to 1, as the symmetry of backscattering peak is greater.

Acknowledgement

The experimental measurements for this study were performed in Prof. Dr. Wolf Weyrich High Energy Spectroscopy Laboratories, Department of Physics, Faculty of Science, Atatürk University. The author thanks Department of Physics, Atatürk University.

REFERENCES

- [1] Udagani C. Study of gamma backscattering and saturation thickness estimation for granite and glass. *Int. J. Eng. Sci. Invention*. 2013;2(6):82-86.
- [2] Udagani C. Study of Gamma Ray Backscattering with Special Reference to Admixture of Kerosene and Petrol. *Int. J. Sci. Res.* 2014; 3(7): 1659-1662.
- [3] Almayahi BA. Backscattering factor measurements of gamma rays of the different thickness of pure concrete. *J. Radiat. Res. Appl. Sci.* 2015;8(3):389-392.
- [4] Singh I, Singh B, Sandhu BS, Sabharwal AD. Experimental evaluation of effective atomic number of composite materials using backscattering of gamma photons. *Radiat. Eff. Defects Solids*. 2017;172(3-4):204-215.
- [5] Singh I, Singh B, Sandhu BS, Sabharwal AD. Determination of effective atomic number of biomedical samples using Gamma ray back-

- scattering. 2nd International Conference on Condensed Matter and Applied Physics, ICC 2017. AIP Conference Proceedings; 2017. 1953(1):140134-1-140134-4.
- [6] Kiran KU, Ravindraswami K, Eshwarappa KM, Somashekarappa HM. Effective atomic number of composite materials by Compton scattering-nondestructive evaluation method. *Int. J. Sci. Eng. Res.* 2014; 5(3):316-325.
- [7] Kiran KU, Ravindraswami K, Eshwarappa KM, Somashekarappa HM. Effective atomic number of selected construction materials using gamma backscattering technique. *Ann. Nucl. Energy.* 2015; 85:1077-1084.
- [8] Uzunoglu Z, Yilmaz D, Sahin Y. Determination of the multiple scattered fraction as a function of target thickness. *Can. J. Phys.* 2017; 95(6):1-5.
- [9] Ravindraswami K, Kiran KU, Eshwarappa KM, Somashekarappa HM. Nondestructive evaluation of selected polymers by multiple scattering of 662 keV gamma rays. *J Radioanal Nucl. Chem.* 2014; 300:997-1003.
- [10] Sharma R, Sharma JK, Singh T. Effective Atomic Numbers for Some Alloys at 662 keV Using Gamma Rays Backscattering Technique. *Phys. Sci. Int. J.* 2016;11(1):1-6.
- [11] Wirawan R, Angraini LM, Qomariyah N, Waris A, Djamal M. Gamma backscattering analysis of flaw types and orientation based on Monte Carlo GEANT4 simulations. *Appl. Radiat. Isot.* 2020; 155:1-7.
- [12] Sabharwal AD, Singh S, Singh B, Sandhu BS. Albedo factors of 279, 320, 511 and 662 keV backscattered gamma photons. *Radiat. Eff. Defects Solids.* 2011;166(6):451-458.
- [13] Naji AT, Jaafar MS, Ali EA, Al-Ani SKJ. Effect of Backscattered Radiation on X-Ray Image Contrast. *Appl. Phys. Res.* 2017; 9(1):105-114.
- [14] Qutub MAZ. Photon backscattering for various stainless-steel thicknesses from 0.25 to 20 MeV using Monte Carlo simulation FLUKA code. *Radiat. Phys. Chem.* 2023; 202:1-7.
- [15] Özdemir Y, Kavaz E, Ahmadi N, Ertugrul M, Ekinci N. Investigation of K X-ray intensity ratios of some 4d transition metals depending on the temperature. *Appl. Radiat. and Isot.* 2016; 115:147-154.
- [16] Gotmar G, Fornstedt T, Guiochonb G. Peak tailing and mass transfer kinetics in linear chromatography Dependence on the column length and the linear velocity of the mobile phase. *J. Chromatogr. A.* 1999; 831:17-35.
- [17] Wahab MF, Patel DC, Armstrong DW. Total peak shape analysis: detection and quantitation of concurrent fronting, tailing, and their effect on asymmetry measurements. *J. Chromatogr. A.* 2017; 509:163-170.
- [18] Tsoufanidis, N. (1983). Measurement and detection of radiation. New York: McGraw-Hill.
- [19] Adams, F., Dams, R., 1970. Applied Gamma Ray Spectrometry, Pergamon Press, 8, Oxford, U.K.

Advanced EEG-Based Analysis for ADHD Identification Utilizing ConvMixer and Continuous Wavelet Transform

Buğra KARAKAŞ^{1*}, Salih Taha Alperen ÖZÇELİK², Hakan UYANIK³, Hüseyin ÜZEN⁴,
Abdulkadir ŞENGÜR⁵

¹ National Education Directorate Department, Elazığ, Türkiye

² Bingöl University, Engineering Faculty, Electrical-Electronics Engineering Department, Bingöl, Türkiye

³ Munzur University, Engineering Faculty, Electrical-Electronics Engineering Department, Tunceli, Türkiye

⁴ Bingöl University, Engineering Faculty, Computer Engineering Department, Bingöl, Türkiye

⁵ Fırat University, Technology Faculty, Electrical-Electronics Engineering Department, Elazığ, Türkiye

Buğra KARAKAŞ ORCID No: 0000-0002-8319-7480

Salih Taha Alperen ÖZÇELİK ORCID No: 0000-0002-7929-7542

Hakan UYANIK ORCID No: 0000-0002-6870-7569

Hüseyin ÜZEN ORCID No: 0000-0002-0998-2130

Abdulkadir ŞENGÜR ORCID No: 0000-0003-1614-2639

*Corresponding author: bugrakarakas@gmail.com

(Received: 10.11.2023, Accepted: 7.01.2024, Online Publication: 26.03.2024)

Keywords

EEG,
Deep learning,
ADHD,
Continuous
wavelet
transform

Abstract: Children with ADHD may experience challenges such as attention deficits, behavioral problems, educational problems, and low self-confidence. This study summarizes research aiming to evaluate the diagnosis of attention deficit hyperactivity disorder (ADHD) with electroencephalography (EEG) signals. The research used EEG data from 30 children diagnosed with ADHD and 30 healthy control groups. EEG data was first processed for noise reduction purposes and then classified using deep learning models such as ConvMixer, ResNet50, and ResNet18. The findings show that ConvMixer demonstrates high accuracy in classification, while requiring low computational resources. Additionally, the effects of different channels on the usability of EEG signals in the diagnosis of ADHD were examined, and the T8 channel was found to be particularly effective. In conclusion, the study emphasizes the effectiveness of lightweight models and underscores the significance of specific EEG channels in diagnosing ADHD using EEG signals.

ConvMixer ve SDD Kullanılarak DEHB Hastalığının EEG Sinyalleri ile Otomatik Olarak Tespit Edilmesi

Anahtar Kelimeler

EEG,
Derin Öğrenme,
DEHB,
Sürekli dalgacık
dönüşümü

Öz: DEHB, çocuklarda dikkat eksikliği, davranış problemleri, eğitimle ilgili sorunlar ve düşük özgüven gibi problemler oluşturabilir. Bu çalışma, Dikkat Eksikliği Hiperaktivite Bozukluğu (DEHB) teşhisini elektroensefalografi (EEG) sinyalleriyle değerlendirmeyi hedefleyen bir araştırmayı özetlemektedir. Araştırma, 30 DEHB tanısı almış çocuk ve 30 sağlıklı kontrol grubunun EEG verilerini kullanmıştır. EEG verileri öncelikle gürültü azaltma amacıyla işlenmiş ve ardından ConvMixer, ResNet50 ve ResNet18 gibi derin öğrenme modelleri kullanılarak sınıflandırılmıştır. Bulgular, ConvMixer'in düşük hesaplama kaynaklarına ihtiyaç duyarak yüksek sınıflandırma başarısı elde ettiğini göstermektedir. Ayrıca, EEG sinyallerinin DEHB teşhisinde kullanılabilirliği konusunda farklı kanalların etkileri incelenmiş ve T8 kanalının özellikle etkili olduğu tespit edilmiştir. Bu çalışma, EEG tabanlı DEHB teşhisi için daha hafif modellerin kullanılabilirliğini ve EEG kanallarının önemini vurgulamaktadır.

1. INTRODUCTION

ADHD is a neurodevelopmental disorder that typically manifests in childhood, affecting at least 5 out of every 100 children today [1]. ADHD can cause problems in children such as attention deficits, behavioral problems, educational problems, and low self-confidence. Early diagnosis of ADHD helps to create a treatment plan appropriate to children's needs, improve school performance, and support social and emotional development. ADHD symptoms cause some changes in brain activity. For this reason, an electroencephalogram (EEG) may reveal some findings that show symptoms of ADHD. Since deep learning methods can automatically analyze EEG data, they can be used as an effective tool to distinguish between individuals with ADHD and healthy individuals.

Numerous studies have been conducted in the literature using artificial intelligence techniques to classify people with ADHD and healthy individuals. Tosun [2] investigated how different frequency light stimuli affected the diagnosis of ADHD. This data set was obtained by the researcher using the power spectral densities and spectral entropy values that were generated from the EEGs of the patients. The researcher created his own data set. The researcher used support vector machines (SVM) and long-short-term memory (LSTM) as classifiers. With the eyes closed, the results showed 88.88% classification accuracy in the Fp1 and F7 channels and 92.15% at rest.

Five Azure Kinect units and depth sensors were used to gather the skeletal data of children as they played a game that Lee et al. [3] designed for the purpose of screening and diagnosing ADHD in children. The child is required to follow a robot that follows a predetermined path in a game meant to screen diagnoses. The skeletal data utilized in this study were separated into two categories: "play" data, which was collected while the child was playing, and "waiting" data, which was collected when the child was waiting while the robot guided. The RNN series, bidirectional layer, and weighted cross-entropy loss function of the GRU, RNN, and LSTM algorithms were used to classify the resultant data. Out of all of these techniques, the LSTM algorithm with a weighted cross-entropy loss function and a bidirectional layer achieved 97.82% classification accuracy.

Two novel deep learning techniques for the classification of ADHD based on functional magnetic resonance imaging (fMRI) were presented by Wang et al. [4]. Convolutional neural networks and independent component analysis were employed in the first. The correlation autoencoder method was applied in the second one. Both approaches outperformed traditional approaches in terms of performance.

The gradient-weighted class activation mapping technique was used by Chen et al. [5] to visualize EEG signals in their investigation. 50 children with attention deficit hyperactivity disorder were studied; 9 girls and 41 boys provided EEG signals for the data collection. From

spatial frequency anomalies in the EEGs, they were able to obtain the power spectral density. The researchers' classification accuracy was 90.29% when they used this feature as the convolutional neural network's (CNN) input.

Lee et al. [6] used deep learning and skeletal data to classify ADHD in children. Data from engaging games were accurately classified into three groups: ADHD, ADHD-RISK, and Normal. 98.15% classification accuracy was attained with the use of bi-directional LSTM and channel attention model. A major contribution to the differentiation of the ADHD-RISK class was made by the study.

Saurabh et al. utilized functional magnetic resonance imaging (fMRI) data during resting-state to diagnose ADHD. They classified ADHD using voxel data in RSN active regions, utilizing a modified BLSTM model [7]. For classification accuracy, the model scored 87.50%. An evaluation was conducted in comparison to alternative approaches.

Tang et al. [8] used the ADHD-200 database as a data set. The suggested network architecture consisted of a modified autocoding network and a binary hypothesis testing framework. The study employed binary hypothesis testing as a means of handling incomplete data, and during feature selection, the brain functional connections from the test and training data sets were combined. The purpose of the modified autocoding network was to capture more useful features. The ADHD-200 database was used for experiments, and the method's average accuracy was 99.6%.

EEG signals were used as the data set by Ahmadi [9], who proposed a computer-aided diagnosis system that can accurately diagnose ADHD. Deep convolutional neural network (CNN) architecture is used in the suggested technique. With the combination of β_1 , β_2 , and γ bands, the highest classification accuracy was obtained. It was discovered that the success rate attained was 99.46%. In this study, deep learning and an EEG signal were used to classify children with ADHD and healthy children.

A total of 121 children and 19 channels, aged 7 to 12, comprised 61 children with ADHD and 60 healthy children [10] were the data set utilized by Maniruzzaman et al. [11]. In the study by et al., key features were chosen using the LASSO logistic regression model after optimal channels were chosen as the network architecture using two different techniques based on SVM and t-test. Consequently, the following six machine learning-based classifiers were employed: logistic regression, multilayer perceptron, k-nearest neighbor, random forest, and Gaussian process classification (GPC). By using these techniques, it was possible to identify children with ADHD from healthy children with an accuracy rate of 97.53%.

Park et al. [12] objectively detected physical aggression in children by utilizing machine learning and physical

activity data from wearable sensors. An activity monitor worn three times a week by 39 individuals with and without ADHD served as the data set for the study conducted by. The random forest method was used to perform machine learning, and patterns describing times of physical aggression were examined. With an 89.3% area under the curve, 82.4% F1 score, 85.0% recall, 82.2% sensitivity, and 82.0% accuracy, the model was able to distinguish between episodes of physical aggression. The sensor's vector magnitude feature was crucial to the model's operation. This research may offer a useful method for remotely identifying and controlling child aggression.

Ghasemi et al. used machine learning to improve the accuracy of ADHD diagnosis. Event-Related Potentials (ERP) data from ADHD patients and healthy control groups were used as the data set in the study by [13]. Features for frequency bands were calculated by processing ERP signals. Seven distinct machine learning algorithms were used for the classification process. Selected features have been combined with care. Deep Learning, Logistic Regression, and Generalized Linear Modeling techniques produced the best classification results. The AUC value is greater than 0.999 and the average accuracy rate is 99.85%. The ability to differentiate ADHD from the control group was better demonstrated by high and low frequencies (Beta, Delta). A machine learning expert system that reduces ADHD misdiagnosis and aids in treatment efficacy evaluation was created in this study.

Mikolas [14] trained a linear SVM classifier with anonymized data from clinical records to identify participants with ADHD from a population presenting a variety of psychiatric conditions. With 66.1% accuracy, children and adolescents diagnosed with ADHD were distinguished from those without the disorder. SVM with single features produced accuracies with slightly different and overlapping standard deviations. Their developed method, which combined 19 features in an automatic feature selection process, produced the best results.

In this study, a deep learning-based method was developed to automatically diagnose ADHD from EEG signals. The open-access data set [10], created with the participation of boys and girls between the ages of 7 and 12, consists of the EEG signals of 61 children with ADHD and 60 healthy children. EEG signals consisting of 19 channels were divided into segments by a multi-part signal segmentation procedure, with each channel becoming a separate vector. Each EEG signal is divided into 4-second segments. A 50Hz notch filter was applied to reduce noise and fluctuation in each EEG segment. Using a continuous wavelet transform, each EEG segment was converted into an image in the frequency-time domain. Each of the 19 channels is classified separately into two classes: ADHD and healthy. In Part 2, the dataset and materials used will be given. In the third part, the findings will be mentioned, and in the fourth part, discussion and conclusions will be given.

2. MATERIAL AND METHOD

2.1. Dataset

In this research, the open-access data set obtained from [10] was used. This data set includes 30 children diagnosed with Attention Deficit Hyperactivity Disorder (ADHD) and 30 healthy controls for whom an experienced child and adolescent psychiatrist confirmed this diagnosis according to DSM-IV criteria. The group diagnosed with ADHD consists of 22 boys and 8 girls, and their average age is 9.62 ± 1.75 years. The healthy control group consists of 25 boys and 5 girls, and their average age is 9.85 ± 1.77 years. Among the children diagnosed with ADHD, 25 had combination subtypes, 3 had attention deficit subtypes, and 2 had hyperactivity subtypes.

Children diagnosed with ADHD were referred to the child and adolescent psychiatry clinic at Roozbeh Hospital, and these children had never used medication before. The control group was selected from two different sources: the first was selected from a primary school with 25 male students; the other 5 female students were selected from an all-female primary school. Children in the control group were evaluated by a child and adolescent psychiatrist to determine possible disorders. As a result of this evaluation, it was determined that none of the children in the control group had psychiatric problems.

Exclusion criteria for children diagnosed with ADHD and healthy controls included history of significant neurological disorder, brain injury (including epilepsy), history of serious medical illness, learning or verbal disability, other psychiatric disorders, and use of benzodiazepine and barbiturate medications. Additionally, after the Raven Progressive Matrices Test was administered to children, participants who showed above-average success were included in the study.

2.2. Preprocessing

EEG signals in the data set were recorded according to the 10-20 standard with a sampling frequency of 128 Hz and were recorded with 19 channels (Fz, Cz, Pz, C3, T3, C4, T4, Fp1, Fp2, F3, F4, F7, F8, P3, P4, T5, T6, O1, O2). Each channel was converted into a separate signal vector. 19 signal vectors were obtained for each sample. Then, a 50 Hz Notch Filter was applied to these signal vectors to minimize noise. Then, each signal vector was divided into 4-second segments without overlapping. For each channel, a total of 79287 segments were obtained, including 2330 ADHD segments and 1843 healthy segments. The pre-processing procedure performed is given in Figure 1.

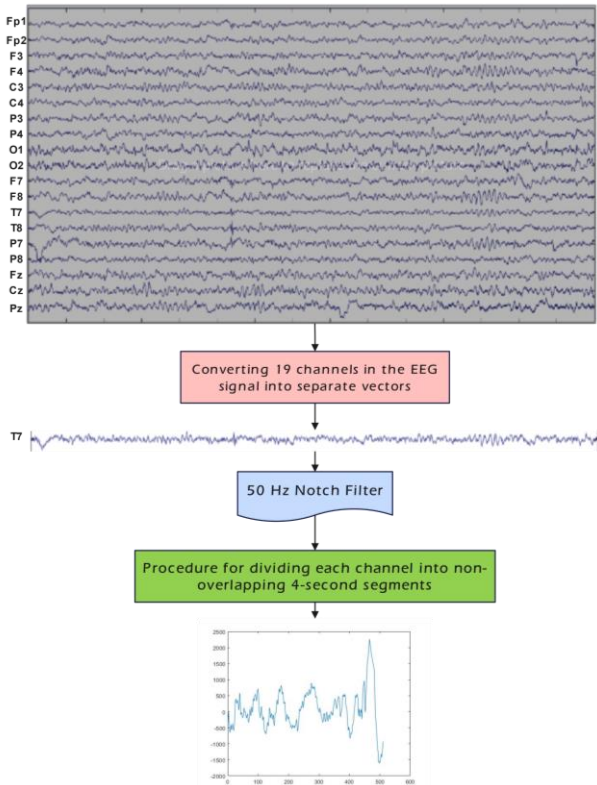


Figure 1. Preprocessing procedure performed

2.3. Continuous Wavelet Transform

Each of the 4-second segments obtained in the pre-processing section was converted into heat map images in the frequency-time domain using the continuous wavelet transform (CWT). The resulting images were set to 224x224, which is the input size of the deep learning networks to be used. CWT is a mathematical process or a spectral analysis method applied to analyze a signal in time-frequency space [15]. EEG signals examine changes in brain activity over time. Frequency components of the EEG are also of high importance. Because oscillations at different frequency levels represent different brain activities [16]. CWT analyzes EEG signals in the time-frequency domain and shows which frequency components are effective in which time interval. The basic equation of CWT is as follows:

$$CWT(a, b) = \int_{-\infty}^{\infty} x(t) \times \psi^* \left(\frac{t-b}{a} \right) dt \quad (1)$$

Here a is the scale factor and determines the time scale of the signal. b is the position parameter and determines the time position of the signal. The result of $CWT(a, b)$ is indexed by time (a) and scale (b). This represents the analysis of the signal at different time scales. $x(t)$ represents the signal under consideration. ψ^* is a wavelet function and is used to measure the frequency components and time positions of the signal. By performing the CWT transformation, wavelet coefficients were obtained as follows:

$$COEFS = CWT(x(t), f_s) \quad (2)$$

Here, $COEFS$ are the wavelet coefficients. f_s is the sampling frequency of the EEG device. Since the sampling frequency is given as 128 Hz in the data set, f_s was chosen as 128 Hz.

The obtained wavelet coefficients were multiplied by a scalar, their logarithm was taken, and then their absolute value was taken.

$$img = \log|COEFS * COEFS| \quad (3)$$

Here img is the resulting image matrix. This matrix was visualized to scale, and a heat map image (HMI) was obtained. For each channel, a total of 79287 HMI was obtained, including 2330 ADHD HMI and 1843 healthy HMI. The stages of obtaining an HMI and an example of the obtained HMI are given in Figure 2.



Figure 2. Stages of obtaining HMI

2.4. Classification Method

The resulting 224x224 size images were classified using Convolutional Neural Network (CNN). The flow diagram of the classification is given in Figure 3.

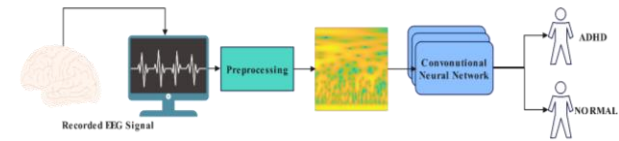


Figure 3. Flow diagram of the applied system

ConvMixer, ResNet50 and ResNet18 were used as classifiers. 70% of the data is reserved for training and 30% for testing. Each channel is classified separately.

2.4.1. ConvMixer

ConvMixer[17] is a deep learning model very similar to MLP-Mixer[18]. In MLP-Mixer, a multilayer perceptron is used to process data in the spatial dimension and mix the channel size, while in ConvMixer, depth convolution called DepthWise is used for spatial mixing. This structure first involves a patch placement layer and is then built by multiple iterations of a simple fully convolutional block. Patch embeddings defined by p and embedding size h can be implemented as a convolution operation with input channels c_{in} , output channels h , kernel size p and step size p :

$$z_0 = BN(\sigma\{conv_{c_{in}} \rightarrow (X, stride = p, kernel_{size} = p)\}) \quad (4)$$

ConvMixer combines several components to process data:

Patch Embedding Layer: Input data is processed with this layer. In this layer, the data is divided into small patch regions and each patch region is converted into a vector by embedding. The stage of converting the input

data into lower-dimensional vector representatives is achieved with this layer.

Convolutional Block: ConvMixer consists of fully connected layers repeated consecutively. These blocks use the basic convolution operation. Each block consists of two steps. The first of these steps is depth convolution, where a convolution is applied where the number of groups is equal to the number of channels. It changes the overall structure of the feature map by comparing channel-level information. The second step is the point convolution step. This step allows further processing of pixel and position features.

Normalization and Activation: Normalization and activation are applied after each convolution. In this way, the model is ensured to stabilize education and learning.

Global Pooling: After a series of repetitions of ConvMixer blocks, global pooling is applied to create a general summary of the entire feature map, and a feature vector is obtained as a result of this process.

Classification Layer: In the final stage, this feature vector is passed to a softmax classification layer and classification of objects or patterns is performed through this layer.

The network architecture used is given in Figure 4.

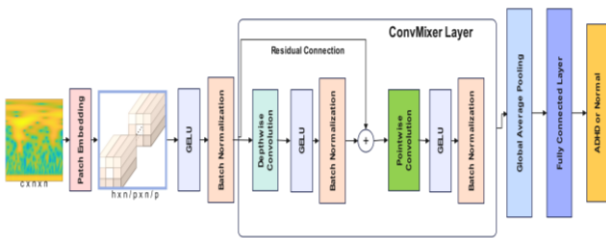


Figure 4. ConvMixer Network Architecture

2.4.2. ResNet50

ResNet [19], developed by Kaiming He and other researchers in 2015, is a family of network architectures. The main feature of ResNet is the use of so-called "skip connections" or "shortcut connections". These connections allow the network to be made deeper, making it easier to train the network and more resistant to overfitting. In this study, ResNet models were also used to classify ADHD and healthy and compare them with the ConvMixer architecture.

Input Layer: ResNet-50 model takes an image of 224x224 pixels as input. This image is usually represented as a tensor consisting of three-color channels (RGB).

Convolution Layers: ResNet-50 contains several convolution layers. Convolution layers are used to capture and extract different features of the image. Each convolution layer implements a convolution operation that comes with weight matrices (W) and bias terms (b).

The mathematical expression of this process is as follows:

$$H_i = f(W_i * H_{i-1} + b_i) \quad (5)$$

Here H_i represents the output of the layer, W_i represents the convolution kernel, H_{i-1} represents the output of the previous layer, b_i represents the bias term and f represents the activation function.

$$Y = f(WX + b) \quad (6)$$

Here Y is the classification result; W, weight matrix; X, feature vector; b is the bias term and f is the activation represents the function.

Skip Connections: ResNet-50 uses connections called "skip connections" or "redundant connections" that specifically help train deeper networks. These connections add the output of one layer to the input of another layer, making the flow of information smoother and allowing the network to become deeper.

2.4.3. ResNet18

Basically, ResNet18 has a similar structure to ResNet50. ResNet18 consists of 18 layers in total, while ResNet50 consists of 50 layers. For this reason, the depth of ResNet50 is greater than ResNet18. This will directly increase the number of parameters of ResNet50 compared to ResNet18. In terms of generalization ability, ResNet50 can generalize better. For this reason, it will work better than ResNet18 in complex situations. Being a model with a higher number of parameters indicates that ResNet50 requires more computational power and memory. In short, while ResNet50 can give better results in larger and more complex data sets, ResNet18 can be described as a simpler model that achieves better results with less data. In the study, classification was performed with both ResNet18 and ResNet50 and these two models were compared in terms of classification success.

Deep learning techniques were applied in a MATLAB environment to automate the classification of Attention Deficit Hyperactivity Disorder (ADHD) using EEG signals. The EEG data, collected from 121 children 60 diagnosed with ADHD and 61 healthy controls were processed into individual vectors for each channel to facilitate detailed analysis. A 50 Hz Notch filter was applied to clean each signal from noise. Each vector, cleared of noise after the Notch filter, was divided into 4-second segments. 4173 segments were obtained for each channel, 2330 of which were ADHD and 1843 were healthy. The resulting 4173 segments were converted into heat map images in the time-frequency domain using the SDD method. The resulting 4173 images were set to 224x224 size. Of these 4173 images, 80% were randomly divided as training data and 20% as test data. For each channel, 3378 training and 835 test images were obtained. A total of 4173*19=79287 images were obtained. In total, 64182 images were allocated to training and 15105 images were allocated to testing.

Some parameters of pre-trained models are given in Table 1.

3. RESULTS OF EXPERIMENTS

Analyzes were carried out in MATLAB environment to automatically classify ADHD disease with deep learning using EEG signals. EEG signals received from a total of 121 children, 60 of whom had ADHD and 61 of whom were healthy, were turned into a separate vector for each channel. A 50 Hz Notch filter was applied to clean each signal from noise. Each vector, cleared of noise after the Notch filter, was divided into 4-second segments. 4173 segments were obtained for each channel, 2330 of which were ADHD and 1843 were healthy. The resulting 4173 segments were converted into heat map images in the time-frequency domain using the SDD method. The resulting 4173 images were set to 224x224 size. Of these 4173 images, 80% were randomly divided as training data and 20% as test data. For each channel, 3378 training and 835 test images were obtained. A total of 4173*19=79287 images were obtained. In total, 64182 images were allocated to training and 15105 images were allocated to testing. Some parameters of pre-trained models are given in Table 1.

Table 1 Parameters for Pre-Trained Models

Model Parameters	ConvMixer	ResNet50	ResNet18
Input Image Size	224x224x3	224x224x3	224x224x3
Mini-batch size	64	64	64
Number of epochs	10	10	10
Initial Learning rate	0.001	0.001	0.001
Optimizer	Adam	Adam	Adam
Activation Function	Softmax	Softmax	Softmax
Verification Frequency	3	3	3
Depth	5	-	-
Patch Size	9	-	-

An example classification process is given in Figure 5.

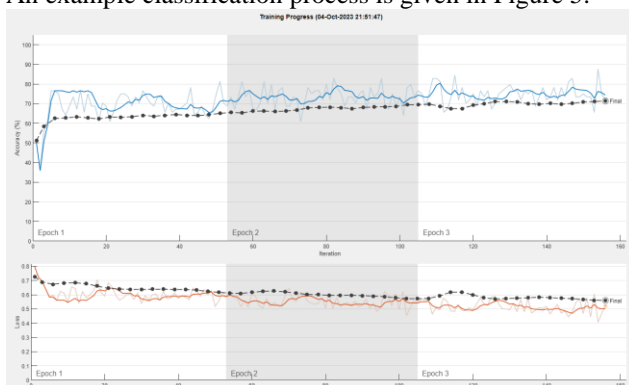


Figure 1 An example for training process

The accuracy rate and average accuracy rate obtained for each channel using ConvMixer in detecting ADHD from EEG signals are as in Table 2.

Table 2 Achieved Classification Accuracy Rates

	ConvMixer	ResNet50	ResNet18	Mean
Fp1	73.16	75.33	72.18	73.5567
Fp2	74.37	73.89	68.82	72.3600
F3	70.9	75.81	76.02	74.2433
F4	70.3	68.74	71.46	70.1667
C3	72.22	77.25	72.18	73.8833
C4	70.18	68.86	69.3	69.44
P3	76.29	76.29	76.26	76.28
P4	65.39	67.19	65.71	66.0967
O1	71.86	71.5	72.66	72.0067
O2	65.15	66.23	67.63	66.3367
F7	73.53	70.9	73.86	72.7633
F8	73.65	73.53	76.74	74.64
T8	75.81	78.92	77.7	77.4767
P7	70.9	74.01	74.82	73.2433
P8	70.9	71.98	75.3	72.7267
Fz	78.68	63.47	64.51	68.8867
Cz	74.13	73.65	76.98	74.92
Pz	77.13	78.8	69.78	75.2367
Mean	72.475	72.575	72.383	

4. DISCUSSION AND CONCLUSION

Table 2 presents the classification results achieved for each channel using pre-trained ResNet and ConvMixer architectures. Classification performance varies for each EEG channel. ConvMixer achieved the highest classification accuracy among all channels, with 78.68% for the Fz channel, while ResNet50 attained the highest accuracy at 78.92% for the T8 channel. ResNet18 achieved the highest classification accuracy among the channels, reaching 76.74% for the F8 channel. Upon examining the classification success obtained by averaging results across 19 channels, ResNet50 exhibited the highest accuracy at 72.575%, followed closely by ConvMixer with 72.475%. ResNet18 gave the lowest classification success with 72.383%. However, all three classifiers gave an average classification accuracy of around 72%.

When their classification success was evaluated, almost three classifiers gave approximately the same classification success. However, when ResNet and ConvMixer are compared, ResNet has many more parameters than ConvMixer architectures. This means that ResNet requires more computational resources than ConvMixer. ConvMixer is a lighter model and consumes less resources. Again, ResNet uses skip connections and cut connections, while ConvMixer focuses on planar comparison of features. In this study, it was revealed that ConvMixer provides features almost as good as ResNet50 with less workload and cost. In addition, the fact that it gives better results than ResNet18 shows that ConvMixer can give better results at some points, even though it has lower depth compared to ResNet architectures.

Another point of focus was which of the 19 channels arranged according to the 10-20 system while recording EEG signals could be more effective in recognizing ADHD with EEG. As stated above, ConvMixer gave high classification success in the Fz probe, ResNet50 gave high classification success in the T8 probe, and ResNet18 gave high classification success in the F8 probe. In this way, it is difficult to deduce which channel

is better for ADHD detection with EEG signal. For this reason, it was estimated which probe would give the best results for automatic ADHD detection by taking the average of the 3 classifiers. As can be seen, the T8 probe was the probe that gave the highest classification success with an average of 77.4767%. This means that the region of the brain where the T8 probe is inserted may be more effective in diagnosing ADHD, and this may be a topic of discussion that may generate new ideas for expert neurologists on this subject.

The biggest disadvantage of this study is its classification accuracy, which is not high. This may be due to the complex and noisy structure of EEG signals.

REFERENCES

- [1] Willcutt, E. G. . The prevalence of DSM-IV attention-deficit/hyperactivity disorder: a meta-analytic review. *Neurotherapeutics*, 2012; 9(3), 490-499.
- [2] Tosun, M. Effects of spectral features of EEG signals recorded with different channels and recording statuses on ADHD classification with deep learning. *Physical and Engineering Sciences in Medicine*, 2021 44(3), 693-702.
- [3] Lee, W., Lee, D., Lee, S., Jun, K., & Kim, M. S. . Deep-Learning-Based ADHD Classification Using Children's Skeleton Data Acquired through the ADHD Screening Game. *Sensors*, 2022; 23(1), 246.
- [4] Wang, D., Hong, D., & Wu, Q.. Attention deficit hyperactivity disorder classification based on deep learning. *IEEE/ACM Transactions on Computational Biology and Bioinformatics*, 2022; 20(2), 1581-1586.
- [5] Chen, H., Song, Y., & Li, X. . Use of deep learning to detect personalized spatial-frequency abnormalities in EEGs of children with ADHD. *Journal of neural engineering*, 2019; 16(6), 066046.
- [6] Lee, W., Lee, S., Lee, D., Jun, K., Ahn, D. H., & Kim, M. S. . Deep Learning-Based ADHD and ADHD-RISK Classification Technology through the Recognition of Children's Abnormal Behaviors during the Robot-Led ADHD Screening Game. *Sensors*, 2023; 23(1), 278.
- [7] Saurabh, S., & Gupta, P. K.. Deep Learning-Based Modified Bidirectional LSTM Network for Classification of ADHD Disorder. *Arabian Journal for Science and Engineering*, 2023; 1-18.
- [8] Tang, Y., Sun, J., Wang, C., Zhong, Y., Jiang, A., Liu, G., & Liu, X. . ADHD classification using auto-encoding neural network and binary hypothesis testing. *Artificial Intelligence in Medicine*, 2022; 123.
- [9] Ahmadi, A., Kashefi, M., Shahrokhi, H., & Nazari, M. A. Computer aided diagnosis system using deep convolutional neural networks for ADHD subtypes. *Biomedical Signal Processing and Control*, 2021; 63, 102227.
- [10] Ali Motie Nasrabadi, Armin Allahverdy, Mehdi Samavati, Mohammad Reza Mohammadi, June 10, 2020, "EEG data for ADHD / Control children", IEEE Dataport, doi: <https://dx.doi.org/10.21227/rzfh-zn36>.
- [11] Maniruzzaman, M., Hasan, M. A. M., Asai, N., & Shin, J. . Optimal Channels and Features Selection Based ADHD Detection From EEG Signal Using Statistical and Machine Learning Techniques. *IEEE Access*, 2023;11, 33570-33583.
- [12] Park, C., Rouzi, M. D., Atique, M. M. U., Finco, M. G., Mishra, R. K., Barba-Villalobos, G., ... & Najafi, B. Machine Learning-Based Aggression Detection in Children with ADHD Using Sensor-Based Physical Activity Monitoring. *Sensors*, 2023; 23(10), 4949.
- [13] Ghasemi, E., Ebrahimi, M., & Ebrahimie, E. Machine learning models effectively distinguish attention-deficit/hyperactivity disorder using event-related potentials. *Cognitive Neurodynamics*, 2022; 16(6), 1335-1349.
- [14] Mikolas, P., Vahid, A., Bernardoni, F., Süß, M., Martini, J., Beste, C., & Bluschke, A. Training a machine learning classifier to identify ADHD based on real-world clinical data from medical records. *Scientific Reports*, 2022; 12(1), 12934.
- [15] Rioul, O., & Duhamel, P. Fast algorithms for discrete and continuous wavelet transforms. *IEEE transactions on information theory*, 1992; 38(2), 569-586.
- [16] Uyanık, H., Ozcelik, S. T. A., Duranay, Z. B., Sengur, A., & Acharya, U. R. Use of differential entropy for automated emotion recognition in a virtual reality environment with EEG signals. *Diagnostics*, 2022; 12(10), 2508.
- [17] Trockman, A., & Kolter, J. Z. Patches are all you need?. *arXiv preprint arXiv:2201.09792*; 2022.
- [18] Tolstikhin, I. O., Houlby, N., Kolesnikov, A., Beyer, L., Zhai, X., Unterthiner, T., ... & Dosovitskiy, A. Mlp-mixer: An all-mlp architecture for vision. *Advances in neural information processing systems*, 2021; 34, 24261-24272.
- [19] He, K., Zhang, X., Ren, S., & Sun, J. Deep residual learning for image recognition. In *Proceedings of the IEEE conference on computer vision and pattern recognition 2016*; (pp. 770-778).

Deceptive Patch Solutions for Protecting Industrial Control Systems Based on Discovered Vulnerabilities

Özlem BATUR DİNLER^{1*} 

¹ Siirt University, Engineering Faculty, Computer Engineering Department, Siirt, Türkiye
Özlem BATUR DİNLER ORCID No: 0000-0002-2955-6761

*Corresponding author: o.b.dinler@siirt.edu.tr

(Received: 30.03.2023, Accepted: 15.01.2024, Online Publication: 26.03.2024)

Keywords

Cybersecurity,
Industrial control
system,
Patch management,
Software
vulnerability
prediction

Abstract: An increase has been observed in concerns about cybersecurity threats in smart energy management on a global scale. Industrial Control Systems, or simply ICSs, are frequently present in industries and essential infrastructures, such as water treatment facilities, nuclear and thermal plants, heavy industries, power production, and distribution systems. ICS devices are high-risk targets for attacks and exploitation with significant security difficulties for ICS vendors and asset owners. Like many consumer electronics, industrial systems are susceptible to a bevy of vulnerabilities that hackers can exploit to launch cyber attacks. Extensive use of ICSs in Critical Infrastructures (CI) increases the vulnerability of CI to cyber attacks and makes their protection a critical subject. This study first contributes to a novel line of research considering how deception can be used by defenders in strategic terms with the objective of introducing uncertainty into an adversary's perception of a system patch management process in order to protect ICSs. Thus, we explore deceptive patch management models for the purpose of providing better insight into developing future cybersecurity techniques for ICS attacks.

26

Keşfedilen Güvenlik Açıklarına Dayalı Endüstriyel Kontrol Sistemlerini Korumaya Yönelik Yanıltıcı Yama Çözümleri

Anahtar Kelimeler

Siber güvenlik,
Endüstriyel kontrol
sistemi,
Yama yönetimi,
Yazılım güvenlik
açığı tahmini

Öz: Küresel ölçekte akıllı enerji yönetiminde siber güvenlik tehditlerine yönelik endişelerde artış gözleniyor. Endüstriyel Kontrol Sistemleri veya kısaca EKS'ler, su arıtma tesisleri, nükleer ve termik santraller, ağır sanayiler, enerji üretimi ve dağıtım sistemleri gibi endüstrilerde ve temel altyapılarda sıklıkla bulunur. EKS cihazları, EKS satıcıları ve varlık sahipleri için önemli güvenlik güçlükleri içeren saldırılar ve istismar için yüksek riskli hedeflerdir. Pek çok tüketici elektroniği gibi, endüstriyel sistemler de bilgisayar korsanlarının siber saldırılar başlatmak için yararlanabilecekleri bir dizi güvenlik açığına karşı hassastır. EKS'lerin Kritik Altyapılarda (KA) yoğun kullanımı, KA'ların siber saldırılara karşı savunmasızlığını artırmakta ve bunların korunmasını kritik bir konu haline getirmektedir. Bu çalışma ilk olarak, EKS'leri korumak için bir düşmanın bir sistem yama yönetimi sürecine ilişkin algısına belirsizliği sokmak amacıyla, aldatmanın savunucular tarafından stratejik terimlerle nasıl kullanılabileceğini ele alan yeni bir araştırma hattına katkıda bulunuyor. Bu nedenle, EKS saldırılarına yönelik gelecekteki siber güvenlik tekniklerinin geliştirilmesine ilişkin daha iyi bir anlayış sağlamak amacıyla aldatıcı yama yönetimi modellerini araştırıyoruz.

1. INTRODUCTION

An Industrial Control Systems (ICS) represents a range of individual control systems and other hardware that operate together with the vulnerability of automating or conducting industrial processes. The ICS domain has

suggested automated tools and environments that are capable of simulating real control system hardware and software behaviors and ensuring a virtualized environment for the purpose of modeling a single type of ICS, such as Programmable Logic Controllers (PLCs),

Distributed Control Systems (ICS), and Supervisory Control and Data Acquisition (CI).

It is vital to enhance the vulnerability of both enterprise networks and ICSs by strengthening cyber security across all points of ICSs. A vulnerability in a computer system represents a weak point, that a hacker can exploit and attack the system. It is possible to categorize the vulnerabilities exploited in the following way: Type 0 indicates zero-day vulnerabilities; Type 1 refers to known vulnerabilities; Type 2 denotes vulnerabilities that originate from protocols, services, and tools that are inherently insecure by nature; Type 3 indicates vulnerabilities related to the insecure configuration of equipment and networks; Type 4 refers to social engineering.

Three main events (discovery, disclosure, and patch) mark a vulnerability's lifecycle. The discovery of a vulnerability by a vendor, third-party institutions, or hackers indicates the lifecycle's beginning. Its public disclosure by the vendor, third-party institutions, or security researchers represents the following event. Black risk refers to the time period between discovery and disclosure. In the said period, the existence of the vulnerability is known only to a closed group of individuals. The patch release by the vendor represents the following event. Gray risk represents the time between the vulnerability disclosure and the patch release date. Nevertheless, the patch will not be installed instantly by all users when it is released by the vendor. White risk denotes the period between the patch date and the date of its installation by all users. A vulnerability's lifecycle comes to an end at the moment of installing the patch by all users.

Patches ensure a direct understanding of the said vulnerabilities in unpatched systems. Conventional patches are capable of weakening systems due to leaking information to an attacker concerning the condition of the system. The patches in question present defects to attackers, which they can use for the purpose of acquiring increased privileges, stealing data, and/or performing malicious unauthorized acts. Deceptive patches impact the decision of an attacker.

The major cybersecurity attacks on ICS infrastructures carried out in the last 20 years represent the most prominent ones with regard to the economic loss described [1]. We investigated them by suggesting possible solutions to prevent such attacks. In Asghar et al. [2], we primarily, examined a number of available studies suggesting several security evaluations, guidelines, and metrics, which might be beneficial for network administrators in predicting the possible risk and guiding them in finding the best solution to protect the ICS from attacks or deliberate assaults. In Upadhyay et al. [3], we presented a timeline analysis of the effect of deceptive patches and ultimately analyzed a formal model of deceptive patches, examining the theoretical security of deceptive patches with a game-theoretic approach. In Mughaid et al. [4], we utilized the world rank of news websites as the primary factor of news accuracy by

employing two common and trusted website rankings. The findings demonstrate that the suggested method yields promising results in comparison to other comparative methods in identifying the accuracy of the news. In Mughaid et al. [5], a methodology for wireless cyber attack detection in 5G networks on the basis of implementing K-Nearest Neighborhood (KNN), Decision Trees (DTs), multi-class Decision Forest (DF), multi-class Decision Jungles, and multi-class Neural Network (NN) techniques. A superior performance was obtained as a result of the experiments carried out, with a 99% accuracy for the KNN algorithm and 93% for DF and NN. The difficulties of implementing traditional security measures for ICS with the objective of addressing security ICS concerning security requirements were highlighted in [6]. Yantz [7] assessed patch management, compliance, and risk management in the business world from the perspective of Operating System (OS) vendors and employee productivity. Hassani [8] provided a strong foundation for the process that could be improved in the future with novel applications, better solutions, and methods for patch management. This research indicated that security patch management is essential in vulnerability management due to its functioning as a remediation plan in vulnerability management. Moreover, a risk-based approach to vulnerability management was presented on a solid basis in [9]. A data set of the gas pipeline control system, one of the essential infrastructures, was employed in [10].

Since reliability and safety represent essential components for an ICS, it is mandatory to understand the attack vectors and threat landscape, involving the resulting threats, to ensure the continued safety and security of control systems. This study contributed to the cybersecurity knowledge by providing patch management solutions for targeted cyber attacks with vulnerabilities of ICSs.

This study contributed to the knowledge of cybersecurity by providing a patch management model of the targeted cyber attacks with vulnerabilities of ICSs. An efficient cybersecurity strategy for an ICS must implement defense-in-depth, which represents a method of layering security mechanisms in order to minimize the failure of a mechanism to a minimum. A vulnerability can be removed by a patch. However, a patch may also present a higher risk from a production or safety perspective. Patch management should be applied as a systematic, documented, and accountable ICS patch management process to manage exposure to vulnerabilities.

The main contributions of the current work are listed below:

- The current study represents the first model defining software security patches and applying deceptive principles to ICSs, making the said methodology a new approach toward efficient analysis and proposing security vulnerability solutions for ICSs.
- The current work presents the novel feasibility of the model based on the basis of deceptive patch models. The most common attacks chosen are used, showing

the possibility of applying deception to patching security vulnerabilities in ICSs.

- We exploit a novel ICS patch management process to capture solutions for the targeted cyber attacks with vulnerabilities of ICSs.
- We investigate how to utilize compensating deception patch-based solutions for security vulnerabilities to reliably secure their control systems.

The organization of the rest of the current article is presented below. Section 2 introduces the overview of the background. Section 3 presents the proposed model. Finally, Section 4 ends with the conclusions and outlines future work.

2. BACKGROUND

2.1. ICS Security Management

Security standards, among the ICS security issues, indicate the need for securing the ICS environment in an explicit way. The standards comprise security concepts, policies, risk management approaches, and security safeguards. The guidelines present suggestions for the measures that should be taken in case of attack detection. Moreover, they suggest the best practices and present an overview of the most essential security measures that all users can comprehend. It is possible to utilize the different

metrics defined in the guidelines for the purpose of assessing cybersecurity strategies.

ICS standard protocols perform the collection and measurement of the system's status, utilize control-layer protocols with the objective of configuring the automation controller, send novel logic, and update the code. Nevertheless, the control layer protocols are predominantly vendor-specific protocols.

Figure 1 shows an overview of the ICS system. It is possible to divide a complete ICS infrastructure into three layers. In the corporate network layer, a supervisory computer or a Human Machine Interface (HMI) can be accessed remotely by managers in a remote way. In the logic control layer (in other words, SCADA/DCS), an HMI or a cloud-based supervisory computer is utilized by system administrators to monitor the purpose of monitoring the status and sending the command for updating the control sequence. Additionally, all control devices (e.g., PLCs and sensors), protocols (e.g. Distributed Network Protocol version 3 (DNP3)/Modbus, and production sites are categorized as physical control layers.

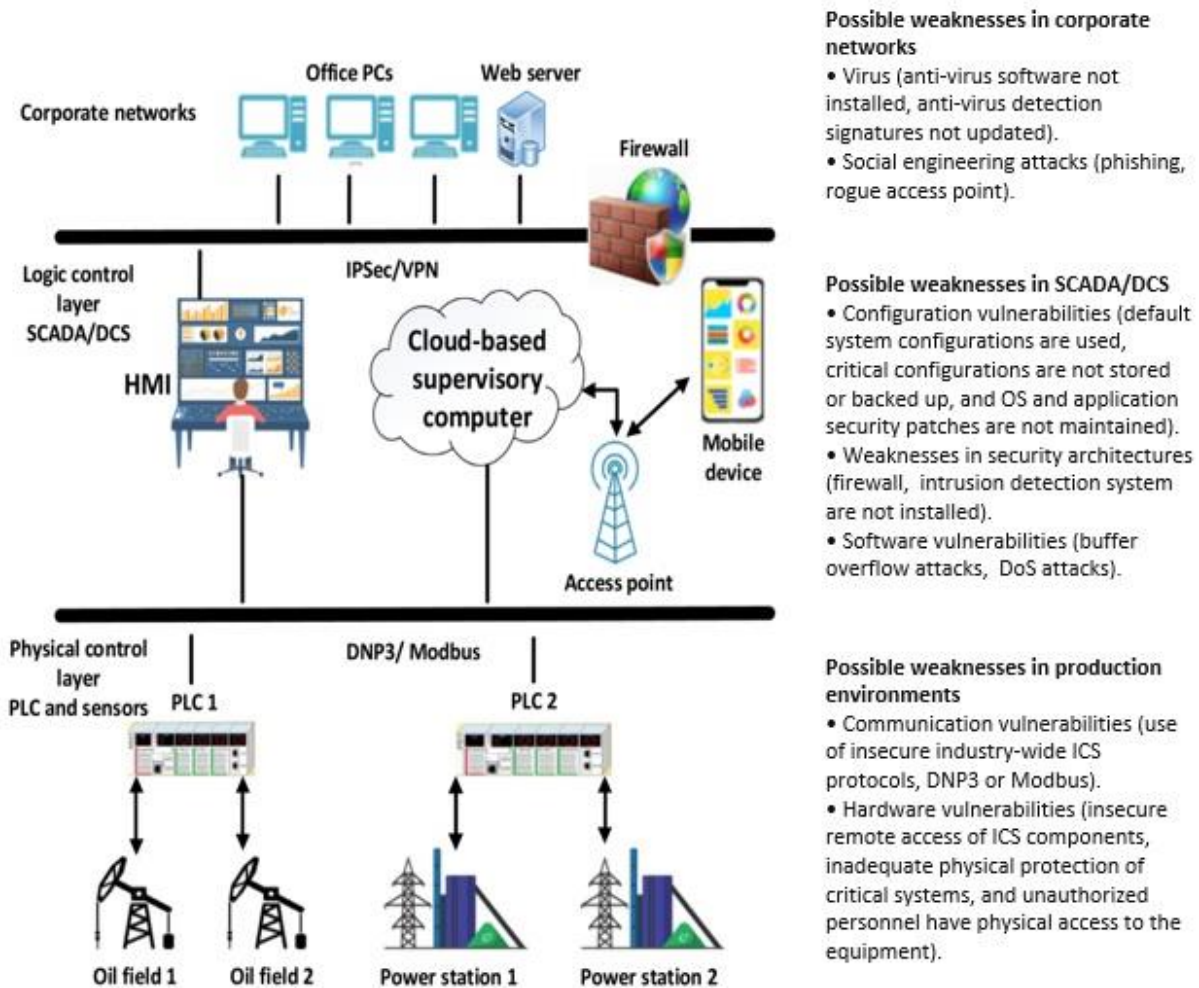


Figure 1. Illustration of overview of the ICS system cyber security [2]

2.2. Patch Management in ICS

Software patch usually represents a piece of code utilized with the objective of fixing, altering, or updating anything in the software. It is necessary not to confuse patches with updates or upgrades since patches are generally employed to deal with single problems, while updates frequently involve a number of patches and improvements, and upgrades usually present novel versions and characteristics.

The deceptive patch types are presented below:

Diverse Patch: Patch diversity deals with the monoculture issue caused by the available patching practices and may adversely influence resources utilized for development and exploitation. Due to the possibility of releasing multiple patches for a vulnerability, attackers should develop many exploits for every version of a patch to owe the potential for a widespread attack.

Faux Patch: A faux patch comprises fake patches for vulnerabilities not existing in the same sense, whereas a traditional patch comprises legitimate patches for existing vulnerabilities. A ghost patch is created by a faux patch when combined with a traditional patch. A faux patch is implemented in the best way to input validation vulnerabilities. In this way, we utilize deception to benefit from this frequently employed technique for the purpose of fixing the vulnerability type in question. Fake patches are similar to decoy passwords and decoy documents.

Obfuscated Patch: A legitimate vulnerability is fixed by an obfuscated patch, which is ideally designed to be infeasible for the purpose of reversing engineer and uncovering the underlying defect. The mentioned patches increase the effort required for the adversary to define the vulnerability being fixed by the patch. Since the said patches fix legitimate vulnerabilities, they change the program's semantics. The objective of the patches in

question is to confuse attackers as they perform exploit development by burying the actual vulnerable code in layers of the obfuscated patch code.

Active: An active response patch fixes the underlying vulnerability but responds to adversarial interaction as if the vulnerability is still present. In the interaction with an active response patch, attackers must, in ideal, be unable to find whether the remote system is patched or vulnerable. The primary aim of the mentioned patches is to impact attackers to make them believe in the success of their exploit, which will ensure that defenders monitor the actions of the adversary during their attack.

A security patch refers to a change in an asset to correct a weakness induced by a vulnerability. The objective of a security patch is preventing exploitation and mitigating threats to an asset. Hackers continuously develop novel techniques with the aim of breaking software and exploiting defects for the penetration of security measures.

Vulnerabilities and bugs in ICS software modules may lead to severe results. However, frequent patching of the said systems can cause mission-CI to be intolerably unavailable. The vulnerability trends in software considerably influence the process of discovery and subsequently trigger a patch deployment for suppressing the potential possibility of a breach.

A patch management program is centered on safe procurement, testing, and implementing the trusted patches to keep ICS more secure. It ensures that the ICS is up-to-date and safeguarded against malware and hackers. It is applicable to all hardware and software components of ICS, in both Information Technology (IT) and OT. Patches are required to assist in resolving security vulnerabilities and addressing functional problems. Table 1 represents Industrial Control System attacks.

Table 1. Industrial Control System Attack

Attack Ref	SRA	PM	CM	NS	SRP	OTD	EAS	ANHSF	SCM	A&T
Slammer [11]		•		•					•	•
Stuxnet [12]			•		•	•	•	•		
VPN Filter [13]		•				•				•
Black Energy [14]	•		•		•	•	•	•		•
NotPetya [15]		•	•	•	•	•	•	•		
Industroyer [16]					•	•	•	•		•
Steel Mill [17]										•
Triton [18]				•	•	•	•	•	•	
Shamoon [19]			•		•	•	•	•		•

SRA: Secure Remote Access, PM: Patch Management, CM: Credential Management, NS: Network Segmentation, SRP: Software Restriction Policies, OTD: Outbound Traffic Detection, EAS: Execution of Explicitly Allowed Software, ANHSF: Audit Network Hosts for Suspicious Files, SCM: Secure Configuration Management, A&T: Awareness and Training

3. PROPOSED MODEL

This study presents novel research, considering the possibility of strategic use of deception by defenders with the aim of introducing uncertainty into the adversary's perception of a system. In the current research, we concentrate on deceptive patches, in which standard software patches are designed for the purpose of limiting

the knowledge that an adversary can acquire about the underlying vulnerability.

This study demonstrates the feasibility of applying deception, in the form of fake patches, to ICS attacks. We believe that the approach in question, either as a stand-alone technique or in combination with other deceptive and detection methods, can cause an exponential increase in program analysis, making exploit generation on the

basis of patches a costly procedure while increasing the program runtime only at a minimal level.

3.1. Deceptive Patch Solutions for ICS Attacks

With the persistence of observed trends in ICS environments, attackers have scant motivation to adjust a set of Tactics, Techniques, and Procedures (TTPs) from currently successful behavior types. What is more important is that security suggestions and guidance should be expanded to involve fundamental detection and monitoring strategies, which are capable of identifying (or

blocking) fundamental behaviors related to available adversary TTPs. Policymakers and defenders should seek avenues with the aim of enhancing defense and response across the whole chain of events constituting and intrusion scenario. In this way, the response is provided at earlier stages, which minimize effects and protect crucial services. In this way, the response is provided at earlier stages, which minimize effects and protects crucial services. Figure 2-3 demonstrates an attack on corporate information system hosts.

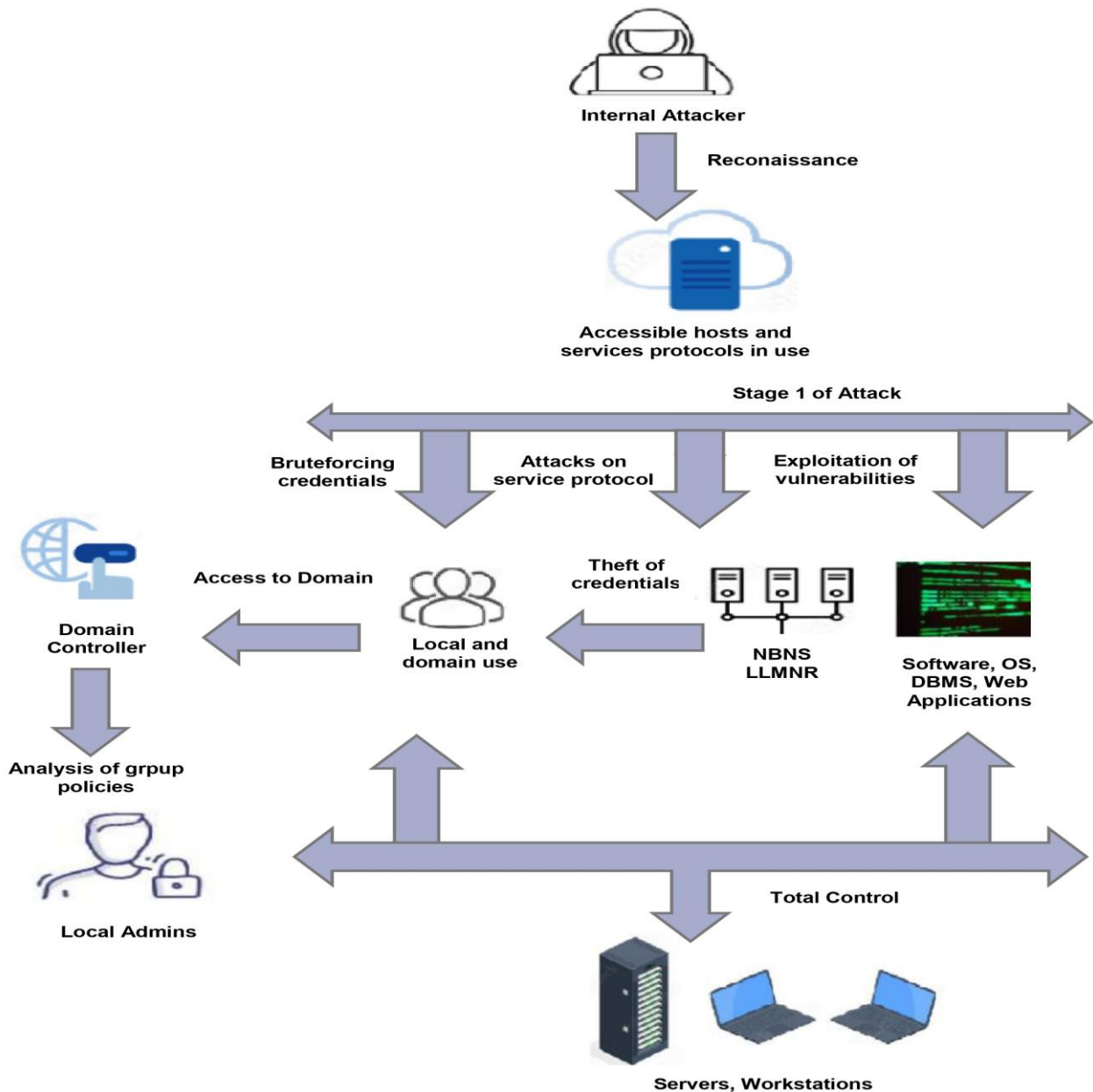


Figure 2. An attack on corporate information system hosts.

Deceptive patches have three general categories: faux patches that present a fix for a vulnerability not exist in reality, obfuscated patches that hide the vulnerability being dealt with, and active response patches that fix the vulnerability while trying to convince adversaries that the system remains unpatched. To analyze ICS attack-based security, we propose to present it based on all types of patch solutions.

In attack [11], a vulnerability in Microsoft SQL Server 2000 constituted the basis of the worm, which penetrated the network of the nuclear power plant through the laptop of a contractor connected to the facility's business network. The worm could access the monitoring system by leveraging incorrect network isolation and made it inaccessible because of the large traffic created.

Remediate Vulnerability; It is necessary to keep ICS isolated from the corporate network utilizing firewalls. While it is understood that there is no possibility for complete ICS isolation, a solution is to limit the number of entry points into the ICS from the corporate network and keep them monitored. It is recommended to update and perform maintenance checks on servers on a regular basis with the objective of reducing the probability of attacks. Following the mentioned event, the update of all Microsoft SQL servers' software in the power plant was updated, and patches were installed.

In attack [12], Stuxnet physically delivered a number of its first infections physically, in other words, through a USB flash drive. Thus, it tried to spread to other workstations in the target network through numerous alternative zero-day vulnerabilities, such as a) USB flash drives, b) the Windows Print Spooler service, c) network shares or the Server Service, and d) local privilege escalation.

Remediate Vulnerability; The attackers employed a workaround method with the aim of bypassing such solutions by infecting the personal computers of individuals with legitimate physical access to the plant's system of the plant. It is also necessary to monitor the physical components of the plant for the purpose of detecting an unusual behavior of a component in order to detect any compromise of the ICS of the plant in the shortest time. It is necessary to authenticate the control loops among the mentioned entities in a proper way and verify the results of their feedback loops.

The proposed deceptive patch solution is an active response patch. An active response patch fixes the underlying vulnerability and responds to adversarial interaction as if the vulnerability no longer exists (and possibly issues an intrusion notification). This type of patch presents deceptive data to attackers in real-time. In other words, data is statically or dynamically produced and introduced to attackers to impact their decision-making process. According to the non-interfering feature, faux patches must not change the program's semantics; the verify step will reveal that fake patches do not change the behavior of the program. In the interaction with an active response patch, attackers must, in ideal, be unable to find whether the remote system is patched or vulnerable. The exploitation of a vulnerability by active response patches, which respond to exploits using the same response as an unpatched program. The said masking will increase the resources required for dynamic analysis tools to recognize unpatched systems.

Attack [14] equipped adversaries with the toolset for the purpose of performing reconnaissance in IT and accessing

software, including VPN and remote access tools. With the above-mentioned access type, attackers can connect to the OT in a direct way and realize their malicious acts.

Remediate Vulnerability; In case of infecting the system with malware, there is a possibility of using decrypting tools to decrypt the Master File Table (MFT) with the aim of recovering files impacted by the attack. Performing the system's regular backups represents another good practice. If damage to the OS cannot be repaired, it is a possibility of reverting back to the version that has been previously saved version in a safe manner. It is possible to employ sandboxing technology for testing emails and documents entering the network and deploy proxy systems for the control of inbound and outbound communication paths. Strong authentication and encrypted communication are needed during remote access to ensure that attackers do not access ICS remotely.

Attack [15] represents a cryptoworm attack against MS Windows-based hosts. A defect in the company's patch update policies ensured that the attackers compromised certain servers. The modification of the malware was performed to utilize an open-source credential dumping tool, showing that user passwords are stored in the memory of the computer for the purpose of spreading across the network. It could be limited by performing frequent updates of the OS and establishing antimalware and antivirus utilities.

Remediate Vulnerability: In case of infecting the system by the malware, there is a possibility of using decrypting tools to decrypt the MFT with the aim of recovering files impacted by the attack. Performing the system's regular backups represents another good practice. If damage to the OS cannot be repaired, it is a possibility of reverting back to the version that has been previously saved version in a safe manner.

The proposed deceptive patch solution is a faux patch. A ghost patch is created by a faux patch when combined with a traditional patch. A faux patch is implemented in the best way to input validation vulnerabilities. In this way, we utilize deception to benefit from this frequently employed technique for the purpose of fixing the vulnerability type in question. Fake patches are similar to decoy passwords and decoy documents. Adding conditional and/or assertion statements to the code, which is capable of detecting invalid input, represents the conventional way to fix the said vulnerability type.

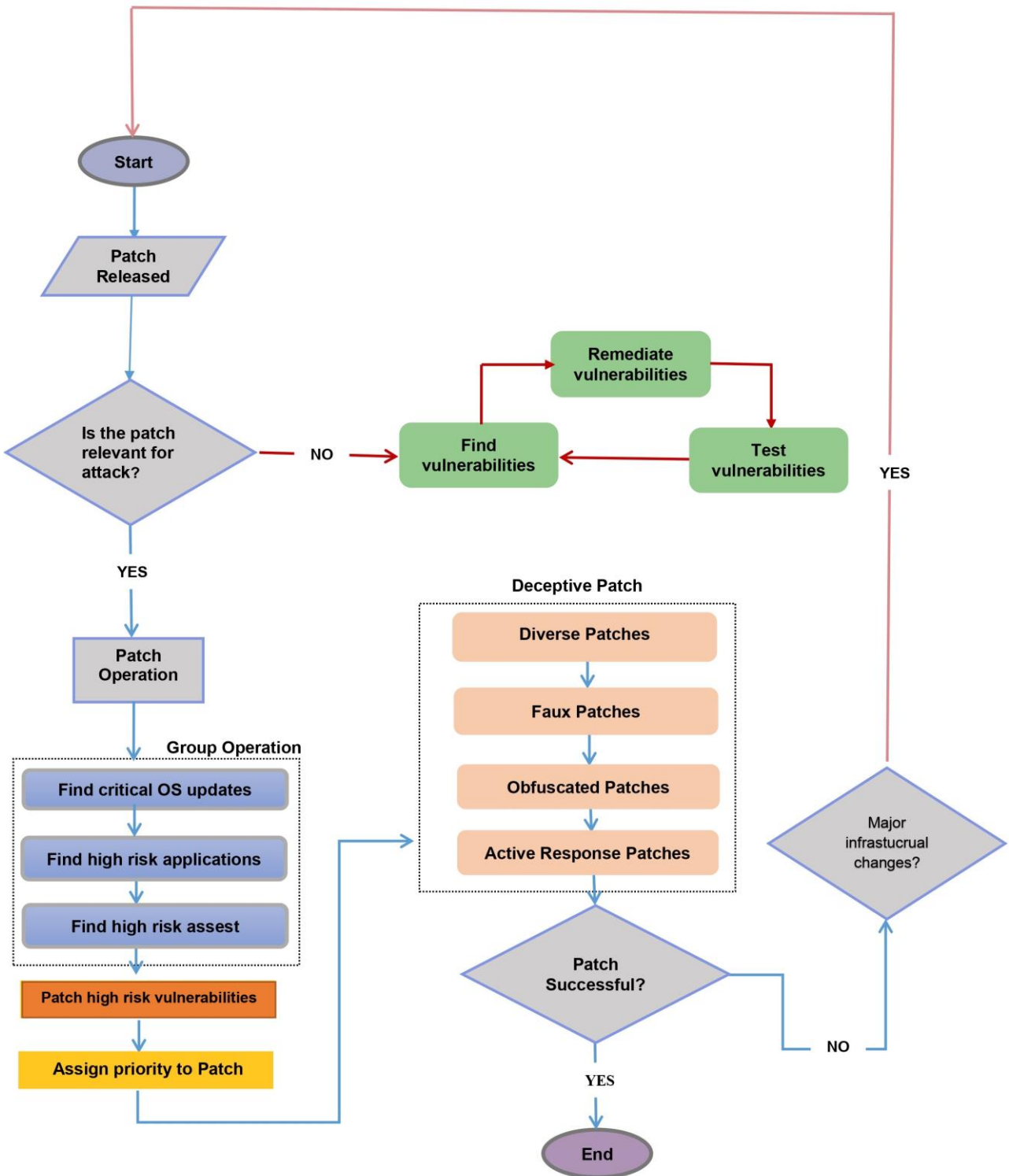


Figure 3. An attack on corporate information system hosts.

In attack [16], the attackers utilized a misconfiguration providing bidirectional data flow, with the objective of gaining a foothold on the ICS network. Industroyer performs scanning and prepares lists of all the OPC servers that the software provides. Moreover, it tries to alter the state of devices that are connected to the said OPC servers. The attackers exploited vulnerabilities targeting the devices of grid operations and network communications, infecting them via spear-phishing campaigns and the fundamental lack of security mechanisms for ICS protocols.

The proposed solution is a diverse patch. Patch diversity deals with the mono-culture issue caused by available patching practices and may adversely affect resources utilized for development and exploitation. Due to the possibility of releasing multiple patches for a vulnerability, attackers should develop many exploits for every version of a patch to owe the potential for a widespread attack. Implementing software diversity in patch development, using deceptive language in patch notifications, and re-releasing the said patches as novel updates may impact attackers by leading to uncertainty in the reconnaissance phase of their attack.

In attack [17], spear-phishing and social engineering tactics were employed by the attackers with the objective of accessing the business network. Thus, they established access to the OT network and could connect to individual control systems.

Remediate Vulnerability; Tools such as defense systems and firewalls must be utilized to protect interconnections between the OT network and the corporate network for the purpose of safeguarding against the above-mentioned intrusions. Additionally, it is necessary to minimize the number of connection interfaces between the corporate network and the OT network. In attack [18], the goal of the malware was to breach the controllers' safety mechanisms in the target facility. Pieces of evidence show that the attackers may have acquired access to the OT network almost a year prior to the incident. Due to a misconfigured firewall, the attackers gained a foothold on the target controller by utilizing a custom-made TRITON attack framework. Attack [19] represents malware aiming to render the computers in the target organizations unusable as a result of wiping their hard drives. The malware could carry out its acts because of the interconnected computers in the business network, stolen credentials, and the usage of a legitimate driver. Because the exchanged data between the OT and IT are utilized for the purpose of determining the requirements and procedures of the business, such terrible attacks on the IT network can deprive the ICS of high-level site operations, supporting the process of production in the OT.

The proposed deceptive patch solution is an obfuscated patch. Implementing polymorphic patches represents a solution to it. Randomization can be employed by ghost patches to create polymorphic patches, which can be distributed based on the basis of various heuristics (such as on the basis of region, OS version, or staggered by time). The non-deterministic characteristics of a polymorphic ghost patch can make exploit development more difficult since the same patch will not be implemented on every end system. In the above-mentioned situation, it will also be necessary to change the conventional patch for every patch instance for the purpose of preventing attackers using multiple instances of a patch to expose the legitimate vulnerability.

4. CONCLUSION

Industrial computer networks have recently been constantly exposed to cyberattacks. The detection and patch philosophy constitute the basis for numerous security solutions in the said area. A systematic approach toward managing and employing software patches may assist organizations in enhancing the general security of their IT systems in an inexpensive way. This study presented the first map for formally modeling the security of the suggested deceptive defense techniques for ICS. The proposed patch methodology is the first work on solutions for ICS software vulnerabilities using deceptive patch types in most common ICS attacks. This paper provided evidence indicating that the applied deceptive patch methodologies keep ICSs more secure.

Investigating and implementing deep learning to deception is a future research field that may have an enormous effect on the way of our defense.

Acknowledgement

This manuscript does not contain any studies with human participants carried out by any of the authors.

REFERENCES

- [1] Alladi T, Chamola V, Zeadally S. Industrial control systems: Cyberattack trends and countermeasures. *Computer Communications*. 2020; 155(22):1–9.
- [2] Asghar MR, Hu Q, Zeadally S. Cybersecurity in industrial control systems: Issues, technologies, and challenges. *Computer Networks*. 2019; (165):1389–1286.
- [3] Upadhyay D, Zaman M, Joshi R, Sampalli S. An efficient key management and multi-layered security framework for SCADA systems. *IEEE Transactions on Network and Service Management*. 2021; 19 (1): 642–660.
- [4] Mughaid A, Al-Zu'bi S, Al Arjan A, Al-Amrat R, Alajmi R, Zitar RA, et al. An intelligent cybersecurity system for detecting fake news on social media websites. *Soft Computing*. 2022; 26(12):5577–5591.
- [5] Mughaid A, AlZu'bi S, Alnajjar A, AbuElsoud E, Salhi SE, et al. Improved dropping attacks in 5G networks using machine learning and deep learning approaches. *Multimedia Tools and Applications*. 2022; 82(1): 1–23.
- [6] Idrissi OE, Mezrioui A, Belmekki A. Cybersecurity challenges and issues of industrial control systems—some security recommendations. *IEEE International Smart Cities Conference (ISC2)*. Casablanca: April; 2019. p. 330-335.
- [7] Yantz M. [Internet]. Importance of patch management to avoid business vulnerabilities; 2023 [cited 2023 March 13]. Available from: <https://itsupportguys.com/importance-of-patch-management-to-avoid-business-vulnerabilities>.
- [8] Hassani P. Implementing patch management process [dissertation]. School of Technology Degree Programme in Information and Communication Technology; 2020.
- [9] Koskenkorva H. The role of security patch management in vulnerability management [dissertation]. Finland: South-Eastern Finland University of Applied Sciences; 2021.
- [10] Söğüt E, Erdem OA. Endüstriyel kontrol sistemlerine (SCADA) yönelik siber terör saldırı analizi. *Politeknik Dergisi*. 2020; 23(2):557-566.
- [11] Holloway M. Slammer worm and David-Besse nuclear plant [Internet]; 2015 [cited 2022 April 12]. Available from: <http://large.stanford.edu/courses/2015/ph241/holloway2/>.
- [12] Nourian A, Madnick S. A systems theoretic approach to the security threats in cyber-physical systems applied to Stuxnet. *IEEE Transactions on*

- Dependable and Secure Computing. 2015;15 (1):2–13.
- [13] Largent W [Internet]. New VPNFilter malware targets at least 500k networking devices worldwide; 2018. [cited 2022 Jun 6]. Available from: <http://blog.talosintelligence.com/2018/05/VPNFilter.html>.
- [14] Xiang Y, Wang L, Liu N. Coordinated attacks on electric power systems in a cyber-physical environment. *Electric Power Systems Research*. 2017;149(6): 156–168.
- [15] Furnell S, Emm D. The ABC of ransomware protection, *Computer Fraud & Security*. 2017;(10):5–11.
- [16] Cherepanov [Internet]. A new threat for industrial control systems; 2021 [cited 10 August 2023]. Available from: <https://www.nae.edu/File.aspx?id=266340>.
- [17] Lee RM, Assante MJ, Conway T. German steel mill cyber attack. *Industrial Control Systems*. 2014;1-15.
- [18] Johnson B, Caban D, Krotofil M, Dan S, Brubaker N, Glyer C [Internet]. Attackers deploy new ics attack framework triton and cause operational disruption to critical infrastructure; 2023 [cited 2023 September 10]. Available from: <https://www.fireeye.com/blog/threat-research/2017/12/attackers-deploy-new-ics-attack-framework-triton.html>.
- [19] Symantec [Internet]. The shamoon attacks. [cited 2022 March 6]. Available from: <http://www.symantec.com/connect/blogs/shamoon-attacks>.
- [20] Panetta K. [Internet]. Gartner top 10 security projects for 2020-2021; 2021.[cited 2023 January 15]. Available from: <https://www.gartner.com/smarterwithgartner/gartner-top-security-projects-for-2020-2021/>
- [21] Olswang A, Gonda T, Puzis R, Shani G, Shapira B, Tractinsky N. Prioritizing vulnerability patches in large networks. *Expert Systems with Applications*.2022; 116467.
- [22] Corallo A, Lazoi M, Lezzi M, Luperto A. Cybersecurity awareness in the context of the Industrial Internet of Things: A systematic literature review. *Computers in Industry*. 2022; 137(4):1-16.
- [23] Bristow M, Sans A [Internet]. A SANS 2021 Survey: OT/ICS Cybersecurity. Survey; 2021. [cited 2023 Januray 15]. Available from: <https://www.sans.org/white-papers/SANS-2021-Survey-OTICS-Cybersecurity/>
- [24] Yang B, Zhang Y. Cybersecurity analysis of wind farm industrial control system based on hierarchical threat analysis model framework. *International Conference on Computing, Communication, Perception, and Quantum Technology, CCPQT 2022*. Xiamen: IEEE p. 6-13.

Investigation of Fourier Transform Infrared (FT-IR) Spectroscopy and Chemometric Analysis Method as an Alternative Method in the Diagnosis of Prostate Cancer

Yılmaz ŞAHİN^{1*} 

¹Atatürk University, Vocational School of Health Services, Department of Therapy and Rehabilitation, Erzurum, Turkey

Yılmaz ŞAHİN ORCID No: 0000-0003-2998-8879

*Corresponding author: yilmazsahin86@gmail.com

(Received: 21.11.2023, Accepted: 17.01.2024, Online Publication: 26.03.2024)

Keywords

FT-IR
Spectroscopy,
Prostate
cancer,
Diagnostic
methods,
Chemometric
Analysis

Abstract: Prostate cancer is one of the most common types of cancer in men. It usually grows slowly and may not show obvious symptoms at first. Prostate cancer can be diagnosed by symptoms or by a doctor performing certain tests during routine health checkups. These tests include physical examination, PSA (Prostate Specific Antigen) Test, biopsy, imaging techniques, and Gleason score. In addition, Fourier transform infrared spectroscopy (FT-IR) is an analysis method used for prostate cancer diagnosis. This study aims to demonstrate FT-IR spectroscopy as an alternative method to other diagnostic methods in the diagnosis of prostate cancer. The FT-IR spectroscopy method is used to examine the molecular structure of samples. For prostate cancer diagnosis, FT-IR spectroscopy can be used to identify molecular changes in prostate tissue and identify characteristics by which cancerous cells differ from healthy cells. FT-IR spectroscopy is based on spectral data obtained by exposing samples to infrared radiation. These spectral data are based on properties associated with the movements of the molecules contained in the samples, such as vibration, rotation and bending. Molecular changes caused by diseases such as prostate cancer may be evident in these spectral data. These changes can provide information about the presence or stage of cancerous cells. Data obtained using FT-IR spectroscopy is processed with statistical analysis methods. These analyses are used to identify molecular differences between cancerous and healthy prostate tissues. In this way, FTIR spectroscopy can help obtain sensitive and accurate results in the diagnosis of prostate cancer.

Prostat Kanseri Tanısında Alternatif Bir Yöntem Olarak Fourier Dönüşümlü Kızılötesi (FT-IR) Spektroskopisi ve Kemometrik Analiz Yönteminin İncelenmesi

Anahtar

Kelimeler

FT-IR
Spektroskopisi,
Prostat kanseri,
Teşhis
yöntemleri,
Kemometrik
Analiz

Öz: Prostat kanseri, erkeklerde en sık görülen kanser türlerinden biridir. Genellikle yavaş büyür ve ilk başlarda belirgin belirtiler göstermeyebilir. Prostat kanseri teşhisi, belirtiler veya rutin sağlık kontrolleri sırasında doktorun belirli testler yapmasıyla konulabilir. Bu testler; Fiziki muayene, PSA (Prostat Spesifik Antijen) Testi, biyopsi, görüntüleme teknikleri, gleason skorudur. Bunların yanısıra, Fourier dönüşümlü kızılötesi spektroskopisi (FT-IR), prostat kanseri teşhisi için kullanılan bir analiz yöntemidir. Bu çalışma da prostat kanseri teşhisinde diğer teşhis yöntemlerinde alternatif bir yöntem olarak FT-IR spektroskopisini göstermektedir. FT-IR spektroskopisi yöntemi, örneklerin moleküler yapısını incelemek için kullanılır. Prostat kanseri teşhisi için FT-IR spektroskopisi, prostat dokusundaki moleküler değişiklikleri belirlemek ve kanserli hücrelerin sağlıklı hücrelerden farklı olduğu özellikleri tespit etmek amacıyla kullanılabilir. FT-IR spektroskopisi, örneklerin infrared radyasyona maruz bırakılmasıyla elde edilen spektral verilere dayanır. Bu spektral veriler, örneklerin içerdiği moleküllerin vibrasyon, rotasyon ve bükülme gibi hareketleriyle ilişkilendirilmiş özelliklere dayanır. Prostat kanseri gibi hastalıkların neden olduğu moleküler değişiklikler, bu spektral verilerde belirgin olabilir. Bu değişiklikler, kanserli hücrelerin varlığı veya evresi hakkında bilgi verebilir. FT-IR spektroskopisi kullanılarak elde edilen veriler, istatistiksel analiz yöntemleriyle işlenir. Bu analizler, kanserli ve sağlıklı prostat dokuları arasındaki moleküler farkları belirlemek için kullanılır. Bu şekilde, prostat kanserinin teşhisinde FTIR spektroskopisi hassas ve doğru sonuçlar elde etmeye yardımcı olabilir.

1. INTRODUCTION

Prostate cancer is the second most common type of cancer among men in the world and is estimated to be the sixth most common cause of cancer-related deaths. Although imaging techniques are advancing today, digital rectal examination (DRM), prostate-specific antigen (PSA) and biopsy indication remain the basic methods for diagnosing prostate cancer [1]. Prostate cancer usually does not cause symptoms in the early stages. Still, in later stages, it may cause symptoms such as frequent urination, pain in the pelvis, difficulty urinating, and blood in the urine. Imaging methods such as positron emission tomography (PET), computed tomography (CT) and magnetic resonance imaging (MRI) are essential methods used today for the advanced diagnosis of prostate cancer [2]. With these imaging methods, it may be difficult to precisely determine the location and boundaries of prostate cancer due to the limitations of a single imaging method, such as insufficient resolution and sensitivity. For this reason, combining more than one imaging method for accurate and definitive diagnosis may sometimes be necessary [3], [4]. FTIR spectroscopy is an essential alternative for many clinical applications, from cancer screening, diagnosis and evaluation of response to treatment to continuous monitoring of disease progression or regression [5]. As with other types of cancer, it is essential to diagnose prostate cancer quickly, cheaply and accurately. Therefore, FT-IR spectroscopy is used as an auxiliary diagnostic method in the diagnosis of prostate cancer, showing high specificity and accuracy. This study aims to show that FT-IR spectroscopy can be used as an alternative method to existing imaging methods in the diagnosis of prostate cancer.

2. MATERIAL AND METHOD

2.1. Fourier Transform Infrared (FT-IR) Spectroscopy

Accurate classification and staging of cancer is one of the most essential uses of FTIR spectroscopy [5]. FTIR spectroscopy is a technique that has been used for many years to analyze chemical components. This infrared spectroscopy has significantly increased its capacity to analyze residual types of biological samples in recent years. Figure 1 shows the FT-IR spectroscopy device. The reason for such approaches is the lack of methods with high sensitivity and specificity for early cancer diagnosis. FT-IR spectroscopy is a technique that examines vibrations at the molecular level. Here, functional groups are associated with characteristic infrared absorption bands corresponding to the fundamental vibration bands of these functional groups [6]. This spectroscopic method allows us to investigate the vibrational properties of amino acids and cofactors sensitive to minimal structural changes. The spectrum of each molecule varies depending on the wavelength and amount of infrared radiation it absorbs. Therefore, the studied sample's absorbance peaks for the multiplex parameters of the lipidome, proteome, metabolome, and genome produce a signature fingerprint. These

biochemical fingerprints are specific to the molecular changes of different diseases and contain essential information in diagnosing each disease. Since biological materials absorb in the mid-IR region (400-4000 cm^{-1}), amide I is the spectral fingerprint region measured to examine these samples (1700-1500 cm^{-1}). The higher wavelength region (3500-2550 cm^{-1}) is associated with stretching vibrations, including C-H, O-H, N-H, and S-H. Low wavelength regions are generally associated with bending and carbon skeleton fingerprint vibrations [7]. Figure 2 shows typical FT-IR spectra of biomolecules and relevant functional groups in biofluids at 3000-800 cm^{-1} wavelengths. In summary, the vibrational frequencies of a particular chemical group are expected to be in certain regions depending on the type of atoms involved and the type of chemical bonds. Tables are available for amino acid side chains and the main chemical groups. One of the most essential advantages of IR spectroscopy is that it offers the opportunity to study solid, liquid, gas, powder and fiber materials with appropriate preparation. With IR spectroscopy, successful results have been obtained by examining proteins, peptides, lipids, biomembranes, carbohydrates, pharmaceuticals, foodstuffs, and plant and animal tissues. One of the most essential advantages of IR spectroscopy is that it offers the opportunity to study solid, liquid, gas, powder and fiber materials with appropriate preparation. With IR spectroscopy, successful results have been obtained by examining proteins, peptides, lipids, biomembranes, carbohydrates, pharmaceuticals, foodstuffs, and plant and animal tissues [8].



Figure 1. FTIR Spectroscopy Device

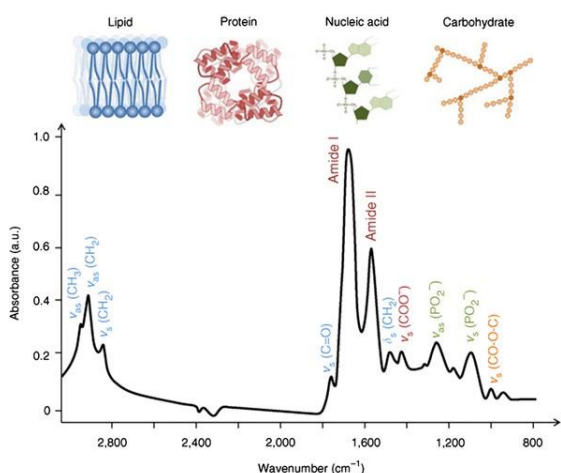


Figure 2. Typical FT-IR spectra of biomolecules and relevant functional groups in biofluids at wavelengths of 3000–800 cm^{-1} [7]

2.2. Chemometric Analysis

As in many fields, multivariate statistical clustering and classification methods are used to analyze spectroscopic data. Multivariate statistical methods try to optimize the use of studies involving more than one measured variable [9]. Since large-scale data generated by spectroscopy-based methods sometimes make it challenging to perform practical analysis with known spectral analysis methods, multivariate chemometric analyses are needed, especially in distinguishing between groups and determining specific spectral biomarkers. One chemometric analysis technique is Principal Component Analysis (PCA). This transformation technique reduces the dimensions of a data set containing many interrelated variables to fewer dimensions while preserving the variance in the data as much as possible. This technique has been combined with portable FT-IR spectroscopy for cancer diagnosis [10] and many cancers as its yield [11] has been noted. PCA can also be used for clustering. Another chemometric analysis technique is hierarchical cluster analysis (HCA). When deciding which clusters should be combined in studies, there must be a similarity measure between data sets. PCA can distinguish these similar variables, but it may not always make a good distinction. This analysis technique mainly aims to group groups based on their characteristic features [11], [12]. This critical analysis technique, developed to improve the noninvasive diagnosis of brain tumors, can provide information from which the relative position and distribution in feature space of selected tumor classes can be calculated from magnetic resonance imaging and spectroscopy data. For example, Figure 3 displays the information obtained with the help of chemometric analysis using magnetic resonance images and spectroscopy in brain tumor classification [12]. In another study where chemometric analysis methods were applied, serum samples taken from nearly 100 prostate cancer patients were examined. The infrared spectrum of serum from these samples, as seen in Figure 4, provided valuable information about biomolecules such as structure, functional groups, bond types and their interactions. Prostate volume, density, etc. Another

method used to diagnose prostate cancer early using features is the Support Vector Machine (SVM) algorithm [13]. SVM is used in pre-processing the Prostate cancer dataset to reduce inhomogeneous distributions in the dataset [14]. Rustam et al. In a study conducted by SVM, it was concluded that SVM was better at classifying prostate cancer data, especially in terms of accuracy. It has also been stated that this method shows promise in allowing healthcare personnel to classify diseases or other medical conditions easily [15].

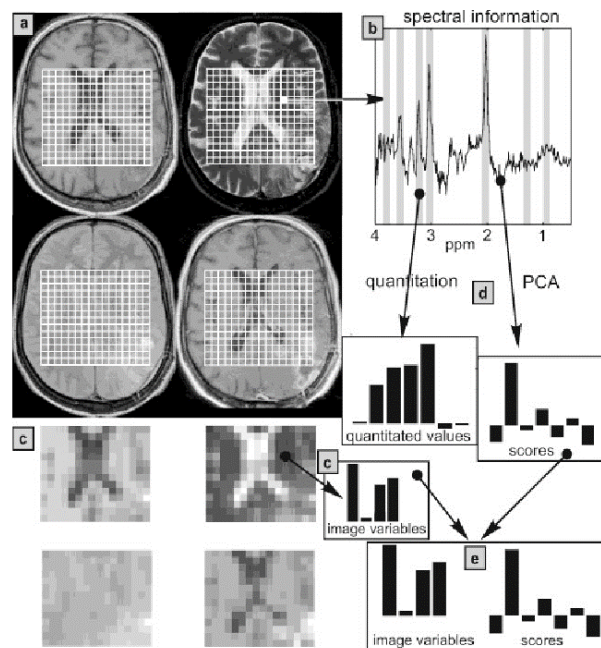


Figure 3. Data processing and data analysis on magnetic resonance images [16].

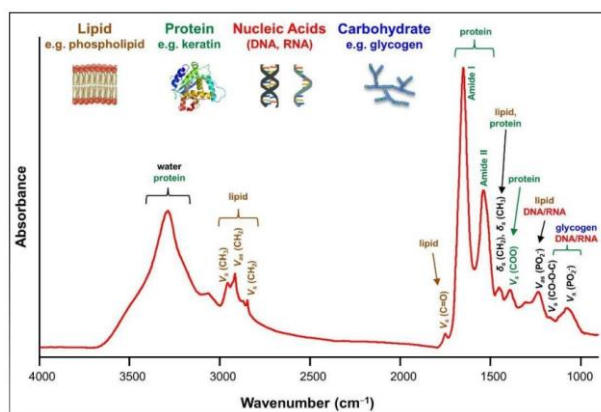


Figure 4. Bond structures corresponding to infrared (FTIR) bands and spectral regions obtained from blood sera from prostate cancer patients [17]

3. RESULTS

In cancer diagnosis, the sensitivity and specificity of biomarkers currently used to detect the disease are generally low. For example, the prostate-specific antigen (PSA) test detects prostate cancer. Although the specificity of this test is as high as approximately 87-95%, its sensitivity is much lower, ranging from 33-59% [14]. FT-IR spectroscopy can distinguish cancer samples from non-cancers with high sensitivity, specificity, and accuracy. Therefore, it can be used as a prospective new

diagnostic method for many different types of cancer. In his study on ten prostate cancer tissues and ten healthy tissues, Albayrak used orthogonal partial minimum analysis, an advanced form of principal component analysis (PCA), to determine the behavior of these 20 samples against infrared light between 50–4000 cm^{-1} applied squares analysis (Orthogonal Partial Least Square, O-PLS) algorithm. He performed O-PLS analysis to distinguish cancerous and healthy cells. The sensitivity and specificity of the proposed method were found to be very high with the help of the Orthogonal Signal Correction (OSC) pre-processing way, thus showing that the FT-IR method could be an alternative method for prostate cancer diagnosis from paraffin blocks [15]. Baker et al. They used 40 prostate cancer tissue biopsy samples obtained as paraffin-embedded blocks from 39 male patient [16]. Serial sections of 10-micron thickness were collected from each sample. Infrared rays were applied to malignant samples of hematoxylin and eosin (H&E) sections. As a result, overall sensitivity and specificity rates of 92.3% and 98.9%, respectively, were recorded [18]. Their results also show that, for the first time, a system based on two-band criteria identifies features that distinguish tumors that are clinically confined to the prostate from those that are clinically invasive. These findings are essential in developing better prostate cancer diagnosis, prognosis, and treatment planning techniques [19]. For example, when defining the tumor volume in patients receiving radiotherapy treatment, determining the border of the clinical target volume (CTV) in the tissue is also crucial regarding possible reactions [20]. FTIR spectroscopy appears promising as an alternative clinical tool to other diagnostic tools in cancer diagnosis. It is a label-free, non-invasive, non-destructive, fast and objective technology for prostate cancer diagnosis and beyond. FTIR spectroscopy provides essential information about the origin and progression of the disease based on biochemical changes in the preliminary diagnosis of the disease. FTIR analysis of urine samples combined with a multivariate (PCA) model (Figure 5) of a simple, rapid, accurate, inexpensive, noninvasive method may be a potential noninvasive alternative for cases where the results of PSA testing are unstable.

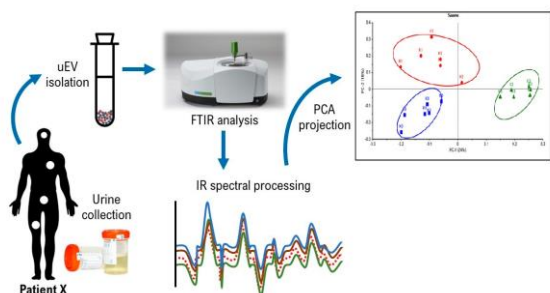


Figure 5. Propose workflow for FTIR analysis and derivation of diagnostic classifier for prostate cancer detection using PCA score plot [21].

Variability from patient to patient, tissue to tissue, and even cell to cell must also be taken into account. Therefore, it isn't easy to access relevant information.

This situation has been implemented and adapted in many techniques.

4. DISCUSSION AND CONCLUSION

The importance of spectral analysis is becoming more important day by day. Especially considering the impact of the results obtained in medical diagnoses, the combination of spectral analysis and data processing must give the "right answer". However, sometimes it can be impossible to find the right answer in real life. Therefore, complex simulated data sets containing measurement artifacts, sample-to-sample variability, and instrumental variability can be critical in validating and optimizing data analysis techniques. Optimized spectroscopic technologies and analysis techniques are essential for disease diagnosis and beyond.

REFERENCES

- [1] M. Bilal, A. Javaid, F. Amjad, T. A. Youssif, and S. Afzal, "An overview of prostate cancer (PCa) diagnosis: Potential role of miRNAs," *Transl. Oncol.*, vol. 26, p. 101542, Dec. 2022, doi: 10.1016/j.tranon.2022.101542.
- [2] T. T. Wheeler, P. Cao, M. D. Ghouri, T. Ji, G. Nie, and Y. Zhao, "Nanotechnological strategies for prostate cancer imaging and diagnosis," *Sci. China Chem.*, vol. 65, no. 8, pp. 1498–1514, Aug. 2022, doi: 10.1007/s11426-022-1271-0.
- [3] W. Hou et al., "Nanoparticles for multi-modality cancer diagnosis: Simple protocol for self-assembly of gold nanoclusters mediated by gadolinium ions," *Biomaterials*, vol. 120, pp. 103–114, Mar. 2017, doi: 10.1016/j.biomaterials.2016.12.027.
- [4] B. Shi et al., "Multifunctional gap-enhanced Raman tags for preoperative and intraoperative cancer imaging," *Acta Biomater.*, vol. 104, pp. 210–220, Mar. 2020, doi: 10.1016/j.actbio.2020.01.006.
- [5] K.-Y. Su and W.-L. Lee, "Fourier Transform Infrared Spectroscopy as a Cancer Screening and Diagnostic Tool: A Review and Prospects," *Cancers (Basel)*, vol. 12, no. 1, p. 115, Jan. 2020, doi: 10.3390/cancers12010115.
- [6] K. M. G. Lima, K. B. Gajjar, P. L. Martin-Hirsch, and F. L. Martin, "Segregation of ovarian cancer stage exploiting spectral biomarkers derived from blood plasma or serum analysis: ATR-FTIR spectroscopy coupled with variable selection methods," *Biotechnol. Prog.*, vol. 31, no. 3, pp. 832–839, May 2015, doi: 10.1002/btpr.2084.
- [7] M. J. Walsh et al., "FTIR Microspectroscopy Coupled with Two-Class Discrimination Segregates Markers Responsible for Inter- and Intra-Category Variance in Exfoliative Cervical Cytology," *Biomark. Insights*, vol. 3, p. BMI.S592, Jan. 2008, doi: 10.4137/BMI.S592.
- [8] Çırak Olgun, "Yıldız Teknik Üniversitesi Fen Bilimleri Enstitüsü Fourier Transform İnfrared Spektroskopisi (FT-IR) İle Sütte Tür Tayini Yapılması," 2017. Accessed: Dec. 26, 2023. [Online]. Available: chrome-

- extension://efaidnbmnnnibpcajpcgglefindmkaj/http s://food.yildiz.edu.tr/media/files/25(4).pdf
- [9] M. J. Baker et al., "Using Fourier transform IR spectroscopy to analyze biological materials," *Nat. Protoc.*, vol. 9, no. 8, pp. 1771–1791, Aug. 2014, doi: 10.1038/nprot.2014.110.
- [10] W. J. Zheng Y, Xiao M, Jiang S, Ding F, "Coating fabrics with gold nanorods for colouring, UV-protection, and antibacterial functions," *Nanoscale*, vol. 5:788, p. 95, 1951.
- [11] L. Wang and B. Mizaikoff, "Application of multivariate data-analysis techniques to biomedical diagnostics based on mid-infrared spectroscopy," *Anal. Bioanal. Chem.*, vol. 391, no. 5, pp. 1641–1654, Jul. 2008, doi: 10.1007/s00216-008-1989-9.
- [12] M. ALBAYRAK, "Fourier Dönüşümlü Kızılötesi Spektroskopisinin Prostat Kanseri Teşhisinde Kullanılabilirliğinin Araştırılması," *Iğdır Üniversitesi Fen Bilim. Enstitüsü Derg.*, vol. 8, no. 4, pp. 223–227, Jun. 2018.
- [13] M. Çınar, M. Engin, E. Z. Engin, and Y. Ziya Ateşçi, "Early prostate cancer diagnosis by using artificial neural networks and support vector machines," *Expert Syst. Appl.*, vol. 36, no. 3, pp. 6357–6361, Apr. 2009, doi: 10.1016/j.eswa.2008.08.010.
- [14] B. A. Akinnuwesi et al., "Application of support vector machine algorithm for early differential diagnosis of prostate cancer," *Data Sci. Manag.*, vol. 6, no. 1, pp. 1–12, Mar. 2023, doi: 10.1016/j.dsm.2022.10.001.
- [15] Z. Rustam and N. Angie, "Prostate Cancer Classification Using Random Forest and Support Vector Machines," *J. Phys. Conf. Ser.*, vol. 1752, no. 1, p. 012043, Feb. 2021, doi: 10.1088/1742-6596/1752/1/012043.
- [16] A. W. Simonetti, W. J. Melssen, M. van der Graaf, G. J. Postma, A. Heerschap, and L. M. C. Buydens, "A Chemometric Approach for Brain Tumor Classification Using Magnetic Resonance Imaging and Spectroscopy," *Anal. Chem.*, vol. 75, no. 20, pp. 5352–5361, Oct. 2003, doi: 10.1021/ac034541t.
- [17] "Prostate Cancer Serum Spectra as Indicators of Early Diagnosis Using FTIR-ATR Fourier Transform Infrared Spectroscopy," *J. Pharm. Negat. Results*, vol. 13, no. SO3, Jan. 2022, doi: 10.47750/pnr.2022.13.S03.126.
- [18] B. Holmstrom, M. Johansson, A. Bergh, U.-H. Stenman, G. Hallmans, and P. Stattin, "Prostate specific antigen for early detection of prostate cancer: longitudinal study," *BMJ*, vol. 339, no. sep24 1, pp. b3537–b3537, Sep. 2009, doi: 10.1136/bmj.b3537.
- [19] M. J. Baker, E. Gazi, M. D. Brown, J. H. Shanks, P. Gardner, and N. W. Clarke, "FTIR-based spectroscopic analysis in the identification of clinically aggressive prostate cancer," *Br. J. Cancer*, vol. 99, no. 11, pp. 1859–1866, Dec. 2008, doi: 10.1038/sj.bjc.6604753.
- [20] O. V. Gul and M. Duzova, "Effect of different CTV shrinkage and skin flash margins on skin dose for left chest wall IMRT: A dosimetric study," *Radiat. Phys. Chem.*, vol. 216, p. 111445, Mar. 2024, doi: 10.1016/j.radphyschem.2023.111445.
- [21] X.-L. Yap, B. Wood, T.-A. Ong, J. Lim, B.-H. Goh, and W.-L. Lee, "Detection of Prostate Cancer via IR Spectroscopic Analysis of Urinary Extracellular Vesicles: A Pilot Study," *Membranes (Basel)*, vol. 11, no. 8, p. 591, Jul. 2021, doi: 10.3390/membranes11080591.

Green Supplier Assessment with Fuzzy Expert System Approach

Çağatay TEKE^{1*} 

¹Bayburt University, Engineering Faculty, Industrial Engineering Department, Bayburt, Türkiye
Çağatay TEKE ORCID No: 0000-0002-6975-8544

*Corresponding author: cagatayteke@bayburt.edu.tr

(Received: 28.08.2023, Accepted: 23.01.2024, Online Publication: 26.03.2024)

Keywords

Fuzzy expert system,
Green supplier,
Green supplier assessment,
Green supply chain management

Abstract: Today, reasons such as increasing pollution on a global extent and limited raw material resources are increasing the interest in green supply chain management (GSCM). GSCM includes the processes starting from the very beginning of the production process of a product, completing the production, delivering the product to the customer, and recycling the product at the end of its useful life. Its main purpose is to eliminate or minimize the damages caused to the environment in all of these processes. In order to achieve this goal, it has great importance to assess the suppliers, which are one of the most important components of the production process, in terms of becoming a green supplier.

In this study, a fuzzy expert system model has been developed to assess the green suppliers based on green production technology, environmental management system, pollution control, product cost, quality, and lead time criteria. To test the performance of the developed model, 32 different suppliers were assessed with this model and the green supplier score was calculated. Also, Mean Square Error (MSE) and coefficient of determination (R^2) have been calculated to measure the performance of the developed model. While the MSE value was found to be 0.0481, the R^2 value was 0.9999. These values show that the green supplier assessment performance of the developed model is quite high.

40

Bulanık Uzman Sistem Yaklaşımı ile Yeşil Tedarikçi Değerlendirmesi

Anahtar Kelimeler

Bulanık uzman sistem,
Yeşil tedarikçi,
Yeşil tedarikçi değerlendirme,
Yeşil tedarik zinciri yönetimi

Öz: Günümüzde küresel ölçekte artan kirlilik ve sınırlı hammadde kaynakları gibi nedenler, yeşil tedarik zinciri yönetimine (YTZY) olan ilgiyi artırmaktadır. YTZY, bir ürünün üretim sürecinin en başından başlayarak, üretiminin tamamlanması, ürünün müşteriye teslim edilmesi ve kullanım ömrü sonunda ürünün geri dönüştürülmesine kadar olan süreçleri kapsamaktadır. Temel amacı, tüm bu süreçlerde çevreye verilen zararları ortadan kaldırmak veya en aza indirmektir. Bu hedefe ulaşmak için üretim sürecinin en önemli bileşenlerinden biri olan tedarikçilerin yeşil tedarikçi olma açısından değerlendirilmesi büyük önem taşımaktadır.

Bu çalışmada, yeşil üretim teknolojisi, çevre yönetim sistemi, kirlilik kontrolü, ürün maliyeti, kalite ve teslim süresi kriterlerine dayalı olarak yeşil tedarikçilerin değerlendirilmesi için bulanık bir uzman sistem modeli geliştirilmiştir. Geliştirilen modelin performansını test etmek amacıyla 32 farklı tedarikçi bu modelle değerlendirilmiş ve yeşil tedarikçi puanı hesaplanmıştır. Ayrıca, geliştirilen modelin performansını ölçmek için Ortalama Karesel Hata (MSE) ve belirlilik katsayısı (R^2) hesaplanmıştır. MSE değeri 0,0481, R^2 değeri ise 0,9999 olarak elde edilmiştir. Hesaplanan bu değerler, geliştirilen modelin yeşil tedarikçi değerlendirme performansının oldukça yüksek olduğunu göstermektedir.

1. INTRODUCTION

Supply chain management (SCM) can be considered as integrating planning, implementation, and control

activities related to the flow of information, services, and materials with a strategic approach in the process from raw materials to finished products in the production process. SCM plays a key role in increasing operational

efficiency in the enterprise. By eliminating unnecessary operations, cost minimization will be ensured and time loss will be prevented. Thus, it will be possible for the enterprise to direct its relevant resources to other areas [1].

When SCM is mentioned, supply chain and supplier concepts come to mind. Supplier is the name given to the external organizations in which the products to be offered to the last users of the enterprise are supplied by purchasing the raw materials or materials used in the production process in the production enterprises. The supply chain, on the other hand, is the process of purchasing and shipping the raw materials of the product desired to be produced in the production enterprises from the supplier and finally entering the warehouse of the enterprise.

Green Supply Chain Management (GSCM) has garnered a great deal of attention with increasing pressures on environmental sustainability. Instead of focusing on products, services, and intra-business organizational activities, the focus has shifted to life cycle analysis, supply chains, and extended producer responsibility. GSCM can be defined in several ways. Most of these definitions depend on the practitioner's or researcher's perspective. This perspective is similar to describing supply chain management in general [2]. GSCM can be defined as integrating environmental thinking into supply chain management, which includes product design, material sourcing, material selection, manufacturing processes, delivery of products to final consumers, and end-of-life management of products. That is, it obliges to include the idea of the environment as a whole in every stage of the product and service [3].

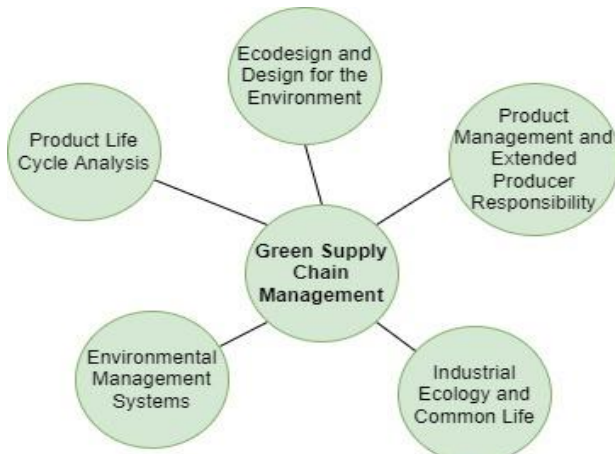


Figure 1. The main corporate, commercial, and technical factors affecting green supply chain management [2]

If we examine the concept of a green supply chain, it aims to reduce environmental degradation through the adoption of green practices in business processes. Air pollution and water pollution can be given as examples of these environmental distortions. It can reduce environmental pollution and production costs, and at the same time promote economic growth. In addition, it can create a competitive advantage with greater customer satisfaction and provide better opportunities for the

enterprise to export its products to environmentally friendly countries [4]. On the other hand, a green supplier can be defined as an external actor in the production process that supplies the raw materials needed by an enterprise in the production process in accordance with the factors in the production environment and environmental standards [5].

The rest of this study has the following structure; Section 2 provides the literature review of the related article. Section 3 proposes a fuzzy expert system model. Section 4 presents the results and discussion. In the final section, the gains obtained through the study were evaluated in a general framework.

2. LITERATURE REVIEW

When the literature is examined, there are many studies on the selection of green suppliers. For example, Daldır and Tosun [6] used multi-criteria decision-making techniques for the selection of green suppliers in their study. Specified criteria for green supplier selection have been identified as green storage, green recycling, green production capacity, green packaging, resource consumption, pollution control, product cost, lead time, error rate, warranty policies, and environmental competencies and documents. Fuzzy analytical hierarchy process (FAHP), one of the multi-criteria decision-making techniques, was used to determine the criterion weights. Within the framework of the existing criteria, five suppliers were evaluated and the Fuzzy WASPAS method was used to select the most suitable green supplier.

Denizhan et al. [7] conducted a study to select the most suitable green supplier. Three alternative suppliers were examined using FAHP and AHP methods, and the most appropriate green supplier selection application was carried out. Within the scope of the study, six main criteria were determined as quality, cost, delivery, service, technical criteria, and green criteria. Four different results were obtained after the application. The first of these is the selection of the most suitable supplier using the FAHP method, and the second is the selection of the most suitable green supplier using the FAHP method. Then, the most appropriate supplier selection and the most appropriate green supplier selection were carried out using the AHP method.

In the study conducted by Çınar and Uygun [8], the criteria of quality conformity, green product design, green purchasing, green production, and environmental management system were based and the intuitive FAHP method, which is one of the multi-criteria decision-making techniques, was used. Three different alternative suppliers were examined and the most suitable one among them was tried to be determined.

Şişman [9] made the selection and assessment of green supplier development programs. In this context, the criteria that will enable the assessment of green supplier development programs with the nominal group technique have been determined first. The specified criteria were

determined as cost, manufacturing output, resource use, quality, technology, environmental design, environmental management system, green image, green purchasing, reverse logistics, manufacturing and use. Then, the fuzzy MOORA method, one of the multi-criteria decision-making techniques, was used to rank and assess alternative programs.

Çalık [10] carried out an application to select the best green supplier among five alternative suppliers by using fuzzy multi-objective linear programming and interval type 2 FAHP method. Within the scope of the study, a manufacturing manager, an academician, and an industrial engineer were first selected and this three-person committee determined the five criteria to be used in practice. These criteria are cost, late delivery, carbon dioxide emission, pollution generation, and the use of environmentally friendly materials. In order to determine the weights of the criteria, interval type 2 FAHP method was used. In the ranking of alternative green suppliers, fuzzy multi-purpose linear programming method was used.

Akın [11] addressed the green supplier selection problem and used the generalized trapezoidal fuzzy flexible sets method to solve this problem. The green supplier selection problem has four criteria and these are service level, quality, price, and environmental management systems. There are a total of eleven suppliers assessed within the scope of the study, of which three are palm oil suppliers, three are sunflower oil suppliers, four are olive oil suppliers and one is a soybean oil supplier. While choosing the best green supplier, it was decided to determine the most suitable supplier for each oil type.

Erbıyık et al. [12] carried out the most appropriate green supplier selection application in the automotive industry by using the Electre method in their study. The criteria for the selection of green suppliers are determined as quality competencies, engineering competencies, green logistics management, cost performance, and management strategies. The SWARA method was used to determine the weights of the criteria. Three alternative suppliers were ranked using the Electre method.

Soyer and Türkay [13] made an application in the white goods industry within the scope of their study. The subject of the application is the selection of green suppliers and the criteria have been determined first in order to make the selection of green suppliers. These criteria are green competencies, environmental effectiveness, organizational factors, costs, and green image. The criteria were determined by a team of fourteen experts, which includes four production managers, one purchasing manager, four quality specialists, four production staff, and one purchasing specialist. The Analytical Network Process (ANP) method was used both in determining the weights of the criteria and in assessing the two alternatives.

Yerlikaya et al. [14] discussed the supplier selection problem based on environmental waste criteria in their study. The problem consists of four alternative suppliers

and five criteria. These criteria are the cost, the percentage of returns, the proportion of chemical waste, the demand, and the percentage of delay in delivery. The entropy method was used to determine the weights of the criteria. In order to determine how much purchase will be made from each supplier, a fuzzy multi-purpose linear programming approach was used.

Çalık [15] conducted a study on the implementation of green supplier selection in the food industry. Nine criteria have been determined within the scope of the application and these criteria are the ratio of cost to price, quality, delivery, technology ability, environmental management system, pollution control, environmental ability, air emissions, and energy consumption. The best worst method, entropy method, and CRITICAL method were used to obtain the criterion weights. The five alternative suppliers were ranked using the COPRAS, WASPAS, and MABAC methods.

Madenöglü [16] discussed the problem of green supplier selection for a business that produces furniture. The relevant problem includes five criteria and three suppliers. The criteria are determined as cost, quality, delivery, technical and green criteria. The Fuzzy SWARA method was used to determine the weights of the criteria. In the ranking of suppliers, fuzzy TOPSIS, fuzzy VIKOR, fuzzy gray relational analysis, and fuzzy ARAS methods were used. A green supplier ranking was performed with each of these methods, and the most suitable supplier turned out to be the same in all four methods.

Lee et al. [17] developed a model for green supplier selection. Firstly, the criteria for the selection of classical suppliers and green suppliers were differentiated using the Delphi method, and the criteria for the selection of green suppliers were determined. These criteria are quality, technology compatibility, total product life cycle cost, green image, pollution control, environmental management, green production, and green competition. For the selection of the most suitable green supplier, the fuzzy extended AHP method was used.

Hashemi et al. [18] proposes a model for selecting green suppliers. While the proposed model uses the ANP approach to determine the criterion weights, it uses the gray relational analysis method in the supplier selection phase. To illustrate how the model works, an exemplary problem in the automotive industry is considered. In addition, the criteria determined for the selection of green suppliers are collected under the main headings of economic criteria and environmental criteria.

Bali et al. [19] proposed an integrated approach for the selection of green suppliers in their study. This approach incorporates intuitionistic fuzzy sets and gray relational analysis methods. The proposed approach was applied to a numerical example. It includes five alternative suppliers and eight assessment criteria. The criteria were determined as service quality, green image, use of green materials, waste control in production, green product,

distribution, reverse logistics, green design-research and development.

Yu and Hou [20] made an application on the green supplier selection problem in an automobile manufacturing company. Four main criteria have been determined in order to assess the five alternative suppliers within the scope of the problem. These criteria are product performance, supplier criterion, cooperation and development potential, and green performance. The modified multiplicative AHP method was used for the assessment of suppliers. In addition, the assessment of suppliers was carried out by the classical AHP method, and the results obtained from both methods were compared.

Freeman and Chen [21] conducted a study using the AHP method, entropy method and TOPSIS method for the selection of green suppliers. Five alternative suppliers were assessed in terms of five main criteria. The main criteria were determined as cost, green competition, quality, delivery schedule, and environmental management performance. The AHP method and entropy methods were used to determine the weights of the criteria. In the process of assessing the alternatives, the TOPSIS method was used.

However, a limited number of studies are available regarding the green supplier assessment [22-26]. On the other hand, no study was found in which a fuzzy expert system model was created based on green production technology, environmental management system, pollution control, product cost, delivery time and quality criteria in order to make a green supplier assessment. Therefore, it can be easily said that this study will be the first research attempt within the framework of this subject. In addition, this study will make a significant contribution to the relevant literature.

3. DEVELOPED FUZZY EXPERT SYSTEM MODEL

The fuzzy expert system is a hybrid artificial intelligence (AI) technique that combines fuzzy logic and expert system methods. Thus, the possibility of combining the advantages of fuzzy set theory with the inference ability of the expert system arises. The working procedure of the fuzzy expert system is shown schematically in Figure 2.

The first step of the fuzzy expert system model developed within the scope of the study is to determine the input and output variables. For this purpose, the opinions of a team of six experts on purchasing and GSCM and the studies in the literature were taken as a basis. As a result, green production technology, environmental management system, pollution control, product cost, quality, and lead time were determined as input parameters. The output parameter is determined as the green supplier assessment score.

The general structure of the developed fuzzy expert system is shown in Figure 3.

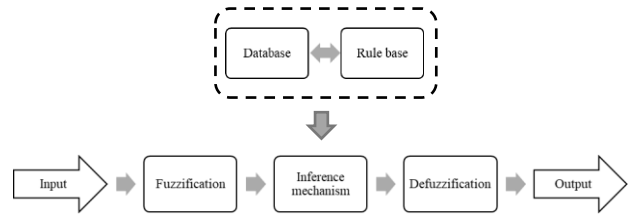


Figure 2. The working procedure of the fuzzy expert system

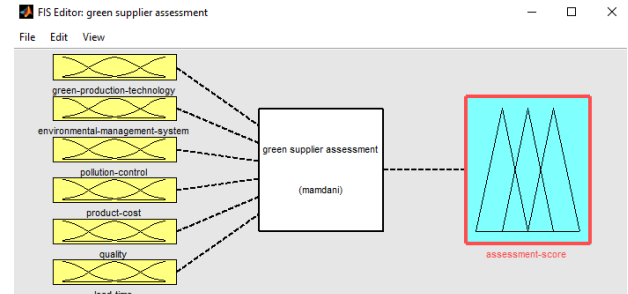


Figure 3. The general structure of the developed fuzzy expert system

Then, fuzzy sets and membership functions of each variable were determined according to the opinions of the expert team. Triangular and trapezoidal membership functions were used as membership functions. The fuzzy sets of the variables are shown in Table 1, and the mathematical representation of the membership functions is as follows:

$$\mu(X_i) = \begin{cases} 0 & , x \leq a_1 \text{ and } x \geq a_3 \\ \frac{x-a_1}{a_2-a_1} & , a_1 < x \leq a_2 \\ \frac{a_3-x}{a_3-a_2} & , a_2 < x < a_3 \end{cases} \quad (1)$$

$$\mu(X_i) = \begin{cases} 0 & , x \leq a \text{ and } x \geq d \\ \frac{x-a}{b-a} & , a < x < b \\ 1 & , b \leq x \leq c \\ \frac{d-x}{d-c} & , c < x < d \end{cases} \quad (2)$$

Afterward, the rule base of the developed fuzzy expert system model has been established by taking into account the expertise of the relevant team. Four input variables have two fuzzy sets. The two input variables have three fuzzy sets each. Therefore, there are a total of $2^4 \times 3^2 = 144$ rules in the rule base. Different methods can be used as an inference mechanism. These are methods Mamdani, Sugeno, Tsukamoto, Larsen, Şen, Zadeh, Dines-Rescher, and Gödel [27]. Mamdani approach was used as the inference mechanism in the model, depending on the type of information modeling. Thus, the output of the model will be included in a fuzzy set.

Table 1. The fuzzy sets of the variables

Variable	Range	Fuzzy set
Green production technology	0	No
	1	Yes
Environmental management system	0	No
	1	Yes
Pollution control	0	No
	1	Yes
Product cost	0-40	Low
	30-70	Medium
	60-100	High
Quality	0-40	Low
	30-70	Medium
	60-100	High
Lead time	0	Delayed
	1	In-time
Assessment score	0-36	Very low
	5-40	Low
	14-86	Medium
	60-95	High
	64-100	Very high

It is necessary to defuzzificate the fuzzy values obtained as a result of inference mechanism. This is done in the defuzzification interface. In this interface, fuzzy values are converted to net values by using the center of gravity method. Finally, the obtained value is the output of the model and gives the assessment score of the green supplier.

4. RESULTS AND DISCUSSION

The surface view of the developed fuzzy expert system model is available in Figure 4.

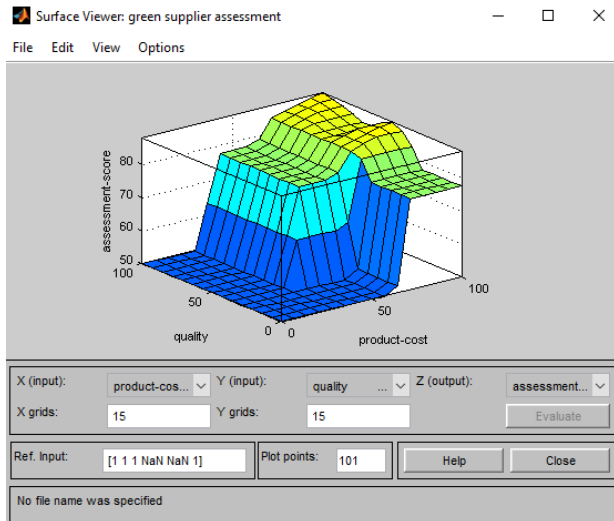


Figure 4. Surface viewer for product cost and quality variables

This surface view shows the impact of quality and product cost variables on the supplier assessment score. Both the quality variable and the product cost variable have a positive relationship with the supplier assessment score. In other words, increasing the value of both variables increases the supplier assessment score.

In order to test the performance of the model, a green supplier assessment of 32 different suppliers was made. A sample of these assessment data is given in Table 2.

Table 2. A small example of the data set

No	GPT	EMS	PC	PCost	Quality	LT	ASM	ASE
1	1	1	0	70	65	1	77.1	77
2	0	1	1	80	45	0	70	70
3	1	0	1	55	70	1	62.6	63
...
15	1	0	0	85	50	0	53.3	53
16	1	1	1	20	95	0	58.7	59
17	0	1	0	30	25	1	38.9	39
...
30	1	1	1	85	80	0	86.8	87
31	1	0	1	65	35	0	45	45
32	0	0	1	40	15	0	20.1	20

GPT: Green Production Technology, EMS: Environmental Management System, PC: Pollution Control, PCost: Product Cost, Quality: Quality, LT: Lead Time, ASM: Assessment Score of the Model, ASE: Assessment Score of the Experts

MSE error type was used to measure the error in green supplier assessment. The formula for this method is as follows:

$$MSE = \frac{1}{n} \sum_{t=1}^n (A_t - F_t)^2 \tag{3}$$

While F_t refers to the estimated value, A_t refers to the actual value. When these definitions are associated with the study, the value obtained from the model is called F_t . A_t is the assessment score of the experts. Additionally, this value represents the average score of the experts. As a result of the calculation made with the available data, the MSE value was found to be 0.0481. In other words, the performance of the developed fuzzy expert system model was determined as 95.19%. In addition, regression analysis was performed to confirm the high prediction performance. The information regarding this analysis is given in Figure 5.

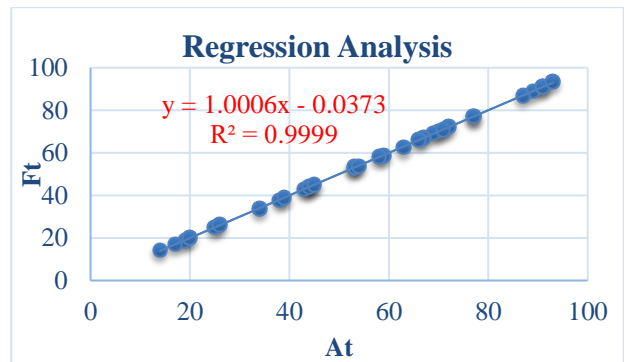


Figure 5. Regression analysis of the developed model

As a result of the regression analysis, the coefficient of determination (R^2) was calculated as 0.999. This value shows that the developed fuzzy expert system model represents the expertise of the experts in the green supplier assessment quite well.

5. CONCLUSION

This study aims to develop a fuzzy expert system model to perform green supplier assessment. In this context, a team of experts in green supplier assessment has been

established. As a result of the expert knowledge of this team and the examination of the studies in the literature, the input variables of the fuzzy expert system model were determined as green production technology, environmental management system, pollution control, product cost, quality, and lead time. The output variable of the model is the green supplier assessment score. MSE and R^2 are calculated to measure the performance of the model. The calculated MSE and R^2 values showed that the developed fuzzy expert system model has a very high performance. Especially in cases where experts in green supplier assessment are limited or difficult to reach, the relevant model will be an important tool for fast and accurate decision making.

AI-driven green supplier assessment will require improving explainable AI for transparent decision-making, integrating the internet of things for real-time environmental monitoring, addressing ethical concerns, ensuring global standardization, and exploring collaborations between humans and AI. Future studies are expected to show a trend in this context.

REFERENCES

- [1] Smith AD. Exploring strategic partnering in supply chain management: case study of successful practices. In: Mamun Habib MD, editor. *Supply chain management: practices, applications and challenges*. New York: Nova Science Publishers; 2016.
- [2] Sarkis J. *Green supply chain management*. New York: ASME Press and Momentum Press; 2014.
- [3] Bhattacharjee K. Green supply chain management-challenges and opportunities. *Asian Journal of Technology & Management Research*. 2015;5(1):14-19.
- [4] Khan SAR. Introduction of green supply chain management. In: Khan SAR, editor. *Green practices and strategies in supply chain management*. Intech Open; 2019.
- [5] Mendoza-Fong JR, García-Alcaraz JL, Ochoa-Domínguez HDJ, Cortes-Robles G. Green production attributes and its impact in company's sustainability. In: García-Alcaraz JL, Alor-Hernández G, Maldonado-Macías AA, Sánchez-Ramírez C, editors. *New perspectives on applied industrial tools and techniques*. 1st ed. Springer Cham; 2018. p. 23-46.
- [6] Daldır I, Tosun Ö. Green supplier selection using fuzzy WASPAS. *Uludağ University Journal of The Faculty of Engineering*. 2018;23(4):193-208.
- [7] Denizhan B, Yılmaz Yağcıner A, Berber Ş. An application of green supplier selection using analytic hierarchy process and fuzzy analytic hierarchy process methods. *Nevşehir Journal of Science and Technology*. 2017;6(1):63-78.
- [8] Çınar A, Uygun Ö. Selecting green supplier using intuitionistic fuzzy AHP. *Journal of Intelligent Systems: Theory and Applications*. 2019;2(2):24-31.
- [9] Şişman B. Evaluating and selection of green supplier development programs by using fuzzy MOORA. *Journal of Yasar University*. 2016;11(44):302-15.
- [10] Çalık A. Green supplier selection with fuzzy multi-objective linear programming and interval type-2 fuzzy AHP method. *The Journal of Selcuk University Social Sciences Institute*. 2018;39:96-109.
- [11] Akın N. Generalized trapezoidal fuzzy soft set: application to green supplier selection problem. *Afyon Kocatepe University Journal of Social Sciences*. 2021;23(1):158-71.
- [12] Erbiyık H, Alkan Kabakçı G, Erdil A. Supplier selection in the automotive sector with the electre method: an application for green supplier selection. *European Journal of Science and Technology*. 2021;(24):421-29.
- [13] Soyer A, Türkay A. Green purchasing and green supplier selection: an application in the white goods sector. *Journal of Engineering Sciences and Design*. 2020;8(4):1202-22.
- [14] Yerlikaya M, Efe B, Efe Ö. Environmental waste criterion-based supplier selection problem. *The International New Issues in Social Sciences*. 2017;5(5):311-22.
- [15] Çalık A. Green supplier selection using group decision making methods: a case study from the food industry. *The International Journal of Economic and Social Research*. 2021;17(1):1-16.
- [16] Madenoğlu F. Green supplier selection in fuzzy multi criteria decision making environment. *Business and Management Studies: An International Journal*. 2019;7(4): 1850-69.
- [17] Lee AHI, Kang H, Hsu C, Hung H. A green supplier selection model for high-tech industry. *Expert Systems with Applications*. 2009;36(4):7917-27.
- [18] Hashemi SH, Karimi A, Tavana M. An integrated green supplier selection approach with analytic network process and improved grey relational analysis. *Int. J. Prod. Econ*. 2015;159:178-91.
- [19] Bali O, Kose E, Gumus S. Green supplier selection based on IFS and GRA. *Grey Systems: Theory and Application*. 2013;3(2):158-76.
- [20] Yu Q, Hou F. An approach for green supplier selection in the automobile manufacturing industry. *Kybernetes*. 2016;45(4):571-88.
- [21] Freeman J, Chen T. Green supplier selection using an AHP-Entropy-TOPSIS framework. *Supply Chain Manag*. 2015;20(3):327-40.
- [22] Agarwal G, Vijayvargy L. (2012). Green supplier assessment in environmentally responsive supply chains through analytical network process. *International MultiConference of Engineers and Computer Scientists, IMECS 2012*. Hong Kong: 2012. p. 1218-23.
- [23] Foroozesh N, Tavakkoli-Moghaddam R. Assessment of green supplier development programs by a new group decision-making model considering possibilistic statistical uncertainty. *Journal of Quality Engineering and Production Optimization*. 2018;3(2):1-10.

- [24] Li L, Wang H. A green supplier assessment method for manufacturing enterprises based on rough ANP and evidence theory. *Information*. 2018;9(7):162.
- [25] Mahdavinia R. Green supplier assessment using fuzzy hierarchical technique at pars khodro company in Iran. 3rd International Conference on Management, Industrial Engineering, Economics and Accounting. Sofia: 2003. p. 1-15.
- [26] Mishra A, Rani P, Pardasani K, Mardani A. A novel hesitant fuzzy WASPAS method for assessment of green supplier problem based on exponential information measures. *J. Clean. Prod.* 2019;238:117901.
- [27] Özkan, M. An application for individual employee performance evaluation by fuzzy inference system. *Cumhuriyet University Journal of Economics and Administrative Sciences*. 2018;19(2):372-88.

Investigation of the Effects of PFKFB3 Small Molecule Inhibitor KAN0438757 on Cell Migration and Expression Level of N-cadherin Protein in Glioblastoma Cell Lines

Seher SARUHAN¹ , Deniz ÖZDEMİR¹ , Remziye SAFA¹ , Can Ali AĞCA^{1*} 

¹Bingöl University, Faculty of Arts and Sciences, Department of Molecular Biology and Genetics, Bingöl, Türkiye

Seher SARUHAN ORCID No: 0000-0003-1641-8519

Deniz ÖZDEMİR ORCID No: 0000-0001-7659-742X

Remziye SAFA ORCID No: 0009-0002-0392-3196

Can Ali AĞCA ORCID No: 0000-0002-0244-3767

*Corresponding author: c.aliagca@gmail.com

(Received: 02.11.2023, Accepted: 10.02.2024, Online Publication: 26.03.2024)

Keywords

KAN0438757,
PFKFB3,
Glioblastoma,
Migration

Abstract: Reprogramming of energy metabolism in cancerous cells plays a crucial role in promoting the epithelial-mesenchymal transition (EMT) program that is linked to malignancy. PFKFB3 (6-phosphofructose-2-kinase/fructose-2,6-bisphosphatase 3), which is responsible for energy metabolism, is a significant glycolytic activator involved in the progression of various types of tumours, including glioblastoma. PFKFB3 has the capacity to alter the expression of EMT-related proteins, thereby influencing the EMT program amongst tumour cells. When undergoing EMT, glioblastoma cells acquire a mesenchymal phenotype associated with augmented cellular motility, invasiveness, and resistance to therapy. Inhibition of PFKFB3 in glioblastoma cells has promising potential as a therapeutic strategy to target EMT and halt cancer progression. PFKFB3 inhibitors are compounds that can block PFKFB3 activity, inhibiting glycolysis in cancer cells. KAN0438757 is a novel, selective inhibitor of PFKFB3 that exhibits anti-tumour effects in various cancer models both *in vitro* and *in vivo*. The study evaluated the impact of a novel inhibitor on the viability, migration, and death of glioblastoma cancer cell lines U373 and U251 using WST-1 cell viability, AO/EtBr staining western blotting, and wound healing assays. The results showed that cell viability decreased and dose-dependent apoptotic morphological changes were observed in glioblastoma cells after KAN0438757 treatment. Moreover, the protein level of EMT-associated N-cadherin decreased, leading to reduced cell migration. In conclusion, it is possible that KAN0438757 could elicit anti-tumour effects in glioblastoma by reversing the EMT programme and inducing apoptotic morphological changes in cancer cells.

PFKFB3 Küçük Molekül İnhibitörü KAN0438757'nin Glioblastoma Hücre Hatlarında Hücre Migrasyonu ve N-kadherin Proteininin Ekspresyon Düzeyi Üzerine Etkilerinin Araştırılması

Anahtar

Kelimeler

KAN0438757,
PFKFB3,
Glioblastoma,
Migration

Öz: Tümör hücrelerinde enerji metabolizmasının yeniden programlanmasının, malign özelliklerle ilişkili epitelyal-mezenkimal geçiş (EMT) programının desteklenmesinde önemli bir rol oynadığı bilinmektedir. Enerji metabolizmasında görev alan PFKFB3 (6-phosphofructose-2-kinase/fructose-2,6-bisphosphatase 3), glioblastoma dahil olmak üzere çoklu tümör tipi ilerlemesinde rol oynayan önemli bir glikolitik aktivatördür. PFKFB3, EMT ile ilişkili proteinlerin ekspresyonunu modüle ederek tümör hücrelerinde EMT programını etkileyebilmektedir. EMT sırasında glioblastoma hücreleri, artan hücre hareketliliği, istilacılık ve tedaviye direnç ile ilişkili bir mezenkimal fenotip kazanmaktadır. Glioblastoma hücrelerinde PFKFB3'ün inhibisyonu, EMT'yi hedeflemek ve kanser ilerlemesini engellemek için potansiyel bir terapötik strateji olarak görülmektedir. PFKFB3 inhibitörleri, PFKFB3'ün aktivitesini bloke edebilen ve dolayısıyla kanser hücrelerinde glikoliz sürecini inhibe edebilen bileşiklerdir. KAN0438757, PFKFB3'ün yeni ve seçici bir inhibitörüdür. KAN0438757'nin hem *in vitro* hem de *in vivo* olarak çeşitli kanser modellerinde anti-tümör etkilerine sahip olduğu gösterilmiştir. Yeni inhibitörün glioblastoma kanseri hücre hatları U373 ve U251'de hücrelerin canlılığı, hücre

göçü ve hücre ölümü üzerindeki etkisi, WST-1 hücre canlılığı, AO/EtBr, boyama western blotlama ve yara iyileştirme testleri ile araştırıldı. Elde ettiğimiz sonuçlarda, glioblastoma hücrelerinde, KAN0438757 tedavisinden sonra hücre canlılığının azaldığı ve doza bağlı apoptotik morfolojik değişiklikler görüldü. Ayrıca EMT ilişkili N-cadherin proteininin düzeyinin azaldığı ve hücre göçünün de baskılandığını gözlemlendi. Sonuç olarak, KAN0438757'nin glioblastomada, EMT programını tersine çevirerek ve kanser hücrelerinin apoptotik morfolojik değişikliklere yol açarak anti-tümör aktiviteye sahip olabileceğini düşündürmektedir.

1. INTRODUCTION

Gliomas constitute approximately 80% of malignant tumours and 30% of brain tumours. Gliomas are classified by the World Health Organization (WHO) as types 1, 2 (low-grade gliomas), 3 (anaplastic glioma) and 4 (Glioblastoma (GBM)) according to their general characteristics [1]. GBM is a highly aggressive form of this type of this classification. Although many treatments have been applied for glioblastoma, according to studies, no further progress has been made in the last decade [2]. To this end, blocking the growth-promoting kinase targets of glioblastoma seems to be a reasonable treatment strategy that requires further study [3]. As with most cancers, glioblastomas tend to favour aerobic glycolysis over oxidative phosphorylation, a phenomenon known as the Warburg effect [4,5]. Glioblastoma cells exhibit elevated levels of fructose-2,6-bisphosphate (F2,6BP), essential controller of 6-phosphofructo-1-kinase, significant enzyme responsible for regulating the rate. Glycolytic flux is controlled through several enzyme steps in glycolysis, including those catalysed by the enzymes phosphofructokinase-1 (PFK1) and 6-phosphofructokinase-2-kinase/fructose-2,6-bisphosphatase (PFKFB) [6]. The bifunctional enzyme family known as PFKFB is expressed by four different genes and is important for cancer metabolism. PFKFB enzymes are crucial for regulating glycolysis. They can be classified into four groups: PFKFB1, PFKFB2, PFKFB3 and PFKFB4 [7]. The activity of the PFKFB3 enzyme plays an important role in glycolysis metabolism because the kinase/phosphatase ratio of PFKFB3 is very high, thus enabling the formation of F-2,6-BP and increased glycolysis [8]. As a result of various studies, PFKFB3 was found to be overexpressed in different human cancers, including malignant glioma [9]. PFKFB3 is overexpressed in GBM and has been shown to promote tumour growth and invasive migration. PFKFB3 promotes GBM growth and invasiveness through several mechanisms; Increasing the production of F2,6BP, a master regulator of glycolysis, can promote Warburg effect, a metabolic change characteristic of cancer cells, and suppress programmed cell death. PFKFB3 can also promote epithelial-mesenchymal transition (EMT) in GBM cells by activating a number of signalling pathways, including the PI3K/AKT/mTOR and the TGF- β 1 pathways [10]. EMT is a complex biological process in which epithelial cells mislay their epithelial properties and take on mesenchymal ones. That procedure crucial for normal embryonic development but may also play a role in cancer progression. Glioblastoma cells often receive EMT to obtain increased invasiveness and disseminate to other parts of the brain [11]. EMT is an a hallmark of cancer

and has been demonstrated to enhance tumor invasion, metastasis, and treatment resistance [12]. The downregulation of epithelial markers (E-cadherin) and the overexpression of mesenchymal markers (N-cadherin) characterize EMT [13]. EMT is a significant factor in the progression of GBM. Promisingly, PFKFB3 inhibitors can halt EMT and offer a new therapeutic strategy for GBM [14]. Furthermore, targeted PFKFB3 inhibition may be an effective treatment for CNS patients. PFKFB3 inhibitor treatment have shown its potential to improve the sensitivity of tumors that are resistant to treatment, both to chemotherapy and radiation [15, 16]. Anti-PFKFB3 and anti-VEGF combination treatment significantly increased the survival rate of preclinical models of glioblastoma and eliminated resistance to anti-angiogenic therapy, as reported by Zhang et al. [17]. In 2018, a specific small molecule inhibitor called KAN0438757 was discovered. It was found to have a high level of selectivity for the PFKFB3 kinase domain. KAN0438757 induced an increase in cell permeability and a decrease in cell viability in various types of cell lines via suppression of PFKFB3-118-20]. Conversely, KAN0438757 treatment produced radiosensitivity and cytotoxicity in cancer cells at concentrations that normal cells tolerated. The use of KAN0438757 after ionising radiation has inhibited the PFKFB3 molecule. This inhibition also prevented PFKFB3, BRCA1 and RAD51 from being nuclear localised. All of these molecules have been deemed essential for proper homologous recombination repair. Furthermore, KAN0438757 efficiently inhibited dNTPs during double-stranded DNA repair by inhibiting homologous recombination repair activity. As a result, H2AX levels increased and ionizing radiation caused cell cycle arrest [19]. In the case of human colorectal cancer cells, cell migration has been inhibited by KAN0438757, along with a decrease in associated PAXLLIN, VINCULIN and CORTACIN genes. *In vivo* administration of KAN0438757 has been found to be non-toxic [20]. However, the effect of KAN0438757 specifically on cell migration in glioblastoma is still mysterious.

This study aimed to is to focus and investigate the anticancer status, cell viability and migration of KAN0438757 in glioblastoma and the EMT-amplified protein N-cadherin.

2. MATERIAL AND METHOD

2.1 Cell Culture

In this study, human glioblastoma U373 and U251 cell lines purchased from ATCC (American Type Culture

Collection) were used. The cells were grown DMEM medium supplemented with 10% fetal bovine serum and 64 µg/ml penicillin + 0.1 mg/ml streptomycin in 5% CO₂/95% air at 37 °C unless otherwise stated.

2.2 WST-1 Viability Test

Water-soluble tetrazolium salts, known as WSTs, are commonly used for testing cell viability. These tests determine cell viability using spectrophotometry. The viability of untreated cells was set as 100%, and the viability of treated cells is expressed as a percentage (%) in comparison. Once the cells had reached a specific density, they were transferred to a 96-well plate with 3000 cells per well and incubated overnight in a CO₂ environment. The plate was then kept in the CO₂ incubator for several hours. Following this, glioma cell lines were treated with varying doses of KAN0438757 for 48 hours. WST-1 dye was added to each well at a volume of 10 µl and left to mix for 2-3 minutes. Afterwards, the plate was measured at 450 nm using the ELISA reader device [21].

2.3 Wound-Healing Migration Assay

The cells were plated onto a 6-well plate with a density of 8,000 cells per well and grown to reach 85-90% confluence. Subsequently, a 100 µL tip were used to produce uniform strips in the cell wells by making a scratch, followed by washing the plates with PBS. After this step, the cells were treated with serum-free DMEM/medium that contained different concentrations of KAN0438757 (5, 10, and 25 µM). The gap regions were photographed with a phase contrast microscope (Olympus, CKX41, Tokyo, Japan) at certain time intervals (0, 24, 48, 72 hours). Wound closure percentage was calculated using ImageJ software based on the cell-free area, as has been previously described [22, 23]. (Wound Closure % = $\{(At=0 - At=\Delta h)/At=0\} * 100$. At=0 = area of the wound measured immediately after scratching. At=Δh = area of the wound measured h hours after the scratch is performed.)

2.4 AO/EBr Staining

In a 6-well plate, U373 and U251 cells were sown (15x10⁴ cells per well) and incubated for overnight. The cells were treated with different concentrations of KAN0438757 (5, 10, and 25 µM). After the treatment period was over, acridine orange ethidium bromide dye was prepared and added to each well from the mixture. Imaging was then carried out under a microscope. Live cells were green under the microscope, but dead cells appeared red [24].

2.5 Western Blotting

Under denaturing conditions, the cells were separated using SDS-PAGE (12%) gel [25]. Proteins were subsequently transferred onto a PVDF membrane following their separation on the gel. Following transfer, the membrane was incubated for 1 hours at room temperature with 5% BSA (Bovine Serum Albumin)

dissolved in 1X TBS-T (TrisBuffered Saline and Tween 20) solution. Membrane were shaken overnight at +4 °C with the appropriate primary antibody (anti-N-cadherin (Santa Cruz, sc-7939, 1:1000) and anti-GAPDH (Santa Cruz, sc-365062, 1:1000). Membrane was rinsed with 1X TBS-T for 5 minutes/5 times the next day before being incubated with secondary antibody (anti-mouse or anti-rabbit) for 60 minutes at room temperature. Images were acquired using the chemiluminescence method after the membrane was washed with 1X TBS-T for 5 minutes/5 times. Image-j was used to determine band intensities densitometrically (National Institute of Health, Bethesda, MD; Image J). Each band's intensity was normalized to the intensity of the matching GAPDH band.

2.6. Statistical Analyses

All results were assessed using the Graph Pad Prism 5.01 software. Statistical analysis was performed through one-way ANOVA followed by post-hoc Tukey test and was repeated three times for reproducibility.

3. RESULTS

3.1 Effect of KAN0438757 on Cell Viability

To investigate the effects of KAN0438757 cell viability, U373 and U251 cell line were treated with different doses of KAN0438757 (5, 10, 25, 50 and 100 µM). According to the data obtained as a result of the measurement, KAN0438757 was shown to impair cell viability in the U373 cell line in a dose-dependent manner, with a sharper drop noted at 25 µM as shown in Figure 1A. Similarly, KAN0438757 reduced cell viability in the U251 cell line Figure 1B. Cell viability was shown to be significantly reduced in both cell lines, particularly after the 10 µM dosage.

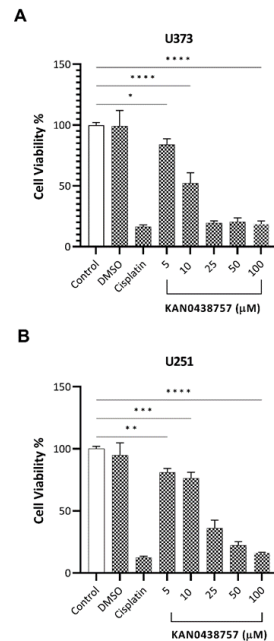


Figure 1. Effect of KAN0438757 on cell viability of human glioblastoma (U373 and U251) cell lines. (A, B) U373, U251 cells were exposed to for 48 hours with KAN0438757 and cell viability was evaluated using WST-1 assays.

3.2 Effect of KAN0438757 on Cell Migration

We further investigated KAN0438757 effects on migration of U373 and U251 cells. The cells received treatment with KAN0438757 (5, 10, and 25 M), as indicated in Figs. 2A and 2B. For 72 hours, wound closure percentages in U373 cells were 20,78% at 10 M and 8,13% at 25 M. Similar to U373 cells, the percentages of wound closure were 38,18 % at 10 μ M and 13,19 % at 25 μ M, respectively in U251 cells. U373 cells treated with low doses of KAN0438757 demonstrated that the intercellular gap was closed after 48 hours. On the other hand, it was showed that the intercellular distance in the cells treated with 25 μ M of KAN0438757 had a very low mobility after 48 hour compared to the control group. At 5 μ M of KAN0438757, there was no statistically significant difference in inhibition effect in both cells lines.

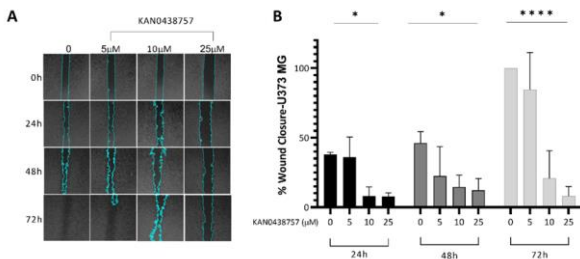


Figure 2. Effect of KAN0438757 on Cell Migration in U373 cell line. KAN0438757 (5-25 M) was applied to U373 cells for 72 hours. Subsequently, the wound-healing assay was conducted to determine cell migration. (A) Microscopic images (4x-500 μ m) of U373 cells following various treatments with KAN0438757. (B) The wound was measured for closure. All of the data given are from three distinct tests.

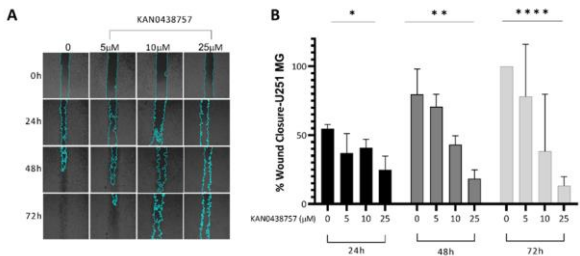


Figure 3. Effect of KAN0438757 on Cell Migration in U251 cell line. The U251 cells were treated with KAN0438757 (5-25 μ M) for 72 hours. Subsequently, the wound-healing assay was conducted to determine cell migration. (A) Images (4x-500 μ m) taken using a microscope of U25 cells following various treatments with KAN0438757. (B) The wound was measured for closure. All of the data given are from three distinct tests.

3.3. Effect of KAN0438757 on Cell Death in U251 and U373 Cells

In order to determine whether the growth inhibition by KAN0438757 was associated with cell death, glioblastoma cells treated with KAN0438757 were analyzed for dual staining (AO/EB staining). Figure. 4-A and B shows that when treated with KAN0438757, the ratio of apoptotic cells significantly increased in cells at high dose of KAN0438757. Given the administered dosage of 5 and 10 μ M, the number of viable cells is relatively considerable. The cells treated with 25 μ M of KAN0438757 were observed to change from green to yellow and orange which suggests that when exposed to

KAN0438757, U251 and U373 cells underwent the typical changes of apoptosis.

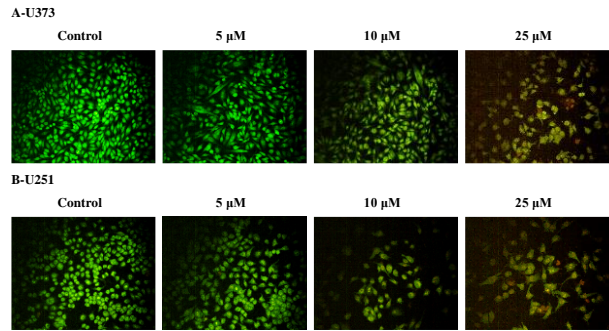


Figure 4. Effect of KAN0438757 on the apoptotic cell death in human glioma cells was evaluated by fluorescence microscopy using acridine orange/propidium iodide double staining. Detection of apoptotic morphology was performed using fluorescent staining of U251 and U373 cell lines with acridine orange-ethidium bromide (AO/EB) after treatment with KAN0438757 (5-25 μ M) for 72 hours. Apoptotic cells emit red fluorescence while as viable cells emit green fluorescence. An increase in the number of apoptotic cells was observed as the KAN0438757 dose increased. This figure presents the outcomes of at least three separate trials (Original magnification 20x).

3.4. Western Blotting

To further investigate the molecular basis effect of KAN0438757 on N-cadherin in glioblastoma cancer cells, we examined the expression N-cadherin after treatment with different concentrations of KAN0438757 by western blot analysis. At 5 μ M of KAN0438757, there was no statistically significant difference in N-cadherin expression in both cells lines (Figure 5B and 5C). N-cadherin, expression levels were decreased after exposure to 25 μ M KAN0438757 compared with the levels in control cells.

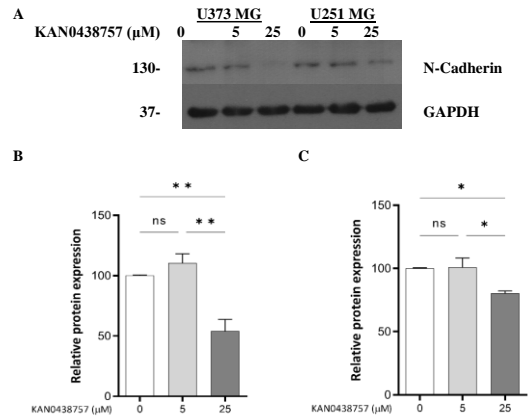


Figure 5. Effect of KAN0438757 on N-cadherin. (A) Western blot bands. (N-cadherin and GAPDH Western blotting was used to evaluate protein expression levels.), (B-C) N-cadherin protein expression levels. GAPDH was used as control. Control group and compared, *P < 0.05, **P < 0.01

4. DISCUSSION AND CONCLUSION

Metastasis, known as the process in which the cancerous cell leaves the primary tumor tissue, passes through the basement membrane to the circulatory system, reaches different tissues and forms a secondary tumor, is the main cause of death from cancer [26]. Despite this important effect on cancer deaths, the molecular

mechanisms of invasion and migration, which form the basis of metastasis, remain unknown. The escape of cancerous cells from the primary tumor tissue is associated with increased migration potential with the reduction of intercellular junction proteins and acquisition of mesenchymal phenotype, called EMT, which has basic functions such as embryogenesis and wound healing in the normal physiological process [27]. The EMT process is mediated by various transcription factors, mainly the Snail, Twist and Zeb family [28]. The roles of transcription factors in EMT are mainly by the regulation of various proteins as an example E and N-cadherin, β -catenin, vimentin and fibronectin and suppression of intercellular tight junctions [29]. Various growth and differentiation factors such as fibroblast growth factor (Fibroblast Growth Factor; FGF), wnt and notch proteins are involved in the initiation of the EMT process. Among these factors, transforming growth factor β (Transforming Growth Factor β ; TGF β), which is an important inducer of EMT, is largely involved in cancer studies [30].

PFKFB3 is an enzyme that is essential in glycolysis, the process by which cells convert glucose into energy [8]. PFKFB3 has been shown to be activated by hypoxia and other stress signals and promotes EMT [31]. EMT is a process in which epithelial cells that are normally tightly packed and adhere to each other lose their cell-cell adhesion and become more mesenchymal-like. Mesenchymal cells are more mobile and can migrate to other parts of the body [32]. EMT is crucial for a diversity of processes, including development, wound healing, and cancer metastasis. In cancer, EMT is thought to promote metastasis by allowing cancer cells to escape from the primary tumor and travel to other parts of the body. PFKFB3 has been shown to be involved in EMT in several ways. First, PFKFB3 can activate transcription factors that promote EMT, such as Snail and Twist [33]. Second, PFKFB3 can increase the production of extracellular matrix proteins that may aid in the migration of cancer cells [34]. Third, PFKFB3 can enhance the generation of reactive oxygen species, which can cause cell-cell adhesions to break down and induce EMT [35]. Here are some additional research findings regarding the relationship between PFKFB3 and EMT; The study in human breast cancer cells showed that inhibition of PFKFB3 reduced EMT and increased the sensitivity of cells to chemotherapy [36]. According to another research in colorectal cancer cells, inhibition of PFKFB3 reduced the cells' ability to metastasize [37]. Overall, the research suggests that PFKFB3 plays a role in EMT and that inhibiting PFKFB3 could be a potential therapeutic strategy for cancer. More study is needed, however, to fully understand the role of PFKFB3 in EMT and to create safe and effective PFKFB3 inhibitors. PFKFB3 is a key enzyme in glycolytic tumor metabolic reprogramming, and protein levels of PFKFB3 are substantially higher in high-grade gliomas (HGGs) than in low-grade gliomas. The significance of PFKFB3 splice variants in glioblastoma development and prognosis is still poorly known. Therefore, it is desired to reveal a new strategy to treat cancer using PFKFB3 inhibitors in the treatment of glioblastoma. Inhibitors

that provide inhibition of PFKFB3 appear as four different molecules: 3PO, PFK15, PFK158 and KAN0438757 [19,40]. Among these inhibitors, KAN0438757 is a new inhibitor that has been studied in recent years, and it has been determined that it selectively inhibits the proliferation of cancer cells. It was also concluded that inhibition of PFKFB3 with KAN0438757 impairs DNA repair, resulting in death of cancer cells. However, there is no study yet to reveal the effects of KAN0438757 inhibitor on glioblastoma cells. As a result, we explored the consequences of the KAN0438757 on cell migration and N-cadherin protein expression levels in glioblastoma cell lines in this study.

In this study, cell viability, cell proliferation, cell death, cell migration, and protein levels such as N-cadherin were analyzed in glioblastoma cell lines U373 and U251 cells. In our study, firstly, the effect of KAN0438757 inhibitor on cell viability were assessed in U373 and U251 cell lines. The WST-1 viability test revealed that cell viability reduced dose-dependently in both cell lines. In the study of Oliveira et al., it was observed that after treatment with KAN0438757 in colorectal cancer cell proliferation was significantly reduced, especially at 50 and 75 μ M doses. In a separate investigation Yan et al. reported that inhibition of PFKFB3 by oxaplatin in colon cancer not only reduces cell viability but also promotes apoptotic cell death [38]. Cell migration was determined by our next experiment, Wound Healing. Glioblastoma cell lines U373 and U251 were treated with KAN0438757 for 0-72 hours. In the U373 cells, it was observed that it inhibited the migration ability of the cells depending on the dose and time. It was concluded that the U251 cell line significantly affected cell migration compared to the U373 cell line and reduced the migration abilities of the cells. According to the information we obtained as a result of these findings, it was determined that the KAN0438757 inhibitor inhibited the migration ability of cells in glioblastoma cells in a time and dose dependent manner. Yan et al. [38] has shown that it significantly reduced cell migration and invasion activity in colorectal cancer cell lines. In another study, Veseli et al. observed that treatment with 3PO, significantly inhibited cell migration in endothelial cells. These results, like the results we obtained in our study, show that PFKFB3 inhibitors have a significant decrease in the migration ability of cancer cells and this has an important role in leading cancer cells to death [41].

Preceding studies has shown that the overexpression of PFKFB3 elevates the migratory and invasive capabilities in tumour cell, while reducing the expression of E-cadherin and upregulating N-cadherin. Specifically, the transcription factors Snail and Twist are notably induced, which have been found to contribute significantly to EMT [14]. Western blot results of the N-cadherin showed that the KAN0438757 caused a decrease in U251 cell lines, especially in the high-dose group compared to the control. In addition, it was determined that KAN0458757 treatment caused a very dramatic decrease in N-cadherin protein expression in U373 cell lines. Yalçın et al. in their study in 2023 showed that silencing of PFKFB3 caused changes in the expressions

of E-cadherin, Vimentin and EMT genes in different cancer cell lines [33]. We have shown that PFKFB3 inhibitor can cause a phenomenon that supports the changes in EMT proteins that we have obtained consistent with this result.

Apoptosis is the removal of infected, damaged, or undesirable cells in order to preserve cell homeostasis. Another experiment, AO/EtBr staining experiments, examined cell death in glioblastoma cell lines after treatment of the KAN0438757 inhibitor. Firstly, it was observed that the cells tended towards death with a reduction in cell count in the U251 cell line, especially in the 25 μ M dose group. On the other hand, in the U373 cell line, it was also detected that in the 25 μ M dose group, significant cells are close to death and some of these even death. In the work of Wang et al. [39] apoptosis was looked at to determine cell death. It was determined that PFK15, an inhibitor of PFKFB3 in rhabdomyosarcoma cells, had a stimulating effect on cell viability loss after induction with 3MA. It has also been observed that PFK15 has multiple cell death-inducing effects other than caspase-dependent apoptosis.

The study shows the significance of PFKFB3-mediated metabolism in the development of EMT in glioblastoma cells and indicates that KAN0438757 could be a fresh approach to treating glioblastoma.

Acknowledgement

This work was partially financed by TUBİTAK under project grant 1919B012108009 and the BUBAP under project grant BAP-FEF.2021.004 and BAP-FEF.2021.005.

REFERENCES

- [1] Weller M. et al. "Glioma". *Nat. Rev. Dis. Prim.* 2015; 1.
- [2] Chen R, Smith-Cohn M, Cohen AL, Colman H. Glioma Subclassifications and Their Clinical Significance. *Neurotherapeutics.*2017;14(2):284–297.
- [3] Bush NAO, Chang SM, Berger MS. "Current and future strategies for treatment of glioma." *Neurosurg. Rev.* 2017;40(1):1–14.
- [4] Bartrons RA, Rodríguez-García, Simon-Molas H, Castaño E, Manzano A, Navarro-Sabaté À. "The potential utility of PFKFB3 as a therapeutic target." *Expert Opinion on Therapeutic Targets.* 2018;22(8):659–674.
- [5] Minchenko OH, Ogura T, Opentanova IL, Minchenko DO, Esumi H. Splice isoform of 6-phosphofructo-2-kinase/fructose-2,6-bisphosphatase-4: Expression and hypoxic regulation. *Mol. Cell. Biochem.*2005;280(1–2):227–234.
- [6] Yalcin A, Telang S, Clem B, Chesney J. Regulation of glucose metabolism by 6-phosphofructo-2-kinase/fructose-2,6-bisphosphatases in cancer." *Exp. Mol. Pathol.* 2009;86(3):174–179.
- [7] Bartrons R, et al. Fructose 2, 6-bisphosphate in cancer cell metabolism. *Front. Oncol.*2018;8(331):1-21.
- [8] Shi L, Pan H, Liu Z, Xie J, Han W. Roles of PFKFB3 in cancer. *Signal Transduct. Target. Ther.* 2017;2(1):1–10.
- [9] Minchenko OH, et al. Single-walled carbon nanotubes affect the expression of the CCND2 gene in human U87 glioma cells. *Materwiss. Werksttech.* 2016;47(2–3)180–188.
- [10] Rodríguez-García A, et al. TGF- β 1 targets Smad, p38 MAPK, and PI3K/Akt signaling pathways to induce PFKFB3 gene expression and glycolysis in glioblastoma cells. *FEBS J.* 2017;284(20):3437–3454.
- [11] Seker-Polat F, Pinarbasi Degirmenci N, Solaroglu I, Bagci-Onder T. Tumor cell infiltration into the brain in glioblastoma: From mechanisms to clinical perspectives. *cancers (Basel).* 2022;14(2):443.
- [12] Younis M, Shaikh S, Khawar, Shahzad K. Long non-coding RNA RP5-821D11.7 promotes proliferation, migration, and epithelial-mesenchymal transition in glioma and glioma stem-like cells *Open Access. Biomed. Lett.* 2023;9:64-74.
- [13] Loh CY, et al. The E-cadherin and N-cadherin switch in epithelial-to-mesenchymal transition: Signaling, therapeutic implications, and challenges. *Cells.* 2019;8(10):1118.
- [14] Lei L, et al. A potential oncogenic role for PFKFB3 overexpression in gastric cancer progression. *Clin. Transl. Gastroenterol.* 2021;12(7):1-10.
- [15] Zhu Y, et al. Targeting PFKFB3 sensitizes chronic myelogenous leukemia cells to tyrosine kinase inhibitor. *Oncogene.* May 2018;37(21):2837–2849.
- [16] Kao GD, Jiang Z, Fernandes AM, Gupta AK, Maity A. Inhibition of phosphatidylinositol-3-OH kinase/Akt signaling impairs DNA repair in glioblastoma cells following ionizing radiation. *J. Biol. Chem.* 2007;282(29):21206–21212.
- [17] Zhang J, et al. Dual inhibition of PFKFB3 and VEGF normalizes tumor vasculature, reduces lactate production, and improves chemotherapy in glioblastoma: insights from protein expression profiling and MRI. *Theranostics.* 2020;10(16):7245–7259.
- [18] Alvarez R, Mandal D, Chittiboina P. Canonical and non-canonical roles of pfkfb3 in brain tumors. *Cells.* 2021;10(11):1–24.
- [19] Gustafsson NMS, et al. Targeting PFKFB3 radiosensitizes cancer cells and suppresses homologous recombination. *Nat. Commun.* 2018;9(1):1–16.
- [20] De Oliveira T, et al. Effects of the novel PFKFB3 inhibitor KAN048757 on colorectal cancer cells and its systemic toxicity evaluation *in vivo.*" *Cancers (Basel).* 2021;13(5):1–24.
- [21] Tykhomyrov A, Nedzvetsky V, Shemet S, Ağca CA. Production and characterization of polyclonal antibodies to human recombinant domain B-free antihemophilic factor VIII. *Turkish J. Biol.* 2017;41(6):857–867.

- [22] Cory G. Scratch-wound assay. *Methods Mol. Biol.* 2011;769:25–30.
- [23] Feoktistova M, Geserick P, Leverkus M. Crystal violet assay for determining viability of cultured cells. *Cold Spring Harb. Protoc.* 2016;4:343-346.
- [24] Kasibhatla S, Amarante-Mendes GP, Finucane D, Brunner T, Bossy-Wetzel E, Green DR. Acridine orange/ethidium bromide (AO/EB) staining to detect apoptosis. *Cold Spring Harb. Protoc.* 2006;3:pdb-prot4493.
- [25] Agca CA, Kırıcı M, Nedzvetsky VS, Gundogdu R, Tykhomyrov AA. The effect of TIGAR knockdown on apoptotic and epithelial-mesenchymal markers expression in doxorubicin-resistant non-small cell lung cancer A549 cell lines. *Chem. Biodivers.* 2020;17(9):e2000441.
- [26] Klein CA. The metastasis cascade. *Science* (80-).2008;1785–1787.
- [27] Roche J. The epithelial-to-mesenchymal transition in cancer. *Cancers.* 2018;10(2):52.
- [28] E. Sánchez-Tilló, et al. EMT-activating transcription factors in cancer: beyond EMT and tumor invasiveness. *Cell. Mol. Life Sci.* 2012;69:3429–3456.
- [29] Zheng H, Kang Y. Multilayer control of the EMT master regulators. *Oncogene.* 2014;33(14):1755–1763.
- [30] Gonzalez DM, Medici D. Signaling mechanisms of the epithelial-mesenchymal transition. *Sci. Signal.* 2014;7(344).
- [31] Marcucci F, Rumio C. Tumor cell glycolysis-at the crossroad of epithelial-mesenchymal transition and autophagy. *Cells.* 2022;11(6):1041.
- [32] Son H, Moon A. Epithelial-mesenchymal transition and cell invasion. *Toxicol. Res.* 2010;26(4):245–252.
- [33] Altunok TH A. PFKFB3 regulates epithelial-to-mesenchymal transition in tumor cells. *Doğu Karadeniz Sağlık Bilim. Derg.* 2023;2(1):15–27.
- [34] Li HM, et al. Blockage of glycolysis by targeting PFKFB3 suppresses tumor growth and metastasis in head and neck squamous cell carcinoma. *J. Exp. Clin. Cancer Res.* 2017;36(1):1–12.
- [35] Jia D, et al. Towards decoding the coupled decision-making of metabolism and epithelial-to-mesenchymal transition in cancer. *Br. J. Cancer.* 2021;124(12):1902–1911.
- [36] Neal JO, et al. Inhibition of 6-phosphofructo-2-kinase (PFKFB3) suppresses glucose metabolism and the growth of HER2+ breast cancer. *Breast Cancer Res. Treat.* 2016;160(1):29–40.
- [37] De Oliveira T, et al. Effects of the novel pfkfb3 inhibitor kan0438757 on colorectal cancer cells and its systemic toxicity evaluation *in vivo*.” *Cancers (Basel).* 2021;13(5):1011.
- [38] Yan S, et al. Necroptosis pathway blockage attenuates PFKFB3 inhibitor-induced cell viability loss and genome instability in colorectal cancer cells. *Am. J. Cancer Res.* 2021;11(5):2062.
- [39] Wang C, Qu J, Yan S, Gao Q, Hao S, Zhou D. PFK15 , a PFKFB3 antagonist , inhibits autophagy and proliferation in rhabdomyosarcoma cells. 2018;21:359–367.
- [40] Pegoraro C, Maczkowiak F, Monsoro-Burq AH. Pfkfb (6-phosphofructo-2-kinase/fructose-2,6-bisphosphatase) isoforms display a tissue-specific and dynamic expression during *Xenopus laevis* development. *Gene Expression Patterns* 2013; 13 (7): 203-211.

Detection of Pneumonia Using A Hybrid Approach Consisting of MobileNetV2 and Squeeze-and-Excitation Network

Hüseyin FIRAT¹ , Hüseyin ÜZEN² 

¹ Dicle University, Faculty of Engineering, Department of Computer Engineering, Diyarbakır, Türkiye

² Bingöl University, Faculty of Engineering-Architecture, Department of Computer Engineering, Bingöl, Türkiye

Hüseyin FIRAT ORCID No: 0000-0002-1257-8518

Hüseyin ÜZEN ORCID No: 0000-0002-0998-2130

*Corresponding author: huseyin.firat@dicle.edu.tr

(Received: 19.09.2023, Accepted: 10.02.2024, Online Publication: 26.03.2024)

Keywords

Deep Learning,
Chest X-Ray
Images,
Pneumonia
Detection,
MobileNet V2,
Squeeze-and-
Excitation
Network

Abstract: Pneumonia is a global health concern, responsible for a significant number of deaths. Its diagnostic challenge arises from visual similarities it shares with various respiratory diseases, such as tuberculosis, complicating accurate identification. Furthermore, the variability in acquiring and processing chest X-ray (CXR) images can impact image quality, posing a hurdle for dependable algorithm development. To address this, resilient data-centric algorithms, trained on comprehensive datasets and validated through diverse imaging methods and radiology expertise, are imperative. This study presents a deep learning approach designed to distinguish between normal and pneumonia cases. The model, a hybrid of MobileNetV2 and the Squeeze-and-Excitation (SE) block, aims to reduce learnable parameters while enhancing feature extraction and classification. Integration of the SE block enhances classification performance, despite a slight parameter increase. The model was trained and tested on a dataset of 5856 CXR images from Kaggle's medical imaging challenge. Results demonstrated the model's exceptional performance, achieving an accuracy of 98.81%, precision of 98.79%, recall rate of 98.24%, and F1-score of 98.51%. Comparative analysis with various Convolutional neural network-based pre-trained models and recent literature studies confirmed its superiority, solidifying its potential as a robust tool for pneumonia detection, thus addressing a critical healthcare need.

54

MobileNetV2 ve Sıkma-Uyarma Ağından Oluşan Hibrit Bir Yaklaşım Kullanılarak Pnömoni Tespiti

Anahtar

Kelimeler

Derin Öğrenme,
Göğüs Röntgeni
Görüntüleri,
Pnömoni
Tespiti,
MobileNet
V2,
Sıkma ve
Uyarma Ağı

Öz: Pnömoni, önemli sayıda ölümden sorumlu olan küresel bir sağlık sorunudur. Teşhis zorluğu, tüberküloz gibi çeşitli solunum yolu hastalıklarıyla paylaştığı ve doğru tanımlamayı zorlaştıran görsel benzerliklerden kaynaklanmaktadır. Ayrıca, göğüs röntgeni görüntülerinin elde edilmesi ve işlenmesindeki değişkenlik, görüntü kalitesini etkileyerek güvenilir algoritma geliştirmenin önünde bir engel oluşturabilir. Bu sorunu çözmek için, kapsamlı veri kümeleri üzerinde eğitilen ve çeşitli görüntüleme yöntemleri ve radyoloji uzmanlığı ile doğrulanan esnek veri merkezli algoritmalar zorunludur. Bu çalışma, normal ve pnömoni vakalarını ayırt etmek için tasarlanmış bir derin öğrenme yaklaşımını sunmaktadır. MobileNetV2 ve Sıkıştırma-Uyarma (SU) bloğunun bir hibriti olan model, özellik çıkarma ve sınıflandırmayı geliştirirken öğrenilebilir parametreleri azaltmayı amaçlamaktadır. SU bloğunun entegrasyonu, hafif bir parametre artışına rağmen sınıflandırma performansını artırmaktadır. Model, Kaggle'ın tıbbi görüntüleme yarışmasından alınan 5856 göğüs röntgeni görüntüsünden oluşan bir veri kümesi üzerinde eğitilmiş ve test edilmiştir. Sonuçlar, %98.81 doğruluk, %98.79 kesinlik, %98.24 geri çağırma oranı ve %98.51 F1 puanı elde ederek modelin olağanüstü performansını göstermiştir. Çeşitli Evrimsel sinir ağı tabanlı önceden eğitilmiş modellerle ve son literatür çalışmalarıyla yapılan karşılaştırmalı analiz, modelin üstünlüğünü doğrulayarak pnömoni tespiti için sağlam bir araç olarak potansiyelini sağlamlaştırdı ve böylece kritik bir sağlık hizmeti ihtiyacını karşıladı.

1. INTRODUCTION

Pneumonia stands as a respiratory ailment provoking inflammation in either one or both lungs, leading to manifestations like coughing, fever, and respiratory distress. The timely identification of pneumonia proves crucial in ensuring effective therapy and enhanced patient recovery. Regrettably, pneumonia constitutes merely one among numerous pulmonary ailments, and as a result, radiographic findings don't consistently verify a pneumonia diagnosis. Consequently, given the present technology available, it remains unfeasible to definitively differentiate pneumonia from alternative lung disorders based on radiological criteria [1,2].

Developing accurate algorithms to detect pneumonia requires large amounts of meticulously annotated data, a task that can be particularly demanding. The complexity escalates when tackling pneumonia, as it necessitates skilled radiologists for data annotation, and the availability of labeled images is limited. Deep learning (DL), a subset of artificial intelligence, has emerged as a formidable tool for pneumonia identification and diagnosis through medical imaging, such as chest X-rays (CXR) [3,4]. DL algorithms possess the capability to undergo training on vast archives of CXR images, enabling them to discern unique features and attributes indicative of pneumonia's presence. This procedure involves utilizing convolutional neural networks (CNNs), a specialized category of DL frameworks exceptionally skilled in tasks related to image recognition. By scrutinizing the texture, shape, and pixel intensity within CXR images, CNNs can develop the ability to precisely identify areas within the image that correspond to regions of the lungs affected by infection or inflammation [5,6].

Following their training, DL models possess the capability to categorize novel CXR images, determining whether they exhibit indications of pneumonia or not. This process can be executed instantly, rendering it a potentially valuable resource for healthcare practitioners in the prompt diagnosis and treatment of pneumonia in patients. Furthermore, DL models can provide support to radiologists in the interpretation of CXR, thereby diminishing the chances of incorrect diagnoses and enhancing patient results [7-9]. Considering these advantages offered by DL techniques, they are commonly employed in scientific studies to diagnose pneumonia through the analysis of CXR images. Some of these studies are as follows.

Reshan et al. [2] introduced an advanced DL model for distinguishing between severe and normal cases of pneumonia. They harnessed eight pretrained models: ResNet50, ResNet152V2, DenseNet121, DenseNet201, Xception, VGG16, EfficientNet. To assess the efficiency of their model, they utilized the identical Kaggle dataset comprising 5856 CXR images. Their findings demonstrated that the MobileNet model yielded the highest accuracy, achieving an impressive 94.23%. In this research, Singh et al. [4] suggested a quaternion-based residual network to classify pneumonia cases in

CXR images. They extended the use of the residual network into the quaternion realm to differentiate between CXR images as either indicative of pneumonia or normal. This approach yielded an accuracy of 93.75% and an F1-score of 0.94, outperforming the traditional real-numbered residual network in terms of performance. Szepesi et al. [10] presented a CNN framework crafted to ensure an accurate and efficient method for detecting pneumonia through the analysis of CXR images. A notable innovation in their approach was the integration of a dropout layer positioned amidst the convolutional layers within the network. Rather than relying on pre-existing networks, they constructed a CNN model from the ground up, incorporating models of transfer learning. The method under consideration underwent training and testing using a collection of 5856 annotated CXR images provided within the context of a medical imaging competition hosted on Kaggle's platform. As a consequence of the experimental investigations, accuracy level of 97.2% was achieved. Ahmad et al. [11] devised an approach to autonomously identify pneumonia by combining pre-trained ResNet and DenseNet169 models. They assessed the model's effectiveness using a set of 5856 CXR images from the well-balanced Kaggle platform. This method attained a 90% accuracy rate in its performance evaluation. Shah et al. [12] suggested a CNN method based on the VGG16 model. They tested the proposed method using 5856 CXR images. They achieved 96.6% accuracy with their proposed method. Stephen et al. [13] presented a CNN model specifically designed to classify and detect the presence of pneumonia in a dataset containing CXR images. They assessed the effectiveness of this innovative approach by employing a dataset consisting of 5856 CXR images, ultimately achieving a classification accuracy of 93.73%. Rajaman et al. [14] introduced a CNN-driven decision support platform for the rapid and precise identification of pneumonia in pediatric CXR. They employed innovative and cutting-edge visualization techniques to elucidate model predictions, which holds great importance in guiding clinical decision-making. Furthermore, the encouraging results exhibited by the tailored VGG16 model, trained on the present tasks, indicate its ability to effectively acquire knowledge from a limited set of intricate data, resulting in reduced bias and enhanced generalization capabilities. They tested the proposed method using 5856 CXR images. They achieved 96.2% accuracy with their proposed method. Toğaçar et al. [15] amalgamated profound attributes extracted from multiple deep models to create an effective deep attribute collection. Subsequently, they employed various algorithms like decision trees and k-nearest neighbors for categorizing this deep attribute ensemble. Additionally, they utilized methods such as linear discriminant analysis and k-nearest neighbors in the realm of pneumonia detection. They tested the proposed method using 5849 CXR images. They achieved 96.84% accuracy with their proposed method. Chouhan et al. [16] introduced a model structured around an ensemble architecture, integrating results from multiple pre-existing models to aid in the diagnosis of pneumonia. They achieved an

accuracy of 96.39% as a result of experimental studies using 5232 CXR images.

In this study, a hybrid MSENNet model consisting of pre-trained MobileNetV2 and Squeeze-and-Excitation (SE) block is proposed to detect normal and pneumonia disease conditions. The purpose of the hybrid MSENNet model is to improve the classification accuracy by decreasing the number of trainable parameters. The number of trainable parameters is reduced with the pre-trained MobileNetV2. Given that the SE block is tailored to enhance the representational quality of the CNN, it is incorporated into CNNs within this investigation to enhance both feature extraction and classification performance. The integration of SE block into the proposed method is driven by their ability to bolster classification performance with only minimal augmentation to the overall parameter count. To assess the performance of the MSENNet model put forward, an examination was conducted using a dataset consisting of 5856 publicly accessible CXR images within the Kaggle platform. While MobileNetV2 achieved 97.78% accuracy, MSENNet, which is a combination of MobileNetV2 and SE block, achieved 98.81% accuracy. MobileNetV2 has the fewest parameters compared to other pre-trained network architectures compared with 2.228.994 trainable parameters. MSENNet has 2.228.995 trainable parameters. Compared to MobileNetV2, the number of trainable parameters increased by 1, while the classification accuracy increased by 1.03%. Besides, the MSENNet model was compared with the pre-trained models and it was observed that it gave the best classification accuracy value. In addition, it was compared with methods from the literature using the same dataset and it was observed that the MSENNet model gave the most successful results.

The remainder of this manuscript comprises three distinct sections. In Section 2, we introduce the CXR image dataset employed in this research. Also, within this section, we delve into the description of our MSENNet approach, along with the theoretical foundation of MobileNetV2 and the SE block. Section 3 outlines the experiments carried out in conjunction with our proposed method. Section 4, Conclusions, provides a comprehensive overview of the entire paper.

2. MATERIAL AND METHOD

2.1. Dataset

The dataset employed in this research was sourced from one of Kaggle's DL competitions [17]. This dataset comprises lung CXR images of children aged one to five years old, sourced from Guangzhou Women and Children's Medical Center. These lung CXR images underwent validation by healthcare experts as part of standard patient care procedures. The dataset consists of a total of 5856 labeled images, with 4273 indicating cases of pneumonia and the remaining 1583 classified as negative cases (normal). All scans were represented as grayscale images, with dimensions varying from 1346x1044 to 2090x1858 pixels. To match the

anticipated input format of most CNN network architectures, all images were resized to dimensions of 224x224x3. Figure 1 displays some sample images from the dataset.

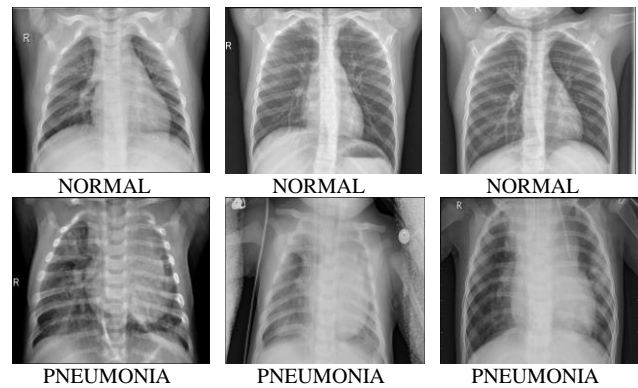


Figure 1. Samples of CXR images

2.2. MobileNetV2

MobileNetV2 stands out as a compact deep neural network, characterized not only by its reduced size but also its computational efficiency, all while delivering strong performance [18]. MobileNetV2 represents an enhanced iteration of MobileNetV1 [19], incorporating a linear bottleneck layer and the inverted residual block as additional components. The network architecture's specifications are detailed in Table 1. Within the inverted residual block (IRB), the initial step involves expanding the input channels via a 1x1 convolution to acquire additional features. Subsequently, feature extraction occurs through a 3x3 convolution, followed by channel reduction via 1x1 pointwise convolution. This entire sequence of operations follows the "expansion-convolution-compression" scheme, which proves to be more efficient and less reliant on parameters compared to the direct utilization of a 3x3 convolutional network.

The linear bottleneck (LB) layer substitutes the ReLU6 activation function within the second-to-last layer with a linear function. This change eliminates the ReLU6 activation between the high-dimensional and low-dimensional sections, effectively addressing the issue of ReLU6 discarding low-frequency information following the IRB. The core structure of MobileNetV2, known as the bottleneck residual block, is created by combining the IRB with the LB layer. When stride (s) equals 1, the shortcut is employed; when s equals 2, the shortcut is omitted, as depicted in Figure 2.

The model took as input the preprocessed chest X-ray images resized to 224x224x3. To start, a convolution operation with 32 channels and a stride of 2 was executed, resulting in a feature layer sized 112x112x32. Subsequently, after applying 7 bottleneck residual blocks, the feature layer expanded to 7x7x320. Following this, a 1x1 convolution operation was applied with 1280 channels and a stride of 1, resulting in a feature layer of 7x7x1280. Ultimately, a global average pooling operation was incorporated to diminish the feature dimensions from 7x7x1280 to a mere 1280, by

implementing a downsizing procedure following this feature map.

Table 1. Parameters defining the structural configuration of the MobileNetV2 feature extraction network

Input	Operator	t	c	n	s (stride)
224x224x3	Conv2D 3x3	-	32	1	2
112x112x32	Bottleneck	1	16	1	1
112x112x16	Bottleneck	6	24	2	2
56x56x24	Bottleneck	6	32	3	2
28x28x32	Bottleneck	6	64	4	2
14x14x64	Bottleneck	6	96	3	1
14x14x96	Bottleneck	6	160	3	2
7x7x160	Bottleneck	6	320	1	1
7x7x320	Conv2D 1x1	-	1280	1	1
7x7x1280	avgpool 7x7	-	-	1	-

Within Table 1, "t" represents the factor by which the initial 1x1 convolutional expansion channel is multiplied within each bottleneck residual block. "c" denotes the count of output feature layer channels, "n" signifies the frequency at which the present convolutional block is iterated, and "s" indicates the convolutional step size utilized within the current convolutional block.

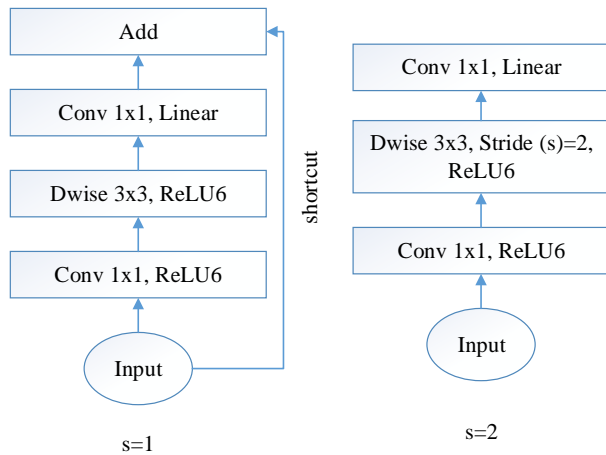


Figure 2. Bottleneck residual block in MobileNetV2

2.3. Squeeze-and-Excitation (SE) Block

The SE block offers a framework for CNNs that enhances channel relationships without substantially increasing computational overhead. This block effectively enhances vital feature information by recalibrating the input features it receives. Utilizing the SE block contributes to the enhancement of interdependencies among channels, thereby augmenting the relevance of feature information for chest X-ray image classification tasks. Figure 3 illustrates the structural outline of the SE block, which functions as follows: Initially, the SE block takes in a feature map along with its current channel count. Subsequently, employing Global Average Pooling (GAP), each channel is transformed into a single numerical value (referred to as "squeeze"). In this process, the feature maps associated with each channel are condensed into 1x1 feature maps using a channel descriptor technique like GAP. This stage produces a scalar value encapsulating general channel information. The primary objective of the "squeeze" operation is to establish a global receptive field, facilitating the utilization of global information even by the lower network layers. Following the

"squeeze" operation, the "excitation" process comes into play, generating weights for individual feature channels based on specified parameters. These parameters are trained explicitly to capture the correlations existing among feature channels. The architecture incorporates two fully connected layers (FC layers) to manage the method's complexity, facilitate generalization, and introduce a bottleneck structure for modeling channel correlations. The initial FC layer serves to reduce the feature dimensions, which are then expanded back to their original size in the subsequent FC layer. Between these two FC layers, the ReLU activation function is employed to infuse non-linearity into the network, allowing it to better adapt to intricate channel correlations. Contrasted with a direct FC layer, the utilization of two FC layers enhances the model's non-linear characteristics, enabling improved accommodation of complex channel relationships while also reducing computational load and parameter count. After the FC-ReLU-FC sequence, the sigmoid function is invoked to compute normalized weights ranging between 0 and 1. Subsequently, a scaling procedure is applied to adjust the normalized weights in accordance with the characteristics of each channel. Importantly, these operations within the SE block incur minimal additional computational overhead. This block can be effortlessly integrated into various methods due to its capability to enhance classification performance [20-22].

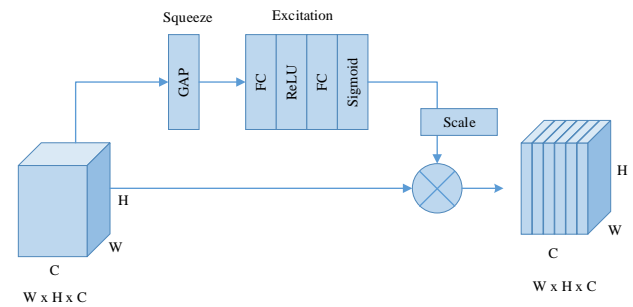


Figure 3. Squeeze-and-Excitation (SE) Block

2.4. Proposed MSENNet Method

The proposed MSENNet model is a hybrid model consisting of MobileNetV2 and SE block as shown in Figure 4. MobileNetV2 aims to decrease the number of trainable parameters. As the SE block is intended to enhance the representational quality of a CNN, this research combines it with MobileNetV2 to enhance both feature extraction and classification performance. Besides, the SE block is integrated into the proposed model as it increases the classification accuracy by minimizing the total number of parameters.

The input image from the proposed MSENNet model is 224x224x3. The MobileNetV2 model was first applied to this image. In the MobileNetV2 model, a convolution process is first applied with a kernel size of 3x3 and a stride value of 2. After this convolution, a feature map of size 112x112x32 is obtained. Then, after applying bottleneck residual blocks seven times in a row, a feature map of size 7x7x320 is obtained. The image size given to the input of each bottleneck residual blocks and the

image size obtained at the output are given in Table 1. After the bottleneck residual blocks, a convolution process of 1x1 size and 1280 filters is implemented to the 7x7x320 feature map. The size of the feature map obtained after this process is 7x7x1280. A global mean pooling process is then applied to this feature map followed by a downscaling procedure to reduce the feature sizes from 7x7x1280 to only 1280. After the operations performed in the MobileNetV2 feature extraction block, the output is given to the input of the SE block. The SE block consists of Squeeze, Excitation and Scaling stages as shown in Figure 3. After these operations are performed in the SE block, GAP and then batch normalization (BN) operations are performed. GAP is a pooling technique designed to substitute the FC layers typically found in standard CNNs. Using GAP, a separate feature map is generated for each category in the classification task's final layer. Instead of introducing FC layers atop these feature maps, each map undergoes averaging, resulting in a vector that is directly passed to the softmax layer. Furthermore, the incorporation of GAP in the proposed method offers the advantage of not having any parameters to optimize in the GAP layer, effectively preventing overfitting. The output of the GAP layer is fed into a softmax function for feature classification and the prediction of CXR images. However, prior to softmax, BN is applied to streamline and accelerate the training process. Finally, Softmax assigns probabilities to each class and the sum of these probabilities equals one.

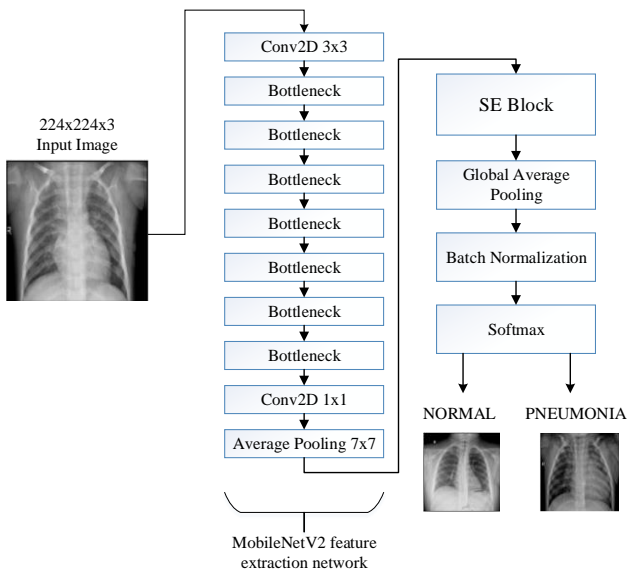


Figure 4. Proposed MSENNet model

3. RESULTS OF EXPERIMENTS

In this section, the hyperparameters used in the experimental studies, the evaluation criteria used, the classification results obtained from the experimental studies and the discussion of these results are presented.

3.1. Parameter Setting

A specific set of hyperparameters is used to train the model using the Keras and TensorFlow library in the

kaggle environment. Experimental studies for the CXR images dataset were performed with TPU VM v3-8, a hardware accelerator in the kaggle environment. Overall, we expect that the use of hyperparameters, optimizers and callbacks in combination with Keras-TensorFlow and the Kaggle environment will allow us to achieve state-of-the-art results with our proposed method architecture. The hyperparameters used include batch size, image size, training-test-validation separation, number of epochs. To train the proposed method, a batch size of 128, an image size of 224x224x3 and a training-test-validation separation of 80%-10%-10% are used. Out of 5856 CXR images, 4684 images were used for training, 586 for validation and 586 for testing. In addition, the model is trained for 100 epochs. Adam optimizer is used to minimize the loss function and optimize the model. In addition to the hyperparameters, two special callbacks are used to optimize the training process. The first callback is the ReduceLROnPlateau callback, which is used to reduce the learning rate when the loss of validation stops the recovery. This helps to stabilize the training process and avoid overlearning. In this callback, 0.000001 is taken as the lower bound of the learning rate (min_learning_rate). Also, the factor value to reduce the learning rate is 0.3. The second callback is the ModelCheckpoint callback, which is used to record model weights at regular intervals during training. This allows us to save the best model based on validation accuracy and load it for future use.

3.2. Performance Metrics

The effectiveness of the proposed approach is gauged by employing performance metrics like precision, F1-score, recall, and classification accuracy. Performance metrics provide a quantitative and objective measure of the effectiveness of a model's predictions. They are also necessary to evaluate classification performance. These metrics provide different perspectives on the performance of the model, each with its own strengths and limitations. A detailed description of these metrics is as follows. Accuracy, a key performance evaluation metric, measures the percentage of correct estimations produced by the method. It is determined as the number of correct estimations divided by the total number of estimations made. The computation of the accuracy value is done as detailed in Equation (1). Precision, a measure of the proportion of true positives in all positive estimations made by the proposed method, is determined as the number of true positives divided by the sum of true positives and false positives. The calculation of the precision value is as in Equation (2). Recall, a metric that measures the proportion of true positives among all true positive samples in the dataset, is determined as the number of true positives divided by the sum of true positives and false negatives. Recall is formulated as in Equation (3). The F1 score, which is the harmonic mean of recall and precision, is an indispensable metric for balancing recall and precision, especially when classes are unbalanced. It ensures a single score that captures both precision and recall, making it a powerful measure for overall model performance evaluation [5,9,23]. The F1 score is computed as outlined in Equation (4).

$$Accuracy (Acc) = \frac{TP + TN}{TP + FP + TN + FN} \quad (1)$$

$$Precision (P) = \frac{TP}{TP + FP} \quad (2)$$

$$Recall (R) = \frac{TP}{TP + FN} \quad (3)$$

$$F1 - score (F1S) = 2 \times \frac{Precision \times Recall}{Precision + Recall} \quad (4)$$

All these performance metrics are deduced from the confusion matrix. An illustrative representation of a confusion matrix can be observed in Figure 5. Within a standard confusion matrix, there exist four primary elements: True Positives (TP): These denote cases where the genuine category is affirmative (for example, class 1), and the model accurately forecasts it as affirmative. True Negatives (TN): These represent instances in which the true category is negative (e.g., class 0), and the model correctly anticipates it as negative. False Positives (FP): These instances arise when the true category is negative, but the model incorrectly anticipates it as affirmative. False Negatives (FN): These arise from situations where the authentic category is affirmative, yet the model erroneously predicts it as negative.

		Actual	
		Positive (P)	Negative (N)
Prediction	Positive (P)	TP	FP
	Negative (N)	FN	TN

Figure 5. Confusion matrix

3.3. Experimental Studies and Results

In order to analyze the classification performance of the proposed MSENNet model, extensive experimental studies were performed on a 2-class (Normal and Pneumonia) CXR images dataset. The confusion matrix of the MSENNet model is given in Figure 6. In the test dataset, 159 out of 164 Normal CXR images and 420 out of 422 Pneumonia CXR images were correctly predicted. It is seen that a total of 579 images are correctly predicted in all classes from a total of 586 test datasets. Based on these results in the confusion matrix, the classification accuracy of the proposed MSENNet model was obtained as 98.81%.

The MobileNetV2 model used in the proposed MSENNet model is a pre-trained model. Accordingly, the MSENNet model is compared with different pre-trained models and the results are given in Table 2. Table 2 shows that 98.81% accuracy, 98.79% precision, 98.24% recall and 98.51% F1-score were obtained with the proposed MSENNet model. The closest accuracy, precision and F1-score values to the proposed method are obtained with

the Xception model with 98.12%, 98.05% and 97.49%, while the closest recall value is obtained with the MobileNetV2 model with 97.22%. The lowest accuracy value was obtained in VGG16 with 96.42%, the lowest precision value was obtained in EfficientNetB0 with 95.94%, the lowest recall value was obtained in VGG16 with 94.32% and the lowest F1-score value was obtained in VGG16 with 95.61%. Considering all the results in Table 2, it is seen that the proposed MSENNet model is more successful than all methods. Considering the parameter numbers of each model, it is seen that the lowest number of parameters is obtained with MobileNetV2. With MobileNetV2, 97.78% accuracy, 97.02% precision, 97.22% recall and 97.12% F1 score values were found. In the proposed MSENNet model, the SE block was added to the MobileNetV2 model. SE block increased the number of parameters by 1. However, it increased the accuracy by 1.03%, precision by 1.77%, recall by 1.02% and F1 score by 1.39%.

The proposed MSENNet model was compared with different studies from the literature using the same dataset and the results are given in Table 3. The proposed MSENNet model achieved 98.81% classification accuracy. The MobileNet model developed by Reshan et al. [2] achieved an accuracy of 94.23%, while the Quaternion CNN model developed by Singh et al. [4] reached 93.75%. Szepesi et al. [10] achieved a 97.2% accuracy using CNN with modified dropout. Ahmad et al. [11] attained 90% accuracy with the Pre-trained ResNet and DenseNet169 models, whereas Shah et al. [12] obtained 96.6% accuracy with the Efficient VGG16 model. Stephen et al. [13] achieved an accuracy of 93.73% using their CNN model when compared to other models. It is evident that the MSENNet model introduced in this study outperforms all other models in terms of success.

	NORMAL	159	5
	PNEUMONIA	2	420
		NORMAL	PNEUMONIA

Figure 6. Confusion matrix of the proposed MSENNet model

Table 2. Comparison of different pre-trained models (%)

Model	Acc	P	R	FIS	#Params
VGG19	96.42	96.94	94.32	95.61	20.026.434
Xception	98.12	98.05	96.94	97.49	20.815.146
ResNet50	97.10	96.43	95.78	96.10	23.542.786
DenseNet121	97.10	96.34	96.14	96.24	6.957.954
NasNetMobile	97.61	96.85	96.85	96.85	4.237.204
EfficientNetB0	96.93	95.94	96.3	96.12	4.012.670
MobileNet	97.44	97.23	96.29	96.76	3.211.074
MobileNetV2	97.78	97.02	97.22	97.12	2.228.994
MSENet	98.81	98.79	98.24	98.51	2.228.995

Table 3. Comparison results with studies in the literature using the same dataset (%)

Study in the Literature	Model	Acc
Reshan et al. [2]	MobileNet	94.23
Singh et al. [4]	Quaternion CNN	93.75
Szepesi et al. [10]	CNN + modified dropout	97.2
Ahmad et al. [11]	Pre-trained ResNet and DenseNet169	90
Shah et al. [12]	Efficient VGG16	96.6
Stephen et al. [13]	CNN	93.73
Proposed MSENet Model	MobileNetV2 and SE block	98.81

4. CONCLUSION

Within the scope of this study, a new DL-based hybrid method for pneumonia detection using CXR images is proposed. The proposed method consists of a combination of pre-trained MobileNetV2 and SE block (MSENet). The primary objective of this proposed MSENet model is to enhance classification accuracy while simultaneously reducing the number of learnable parameters. The utilization of pre-trained MobileNetV2 effectively reduces the count of learnable parameters, a significant aspect of our approach. The SE block is specifically tailored to augment the quality of representation within CNNs, and it is seamlessly integrated into our investigation to amplify both feature extraction and classification performance. The integration of the SE block into our proposed MSENet model is driven by its capability to enhance classification performance with only marginal adjustments to the overall parameter count. To assess the performance of the MSENet model proposed in this study, we employed a dataset consisting of 5856 publicly available CXR images within the Kaggle environment. MobileNetV2 achieved an accuracy of 97.78%, whereas the combined MSENet, comprising MobileNetV2 and the SE block, achieved an accuracy of 98.81%. It's worth noting that MobileNetV2 boasts the lowest parameter count compared to other pre-trained network architectures, with a mere 2.228.994 trainable parameters. In contrast, the MSENet incorporates 2.228.995 trainable parameters. This results in a minor increase of just 1 parameter compared to MobileNetV2, while concurrently achieving a notable increase in classification accuracy by 1.03%. Furthermore, when compared to various pre-trained models, our proposed MSENet demonstrated the highest classification accuracy. Additionally, in a comparative analysis with existing literature methods on the same dataset, the MSENet approach exhibited the most remarkable results.

REFERENCES

- [1] Hu Z, Yang Z, Lafata KJ, et al. A radiomics-boosted deep-learning model for COVID-19 and non-COVID-19 pneumonia classification using chest x-ray images. *Med Phys.* 2022; 49: 3213–3222.
- [2] Reshan MS Al, Gill KS, Anand V, et al. Detection of Pneumonia from Chest X-ray Images Utilizing MobileNet Model. *Healthc*; 11. Epub ahead of print 2023. DOI: 10.3390/healthcare11111561.
- [3] Jaiswal AK, Tiwari P, Kumar S, et al. Identifying pneumonia in chest X-rays: A deep learning approach. *Meas J Int Meas Confed.* 2019; 145: 511–518.
- [4] Singh S, Tripathi BK. Pneumonia classification using quaternion deep learning. *Multimed Tools Appl.* 2022; 81: 1743–1764.
- [5] Zhang D, Ren F, Li Y, et al. Pneumonia detection from chest x-ray images based on convolutional neural network. *Electron*; 10. Epub ahead of print 2021. DOI: 10.3390/electronics10131512.
- [6] Kundu R, Das R, Geem ZW, et al. Pneumonia detection in chest X-ray images using an ensemble of deep learning models. *PLoS One*; 16. Epub ahead of print 2021. DOI: 10.1371/journal.pone.0256630.
- [7] Mercaldo F, Belfiore MP, Reginelli A, et al. Coronavirus covid-19 detection by means of explainable deep learning. *Sci Rep.* 2023; 13: 1–11.
- [8] Ayan E, Ünver HM. Diagnosis of pneumonia from chest X-ray images using deep learning. 2019 *Sci Meet Electr Biomed Eng Comput Sci EBBT 2019*. İstanbul: IEEE; 2019; p. 0–4.
- [9] Sharma S, Guleria K. A Deep Learning based model for the Detection of Pneumonia from Chest X-Ray Images using VGG-16 and Neural Networks. *Procedia Comput Sci.* 2023; 218: 357–366.
- [10] Szepesi P, Szilágyi L. Detection of pneumonia using convolutional neural networks and deep learning. *Biocybern Biomed Eng.* 2022; 42: 1012–1022.
- [11] Al-Taani AT, Al-Dagameh IT. Automatic Detection of Pneumonia Using Concatenated Convolutional Neural Network. *Jordanian J Comput Inf Technol.* 2023; 9: 118–136.
- [12] Shah U, Abd-Alrazeq A, Alam T, et al. An efficient method to predict pneumonia from chest X-rays using deep learning approach. *Stud Health Technol Inform* 2020; 272: 457–460.
- [13] Stephen O, Sain M, Maduh UJ, et al. An Efficient Deep Learning Approach to Pneumonia Classification in Healthcare. *J Healthc Eng*; 2019. Epub ahead of print 2019. DOI: 10.1155/2019/4180949.
- [14] Rajaraman S, Candemir S, Kim I, et al. Visualization and interpretation of convolutional neural network predictions in detecting pneumonia in pediatric chest radiographs. *Appl Sci*; 8. Epub ahead of print 2018. DOI: 10.3390/app8101715.
- [15] Toğaçar M, Ergen B, Cömert Z, et al. A Deep Feature Learning Model for Pneumonia Detection

- Applying a Combination of mRMR Feature Selection and Machine Learning Models. *Irbm*. 2020; 41: 212–222.
- [16] Chouhan V, Singh SK, Khamparia A, et al. A novel transfer learning based approach for pneumonia detection in chest X-ray images. *Appl Sci*; 10. Epub ahead of print 2020. DOI: 10.3390/app10020559.
- [17] Mooney P. Chest X-Ray Images (Pneumonia). Kaggle, <https://www.kaggle.com/datasets/paultimothymooney/chest-xray-pneumonia> (accessed 10 September 2023).
- [18] Sandler M, Howard A, Zhu M, et al. MobileNetV2: Inverted Residuals and Linear Bottlenecks. *Proc IEEE Comput Soc Conf Comput Vis Pattern Recognit 2018*. Salt Lake City: IEEE; 2018. p. 4510–4520.
- [19] Howard AG, Zhu M, Chen B, et al. MobileNets: Efficient Convolutional Neural Networks for Mobile Vision Applications, <http://arxiv.org/abs/1704.04861> (2017).
- [20] Hu J, Shen L, Sun G. Squeeze-and-Excitation Networks. *Proc IEEE Comput Soc Conf Comput Vis Pattern Recognit 2018*. Salt Lake City: IEEE; 2018. p.7132–7141.
- [21] Fırat H. Sıkma - Uyarma Artık Ağı kullanılarak Beyaz Kan Hücrelerinin Sınıflandırılması. *Bilişim Teknol Derg*. 2023; 16: 189–205.
- [22] Asker ME. Hyperspectral image classification method based on squeeze-and-excitation networks, depthwise separable convolution and multibranch feature fusion. *Earth Sci Informatics*. 2023; 1427–1448.
- [23] Dayı B, Üzen H, Çiçek İB, et al. A Novel Deep Learning-Based Approach for Segmentation of Different Type Caries Lesions on Panoramic Radiographs. *Diagnostics*. 2023; 13: 202.

Purification, Characterization of Glutathion Reductase Enzyme From Sheep Spleen Tissue and Investigation of the Effects of Some Antibiotics on Enzyme Activity

Çiğdem ÇOBAN¹, Yusuf TEMEL², Mehmet ÇİFTÇİ³

¹ Bingöl University, Solhan Health Services Vocational School, Bingöl, Türkiye

² Bingöl University, Solhan Health Services Vocational School, Bingöl, Türkiye

³ Bingöl University, Faculty of Veterinary, Bingöl, Türkiye

Çiğdem ÇOBAN ORCID No: 0000-0003-1141-544X

Yusuf TEMEL ORCID No: 0000-0001-8148-3718

Mehmet ÇİFTÇİ ORCID No: 0000-0002-1748-3729

*Corresponding author: mciftci@bingol.edu.tr

(Received: 27.07.2023, Accepted: 20.02.2024, Online Publication: 26.03.2024)

Keywords

Glutathione reductase, Sheep spleen, Purification, Antibiotic, Inhibition

Abstract: In this study, glutathione reductase (EC 1.8.1.7; GR, Glutathione: NADP⁺ oxidoreductase), which is the key enzyme of antioxidant metabolism, was purified from sheep spleen using ammonium sulfate precipitation and 2', 5'-ADP Sepharose-4B affinity chromatography. As a result of purification, the GR enzyme was purified, with 20.03 EU/mg of specific activity, 1564.8 times a yield of 40.61%. The purity of the enzyme was checked by SDS-PAGE. In the characterization studies, optimum pH, optimum ionic strength, stable pH, optimum temperature and subunit molecular mass of the enzyme were determined. In addition, K_M and V_{max} values were found to determine the enzyme's affinity for GSSG and NADPH substrates. It was determined as K_M constant 0.0061 mM and V_{max} value 0.259 EU/mL, for NADPH, K_M constant was determined as 0.351 mM and V_{max} value was determined as 0.604 EU/mL for GSSG. In addition, the effects of ampicillin, streptomycin sulfate, gentamicin, cefoperazone sodium and precort-lyo on enzyme activity were investigated. It was determined that these drugs showed an inhibitory effect on GR enzyme activity purified from sheep spleen tissue. The IC₅₀ values for precort-lyo, ampicillin, streptomycin sulfate, cefoperazone sodium, and gentamicin were 1.27, 3.22, 7.95, 16.97, and 17.20 mM, respectively; and K_i constants were calculated as 0.466±0.387 (competitive), 1.057±0.110 (non-competitive), 3.386±1.305 (competitive), 4.910±0.960 (competitive), and 20.770±8.169 mM (non-competitive), respectively.

Koyun Dalak Dokusundan Glutatyon Redüktaz Enziminin Saflaştırılması, Karakterizasyonu Ve Bazı Antibiyotiklerin Enzim Aktivitesi Üzerine Etkilerinin Araştırılması

Anahtar

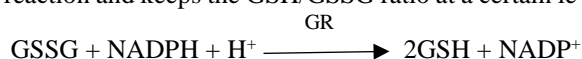
Kelimeler
Glutatyon redüktaz, Koyun dalak, Saflaştırma, Antibiyotik, İnhibisyon

Öz: Bu çalışmada, antioksidan metabolizmanın anahtar enzimi olan glutatyon redüktaz (EC 1.8.1.7; GR, Glutatyon: NADP⁺ oksidoredüktaz), koyun dalak dokusundan amonyum sülfat çöktürmesi ve 2', 5'-ADP Sefaroz-4B afinite kromatografisi kullanılarak, 20.03 EÜ/mg spesifik aktivite ile %40.61 verimle 1564.8 kat saflaştırıldı. Enzimin saflığı SDS-PAGE ile kontrol edildi. Enzime ait karakterizasyon çalışmalarında, optimum pH, optimum iyonik şiddet, stabil pH, optimum sıcaklık ve alt birim molekül kütlesi belirlendi. Ayrıca enzimin GSSG ve NADPH substratlarına ait olan K_M ve V_{max} değerleri bulundu. NADPH için K_M sabiti 0,0061 mM ve V_{max} değeri 0,259 EU/mL, GSSG için K_M sabiti 0,351 mM ve V_{max} değeri 0,604 EU/mL olarak belirlendi. Buna ilaveten ampisilin, streptomisin sülfat, gentamisin, sefoperazon sodyum ve prekort-lyo'nun enzim aktivitesi üzerine etkileri araştırıldı. Bu ilaçların koyun dalak dokusundan saflaştırılan GR enzim aktivitesi üzerinde inhibitör etki gösterdiği belirlendi. Prekort-liyo, ampisilin, streptomisin sülfat, sefoperazon sodyum ve gentamisin ilaçları için IC₅₀ değerleri sırasıyla 1.27, 3.22, 7.95, 16.97 ve 17.20 mM ve K_i sabitleri sırasıyla 0,466±0,387 (yarışmalı), 1,057±0,110 (yarışmasız), 3,386±1,305 (yarışmalı), 4,910±0,960 (yarışmalı) ve 20,770±8,169 mM (yarışmasız) olarak hesaplanmıştır.

1. INTRODUCTION

Glutathione (GSH, γ -L-glutamyl-L-cysteinyl-glycine) is a low molecular weight thiol that is responsible for protecting organisms from the harmful effects of reactive oxygen species (ROS) and reactive nitrogen species (RNS) [1]. GSH is highly reactive and often conjugates with other molecules via its sulfhydryl moiety. GSH, detoxification of intracellular free radicals, xenobiotics, some antineoplastic drugs and some metabolic end products by conjugation, protection of thiol groups of some proteins such as hemoglobin and various enzymes, DNA and protein synthesis, amino acid transport, breaking of disulfide bonds of some proteins such as insulin, intracellular cysteine. It plays a role in many vital reactions inside the cell. GSH metabolism may play both a protective and pathogenic role in cancer. It is very important in the removal and detoxification of carcinogens, and reactions in this pathway can have a significant impact on cell survival [2,3].

Glutathione reductase (E.C. 1.8.1.7; GR) is in the group of oxidoreductases [4]. GR is an important enzyme that catalyzes the conversion of oxidized glutathione (GSSG) to reduced glutathione (GSH) according to the following reaction and keeps the GSH/GSSG ratio at a certain level.



The GSH/GSSG ratio in erythrocyte cells is approximately 500/1. A decrease in this ratio in erythrocyte cells causes hemolysis [5]. For the reaction catalyzed by GR to occur, NADPH supplied from the pentose phosphate pathway is needed [6].

GR is found in prokaryotes in the periplasmic space in relation to the inner membrane facing the cytoplasm, in the cytoplasm in eukaryotes, and in organelles including the nucleus and mitochondria [7]. It was determined that the enzyme, whose structure was first determined by Meldrum and Tarr in 1935, carried out the reduction reaction of GSSG in the blood and NADPH was a cofactor in this reaction [8]. In previous studies, GR enzyme, porcine erythrocyte, bovine erythrocyte, rat liver, bovine liver, sheep brain, mammalian tissues such as sheep liver, rainbow trout and turkey liver tissue, fungi, microorganisms such as cyanobacteria, vegetable plants such as wheat, corn, pea and spinach. It has been characterized by purification from many prokaryotic and eukaryotic sources [9,10].

Antibiotics are drugs that treat infectious diseases as well as enable many modern medical procedures, including cancer treatment, organ transplants, and open heart surgery. However, the misuse of these drugs causes the patient to suffer from drug side effects, as well as financial losses and a rapid increase in antimicrobial resistance (AMR), where some infections can no longer be effectively treated [11]. In kinetic studies on enzymes, it has been determined that drugs, including antibiotics, interact with enzymes and affect enzymes in vivo and in vitro [12, 13]. In studies carried out to date, it has been

determined that the GR enzyme has not been purified from sheep spleen.

The aim of this study is to purify and characterize the glutathione reductase enzyme, which has an important effect on the regulation of glutathione metabolism in the cell and accordingly the functioning of the antioxidant system, from sheep spleen, and amoxicillin, tylosin, ampicillin, streptomycin sulfate, gentamicin, cefuroxime sodium, cefazolin sodium, cefaperazone sodium, lincomycin, and clindamycin. To investigate the in vitro effects of novamizole, ketogenic and precort-lyo drugs on enzyme activity.

2. MATERIAL AND METHOD

2.1. Material and Method Subheading

2.1.1. Material

NADPH, NADP⁺, GSH, GSSG, bovine serum albumin (BSA), N,N,N',N'-tetramethyl ethylenediamine TEMED, sodium bicarbonate, ethylenediaminetetraacetic acid (EDTA), Coomessie Brilliant Blue G-250, sodium dodecylsulfate (SDS), ammonium sulfate, trihydroxymethylaminomethane (Tris), Acryamide, N,N'-methylene bisacrylamide, 2', 5'-ADP Sepharose-4B were obtained from Sigma Chemical Comp. and E.Merc AG.

2.1.2. Supply of sheep spleen tissue and preparation of homogenate

The sheep spleen used in the study was obtained from the Meat and Milk Institution of Bingöl and brought to the laboratory according to the cold chain rules. 15 g of fresh spleen tissue was suspended in 45 mL of 50 mM KH₂PO₄ (pH: 7.5) buffer. Then it was centrifuged at 13.000 g for 1 hour and homogenate was formed by discarding the precipitate. All operations were carried out at +4 °C [9, 14].

2.1.3. Measuring enzyme activity

The activity measurement of the GR enzyme purified from sheep spleen tissue was carried out according to the method described by Carlberg and Mannervik [15]. This method is based on the determination of the amount of NADPH at 340 nm, which decreases due to the oxidation of NADPH in the presence of oxidized glutathione (GSSG).

2.1.4. Ammonium sulphate precipitation and dialysis

Ammonium sulfate precipitation was performed for the prepared homogenate. For this purpose, precipitation was performed in the ranges of 0% - 20%, 20% - 30%, 30% - 40%, 40% - 50%, 50% - 60%, 60% and 70%, respectively, and the interval in which the enzyme precipitated was determined [16].

2.1.5. Enzyme purification by 2', 5'-ADP sepharose-4B affinity chromatography

The supernatant obtained as a result of homogenate preparation and ammonium sulfate precipitation was applied to the 2', 5'-ADP Sepharose-4B affinity chromatography column. For this; 2',5'-ADP sepharose-4B gel was weighed 2 g dry. Afterwards, this gel was washed several times with 400 mL of distilled water to remove impurities, and the gel was swollen during this time. The air formed due to inflation was removed by vacuuming method using a water trumpet. The prepared gel was packed into a cooled column consisting of a 1x10 cm closed system. The column is 0.1 M K-acetate/0.1 M K-phosphate (pH=7.85), 0.1 M K-phosphate/0.1 M KCl (pH=7.85) and 50 mM KH₂PO₄ washed with /1 mM EDTA (pH=7) buffers. After washing the column, the enzyme was eluted with elution buffer (50 mM KH₂PO₄/1 mM EDTA, 1mM GSH and 0.5 mM NADPH, pH 7.3). The equilibration of the column was understood from the approximate equalization of the absorbance at 280 nm with the buffer passed through the column. Elutions were taken into 1.5 mL eppendorf tubes and activity measurements were made [14, 17, 18].

2.1.6. Control of enzyme purity and determination of molecular mass by SDS-PAGE

The degree of purity of the GR enzyme purified from sheep spleen tissue and the molecular mass of the possible subunit of the enzyme were determined by SDS-PAGE based on the Laemmli method [19].

2.1.7. Protein determination

The protein amounts in the supernatants obtained as a result of homogenate, ammonium sulfate precipitate and 2', 5'-ADP Sepharose-4B affinity chromatography were determined by Bradford method. Standard bovine albumin solution (containing 1 mg protein in 1 mL) was used to create a standard graph, and protein amounts were determined by using the standard graph.

2.1.8. Optimum pH studies

Tris-HCl with pH values of 7, 7.5, 8.0, 8.5 and 9.0 for the determination of the optimum pH of the GR enzyme purified from sheep spleen tissue and pH of 5.5, 6.0, 6.5, 7.0, 7.5 and 8.0 KH₂PO₄ buffers were used.

2.1.9. Optimum ionic strength studies

To determine the optimum ionic strength of the GR enzyme purified from sheep spleen tissue, activity measurements were made using 0.01, 0.02, 0.04, 0.06, 0.08, 0.1, 0.2, 0.4, 0.5, 0.8 and 1 M KH₂PO₄ solutions at optimum pH.

2.1.10. Stable pH studies

For the determination of stable pH value of GR enzyme purified from sheep spleen tissue, KH₂PO₄ with pHs of 5, 5.5, 6, 6.5, 7.0, 7.5 and 8.0 and pH of 7, 7.5, 8.0, 8.5 and 9.0 Tris-HCl buffers were used. Measurements were made for 7 days and the stable pH of the enzyme was determined.

2.1.11. Effect of optimum temperature on enzyme activity

In order to determine the effect of optimum temperature on the GR enzyme purified from sheep spleen tissue, activity measurements were made between 0°C and 90°C at 10°C intervals.

2.1.12. Kinetic studies

In order to determine the K_M constant and V_{max} value of the substrates of the GR enzyme purified from sheep spleen tissue, activity measurements were made at 5 different concentrations, which are the substrates of the enzyme, GSSG and NADPH. Lineweaver-Burk graphs were drawn and K_M and V_{max} values were determined for NADPH and GSSG substrates with the help of these graphs [20].

2.1.13. *In vitro* inhibition studies

In order to examine the effects of some drugs on the GR enzyme activity purified from sheep spleen tissue, drugs at different concentrations were taken and added to the cuvette medium. IC₅₀ values for drugs that cause enzyme inhibition, such as prekort-lyo, ampicillin, streptomycin sulfate, cefoperazone sodium and gentamicin, were calculated using the Activity%-[I] graphs drawn. In order to determine the Ki constants of these drugs showing inhibitory effect, enzyme activities were measured at 3 different fixed concentrations and 5 different substrate concentrations. Lineweaver-Burk graphs were created by converting each activity value to enzyme unit and calculating 1/V and 1/[S] values. Using these graphs, Ki constants and inhibition types were determined.

3. RESULTS

In this study, the GR enzyme was purified with a specific activity of 20.03 EU/mg, 40.61% yield and 1564.8-fold from sheep spleen tissue using homogenate preparation, ammonium sulfate precipitation and 2', 5'-ADP Sepharose-4B affinity chromatography. Purification results of GR enzyme purified from sheep spleen tissue are given in Table 3.1.

Table 3.1. Purification steps of glutathione reductase enzyme

Purification step	Total Volume (mL)	Activity (EU/mL)	Protein (mg/mL)	Total Protein (mg)	Total Activity (EU)	Specific Activity (EU/mg)	Yield %	Pur. fold
Homogenate	25	0.523	40.85	1021	13.075	0.0128	100	1
Ammonium sulfate precipitation (40-70%)	13	0.689	52.94	688	8.957	0.0130	68.50	1.015
Affinity Chromatog.	9	0.590	0.029	0.265	May.31	20.Mar	40.61	1564.8

3-8% SDS-PAGE was performed to determine the purity of the GR enzyme purified from sheep spleen tissue. The SDS-PAGE photograph is shown in Figure 3.1. The logMK-Rf graph was drawn for the determination of the molecular mass of the possible subunit of the enzyme. The molar mass of sheep spleen GR enzyme was calculated as approximately 91 kDa by using the graphic equation.

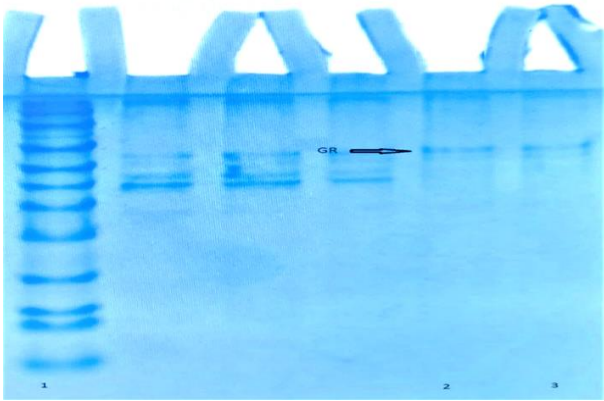


Figure 3.1. SDS-PAGE photograph obtained for the GR enzyme. Well 1: standard protein (molecular size of the markers; 175, 130, 95, 70, 62, 51, 42, 29, 22, 14 and 10.5 kDa), wells 2 and 3: pure GR enzyme from the affinity column.

The optimum pH of GR enzyme purified from sheep spleen tissue was determined as 8.0 (KH₂PO₄ buffer), optimum ionic strength was 0.1 M (KH₂PO₄ buffer), stable pH was 7.0 (KH₂PO₄ buffer) and figures 3.2, 3.3 and figures shown in 3.4. In addition, in studies conducted to determine the effect of temperature on the GR enzyme, the temperature with the highest enzyme activities was determined as 40°C and is shown in figure 3.6.

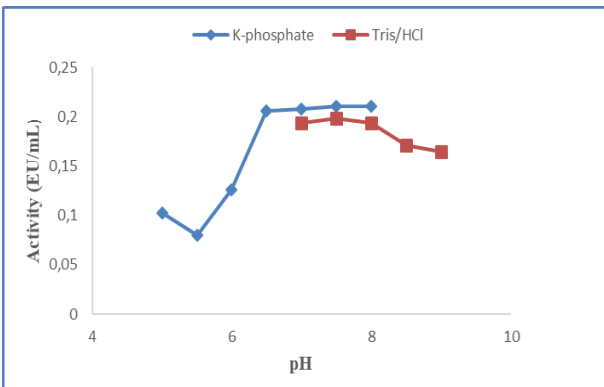


Figure 3.2. pH-Activity graph showing the result of the optimum pH study for sheep spleen tissue GR enzyme.

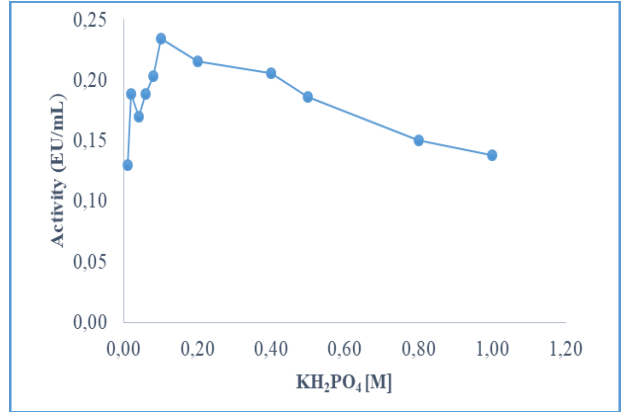


Figure 3.3. pH-Activity graph showing the result of the optimum pH study for sheep spleen tissue GR enzyme.

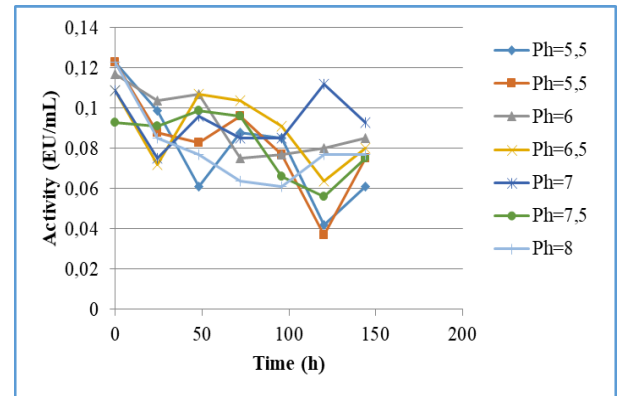


Figure 3.4. Stable pH graph for sheep spleen tissue GR enzyme using KH₂PO₄ buffer solution at different pHs

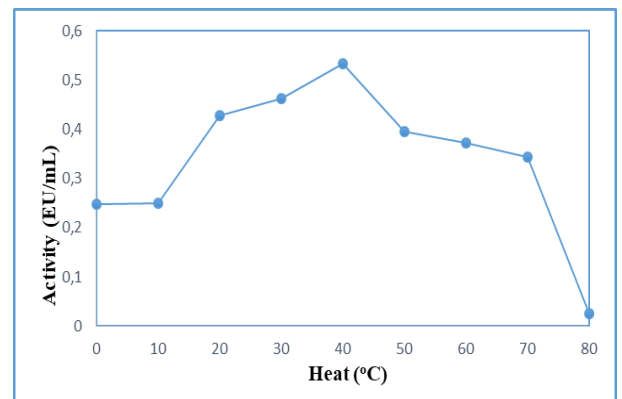


Figure 3.5. Sheep spleen tissue GR enzyme, activity-temperature change graph.

Lineweaver-Burk plot was drawn to determine the K_M constant and V_{max} value for GSSG and NADPH, which are the substrates of the GR enzyme purified from sheep spleen tissue. Using the graph, the K_M constant was 0.0061 mM and the V_{max} value was 0.259 EU/mL for NADPH, and the K_M constant was 0.351 mM and the V_{max} value was 0.604 EU/mL for GSSG, it was shown in Figures 3.6 and 3.7.

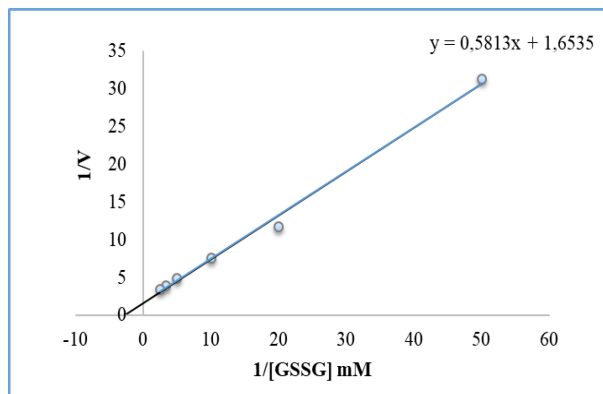


Figure 3.6. Plot $1/V-1/[S]$ plotted to determine the K_M constant and V_{max} of the GSSG substrate

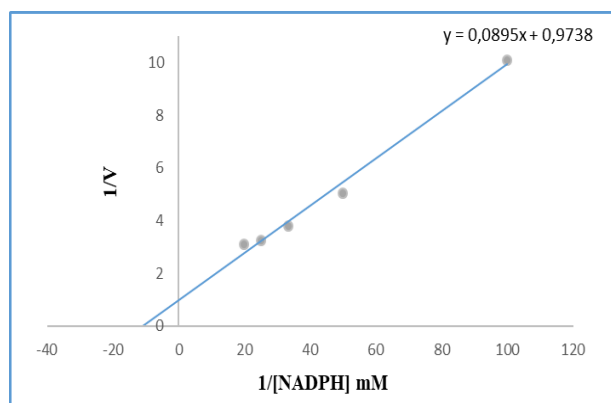


Figure 3.7. Plot $1/V-1/[S]$ plotted to determine the K_M constant and V_{max} of the NADPH substrate

As a result of the kinetic studies, ampicillin, streptomycin sulfate, gentamicin, cefoperazone sodium and precort-lyo showed an inhibitory effect on the GR enzyme activity. It was determined that amoxicillin, tylosin, cefuroxime sodium, cefazolin sodium, lincomycin, novamizole, ketogenic and clindamycin drugs did not show any activation or inhibition effect on the GR enzyme activity. For ampicillin, streptomycin sulphate, gentamicin, cefoperazone sodium and precort-lyo drugs showing inhibitory effects on the enzyme, Activity%-[I] graphs were drawn and IC_{50} values were calculated with the help of these graphs (Figure 3.8-3.9 and Table 3.2).

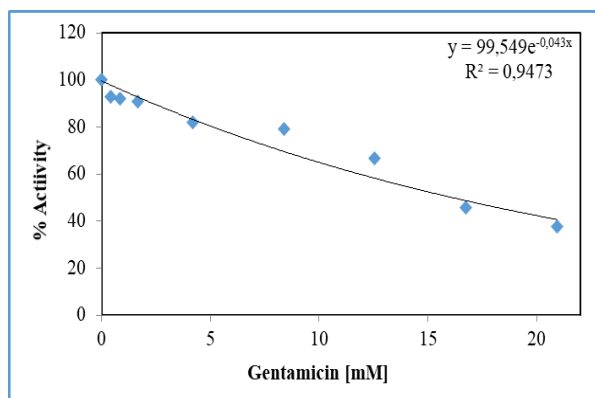


Figure 3.8. Effect of ampicillin on sheep spleen GR enzyme

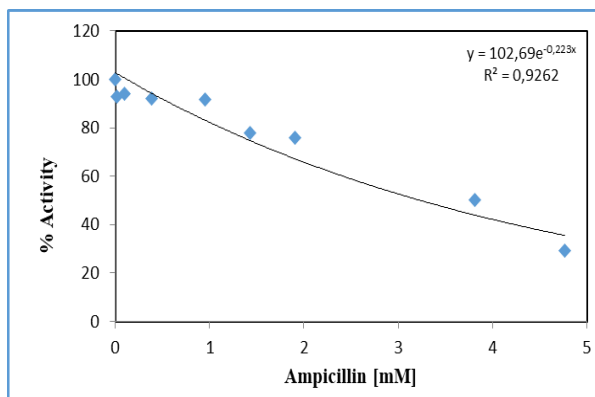


Figure 3.9. Effect of gentamicin on sheep spleen GR enzyme

Table 3.2. IC_{50} values found for some drugs

Drug	IC_{50} (mM)
Precort-lyo	1.27
Ampicillin	3.22
Streptomycin sulfate	7.95
Cefoperazon sodium	16.97
Gentamicin	17.20

Lineweaver-Burk graphs were drawn for ampicillin, streptomycin sulfate, gentamicin, Cefoperazone sodium and precort-lyo drugs, which had an inhibitory effect on GR enzyme activity purified from sheep spleen tissue, and K_i constants and inhibition types were determined with the help of these graphs (Figure 3.10-3.11 and Table 3.3).

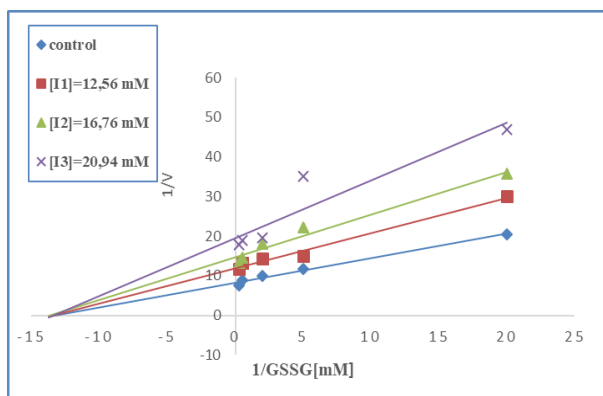


Figure 3.10. Lineweaver-Burk plot for determination of K_i constant for gentamicin sulfate plotted on five different substrates and three different inhibitor concentrations

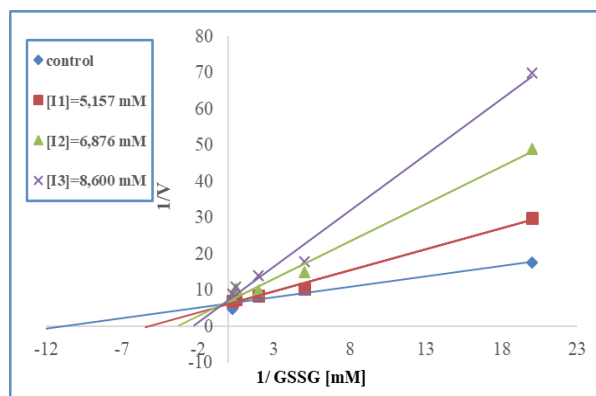


Figure 3.11. Lineweaver-Burk plot for determination of K_i constant for streptomycin sulfate plotted on five different substrates and three different inhibitor concentrations

Table 3.3. K_i values and inhibition types calculated from Lineweaver-Burk plots plotted for sheep spleen GR enzyme at five different substrates and three different concentrations of constant inhibitor

Inhibitor	[I] (mM)	K_i (mM)	Average K_i (mM)	Type of inhibition
Ampicillin	[I1] = 2.862 mM [I2] = 3.816 mM [I3] = 4.770 mM	[I1] = 1.172 mM [I2] = 1.048 mM [I3] = 0.951 mM	1.057 ± 0.11	non-competitive
Gentamicin sulfate	[I1] = 12.56 mM [I2] = 16.76 mM [I3] = 20.94 mM	[I1] = 28.55 mM [I2] = 21.50 mM [I3] = 12.26 mM	20.770 ± 8.17	non-competitive
Streptomycin sulfate	[I1] = 5.157 mM [I2] = 6.876 mM [I3] = 8,600 mM	[I1] = 4.83 mM [I2] = 3.04 mM [I3] = 2.29 mM	3.386 ± 1.31	competitive
Cefoperazon sodium	[I1] = 4.992 mM, [I2] = 9.984 mM, [I3] = 19.968 mM.	[I1] = 3.88 mM [I2] = 5.07 mM [I3] = 5.78 mM	4.910 ± 0.96	competitive
Precort-lyo	[I1] = 0.089 mM, [I2] = 0.356 mM, [I3] = 1.780 mM	[I1] = 0.19 mM [I2] = 0.30 mM [I3] = 0.91 mM	0.466 ± 0.39	competitive

4. DISCUSSION AND CONCLUSION

The GR enzyme (E.C. 1.8.1.7; GR), which belongs to the oxidoreductases (NADP⁺ oxidoreductase) enzyme group, catalyzes electron transfer between reduced pyridine nucleotides and disulfide substrates. GR enzyme is a very important enzyme for glutathione metabolism, which plays a major role in the balanced and regular conduct of biochemical events in the cell by converting more than 99% of oxidized glutathione (GSSG) into reduced glutathione (GSH) in the reaction it catalyzes [21].

In this study, the GR enzyme, whose importance was explained above, was first purified and characterized from sheep spleen tissue using ammonium sulfate precipitation and 2', 5'-ADP Sepharose-4B affinity chromatography, and the effects of some drugs on enzyme activity were also investigated. In this method, there is an advantage in terms of using less chemicals in a shorter time and reuse of the used materials, purification at once and applying a high volume of substance. When the literature studies are examined, GR enzyme was purified 5 456 times from bovine liver with 38.4% yield by 2', 5'-ADP Sepharose-4B affinity chromatography [10]. GR enzyme was purified from rainbow trout liver 1654 times with 41% efficiency [22]. In another study, it was purified 5.823 times from human erythrocytes with 24% yield [23].

SDS-polyacrylamide gel electrophoresis method was performed according to Laemmli (1970) procedure in order to control the purity of the enzyme and to determine the molecular mass of its possible subunit. The subunit molecular mass of the GR enzyme was calculated as approximately 91 kDa. This value found in the study shows similarities with mouse kidney and liver, sheep liver [24, 25, 26].

In our study, the optimum pH for the GR enzyme was determined as 8.0 (in 0.1 M KH₂PO₄ buffer). In the literature search, it was seen that the optimum pH of the GRs purified from different sources was between 7 and 8.5 [4, 10, 22, 27, 28].

Sheep spleen GR enzyme was determined as optimum ionic strength 100 mM KH₂PO₄ buffer. This value was found to be close to the values found in studies conducted in various sources before [4, 22, 25, 27]. Considering the activities measured for 7 days, it is seen that the stable pH is 7.0 K-phosphate buffer. It was determined that this pH value is close to stable pH values of GR enzyme purified from bovine erythrocyte, rainbow trout liver and turkey liver [4, 22, 27]. By examining the effect of temperature on the enzyme, the temperature at which the enzyme showed the highest activity was determined as 40°C. In previous studies, these values were determined as 55°C for bovine erythrocytes, 60°C for sheep liver, 55°C for

beef liver, 10°C for trout liver, 40°C for turkey liver, 35-50°C for sheep spleen [4, 22, 25, 27, 29].

In studies conducted to determine the K_M constant and V_{max} value for GSSG and NADPH, which are the substrates of sheep spleen GR enzyme, the K_M constant is 0.0061 mM and the V_{max} value is 0.259 EU/mL for NADPH, and the K_M constant is 0.351 mM and the V_{max} value is 0.604 EU/mL for GSSG was determined. According to these results; It was determined that the affinity of the GR enzyme to the NADPH substrate was higher than its affinity to the GSSG substrate. This result is in agreement with the values found for sheep liver and bovine erythrocyte GR enzymes [10,27].

In our study, the effects of some drugs on enzyme activity were also investigated. In inhibition studies, it was determined that ampicillin, streptomycin sulfate, gentamicin, cefoperazone sodium and precort-lyo substances inhibited the enzyme, but amoxicillin, tylosin, cefuroxime sodium, cefazolin sodium, lincomycin, novamizole, ketogenic and clindamycin substances did not affect the enzyme activity. Precort-lyo, ampicillin, streptomycin sulfate, cefoperazone sodium and gentamicin showing inhibitory effects found IC_{50} values of 1.27, 3.22, 7.95, 16.97 mM and 17.20 mM, respectively, and K_i constants 0.466 ± 0.387 (competitive), 1.057 ± 0.110 (non-competitive), 3.386 ± 1.305 (competitive), 4.910 ± 0.960 (competitive), 20.770 ± 8.169 (non-competitive) mM. According to these results, it was determined that the drug with the most effective inhibitory effect on sheep spleen GR enzyme activity was precort-lyo, and the drug with the lowest inhibitory effect was gentamicin.

Today, many of the drugs that are used intensively for treatment in human and veterinary medicine act on regulatory enzymes that have important roles in metabolism [28-33]. An inhibition that may occur in the activity of these enzymes may play a role in eliminating any problem in cell metabolism or in correcting the situation caused by a pathogenic microorganism in the cell. The results of this study show that ampicillin, gentamicin, streptomycin sulfate, cefoperazone sodium and precort-lyo drugs have inhibitory effects on GR enzyme purified from sheep spleen. From this perspective, it may be a guide for treatments in which the GR enzyme is used as a target in human and veterinary medicine and for future studies on this enzyme.

Acknowledgement

We would like to thank Bingöl University Scientific Research Projects Coordination Unit (BÜBAP) for their financial support with the project numbered BAP-FEF-2019.00.007.

REFERENCES

- [1] Winterbourn CC. Regulation of intracellular glutathione. *Redox Biol* 2019; 22: 101086.
- [2] Balendiran GK, Dabur R, Fraser D. The role of glutathione in cancer. *Cell Biochem Funct* 2004; 22(6): 343–52.
- [3] Temel Y, Kufrevioglu OI, Ciftci M. Investigation of the effects of purification and characterization of turkey (*Meleagris gallopavo*) liver mitochondrial thioredoxin reductase enzyme and some metal ions on enzyme activity. *Turkish J Chem* 2017;41(1): 48–60.
- [4] Taser P, Ciftci M. Purification and characterization of glutathione reductase from turkey liver 2012; 36(5): 546–53.
- [5] Ballatori N, Krance SM, Notenboom S, Shi S, Tieu K, Hammond CL. Glutathione dysregulation and the etiology and progression of human diseases. *Biol Chem* 2009; 390(3): 191–214.
- [6] Temel Y, Taysi MŞ. The Effect of Mercury Chloride and Boric Acid on Rat Erythrocyte Enzymes. *Biol Trace Elem Res* 2019; 191(1): 172–187.
- [7] Couto N, Wood J, Barber J. The role of glutathione reductase and related enzymes on cellular redox homeostasis network. *Free Radic Biol Med* 2016; 95: 27–42.
- [8] Meldrum NU, Tarr HL. The reduction of glutathione by the Warburg-Christian system. *Biochem. J.* 1935; 29: 108-15
- [9] Can B, Kulaksiz Erkmen G, Dalmizrak O, Ogus I H, Ozer N. Purification and characterisation of rat kidney glutathione reductase. *Protein J.* 2010; 29: 250-256.
- [10] Kuzu M, Aslan A, Ahmed I, Comakli V, Demirdag R, Uzun N. Purification of glucose-6-phosphate dehydrogenase and glutathione reductase enzymes from the gill tissue of Lake Van fish and analyzing the effects of some chalcone derivatives on enzyme activities. *Fish Physiol Biochem* 2016; 42(2): 483–91.
- [11] Ulusu NN, Tandoğan B. Purification and kinetic properties of glutathione reductase from bovine liver. *Mol Cell Biochem* 2007; 303(1–2): 45–51.
- [12] Hutchings M, Truman A, Wilkinson B. Antibiotics: past, present and future. *Curr Opin Microbiol* 2019;51:72–80.
- [13] Beydemir S, Ciftci M, Ozmen İ, Buyukkuroglu ME, Ozdemir H, Kufrevioglu OI. Effects of some medical drugs on enzyme activities of carbonic anhydrase from human erythrocytes in vitro and from rat erythrocytes in vivo. *Pharmacol.Res* 2000; 42: 187-191.
- [14] Erat M, Sakiroglu H, Ciftci M. Effects of some Antibiotics on Glutathione Reductase from Bovine Erythrocytes. *Vet. Med. Czech* 2003; 48(11): 305–312.
- [15] Temel Y, Bozkus T, Karagözoglu Y, Ciftci M. Purification and Characterization of Glutathion Reductase Enzyme From Japanese Quail (*Coturnix coturnix japonica*) 2017; 7(3): 143–50.
- [16] Carlberg I, Mannervik B. Purification and characterization of glutathione reductase from calf liver. An improved procedure for affinity chromatography on 2', 5'-ADP Sepharose-4B. *Anal. Biochem* 1981; 116:531–536.
- [17] Smith LL. Cholesterol autoxidation. *Chem. Phys. Lipids* 1987; 44: 87-125.
- [18] Adem S, Ciftci M. Purification of rat kidney glucose 6-phosphate dehydrogenase, 6-phosphogluconate

- dehydrogenase, and glutathione reductase enzymes using 2',5'-ADP Sepharose-4B affinity in a single chromatography step. *Protein Expr Purif* 2012; 81(1):1-4.
- [19] Temel Y, Kocyigit UM. Purification of glucose-6-phosphate dehydrogenase from rat (*Rattus norvegicus*) erythrocytes and inhibition effects of some metal ions on enzyme activity. *J Biochem Mol Toxicol* 2017; 31(9): e21927.
- [20] Laemmli DK. Cleavage of structural proteins during in assembly of the heat ofbacteriophage T4. *Nature*, London, 1970 s. 227-680.
- [21] Lineweaver H, Burk D The determination of enzyme dissociation constants. *J Amer Chem Soc* 1934; 56(3):658-666.
- [22] Keha E, Kufrevioglu OI. *Biyokimya, Aktif Yayınevi, Erzurum*; 2010, s. 653.
- [23] Tekman B, Ozdemir H, Senturk M, Ciftci M. Purification and characterization of glutathione reductase from rainbow trout (*Oncorhynchus mykiss*) liver and inhibition effects of metal ions on enzyme activity. *Comparative Biochemistry and Physiology* 2008; 148: 117-121.
- [24] Erat M, Ciftci M. Effect of Melatonin on Enzyme Activities of Glutathione Reductase from Human Erythrocytes In Vitro and from Rat Erythrocytes In Vivo. *Eur.J. Phlogy* 2006; 537: 59-63.
- [25] Güller P. Gentamisin, amoksisilin ve sefazolin sodyum antibiyotiklerinin fare karaciğer ve böbrek glutatyon redüktaz enziminin aktivite, protein ve gen ekspresyon düzeyleri üzerine etkilerinin incelenmesi. Kimya anabilim dalı, Atatürk üniversitesi, Erzurum, Türkiye, 2015.
- [26] Ulusu G, Erat M, Ciftci M, Sakiroglu H, Bakan E. Purification and characterization of glutathione reductase from sheep liver. *Turkish Journal of Veterinary and Animal Sciences* 2005; 29(5): 1109-1117.
- [27] Erat M, Ciftci M. In vitro effects of some antibiotics on glutathione reductase from sheep liver. *Journal of Enzyme and Medicinal Chemistry* 2003; 18: 545-550.
- [28] Erat M. Purification of human and bovine erythrocyte glutathione reductase enzyme, investigation of the inhibition or activation effects of some drugs and chemicals. Department of Chemistry, Atatürk University, Erzurum, Turkiye, 2002.
- [29] Bilir G. Purification of glutathione reductase enzyme from soybean seed (*glycine max l.*) and examination of the inhibition kinetics of some heavy metals. Department of agricultural biotechnology, Ondokuz Mayıs University, Samsun, Turkiye, 2017.
- [30] Kavutçu M. Isolation, purification and investigation of physicochemical and kinetic properties of adenosine deamylase enzyme from sheep spleen. Department of Biochemistry, Ankara University, Ankara, Türkiye, 1995.
- [31] Temel Y, Ayna A, Hamdi Shafeeq I, Ciftci M. In vitro effects of some antibiotics on glucose-6-phosphate dehydrogenase from rat (*Rattus norvegicus*) erythrocyte. *Drug and chemical toxicology* 2020; 43(2): 219-223.
- [32] Bayindir S, Ayna A, Temel Y, Ciftci M. The synthesis of new oxindoles as analogs of natural product 3, 3'-bis (indolyl) oxindole and in vitro evaluation of the enzyme activity of G6PD and 6PGD. *Turkish Journal of Chemistry* 2018; 42(2):332-345.
- [33] Ayna A, Khosnaw L, Temel Y, Ciftci M. Antibiotics as inhibitor of glutathione S-transferase: biological evaluation and molecular structure studies. *Current drug metabolism* 2021; 22(4): 308-314.

An Investigation on the Use of Clustering Algorithms for Data Preprocessing in Breast Cancer Diagnosis

Ali ŞENOL^{1*} , Mahmut KAYA² 

¹ Tarsus University, Engineering Faculty, Department of Computer Engineering, Mersin, Türkiye

² Fırat University, Engineering Faculty, Department of Artificial Intelligence and Data Engineering, Elazığ, Türkiye

Ali ŞENOL ORCID No: 0000-0003-0364-2837

Mahmut KAYA ORCID No: 0000-0002-7846-1769

*Corresponding author: alisenol@tarsus.edu.tr

(Received: 21.09.2023, Accepted: 26.02.2024, Online Publication: 26.03.2024)

Keywords

Outlier detection, Clustering, Classification, Breast cancer diagnosis.

Abstract: Classification algorithms are commonly used as a decision support system for diagnosing various diseases, such as breast cancer. However, the accuracy of classification algorithms can be affected negatively if the data contains outliers and/or noisy data. For this reason, outlier detection methods are frequently used in this field. In this study, we propose and compare various models that use various clustering algorithms to detect outliers in the data preprocessing stage of classification to investigate their effects on classification accuracy. Clustering algorithms such as DBSCAN, HDBSCAN, OPTICS, FuzzyCMeans, and MCMSTClustering (MCMST) were used separately in the data preprocessing stage of the k Nearest Neighbor (kNN) classification algorithm for outlier elimination, and then the results were compared. According to the results, the kNN + MCMST model most effectively eliminated outliers. The classification accuracy of the kNN + MCMST model was 0.9834, which was the best one, while the accuracy of the kNN algorithm without using any data preprocessing was 0.9719.

70

Meme Kanseri Teşhisinde Kümeleme Algoritmalarının Veri Ön İşleme Amacıyla Kullanılması Üzerine Bir İnceleme

Anahtar Kelimeler

Sapan veri tespiti, Kümeleme, Sınıflandırma, Meme kanseri teşhisi.

Öz: Sınıflandırma, meme kanseri teşhisinde olduğu gibi pek çok hastalığın teşhisi konusunda karar destek sistemleri olarak kullanılmaktadır. Verilerin sapan ve/veya gürültülü veri içermesi durumunda sınıflandırma algoritmalarının başarısı olumsuz etkilenebilmektedir. Bu nedenle bu alanda sapan veri tespit yöntemleri sıkça kullanılmaktadır. Bu çalışmada sapan verileri tespit etmek amacıyla çeşitli kümeleme algoritmalarının sınıflandırmanın veri ön işleme aşamasında kullanılması durumunda sınıflandırma başarısının nasıl etkileneceğine yönelik modeller önerilmekte ve kıyaslanmaktadır. Kümeleme algoritmalarından DBSCAN, HDBSCAN, OPTICS, FuzzyCMeans ve MCMSTClustering (MCMST) algoritmaları k en yakın komşu (kNN) sınıflandırma algoritmasının veri ön işleme aşamasında sapan verileri ortadan kaldırma amacıyla ayrı ayrı kullanılmış ve sonuçlar karşılaştırılmıştır. Elde edilen sonuçlara göre MCMST algoritmasının sapan verileri ortadan kaldırmada daha başarılı olduğu tespit edilmiştir. Veri ön işleme işlemi yapılmaksızın kNN algoritmasının kullanılması durumunda sınıflandırma başarısı 0.9719 iken; en yüksek sınıflandırma başarısına ulaşan kNN + MCMST modelinin doğruluk oranının 0.9834 olduğu tespit edilmiştir.

1. INTRODUCTION

Breast cancer is the most common type of cancer among women and has a high mortality rate if not diagnosed and treated in time. Every year, 2 million 800 thousand women worldwide are diagnosed with breast cancer. However, 90% of patients successfully overcome breast

cancer with early diagnosis and treatment [1]. This underscores the critical importance of early detection strategies in combating breast cancer and reducing its mortality rates.

Classification, a sub-branch of machine learning, is used in many areas [2-6]. One of these areas is health

applications. The use of classification algorithms as a decision support system contributes significantly to the diagnosis of diseases. Several classification algorithms are commonly employed in healthcare settings for disease diagnosis, including breast cancer. Because, classification algorithms can predict new arrival data by learning from existing ones. Naïve Bayes [7], Support Vector Machines (SVM) [8], kNN [9], Decision Trees [10], and Artificial Neural Networks [11] are widely used in this field. These algorithms demonstrate varying degrees of effectiveness in accurately classifying medical data and assisting healthcare professionals in making informed decisions regarding patient care.

The most important factor that reduces the classification accuracy of classification algorithms in machine learning is the presence of outliers and noisy data. Outlier data can arise due to data processing errors, sampling errors, data entry errors, and natural causes (changes in the data). This kind of data can cause classification algorithms to learn the data incorrectly, thus reducing their accuracy. Data preprocessing serves as a crucial step in enhancing the robustness of classification algorithms against outliers. Numerous methods have been proposed in the literature to detect outliers. Isolated Forests [12], Local Outlier Factor (LOF) [13] One-Class SVM [14], and IQR [15, 16] are the leading methods of this area. In addition, clustering algorithms are also frequently used to detect outliers. K-means [17] and DBSCAN [18] are two of these algorithms. Clustering algorithms are used to detect outliers as they can assume that data outside clusters are outliers.

Efficient outlier detection holds paramount importance in classification tasks, particularly in healthcare applications such as breast cancer diagnosis. Identifying and mitigating outliers not only improves the accuracy of classification algorithms but also enhances the reliability of diagnostic decisions. By leveraging advanced outlier detection techniques, healthcare professionals can ensure that classification models are trained on high-quality, representative data, leading to more precise and actionable insights. Thus, the integration of robust outlier detection methodologies into the data preprocessing pipeline is essential for optimizing the performance of classification algorithms and ultimately improving patient outcomes.

In this study, DBSCAN [18], HDBSCAN [19], OPTICS [20], FuzzyCMeans [21], and MCMST [22] clustering algorithms were used to reveal their contribution to the success of classification algorithms when they are used to detect outliers in the data preprocessing stage of classification. To reveal the performance of the models, the obtained results were compared in terms of both classification success and run-time complexity. So, the main contribution of this study to the literature can be summarized as follows:

- Different clustering algorithms were used in the data preprocessing stage of classification and their contribution to classification accuracy was analyzed.

- The MCMST algorithm was used for the first time in this study to detect outliers in data preprocessing and contributed significantly to high classification accuracy.

The rest of the paper is organized as follows: The second section discusses the literature review, while the third section provides information about the algorithms used in this paper. Next, section four presents detailed information about the proposed models. Then, in the fifth section, we provide details about the experimental study and setup. In the sixth section, we share and discuss the results. Finally, in the seventh section, we conclude the study and share plans for future works.

2. LITERATURE REVIEW

In recent years, numerous studies have explored the application of machine learning algorithms, including ANNs, SVM, Naïve Bayes, and kNN, for breast cancer diagnosis using the Wisconsin Breast Cancer Dataset (WBCD). While these studies have reported high classification accuracies, a critical examination reveals certain drawbacks and gaps that warrant further investigation.

One of these studies was proposed by Chen et al. in [23] in 2011. The authors aimed to diagnose breast cancer using rough sets and SVM. Their proposed model achieved 99.41% classification accuracy. Marcano-Cedeno and Andina [24] used ANN with metaplasticity-based multilayer perceptron algorithm for breast cancer diagnosis and achieved 96.26% accuracy. In another study, Seera and Lim [25], proposed an intelligent system for breast cancer diagnosis with a hybrid model including a Fuzzy Min-Max Neural Network, Regression Tree, and Random Forest algorithms. It was found that the model they proposed reached 98.84% classification accuracy. In the proposed model, the Fuzzy Min-Max Neural Network was responsible for incremental learning, the Regression Tree for data intelligibility, and the Random Forest for improving prediction accuracy. Another study in this field was carried out by Zheng et al. [26] to classify breast cancer dataset using SVM with k-means clustering algorithm. In their proposed model, the k-means algorithm clusters the data into cancerous and non-cancerous clusters, while SVM classifies the data using these clusters. The accuracy of their models was measured as 97.38%. In the work presented in [27], Jabbar aimed to improve the accuracy of breast cancer diagnosis using a community learning approach. For this purpose, Bayesian Networks and Radial Basis Function are used in the proposed method. According to the findings, the proposed model reaches 97% classification accuracy. Similarly, Abdel-Zaher and Eldeib in [28] used Deep Belief Networks to diagnose breast cancer. According to the obtained results, their proposed system achieves an accuracy of 99.68%. In addition, Kamel et al. in [29] aimed to classify breast cancer data with the Gaussian Naive Bayes algorithm and achieved 98% accuracy.

In addition to these studies, artificial neural networks and deep learning-based models have been proposed for breast cancer diagnosis and classification, especially in recent years. In one of them, Alickovic and Subasi in [30] aimed to classify a breast cancer dataset using Normalized Neural Networks. According to the experimental results, it was found that their models achieved 99.27% classification accuracy. Similarly, Singh et al. [31] used a Feature Importance Score-Based Functional Link Artificial Neural Networks to classify the same dataset. The proposed model achieved classification with 99.41% accuracy. In addition, in the work given in [32], Kaur proposed a Dense Convolutional Neural Network-based framework for the same aim. His model's performance was also successful, similar to that of other ANN-based models. Its classification accuracy was 98.2%.

Along with the machine learning algorithms shared above, the kNN classification algorithm is also widely used for breast cancer diagnosis in various hybrid structures. In [33], one of these studies, Pawlovsky and Matsuhashi used Genetic Algorithm (GA) for component selection to improve the accuracy of kNN. For this purpose, they tried to make the GA select the best chromosomes. According to the experimental results, their proposed model achieved better results than the standard kNN on UCI's breast cancer dataset. While the standard kNN classifies the data with an accuracy of 76%, the proposed model classifies the data with an accuracy of 79%. In another study, Rajaguru and Chakravarthy [34] performed feature selection on breast cancer data using Principal Component Analysis and then classified the dataset using kNN and Decision Networks to compare the results. According to the results, kNN classified the dataset with 95.61% accuracy, while the Decision Tree classified it with 91.23%. In [35], Admassu performed hyperparameter optimization to determine the most accurate value of k for the kNN algorithm. The most appropriate k values for the breast cancer dataset were determined as 8 and 39, according to the findings. It was observed that the classification performance was 94.35% for the mentioned k values. Besides, in [36], Henderi et al. studied the effect of normalization on classification performance. They normalized the breast cancer dataset with Min-Max and Z-Score Normalization methods and classified it with kNN. The classification accuracy of their model was 98%. In [37], another study in this field, Tounsi et al. examined the effect of feature selection methods on the classification accuracy of breast cancer dataset. For this purpose, they classified the data using SVM and kNN after feature selection. The findings determined that kNN can classify with 96.83% when Ant Colony Optimization is used as the feature selection method. Another study aiming to classify breast cancer dataset with kNN and using feature selection was proposed by Priyadarshini et al. in [38]. The authors applied various feature selection methods to various datasets, including a breast cancer dataset, and then classified them with kNN. The results show 99.51% accuracy can be achieved when the kNN classification algorithm is used with the Equilibrium Optimizer.

As can be seen from the studies we have discussed in this section, clustering algorithms are underutilized for breast cancer diagnosis. This is one of the most critical drawbacks of existing studies. Specifically, density-based clustering algorithms like MCMST, which is very successful in detecting outliers, are anticipated to contribute to classification success significantly. To address this shortcoming in this area, this study is also crucial.

3. PRELIMINARIES

3.1. kNN (k-Nearest neighbors)

kNN is a simple and easy-to-understand algorithm with few parameters (k parameters representing only the k nearest neighbors) and high classification ability. As can be seen in Figure 1, kNN decides which class to assign the data to by looking at its k nearest neighbors. The dominant class among these k neighbors is determined as the class to which the relevant data will be assigned.

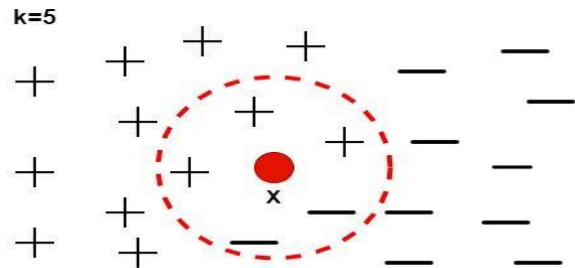


Figure 1. A kNN example ($k=5$).

3.2. Clustering Algorithms

Clustering algorithms are unsupervised learning algorithms that define clusters based on similarities and dissimilarities and do not require class labels. They are machine learning methods that can provide excellent results, especially when class labels are missing, incomplete, or inconsistent. For this purpose, they usually use the distances among the data as the similarity criteria. Euclidean distance, Mahalanobis, City Block, and Manhattan are commonly used distance calculation methods. K-means [17], DBSCAN [18], HDBSCAN [19], OPTICS [20], FuzzyCMeans [21], and MCMST [22] are some examples of these kinds of algorithms.

3.3. Outlier Detection

As shown in Figure 2, outliers refer to data that exhibit characteristics outside the normal. Outlier detection methods, also called anomaly detection, are proposed to detect such abnormal data. Various methods have been proposed to detect outliers, including IForest, MAD, IQR, and LOF. The main goal of such methods is to detect outliers through various mathematical and/or statistical calculations. Apart from such methods, clustering algorithms are also used to detect outliers. The main idea behind using clustering algorithms for detecting outliers is to detect data that fall outside

clusters by defining clusters. In particular, density-based clustering algorithms such as DBSCAN achieve very successful results in this regard.

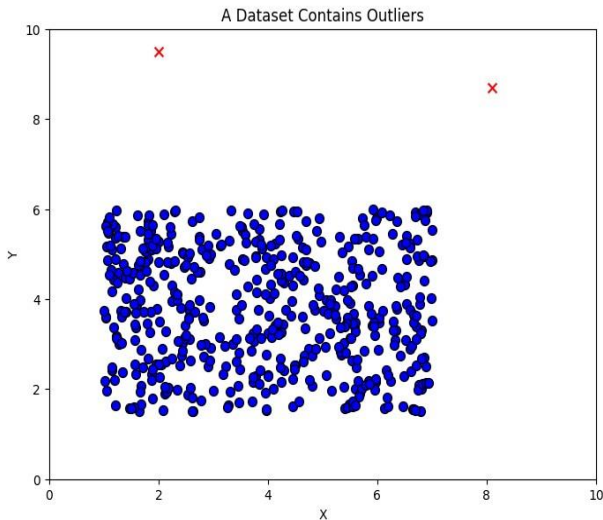


Figure 2. An example that shows outliers.

3.4. MCMST Algorithm

The MCMST algorithm is a density-based clustering algorithm that achieves high clustering success by using a KD-Tree data structure to define micro-clusters and then applying the Minimum Spanning Tree to these micro-clusters to identify the macro clusters [22]. As can be seen in Figure 3, since the MCMST algorithm is a density-based clustering algorithm, it is an algorithm that can both define clusters in arbitrary-shapes and detect outliers with high accuracy.

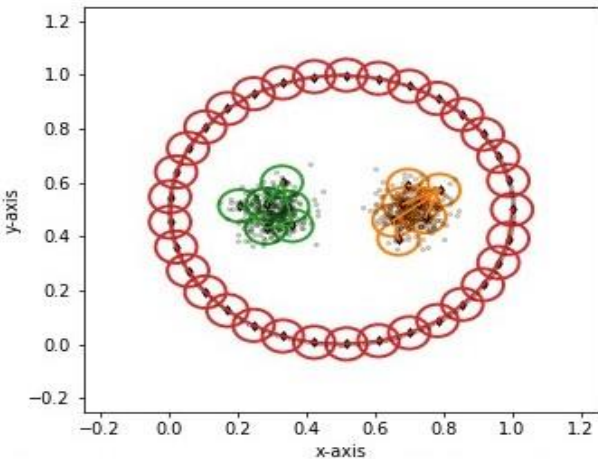


Figure 3. Clustering example with MCMST [22].

4. PROPOSED MODELS: CLUSTERING-BASED OUTLIER DETECTION AND KNN CLASSIFIER MODELS FOR BREAST CANCER DIAGNOSIS

This section provides detailed information about the proposed models. In this study, DBSCAN, HDBSCAN, OPTICS, FuzzyCMeans, and MCMST clustering algorithms were used as clustering algorithms. As seen in Figure 4, the proposed model first passes the dataset through an outlier filter using various clustering algorithms. Then, the data set, which has been cleaned from outliers, is subjected to classification with the kNN

classifier. In the last stage, the obtained results are evaluated.

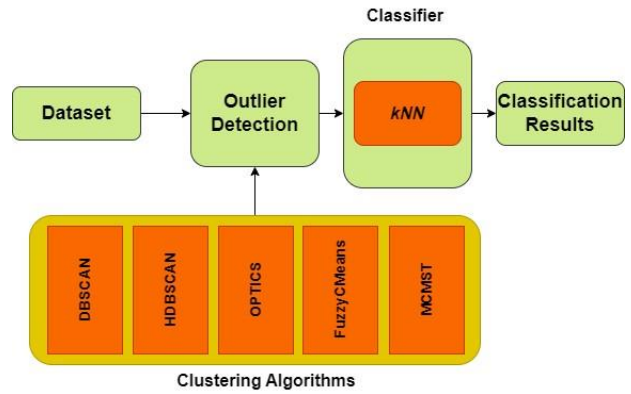


Figure 4. Proposed model.

4.1. Outlier Detection Using Clustering Algorithms

Clustering algorithms are methods that classify data into groups according to the similarities among them. In particular, density-based methods use various parameters for clustering. In short, an amount of data group with an enough density in a certain area that is above a certain threshold value are defined as clusters. Data groups that fall below this threshold are defined as outlier data. At this point of view, clustering algorithms are widely used in the data preprocessing stage to detect outliers. As illustrated in Figure 5, the process of eliminating the outliers is expected to have a positive effect on the clustering success. The first figure indicates the raw data with outliers, while the second figure illustrates the processed data. In this study, we use various clustering algorithms in the data preprocessing stage of classification algorithms to eliminate outliers and examine the possible impact of clustering algorithms on classification performance.

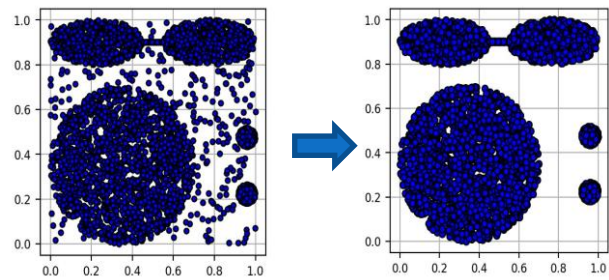


Figure 5. An example of outliers' elimination.

4.2. Classifier

In this study, we used the kNN as a classifier because it is easy to use, simple, and achieves successful results. Another important advantage of the kNN is that it uses only one parameter.

5. EXPERIMENTAL STUDY

In this section, we share detailed information about the experimental studies carried out to demonstrate the performances of the proposed models.

5.1. Used Dataset and Data Preprocessing

In this study, the Wisconsin Breast Cancer Dataset is used to measure the success of the proposed models. The dataset contains information about breast cancer diagnoses of 569 patients. Each record consists of 30 features. To make the parameter selection process easier, the data were normalized using Min-Max Normalization. Let x_{MinMax} be Min-Max Normalization of feature x that is the scaled value between $[0, 1]$, x_{min} be the minimum value of x feature, and x_{max} be the maximum value of x ; x_{MinMax} is calculated using Eq. (1).

$$x_{MinMax} = \frac{x - x_{min}}{x_{max} - x_{min}} \quad (1)$$

5.2. Parameter Setting

Both clustering algorithms and kNN use various parameters. To understand which parameters achieve the best results, a random search method was performed for each algorithm. The range of parameters used is provided in Table 1. In addition, k-fold cross-validation was used to ensure that the results of the models were properly tested. Here, k is set to 5, and the dataset is divided into 75% training and 25% test data.

Table 1. Range of parameters.

Algorithm	Parameter range
kNN	$k=[1, 20]$
kNN + DBSCAN	$k=[1, 20]$, $\text{eps}=[0.01, 1]$, $\text{min_samples}=[1, 30]$
kNN + HDBSCAN	$k=[1, 20]$, $\text{min_cluster_size}=[1, 20]$, $\text{min_samples}=[1, 30]$
kNN + OPTICS	$k=[1, 20]$, $\text{eps}=[0.01, 1]$, $\text{min_samples}=[1, 30]$
kNN + FuzzyCMeans	$k=[1, 20]$, $c=[1, 30]$, $m=[1, 30]$
kNN + MCMST	$k=[1, 20]$, $N=[1, 30]$, $r=[0.01, 1]$, $n_micro=[1, 30]$.

5.3. Metrics to Measure the Classification Performance

Since a classification model was used in this study, the Accuracy, Precision, Recall, and F1-Score, commonly used metrics, were used to measure classification success. These metrics are calculated from the confusion matrix given in Table 2. Let True-Positive be TP, True Negative be TN, False Positive be FP, and False Negative be FN; each metric is calculated by Eq. (2), (3), (4), and (5), respectively.

$$\text{Accuracy} = \frac{TP + TN}{TP + TN + FP + FN} \quad (2)$$

$$\text{Precision} = \frac{TP}{TP + FP} \quad (3)$$

$$\text{Recall} = \frac{TP}{TP + FN} \quad (4)$$

$$F1 - \text{Score} = \frac{2 * \text{Precision} * \text{Recall}}{\text{Precision} + \text{Recall}} \quad (5)$$

Table 2. Confusion matrix.

Predicted	Actual	
	TP	FP
FN		
TN		

6. EXPERIMENTAL RESULTS AND DISCUSSION

In order to determine which clustering algorithm is more successful in detecting outliers, each clustering algorithm was run on the WBCD dataset with parameters randomly selected from the range given in Table 1. Then the results were analyzed by classifying with kNN. Each algorithm was run 100 times and the parameters given in Table 3 that provided the highest classification accuracy were determined. Each clustering algorithm detected a different number of outliers with these parameters, as shown in Table 4. Likewise, the classification successes shown in Table 5 were obtained when the models were tested with these parameters.

Table 3. The best parameters for each algorithm.

Algorithm	Parameters
kNN	$k=12$
kNN + DBSCAN	$k=5$, $\text{eps}=0.54$, $\text{min_samples}=5$
kNN + HDBSCAN	$k=3$, $\text{min_cluster_size}=3$, $\text{min_samples}=2$
kNN + OPTICS	$k=16$, $\text{eps}=0.32$, $\text{min_samples}=13$
kNN + FuzzyCMeans	$k=8$, $c=13$, $m=2$
kNN + MCMST	$k=4$, $N=4$, $r=0.58$, $n_micro=24$,

When the results are analyzed, it is seen that the MCMST + kNN model gives the highest classification performance. If the dataset was subjected to classification with kNN without using any outlier detection method, kNN classified the dataset with an accuracy of 0.9719. However, an accuracy rate of 0.9834 was achieved when the outliers were detected and deleted with the MCMST clustering algorithm on the dataset and then classified with kNN. If the effects of other clustering algorithms on the classification performance of kNN are analyzed, we can see that DBSCAN and FuzzyCMeans algorithms slightly increase the classification success, although not as much as MCMST. However, it is seen that HDBSCAN and OPTICS algorithms have a negative impact on classification performance.

Table 4. Number of detected outliers for the models.

Algorithm	# of Detected Outliers	Outliers Ratio (%)
kNN	-	-
kNN + DBSCAN	48	8.44
kNN + HDBSCAN	42	7.38
kNN + OPTICS	41	7.21
kNN + FuzzyCMeans	24	4.22
kNN + MCMST	7	1.23

Table 5. Comparison of classification performance of models.

	Accuracy	Precision	Recall	F1-Score
kNN	0.9719	0.9634	0.9771	0.9694
kNN + DBSCAN	0.9769	0.9702	0.9789	0.9742
kNN + HDBSCAN	0.9696	0.9596	0.9715	0.9651
kNN + OPTICS	0.9646	0.9495	0.9703	0.9584
kNN + FuzzyCMeans	0.9755	0.9677	0.9759	0.9714
kNN + MCMST	0.9834	0.9796	0.9846	0.9817

When kNN was applied to the dataset without performing any preprocessing related to outlier detection, the confusion matrices shown in Figure 6 were obtained. On the other hand, when the MCMST clustering algorithm, which had the highest classification accuracy, was used with kNN, the confusion matrices given in Figure 7 were obtained.

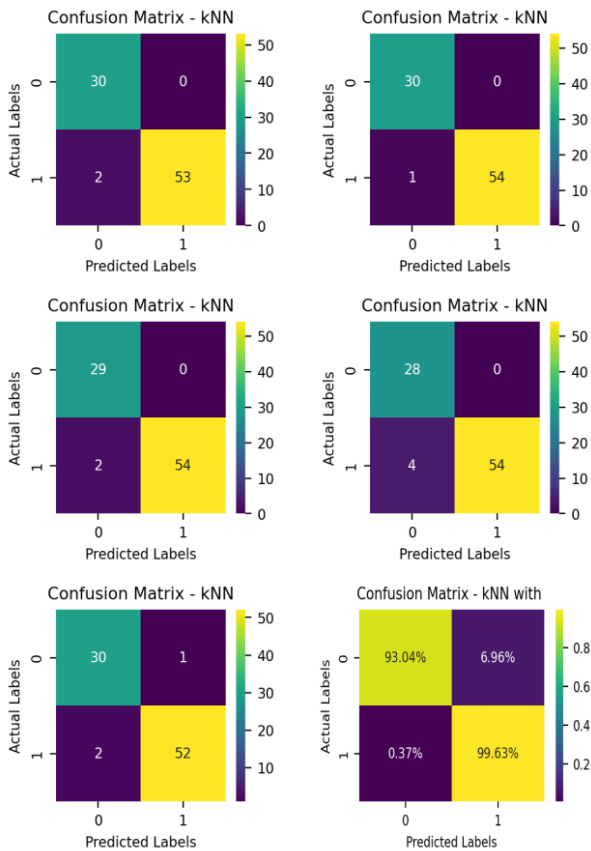


Figure 6. Confusion matrices and their average obtained from k-fold cross-validation for kNN (k=5).

Another point that we analyzed in the proposed study is the run-time complexity of models. As shown in Figure 8, the fastest model among others was the one in which the kNN was run alone. However, it should be noted that no outlier detection is performed in this model. In contrast, the model with the highest run-time was kNN + OPTICS. When the kNN + MCMST model, which achieves the highest classification success, is examined, it is seen that although it is slower than the other 4 models, it is considerably faster than the kNN + OPTICS model.

After determining that the model with the highest classification success was kNN + MCMST, we examined the effect of kNN's single parameter k on the

classification success. We chose k from [1, 50] interval and ran the model for each value of k. The obtained results are illustrated in Figure 9. When the results are analyzed, it can be said that the k value affects model success, but it does not have a great effect. However, the value k = 4 gives the highest classification success.

The MCMST algorithm, as mentioned in the related study, is a very successful algorithm for detecting outliers. This is because this algorithm identifies clusters with a micro-cluster-based density approach. This approach makes the detection of outliers more efficient. Therefore, the MCMST + kNN model is expected to give better results than other models. The results obtained also support this expectation.

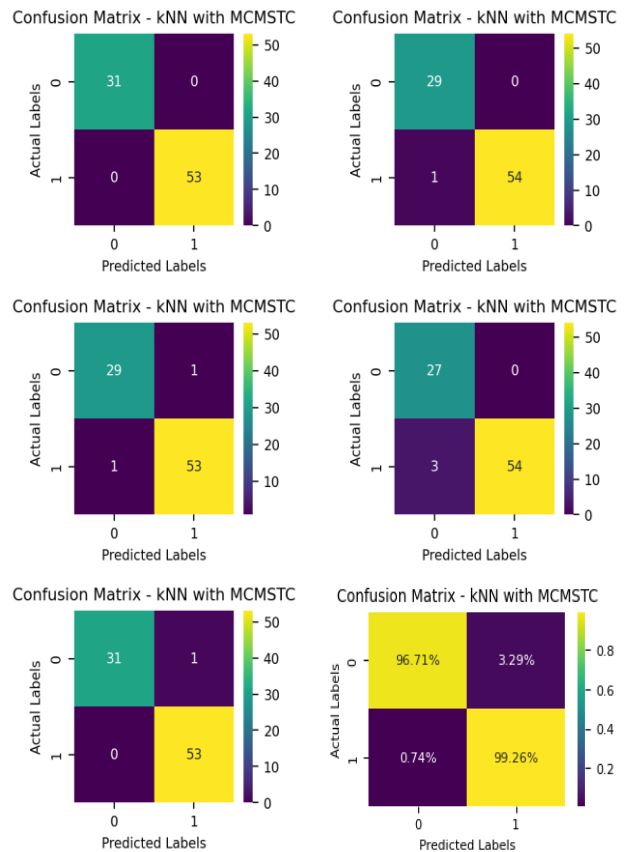


Figure 7. Confusion matrices and their average obtained from k-fold cross-validation for kNN + MCMST (k=5).

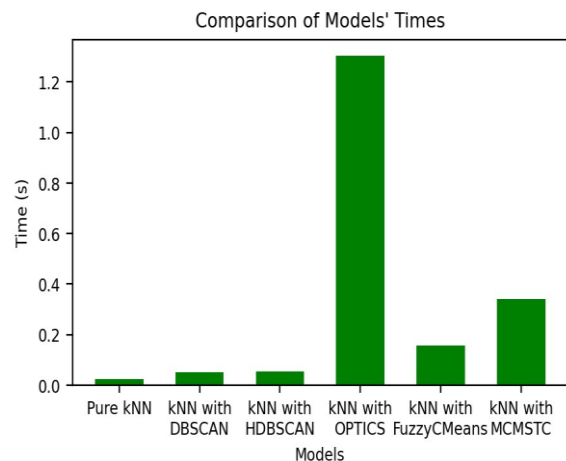


Figure 8. Comparison of the run-time complexity of the models.

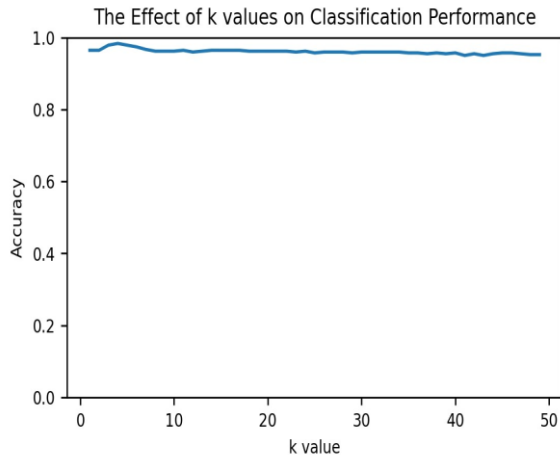


Figure 9. The effect of k values on the kNN + MCMST model classification.

7. CONCLUSION

In this study, the effect of using clustering algorithms in the data preprocessing stage to eliminate outliers on the classification accuracy of the WBCD dataset was investigated. For this purpose, the mentioned dataset was first processed with DBSCAN, HDBSCAN, OPTICS, FuzzyCMeans, and MCMST clustering algorithms to identify and eliminate outliers and then these data were separately classified with kNN that is a simple and effective algorithm.

According to the results, kNN + MCMST was the model with the highest classification performance. The highest classification accuracy was achieved by the kNN + MCMST model, which had an accuracy of 0.9834. In contrast, the accuracy of the kNN method without any data preprocessing was 0.9719. Although the run-time of the model is a little high, it is at an acceptable level. However, three predefined parameters for MCMST are difficult for regular users to determine. This is the most crucial limitation of the model. Given the success of the MCMST clustering algorithm in enhancing classification accuracy, future studies could investigate its integration with deep learning-based models. We can achieve even higher classification accuracy and robustness by leveraging the strengths of both clustering algorithms and deep learning architectures, such as convolutional neural networks (CNNs) or recurrent neural networks (RNNs). This hybrid approach could offer novel insights into the complex patterns underlying breast cancer diagnosis and contribute to the development of more effective diagnostic tools. The models to be developed are planned to be tested in different clinical data sets and in different fields. This will be important in testing the proposed model's effectiveness in different fields.

REFERENCES

[1] Sağlık, A. Rakamlarla Meme Kanseri. 2023 [cited 2023 12.09.2023]; Available from: <https://www.anadolusaglik.org/blog/rakamlarla-meme-kanseri>.

[2] Şenol, A., Canbay, Y. and Kaya, M., Trends in Outbreak Detection in Early Stage by Using

Machine Learning Approaches. *Bilişim Teknolojileri Dergisi*. 14(4): p. 355-366.

[3] Khaire, U.M. and R. Dhanalakshmi, Stability of feature selection algorithm: A review. *Journal of King Saud University-Computer Information Sciences*, 2022. 34(4): p. 1060-1073.

[4] Zhou, H., X. Wang, and R. Zhu, Feature selection based on mutual information with correlation coefficient. *Applied Intelligence*, 2022: p. 1-18.

[5] Heidari, A., et al., Machine learning applications for COVID-19 outbreak management. *Neural Computing Applications*, 2022. 34(18): p. 15313-15348.

[6] Deiana, A.M., et al., Applications and techniques for fast machine learning in science. 2022. 5: p. 787421.

[7] Russell, S.J., *Artificial intelligence a modern approach*. 2010: Pearson Education, Inc.

[8] Manevitz, L.M. and M. Yousef, One-class SVMs for document classification. *Journal of machine Learning research*, 2001. 2(Dec): p. 139-154.

[9] Ali, N., D. Neagu, and P. Trundle, Evaluation of k-nearest neighbour classifier performance for heterogeneous data sets. *SN Applied Sciences*, 2019. 1: p. 1-15.

[10] Fürnkranz, J., Decision Tree, in *Encyclopedia of Machine Learning and Data Mining*, C. Sammut and G.I. Webb, Editors. 2017, Springer US: Boston, MA. p. 330-335.

[11] Jain, A.K., J. Mao, and K.M. Mohiuddin, Artificial neural networks: A tutorial. *J Computer*, 1996. 29(3): p. 31-44.

[12] Liu, F.T., K.M. Ting, and Z.-H. Zhou, Isolation-Based Anomaly Detection. *ACM Trans. Knowl. Discov. Data*, 2012. 6(1): p. Article 3.

[13] Breunig, M.M., et al., LOF: identifying density-based local outliers. *SIGMOD Rec.*, 2000. 29(2): p. 93-104.

[14] Schölkopf, B., et al., Estimating the support of a high-dimensional distribution. *Neural Computation*, 2001. 13(7): p. 1443-1471.

[15] Rousseeuw, P.J. and C. Croux, Alternatives to the Median Absolute Deviation. *Journal of the American Statistical Association*, 1993. 88(424): p. 1273-1283.

[16] Ahmad, S., et al., On efficient monitoring of process dispersion using interquartile range. *Open journal of applied sciences*, 2012. 2(04): p. 39-43.

[17] Hartigan, J.A. and M.A. Wong, A k-means clustering algorithm. *JSTOR: Applied Statistics*, 1979. 28(1): p. 100-108.

[18] Ester, M., et al., A density-based algorithm for discovering clusters in large spatial databases with noise, in *Proceedings of the Second International Conference on Knowledge Discovery and Data Mining*. 1996, AAAI Press: Portland, Oregon. p. 226-231.

[19] Campello, R.J.G.B., D. Moulavi, and J. Sander. Density-Based Clustering Based on Hierarchical Density Estimates. in *Pacific-Asia Conference on Knowledge Discovery and Data Mining*. 2013.

- [20] Ankerst, M., et al., OPTICS: ordering points to identify the clustering structure. *SIGMOD Rec.*, 1999. 28(2): p. 49–60.
- [21] Bezdek, J.C., R. Ehrlich, and W. Full, FCM: The fuzzy c-means clustering algorithm. *Computers & Geosciences*, 1984. 10(2): p. 191-203.
- [22] Şenol, A., MCMSTClustering: defining non-spherical clusters by using minimum spanning tree over KD-tree-based micro-clusters. *Neural Computing and Applications*, 2023. 35(18): p. 13239-13259.
- [23] Chen, H.-L., et al., A support vector machine classifier with rough set-based feature selection for breast cancer diagnosis. *Expert Syst. Appl.*, 2011. 38(7): p. 9014–9022.
- [24] Marcano-Cedeño, A., J. Quintanilla, and D. Andina, WBCD breast cancer database classification applying artificial metaplasticity neural network. *Expert Systems with Applications*, 2011. 38: p. 9573-9579.
- [25] Seera, M. and C.P. Lim, A hybrid intelligent system for medical data classification. *Expert Systems with Applications*, 2014. 41(5): p. 2239-2249.
- [26] Zheng, B., S.W. Yoon, and S.S. Lam, Breast cancer diagnosis based on feature extraction using a hybrid of K-means and support vector machine algorithms. *Expert Systems with Applications*, 2014. 41(4, Part 1): p. 1476-1482.
- [27] Jabbar, M.A., Breast Cancer Data Classification Using Ensemble Machine Learning. *Engineering and Applied Science Research*, 2021. 48(1): p. 65-72.
- [28] Abdel-Zaher, A.M. and A.M. Eldeib, Breast cancer classification using deep belief networks. *Expert Systems with Applications*, 2016. 46: p. 139-144.
- [29] Kamel, H., D. Abdulah, and J.M. Al-Tuwaijari. Cancer Classification Using Gaussian Naive Bayes Algorithm. in 2019 International Engineering Conference (IEC). 2019.
- [30] Alickovic, E. and A. Subasi. Normalized Neural Networks for Breast Cancer Classification. in *CMBEBIH 2019*. 2020. Cham: Springer International Publishing.
- [31] Singh, S., et al., Feature Importance Score-Based Functional Link Artificial Neural Networks for Breast Cancer Classification. *BioMed Research International*, 2022. 2022: p. 2696916.
- [32] Kaur, H., Dense Convolutional Neural Network Based Deep Learning Framework for the Diagnosis of Breast Cancer. *Wireless Personal Communications*, 2023.
- [33] Pawlovsky, A.P. and H. Matsuhashi. The use of a novel genetic algorithm in component selection for a kNN method for breast cancer prognosis. in 2017 Global Medical Engineering Physics Exchanges/Pan American Health Care Exchanges (GMEPE/PAHCE). 2017.
- [34] Rajaguru, H. and S. Chakravarthy, Analysis of Decision Tree and K-Nearest Neighbor Algorithm in the Classification of Breast Cancer. *Asian Pacific journal of cancer prevention : APJCP*, 2019. 20: p. 3777-3781.
- [35] Admassu, T., An optimized K-Nearest Neighbor based breast cancer detection. *Journal of Robotics and Control (JRC)*, 2021. 2.
- [36] Henderi, H., Comparison of Min-Max normalization and Z-Score Normalization in the K-nearest neighbor (kNN) Algorithm to Test the Accuracy of Types of Breast Cancer. *IJIS: International Journal of Informatics and Information Systems*, 2021. 4: p. 13-20.
- [37] Tounsi, S., I.F. Kallel, and M. Kallel. Breast cancer diagnosis using feature selection techniques. in 2022 2nd International Conference on Innovative Research in Applied Science, Engineering and Technology (IRASET). 2022.
- [38] Priyadarshini, J., et al. Analyzing Physics-Inspired Metaheuristic Algorithms in Feature Selection with K-Nearest-Neighbor. *Applied Sciences*, 2023. 13(2), 906.

Protective Effect of Royal Jelly on Some Hematologic Parameters Against Sodium Arsenite Toxicity: A Study in Rats

Enes KAYA^{1*}, Halil ŞİMŞEK²

¹ Bingöl University, Bee and Natural Products R&D and P&D Application and Research Center, Bingöl, Türkiye

² Bingöl University, Vocational School of Health Services, Department of Medical Services and Techniques, Bingöl, Türkiye

Enes KAYA ORCID No: 0000-0003-3973-168X

Halil ŞİMŞEK ORCID No: 0000-0002-9637-1265

*Corresponding author: eneskaya@bingol.edu.tr

(Received: 10.10.2023, Accepted: 29.02.2024, Online Publication: 26.03.2024)

Keywords

Royal jelly,
sodium
arsenite,
hematological
parameters,
heavy metal
toxicity

Abstract: This study examined the effect of royal jelly on some hematological values against sodium arsenite (NaAsO₂)-induced toxicity in rats. Royal jelly is a known functional bee product; therefore, its potential to protect against these effects is of great importance. In this study, the effects of royal jelly on hematologic changes were investigated. In the study, 35 healthy Wistar albino male rats weighing 250–300 g and 12–13 weeks old were used. Rats were administered daily by gavage for 14 days. WBC, LYM, MID, GRA, RBC, HGB, MCHC, MCH, MCV, HCT, PLT, MPV, and PDW values were measured in blood samples. When the measured values were analyzed, the MID, RBC, MCHC, MCH, MCV, and PDV values did not show statistical significance in all experimental groups ($P > 0.005$). However, significant decreases in %LYM, %MID, HCT, and PLT values and increases in WBC, GRA, and %GRA counts were observed in all groups ($P < 0.005$). This review shows that royal jelly has a potential effect on the hematological and immune systems against toxicity caused by harmful heavy metals such as arsenic. In particular, further research is required to identify the most effective dosage of royal jelly. The results highlight the protective potential of royal jelly against toxicity, which requires further investigation.

Arı Sütünün Sodyum Arsenit Toksikitesine Karşı Bazı Hematolojik Parametreler Üzerindeki Koruyucu Etkisi: Ratlarda Bir İnceleme

Anahtar Kelimeler

Arı sütü,
sodyum arsenit,
hematolojik
parametreler,
ağır metal
toksitiesi

Öz: Bu çalışma, ratlarda sodyum arsenit (NaAsO₂) kaynaklı toksisiteye karşı arı sütünün bazı hematolojik değerlere olan etkisini incelemektedir. Arı sütü, bilinen fonksiyonel bir arı ürünüdür ve bu nedenle, bu etkilere karşı koruma sağlama potansiyeli büyük önem taşımaktadır. Çalışmada, hematolojik değişiklikler üzerinden arı sütünün etkileri araştırılmaktadır. Çalışmada, 250-300 gram ağırlığındaki 12-13 haftalık 35 sağlıklı Wistar albino erkek sıçan kullanıldı. Sıçanlara 14 gün boyunca gavaj yolu ile günlük olarak uygulama yapıldı. Kan örneklerinde WBC, LYM, MID, GRA, RBC, HGB, MCHC, MCH, MCV, HCT, PLT, MPV ve PDW değerleri ölçüldü. Ölçülen değerler incelendiğinde, MID, RBC, MCHC, MCH, MCV ve PDV değerleri tüm deney gruplarında istatistiksel olarak anlamlılık göstermedi ($P > 0.005$). Ancak, %LYM, %MID, HCT ve PLT değerlerinde tüm gruplarda önemli düşüşler, WBC, GRA ve % GRA sayılarında ise artışlar gözlemlendi ($P < 0.005$). Bu inceleme, arı sütünün arsenik gibi zararlı ağır metallerin neden olduğu toksisiteye karşı hemotolojik sistem ve bağışıklık sistemi üzerinde potansiyel bir etkisi olduğunu göstermektedir. Özellikle, arı sütünün en etkili dozajının belirlenmesi için daha fazla araştırmaya ihtiyaç vardır. Sonuçlar, arı sütünün toksisiteye karşı koruyucu potansiyelini vurgulamakta olup, bu potansiyelin daha fazla araştırılması gerekmektedir.

1. INTRODUCTION

Royal jelly is an extremely valuable bee product that provides numerous benefits in terms of nutrition and bee diversity. Interestingly, although all bees have the same genetic makeup, queen bees, and worker bees differ significantly in their physiology and morphology - this difference can be attributed to the exclusive consumption of royal jelly by queen bees [1]. Royal jelly is known as a nutrient considered extremely valuable for health and is used as a cosmetic and dietary supplement, with the belief that its effects on bees will have similar effects on humans. Royal jelly is notable for its unique biochemical composition, a special secretion produced by bees of the *Apis mellifera* species. Its proteins, lipids, vitamins, minerals, and bioactive peptides support the potential health benefits of these components on the body. The health benefits of royal jelly have been studied in various aspects such as immune system modulation, antioxidant effects, maintenance of skin health, and alleviation of aging processes [2]. The pharmacological properties of royal jelly have been characterized by a range of biological activities observed in experimental animals. These activities include growth-promoting, antiseptic, antitumor, antibacterial, antioxidant, immunomodulatory, antihypertensive, and anti-inflammatory activities. In addition, royal jelly is believed to have anti-aging, healing, hypoglycemic (anti-diabetic) and anti-cancer properties. Biologically, the special components in royal jelly form the basis for these various pharmacological effects. For example, proteins may support the mechanisms behind growth-promoting effects, while antioxidants may be effective in reducing cellular damage. The immunomodulatory effects of royal jelly can be explained by exerting a regulatory effect on the immune system [3].

Heavy metals are elements that have a high atomic mass, metallic properties, a density greater than 5 g/cm³, and are chemically stable and widely distributed in nature. Heavy metals are elements that can enter the body through the mouth, respiratory tract, and skin. These metals can have toxic effects even at low concentrations, meaning they can be harmful even in very small amounts. These dangerous properties arise because heavy metals are easily absorbed in the body, but cannot be effectively eliminated from the body. In living organisms, heavy metals can accumulate and concentrate. These metals can cause serious health problems when they exceed a certain threshold dose. These problems can include poisoning, organ damage, and even death [4]. Although industrialization has brought many economic and technological benefits to humanity, it is also an important factor that has led to an increase in environmental problems. This process has led to the emergence of environmental problems such as heavy metal pollution and these problems have reached great dimensions over time. With the increase in industrial activities around the world, the number of metal elements exposed to the external environment has also increased. More than 35 of these metals have been detected in the external environment and 23 of these elements are heavy metals. Heavy metals are elements

found in nature and can be released into the environment as a result of human activities such as various industrial processes, mining activities, energy production, and vehicular traffic. Many of these metals can enter the body through the mouth, respiratory tract, and skin and therefore have the potential to harm human health and the environment [5].

Arsenic (As) is one of the twenty most common elements in the earth's crust and is classified as a metal and nonmetal element in terms of its chemical properties. Because of this property, arsenic is also called a metalloid. Arsenic occurs naturally in different parts of the Earth's crust and is present as part of various minerals and ores. Industrial and agricultural practices can lead to the release of arsenic into the environment, which can cause arsenic contamination in water sources and soils. Arsenic can pose a significant hazard to human health. Exposure to high levels of arsenic can cause serious health problems and have carcinogenic effects. It is therefore important to monitor and control arsenic contamination. Arsenic, as an element released into the environment by both natural processes and human activities, is of great importance in the fields of environmental chemistry and health sciences. Its environmental and human health impacts are the focus of scientific research and it is important to learn more about arsenic from an environmental and human health perspective [6].

Hematology is an intriguing field of research that focuses on the cellular components of blood, including erythrocytes (red blood cells), leukocytes (white blood cells), and platelets (thrombocytes), and studies the relationship between the physiology and pathology of these components. By understanding the normal functioning of these cells, hematologists can identify and treat a range of blood-related health conditions. Blood studies provide deep knowledge about the functions and changes of these cellular components, which contributes significantly to our understanding of the functioning of the human body. Hematology sheds light on understanding and treating blood diseases, immune system problems, and other health conditions related to the circulatory system. Blood analysis and the study of cellular components help diagnose diseases early, formulate treatment plans, and monitor patients' health [7].

Hematological parameters such as red blood cell count, white blood cell count, and hemoglobin concentration are widely used as clinical indicators of health and disease. These parameters are a reflection of the biochemical components and cellular structure of the blood and provide important information about the overall health status of the body. Red blood cell count correlates with hemoglobin levels, reflecting the body's capacity to transport oxygen. Hemoglobin is an important molecule that determines the blood's ability to carry oxygen. Therefore, red blood cell count and hemoglobin concentration are critical in diagnosing and monitoring oxygen transport problems such as anemia. White blood cell count reflects the activity of the

immune system and is used to monitor various health problems, such as infections and inflammatory conditions. The number and types of white blood cells help determine the type and severity of infections. These hematologic parameters play an important role in establishing medical diagnoses and treatment plans. They are also regularly monitored to monitor patients' health status and assess their response to treatment. Thus, hematologic parameters are an indispensable tool for disease diagnosis and treatment management in the medical field [8]. Leukocytes, also known as white blood cells, are essential in the immune system and are divided into two main categories: granulocytes and agranulocytes. Granulocytes, with small particles, are the first line of defense against diseases, while agranulocytes, monocytes, and lymphocytes are the immune system's clean-up crew and direct long-term immune responses, creating specialized defense mechanisms like antibodies [9]. Leukocytosis is a condition where the number of white blood cells in the body exceeds normal levels, often indicating health issues and being linked to the immune system. It is crucial to identify and treat the cause of leukocytosis to ensure proper health outcomes [10]. White blood cells (WBCs) are vital in our body's defense system, constantly active in the bloodstream. They protect against threats and are activated by pathogens or harmful substances. This self-defense mechanism increases leukocyte numbers, preventing infections and maintaining health. Leukocytosis, a natural defense mechanism, can signal health problems like infections. The WBC value includes neutrophils, eosinophils, lymphocytes, monocytes, atypical leukocytes, or any combination thereof [12]. Lymphocytes, agranulocytes, are white blood cells that play a crucial role in the immune system. They detect and respond to antigens, forming an essential part of the body's defense mechanism against infections. Lymphocytes identify foreign organisms or pathogens, activating other immune system components to protect against infections. Their role is vital in maintaining the health of the immune system and protecting the body from harmful agents [13]. Monocytes, agranulocytes, are white blood cells that play a crucial role in the body's immune system. They detect, engulf, and eliminate foreign substances through phagocytosis, acting as the first line of defense against infectious agents in rats. Monocytes recognize harmful organisms or foreign substances and neutralize them, making them a vital component of the immune response. Their role is vital for the body's health and the effectiveness of the immune system, making their function crucial [14]. Platelets, a small, reactive blood cell, play crucial roles in fibrosis and blood clotting processes. They undergo changes when stimulated by inflammatory cytokines and classical activators, altering cell shape, forming pseudopodia, and releasing cytoplasmic granules. Platelets accumulate rapidly at damaged sites and form the first line of defense, making their multifaceted role critical for maintaining body health [15].

Previous studies on the effect of arsenic on the hematopoietic system indicate that exposure to high

doses of arsenic can affect and alter the hematopoietic system and these hematopoietic parameters [16]. In blood samples, blood leukocyte parameters, blood erythrocyte-hemoglobin, hematocrit parameters, platelet-related parameters WBC, LYM, MID, GRA, RBC, HGB, MCHC, MCH, MCV, HCT, PLT, MPV, and PDW values were examined and the potential effect of royal jelly on the hematological system and immune system against the toxicity caused by sodium arsenic was evaluated.

2. MATERIAL AND METHOD

2.1. Animal Selection and Permissions: Thirty-five male Wistar albino rats weighing 250-300 grams and 12-13 weeks old were used for the experiment. Animal experiments were performed at Bingöl University Animal Experiment Center. The permission for the experiment was obtained from Bingöl University Animal Experiments Local Ethics Committee with the decision number 07/01 dated 09.12.2021.

2.2. Animal Care: Rats were kept in a control room with a temperature of 24-25°C and a twelve-hour dark photoperiod (19:00-07:00 dark; 07:00-19:00 light). Animals were given unlimited access to water and standard food. Rats were rested and acclimatized for one week while they were maintained in cages.

2.3. Experimental Groups: Rats were randomly divided into five different groups:

a) Control Group (C): Rats were given 0.5 cc saline by gavage for 14 days.

b) Royal Jelly Group (R): Rats were given 1 g royal jelly at a dose of 200 mg/kg, dissolved in 10 cc distilled water, and given 0.5 cc by gavage for 14 days (Solution was prepared daily).

c) NaAsO₂ Group (Arc): Rats were given NaAsO₂ at a dose of 10 mg/kg for 14 days, 1.250 g NaAsO₂ was dissolved in 250 cc distilled water to form a stock solution and given 0.5 cc by gavage.

d) NaAsO₂ + Royal Jelly 100 mg/kg Group (Arc-R-100): Rats were given NaAsO₂ at a dose of 10 mg/kg from the stock solution orally for 14 days. Royal jelly was administered 30 minutes before NaAsO₂ administration at a dose of 100 mg/kg by dissolving 0.250 g royal jelly in 5 cc distilled water and administering 0.5 cc by gavage (Solution was prepared daily).

e) NaAsO₂ + Royal Jelly 200 mg/kg Group (Arc-R-200): Rats were given NaAsO₂ at a dose of 10 mg/kg from the stock solution orally for 14 days. Royal jelly was administered 30 minutes before NaAsO₂ administration at a dose of 200 mg/kg by dissolving 1 g royal jelly in 10 cc distilled water and administered by 0.5 cc gavage.

2.4. Sample Collection and Determination of Hematologic Parameters

One day after the end of the study period, animals were decapitated under sevoflurane anesthesia, and blood samples were collected in 3 ml EDTA vacuum tubes. Blood samples were analyzed for White Blood Cell Count (WBC), Lymphocyte (LYM), Monocyte (MID), Granulocyte (GRA), Erythrocyte (RBC), Hemoglobin (HGB), Mean Corpuscular Hemoglobin Concentration (MCHC), Mean Corpuscular Hemoglobin (MCH), Mean Corpuscular Volume (MCV), Hematocrit (HCT), Platelet Count (PLT), Mean Platelet Volume (MPV), Platelet Distribution Width (PDW) parameters were analyzed. Blood samples were read on BeneSphera™ Brand Hematology Analyzer. Analyses were performed using standard methods [17].

2.5. Statistical Analysis

Differences between the experimental groups were determined using IBM SPSS Statistical software (Version 27) (USA). Statistical evaluation of the data was performed using One-Way ANOVA and Bonferroni test as post hoc. Values were considered statistically significant at $P < 0.005$.

3. RESULTS

WBC, LYM, MID, GRA, RBC, HGB, MCHC of (C), (R), (Arc), (Arc-R-100), (Arc-R-200) groups, MCH, MCV, HCT, PLT, MPV, PDW values are given in Table 1. Statistical comparison was made between the (C) group, (R) group, (Arc) group, (Arc-R-100) group, and (Arc-R-200) group. Values are the mean values of seven separate observations with a standard deviation. Statistically significant values are marked in the table. In all experimental groups, MID, RBC, MCHC, MCH, MCV, PDV hematologic values were statistically insignificant in all groups.

3.1. When the control group and other groups were compared statistically; the following hematologic values were found significant ($P < 0,005$) (Table 1).

- i. Between (C) + (R) group; A statistically significant difference was found in %LYM value. This indicates that royal jelly may affect the percentage of lymphocytes.
- ii. Between (C) + (Arc) group; Statistically significant differences were found in WBC, GRA, %LYM, %MID, %GRA, PLT, HCT values. This indicates that arsenic exposure may affect these parameters.
- iii. Between (C) + (Arc-R-100) group; Significant differences were found in WBC, GRA, %LYM, %MID, %GRA values. This indicates that there were significant differences in the values of white blood cells (WBC), granulocytes (GRA), the percentage of lymphocytes (%LYM), the percentage of medium-sized cells (%MID), and the percentage of granulocytes (%GRA) between the group treated with 100 mg/kg royal jelly (Arc-R-100) and the control group. These results indicate

that royal jelly has a protective effect against arsenic toxicity.

- iv. Between (C) + (Arc-R-200) group; Significant differences were found in %LYM, %MID, %GRA, HCT values. This indicates that there were significant differences in the percentage of lymphocytes (%LYM), the percentage of medium-sized cells (%MID), the percentage of granulocytes (%GRA), and hematocrit (HCT) values between the group treated with 200 mg/kg royal jelly (Arc-R-200) and the control group ©. These results may indicate that royal jelly has a protective effect against arsenic toxicity.

3.2. When the royal jelly group was compared with the other groups; the following hematologic values were found significant ($P < 0,005$) (Table 1).

- i. Between (R) + (Arc) group; A significant difference was found in the PLT value. This indicates that arsenic exposure may affect the platelet count.
- ii. Between (R) + (Arc-R-100) group; Significant differences were found in WBC and LYM values. This indicates that royal jelly may affect these parameters.
- iii. Between (R) + (Arc-R-200) group; A significant difference in HGB value was found. This indicates that royal jelly may affect hemoglobin levels.

3.3. When the arsenic group and other groups were compared statistically; the following hematologic values were found significant ($P < 0,005$) (Table 1).

- i. Between (Arc) + (Arc-R-100) group, PLT
- ii. Between (Arc) + (Arc-R-100) group; PLT, MPV

Significant differences were found in PLT and MPV values. This indicates that royal jelly may modify the effect of arsenic exposure on these parameters.

3.4. When NaAsO₂ + royal jelly 100 mg/kg group and NaAsO₂ + royal jelly 200 mg/kg group were compared statistically; the following hematologic values were found significant ($P < 0,005$) (Table 1).

Between (Arc-R-100) + (Arc-R-200); the HGB value ($P < 0,005$) was found significant, while other hematological values ($P > 0,005$) were found statistically insignificant. This indicates that different doses of royal jelly may have different effects on hemoglobin levels.

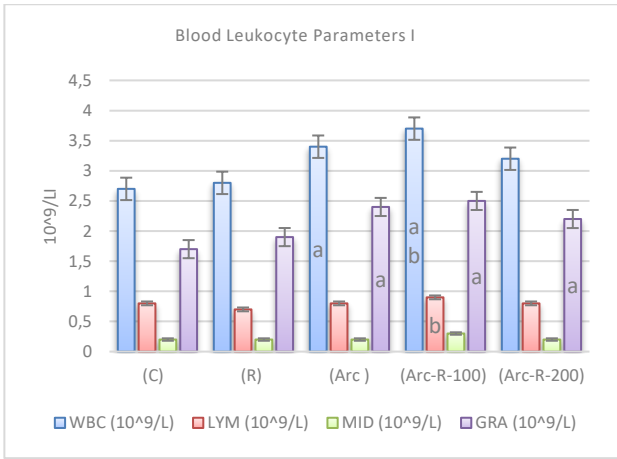


Figure 1. Blood Leukocyte Parameters in Control and Experimental Groups a- The difference compared to the control group is statistically significant (P<0.005) b- The difference according to the royal jelly group is statistically significant (P<0.005)

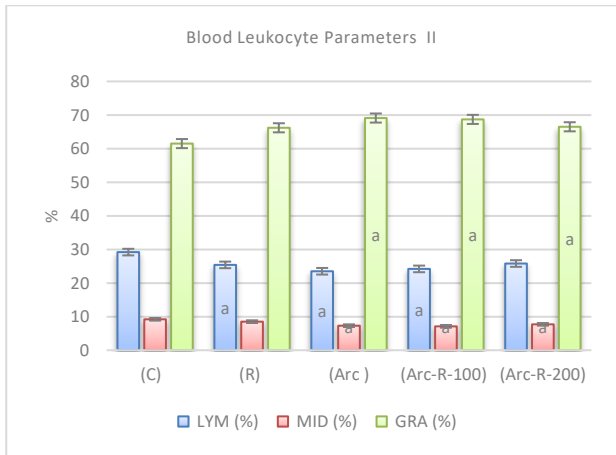


Figure 2. Percent Blood Leukocyte Parameters in Control and Experimental Groups a- The difference compared to the control group is statistically significant (P<0.005)

When the blood leukocyte parameters in the control and experimental groups were examined, the effects of different treatments (Control Group, Royal Jelly Group, NaAsO₂ Group, and different concentrations of Royal Jelly & NaAsO₂) on blood leukocyte parameters were revealed. Compared to the control group, significant changes were observed in the blood leukocyte parameters of the royal jelly group and NaAsO₂ Group. In particular, WBC (10⁹/L) values were significantly higher in the Royal Jelly Group compared to the control group (P<0.005). Furthermore, a significant decrease was observed in LYM (%) and GRA (%) values in the NaAsO₂ group compared to the control group (P<0.005) (Figure 1-2).

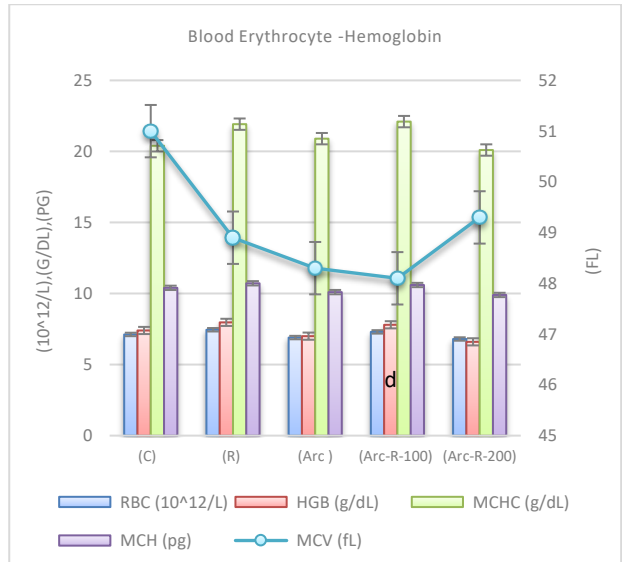


Figure 3. Blood Erythrocyte-Hemoglobin Parameters in Control and Experimental Groups d- There is a significant difference between the 100 mg/kg group of royal jelly and the 200 mg/kg group of royal jelly (P<0.005)

When the blood erythrocyte-hemoglobin parameters in the control and experimental groups were examined, the effects of different treatment groups (control, royal jelly, NaAsO₂, and royal jelly + NaAsO₂ combinations) on RBC, HGB, MCHC, MCH, and MCV values were shown. A significant difference was found between the 100 mg/kg royal jelly group and the 200 mg/kg royal jelly group in the HGB parameter (P<0.005). The findings indicate that royal jelly dosage has a significant effect on blood erythrocyte-hemoglobin parameters. In particular, a significant difference was found between 100 mg/kg and 200 mg/kg royal jelly doses, indicating that royal jelly has a dose-dependent effect on these parameters (Figure 3).

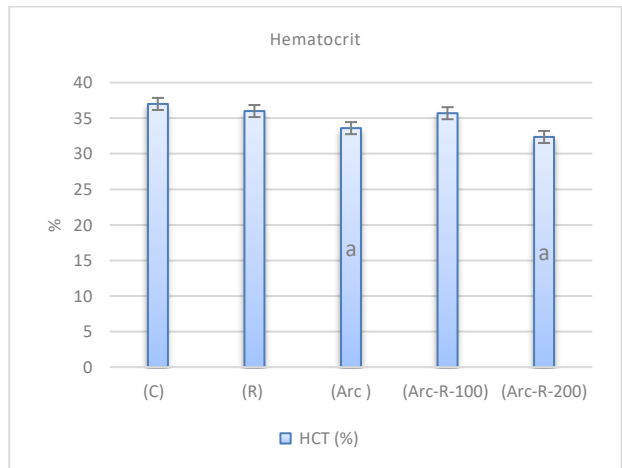


Figure 4. Hematocrit Parameter in Control and Experimental Groups a- The difference compared to the control group is statistically significant (P<0.005)

The control group and Royal Jelly Group had higher hematocrit levels than the NaAsO₂-exposed groups, while the hematocrit levels decreased in the NaAsO₂-exposed groups. However, when royal jelly was given before NaAsO₂ exposure, there was a partial improvement in hematocrit levels. This suggests a

potential protective effect of royal jelly against NaAsO₂ toxicity. These findings are statistically significant (P<0.005)

significant (P<0.005) b- The difference according to the royal jelly group is statistically significant (P<0.005) c- The difference compared to the arsenic group is statistically significant (P<0.005)

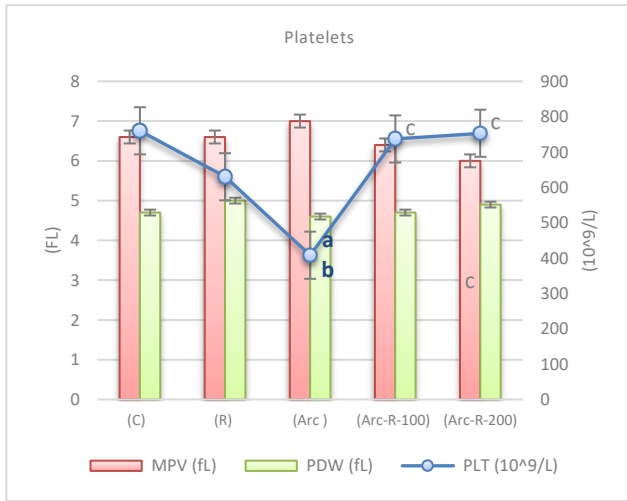


Figure 5. Platelet-Related Parameters in Control and Experimental Groups a- The difference compared to the control group is statistically significant (P<0.005)

There was no statistically significant difference in PDW values between any groups. The decrease in the MPV value indicates a decrease in the size of platelets. The decrease in MPV values compared to the arsenic group may indicate that royal jelly may have a protective effect against arsenic toxicity. Arsenic can impair the formation and function of blood cells. This can lead to changes in the size and number of platelets. However, a reduction in MPV values was observed in the royal jelly group, suggesting that royal jelly may mitigate these negative effects. Compared to the control group and the royal jelly group, a significant decrease in PLT levels was observed in the NaAsO₂ group. However, in the royal jelly-treated groups Arc-R-1 and Arc-R-2, PLT levels were higher than in the NaAsO₂ group. This suggests that royal jelly has a protective effect against NaAsO₂ -induced toxicity (Figure 5).

Table 1. Some Hematological Parameters in Control and Experimental Groups a- The difference compared to the control group is statistically significant (P<0.005) b- The difference according to the royal jelly group is statistically significant (P<0.005) c- The difference compared to the arsenic group is statistically significant (P<0.005) d- There is a significant difference between the 100 mg/kg group of royal jelly and the 200 mg/kg group of royal jelly (P<0.005)

Hemogram	Control Group +SD	Royal Jelly Group +SD	NaAsO ₂ Group +SD	100 mg/kg Royal Jelly + NaAsO ₂ Group +SD	200 mg/kg Royal Jelly+ NaAsO ₂ Group +SD
WBC (10⁹/L)	2,7 ± 0,13	2,8 ± 0,17	3,4 ± 0,43 ^a	3,7 ± 0,21 ^{a b}	3,2 ± 0,36
LYM (10⁹/L)	0,8 ± 0,06	0,7 ± 0,00	0,8 ± 0,10	0,9 ± 0,02 ^b	0,8 ± 0,13
MID (10⁹/L)	0,2 ± 0,05	0,2 ± 0,04	0,2 ± 0,05	0,3 ± 0,06	0,2 ± 0,04
GRA (10⁹/L)	1,7 ± 0,10	1,9 ± 0,15	2,4 ± 0,30 ^a	2,5 ± 0,55 ^a	2,2 ± 0,29
LYM (%)	29,2 ± 1,50	25,4 ± 2,40 ^a	23,5 ± 0,68 ^a	24,2 ± 1,16 ^a	24,6 ± 3,74 ^a
MID (%)	9,2 ± 0,60	8,5 ± 1,07	7,3 ± 0,42 ^a	7,1 ± 0,74 ^a	7,7 ± 0,40 ^a
GRA (%)	61,5 ± 2,03	66,2 ± 3,36	69,1 ± 0,79 ^a	68,7 ± 1,90 ^a	67,6 ± 4,10 ^a
RBC (10¹²/L)	7,12 ± 0,68	7,45 ± 0,34	6,9 ± 0,35	7,3 ± 0,16	6,8 ± 0,49
HGB (g/dL)	7,4 ± 0,35	7,97 ± 0,68	7,0 ± 0,62	7,8 ± 0,15 ^d	6,6 ± 0,64 ^b
MCHC (g/dL)	20,4 ± 1,46	21,92 ± 1,65	20,9 ± 1,37	22,1 ± 0,76	20,1 ± 1,12
MCH (pg)	10,4 ± 1,0	10,72 ± 0,76	10,1 ± 0,81	10,6 ± 0,26	9,9 ± 0,80
MCV (fL)	51,0 ± 1,79	48,9 ± 1,75	48,3 ± 1,12	48,1 ± 0,66	49,3 ± 1,34
HCT (%)	37 ± 2,50	36 ± 1,10	33,6 ± 2,18 ^a	35,7 ± 0,39	32,36 ± 1,14 ^a
PLT (10⁹/L)	760 ± 46,57	630 ± 115,51	408 ± 105,26 ^{a b}	737 ± 47,75 ^{a c}	753 ± 82,59 ^c
MPV (fL)	6,6 ± 0,19	6,6 ± 0,44	7,0 ± 0,72	6,4 ± 0,08	6 ± 0,28 ^c
PDW (fL)	4,7 ± 0,22	5 ± 0,26	4,6 ± 0,92	4,7 ± 0,14	4,9 ± 0,12

4. DISCUSSION

Royal jelly is a natural product produced by the hypopharyngeal and mandibular glands of worker bees and has been widely used in alternative medicine for centuries. Rich in ingredients, royal jelly is abundant in proteins, lipids, amino acids, minerals, and vitamins. It also contains bioactive compounds such as peptides, flavonoids, fatty acids, and phenolic acids [18]. Heavy metal pollution is a serious concern for the environment and human health. However, some supplements may play a potential role in reducing the harmful effects caused by heavy metals in the body. These supplements may help prevent the accumulation of heavy metals in the body or reduce their toxicity [19]. Thanks to its antioxidant properties, royal jelly can reduce cellular oxidative stress, regulate the immune system, suppress inflammation, and reduce the effects of aging. It can also fight germs with antibacterial and disinfectant properties, have anti-cancer potential, lower blood pressure by dilating blood vessels, improve cholesterol levels, protect liver health, and inhibit tumor development. Royal jelly is, therefore, a valuable natural supplement that offers many important health benefits [20]. Arsenic is one of the heavy metals found in nature, and humans can be exposed to it through inhaled air, consumption of food and water, and skin contact. Once in the body, it can affect many organ systems, including the skin, respiratory, cardiovascular, immune, reproductive and urinary systems, digestive, and nervous systems [21]. Hematology and biochemical indicators are reliable parameters for assessing the health status of humans and animals suffering from arsenic poisoning. These indicators are important for monitoring the effects of arsenic exposure and determining the degree of toxicity. Hematological parameters provide information on blood composition and circulatory system health, while biochemical indicators assess body functions and organ systems. These parameters play a critical role in detecting arsenic poisoning and guiding treatment processes [22]. This research was conducted to predict the extent to which the harmful effects caused by arsenic exposure can be reduced by royal jelly. This evaluation included hematological parameters, as these parameters can help determine the degree of harmful effects on the blood components of animals. The monitoring of hematological parameters was used as an important tool to evaluate the protective effect of royal jelly against arsenic and arsenic-induced toxicity and to provide important information in this regard. Some values from studies on sodium arsenite exposure in rats are as follows. Kumari et al. [23] observed a significant decrease in WBC, RBC, Hb, Hct, MCV, and MCH in rats exposed to sodium arsenite. However, MCHC remained the same. Sharma and Rani [24] reported a decrease in RBC, Hb, HCT, and PLT and an increase in WBC values. Ola-Davies et al. [11] found significant decreases in PCV, Hb, and RBC, increases in WBC, platelets, lymphocytes, and eosinophils, and decreases in neutrophils and monocytes. The reasons for the differences in the data obtained from different studies may be various environmental factors such as application method, dose, and application time.

Granulocytes are white blood cells that play an important role in the immune system's response to conditions such as infection, allergies, and asthma. Granulocytes are the most common type of white blood cells and are usually divided into three main categories: neutrophils, eosinophils, and basophils. These cells play important roles in various immune responses [25]. Kumari et al. found that granulocyte values were significantly higher in rats exposed to sodium arsenite compared to the control group. In our study, a significant increase in granulocytes was observed in rats exposed to sodium arsenite compared to the control group ($P < 0.005$). This increase was not significant in the royal jelly group ($P > 0.005$). The results suggest that royal jelly, instead of lowering granulocyte levels, may stimulate more granulocyte production by making the immune system more active.

White blood cells or leukocytes play a vital role in phagocytosis, immunity, and defense against infection [26]. Increased white blood cell counts are known to be a normal reaction to foreign bodies [27]. Ewere et al. [28] found that WBC values in rats exposed to sodium arsenite increased significantly compared to the control group. In our study, an increase in WBC levels was observed. Especially in Arc and Arc-R-100 groups, this increase in WBC levels was found to be statistically significant. In addition, it was observed that this increase became insignificant compared to the control group when the amount of royal jelly in the Arc-R-100 group was increased to 200 mg/kg in the Arc-R-200 group and the values approached the control values. This shows that the amount of royal jelly can affect WBC levels and can be considered an indicator of recovery. These results indicate that royal jelly has a protective effect against sodium arsenite exposure and has a positive effect on the immune system.

Lymphocytes are an important part of the immune system and initiate immune responses by sensing pathogens entering the body. A low lymphocyte count can cause the body to become vulnerable to germs and diseases. This can reduce the body's ability to maintain an effective defense mechanism against harmful microorganisms. Individuals with a low lymphocyte count may therefore have an increased risk of infection and may need to take extra precautions [29]. Ola-Davies et al. found that LYM values increased in rats exposed to sodium arsenite compared to the control group. Our research findings show a significant increase in LYM levels between the R group and the combination groups Arc-R-100 and Arc-R-200. This suggests that royal jelly may have a positive effect on the immune system by increasing the number of lymphocytes. Furthermore, the lymphocyte percentage values were statistically significantly increased in the arsenic-exposed groups unlike the other groups ($P < 0.005$). This supports the hypothesis that royal jelly has the potential to increase the HCT count of other shaped elements in the bloodstream and suggests that royal jelly may have positive effects on the immune system and provide a protective effect against toxicity.

Monocytes play a critical role in the immune system, having the ability to transform into macrophages and dendritic cells when needed to fight against infections. When they move into infected tissues, they help to activate the adaptive immune system by initiating an inflammatory response. The versatility of monocytes is considered a vital component of the immune system's defense against harmful pathogens [9]. Ola-Davies et al. observed that % LYM values decreased in rats exposed to sodium arsenite compared to the control group. According to our study, a significant decrease in the number of monocytes was observed in rats exposed to sodium arsenite. This decrease was valid for all groups except for the royal jelly group. These results are in line with the study conducted by him and his team. In addition, while the MID value in the Arc-R-100 group showed the lowest value in percentage terms, it was observed that these values gradually approached the control group with the increase in the amount of royal jelly in the Arc-R-200 group. This finding again refers to the potential of royal jelly to support the immune system.

Arsenic can negatively affect heme metabolism by binding to hemoglobin. This effect results in a decrease in hemoglobin levels inside red blood cells. Hemoglobin is a critical component that ensures the ability of red blood cells to transport oxygen. Due to its effect on hemoglobin, arsenic can impair the function of red blood cells and negatively affect oxygen transportation throughout the body. Therefore, it is important to monitor hematological parameters to understand and prevent arsenic-related health problems [30]. Arsenic exposure has been reported to contribute to anemia in humans and rodents by suppressing bone marrow function [31]. There appears to be a possible correlation between arsenic exposure and RBC and HGB levels. This relationship may be attributed to the reduced capacity of the bone marrow to produce red blood cells, leading to anemia in these groups [32]. Basher et al. [33] reported that HGB and RBC values decreased in rats exposed to sodium arsenite compared to the control group. In our study, HGB and RBC values decreased compared to the control group. There was a significant decrease in HGB level ($P < 0.005$) between the R group and Arc-R-2 and between Arc-R-1 and Arc-R-2 groups. Although these decreases were not significant in the RBC parameter, they were parallel in terms of significance. Although the group given royal jelly alone (R) had the highest HGB and RBC counts, the combination of sodium arsenite and royal jelly and the increased dose of royal jelly caused a greater decrease in HGB and RBC counts. This may be because individuals administered sodium arsenic may have experienced anemia due to persistent high levels of this substance in their bloodstream, which may have triggered erythrocyte hemolysis and subsequent decrease in hemoglobin levels.

Hematocrit, also known as packed cell volume, is used to determine the percentage of red blood cells in whole blood. Automated methods calculate this value by multiplying the number of RBCs and the average cell volume, while manual methods involve measuring the

hematocrit after centrifugation of a microcapillary tube filled with whole blood [7]. Hematocrit refers to the percentage of packed blood cells relative to the total blood volume. The formula $HCT = (RBC \times MCV)/10$ is used to calculate hematocrit. Following research, it has been found that chronic exposure to low levels of arsenic can negatively affect the body's red blood cells, hematocrit, and hemoglobin levels [16]. There appears to be a discernible association between arsenic exposure and decreased RBC and HCT/PCV measurements [30]. Sharma and Rani observed that arsenic exposure significantly decreased HCT levels in albino rats. In this study, the lowest HCT level was observed only in the group given sodium arsenite. Recent research suggests that low HCT levels may indicate different health conditions. Low HCT values may be a result of conditions such as anemia, excessive fluid intake, renal failure, or chronic inflammatory diseases [34]. The highest HCT level was detected only in the royal jelly group, suggesting that royal jelly may increase hematocrit levels. In conclusion, in the study, hematocrit levels increased in royal jelly-treated groups but decreased in sodium arsenite-treated groups. This suggests that royal jelly may increase hematocrit levels and arsenic exposure may decrease hematocrit levels.

One of the important values in hematologic analysis is the Mean Platelet Volume and Platelet count. MPV shows the average size of platelets and often reflects platelet activity. These parameters are vital for understanding the functioning of the blood coagulation system and for diagnosing various hematological disorders [35]. Mean Platelet Volume determines the overall size of blood cells by measuring the size of platelets. These parameters are used in routine blood morphology tests and play an important role in assessing blood clotting ability [36]. In the study, it was found that the highest MPV rate was in the Arc group and the lowest MPV rate was in the Arc-R-200 group. Kalia et al. reported that arsenic exposure caused a decrease in platelet levels in their study [37]. The highest mean PLT value was observed in the Arc-R-100 and Arc-R-200 groups. The reason for this is that MPV is inversely proportional to platelet count under normal physiologic conditions. That is, the higher the platelet count, the lower the mean volume of platelets, and this is associated with maintaining blood clotting ability and maintaining a constant mass of platelets. [38]. This suggests a decrease in the average volume of platelets accompanying their increased production. In different pathological conditions, this normal physiological ratio can be disrupted. In particular, increased or abnormal platelet production, increased destruction of platelets, or the effect of activation factors on platelets can lead to changes in the ratios between MPV and PLT. These changes can be observed during hematologic analyses and can provide healthcare professionals with important information about the condition of blood cells.

5. CONCLUSION

Sodium arsenite exposure can cause hematologic changes in rats. These changes include an increase in

white blood cells and decreased levels of red blood cells, hemoglobin, and hematocrit. An increase in granulocytes, a marked increase in lymphocytes, and a decrease in monocytes have also been observed. Arsenic exposure can also cause a decrease in hemoglobin and erythrocyte levels and a decrease in hematocrit levels. These findings emphasize that arsenic exposure can have serious effects on hematological parameters. It is suggested that royal jelly administration may influence these changes and in some cases may be protective against arsenic exposure. In particular, royal jelly may have the potential to protect the body against toxicity by increasing white blood cell count and lymphocyte count. Changes in mean platelet volume and platelet count were also observed and it is thought that royal jelly may affect these changes. Royal jelly may have protective effects against sodium arsenite toxicity and has been shown to have positive effects on the immune system. However, decreases in red blood cells, hemoglobin, and hematocrit levels have been noted and further research is needed. Further studies are also needed to identify the components of royal jelly that contribute to these positive effects.

The study did not show significant differences in hematologic parameters such as MID, RBC, MCHC, MCH, MCV, and PDW. However, decreases in %LYM, %MID, HCT, and PLT values and increases in WBC, GRA, and %GRA values were observed in all experimental groups. These results indicate that royal jelly may strengthen the immune system against the effects of harmful substances such as arsenic. The study also emphasizes the possible protective role of royal jelly against toxic effects. This suggests that royal jelly may provide positive effects on health and may be a valuable complementary food for those aiming to improve health. However, further research is needed to determine the appropriate royal jelly dosage and to understand the mechanisms in more depth. This information highlights the potential protective effects of royal jelly and its positive effects on the immune system.

REFERENCES

- [1] Beltekin B, Demir N. International Journal of Food, Agriculture and Animal Sciences (IJFAA) Production and Some Bioactive Properties of Royal Jelly- A Review Arı Sütü Üretimi ve Bazı Biyoaktif Özellikleri - Derleme. 2022; 2(1): 38–46.
- [2] Ramadan MF, Al-Ghamdi A. Bioactive Compounds and Health-Promoting Properties of Royal Jelly: A Review. J. Funct. Foods 2012; 4(1): 39–52.
- [3] Fratini F, Cilia G, Mancini S, Felicioli A. Royal Jelly: An Ancient Remedy with Remarkable Antibacterial Properties. Microbiol. Res. 2016; 192: 130–141.
- [4] Özbolat G, Tuli A. Ağır Metal Toksikitesinin İnsan Sağlığına Etkileri. Arşiv Kaynak Tarama Derg. 2016; 25(23783): 502–521.
- [5] Seven T, Can B, Darende BN, Ocak S. Hava ve Toprakta Ağır Metal Kirliliği. Ulus. Çevre Bilim. Araştırma Derg. 2018; 1(2): 91–103.
- [6] Başkan MB, Pala A. İçme Sularında Arsenik Kirliliği: Ülkemiz Açısından Bir Değerlendirme. Pamukkale Üniversitesi Mühendislik Bilim. Derg. 2009; 15(1): 69–79.
- [7] Bolliger AP, Everds N. Haematology of the Mouse. Lab. Mouse 2012: 331–347.
- [8] Kelada SNP, Aylor DL, Peck BCE, Ryan JF, Tavarez U, Buus RJ, Chesler DRM, Threadgill DW, Churchill GA, de Villena FPM, Collins FS. Genetic Analysis of Hematological Parameters in Incipient Lines of the Collaborative Cross. G3 Genes, Genomes, Genet. 2012; 2(2): 157–165.
- [9] Lakna. DifferencACe Between Gram Positive and Gram Negative Bacteria Stunning Images of Cells Discover How Scientists Use Main Difference AC–Gram Positive vs Gram Negative Bacteria. Pediaa 2017; (April): 13.
- [10] Kumar V. R. Robbins Temel Patoloji. İstanbul: Nobel 2003.
- [11] Ola-Davies OE, Akinrinde AS. Acute Sodium Arsenite-Induced Hematological and Biochemical Changes in Wistar Rats: Protective Effects of Ethanol Extract of Ageratum Conyzoides. Pharmacognosy Res. 2016; 8(Suppl 1): S26.
- [12] Mank V, Azhar W, Brown K. Leukocytosis. StatPearls 2023.
- [13] Tigner A, Ibrahim SA, Murray I V. Histology, White Blood Cell. StatPearls 2022.
- [14] Frandson RD, Wilke WL, Fails AD. Anatomy and Physiology of Farm Animals. 2009: 512.
- [15] Linke B, Schreiber Y, Picard-Willems B, Slattery P, Nüsing RM, Harder S, Geisslinger G, Scholich K. Activated Platelets Induce an Anti-Inflammatory Response of Monocytes / Macrophages through Cross-Regulation of PGE 2 and Cytokines. 2017; 2017.
- [16] Ciarrocca M, Tomei G, Palermo P, Caciari T, Cetica C, Fiaschetti M, Gioffrè PA, Tasciotti Z, Tomei F, Sancini A. Environmental and Biological Monitoring of Arsenic in Outdoor Workers Exposed to Urban Air Pollutants. Int. J. Hyg. Environ. Health 2012; 215(6): 555–561.
- [17] Dacie J V, Lewis SM. Practical Haematology. 1995: 609–609.
- [18] Kaya E, Şimşek H, Çakar F. Arı Sütünün Senesens ve Telomer Etkisi. In: Sağlık Bilim. Alanında Uluslararası Araştırmalar IX. 2022; 83–95.
- [19] Nikolić R, Krstić N, Jovanović J, Kocić G, Cvetković TP, Radosavljević-Stevanović N. Monitoring the Toxic Effects of Pb, Cd and Cu on Hematological Parameters of Wistar Rats and Potential Protective Role of Lipoic Acid and Glutathione. Toxicol. Ind. Health 2015; 31(3): 239–246.
- [20] Ramadan MF, Al-Ghamdi A. Bioactive Compounds and Health-Promoting Properties of Royal Jelly: A Review. J. Funct. Foods 2012; 4(1): 39–52.
- [21] Smedley PL, Kinniburgh DG. United Nations Synthesis Report on Arsenic in Drinking Water Developed on Behalf of the United Nations Administrative Committee on Cooperation Sub-Committee on Water Resources, with Active

- Participation of UNICEF, UNIDO, IAEA, and the World Bank. *Br. Geol. Surv. Wallingford* 2001:1–390.
- [22] Ohaeri CC, Eluwa MC. Abnormal Biochemical and Haematological Indices in Trypanosomiasis as a Threat to Herd Production. *Vet. Parasitol.* 2011; 177(3–4): 199–202.
- [23] Kumari S, Rani S, Kumar A. Ameliorative Effect of *Panax Quinquefolius* on Sodium Arsenite Induced Toxicity in Charles Foster Rats. *J. Appl. Nat. Sci.* 2022; 14(4): 1532–1541.
- [24] Sharma S, Rani S. Possible Protective Role of Aqueous Tomato Extract on Hemato-Biochemical Parameters against Sodium Arsenite Toxicity in Albino Rats. *J. Pharm. Res. Int.* 2022; 34(14B): 12–22.
- [25] Lin A, Loré K. Granulocytes: New Members of the Antigen-Presenting Cell Family. *Front. Immunol.* 2017; 8(DEC): 1781.
- [26] Blumenreich MS. The White Blood Cell and Differential Count. *Clin. Methods Hist. Phys. Lab. Exam.* 1990.
- [27] Adebayo AH, Zeng GZ, Fan JT, Ji CJ, He WJ, Xu JJ, Zhang YM, Akindahunsi AA, Kela R, Tan NH. Biochemical, Haematological and Histopathological Studies of Extract of *Ageratum Conyzoides* L. in Sprague Dawley Rats. *J. Med. Plants Res.* 2010; 4(21): 2264–2272.
- [28] Ewere EG, Okolie NP, Ndem JI, Oyebadejo SA, Ewere EG, Okolie NP, Ndem JI, Oyebadejo SA. Immunological and Hematological Effects of *Irvingia Gabonensis* Stem Bark in Sodium Arsenite-Exposed Rats. <https://Gsconlinepress.Com/Journals/Gscbps/Sites/Default/Files/GSCBPS-2021-0089.Pdf> 2021; 15(1): 027–037.
- [29] NHLBI, NIH. Lymphopenia - What Is Lymphopenia? <https://www.nhlbi.nih.gov/health/lymphopenia> Date Accessed 2023-09-07 2022.
- [30] Lu M, Wang H, Li XF, Lu X, Cullen WR, Arnold LL, Cohen SM, Le XC. Evidence of Hemoglobin Binding to Arsenic as a Basis for the Accumulation of Arsenic in Rat Blood. *Chem. Res. Toxicol.* 2004; 17(12): 1733–1742.
- [31] Szymańska-Chabowska A, Antonowicz-Juchniewicz J, Andrzejak R. Some Aspects of Arsenic Toxicity and Carcinogenicity in Living Organism with Special Regard to Its Influence on Cardiovascular System, Blood and Bone Marrow. *Int. J. Occup. Med. Environ. Health* 2002; 15(2): 101–116.
- [32] Ferland R, Gadahi JA, Saleha S, Ali Q. Histological and Haematological Disturbance Caused by Arsenic Toxicity in Mice Model. *Pakistan J. Biol. Sci.* 2008; 11(11): 1405–1413.
- [33] Basher MK, Sarkar S, Mobarak MH, Islam MR. Inorganic Arsenic Exposure during Pregnancy Affects Post-Natal Growth, Blood Parameters, and Organ Development of Mice Offspring. *J. Adv. Biotechnol. Exp. Ther.* 2023; 6(2): 445–457.
- [34] Kundrapu S, Noguez J. *Laboratory Assessment of Anemia*, vol. 83. Elsevier Inc. 2018.
- [35] Korniluk A, Koper-Lenkiewicz OM, Kamińska J, Kemona H, Dymicka-Piekarska V. Mean Platelet Volume (MPV): New Perspectives for an Old Marker in the Course and Prognosis of Inflammatory Conditions. *Mediators Inflamm.* 2019; 2019.
- [36] Sikora J, Kostka B. Blood Platelets as Pharmacological Mode. *Postępy Biol. Komórki* 2005.
- [37] Kalia K, Narula GD, Kannan GM, Flora SJS. Effects of Combined Administration of Captopril and DMSA on Arsenite Induced Oxidative Stress and Blood and Tissue Arsenic Concentration in Rats. *Comp. Biochem. Physiol. C. Toxicol. Pharmacol.* 2007; 144(4): 372–379.
- [38] Thompson CB, Jakubowski JA. The Pathophysiology and Clinical Relevance of Platelet Heterogeneity. *Blood* 1988; 72(1): 1–8.

PSO Training Neural Network MPPT with CUK Converter Topology for Stand-Alone PV Systems Under Varying Load and Climatic Conditions

Mehmet YILMAZ¹ , M. Fatih ÇORAPSIZ^{1*} 

¹ Ataturk University, Engineering Faculty, Electrical-Electronics Engineering, Erzurum, Türkiye
Mehmet YILMAZ ORCID No: 0000-0001-7624-4245
M. Fatih ÇORAPSIZ ORCID No: 0000-0001-5692-8367

*Corresponding author: corapsiz@atauni.edu.tr

(Received: 22.01.2024, Accepted: 01.03.2024, Online Publication: 29.03.2024)

Keywords

Maximum power point tracking, Particle swarm optimization based neural network, CUK converter, Boost converter

Abstract: Temperature and irradiance levels are two examples of environmental variables that affect the power value produced by photovoltaic panels. Therefore, in order to transfer the maximum power value from the PV panel to the load under varying climatic conditions, maximum power point tracking (MPPT) algorithms and DC-DC converter topologies are used. In this study, the performances of boost converter and CUK converter circuit topologies are investigated under variable irradiance and variable load conditions by using a neural network-based MPPT algorithm learning particle swarm optimization (PSO). As the first scenario, it is analyzed assuming that the temperature and irradiance values coming to the panel are constant. As the second scenario, the performance evaluation of the converter topologies according to the current, voltage and power parameters is made for the variable load situation. As the last scenario, the difference in the irradiance value coming to the panel depending on the sun's condition during the day has been examined. Canadian Solar CS6P-250P PV panel is used in the study. 50 kHz is selected as the switching frequency. According to the results obtained, it has been observed that the CUK converter circuit topology reaches the maximum power point faster than the boost converter circuit topology both in dynamic environmental conditions and load change, and the oscillation at this point is less. It is aimed to increase the performance of this method, which uses boost converter topology and MPPT in the literature, by applying CUK converter topology.

Değişken Yük ve İklim Koşulları Altında Müstakil Çalışan PV Sistemleri için CUK Dönüştürücü Topolojili PSO Eğitilmiş Sinir Ağı Tabanlı MPPT

Anahtar

Kelimeler

Maksimum güç noktası takibi, Parçacık sürü optimizasyon tabanlı sinir ağı, CUK dönüştürücü, Yükselten tip dönüştürücü

Öz: PV panellerden elde edilen güç değeri sıcaklık ve ışınım değerleri gibi çevresel faktörlere bağlı olarak değişmektedir. Bu nedenle değişen iklim koşullarında PV panelden maksimum güç değerinin yüke aktarılması için maksimum güç noktası izleme (MPPT) algoritmaları ve DC-DC dönüştürücü topolojileri kullanılmaktadır. Bu çalışmada, parçacık sürü optimizasyonu (PSO) öğrenen sinir ağı tabanlı MPPT algoritması kullanılarak, yükselten tip dönüştürücü ve CUK dönüştürücü devre topolojilerinin performansları değişken ışınım ve değişken yük koşulları altında incelenmiştir. İlk senaryo olarak panele gelen sıcaklık ve ışınım değerlerinin sabit olduğu varsayılarak analiz edilmiştir. İkinci senaryo olarak değişken yük durumu için akım, gerilim ve güç parametrelerine göre dönüştürücü topolojilerinin performans değerlendirmesi yapılmıştır. Son senaryo olarak ise gün içerisinde güneşin durumuna bağlı olarak panele gelen ışınım değerindeki farklılık incelenmiştir. Çalışmada Canadian Solar CS6P-250P PV panel kullanılmıştır. Anahtarlama frekansı olarak 50 kHz seçilmiştir. Elde edilen sonuçlara göre CUK dönüştürücü devre topolojisinin hem dinamik çevre koşullarında hem de yük değişiminde yükselten tip dönüştürücü devre topolojisine göre maksimum güç noktasına daha hızlı ulaştığı ve bu noktadaki salınımın daha az olduğu görülmüştür. Literatürde yükselten tip dönüştürücü topolojisi ve MPPT kullanan bu yöntemin performansının CUK dönüştürücü topolojisi uygulanarak artırılması hedeflenmiştir.

1. INTRODUCTION

Due to factors such as technological developments, increasing population and developing industry, the need for electrical energy is increasing over time. Fossil energy fuels, which are used to meet the energy needs, that are of primary importance in the development of countries, are gradually depleted. The use of fossil energy fuels is decreasing day by day due to the harmful gases they emit to the environment. Renewable energy sources have been used in order to meet the increasing energy demand in recent years. The most important advantages of these resources are that they are clean, constantly renewable, reduce environmental pollution and have low operating costs. The most important renewable energy sources used today are hydroelectric energy, wind energy, solar energy, geothermal energy and wave energy. Solar energy systems are preferred because they have no fuel costs, contain no moving parts, are resistant to climate changes and directly convert solar energy into electrical energy. Photovoltaic (PV) panels are the most important part of solar energy systems. PV panels are obtained from the combination of PV cells. PV panels are connected in series or parallel to create an energy system at the desired power level. Another important factor affecting the PV panel efficiency is the amount of solar irradiance reaching to the panel. During the day, the amount of irradiance reaching to the panel is reduced in cases such as cloudy weather and tree shadows. As a result, the amount of power produced decreases and the panel efficiency decreases. For these reasons, MPPT algorithms are used to increase panel efficiency. MPPT algorithms basically try to provide maximum energy to the load by optimizing the duty ratio of the DC-DC converters that provide the connection between the PV panel and the load. MPPT control algorithms are divided into two groups as analog and digital control. MPPT is provided with the help of conventional controllers by comparing the reference voltage and output voltage produced PV panel in analog control. In the digital control method, the control signal is produced directly by the pulse width modulation (PWM) generator.

In both control methods, the aim is to transfer the power obtained from the PV panel to the load with the highest possible efficiency through optimization algorithms. Optimization algorithms are classified as classical and metaheuristic. Classical optimization algorithms are frequently preferred in real-time applications due to their advantages such as simple structure and easy applicability. The most used optimization algorithms for MPPT applications are perturb and observe algorithm (P&O) [1-8], incremental conductance algorithm (INC) [9]. MPPT is preferred as analog control method in fuzzy logic-based algorithms (FLC) [3,10-11], neural network-based (NN) [12-16] and machine learning based [17] algorithms. Under partial shading conditions, bypass diodes cause multiple local maximum points in the P-V characteristic. In this case, classical optimization algorithms cannot reach the global maximum because they follow the local maximum. Metaheuristic

optimization algorithms are used to increase PV panel efficiency. Major metaheuristic optimization algorithms; African vulture optimization algorithm (AVOA) [18], crow search algorithm (CSA) [19], butterfly optimization algorithm (BOA) [20], whale optimization algorithm (WOA) [21], most valuable player algorithm (MVPA) [22], squirrel search algorithm (SSA) [23], shuffled frog-leaping algorithm (SFLA) [24,25], BAT search [26], Harris hawk optimization (HHO) [27], search and rescue algorithm (SRA) [28] and particle swarm optimization (PSO) [7,29-33]. There are comparisons of some metaheuristic optimization algorithms based on performance parameters such as complexity, efficiency, and convergence time [34,35]. Al-Majidi et al designed a feedforward artificial neural network (ANN) for MPPT. In order to increase the accuracy of the model designed for MPPT, the PSO algorithm is used for the initial weights and selection of the best topology. While training, irradiance values and temperature values are determined as input variables, and power value is determined as output variable. In order to prove the accuracy of the designed model, a real-time data collection system is created. With this system, 48500 data are collected in a year on sunny and cloudy days. The suggested approach is compared with P&O, FLC, and traditional ANN algorithms. The outcomes gained show that the proposed strategy is successful. A boost converter topology is recommended to raise the input voltage produced by the PV panel [36]. In this study, it is aimed to increase the performance of the proposed method by applying it to amplifying type and CUK converter circuit topologies. This paper is structured as follows: PV cell model, boost converter, CUK converter, PSO, NN and PSO training NN are explained in Sect. 2. The simulation model created to compare the performance of the boost converter and CUK converter circuit topologies and the results are presented comparatively in Sect. 3. Finally, conclusions are given in Sect. 4.

2. MATERIAL AND METHOD

2.1. PV Cell Model

PV cells are obtained from the combination of p-n semiconductor elements. PV cells are semiconductor materials that generate current depending on the irradiance value. The most frequently used single-diode PV cell model in the literature for modeling PV cells is shown in Figure 1 [37]. I_{pv} is the current produced by light photons, I_d is the diode current, G is the irradiance value from the sun, T is the temperature value, V_p is the voltage value obtained from the PV panel. In materials with a thin film structure made up of extremely thin layers, R_p represents the total of the resistances formed between the layers and surrounding the cell, and R_s represents the sum of the resistances of the semiconductor material forming the cell and the contact resistances formed at the junction points of the cells.

Nomenclature	Abbreviation		
PV	Photovoltaic	BOA	Butterfly optimization algorithm
MPPT	Maximum power point tracking	WOA	Whale optimization algorithm
PWM	Pulse width modulation	MVPA	Most valuable player algorithm
P&O	Perturb and observe	SSA	Squirrel search algorithm
FL	Fuzzy logic	SFLA	Shuffled frog-leaping algorithm
P&O	Perturb and observe	HHO	Harris hawk optimization
INC	Incremental Conductance	SRA	Search and rescue algorithm
NN	Neural networks	PSO	Particle swarm optimization
CSA	Cuckoo search algorithm	ANN	Artificial neural network
BLDC	Brushless direct current	ML	Machine Learning
AVOA	African vulture optimization algorithm		

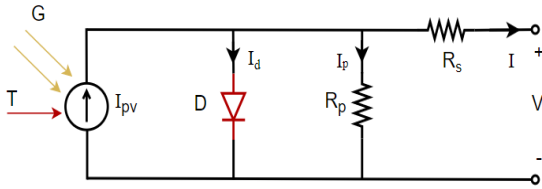


Figure 1. Single diode PV cell model [16]

The equations for modeling PV panels are given in Equations (1-5).

$$I = I_{pv} - I_d - I_p \tag{1}$$

$$I_d = I_0 \left(e^{\frac{qV_d}{kT}} - 1 \right) \tag{2}$$

$$V_d = V + IR_s \tag{3}$$

$$I_d = I_0 \left(e^{\frac{q(V+IR_s)}{nkT}} \right) \tag{4}$$

$$I = I_{pv} - I_0 \left(e^{\frac{q(V+IR_s)}{nkT}} \right) - \frac{V + IR_s}{R_p} \tag{5}$$

Where n represents the diode ideality constant, T represent for the cell temperature (K), k is the Boltzman constant (J/K), q is the electron charge (C) and I_0 represents reserve saturation current (A). Canadian Solar CS6P-250P was used as PV panel in the study. The features of this panel are given in Table 1.

Table 1. Canadian Solar CS6P-250P

Parameters	Value
Maximum Power	249.83 W
Open Circuit Voltage	37.2 V
Vmp	30.1 V
Isc	8.87 A
Imp	8.3 A
Temperature coefficient of Isc (%/deg.C)	0.063698
Temperature coefficient of Voc (%/deg.C)	-0.3654
Ncell	60

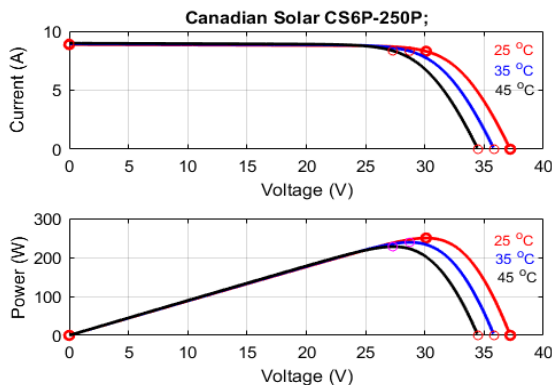


Figure 2. PV system curves at fixed 1000 W/m2 irradiance value

The two most significant factors influencing PV panel output power are temperature and irradiance levels. Figure 2 shows the voltage dependent variation of the output power and current of the Canadian Solar CS6P-250P PV panel according to the constant irradiance and variable temperature values. It is seen that as the temperature value increases, the voltage value decreases and the power value increases in Figure 2.

Figure 3 illustrates the variation of the output power and current depending on the voltage, according to the constant temperature and variable irradiance values. As can be seen from Figure 3, the current value decreases as the irradiance value decreases. In addition, since the power value depends on the voltage and current values, it is seen that there is a decrease in this value.

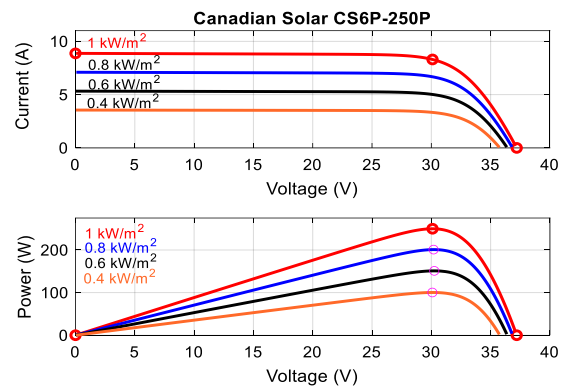


Figure 3. PV system curves at fixed 25°C temperature value

2.2. Boost Converter Model

Step up circuit topologies that transfer the unadjusted DC voltage value applied to the input to the output at higher levels and adjustable. It is also known as step up converter. It operates in two different states depending on the open or close state of the switching element. In the case of switching is ON-mode, the diode is polarized in the opposite direction and shows open circuit property. In the case of switching is OFF-mode, the diode is forward-biased and shows short-circuit characteristics. The boost converter circuit topology is shown in Figure 4 [16].

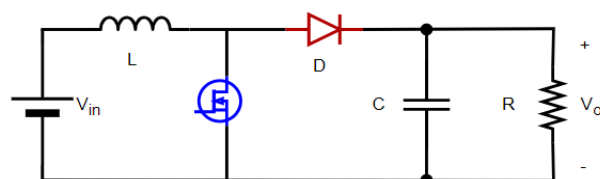


Figure 4. Boost converter circuit topology

The boost converter parameters are determined using the following equations. Average output current;

$$I_0 = \frac{P}{V_0} \quad (6)$$

$$\Delta I = (0.05) \frac{I_0 V_0}{V_{in}} \quad (7)$$

$$\Delta V = V_0(0.01) \quad (8)$$

Inductance;

$$L = \frac{V_{in} (V_0 - V_{in})}{f \Delta I V_0} \quad (9)$$

Capacitance;

$$C = \frac{V_{in} (V_0 - V_{in})}{f \Delta I V_0} \quad (10)$$

The circuit parameters of the boost converter used in simulation studies are given in Table 2.

Table 2. The parameters of Boost converter topology

Parameters	Value
L	1 mH
C _{in} and C ₂	100 μF- 42.5 μF
R _L	30 Ω
Switching Frequency (f)	50 kHz

2.3. CUK Converter Model

CUK circuit topologies that transfer the DC voltage value applied to the input to the output at higher or lower levels. Today, CUK converters are used in brushless direct current (BLDC) motor driver circuits, renewable energy systems and pulse width modulation (PWM) based PV systems. The most important difference of CUK converters from other converters is the use of capacitors for energy transfer. The CUK converter circuit topology is shown in Figure 5.

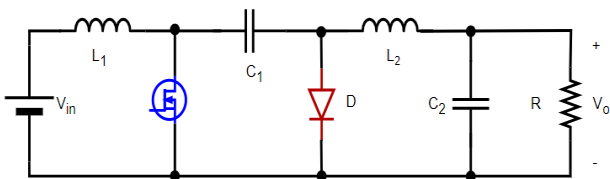


Figure 5. CUK converter circuit topology

The following equations are used in the CUK converter design given in Figure 5;

Duty ratio;

$$D = - \frac{V_0}{V_{in} - V_0} \quad (11)$$

Average inductance currents;

$$i_{L1} = \frac{P_s}{V_{in}} \quad (12)$$

$$i_{L2} = \frac{P_s}{-V_0} \quad (13)$$

Rate of change inductance currents;

$$\Delta i_{L1} = i_{L1} (\%10) \quad (14)$$

$$\Delta i_{L2} = i_{L2} (\%10) \quad (15)$$

Inductances;

$$L_1 = \frac{V_{in} D}{f \Delta i_{L1}} \quad (16)$$

$$L_2 = \frac{V_{in} D}{f \Delta i_{L2}} \quad (17)$$

Rate of change capacitance voltage;

$$\Delta V_{C1} = (V_{in} - V_0) 0.01 \quad (18)$$

Load resistance;

$$R = \frac{V_0^2}{P} \quad (19)$$

Capacitances;

$$C_1 = \frac{V_0 D}{R f \Delta V_{C1}} \quad (20)$$

$$C_2 = \frac{1 - D}{0.01 f^2 8 L_2} \quad (21)$$

where we have; V_{in} input voltage (V), V_0 output voltage (V), i_L average inductance current (A), D duty ratio, Δi_L rate of change inductor current, L inductance (H), C capacitance (F), ΔV_c rate of change capacitor voltage, R load resistance (Ω), f switching frequency (Hz), r ripple, r_{c1} ripple at C_1 .

Circuit parameters of the CUK converter used in simulation studies are given in Table 3.

Table 3. The parameters of CUK converter

Component	Parameters
L ₁ and L ₂	5.74 μH- 1.59 μH
C ₁ and C ₂	39.5 μF- 8.36 μF
R _L	30 Ω
Switching Frequency	50 kHz

2.4. Particle Swarm Optimization

The PSO algorithm was first developed in 1995 by R.C. It was introduced by Eberhart and J. Kennedy. The basis of the algorithm is based on the behavior of flocks of birds. Swarms are made up of particles. Each particle adjusts its position to its best position, taking advantage of its previous experience. Afterwards, all particles update their position according to the best particle of the swarm. This process continues until the goal is reached. In Figure 6, the flow chart of the PSO algorithm is given. The particle velocity and position are shown in the equations below. The velocity and position information of the particles are calculated according to Equation 22 and Equation 23 [31].

$$v_{k+1}^i = w v_k^i + c_1 r \text{and} \frac{p^i - x_k^i}{\Delta t} + c_2 r \text{and} \frac{p_k^g - x_k^i}{\Delta t} \quad (22)$$

$$x_{k+1}^i = x_k^i + v_{k+1}^i \quad (23)$$

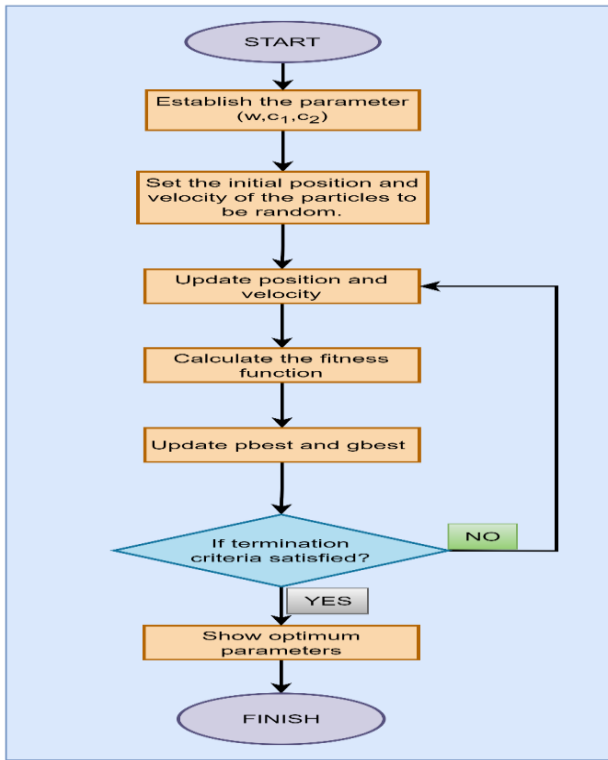


Figure 6. PSO flowchart

2.5. Neural-Network Model

The first artificial neural network model was created in 1943 by W. McCulloch and W. Pitts. In general, neural networks have usage areas such as system modeling, handwriting recognition, automatic vehicle control, voice recognition, fingerprint recognition and meteorological interpretation. An artificial neuron is shown in Figure 7.

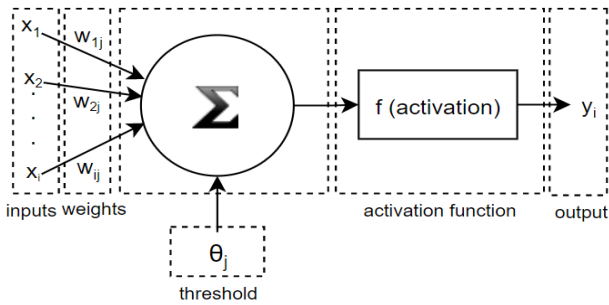


Figure 7. Artificial neuron

2.6. PSO training Neural-Network Model

PSO algorithm is used in training neural networks in order to obtain faster training process and convergence time. The algorithm is started by choosing a random location for each particle. The velocity and position information of each particle is updated using Equation 22 and Equation 23 by creating loops as many as the number of particles. Then the *Gbest* value is updated by comparing it with the *Pbest* values in each iteration. Finally, the algorithm is terminated by looking at the stopping criteria. The flowchart of NN training with PSO is shown in Figure 8.

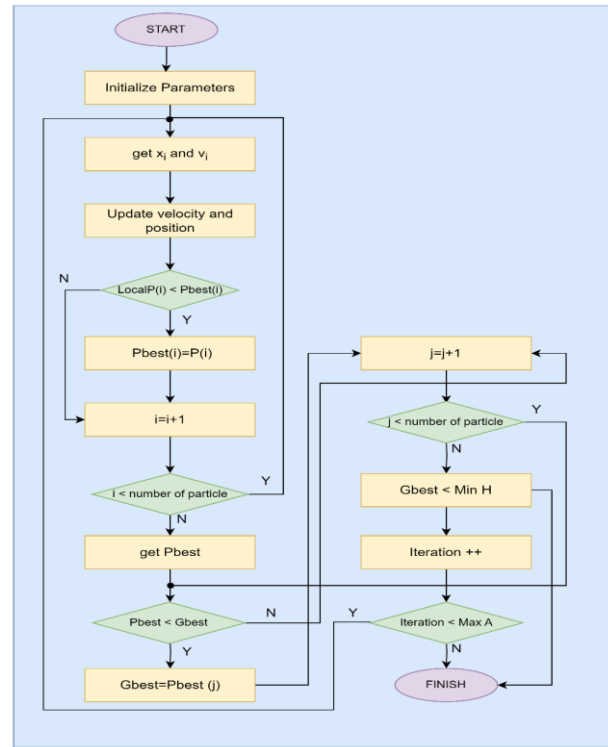


Figure 8. PSO training NN Algorithm [38]

3. RESULTS AND DISCUSSION

The simulation model shown in Figure 9 was created to compare the performances of the boost converter and the CUK converter. While creating the simulation model, Canadian Solar CS6P-250P was chosen as the PV panel. Boost converter and CUK converter circuit topologies are utilized as DC-DC converter architectures to raise the voltage at the panel output. 30Ω resistive as load, PSO trained neural network maximum power point tracking (NN MPPT) algorithm is used to optimize the duty ratios of converter topologies. The irradiance values were determined as 1000 W/m², 800 W/m², 600 W/m², 400 W/m² in the first case, constant 700 W/m² in the second case and a *trapezoidal function* in the last case. Irradiance values for different scenarios are shown in Figure 10.

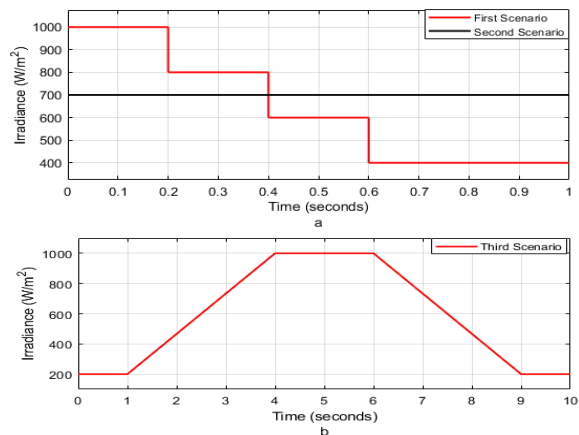


Figure 10. Irradiance values for a) first and second scenarios, b) third scenario

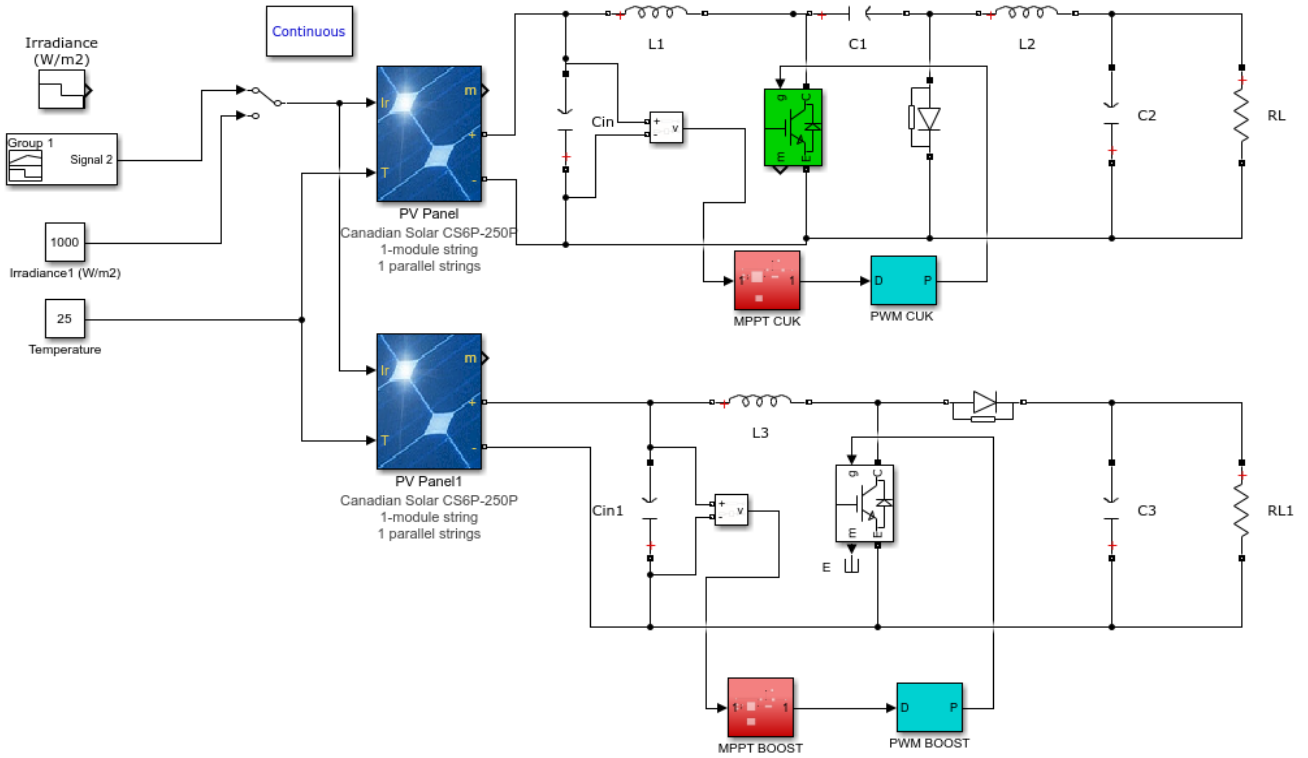


Figure 9. Simulation Model

First Scenario: In the first scenario, the irradiance value was initially selected as 1000 W/m^2 and the converter performances were examined by reducing 200 W/m^2 in 0.2 s intervals. The irradiance value was determined as 800 W/m^2 in the $0.2-0.4 \text{ s}$ time interval, 600 W/m^2 in the $0.4-0.6 \text{ s}$ time interval and 400 W/m^2 in the $0.6-0.9 \text{ s}$ time interval. Irradiance values are chosen as high, medium and low irradiance levels and the changes in current, voltage and power at these values are investigated. The temperature was determined as 25°C fixed values. Figure 11 shows the time-dependent variation of the load currents of the boost converter and CUK converter circuit topologies.

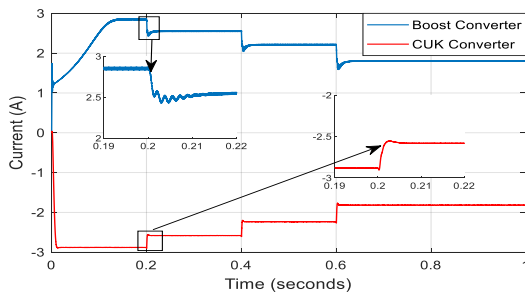


Figure 11. Boost converter and CUK converter output currents

In Table 4, the current values of both converters are given for the scenario determined above.

Table 4. The performance of Boost and CUK converter topologies

Time	Irradiance Value	Boost Converter	CUK Converter
0-0.2s	1000 W/m^2	2.856A	-2.88A
0.2-0.4s	800 W/m^2	2.558A	-2.58A
0.4-0.6s	600 W/m^2	2.21A	-2.24A
0.6-1s	400 W/m^2	1.81A	-1.83A

In Figure 12, the change in the voltage values of the boost converter topology and the CUK converter topology due to the decrease in the irradiance value at certain time intervals is shown.

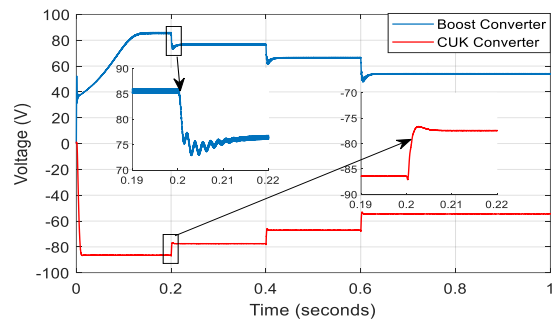


Figure 12. Boost converter and CUK converter output voltages

The variation of the load voltage obtained depending on the irradiance value with respect to time is given in Table 5.

Table 5. The performance of Boost and CUK converter topologies

Time	Irradiance Value	Boost Converter	CUK Converter
0-0.2s	1000 W/m^2	85.6V	-86.5V
0.2-0.4s	800 W/m^2	76.6V	-77.5V
0.4-0.6s	600 W/m^2	66.5V	-67V
0.6-1s	400 W/m^2	54V	-54.5V

In Figure 13, the variation of the power consumed on the load connected to the output in DC-DC converter topologies according to time is given.

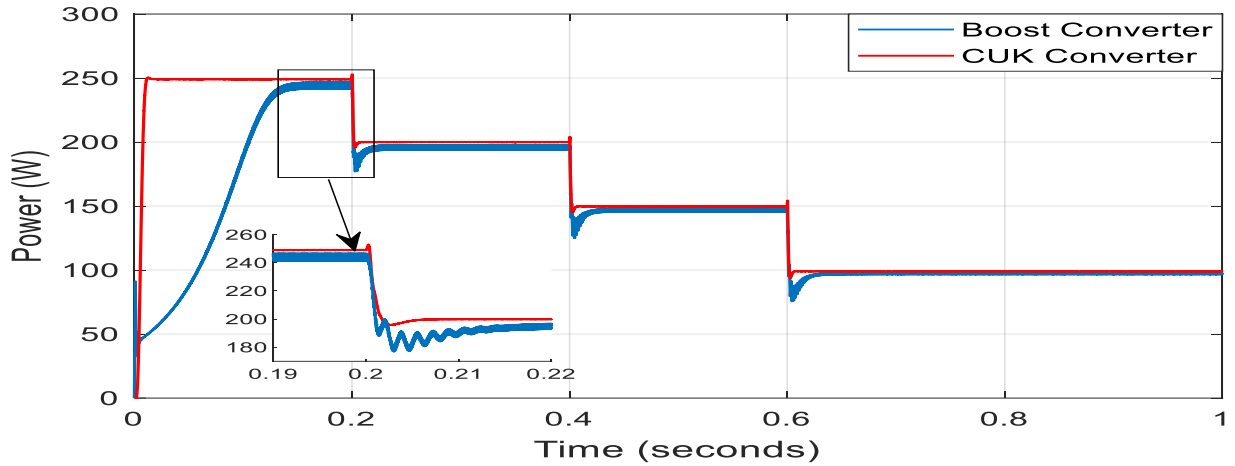


Figure 13. Boost converter and CUK converter output powers

In Table 6, the power values transferred to the load for the first scenario are shown in comparison.

Table 6. The performance of Boost and CUK converter topologies

Time	Irradiance Value	GMPP	Boost Converter	CUK Converter
0-0.2s	1000 W/m ²	249.83W	244.5W	249.12W
0.2-0.4s	800 W/m ²	201.56W	196 W	200.5W
0.4-0.6s	600 W/m ²	152.01W	147W	150.6W
0.6-1s	400 W/m ²	101.36W	98W	99.5W

When the results of both converters are examined, it is seen that the CUK converter circuit topology reaches the MPP point in a shorter time compared to the boost converter topology for the first scenario. In addition, it has been observed that there is less oscillation in the current, voltage and power values of the CUK converter circuit topology at the MPP point. The performance criteria such as settling time, rise time and oscillation (output power) of these two converters are shown in Table 7 comparatively.

Table 7. Comparison of Boost and CUK converter performance (0-0.2s)

Performance Metrics	Boost Converter	CUK Converter
Settling time (sec)	132 ms	10 ms
Rise time (sec)	110 ms	5.14 ms
Oscillation (%) (Power)	% 1.78	% 0.22

Second Scenario: In the second scenario, the effect of load change on converter performance (current, voltage and power) was examined by keeping the irradiance value and temperature constant. For this purpose, the irradiance value is determined as 700 W/m² and the temperature was determined as 25°C fixed values. The situation where the load value changes at intervals of 0.3s has been examined. The load value was determined as 20Ω in the 0-0.3s time interval, the load value in the 0.3-0.6s time interval as 25Ω and the load value in the 0.6s and later time period as 30Ω.

Figure 14 shows the variation of the currents of the boost converter and CUK converter circuit topologies for the load change situation at certain time intervals.

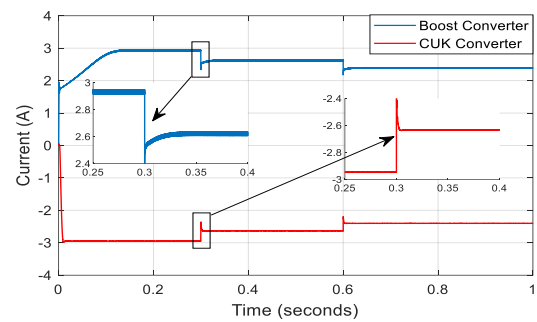


Figure 14. Boost converter and CUK converter output currents

As the load value connected to the output of the converter changes, the current value also changes accordingly. The current values obtained for this scenario are shown in Table 8.

Table 8. The performance of Boost and CUK converter topologies

Time	Irradiance Value	Load	Boost Converter	CUK Converter
0-0.3s	700 W/m ²	20Ω	2.98A	-2.95A
0.3-0.6s	700 W/m ²	25Ω	2.62A	-2.63A
0.6-1s	700 W/m ²	30Ω	2.39A	-2.4A

Figure 15 shows the time-dependent variation of the output voltages of the second scenario boost converter and CUK converter.

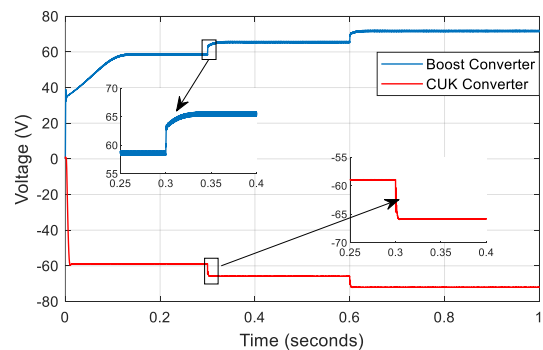


Figure 15. Boost converter and CUK converter output voltages

The change in the current value affects the voltage value so that the power transferred to the load remains constant. The output voltage values of both converters for 700 W/m² fixed irradiance value and variable load values are given in Table 9.

Table 9. The performance of Boost and CUK converter topologies

Time	Irradiance Value	Load	Boost Converter	CUK Converter
0-0.3s	700 W/m ²	20Ω	58.6V	-59V
0.3-0.6s	700 W/m ²	25Ω	65.5V	-65.8V
0.6-1s	700 W/m ²	30Ω	71.8V	-72.1V

Figure 16 is given for the type converter and the CUK converter topology that amplify the time-dependent variation of the power dissipated on the load.

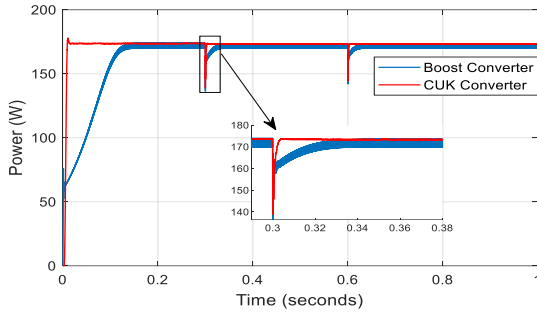


Figure 16. Boost converter and CUK converter output powers

In Table 10, the power values transferred to the load for the second scenario situation are presented.

Table 10. The performance of Boost and CUK converter topologies

Time	Irradiance Value	Load	GMPP	Boost Converter	CUK Converter
0-0.3s	700 W/m ²	20Ω	176.941 W	171.6W	174W
0.3-0.6s	700 W/m ²	25Ω	176.941 W	171.6W	174W
0.6-1s	700 W/m ²	30Ω	176.941 W	171.6W	174W

It has been observed that the CUK converter circuit topology reaches the MPP point quickly for the situation where the load value changes at certain intervals, while the boost converter topology cannot fully reach the MPP point and oscillates more in current, voltage and power values. DC-DC converters performance parameters rise time, settling time and oscillation (%) for the two designed models are given in Table 11.

Table 11. Comparison of Boost and CUK converter performance (0-0.2s)

Performance Metrics	Boost Converter	CUK Converter
Settling time (sec)	122 ms	9 ms
Rise time (sec)	90 ms	4.1 ms
Oscillation (%) (Power)	% 2.298	% 0.115

Third Scenario: As the last scenario, the difference in the irradiance value coming to the panel depending on the sun's condition during the day has been examined. In order to evaluate this situation, a function whose irradiance value changes trapezoidal is chosen. The variation of irradiance with time for this scenario is shown in Figure 10b. At 700 W/m², 25 °C, GMPP is 50.027W, while for 1000 W/m², 25 °C, the GMPP is 249.83W. The boost converter output power is given in Figure 17.

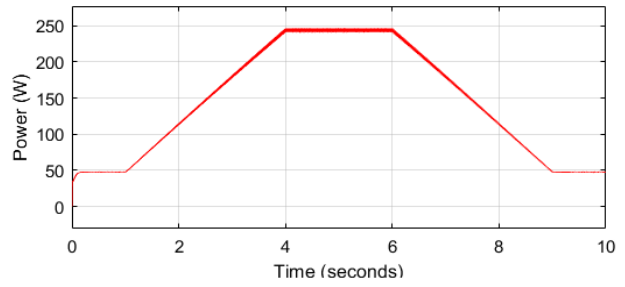


Figure 17. Boost converter output power

The irradiance value was determined as 200 W/m² in the 0-1s time interval. In this case, the settling time is 0.123s and the output power is 47.5W. In the 1-4s time interval, the irradiance value increased linearly. Depending on the increase in irradiance, the power value transferred to the load also increased. In the case of 1000 W/m² irradiance in the 4-6s time interval, the power value is 244.5W. While the irradiance decreases linearly between 6-9s, the power value also decreases as the power value changes directly proportional to the irradiance. Finally, when the irradiance value is considered 200 W/m² again, the output power value is measured as 47.5W.

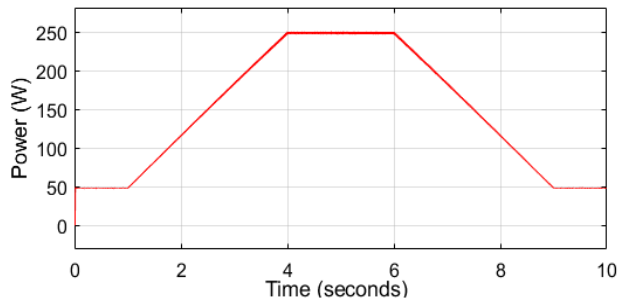


Figure 18. Boost converter output power

The CUK converter output power is seen in Figure 18. The output power value transferred to the load in the 0-1s time interval was measured as 48W in 0.016s. Figure 18 shows an increasing power change in response to the increasing irradiance value in the 1-4s time interval, and a decreasing power change depending on the decreasing irradiance value in the between 6-9s. The power is 249.6W in the between 4-6s. Finally, when the irradiance value is considered as 200 W/m² again, the power value is measured as 48W.

4. CONCLUSION

Solar energy systems are the most preferred renewable energy source due to their low maintenance costs. In order to adjust the output voltage of the PV panel to the desired values, booster type and CUK converter topologies are used. In this study, the PSO-based NN optimization algorithm was applied to both converter topologies. The performance of the converters for different scenarios was compared according to parameters such as settling time, rise time and oscillation. Firstly, DC-DC converter topologies for variable irradiance conditions are compared and performance criteria are presented. As the second scenario, the performance evaluation of the converter topologies according to the current, voltage and power parameters is made for the variable load situation.

In this situation, the CUK converter topology has reached its MPP by responding faster to all load change situations. Since the angle of incidence of the sun rays cannot reach the panels at the same rate during the day, the irradiance value is determined as a trapezoidal function in order to evaluate this scenario. The performance of the DC-DC converters under these scenarios is investigated. It is observed that the CUK converter responds faster to changes and reaches MPP earlier than the boost converter. In studies conducted for three different cases, it is observed that the CUK converter reaches the MPP faster and oscillates less than the boost converter. Matlab/Simulink program is used for simulation studies. PSO algorithm is frequently preferred in optimization problems due to its advantages such as simple structure and easy applicability. In this study, the panel data is trained with a neural network based on the PSO optimization algorithm. CUK converter circuit topology has been applied to this method, which is mostly used with boost converter structure in the literature, and it has been tried to contribute to the relevant field and successful results have been obtained. As a future research, the application of different optimization algorithms that have not yet been applied in this field to these systems will be studied.

REFERENCES

- [1] Kamran M, Mudassar M, Fazal MR, Asghar MU, Bilal M, Asghar R. Implementation of improved Perturb & Observe MPPT technique with confined search space for standalone photovoltaic system. *Journal of King Saud University-Engineering Sciences*.2020; 32(7), 432-441.
- [2] Pillai DS, Ram JP, Ghias AM, Mahmud MA, Rajasekar N. An accurate, shade detection-based hybrid maximum power point tracking approach for PV systems. *IEEE Transactions on Power Electronics*. 2019; 35(6), 6594-6608.
- [3] Khan MJ, Pushparaj. A novel hybrid maximum power point tracking controller based on artificial intelligence for solar photovoltaic system under variable environmental conditions. *Journal of Electrical Engineering & Technology*. 2021; 16(4), 1879-1889.
- [4] Sundaram BM, Manikandan BV, Kumar BP, Winston DP. Combination of novel converter topology and improved MPPT algorithm for harnessing maximum power from grid connected solar PV systems. *Journal of Electrical Engineering & Technology*. 2019; 14, 733-746.
- [5] Padmavathi N, Chilambuchelvan A, Shanker NR. Maximum power point tracking during partial shading effect in PV system using machine learning regression controller. *Journal of Electrical Engineering & Technology*. 2021; 16, 737-748.
- [6] Kumari N, Kumar SS, Laxmi V. Design of an efficient bipolar converter with fast MPPT algorithm for DC nanogrid application. *International Journal of Circuit Theory and Applications*. 2021; 49(9), 2812-2839.
- [7] Thankakan R, Samuel Nadar ER. Investigation of the double input power converter with N stages of voltage multiplier using PSO-based MPPT technique for the thermoelectric energy harvesting system. *International Journal of Circuit Theory and Applications*. 2020; 48(3), 435-448.
- [8] Kofinas P, Dounis AI, Papadakis G, Assimakopoulos MN. An Intelligent MPPT controller based on direct neural control for partially shaded PV system. *Energy and Buildings*. 2015; 90, 51-64.
- [9] Kumar R, Khandelwal S, Upadhyay P, Pulipaka S. Global maximum power point tracking using variable sampling time and pv curve region shifting technique along with incremental conductance for partially shaded photovoltaic systems. *Solar Energy*. 2019; 189, 151-178.
- [10] Bouarroudj N, Benlahbib B, Houam Y, Sedraoui M, Batlle VF, Abdelkrim T, et al. Fuzzy based incremental conductance algorithm stabilized by an optimal integrator for a photovoltaic system under varying operating conditions. *Energy Sources, Part A: Recovery, Utilization, and Environmental Effects*. 2021; 1-26.
- [11] Nasir A, Rasool I, Sibtain D, Kamran R. Adaptive Fractional Order PID Controller Based MPPT for PV Connected Grid System Under Changing Weather Conditions. *Journal of Electrical Engineering & Technology*. 2021; 16(5), 2599-2610.
- [12] Jiang M, Ghahremani M, Dadfar S, Chi H, Abdallah YN, Furukawa N. A novel combinatorial hybrid SFL-PS algorithm based neural network with perturb and observe for the MPPT controller of a hybrid PV-storage system. *Control Engineering Practice*. 2021; 114, 104880.
- [13] Hamdi H, Regaya C B, Zaafouri A. Real-time study of a photovoltaic system with boost converter using the PSO-RBF neural network algorithms in a MyRio controller. *Solar energy*. 2019; 183, 1-16.
- [14] Saidi AS, Salah CB, Errachdi A, Azeem MF, Bhutto JK, Ijyas VT. A novel approach in stand-alone photovoltaic system using MPPT controllers & NNE. *Ain Shams Engineering Journal*. 2021; 12(2), 1973-1984.
- [15] Fathi M, Parian JA. Intelligent MPPT for photovoltaic panels using a novel fuzzy logic and artificial neural networks based on evolutionary algorithms. *Energy Reports*. 2021; 7, 1338-1348.
- [16] Yılmaz M, Çorapsız MF. Artificial Neural Network based MPPT Algorithm with Boost Converter topology for Stand-Alone PV System. *Erzincan University Journal of Science and Technology*. 2022; 15(1), 242-257.
- [17] Yılmaz M, Kaleli A, Çorapsız MF. Machine learning based dynamic super twisting sliding mode controller for increase speed and accuracy of MPPT using real-time data under PSCs. *Renewable Energy*. 2023; 219, 119470.
- [18] Ghazi GA, Hasanien HM, Al-Ammar EA, Turkey RA, Ko W, Park S, Choi HJ. African vulture optimization algorithm-based PI controllers for performance enhancement of hybrid renewable-energy systems. *Sustainability*. 2022; 14(13), 8172.

- [19] Houam Y, Terki A, Bouarroudj N. An efficient metaheuristic technique to control the maximum power point of a partially shaded photovoltaic system using crow search algorithm (CSA). *Journal of Electrical Engineering & Technology*. 2021; 16, 381-402.
- [20] Aygül K, Cikan M, Demirdelen T, Tumay M. Butterfly optimization algorithm based maximum power point tracking of photovoltaic systems under partial shading condition. *Energy Sources, Part A: Recovery, Utilization, and Environmental Effects*. 2023; 45(3), 8337-8355.
- [21] Tao H, Ghahremani M, Ahmed FW, Jing W, Nazir MS, Ohshima K. A novel MPPT controller in PV systems with hybrid whale optimization-PS algorithm based ANFIS under different conditions. *Control Engineering Practice*. 2021; 112, 104809.
- [22] Pervez I, Shams I, Mekhilef S, Sarwar A, Tariq M, Alamri B. Most valuable player algorithm based maximum power point tracking for a partially shaded PV generation system. *IEEE Transactions on Sustainable Energy*. 2021; 12(4), 1876-1890.
- [23] Fares D, Fathi M, Shams I, Mekhilef S. A novel global MPPT technique based on squirrel search algorithm for PV module under partial shading conditions. *Energy Conversion and Management*. 2021; 230, 113773.
- [24] Mohammadinodoushan M, Abbassi R, Jerbi H, Ahmed FW, Rezvani A. A new MPPT design using variable step size perturb and observe method for PV system under partially shaded conditions by modified shuffled frog leaping algorithm-SMC controller. *Sustainable Energy Technologies and Assessments*. 2021; 45, 101056.
- [25] Aldosary A, Ali ZM, Alhaider MM, Ghahremani M, Dadfar S, Suzuki K. A modified shuffled frog algorithm to improve MPPT controller in PV System with storage batteries under variable atmospheric conditions. *Control Engineering Practice*. 2021; 112, 104831.
- [26] Eltamaly AM, Al-Saud MS, Abokhalil AG. A novel bat algorithm strategy for maximum power point tracker of photovoltaic energy systems under dynamic partial shading. *IEEE Access*. 2020; 8, 10048-10060.
- [27] Mansoor M, Mirza AF, Ling Q. Harris hawk optimization-based MPPT control for PV systems under partial shading conditions. *Journal of Cleaner Production*. 2020; 274, 122857.
- [28] Zafar MH, Khan NM, Mirza AF, Mansoor M, Akhtar N, Qadir MU, ... & Moosavi, et al. A novel meta-heuristic optimization algorithm based MPPT control technique for PV systems under complex partial shading condition. *Sustainable Energy Technologies and Assessments*. 2021; 47, 101367.
- [29] Basha CH, Murali M. A new design of transformerless, non-isolated, high step-up DC-DC converter with hybrid fuzzy logic MPPT controller. *International Journal of Circuit Theory and Applications*. 2022; 50(1), 272-297.
- [30] Kumar N, Hussain I, Singh B, Panigrahi BK. Rapid MPPT for uniformly and partial shaded PV system by using JayaDE algorithm in highly fluctuating atmospheric conditions. *IEEE Transactions on Industrial Informatics*. 2017; 13(5), 2406-2416.
- [31] Alshareef M, Lin Z, Ma M, Cao W. Accelerated particle swarm optimization for photovoltaic maximum power point tracking under partial shading conditions. *Energies*. 2019; 12(4), 623.
- [32] Bounabi M, Kaced K, Ait-Cheikh MS, Larbes C, Ramzan N. Modelling and performance analysis of different multilevel inverter topologies using PSO-MPPT technique for grid connected photovoltaic systems. *Journal of Renewable and Sustainable Energy*. 2018; 10(4).
- [33] Eltamaly AM, Farh HM, Abokhalil AG. A novel PSO strategy for improving dynamic change partial shading photovoltaic maximum power point tracker. *Energy sources, part a: recovery, utilization, and environmental effects*. 2020; 1-15.
- [34] Kamarzaman NA, Tan CW. A comprehensive review of maximum power point tracking algorithms for photovoltaic systems. *Renewable and Sustainable Energy Reviews*. 2014; 37, 585-598.
- [35] Pal RS, Mukherjee V. Metaheuristic based comparative MPPT methods for photovoltaic technology under partial shading condition. *Energy*. 2020; 212, 118592.
- [36] Al-Majidi SD, Abbod MF, Al-Raweshidy HS. A particle swarm optimisation-trained feedforward neural network for predicting the maximum power point of a photovoltaic array. *Engineering Applications of Artificial Intelligence*. 2020; 92, 103688.
- [37] Reddy SS, Yammani C. A novel two step method to extract the parameters of the single diode model of Photovoltaic module using experimental Power-Voltage data. *Optik*. 2021; 248, 167977.
- [38] Çevik K, Koçer H. A Soft Computing Application Based on Artificial Neural Networks Training by Particle Swarm Optimization. *Süleyman Demirel University Journal of Natural and Applied Sciences*. 2013; 17(2), 39-45.

The Effect of Cadmium and Lead Exposure on the Development and Physical Structure of Quinoa (*Chenopodium quinoa* Willd.)

Zeynep GÜL^{1*} , Abdullah YAZICI² , Özlem ÇAKIR³ 

¹ Atatürk Üniversitesi, Bitkisel Üretim ve Uygulama Merkezi, Erzurum, Türkiye

² Atatürk Üniversitesi, Ziraat Fakültesi, Tarla Bitkileri Bölümü, Erzurum, Türkiye

³ Bayburt Üniversitesi, Mühendislik Fakültesi, Gıda Mühendisliği Bölümü, Bayburt, Türkiye

Zeynep GÜL ORCID No: 0000-0003-2961-1473

Abdullah YAZICI ORCID No: 0000-0003-0362-2799

Özlem ÇAKIR ORCID No: 0000-0002-5080-7721

*Corresponding author: zdumlu@atauni.edu.tr

(Received: 06.10.2023, Accepted: 07.03.2024, Online Publication: 26.03.2024)

Keywords

Quinoa,
Chenopodium quinoa Willd.,
Heavy Metal,
Cadmium,
Lead

Abstract: The presence of soil affected by cadmium (Cd) and lead (Pb) and their metals is increasing daily. Quinoa is a plant that can grow in harsh conditions due to being a halophyte plant. This study was planned to examine the effects of lead and cadmium metals, two of the most common metals today, on plant growth, physiology and some biochemical properties of quinoa. Within the scope of the study, heavy metal applications were made as 1 control (no application), 4 doses of Cd (50, 100, 150 and 200 mg/kg), and 4 doses of lead (500, 1000, 1500, 2000 mg/kg). In this study, which was carried out in Atatürk University Plant Production and Application Center greenhouse conditions, it is observed that the metals applied negatively affected the parameters in the plant, and cadmium metal had a more toxic effect than lead metal. It is determined that the fresh weight of the plant lost 62% at the Cd 200 level and 45% at the Pb 2000 level compared to the control group.

98

Kadmiyum ve Kurşun Uygulamalarının Kinoa'nın (*Chenopodium quinoa* Willd.) Gelişimi ve Fiziksel Yapısı Üzerine Etkisi

Anahtar Kelimeler

Kinoa,
Chenopodium quinoa Willd.,
Ağır Metal,
Kadmiyum,
Kurşun

Öz: Cd ve Pb metallerinin etkilediği toprak varlığı her geçen gün artmaktadır. Kinoa halofit bir bitki olduğundan tuzlu topraklarda yetişme kabiliyetine sahiptir. Bu çalışma, günümüzde sıkça rastlanan metallerden ikisi olan kurşun ve kadmiyumun, kinoa bitki büyümesi, fizyolojisi ve bazı biyokimyasal özelliklerine olan etkilerini incelemek için planlanmıştır. Çalışma kapsamında 1 kontrol (hiçbir uygulama yapılmayan), Cd 4 doz (50, 100, 150 ve 200 mg/kg), kurşun 4 doz (500, 1000, 1500, 2000 mg/kg) olacak şekilde ağır metal uygulamaları yapılmıştır. Atatürk Üniversitesi Bitkisel Üretim ve Uygulama Merkezi sera koşullarında yapılan bu çalışmada uygulanan metallerin bitkideki parametreleri olumsuz etkilediği, kadmiyum metalinin, kurşun metalinden daha toksik bir etkiye sahip olduğu görülmüştür. Bitki yaş ağırlığının Cd 200 seviyesinde kontrol grubuna göre %62, Pb 2000 seviyesinde ise %45 oranında kayba uğradığı tespit edilmiştir.

1. INTRODUCTION

Quinoa (*Chenopodium quinoa* Willd.) belongs to the Chenopodiaceae family, growing in the Andes Mountains region of South America [1]. Its extraordinary adaptation to climate and soil conditions increases the spreading worldwide. It is widely grown worldwide, including Europe, North America, North Africa and Asia [2, 3]. The chemical and nutritional compositions of quinoa are

greatly affected by genetic diversity, geographical locations and growing environmental conditions [4]. It is reported that the number of countries where quinoa grows was 8 in 1980 and 40 in 2010, which is more than 100 in 2021 [5]. Quinoa cultivation in Turkey started in the 2000s. It was initially a product exported from South American countries and sold in luxury markets at high prices, but today, it has begun to take place at more affordable prices with the spread of domestic production.

Studies on identifying and developing suitable varieties for Turkey among the quinoa species brought from abroad are continuing. Limtar White, the first possible variety for Turkey, received production permission in 2016. According to unofficial figures, it is estimated that it is cultivated in approximately 15 thousand decree areas in our country [6].

Quinoa seeds are used in human nutrition, like bulghur and rice, and since it does not contain gluten, they are known as a safe food source for celiac patients, a genetic disease [7]. The protein content of quinoa seeds is between 7.5% and 22.1%, which means that the plant is a good protein source [8, 9]. Quinoa is also used as a forage plant and in animal nutrition in dry grass and silage form due to its ability to be easily ensiled [10]. The straw and hay of the plant have been included in the nutrition programs of sheep, cattle and horses in South America for many years [11].

Quinoa is known as one of the most essential grains of the 21st century due to its nutritional and biological properties and its resistance to environmental conditions [12]. There is particular interest in quinoa due to its ability to adapt to harsh conditions, including saline soils, drought and stressful environments. The reason why it is resistant to arid conditions is that it has a tap root system. [13]. Most scientific research on quinoa focuses on its behavior on abiotic stresses such as drought and salinity. In recent years, many studies have been conducted on this plant's harsh temperature conditions and heavy metal stress [14]. Some quinoa varieties can accumulate high amounts of metal in their leaf tissues even if the soil or environment contains a low rate of heavy metal. This situation increases the importance of the plant when assessed with heavy metal pollution increasing [15].

Overuse of chemical fertilizers in agricultural activities causes the accumulation of potassium, nitrogen, phosphorus and some nutrients in the soil. Disproportional use of pesticides and chemical fertilizers, industrial activities and environmental pollution cause heavy metal accumulation. It is reported heavy metal pollution affects approximately 235 million hectares of arable land worldwide [16]. As seen in all kinds of pollution, firstly plants are affected by heavy metal pollution [17]. Heavy metals accumulate in soils on the surface or at depths near the surface [18]. Heavy metal stress conditions negatively affect plant growth, yield and productivity. As a result of these adverse effects, the plants' metabolic, physiological and biochemical properties are involved [19]. These metals, which accumulate in plants, enter the food chain, reach other living organisms, and can increase toxic levels for human health. Each plant has the potential to absorb and accumulate heavy metals. Many studies have shown variations in metal uptake, even among different genotypes of the same plant species [20].

Cadmium and lead are the most known heavy metals. Cd enters the human body through the food chain and causes serious health problems [21]. The use of cadmium in many industrial branches increases the risk of contamination of foodstuffs with soil, air and water. It is

one of the leading metals from agricultural activities [22, 23]. It causes oxidative stress, growth delay and inhibition of plant enzymatic reactions [24, 25, 26]. In addition, it causes chlorosis (yellowing) and color change (browning) at the root tips and that can cause plant death.

Heavy metals prevent the transportation of nutrients from the root to the leaves and branches and negatively affect photosynthesis by suppressing chlorophyll biosynthesis [27, 28]. Also, some lead is present in plants, but that does not mean lead is an essential component in metabolism [29]. Increasing its concentration in the soil suppresses the growth and development of plants and decreases yield [30, 31]. Additionally, Pb negatively affects seed germination and suppresses the plant's root development, even causing the death of the plant [32, 33, 34, 35]. Halophytic plants such as quinoa can be used for cleaning soils contaminated with lead and cadmium metals [19]. Within the scope of this study, the effects of different doses of cadmium and lead metals on plant growth, physiology and some biochemical properties of quinoa were examined.

2. MATERIAL AND METHOD

The study uses the seeds of the Titicaca variety of quinoa (*Chenopodium quinoa* Willd.). The experiment was performed for 9 different applications (control + 4 Cd applications + 4 Pb applications) and three replications for each. There were two pots in each repetition. It was applied in a completely randomized design with 54 (9x3x2=54) pots. The volume of each pot is 2 liters and it was filled with a mixture of garden soil, peat and sand. In the control group, heavy metal application was not made. Heavy metal applications were performed by four different doses of cadmium and lead. Cd dose was performed by using CdSO₄.8H₂O with 50, 100, 150 and 200 mg/kg. Lead doses were applied using PbNO₃ with 500, 1000, 1500 and 2000 mg/kg. Heavy metals were added into the soil mixture in each pot by a homogeneous mixture and each incubation period was performed for three weeks. Soil and heavy metal concentration rates were determined from the literature reviews [36, 37, 38]. At the end of the incubation period, 7 seeds were planted in each pot with a depth of 1 to 1.5 cm. After the seedlings were formed, thinning was done and 4 seedlings were left in each pot. The moisture rate of the soil was constantly checked and required watering was applied at appropriate rates. The potting work was completed in 50 days. Afterwards, the following measurements and analyzes were made.

2.1. Physical Methods

Within the scope of the study, seedling height (cm) and number of leaves are measured. Additionally, fresh and dry weights (g) of roots and above-ground plant parts were determined. The samples were kept at 68 °C to determine the dry weights until they reached constant weight. LICOR, LI-3100 model (Lincoln, NE, USA) device was used for leaf area measurement and SPAD-502 model chlorophyllometer (Konica Minolta Sensing, Inc., Japan brand) was used for chlorophyll determination.

2.2. Electrical Conductivity (EC)

When plants are exposed to stress, the damage usually occurs in leaf tissue or cell membranes. The damage rate is measured by measuring the electrical conductivity in fresh leaf tissues. In this study, two plants were randomly selected from each replicate and the youngest leaf on the plant was used for electrical conductivity measurement. Samples taken from the leaves with a diameter of 1 cm were put in 20 ml of pure water and shaken for 24 hours and then electrical conductivity was measured [39]. In this way, permeability, which also indicates damage in the cell membranes, was determined (EC1). Afterwards, the samples were put in an autoclave at 121 °C for 20 minutes to ensure the complete disintegration of cells and tissues and then the second measurement was performed (EC2). Finally, the required calculation determines the relative electrical conductivity ratio (EC1/ EC2) [39].

2.3. Leaf relative water content (LRWC)

Leaf relative water content (LRWC) was determined according to [39].

2.4. Hydrogen Peroxide (H₂O₂) Analysis

For this analysis, the methods and applications mentioned in the studies of Sahin et al. and Caşka Kılıçaslan et al. were preferred [40, 41]. The procedures and sequences mentioned here were applied to quinoa with minor modifications. In this context, firstly, leaf tissues were homogenized in 0.1% (w/v) TCA solution on ice and the homogenate was centrifuged at 12,000 g for 15 minutes. The resulting supernatant was added to the mixture of 10 mmol l⁻¹ potassium phosphate buffer (pH 7.0) and 1 mol l⁻¹ potassium iodide. Following this process, measurements were made at a 390 nm absorbance level. Measures made at different intervals were evaluated using a standard curve created under appropriate conditions.

2.5. Lipid Peroxidation (Malondialdehit-MDA) Analysis

For MDA analysis, the methods mentioned in the studies of Sahin et al. and Caşka Kılıçaslan et al. were used [40, 41]. The leaves were put into the fine powder using liquid nitrogen and then leaf extracts were extracted using cold ethanol. The obtained crude extracts were centrifuged at 12,000 g for 20 minutes with heated trichloroacetic acid, thiobarbituric acid, butylated hydroxytoluene and a supernatant mixture. Then, the mixture was cooled in an ice bath and centrifuged again. Finally, measurements were made at 400, 500 and 600 nm absorbance values. Finally, the MDA concentration is defined with the help of a coefficient of 155 mmol L⁻¹ cm⁻¹.

2.6. Statistical Assessment

Within the scope of the study, a random parcel trial design was preferred and three repetitions were made. SPSS 18 package program was used to evaluate the results,

analysis of variance and Duncan's multiple comparison test was applied.

3. RESULTS

The effects of cadmium and lead metals at different concentrations on quinoa development are presented in Table 3.1. The plant height is negatively affected by Cd and Pb applications. The results for both metals are statistically in the same group. The lowest values for fresh and dry weights of plants and roots were determined at the highest metal concentrations. For the Cd 200 level, fresh plant weight decreases by 62% compared to the control, and for the Pb 2000 level, it reduces by 45%. Heavy metals are known to prevent the plant from absorbing nutrients from the soil. This situation restricts plant growth parameters such as plant and root lengths, number of leaves and leaf area [42, 43]. Similar results were obtained in our study when compared to previous studies. Fresh root weight decreases by 64% and 50% in Cd 200 and Pb 2000 exposures. Heavy metal deconstructs the structure of cell membranes and damages the root surfaces, negatively affecting root length [44]. In a similar study made on quinoa, root dry weight decreased by 66-63% in Cd 90 and Pb 150 applications [19]. In another study, where the heavy metal concentrations were applied to annual grass (*Lolium multiflorum* Lam.) at the same rate, even seed emergence was not achieved with the last two doses of cadmium metal, while all seeds emerged ultimately in quinoa [45].

Table 3.1. Effect of Cd and Pb exposure on quinoa development

Exposure	Plant length (cm)	Plant fresh weight (g)	Plant Dry Weight (g)	Root Fresh Weight (g)	Plant Dry Weight (g)
Control	9,350±1,3 43a	1,910±0,4 95a	0,300±0,1 41a	0,145±0,0 07bc	0,100±0,0 14b
Cd 50	9,433±1,1 01a	1,600 ±0,150ab	0,227±0,0 28ab	0,120±0,0 17de	0,097±0,0 06b
Cd 100	9,233±1,6 92a	1,300±0,2 36bc	0,153±0,0 25bc	0,110 ±0,100e	0,083±0,0 06b
Cd 150	10,400±2, 007a	1,397±0,5 06abc	0,163±0,0 0bc	0,087±0,0 06f	0,067±0,0 06bc
Cd 200	9,133±0,9 24a	0,723 ±0,171d	0,117±0,0 28c	0,053±0,0 06g	0,027±0,0 06d
Pb 500	9,667±1,0 69a	1,583± 0,231ab	0,167± 0,035bc	0,170±0,0 10a	0,103±0,0 06b
Pb 1000	10,500±0, 854a	1,677±0,1 40ab	0,200±0,0 17bc	0,157 ±0,012ab	0,867±0,0 57a
Pb 1500	9,833±0,4 16a	1,407±0,0 86abc	0,177±0,0 06bc	0,134±0,0 06cd	0,080±0,0 10b
Pb 2000	9,734±0,3 21a	1,057±0,2 06cd	0,140 ±0,026bc	0,073±0,0 23fg	0,040±0,0 10cd

There is no statistical difference between the means shown with the same letter given. The effects of lead and cadmium applications on the number of leaves in quinoa are shown in Table 3.2. The leaf area of the control group, which is 12,750, decreased to 9,667 for cadmium 200 (24% decrease). It is reported that heavy metals decompose the chloroplast structure and thus reduce the chlorophyll content of plants. However, it also negatively affects stomatal conductance in plants, preventing the continuity of the photosynthesis process and reducing water consumption. As a result, yield and product quality are also negatively affected [46]. Although the amount of chlorophyll in some applications decreases in this study compared to the control group, it is included in the same

statistical group (Table 3.2). Leaf area decreases with the increase in heavy metal. At the highest dose of cadmium, the leaf area had the lowest value among all samples (42,570 cm²/plant). Lead applications negatively affect the leaf area, and the results of Pb 1500 and 2000 applications were in the same statistical group. Electrical conductivity increases with heavy metal applications, and LRWC value decreases. The decrease in LRWC value may be due to heavy metal-induced reductions in hydraulic conductivity [47].

Table 3.2. Effects of Cd and Pb exposure on physical properties

Exposure	Leaf Number (for each plant)	Chlorophyll (SPAD)	Leaf area (cm ² /plant)	EC (%)	LRWC (%)
Control	12,750±0, 636ab	43,400±1, 697a	98,640±13, 641a	54,815±4, 772c	82,745±4, 433a
Cd 50	13,533±0, 585a	42,367±3, 564a	76,163±19, 247abc	65,153±5, 505b	80,837±1, 385a
Cd 100	10,800±2, 066bc	39,00±6, 090a	67,090±12, 588abc	72,050±1, 516a	72,923±1, 414bc
Cd 150	11,600±1, 558abc	42,20±1, 509a	74,907±21, 010abc	72,170±1, 607a	68,760±1, 711d
Cd 200	9,667±1,2 42c	40,767±5, 670a	42,570±3,7 12c	73,843 ±3,112a	63,837±2, 169e
Pb 500	10,900±1, 015bc	41,90±3, 650a	77,503±16, 840abc	65,593±0, 115b	76,790±2, 931b
Pb 1000	12,300±1, 277ab	43,734±2, 040a	89,510 ±18,312ab	71,970±1, 573a	69,260±1, 905cd
Pb 1500	11,267±0, 058abc	40,334±6, 407a	58,313±11, 553bc	73,827±0, 769a	66,537 ±2,188de
Pb 2000	12,734±1, 021ab	42,267±2, 532a	63,397±28, 080bc	74,736±0, 788a	63,863±1, 824e

*There is no statistical difference between the means shown with the same letter given

The effects of Cd and Pb on H₂O₂ and MDA values are presented in Table 3.3. As can be seen from the table, an increase in H₂O₂ and MDA enzyme activities is observed as a result of heavy metal applications. H₂O₂ activity, which is 89,400 in the control group, increased to 136,00 mmol/kg with Cd application. Higher values were obtained in Pb applications than in the control, except for the Pb 500 application. Pb 1000 and Pb 2000 applications were stayed in the same statistical group. The type of stress factor varies depending on many factors such as the processes occurring in the plant and the type of plant [48]. As the ratio of applied Cd and Pb elements increases, the MDA content in quinoa rises steadily. The enzyme activity known as malondialdehyde (MDA) varies depending on the type and severity of stress [49]. In a study investigating the effects of drought stress on quinoa, it is reported that, due to the increase in the stress factor, root length, root fresh-dry weight and chlorophyll amount in plants decreases compared to the control group, the MDA value increases by 82% [50]. Researchers attributed these results to the severe damage caused by heavy metal stress in plant cells [51].

Table 3.3 Effect of Cd and Pb on enzymes of quinoa

Exposure	H ₂ O ₂ (mmol kg ⁻¹)	MDA (nmol g ⁻¹)
Control	89,400± 23,416bc	5,876± 0,655ab
Cd 50	122,533± 11,582ab	6,367± 1,787ab
Cd 100	122,700± 13,323ab	6,334± 0,631ab
Cd 150	135,933± 22,982a	6,627± 0,340ab
Cd 200	136,00± 24,093a	7,107 ± 0,304a
Pb 500	75,166± 20,004c	5,467 ± 0,093b
Pb 1000	109,133± 28,916c	5,573± 0,466b
Pb 1500	125,300± 4,479ab	6,474± 0,271ab
Pb 2000	115,833± 11,202a	6,850± 0,685ab

*There is no statistical difference between the means shown with the same letter given

As it is known, plants exposed to some environmental effects or stresses are treated differently. The most common of these is some reactive oxygen species accumulation in plant tissues [41]. Some free radicals resulting from oxidative stress provoke lipid peroxidation in the cell membrane, leading to malondialdehyde (MDA) formation. Many scientific studies address this issue and investigate possible harms and treatments [52, 53, 40, 55]. This study observed that both H₂O₂ and MDA levels increased significantly due to the Cd and Pb heavy metal stress applied. This situation can be expressed as an effort to adapt quinoa to current conditions to reduce the harmful effects of relevant heavy metals or eliminate these effects. Some studies have reported that quinoa plants exposed to heavy metals or different stresses have effective mechanisms in these and similar ways [56, 57, 58].

4. CONCLUSION

The results showed that quinoa was negatively affected by Pb and Cd metals in all parameters, and its toxic effect increased depending on the increase in concentration. Seed germination occurred at all concentrations of both metals. Cd had a more toxic effect compared to Pb metal. Quinoa has a defense mechanism against heavy metals by increasing enzyme activity. More detailed studies are needed to understand the defense mechanism of quinoa, which is known to be resistant to abiotic stresses.

Ethics Statement

The authors of this article declare that the materials and methods used in this study do not require ethics committee approval and legal-specific permission.

Conflicts of interest

As the authors of this study, we declare that there is no financial conflict of interest with any institution, organization, or person related to this article and no conflict of interest between the authors.

Acknowledgements

This study was supported by BAP (The Coordination Unit of Scientific Research Projects, Project No: 2020-8494). The authors thank BAP for funding

REFERENCES

- [1] Mu H, Xu S, Sun Q, Shi J, Zhang D, Wan D, Wei J. Research Progress of Quinoa Seeds (*Chenopodium quinoa* Willd.): Nutritional Components, Technological Treatment, and Application. Foods. 2023; 12(10), 2087.
- [2] Tang Y, Li X, Zhang B, Chen P.X, Liu R, Tsao R. Characterisation of phenolics, betanins and antioxidant activities in seeds of three *Chenopodium quinoa* Willd. genotypes. Food Chem. 2015; 166: 380–388. [CrossRef]
- [3] Aziz A, Akram N.A, Ashraf M. Influence of natural and synthetic vitamin C (ascorbic acid) on primary and secondary metabolites and associated

- metabolism in quinoa (*Chenopodium quinoa* Willd.) plants under water deficit regimes. *Plant Physiol. Biochem.* 2018; 123: 192–203. [CrossRef]
- [4] Pedrali D, Giupponi L, De la Peña-Armada R, Villanueva-Suárez M, Mateos-Aparicio I. The quinoa variety influences the nutritional and antioxidant profile rather than the geographic factors. *Food Chem.* 2023; 402, 133531. [CrossRef] [PubMed]
- [5] Pathan S, Siddiqui R.A. Nutritional composition and bioactive components in quinoa (*Chenopodium quinoa* Willd.) greens: A review. *Nutrients.* 2022; 14(3), 558.
- [6] Tan M, Temel S. Her Yönüyle Kkinoa Önemi, Kullanılması ve Yetiştiriciliği. Iksad Publishing House, Ankara; 2019.
- [7] Jacobsen SE. The worldwide potential for quinoa (*Chenopodium quinoa* Willd.). *Food Rev Int.* 2003; 19(1-2): 167–177.
- [8] Cardozo A, Tapia M. Valor nutritivo. In: Tapia M., Gandarillos H., Alandia S., Cardozo A., Mujica A. (Eds.) *Quinoa y kaniwa, cultivos Andinos.* Bogota CIID, Oficina Rgiond para la america Lotina. 1979. pp. 149-192, ISBN: O344 88936- 200-9.
- [9] Kır A.E, Temel S. Sulu koşullarda farklı kinoa (*Chenopodium quinoa* Willd.) genotiplerinin tohum verimi ile bazı tarımsal özelliklerinin belirlenmesi. *Iğdır Üniv. Fen Bilimleri Enst. Derg.* 2017; 7(1): 353-361.
- [10] Tan M, Temel S. Erzurum ve Iğdır şartlarında yetiştirilen farklı kinoa genotiplerinin kuru madde verimi ve bazı özelliklerinin belirlenmesi. *Iğdır Üni. Fen Bilimleri Enst. Der.* 2017; 7(4): 257-263.
- [11] FAO. Plant Production and Protection Series. In: Hernandez, J.E, Leon, J. (Eds.), *Neglected crops 1492 from a different perspective.* 1994. No. 26, Available at <http://www.fao.org/docrep/T0646E/T0646E00.htm> (accessed March 2014).
- [12] FAO. La Quinoa: Cultivo milenario para contribuir a la se-guridad alimentaria mundial. Oficina Regional Para America Latina Y El Caribe, FAO, 2011; 37, 66. <https://doi.org/10.1016/j.jaridenv.2009.03.010F>
- [13] Gonzalez J.A, Gallardo M, Hilal, M, Rosa, M. Prado F.E. Physiological responses of quinoa (*Chenopodium quinoa* Willd.) to drought and waterlogging stresses: Dry matter partitioning. *Bot. Stud.* 2009; 50(1): 35-42.
- [14] Hinojos L, González J.A, Barrios-Masias F. H, Fuentes F, Murphy K.M. Quinoa abiotic stress responses: A review. *Plants.* 2018; 7(4), 106.
- [15] Bhargava A, Shukla S, Srivastava J, Singh N, Ohri D. Genetic diversity for mineral accumulation in the foliage of *Chenopodium* spp. *Scientia Horticulturae.* 2008; 118(4): 338-346.
- [16] Bermudez G.M.A, Jasan R, Pla R, Pignata M.L. Heavy metals and trace elements in atmospheric fall-out: Their relationship with topsoil and wheat element composition. *Journal of Hazardous Materials.* 2012; 213-214: 447-456.
- [17] Yaldız G, Şekeroğlu N. Tıbbi ve aromatik bitkilerin bazı ağır metallere tepkisi, *Türk Bilimsel Derlemeler Dergisi.* 2013; 6(1): 80- 84.
- [18] Arıkan E.N. Bazı ağır metallerce kirlenmiş tarım topraklarının çim bitkisi (*Lolium perenne* L.) kullanılarak fitoremediasyon yöntemleriyle doğal arıtımı [dissertation]. Nevşehir: Nevşehir Hacı Bektaş Veli University; 2021.
- [19] Amjad M, Iqbal M.M, Abbas G, Farooq A.B.U, Naeem M.A, Imran M, et al. Assessment of cadmium and lead tolerance potential of quinoa (*Chenopodium quinoa* Willd) and its implications for phytoremediation and human health. *Environmental Geochemistry and Health.* 2021; 1-14.
- [20] Hassan MJ, Zhang G, Zhu Z. Influence of cadmium toxicity on plant growth and Nitrogen Uptake in Rice as Affected by Nitrogen Form. *J. Plant Nutr.* 2008; 31: 251–262.
- [21] Çağlarırnak N, Hepçimen A. Z. Ağır metal toprak kirliliğinin gıda zinciri ve insan sağlığına etkisi. *Akademik Gıda.* 2010; 8(2): 31-35.
- [22] Özkan A. Antakya-Cilvegözü karayolu etrafındaki tarım arazilerinde ve bitkilerdeki ağır metal kirliliği. *Çukurova Üniversitesi Mühendislik Mimarlık Fakültesi Dergisi,* 2017; 32(3): 9–18.
- [23] Kabata-Pendias A. Trace elements in soils and plants, 4th edn. CRC Press, Boca Raton. 2011.
- [24] Prasad M.N.V. Cadmium toxicity and tolerance in vasculer plants. *Environmental and Experimental Botany.* 1995; 35, 525–545.
- [25] Ramos I, Esteban E, Lucena J.J, Garate A. Cadmium uptake and subcellular distribution in plants os *Lactuca* sp. Cd- Mn Interaction. *Plant Science.* 2002; 162: 761– 767.
- [26] Jali P, Pradhan C, Das A.B. Effects of cadmium toxicity in plants: a review article. *Scholars Academic Journal of Biosciences.* 2016; 4(12):1074-1081.
- [27] Benavides M.P, Gallego S. M, Tomaro M.L. Cadmium toxicity in plants. *Brazilian Journal of Plant Physiology.* 2005; 17(1): 21-34.
- [28] Nagajyot P, Lee K, Sreekanth T. Heavy metals, occurrence and toxicity for plants a review. *Environmental Chemistry Letters.* 2010; 8(3):199-216.
- [29] Kabata-Pendias A, Pendias H. Trace element in the soil and plants. CRC Press Florida. 1984.
- [30] Wang G, Su M.Y, Chen Y.H, Lin F.F, Luo D, Gao S.F. Transfer characteristics of cadmium and lead from soil to the edible parts of six vegetable species in southeastern. *China Environ. Pollut.* 2006; 144(1): 127-35.
- [31] Zheljzkov V.D, Craker L.E, Xing B. Effects of Cd, Pb, and Cu on growth and essential oil contents in dill, peppermint, and basil. *Environmental and Experimental Botany.* 2006; 58 (1-3): 9-16. DOI: 10.1016/j.envexpbot.2005.06.008
- [32] Mrozek Jr E, Funicelli N.A. Effect of zinc and lead on germination of *Spartina alterniflora* Loisel seeds at various salinities. *Environmental and Experimental Botany.* 1982; 22(1): 23-32.

- [33] Symeonidis L, McNeilly T, Bradshaw A.D. Differential tolerance of three cultivars of *Agrostis capillaris* L. to cadmium, copper, lead, nickel and zinc. *New Phytologist.*, 1985; 101: 309–315.
- [34] Dabas S. To study the effect of lead on efficiency of nitrogen fixation and nitrogen assimilation in *Vigna radiata* (L.) Wilczek. Ph.D. Thesis, M.D. University, Rohtak. 1992.
- [35] Çolak U. Gaziantep ilinde Ekimi Yapılan Ekmeklik Buğday Çeşitlerinde (Tosunbey, Ceyhan 99) Kurşun Stresinin Fizyolojik ve Morfolojik Etkileri ile Kurşuna Tolerans Düzeylerinin Belirlenmesi [dissertation]. Gaziantep: Gaziantep University; 2009.
- [36] Alım Z. Hümik Asit Uygulamalarının Ağır Metal Stresi Altında Yetiştirilen Terede Bitki Gelişimi ile Bazı Fizyolojik ve Biyokimyasal Özellikler Üzerine Etkileri [dissertation]. Erzurum: Atatürk University; 2020.
- [37] Yıldırım E, Ekinci M, Turan M, Açar G, Örs S, Dursun A, Kul R, Balcı T. Impact of Cadmium and Lead Heavy Metal Stress on Plant Growth and Physiology of Rocket (*Eruca sativa* L.). *KSU J. Agric Nat.* 2019; 22(6): 843-850.
- [38] Lambrechts T, Lequeue G, Lobet G, Lutts S. Impact of cadmium and zinc on root system of *Lolium perenne* and *Trifolium repens*. *Communications in Agricultural and Applied Biological Sciences.* 2013; 78(1): 19-24.
- [39] Kaya C, Higgs D, Ince F, Amador B.M, Cakir A, Sakar E. Ameliorative effects of potassium phosphate on salt-stressed pepper and cucumber. *J. Plant Nutrition.* 2003; 26: 807-820.
- [40] Sahin U, Ekinci M, Ors S, Turan M, Yıldız S, Yıldırım E. Effects of individual and combined effects of salinity and drought on physiological, nutritional and biochemical properties of cabbage (*Brassica oleracea* var. *capitata*). *Scientia Horticulturae.* 2018; 240, 196-204.
- [41] Caşka Kılıçaslan, S, Yıldırım E, Ekinci M. Kul R. Kuraklık stresinin fasulyede bitki Gelişimi, Bazı Fizyolojik ve Biyokimyasal Özellikler Üzerine Etkisi. *Erciyes Üniversitesi Fen Bilimleri Enstitüsü Fen Bilimleri Dergisi.* 2020; 36 (2):264-273.
- [42] Mengoni A, Gonnelli C, Galardi F, Gabbrielli R, Bazzicalupo M. Genetic diversity and heavy metal tolerance in populations of *Silene paradoxa* L. (Caryophyllaceae): a random amplified polymorphic DNA analysis. *Molecular Ecology.* 2000; 9:1319-1324.
- [43] Jayakumar K, Jaleel C.A, Vijayarengan P. Changes in growth, biochemical constituents, and antioxidant potentials in radish (*Raphanus sativus* L.) under cobalt stress. *Turkish Journal of Biology.* 2007; 31(3):127–136.
- [44] Soudek P, Katrusakova A, Sedlacek L, Petrova S, Koci V, Marsik P. Effect of heavy metals on inhibition of root elongation in 23 cultivars of flax (*Linum usitatissimum* L.). *Archives of Environmental Contamination and Toxicology.* 2010; 59(2): 194-203.
- [45] Gül Z, Yazıcı A. Farklı Ağır Metal Uygulamalarının Tek Yıllık Çim (*Lolium multiflorum*) Bitki Gelişimi ve Fizyolojisi Üzerine Etkisi. *MAS Journal of Applied Sciences.* 6 (Özel Sayı), 2021; 1110-1117.
- [46] Tunc T, Sahin U. The changes in the physical and hydraulic properties of a loamy soil under irrigation with simpler-reclaimed wastewaters. *Agricultural Water Management.* 2015; 158:213-224.
- [47] Ehlert C, Maurel C, Tardieu F, Simonneau T. Aquaporin mediated reduction in maize root hydraulic conductivity impacts cell turgor and leaf elongation even without changing transpiration. *Plant Physiology.* 2009; 150(2), 1093-1104.
- [48] Bhaduri A.M, Fulekar M.H. Antioxidant enzyme responses of plants to heavy metal stress. *Reviews in Environmental Science and Bio-Technology.* 2012; 11: 55–69.
- [49] Tunçtürk R, Tunçtürk M, Oral E. Kuraklık stresi koşullarında yetiştirilen soya fasulyesinin (*Glycine max* L.) bazı fizyolojik özellikleri üzerine rizobakterium (PGPR) uygulamalarının etkisi. *ÇOMÜ Ziraat Fakültesi Dergisi.* 2021; 9 (2): 359-368. DOI: 10.33202/comuagri.881226.
- [50] Aslam M.U, Raza M.A.S, Saleem M.F, Wagas M, Iqbal R, Ahmad S, Haider I. Improving strategic 327 growth stage-based drought tolerance in quinoa by rhizobacterial inoculation. *Community Soil Science Plant. Anal.* 2020; 51 (5): 1-16.
- [51] Kirecci O.A. *Saccharomyces Cerevisiae*'nın Gelişme Ortamına İlave Edilen Ağır Metallerin (Mn, Mg, Cd, Fe) Bazı Biyokimyasal Parametrelere Etkileri. *KSU Doğa Bilimleri Dergisi.* 2017; 20(3): 175- 184.
- [52] Sairam R.K, Srivastava G.C, Agarwal S, Meena R.C. Differences in Antioxidant Activity in Response to Salinity Stress in Tolerant and Susceptible Wheat Genotypes, *Biol. Plant.* 2005; 49: 85-91.
- [53] Kuşvuran Ş. Kavunlarda Kuraklık ve Tuzluluğa Toleransın Fizyolojik Mekanizmaları Arasındaki Bağlantılar [dissertation]. Adana: Çukurova University; 2010.
- [54] Yaqoob H, Akram N.A, Iftikhar S, Ashraf M, Khalid N, Sadiq M, et al. Seed Pretreatment and Foliar Application of Proline Regulate Morphological, Physio-Biochemical Processes and Activity of Antioxidant Enzymes in Plants of Two Cultivars of Quinoa (*Chenopodium quinoa* Willd.). *Plants.* 2019; 8(12):588. <https://doi.org/10.3390/plants8120588>
- [55] Parvez S, Abbas G, Shahid M, Amja M, Hussain M, Asad S.A, et al. Effect of salinity on physiological, biochemical and photostabilizing attributes of two genotypes of quinoa (*Chenopodium quinoa* Willd.) exposed to arsenic stress. *Ecotoxicology and Environmental Safety.* 2020; 187, 109814. <https://doi.org/10.1016/j.ecoenv.2019.109814>
- [56] Khalofah A, Migdadi H, El-Harty E. Antioxidant Enzymatic Activities and Growth Response of Quinoa (*Chenopodium quinoa* Willd.) to Exogenous Selenium Application. *Plants.* 2021; 10: 719. <https://doi.org/10.3390/plants10040719>
- [57] Tüver G.Y, Ekinci M, Yıldırım E. Morphological, physiological and biochemical responses to combined cadmium and drought stress in radish (*Raphanus sativus* L.). *Rend. Fis. Acc. Lincei.* 2022.

Screening Some Advanced Upland Cotton (*Gossypium Hirsutum* L.) Genotypes Tolerance Under Water Deficit Stress

Sadettin ÇELİK^{1*} 

¹University of Bingol, Genç vocational school, Department of Forestry, 12500, Genç, Bingol/ Turkey

Sadettin ÇELİK ORCID No: 0000-0002-8396-4627

*Corresponding author: sadettincelik@bingol.edu.tr

(Received: 07.11.2023, Accepted: 07.03.2024, Online Publication: 26.03.2024)

Keywords

Drought tolerance,
Cotton,
Cluster,
Morphological
traits,
Stress factors

Abstract: Upland cotton is the most widely cultivated among cotton species and is the best natural fiber source for the textile industry. However, abiotic stress, particularly drought stress, adversely affects important cotton planting regions. This study uses phenotypic drought markers to ascertain the tolerances of some advanced cotton lines under the limited irrigation conditions obtained from the drought-tolerant variety development breeding program. The study was conducted according to the completely randomized design with three replications. A total of 16 genotypes were used, with fourteen lines selected from the F₂ segregation stage of the drought-tolerant variety breeding program, and two varieties used as control varieties. Variance analysis (ANOVA) was conducted, and the results revealed highly significant variations between the means ($P<0.01$). The highest root length (RL, 46 cm) was recorded in the Aras 24 genotype, while the lowest was in Aras 28 (15 cm). Aras 40 showed the highest root weight (RW, 0.241 g) value, followed by Aras 24 (0.210 g) and TEX (control 0.206 g). The lowest RW values were seen in Aras 28 (0.086 g) and Aras 29 (0.089 g). Regarding lateral fresh weight (LFW), Aras 28 recorded the lowest (0.019 g), while Aras 24 recorded the highest value (0.088 g). Lastly, Aras 41 showed the highest relative water content (RWC) value of 92%, followed by Aras 38 (89) and TEX (76). In conclusion, if the breeding program is continued with Aras 41, Aras 40, and Aras 24 varieties, it will significantly contribute to the goal.

Bazı Upland Pamuk (*Gossypium hirsutum* L.) Pamuk Genotiplerinin Su Noksanlığı Stresi Altında Toleranslıklarının Görüntülenmesi

Anahtar Kelimeler

Kuraklık toleransı,
Pamuk,
kümelenme,
Morfolojik
özellikler,
Stres faktörleri

Öz: Upland pamuğu bütün pamuk türleri arasında en fazla yetiştiriciliği yapılan pamuk türüdür ve tekstil endüstrisi için en iyi doğal lif kaynağıdır. Ancak, özellikle kuraklık stresi gibi abiyotik stres faktörü pamuk yetiştirilen alanları olumsuz yönde etkilemektedir. Bu çalışma, kuraklığa dayanıklı çeşit geliştirme ıslah programından elde edilen bazı ileri pamuk hat ve genotiplerinin kısıntılı sulama koşulları altındaki toleranslarını belirlemek için fenotipik kuraklık markörlerinden yararlanılarak yürütülmüştür. Araştırma tesadüf parselleri deneme desenine göre 3 tekerrürlü olarak yürütülmüştür. Kuraklığa toleranslı çeşit geliştirme programının F₂ segregasyon aşamasından seçilen on dört adet hat, iki çeşit de kontrol olmak üzere 16 genotip kullanılmıştır. Varyans analizi (ANOVA) sonucunda ortalamalar arasındaki farklılıklar önemli bulunmuştur ($P<0.01$). En yüksek kök uzunluğu (RL) Aras 24 genotipinde (46 cm), en düşük kök uzunluğu (RL) değeri ise Aras 28 (15 cm)'de kaydedilmiştir. Aras 40 en yüksek Kök ağırlığı (RW) (0.241 g) değerini göstermiş ve bunu Aras 24 (0.210 g) ve TEX (0.206 g) kontrol çeşidi takip etmiştir. En düşük RW değeri ise Aras 28 (0.086 g) ve Aras 29 (0.089 g) genotiplerinde görülmüştür. Lateral taze ağırlığı (LFW) ise en düşük değer Aras 28 (0.019 g), en yüksek değer Aras 24 (0.088 g) genotipinde kaydedilmiştir. Aras 41 genotipi en yüksek bağıl su içeriği (RWC, 92) değerini göstermiş ve bunu Aras 38 (89) ve TEX (76) kontrol çeşidi takip etmiştir. Sonuç olarak, kuraklığa karşı tolerant çeşit geliştirme ıslah programına Aras 41, Aras 40 ve Aras 24 ile devam edilmesi halinde bu ıslah programının başarıya ulaşmasında önemli katkılar sağlayacağı anlaşılmıştır.

1. INTRODUCTION

Upland cotton (*Gossypium hirsutum* L.) with allotetraploid ($2n=4x=52$; AADD) genome is one of the most important field crops in the world [1]. Since it is the largest source of natural fiber consumed worldwide, it meets approximately 90% of the world's cotton production [2]. In addition to being an oil plant in terms of oil obtained from its seeds, it also provides raw materials for many industries. It constitutes the primary source of income for millions of people. Due to drought around the world, cotton production in the last five years has decreased from 13,960 million bales to 11,935 million bales, resulting in a decrease in production by approximately 14% [3]. Although the cotton plant (*Gossypium spp.*) has a higher tolerance to abiotic stress factors such as drought than other important industrial field crops, profound decreases are observed in its yield when exposed to drought stress for a long time [4].

High temperatures caused by global warming increase evaporation." This leads to the induction of water stress in the cotton plant. It causes the cotton plant to enter into water stress. Without water, it becomes imperative to turn to many alternatives. Considering the importance of reducing the expenses of the enterprises, it is seen that the breeding studies to be carried out to increase the tolerance of water stress, which is one of the biggest problems in the cultivation of cotton plants, are of critical importance. Due to the narrow genetic diversity in the Upland cotton species, it is challenging to select varieties for cultivars with high drought stress tolerance [5].

Genetic diversity consists of allelic variations of genes; differences in the plant genome sequence are the result of the reflections in the phenotype as a result of factors such as changes in the gene pool and population of the cotton species [6]. The drought resistance of plants can be followed by morphological characteristics [7]. Saad et al. [8] investigated the relationship between morphophysiological selection and linkage among traits in a study on cotton. The narrowing genetic diversity of Upland cotton in various ways makes it difficult to be successful in intraspecies crossing studies. Studies have shown that the selection of the varieties that will participate in the variety development breeding program as parents among the commercial varieties increases the success of the crossbreeding breeding program to be carried out for

the variety breeding since the commercial varieties have high values in terms of agronomic and technological parameters, that is, they have high allele frequency [9].

Since the seedling period is the most sensitive period of cotton, it is a critical period for the following growth stages, when drought stress is most evident [10]. Various parameters are used to evaluate the reactions of cotton genotypes to drought stress during the seedling period. Parameters such as root length (RL), excised leaf water loss, root weight (RW), leaf area (Leaf Area, LA), stomatal conductivity and density, number of lateral roots (LNR), and relative water content (RWC) are the extensively used to assess the drought tolerance of plants [11]. Again, to understand the genetic potential and performance of the plant under drought stress during the seedling period, besides the root system-related parameters, morphological characters [12], cotton seedling period characters [13], seed germination characters [14], and relative growth rate [15]. are used.

This study aims to determine the tolerances of some advanced cotton lines under the deficit irrigation conditions obtained from the drought-tolerant variety development breeding program using morphological drought markers such as germination rate (%) fresh lateral weight (LFW) and Relative Water Content (RWC), Root length (RL), and Root weight (RW). These parameters were used to determine the tolerance level and genotypes of the cotton lines to facilitate the decision regarding which genotype to choose to continue with the breeding program.

2. MATERIAL AND METHOD

2.1. Plant Materials and Climatic Parameters

In the experiment, 14 genotypes provided from STAR SEED company (www.startohum.com) of Upland (*G. hirsutum* L.) cotton genotypes obtained from the F₂ segregation stage of the variety development breeding program against drought were used as plant material. As control varieties, TEX and Beyaz Altın 119 (BA-119) commercial varieties were used, which are not only tolerant to drought stress, but also have wide adaptability, are highly productive, and are intensively planted in the Southeastern Anatolia region, one of the regions where cotton cultivation is done in Turkey.

Table 1. The long-term climatic parameters for all months in the province of Bingol (URL 1, 2022)

Long-term climate data of Bingol province (1927-2021)													
	MONTHS												Annual
	1	2	3	4	5	6	7	8	9	10	11	12	
Average Temperature (°C)	-2.3	-1.1	4.2	10.8	16.3	22.0	26.7	26.5	21.3	14.2	6.8	0.6	12.2
Average Maximum Temperature (°C)	2.3	3.9	9.5	16.7	22.9	29.4	34.6	34.7	29.8	21.6	12.6	5.1	18.6
Average Lowest Temperature (°C)	-5.9	-4.9	-0.1	5.8	10.2	14.7	19.0	18.7	13.6	8.3	2.2	-2.8	6.6
Average Sunbathing Time (hours)	3.4	4.4	4.9	5.5	7.1	9.1	9.4	9.0	8.1	6.1	4.5	3.2	6.2
Average Number of Rainy Days	1.10	1.9	1.12	1.12	1.12	1.3	1.1	1.1	1.3	8.8	1.8	1.10	95.1
Average Monthly Total Rainfall (mm)	140.4	128.7	129.8	116.4	76.2	20.6	7.0	4.2	12.6	66.2	106.1	136.4	944.6
Highest Temperature (°C)	13.3	16.2	22.3	30.3	33.9	38.0	42.0	41.3	37.8	32.1	25.5	22.8	42.0
Lowest Temperature (°C)	-23.2	-21.6	-20.3	-9.2	1.0	3.5	8.8	7.8	4.2	-2.4	-15.0	-25.1	-25.1

2.2. Method

2.1.1. Calculation of germinating percentages

Humus soil taken from forest areas was used to prepare the seedbed. By making three holes in the bottoms of 5-liter pots, the water given to them remained in the root zone, preventing the genotypes from being exposed to physiological drought stress. Drought-tolerant Ba 119 and TEX were used as control cultivars in the experiment, which was established with three replications according to the completely randomized design.

The pots experiment involved thoroughly watering all pots until they reached a field capacity (800 m L⁻¹), utilizing the following formula to determine field capacity.

Field capacity= (Weight of soil at maximum water holding-weight of oven-dried soil)/weight of oven-dried soil) (Junker et al., 2015).

To reach the field capacity, 800 m L⁻¹ water was given to the plants during sowing (100% field capacity, Control). 25 days after sowing (DAS), all plants germinated and emerged, drought stress treatments were started to be applied. These treatments included slight drought at 75% field capacity (600 m L⁻¹), moderate drought at 50% field capacity (400 m L⁻¹), and severe drought at 25% field capacity (200 m L⁻¹).

The trial, which was established on Jul 30, 2022, in Turkey-Bingöl Genç (Coordinates: 38 ° 44' 58" N and 40 ° 32' 11" E), was terminated on September 20 (52 days).

was terminated. Observations were made for the genotypes' germination percentages (%) 15 days after sowing using the formula mentioned below:

$$\text{Germination percentage (\%)} = \frac{\text{Germinated seeds}}{\text{Total seeds}} \times 100$$

Measurement of relative water content: Root weight (g) and Lateral fresh weight (g) were directly measured on a precision balance. After the experiment was terminated, the root length (cm) was measured without damaging the roots. The following formula was used to obtain the Relative Water Content (RWC) value:

$$\text{Relative Water Content (RWC)} = \frac{(\text{FW}-\text{DW})}{(\text{TW}-\text{DW})} \times 100 \quad [16]$$

FW is fresh weight, DW is dry weight while TW is Turgid weight.

Fresh weights of 0.6 cm radius discs cut from leaves of each genotype were weighed for turgid weight approximately four days after the last exposure to drought stress. These were placed in Petri dishes filled with distilled water (dH₂O), and turgid weights were

measured after 4 hours. After this stage, the leaf discs' dry weights were measured at 60 °C in the oven, and the Relative water content (RWC) values were calculated.

2.3. Statistical Analysis

The means of morphological markers that reflect drought stress in phenotype, such as root length (RL), root weight (RW), lateral fresh weight (LFW), and relative water content (RWC), were compared using analysis of variance (ANOVA) to assess the significance of the differences. The means were compared with the Least Significant Difference (LSD) test at the p<0.05 significance level. The phylogenetic tree was built using the means of drought-related morphological traits based on the kinship of genotypes using JMP 17.0 (JMP®, Version <17>).

3. RESULTS AND DISCUSSIONS

The majority of breeding programs primarily select cotton with high seed yield and fiber quality under ideal field conditions. The environmental factors effect, which results in low heritability of seed yield and yield parameters [18], however, means that the response to selection is low under inappropriate conditions. Additionally, there are unfavorable correlations between yield and fiber quality traits. In order to simultaneously increase yield and fiber quality, it is crucial to screen cotton for drought tolerance under field conditions. This is because of other abiotic stress factors, such as heat, salt, and biotic stresses, can also have an impact on the results. Although it is more practical to screen a large collection of germplasm at the seedling phase in a greenhouse [19], the true value of a genotype must be evaluated in the field before being used in breeding for drought tolerance. Utilizing a small part of genotypes from one to some cultivars and breeding lines, efforts have been made to develop cotton under drought conditions so far [20, 21, 22].

A large genetic and breeding population for drought tolerance was only briefly evaluated in a few studies [23, 24, 25, 26]. However, research on how drought stress effects cotton yield at the crucial seedling stage is lacking. Therefore, the cotton seeds of advanced genotypes under water-stressed conditions were measured to calculate various sensitivity and tolerance indices to investigate suitable stress resistance indices for screening of cultivars under drought.

As a result of the analysis of variance performed at a 95% confidence level, the differences between genotypes for all phenotypic markers were found to be very significant (P<0.01), except for the lateral root weight. Accordingly, while the highest germination rate (%) was recorded in the Aras 30 (90%) genotype, the lowest germination rate was observed in the Aras 24 (40%) genotype.



Figure 1. *G. hirsutum* L. Morphological structure of roots and root lengths

Genotypes Germination, Percent (%), Root Length (RL) seedling stage is lacking. Therefore, cotton seeds of advanced genotypes under water-stressed conditions were measured in order to the highest average root length was Aras 24 (46 cm), while the lowest was Aras 28 (15 cm). Regarding root length, the mean for all the genotypes was 27 cm. A root length above the average was obtained in half of the genotypes. In contrast, a root length close to the average was obtained in the other half (Table 2, Fig. 1). A replication of the Aras 24 genotype resulted in 52 cm of taproot length (Fig. 1). Zahid et al. [27] observed an average Root length of 5.163 cm in their trials in which they investigated the reactions of 23 cotton genotypes to drought stress during the seedling period. They obtained a lower average root length compared to our study because the cotton plant terminated the experiment when it reached the level of 4 true leaves. Studies have shown that the deep root system increases drought tolerance, improves water and nitrogen uptake from the soil, and reduces Axial root and lateral branching, which puts an extra load on the plant under drought stress [28].

Table 2. The means of some drought traits of Upland cotton species

GENO.	GP	RL	RW	LFW	RWC
Aras 21	77ad	32bc	0.132bc	0.024c	0
Aras 22	67ad	27be	0.119c	0.056bc	65ac
Aras 24	40d	46a	0.210ab	0.088ab	42bc
Aras 25	43cd	33bc	0.147bc	0.024c	42bc
Aras 28	87a	15f	0.086c	0.019c	47bc
Aras 29	47bd	24cf	0.089c	0.029bc	42bc
Aras 30	90a	18ef	0.095c	0.056bc	62ac
Aras 36	73ad	19df	0.118c	0.026c	36cd
Aras 37	80ac	29be	0.085c	0.047bc	70ac
Aras 38	83ab	26bf	0.113c	0.048bc	89a
Aras 39	80ac	25cf	0.131bc	0.059bc	68ac
Aras 40	60ad	37ab	0.241 a	0.084ac	74ac
Aras 41	70ad	30bd	0.159ac	0.036bc	92a
Aras 42	70ad	22cf	0.135bc	0.057bc	41bc
Ba 119	73ab	22cf	0.160ac	0.067bc	62ac
TEX	83ab	29be	0.206ab	0.087ab	76ab
Mean	70 ad	27be	0.13bc	0.079ac	56

The highest root weight was measured in the Aras 40 genotype with an average of 0.241 g, followed by Aras 24 (0.210 g) and control variety TEX (0.206 g). In the experiment, where the mean root weight of all genotypes was measured as 0.13 g, the lowest average root weight was observed in the Aras 28 (0.086 g) and Aras 29 (0.089) genotypes, respectively. Some plants, such as cotton, try to reach deep or distant waters by developing their root systems in the first stages of drought stress.

Developing the root system in field crops is possible not only by root length but also by increasing root weight, number of laterals, and root density per plant. Although the cotton plant develops a root system that is 10 times the length above the ground under drought stress in the first place, it shows that the root system weakens over time under long-term drought stress [29]. In addition, stomata, which close in order to minimize water loss in water deficiency, will reduce the uptake of CO₂, which is a component of photosynthesis, so the rate of photosynthesis decreases and the growth of cotton decreases and as a result, the yield decreases [30]. Riaz et al. [31] conducted a 52-day experiment to monitor drought stress using forward-line genotypes in greenhouse conditions. As a result of the experiment, they stated that the new genotypes' root weight (RFW, Root fresh weight) varied between 0.39 and 0.57 g. Although parallel to our study, their superior root weight can be associated with the stabilization of humidity and temperature under controlled conditions or the frequency of irrigation.

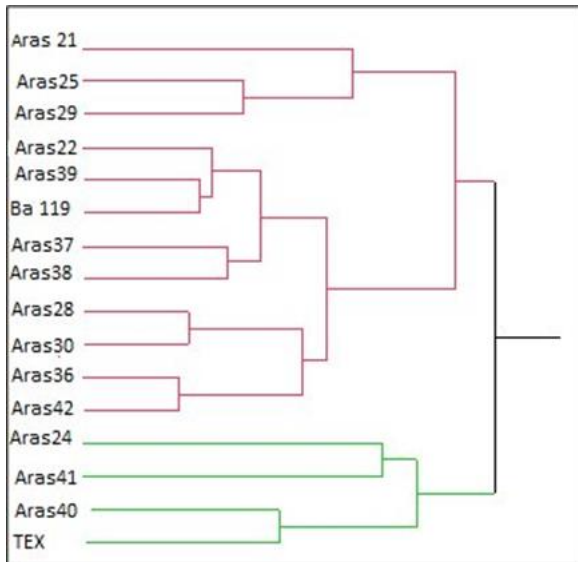


Figure 2. The Phylogenetic Tree of Upland cotton genotypes under drought-stress using JMP 17.0 ver. Software

Genotypes were divided into two main clusters, as seen in Fig. 2. While Aras 24, Aras 40, Aras 41, and control variety TEX were clustered in the first cluster, the remaining genotypes formed a separate cluster. They were divided into two sub-clusters among themselves. Genotypes close to a common ancestor come together in the same cluster, while genotypes far from each other in origin are classified in clusters far from each other.

While the number of lateral roots provides the opportunity to take water and nutrients by spreading over a vast extent in the root area, the weight of the lateral roots tries to increase tolerance to drought stress by storing Glucose (C₆H₁₂O₆) compound in the roots when the cotton plant starts to experience water stress. In this study, Aras 24 showed the highest (0.088 g) LFW, followed by TEX with a 0.087 g average.

In the experiment in which the lateral fresh weights mean of the genotypes were calculated as 0.079 g, the

lowest average was followed by Aras 28 with an average of 0.19 g and Aras 25 and Aras 21 genotypes with an average of 0.024 g.

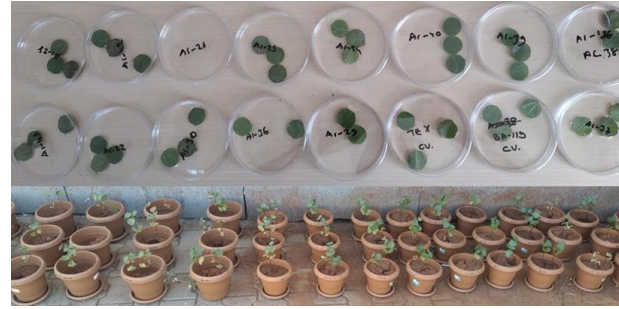


Figure 3. Screening the drought effects of *G. hirsutum* L. Cotton genotypes.

The water content in the leaves is one of the essential drought indicators showing the drought stress tolerance of the cotton plant. Generally, plants with high leaf water content are drought-tolerant [32]. Fig. 3 shows *G. hirsutum* L. cotton genotypes being screened for their drought resistance. Relative Water Content (RWC) content should be mentioned because Aras 21 genotype dries up at the last stage of the limited irrigation application in the experiment. However, while Aras 41 genotype showed the highest value with an RWC of 92 %, Aras 38 (89%) and control variety TEX (76%) followed it. The lowest value was measured in Aras 36 (36%) genotypes, followed by Aras 42 (41%), Aras 24 (42%), and Aras 25 (42%) genotypes. The average RWC values of all genotypes were recorded as 56 % (Table 2). Similar RWC values have been found by Akbar and Hussain [33] and Eid et al.[34]. The RWC value decreases under long-term water stress (Ullah et al., 2012) [35].

4. CONCLUSION

The current study's analysis of morphological parameters such as RW, RL, LFW, and RWC allowed for the conclusion that these indices serve as the most accurate predictors of yield in drought-stressed environments. The genotypes that exhibited high values for the parameters mentioned above were capable of producing high yields under stress environments.

As a result, it has been observed that if the cultivar development breeding program is continued with Aras 41, Aras 40, and Aras 24 varieties, it will significantly contribute to the goal. The genotypes that are promising under drought stress need to be planted in uncontrolled field conditions for a more comprehensive evaluation.

Acknowledgment

I would like to acknowledge to Dr. Sedat SÜLLÜ, who supplied us with seeds from Star SEED company, and Ms. Seda ÇELİK, who helped in the establishment of the experiment and the cultural processes.

REFERENCES

- [1] Li, F., Fan, G., Lu, C. *et al.* Genome sequence of cultivated Upland cotton (*Gossypium hirsutum* TM-1) provides insights into genome evolution. *Nat Biotechnol* 33, 524–530 (2015). <https://doi.org/10.1038/nbt.3208>.
- [2] Hu Y, Chen J, Fang L, Zhang Z, Ma W, Niu Y, Ju L, Deng J, Zhao T, Lian J, Baruch K. *Gossypium barbadense* and *Gossypium hirsutum* genomes provide insights into the origin and evolution of allotetraploid cotton. *Nature genetics*. 2019, Apr;51(4):739-48.
- [3] Anonymous. Economic Survey, Pakistan Bureau of Statistics, Agriculture.2017. Chapter-2. Available online at: http://www.finance.gov.pk/survey/chapter_10/02_agriculture.pdf.
- [4] Parida AK, Dagaonkar VS, Phalak MS, Umalkar GV, Aurangabadkar LP. Alterations in photosynthetic pigments, protein, and osmotic components in cotton genotypes subjected to short-term drought stress followed by recovery. *Plant Biotechnology Reports*. 2017, Apr;1(1):37-48.
- [5] Tyagi P, Gore MA, Bowman DT, Campbell BT, Udall JA, Kuraparthy V. Genetic diversity and population structure in the US Upland cotton (*Gossypium hirsutum* L.). *Theoretical and Applied Genetics*.2014, Feb;127(2):283-95.
- [6] Bhandari HR, Bhanu AN, Srivastava K, Singh MN, Shreya HA. Assessment of genetic diversity in crop plants-an overview. *Adv. Plants Agric. Res*. 2017;7(3):279-86.
- [7] Tuberosa R. Phenotyping for drought tolerance of crops in the genomics era. *Front. Physiol.* 3: 347. 2012.
- [8] Saad M, Nazeer W, Naeem M, Sarwar M, Zia ZU, Tipu AL, Hussain K, Hossain MF, Ahmad F. Morpho-Physiological Indicators for Selection of High-Yielding Cotton (*Gossypium Hirsutum* L.) Cultivars. *Bangladesh Journal of Botany*. 2022. Mar 31;51(1):17-22.
- [9] Santos IG, Teodoro PE, Farias FC, Farias FJ, de CARVALHO LP, Rodrigues JI, Cruz CD. Genetic diversity among cotton cultivars in two environments in the State of Mato Grosso.
- [10] Hou S, Zhu G, Li Y, Li W, Fu J, Niu E, Li L, Zhang D, Guo W. Genome-wide association studies reveal genetic variation and candidate genes of drought stress-related traits in cotton (*Gossypium hirsutum* L.). *Frontiers in Plant Science*. 2018, Sep 3;9:1276.
- [11] Veesar NF, Jatoi WA, Gandahi N, Aisha G, Solangi AH, Memon S. Evaluation of Cotton Genotypes for Drought Tolerance and Their Correlation Study at Seedling Stage. *Biomedical Journal of Scientific & Technical Research*. 2020. 29(1):22090-9.
- [12] Singh B, Norvell E, Wijewardana C, Wallace T, Chastain D, Reddy KR. Assessing Morphological characteristics of elite cotton lines from different breeding programs for low temperature and drought tolerance. *J Agron Crop Sci*.2018, 204:467–476.
- [13] Megha BR, Mummigatti UV, Chimmad VP, Aladakatti YR. Evaluation of hirsutum cotton genotypes for water stress using peg-6000 by slanting glass plate technique. *Int J Pure Appl Biosci*. 2017, 5:740–50.
- [14] Singh B, Raja Reddy K, Redoña ED, Walker T 2017. Developing a screening tool for osmotic stress tolerance classification of rice cultivars based on in vitro seed germination. *Crop Sci*.2017, 57:387–394. doi: 10.2135/cropsci2016.03.0196.
- [15] Sekmen AH, Ozgur R, Uzilday B, Turkan I. Reactive oxygen species scavenging Capacities of cotton (*Gossypium hirsutum*) cultivars under combined drought and heat induced oxidative stress. *Environ Exp Bot*. 2014, 99:141–149.
- [16] Pieczynski M, Marczewski W, Hennig J, Dolata J, Bielewicz D, Piontek P, Wyrzykowska A, Krusiewicz D, Strzelczyk-Zyta D, Konopka-Postupolska D, Krzeslowska M. Down-regulation of CBP 80 gene expression as a strategy to engineer a drought-tolerant potato. *Plant biotechnology journal*. 2013, May;11(4):459-69.
- [17] JMP®, Version <17>. SAS Institute Inc., Cary, NC, 1989–2021.
- [18] Percy RG, Cantrell RG, Zhang J. Genetic variation for agronomic and fiber properties in an introgressed recombinant inbred population of cotton. *Crop Science*. 2006 May;46(3):1311-7.
- [19] Abdelraheem A, Hughs SE, Jones DC, Zhang J. Genetic analysis and quantitative trait locus mapping of PEG-induced osmotic stress tolerance in cotton. *Plant Breeding*. 2015 Feb;134(1):111-20.
- [20] Levi A, Paterson AH, Barak V, Yakir D, Wang B, Chee PW, Saranga Y. Field evaluation of cotton near-isogenic lines introgressed with QTLs for productivity and drought-related traits. *Molecular Breeding*. 2009 Feb; 23:179-95.
- [21] Wang R, Ji S, Zhang P, Meng Y, Wang Y, Chen B, Zhou Z. Drought effects on cotton yield and fiber quality on different fruiting branches. *Crop Science*. 2016 May;56(3):1265-76.
- [22] Zhang D, Luo Z, Liu S, Li W, Dong H. Effects of deficit irrigation and plant density on the growth, yield and fiber quality of irrigated cotton. *Field Crops Research*. 2016 Oct 1; 197:1-9.
- [23] Nasimi RA, Khan IA, Iqbal MA, Khan AA. Genetic analysis of drought tolerance with respect to fiber traits in upland cotton. *Genet Mol Res*. 2016 Oct 5;15(4):1-6.
- [24] Pauli D, Andrade-Sanchez P, Carmo-Silva AE, Gazave E, French AN, Heun J, Hunsaker DJ, Lipka AE, Setter TL, Strand RJ, Thorp KR. Field-based high-throughput plant phenotyping reveals the temporal patterns of quantitative trait loci associated with stress-responsive traits in cotton. *G3: Genes, Genomes, Genetics*. 2016 Apr 1;6(4):865-79.
- [25] Dabbert TA, Gore MA. Challenges and perspectives on improving heat and drought stress resilience in cotton. *Journal of Cotton Science*. 2014;18(3):393-409.
- [26] Abdelraheem A, Fang DD, Zhang J. Quantitative trait locus mapping of drought and salt tolerance in

- an introgressed recombinant inbred line population of Upland cotton under the greenhouse and field conditions. *Euphytica*, 2017 214(1). <https://doi.org/10.1007/s10681-017-2095-x>.
- [27] Zahid Z, Khan MK, Hameed A, Akhtar M, Ditta A, Hassan HM, Farid G. Dissection of drought tolerance in upland cotton through morpho-physiological and biochemical traits at the seedling stage. *Frontiers in Plant Science*.2021. Mar 12;12: 627107.
- [28] Lynch JP. Harnessing root architecture to address global challenges. *Plant J*. 2022,109:415–431. doi: 10.1111/tbj.15560.
- [29] Abdelraheem A, Esmacili N, O’Connell M, & Zhang J. Progress and perspective on drought and salt stress tolerance in cotton. *Industrial Crops and Products*,2019 pp. 130, 118–129. doi:10.1016/j.indcrop.2018.12.070.
- [30] Chastain DR, Snider JL, Collins GD, Perry CD, Whitaker J, Byrd SA. Water deficit in field-grown *Gossypium hirsutum* primarily limits net photosynthesis by decreasing stomatal conductance, increasing photorespiration, and increasing the ratio of dark respiration to gross photosynthesis. *Journal of plant physiology*. 2014, Nov 1;171(17).
- [31] Riaz M, Farooq J, Sakhawat G, Mahmood A, Sadiq MA, Yaseen M. Genotypic variability for root/shoot parameters under water stress in some advanced lines of cotton (*Gossypium hirsutum* L.). *Genet. Mol.* 2013, Res. Feb 27;12(1):552-61.
- [32] Brito GG, Sofiatti V, Lima MM, Carvalho LP, Silva Filho JL. Physiological traits for drought phenotyping in cotton. *Acta Scientiarum. Agronomy*. 2011, 33:117-25.
- [33] Akbar M, Hussain SB. Assessment of drought-tolerant cotton genotypes based on seedling & physiological attributes at different moisture levels. *Pure and Applied Biology*. 2019. (PAB). 2019 Feb 27;8(1):93-107.
- [34] Eid MA, El-hady MA, Abdelkader MA, Abd-Elkrem YM, El-Gabry YA, El-temsah ME, ElAreed SR, Rady MM, Alamer KH, Alqubaie AI, Ali EF. 2022.ResponseinPhysiological Traits and Antioxidant Capacity of Two Cotton Cultivars under Water Limitations. *Agronomy*.2022, Mar 26;12(4):803.

Isolation, Identification and Molecular Characterization of Lactic Acid Bacteria from Raw Milk Samples Collected from Erzurum Region

Selcan DOĞAN¹ , Gulsah ADIGUZEL^{1*} 

¹Ataturk University, Faculty of Veterinary Science, Department of Food Science and Technology, Erzurum, Türkiye
Selcan DOĞAN ORCID No: 0000-0001-6196-7950
Gulsah ADIGUZEL ORCID No: 0000-0003-1207-6742

*Corresponding author: gulsah@atauni.edu.tr

(Received: 24.01.2024, Accepted: 11.03.2024, Online Publication: 26.03.2024)

Keywords

Raw milk,
Lactic acid
bacteria,
Identification,
rep-PCR,
16S-rRNA
sequence
analysis

Abstract: Due to its high-water content, milk is an important source of different microbial contents, especially lactic acid bacteria. This study aims to isolate and identify lactic acid bacteria from raw milk samples collected from Erzurum and its surroundings, and to introduce possible new species, or genera, to the taxonomy. For this purpose, DNAs of pure bacterial cultures obtained from 50 raw milk samples were isolated, isolates that differed from each other were selected by rep-PCR. A total of 11 different species and subspecies [*Corynebacterium casei*, *Enterococcus italicus*, *E. durans*, *Lactococcus lactis*, *Lactococcus lactis* subsp. *lactis*, *Lactococcus lactis* subsp. *hordniae*, *Lactobacillus paracasei*, *Leuconostoc lactis*, *Staphylococcus succinis*, *Streptococcus parauberis* and *S. uberis*] were determined in raw milk samples by 16S rRNA sequence analysis. It was concluded that the (GTG)₅-PCR method was more successful than BOX-PCR in the identification of lactic acid bacteria isolated from raw milk samples at a species and subspecies level, and the isolate TS10, which was 98% similar to *S. uberis*, maybe a new species and should be re-examined with advanced diagnostic techniques.

Erzurum Yöresinden Toplanan Çiğ Süt Örneklerinden Laktik Asit Bakterilerinin İzolasyonu, İdentifikasyonu ve Moleküler Karakterizasyonu

Anahtar Kelimeler

Çiğ süt,
Laktik asit
bakteri,
İdentifikasyon,
rep-PCR,
16S-rRNA
sekans analizi

Öz: Süt, sahip olduğu yüksek su aktivitesi nedeniyle başta laktik asit bakterileri olmak üzere, farklı mikrobiyal içerikler açısından önemli bir kaynaktır. Bu çalışmada Erzurum ve çevresinden toplanan çiğ süt örneklerinden, laktik asit bakterilerinin izolasyonu, identifikasyonu ve olası yeni tür veya cinslerin taksonomiye kazandırılması hedeflenmiştir. Bu amaçla, Erzurum ve ilçelerindeki üreticilerden toplanan 50 adet çiğ süt örneğinden elde edilen saf bakteri kültürlerinin DNA'ları izole edilerek, rep-PCR ile birbirinden farklı olan izolatlar seçilmiş ve 16S rRNA sekans analizi ile çiğ süt örneklerinde 11 farklı tür ve alt-türün [*Corynebacterium casei*, *Enterococcus italicus*, *E. durans*, *Lactococcus lactis*, *Lactococcus lactis* subsp. *lactis*, *Lactococcus lactis* subsp. *hordniae*, *Lactobacillus paracasei*, *Leuconostoc lactis*, *Staphylococcus succinis*, *Streptococcus parauberis* ve *S. uberis*] varlığı tespit edilmiştir. İncelenen çiğ süt örneklerinden izole edilen laktik asit bakterinin tür ve tür altı düzeyde identifikasyonunda (GTG)₅-PCR yönteminin, BOX-PCR'a göre daha başarılı olduğu, %98 oranında *S. uberis*'e benzerlik gösteren TS10 kodlu izolatın yeni tür olabileceği ve ileri tanı teknikleri ile yeniden incelenmesi gerektiği sonucuna varılmıştır.

1. INTRODUCTION

People need high-quality foods with high nutritional value to sustain their essential activities. The most preferred and first thing that comes to mind is milk and dairy products. "Raw milk" is defined as milk that is milked from the animal at certain intervals, from which no components are removed, or any other substance is

added, and which is not subjected to any prior processing, such as being sent to a factory to be processed [1].

Milk is a nutriment that has a key position in the nutrition process, containing high-quality protein, minerals such as calcium, phosphorus and zinc, and vitamins such as carotenoids, riboflavin, A, D, E, K, B1

(thiamine), B6, B12 and niacin. Since the foods in the milk and dairy products group are rich in calcium, they are important for the healthy development of bones and teeth of individuals, especially in the age groups between adolescence and adulthood; in adults, it has a key role in protecting against cardiological problems, high blood pressure, stroke, osteoporosis, Type 2 diabetes, and colon cancer [2].

Milk allows microorganisms to multiply rapidly under inappropriate milking and storage conditions. Microbial contamination, especially results after milking, increases the acidity in milk and therefore causes coagulation in milk. Medicines used in disease treatment, pesticides, antibiotics, detergent residues, estrus, gestation, and body secretions affect the structure of raw milk. Therefore, in cases where the microorganism load in raw milk is not at an acceptable level, human health will be threatened, and serious milk production losses will grow up [1].

The first diagnosis of lactic acid bacteria as a group was made based on their ability to ferment and coagulate milk with coliform bacteria. Coliform bacteria were separated from the lactic acid bacteria group, with the introduction of microorganisms of the *Lactobacillus* type into taxonomy by Beijerinck in 1901. Lactic acid bacteria are defined as cocci or rod-shaped microorganisms that are gram-positive, endospore, oxidase, catalase-negative, anaerobic, or facultative aerobic, can tolerate acid, can grow at low pH and salt concentrations, are strongly fermentative, produce lactic acid as the final product during sugar fermentation [3,4]. While morphological and physiological tests are widely used in the diagnosis of lactic acid bacteria, now, additional molecular tests (such as API, FAME, SDS-PAGE, PCR-RFLP, rep-PCR and 16S rRNA sequence analysis) are also conducted since merely conventional analyses (such as gram; endospore staining; determination of salt, pH and temperature values at which bacteria develop optimally; motility; catalase; oxidase; and gas production test from glucose) are insufficient for identification [1,5,6].

Most of the lactic acid bacteria found in milk and used as probiotics are classified as GRAS (Generally Recognized as Safe) microorganisms because they are not pathogenic, they produce antimicrobial substances, they are suitable for technological and industrial processes, and they are tolerant to acid and bile. In the last decade, there has been a significant increase in research based on the isolation and identification of lactic acid bacteria from different sources and the determination of their potential to be used as probiotics [1,6]. This study aims to isolate and identify lactic acid bacteria, which are very important for public health and food safety, from raw milk samples collected from Erzurum and its surroundings, and to introduce possible new species or genera into taxonomy.

2. MATERIAL AND METHOD

2.1. Material

50 raw milk samples collected under aseptic conditions from different locations, including Erzurum and its districts (Aziziye, Pasinler, Yakutiye (Dumlu), Tekman, Ispir and Koprukoy) in the summer period, were brought to the laboratory under the cold chain. The analyses and further processing were started immediately.

2.2. Isolation of Lactic Acid Bacteria

For the isolation of test bacteria, a serial dilution tube (10^{-1} - 10^{-7}) was prepared using 0.85% sterile physiological water. Subsequently, 0.1 ml of these dilutions was taken and dispersed on MRS (de Man, Rogosa and Sharpe) and M17 Agar and incubated at 35 °C for 48 hours under both aerobic and anaerobic conditions. At the end of this period, isolates that are believed to be different from the developing colonies in terms of cell and colony morphology were selected. Three phase lines were inoculated onto MRS and M17 Agar and incubated at 35 °C. Afterward, colonies were taken from each pure culture with a sterile loop, inoculated into MRS Broth/M17 Broth and kept in a shaking incubator at 35 °C for 24-48 hours. At the end of this period, stock tubes were prepared from the test strains and stored at -86°C until further analysis [7].

2.3. Identification of Isolates Using Conventional Methods

Bacteria from the stock were revived using MRS/M17 agar before the test isolates were diagnosed using conventional methods. Subsequently, morphological, physiological, and biochemical characteristics of the isolates were determined [8,9]. Different strains were selected and subjected to molecular characterization.

2.4. Molecular Characterization of Isolates

2.4.1. Genomic DNA isolation and molecular fingerprinting

A single colony was taken from the Petri dishes of each test strain revived on MRS/M17 agar, inoculated into MRS/M17 Broth, and incubated for 48 hours. At the end of this period, the genomic DNA of bacteria was isolated according to the Promega Wizard^R genomic DNA purification kit (A2360) protocol [10]. Subsequently, the amount of DNA was adjusted by spectrophotometer to be between A260/A280=1-1.9. To reveal the genomic differences between the test isolates, rep-PCR [BOX-PCR and (GTG)₅-PCR] genomic fingerprint analysis was performed using BOXA1R (5'-CTACGGCAAGGCGACGCTGACG-3') and (GTG)₅ primers (5'-GTGGGTGGTGGTGGTG-3'). To obtain PCR products, 27 µL reaction mixture was prepared as follows: 5 µL Specific Gitschier Buffer, 2.5 µL dimethyl sulfoxide (100%, 20X), 1.25 µL dNTPs (10 mM), 1.25 µL bovine serum albumin (20 gL⁻¹), 3.0 µl primers (5 mM), 0.3 µL Taq polymerase (250 U) and 13.7 µL PCR

grade water. In conclusion, 3 μ L of DNA whose concentration was adjusted to 50 ng was added to each PCR tube (excluding the negative). PCR reactions were conducted employing a thermal cycler, with the specified conditions for (GTG)₅-PCR as follows: initial denaturation at 94 °C for 7 minutes; 36 cycles at 94 °C for 1 minute, annealing at 53 °C for 1 minute utilizing the (GTG)₅ primer, and extension at 65 °C for 8 minutes; followed by a final polymerization at 65 °C for 16 minutes before cooling at 4 °C. In the case of BOX-PCR, the process involves an initial denaturation at 95 °C for 7 minutes, followed by 36 cycles that include 94 °C for 1 minute, annealing at 53 °C for 1 minute using the BOX primer, extension at 65 °C for 8 minutes, and concluding with a final polymerization at 65 °C for 16 minutes in advance of cooling to 4 °C [11-13].

2.4.2. 16S rRNA-PCR

The evolutionarily conserved 16S rRNA gene region is very important in terms of bacterial taxonomy. For this purpose, the 16S rRNA region was amplified using primers 27F (5'-AGAGTTTGATCCTGGCTCAG-3') and 1492R (5'-GGTTACCTTGTTACGACTT-3') [14,15]. 13.1 μ l ddH₂O, 3 μ l 10X PCR buffer, 1.8 μ l MgCl₂, 1.2 μ l DMSO, 0.6 μ l dNTP, 3 μ l (5 μ M) forward primer (27F), 3 μ l (5 μ M) reverse primer (1492R), 0.3 μ l Taq DNA polymerase and 4 μ l template DNA (50 ng). The resulting 16S rRNA PCR products were cloned into the pGEM-T Easy Cloning Vector (Promega, Southampton, UK) using *Escherichia coli* JM101 strain according to the manufacturer's instructions. After cloning, colonies that gave positive results were selected; plasmid isolation was performed and sent to Macrogen Company (Netherlands) for sequence analysis. The obtained 16S rRNA sequence results were compared with other bacteria in GenBank® and EzTaxon (https://blast.ncbi.nlm.nih.gov/Blast.cgi?PROGRAM=blastn&PAGE_TYPE=BlastSearch&LINK_LOC=blasthome and <http://www.ezbiocloud.net/eztaxon/identify>), the similarity ratios between them were determined and their GenBank® No's were achieved [16,17].

3. RESULTS AND DISCUSSION

Lactic acid bacteria have great industrial importance because they are used as starter cultures in the production of various foods, produce antimicrobial substances and included in the formulations of probiotic products. Many dairy products, such as raw milk, kefir and white cheese, are good sources of lactic acid bacteria. Lactic acid bacteria play a very important role in the formation of the unique taste and aroma characteristics of different fermented dairy products. Therefore, the isolation and identification of lactic acid bacteria from natural sources is of great importance [18]. In this study, conventional and molecular characterization of 11 different species and sub-species from raw milk samples collected from Erzurum and its districts were performed.

3.1. Isolation and Identification of Lactic Acid Bacteria

In this study, a total of 150 bacteria were purified (Table 1) isolating from 50 raw milk samples taken from milk producers via cold chain in Erzurum Aziziye, Pasinler, Yakutiye (Dumlu), Tekman, Ispir and Koprukoy districts under aseptic conditions, and stock cultures were prepared.

Table 1. The localities of raw milk samples and Isolated Lactic acid bacteria strains

Location of Isolates	Isolates
Aziziye	TS4,TS19,TS7
Pasinler	TS5,TS6,TS8
Tekman	TS10,TS17
Yakutiye (Dumlu)	TS1,TS2,TS3
Ispir	TS9,TS11
Koprukoy	TS13,TS18

150 pure isolates were subjected to pre-screening in terms of colony morphology, Gram, catalase, and oxidase properties. Consequently, DNA isolations of selected 130 isolates, which were believed to be phenotypically different, were differentiated using rep-PCR [BOX and (GTG)₅-PCR], and the presence of 15 different isolates was observed (Figure 1 and Figure 2).

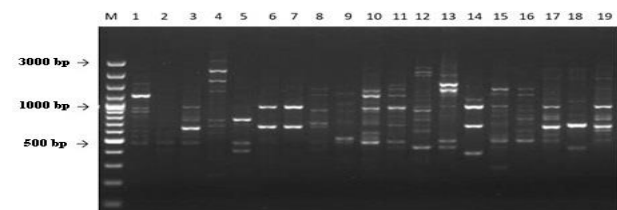


Figure 1. BOX-PCR of test isolates: M [Marker (BioLabs N0550S);100, 200, 300, 400, 500, 600, 700, 800, 900,1000, 1200, 1500, 2000, 3000, 4000, 6000 and 1-19; samples]

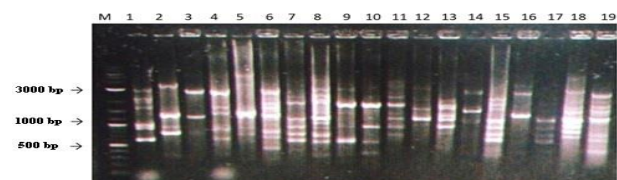


Figure 2. (GTG)₅-PCR of test isolates: M [Marker (BioLabs N0550S);100, 200, 300, 400, 500, 600, 700, 800, 900,1000, 1200, 1500, 2000, 3000, 4000, 6000 and 1-19; samples]

In the BOX-PCR analysis performed for this purpose, it was determined that the isolates contained at least two polymorphic bands between 650-3000 bp and a maximum of 11 polymorphic bands between 400-6500 bp. As a result of the later (GTG)₅-PCR analysis; it was determined that the test strains gave at least 3 polymorphic bands between 600-3000 bp and a maximum of 14 polymorphic bands between 300-6500 bp. (GTG)₅-PCR was more effective in revealing genomic differences between strains than BOX-PCR. Ledina *et al.* [19] performed the isolation and identification of lactic acid bacteria from raw milk and cheese samples in their study, and like our study, they concluded that the (GTG)₅ fingerprint analysis method was highly successful in revealing the distinction between strains. The 16S rRNA gene region of 15 test strains which were believed to be different according to

the results of the genomic fingerprint analysis, was amplified with universal primers (27F and 1492R). Afterward, PCR products were run on agarose gel (1%) and it was observed that all isolates gave a single band (1500 bp) (Figure 3). 16S rRNA PCR products were cloned using the appropriate vector system. Colony PCR (Figure 4) was performed by selecting white colonies containing the relevant gene, and plasmid isolation was performed using the isolation kit (A1330) from Promega.

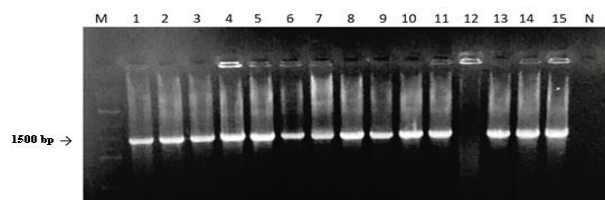


Figure 3. Gel image of 16S rRNAs of various isolates: M [Marker (BioLabs N0550S)];100, 200, 300, 400, 500, 600, 700, 800, 900,1000, 1200, 1500, 2000, 3000, 4000, 6000, N; Negative Control and 1-15; samples]

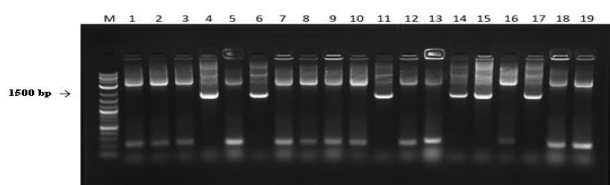


Figure 4. Colony PCR image: M [Marker (BioLabs N0550S)];100, 200, 300, 400, 500, 600, 700, 800, 900,1000, 1200, 1500, 2000, 3000, 4000, 6000 and 1-19; samples]

Then, whether the plasmid carried the desired gene region was analysed using the EcoRI rapid cut-off enzyme. Samples that gave positive results and had the optimum concentration were sent to Macrogen (Netherlands) for sequence analysis [20]. After the 16S rRNA sequence data were made significant, they were compared (Blast) with the sequences in Eztaxon and GenBank®, and then GenBank® numbers were obtained from NCBI (Table 2).

Table 2. 16S rRNA sequence analysis results, similarity ratios and GenBank® No's of test isolates

Code of Isolate	Name of Isolate	Similarity Ratio (%)	GenBank® No
TS1	<i>Enterococcus italicus</i>	99.43	MW433826
TS2	<i>Leuconostoc lactis</i>	99.50	MW433829
TS3	<i>Enterococcus italicus</i>	99.23	MW433845
TS4	<i>Streptococcus parauberis</i>	99.50	MW433848
TS5	<i>Enterococcus durans</i>	99.43	MW433847
TS6	<i>Corynebacterium casei</i>	99.20	MW450777
TS7	<i>Lactococcus lactis</i>	99.36	MW450701
TS8	<i>Lactococcus lactis</i>	99.50	MW450781
TS9	<i>Enterococcus italicus</i>	99.36	MW450782
TS10	<i>Streptococcus uberis</i>	98	MW450783
TS11	<i>Enterococcus italicus</i>	99.93	MW450787
TS13	<i>Staphylococcus succinus</i>	99.9	MW450820
TS17	<i>Lactococcus lactis</i> subsp. <i>lactis</i>	99	MW4508551
TS18	<i>Lactococcus lactis</i> subsp. <i>hordniae</i>	99.85	MW450862
TS19	<i>Lactocaseibacillus paracasei</i> subsp. <i>paracasei</i>	99.50	MW463461

Using the data obtained within the scope of the study, a phylogenetic tree was drawn with the NJ (Neighbor-Joining) method to reveal the phylogenetic relationship between lactic acid bacteria (Figure 5).

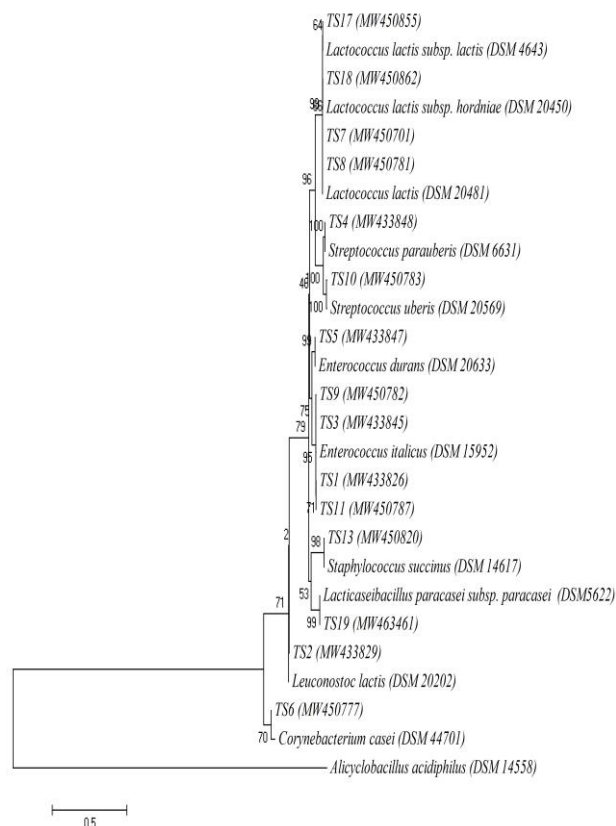


Figure 5. Neighbor-Joining-Phylogenetic tree created with 16S rRNA sequence analysis of lactic acid bacteria and reference strains

In the study conducted by Lusk *et al.* [21], it was concluded that the amplification of the 16S rRNA gene region was highly successful in the identification of the microflora in cheese, especially at the species level. Similar results have been presented by different scientists, and these data are compatible with our results [22,23]. From the test isolates; it was concluded that TS1, TS3, TS9 and TS11 are similar to *Enterococcus italicus*; TS2 is similar to *Leuconostoc lactis*; TS4 is similar to *Streptococcus parauberis*; TS5 is similar to *E. durans*; TS6 is similar to *Corynebacterium casei*; TS7 and TS8 is similar to *Lactococcus lactis*; TS13 is similar to *Staphylococcus succinus*; TS17 is similar to *L. lactis* subsp. *lactis*; TS18 is similar to *L. lactis* subsp. *hordniae*; TS19 is similar to *Lactobacillus paracasei* ($\geq 99\%$), and the isolate TS10 showed 98% similarity to *Streptococcus uberis*, TS10 which is similar to *S. uberis*, maybe a new species and should be investigated with further diagnostic techniques (Table 2).

In the study conducted by Kirmaci [24], 143 isolates were obtained from raw sheep milk and the species-level identification of the samples was carried out by 16S rRNA sequence analysis. It was determined that 48.95% of 143 isolates are *Enterococcus* spp., 40.55% are *Lactococcus* spp., 9.10% are *Lactobacillus* spp., 0.69% are *Streptococcus* spp. and 0.69% are *Leuconostoc* spp. As a result, it was observed that samples of the

Enterococcus and *Lactococcus* genera constituted the dominant flora. Results like the literature data were obtained in the performed study. Detailed morphological, physiological, and biochemical characteristics of 11 different strains were investigated by randomly selecting one of the isolates belonging to the same species (TS1 from TS1, TS3, TS9 and TS11 isolates; TS7 from TS7 and TS8 strains) that were believed to be different. As a result of this study, it was observed that all the isolates were Gram-positive, endospore negative, nonmotile, with stem cell morphology (excluding TS6 and TS19), catalase (excluding TS6 and TS13) and oxidase (excluding TS4 and TS13) negative, and homofermentative (TS2, TS7 and TS19 are heterofermentative). In their study, Fortina *et al.* [25] revealed that the *Enterococcus italicus* species was gram-positive; it had an endospore, catalase, oxidase negative, homofermentative, nonmotile and stem cell morphology and can grow at 10-45 °C, pH 9 and 6% NaCl concentration. TS1, TS3, TS9 and TS11 isolates which were isolated within the scope of our study, showed 99% similarity to the *Enterococcus italicus* species and also showed characteristics parallel to the literature data.

It was determined that the isolate TS10, which has a 98% similarity to *Streptococcus uberis* was gram-positive, catalase-negative, and grown in the 0-6% salt concentration range, at 15-50 °C. In the study conducted by Odierno *et al.* [26], the same bacterial species were isolated from raw milk, identification was performed, and similar results were obtained. Unlike others, the genomic similarity ratio of the isolate we obtained to the strains in GenBank® is 98% instead of 99%.

As a result of the studies carried out to determine the salt tolerance (0-12%) of the isolated lactic acid bacteria: it was determined that test isolates TS1, TS2, TS6, TS7, TS12, TS13 and TS18 were grown at 0-8%; the samples TS4, TS5 and TS10 were grown in the 0-6% salt range, and the TS17 was grown in the 0-10% salt range. In the study conducted to determine the pH ranges in which test strains can grow: it was observed that isolates TS1, TS2, TS5 and TS18 were grown in the pH range of 5-11; isolates TS4, TS7, TS17 and TS19 were grown in the pH range of 5-9; isolates coded TS6, TS10 and TS13 were grown in the pH range of 3-11. Furthermore, it was determined that all the strains grew at 20-50 °C (except for isolates TS7, TS17 and TS19, these strains can grow at the highest temperature of 45 °C), while isolates TS10 and TS13 could also grow at low temperatures such as 15 °C.

In the study conducted by Tangler [27], it was determined that *Lactobacillus*, *Pediococcus* and *Leuconostoc* genera isolated from turnip juice grew at pH 4 but could not grow at pH 9.6. It was determined that other bacteria, except *L. buchneri*, from the species *Lactobacillus plantarum*, *L. buchneri*, *L. brevis*, *L. fermentum* and *L. delbrueckii*, which were used as controls for the same study, grew at pH 4.4. It was determined that the TS2 determined as *Leuconostoc lactis* grew in the pH range of 5-11, unlike the literature.

Kuikui *et al.* [28] isolated lactic acid bacteria from rice silage and identified those using phenotypic and genotypic methods. Because of the phenotypic characterization, it was observed that most of the isolates did not show any growth at low pH and temperature values such as pH 3 at 45 °C and could only grow at a maximum salt concentration of 6.5%. In our study, contrary to the literature data of the isolates; it has been determined that most of the isolates can grow at 20-50 °C, in the pH range of 3-11, and at 0-8% salt concentration. This reveals that the physiological characteristics of isolates may vary depending on the location and the difference in isolated sources.

In this study conducted by Brennan *et al.* [29], it was determined that *Corynebacterium casei* LMG S-19264^T standard strain obtained from cheese is a catalase-positive, oxidase negative, non-motile and non-spore-forming bacterium. In parallel with the literature data, it was determined that the isolate TS6 (*C. casei*) obtained from raw milk was catalase positive, oxidase negative, non-motile, grew at 0-8% salt concentration, in the pH range of 3-11 at 20-50 °C.

In the study conducted by Sánchez *et al.* [30], it was determined that the optimum pH at which the isolate CRL264, which is like *Lactococcus lactis*, could grow was 6.6 and the temperature was 30 °C. In parallel with the literature data, it was observed that the TS7 obtained in our study showed growth at pH 5-9 and 20-45 °C.

4. CONCLUSION

As a result of the research, it was concluded that raw milk samples collected from Erzurum and its districts have a very wide microflora most of the species belonging to the genera *Lactococcus* and *Enterococcus* constitute the dominant flora compared to other species according to conventional test results that must be supported by molecular methods. Among the rep-PCR methods, (GTG)₅-PCR is more effective in the identification of lactic acid bacteria at the species and sub-species level than the BOX-PCR method, in view of the fact that isolates survive a wide range of pH, temperature and salt concentrations. Some differences between the physiological characteristics of the bacterial strains isolated within the scope of the study and the literature data may depend on the source from which the strains were isolated, ambient conditions and the isolated habitat. These isolated and identified strains are applicable in biotechnological processes, and also according to the 16S rRNA gene analysis results, the TS10 showed 98% similarity to the *Streptococcus uberis*, maybe a new species and must be analysed with further diagnostic techniques.

REFERENCES

- [1] Dogan S. Isolation Identification and Molecular Characterization of Lactic Acid Bacteria From Raw Milk Samples Collected from Erzurum Region. Master of Science thesis, Ataturk University, Graduate School of Health Sciences, Erzurum, Turkey; 2021.
- [2] Gürsoy A. [Internet]; 2011. *Süt Kimyası ve Biyokimyası*. <https://acikders.ankara.edu.tr/course/view.php?id=5685>.
- [3] TÜİK Verileri; 2020. https://data.tuik.gov.tr/Bulten/Index?p=Dis-Ticaret-Isstatistikleri-Temmuz-2020-3385.5_Temmuz_2020.
- [4] Yalçın H, Özdemir S, Gökalp HY, Kurt A. Ziraat Fakültesi Süt Fabrikasına Farklı Kaynaklardan Gelen İnek Sütlerinde Total, Psikrofilik, Laktik Asit, Koliform Grubu ve *S. aureus* Bakteri Sayılarının Belirlenmesi. Atatürk Üniversitesi Ziraat Fakültesi Dergisi, 1991; 22: 38-45.
- [5] Yerlikaya O. Starter cultures used in probiotic dairy product preparation and popular probiotic dairy drinks. Food Science Technology, 2014; 34: 221-29.
- [6] Akbulut S, Baltacı MO, Adigüzel G, Adigüzel A. Identification and potential Biotechnological Characterization of Lactic Acid Bacteria Isolated from White Cheese Samples. Journal of Pure and Applied Microbiology, 2022;16(4):2912-22.
- [7] Akbulut S. Investigation of the potential use of locally isolated lactic acid bacteria as probiotics. PhD thesis, Graduate School at Natural and Applied Sciences, Atatürk University, Graduate School at Natural and Applied Sciences, Erzurum, Turkey; 2023.
- [8] Arslan, S. Isolation, identification and molecular characterization of lactic acid bacteria from different regions of Turkey white cheese samples. MS thesis, Graduate School at Natural and Applied Sciences, Erzurum, Turkey; 2017.
- [9] Adigüzel, G. Phenotypic and genotypic characterization of lactic acid bacteria isolated from Turkish dry fermented sausage. PhD. thesis, Graduate School of Health Sciences, Ataturk University, Graduate School of Health Sciences, Erzurum, Turkey; 2008.
- [10] Sari B, Faiz O, Genc B, Sisecioglu M, Adigüzel A and Adigüzel G. New xylanolytic enzyme from *Geobacillus galactosidarius* BS61 from a geothermal resource in Turkey. International Journal of Biological Macromolecules, 2018; 119: 1017-26.
- [11] Gevers D, Huys G and Swings J. Applicability of rep-PCR fingerprinting for identification of *Lactobacillus* species. FEMS Microbiology Letters, 2001; 205: 31-36.
- [12] Saez GD, Hebert EM, Saavedra L, Zarate G. Molecular identification and technological characterization of lactic acid bacteria isolated from fermented kidney beans flours (*Phaseolus vulgaris* L. and *P. coccineus*) in northwestern Argentina. Food Research International. 2017;102: 605-15.
- [13] Erkaya E, Genc B, Akbulut S, Adigüzel G, Omeroglu MA, Ozkan H, Adigüzel A. Bacteriocin Producing Bacteria Isolated from Turkish Traditional Sausage Samples. Journal of Pure and Applied Microbiology, 2020;14(2):1567-76.
- [14] Hongoh Y, Yuzawa H, Ohkuma M, Kudo T. Evaluation of primers and PCR conditions for the analysis of 16S rRNA genes from a natural environment. FEMS Microbiology Letters, 2003; 221(2): 299-304.
- [15] Genc B, Tunc MT, Adigüzel A. Characterization of Water-Soluble Extracellular Polysaccharide from *Aeribacillus pallidus* IM17, Indian Journal of Microbiology, <https://doi.org/10.1007/s12088-023-01178-2>
- [16] Nadaroglu H, Mosber G, Alayli Gungor A, Adigüzel G, Adigüzel A. Biodegradation of some azo dyes from wastewater with laccase from *Weissella viridescens* LB37 immobilized on magnetic chitosan nanoparticles, Journal of Water Process Engineering, 2019; 31; 100866.
- [17] Altınok F, Albayrak S, Arslan NP, Taskin M, Aygun E, Sisecioglu M, Adigüzel A. Application of *Anoxybacillus gonensis* UF7 lipase as a catalyst for biodiesel production from waste frying oils. Fuel, 2023; 334(1): 126672.
- [18] Heredia Y, Castro J. Antimicrobial activity and partial characterization of bacteriocin-like inhibitory substances produced by *Lactobacillus* spp. isolated from artisanal Mexican cheese. Journal of Dairy Science, 2015;12: 8285-93.
- [19] Ledina T, Mohar P, Golop M. Tetracycline resistance in *Lactobacilli* isolated from Serbian traditional raw milk cheeses. Journal of Food Science and Technology-Mysore, 2018;55: 1426-34.
- [20] Baltacı MO, Omeroglu MA, Albayrak S, Adigüzel G, Adigüzel A. Production of Endoglucanase by *Exiguobacterium mexicanum* OB24 Using Waste Melon Peels as Substrate. Anais da Academia Brasileira de Ciências, 2022;94:e20220151.
- [21] Lusk TS, Ottesen AR, White JR, Allard MW, Brown EW, Kase JA. Characterization of microflora in Latin-style cheeses by next generation sequencing technology. BMC Microbiology, 2012;12: 254.
- [22] Quilodrán-Vega, Villena SR, Valdebenito J, Salas J, Parra MJ, Ruiz C, Kitazawa A, García HA. Isolation of lactic acid bacteria from swine milk and characterization of potential probiotic strains with antagonistic effects against swine-associated gastrointestinal pathogens. Canadian Journal of Microbiology, 2016;6: 514- 24.
- [23] Gebru YA, Sbhata DB. Isolation and characterization of probiotic LAB from kimchi and spontaneously fermented teff (*Eragrostis tef* (Zucc.) Trotter) batter: their effects on phenolic content of teff during fermentation. Hindawi BioMed Research International, 2020;2020: 4014969.

- [24] Kirmaci HA. Isolation, molecular characterization of lactic acid bacteria in traditional Urfa cheese and possible use as a starter culture. PhD. thesis, Graduate School at Natural and Applied Sciences, Harran University, Sanliurfa, Turkey, 2010.
- [25] Fortina MG, Ricci G, Mora D, Manachini PL. Molecular analysis of artisanal Italian cheeses reveals *Enterococcus italicus* sp. nov. International Journal of Systematic and Evolutionary Microbiology, 2004;54: 1717-21.
- [26] Odierno L, Calvino L, Traversa P. Conventional identification of *Streptococcus uberis* isolated from bovine mastitis in Argentinean dairy herds. Journal of Dairy Science, 2006; 89: 3886-90.
- [27] Tanguler H. Identification of predominant lactic acid bacteria isolated from salgam beverage and improvement of its production technique. PhD, thesis, Graduate School at Natural and Applied Sciences, Cukurova University, Adana, Turkey, 2010.
- [28] Kuikui N, Yanping W, Yimin C. Natural Lactic Acid Bacteria Population and Silage Fermentation of Whole-crop Wheat. Asian Australasian Journal of Animal Sciences. 2015; 28: 1123-32.
- [29] Brennan NM, Brown R, Goodfellow M, Cogan TM. *Corynebacterium mooreparkense* sp. nov. and *Corynebacterium casei* sp. nov., isolated from the surface of a smear-ripened cheese. International Journal of Systematic and Evolutionary Microbiology, 2001; 51: 843-52.
- [30] Sánchez C, Neves AR, Cavalheiro J, Santos H. Contribution of citrate metabolism to the growth of *Lactococcus lactis* CRL264 at low pH. Applied and Environmental Microbiology, 2008; 74: 1136-44.

Ergonomics in Beekeeping Activities

Özgür ÖZGÜN^{1*}, Timuçin ÇİNKİLİÇ¹, İsa AK¹

¹ Bingöl University, Health Sciences Faculty, Occupational Health and Safety Department, 12000, Bingöl, Türkiye
Özgür ÖZGÜN ORCID No: 0000-0003-3816-6746
Timuçin ÇİNKİLİÇ ORCID No: 0009-0006-1812-9680
İsa AK ORCID No: 0009-0009-6862-4526

*Corresponding author: oozgun@bingol.edu.tr

(Received: 15.12.2023, Accepted: 11.03.2024, Online Publication: 26.03.2024)

Keywords

Beekeeping,
Ergonomics,
Beekeeper
health risks,
Musculoskeletal
health

Abstract: Most of the academic research that has been done on beekeeping focuses on bee health, ways to protect bees from diseases, and how to get more yield. However, there are also ergonomic risks during beekeeping activities that affect the health of beekeepers and indirectly affect productivity. In this study, ergonomic risks that threaten the health of beekeepers were investigated. The most important ergonomic risks for beekeepers are those that threaten the health of the musculoskeletal system. These risks arise from working with improper body posture for long periods, manual handling/lifting, and the use of non-ergonomic hand tools. Measures and solutions that can be applied to protect the health of beekeepers against ergonomic risks and to increase working efficiency are presented.

Arıcılık Faaliyetlerinde Ergonomi

118

Anahtar Kelimeler

Arıcılık,
Ergonomi,
Arıcı sağlık
riskleri,
Kas-iskelet
sistemi sağlığı

Öz: Arıcılık üzerine yapılan akademik araştırmaların çoğu arı sağlığı, arıları hastalıklardan koruma yolları ve nasıl daha fazla verim alınabileceği üzerine odaklanmaktadır. Bununla birlikte, arıcılık faaliyetleri sırasında arıcıların sağlığını etkileyen ve dolaylı olarak verimi etkileyen ergonomik riskler de vardır. Bu çalışmada, arıcıların sağlığını tehdit eden ergonomik riskler araştırılmıştır. Arıcılar için en önemli ergonomik riskler kas-iskelet sistemi sağlığını tehdit eden risklerdir. Bu riskler, uzun süreler boyunca uygun olmayan vücut duruşu ile çalışma, elle taşıma/kaldırma ve ergonomik olmayan el aletlerinin kullanımından kaynaklanmaktadır. Ergonomik risklere karşı arıcıların sağlığını korumak ve çalışma verimini artırmak için uygulanabilecek önlemler ve çözümler sunulmuştur.

1. INTRODUCTION

Beekeeping activities, which date back to 4500 BC [1], turned into a large-scale individual and commercial practice with the development of hives with removable frames in the 1800s [2]. The beekeeping industry and the extraction of honey have always been important for the global economy [3] and are also of great importance for the economy of our country [4]. In the last 10 years, there have been a total of 180 thousand beekeepers in Turkey, 140 thousand of which are stationary and 40 thousand are itinerant [4]. Although beekeeping is an important sector, it has not reached its real potential. The main reasons for this are lack of experience and knowledge, accommodation, marketing and bee diseases [5]. Solutions to these problems in the beekeeping sector are possible through technological and engineering

interventions and innovations [2]. However, there are also risk factors that threaten the health of beekeepers such as environmental factors, especially climatic conditions, psychological difficulties and mechanical hazards [6]. A limited number of studies have been conducted on what these risk factors that threaten the health of beekeepers are and how they can be prevented [2]. One of these health problems is musculoskeletal disorders. The most common health problems of beekeepers are pain in the back and lumbar regions [7].

Ergonomics is an interdisciplinary science aimed at adapting the work environment and conditions to the physiological and psychological capabilities of individuals, thereby reducing stress and fatigue in employees and enhancing productivity [4]. Effective application of ergonomics in the workplace significantly

contributes to the prevention of musculoskeletal disorders and occupational diseases among employees. Ergonomic studies include training on risky situations, body mechanics and exercise. In addition to preventing occupational accidents and occupational diseases, mental and physical protection of employees is among the goals of ergonomics [8].

In this study, the ergonomic risks that beekeepers are exposed to were investigated and the measures and solutions that can be applied to protect the health of beekeepers and increase their working efficiency against these risks were discussed.

2. METHOD

In the present study, ergonomic risk factors that beekeepers are exposed to during bee care and honey harvesting processes were determined in Bingöl. The most significant ergonomic risk factors are those that threaten musculoskeletal health. The methods used to assess exposures leading to musculoskeletal diseases are divided into three classes; personal survey methods, methods based on systematic observations and direct measurement methods [9]. In the study, ergonomic risk factors identified using methods based on systematic observations were photographed and recorded.

Ergonomic risk factors such as manual lifting and carrying, working in improper body postures, prolonged standing, and the use of hand tools were identified. Suggestions for eliminating or mitigating these risk factors through regulations and techniques that do not endanger the musculoskeletal system are presented.

3. RESULTS AND DISCUSSION

The most common health problems among beekeepers are low back and back pain. These health problems are caused by the fact that the hives that beekeepers often have to carry have a weight of about 30-40 kg and beekeepers work in the wrong body posture for a long time [7]. Figure 1 shows pictures of manual lifting and carrying in beekeeping activities. When Figure 1 is examined, it is seen that the beekeeper grasps the load by leaning his body forward to lift a hive on the ground. During this type of lifting, the load is lifted using the lumbar and back muscles, which causes a great deal of force to be applied to the intervertebral discs. The weight of the hives usually ranges between 30-40 kg. It has been reported that if a load of 40 kg is lifted from the floor by bending the torso forward, a load of 450 kg can act on the discs between the vertebrae [10]. Such large loads acting on the disc structures between the vertebrae can cause serious damage to the spine. One of these damages is injuries such as hernias, which occur as a result of slipping of the discs between the vertebrae or ejection of the support fluid sacs in these discs. Industrial lifting principles have been developed to protect the health of the spine during the lifting of loads on the ground in industry. Leg muscles, which are biomechanically much more advantageous and stronger, should be used instead of anatomically weak lumbar muscles when lifting loads on the floor [10]. As

shown schematically in Figure 2, the principle should be to approach the load by bending the knees to keep the body as upright as possible and to perform the lifting process using the leg muscles. Beekeepers should be informed about this industrial lifting principle. Thus, it will be possible to prevent spinal disorders that may be caused by load lifting. Another measure that can be taken to prevent the torso from leaning forward during the lifting of the hives is the use of stands with a height suitable for the anthropometric characteristics of the beekeeper. What is meant by the appropriate height here is that the handles of the hive should be raised to a level between the beekeeper's fingertips and waist. In this way, the beekeeper will be able to grasp the hive by keeping his body upright and will be relieved of large loads that may affect the cartilage discs between the vertebrae during lifting from the ground.



Figure 1. Wrong lifting procedures that threaten spinal health

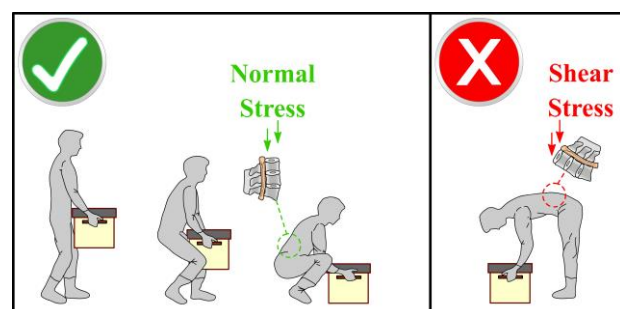


Figure 2. Industrial load lifting principle

Figure 3 depicts images related to the transportation of heavy loads in beekeeping work. Carrying or supporting heavy loads under inappropriate ergonomic conditions increases the risk of injury [11]. Two different groups of injuries can occur in handling operations using the hands. The first group includes cuts, bruises, and fractures resulting from accidents, while the second group comprises musculoskeletal injuries [12]. Musculoskeletal injuries can affect muscles, tendons, ligaments, joints, nerves, blood vessels or related soft tissues as a result of incorrect body posture, repetitive movements and vigorous exertion [13]. These injuries often lead to decreased work performance among employees, consequently reducing the quality and efficiency of their work. Most beekeepers complain of fatigue, back pain, upper body and neck pain, hand or arm pain due to manual material handling [7]. In addition, muscle fatigue and pain in the shoulders may occur as a result of weight bearing and increased duration of this carrying [14]. Local muscle fatigue is a result of increased intramuscular pressure and decreased blood flow in the muscles of the upper extremities as the arm is lifted. Restriction of muscle blood flow impairs muscle metabolism and increases metabolite accumulation, thus causing muscle fatigue [15].



Figure 3. Transportation of heavy loads in beekeeping

Lifting, holding, and carrying heavy loads can quickly lead to fatigue, strain, and health problems [10]. It is of paramount importance for beekeepers to adhere to the following recommendations while lifting and carrying loads, such as hives, to prevent musculoskeletal disorders.

- To prevent the torso from bending forward when lifting the hives, the position of the hive handles should be between the fingertips and waist level.
- Lifting the hives with mechanical lifts to waist height will reduce the risk of spinal or muscle damage.
- It is important that the handles that enable the gripping of the hives or loads have the appropriate geometry and dimensions. The geometry and dimensions of the handles are among the factors that determine the limit values in load lifting. The small size of the handles reduces the grip and the force that can be applied, making transportation difficult on the one hand, and on the other hand, it can cause accidents and injuries as a result of slipping. In addition, the handles should not have sharp corners [10].
- A hive or load being transported should be kept as close to the body as possible.
- If possible, it is easier and safer to transport hives or loads by mechanical means such as wheelbarrows.
- Transportation should not be performed on rough or uneven ground [15]. During transportation on uneven or uneven ground, it may be necessary to apply momentarily very large forces that can cause injuries to muscles and tendons in order to maintain balance. In order to prevent this, a place with a smooth ground should be selected as much as possible or corrections should be made on the ground.

Figure 4 shows images related to working in the wrong body posture. During the bee care and honey harvesting processes related to beekeeping, it is necessary to work for a long time in inappropriate wrong body postures as shown in the figure. The opposite of the wrong body posture is referred to as neutral posture. The term neutral posture is used for the torso as well as for different joints. For the torso, neutral posture is the posture in which the natural curvature of the spine is maintained during sitting or standing, and the body is aligned and balanced [10]. Incorrect body posture is a major problem that affects the balance and proper alignment of the body. Incorrect body posture leads to unbalanced use of muscle groups, resulting in pain, strain and muscle strains. In addition, long-term incorrect body posture can lead to serious health problems such as chronic back pain, neck problems and spinal curvature. Beekeepers' frequent movements such as squatting, bending, twisting, reaching, and working on the knees can cause posture disorders [7]. Especially during bee care and honey harvesting, arrangements must be made to ensure the maintenance of neutral body posture by preventing repetitive and prolonged movements that cause incorrect body postures such as squatting, bending, reaching and turning with waist and shoulder bending. One of these arrangements is to raise the hives to a height suitable for the anthropometric measures of the beekeeper. This can be achieved by using hive stands. Aiyeloja et al [3] conducted a study on the ergonomics of hive stands height and hive type in honey harvesting. In this study, it was

reported that hives usually have a height of 30 cm and for human height of 150-180 cm, placing stands with a height of 70 cm under the hives moderately improves ergonomic conditions. For the best working conditions, it was recommended to place stands with a height of 80-84 cm under the hives [3]. To avoid incorrect body postures, the body should be in neutral posture, facing and close to the work being done. It is also important for the health of the spine that rotational movements are made on the feet, not on the waist and shoulders. In order to avoid turning and bending movements in the back area, the employee should be careful not to go beyond the reach of their arms.

Beekeepers have to working in a standing posture for long periods of time during bee care and honey harvesting processes, which can adversely affect musculoskeletal health. Prolonged standing without adequate rest breaks may lead to joint disorders, back pain, swelling in the feet and legs and muscle fatigue, as well as heart and circulatory disorders [16]. Working in a sitting posture is not an alternative to working in a standing posture. It is useful to sit, walk and do stretching exercises intermittently to prevent the adverse effects of prolonged standing [7].



Figure 4. Working in the wrong body posture during bee care

Beekeeping is an occupational group in which hand and wrist areas are used intensively. During bee care and honey harvesting, repetitive movements are performed using some hand tools. Examples of these repetitive movements include the use of bee smoker and hive tool as shown in Figure 5. The uncapping fork, wire embedder

and bee brush are also frequently used hand tools in beekeeping. Continuous and repetitive hand movements can lead to carpal tunnel syndrome over time. Carpal tunnel syndrome causes numbness, tingling and pain in the hand as a result of compression of the nerves on the inside of the wrist [17]. Measures such as maintaining a neutral wrist posture during beekeeping activities and taking periodic rest breaks are important to reduce the risk of beekeepers encountering such health problems.



Figure 5. Wrist working in a non-neutral position during the use of hand tools.

4. CONCLUSIONS

In this study, ergonomic risks to which beekeepers are exposed were investigated. Measures that can be taken to protect the health of beekeepers against the identified risks and suggestions for improving working conditions in ergonomic terms are presented. Musculoskeletal system diseases are the leading ergonomic risks for beekeepers. To prevent these risks, the following recommendations should be taken into consideration:

- It is of great importance to comply with the industrial load lifting principle in manual lifting operations and to raise awareness of beekeepers in this regard.
- Manual handling of heavy loads should be avoided, and mechanical means should be used for such loads.
- Neutral body posture should be maintained during bee care and honey harvesting operations by placing stands under the hives. In order to maintain a neutral body posture, it is also important that the body is facing and close to the work being done. Bending, turning or over-reaching movements should be avoided, especially using the waist and shoulders.
- If prolonged standing work is necessary, intermittent sitting, walking or stretching exercises should be performed.
- The neutral position of the joints must be maintained during the use of hand tools.

REFERENCES

- [1] Crane EE. The world history of beekeeping and honey hunting. New York: Taylor & Francis; 1999.
- [2] Fels DI, Balcker A, Cook D, Foth M. Ergonomics in apiculture: A case study based on inspecting movable frame hives for healthy bee activities. *Heliyon*. 2019;5(7):1-9.
- [3] Aiyeloja AA, Adedeji GA, Emerhi EA. Impacts of beehive stands' heights and hives' types on the ergonomics of honey harvesting in Port Harcourt, Nigeria. *New York Science Journal*. 2015;8(4):23-27.
- [4] <https://www.researchgate.net/publication/322298875> (Date Accessed: 22 Mayıs 2023).
- [5] Küçük A, Saylam A, Al A, Şahinoğlu OA. Beekeeping problems and solution suggestions in forest villages (Trabzon Regional Directorate of Forestry example). *Turkish Journal of Forestry Research*. 2022;9(2):122-134.
- [6] Topal E, Saner G, Yücel B, Strant M, Üçeş E, Olgun T, Şengül Z. An evaluation on beekeeper's health risk and some other risk factors in beekeeping farms: A case of Izmir-Turkey. *Turkish Journal of Agricultural Economics*. 2019;25(2):149-159.
- [7] Özdemir M. A research of occupational health and safety risks in the beekeeping sector: upper çoruh valley region and bayburt example [PhD Thesis]. Trabzon: Avrasya University; 2021.
- [8] Gümüş GL. Awareness of occupational health and safety in architectural offices and investigation of ergonomics in terms of working environment in Kayseri [Master Thesis]. Kayseri: Erciyes University; 2022.
- [9] Özel E, Çetik O. Tools used in the analysis of occupational duties and a sample application. *Journal of Science and Technology of Dumlupınar University*. 2010;22:41-52.
- [10] Üçüncü K. Ergonomics lecture notes. Trabzon: Karadeniz Technical University; 2020.
- [11] Guidance on the management of manual material handling in the workplace. Dublin: Health and Safety Authority; 2005.
- [12] Hazards and risks associated with manual handling in the workplace, European Agency for Safety and Health at Work; available at <http://osha.europa.eu>.
- [13] Ergonomics Guidelines For Manual Material Handling, WorksafeNB, 2010.
- [14] Lin CL, Wang MJ, Drury CG, Chen Y. Evaluation of perceived discomfort in repetitive arm reaching and holding task. *International Journal of Industrial Ergonomics*. 2010;40:90-96.
- [15] Al Amin MS, Nuradilah Z, Isa H, Nor Akramin M, Febrian I, Taufik M. A review on ergonomics risk factors and health effects associated with manual materials handling. *Advanced Engineering Forum*. 2013;10:251-256.
- [16] Yapıcı G. Working in a Standing Posture and Health Effect. *Journal of Turgut Ozal Medical Center*. 2011;18:194-198.
- [17] Padua L, Coraci D, Erra C, Pazzaglia C, Paolasso I, Loreti C, Caliandro P, Hobson-Webb LD. Carpal tunnel syndrome: clinical features, diagnosis, and management. *The Lancet Neurology*. 2016;15(12):1273-1284.

**Partially Purification and Biochemical Characterization of Phytase Enzyme from
Lactobacillus brevis Isolated from Fresh Kashar Cheese**

Neslihan DİKBAŞ^{1*}, Şeyma ALİM¹, Sümevra UÇAR¹, Sevda UÇAR², Ayşe Gül KASAPOĞLU³
Esmâ YİĞİDER¹

¹ Ataturk University, Agricultural Faculty, Department of Agricultural Biotechnology, Erzurum, Türkiye

² Sivas Science and Technology University, Faculty of Agricultural Sciences and Technology
Department of Herbal Production and Technologies, Sivas, Türkiye

³ Erzurum Technical University, Faculty of Science, Department of Molecular Biology and Genetics, Erzurum,
Türkiye

Neslihan DİKBAŞ ORCID No: 0000-0001-9096-2761

Şeyma ALİM ORCID No: 0000-0001-6684-7974

Sümevra UÇAR ORCID No: 0000-0002-7629-0206

Sevda UÇAR ORCID No: 0000-0002-3612-457X

Ayşe Gül KASAPOĞLU ORCID No: 0000-0002-6447-4921

Esmâ YİĞİDER ORCID No: 0000-0002-6896-0193

*Corresponding author: neslidikbas@atauni.edu.tr

(Received: 21.02.2024, Accepted: 15.03.2024, Online Publication: 26.03.2024)

Keywords
Lactobacillus brevis,
Phytase,
Enzyme
purification

Abstract: In the last 20 years, phytase enzyme has attracted the attention of scientists in the fields of environmental protection, nutrition and biotechnology. Myo-inositol hexaphosphate phosphohydrolase (phytase), which is a type of phosphatase enzyme, catalyzes the hydrolysis of phytate into less phosphorylated inorganic phosphates and phytate. Phytases of microbial origin are widely used in biotechnological applications (paper industry, feed industry, food industry and soil improvement). In the present study, phytase enzyme was partially purified from *Lactobacillus brevis* NM-34 strain isolated from fresh kashar cheese and the pH and temperature values at which the enzyme showed optimum activity were determined. *L. brevis* NM-34 exhibited a phytase activity of 243.80 U/mL as a result of ammonium sulphate precipitation. In the ammonium sulfate range (40-60%), where the highest phytase activity was observed, the protein concentration was measured as 0.989 mg/mL. K_m and V_{max} values of phytase enzyme were determined as 0.0146 mM and 1.6 $\mu\text{mol}/\text{min}$, respectively. The pH and temperature values at which the partially purified phytase showed optimum activity were found to be pH 5 and 50 °C, respectively. Based on the findings from our research, the enzyme purified from this bacterium was found to have unique properties that make it suitable for use in industrial applications.

**Taze Kaşar Peynirinden İzole Edilen *Lactobacillus brevis*'ten Fitaz Enziminin Kısmi
Saflaştırılması ve Biyokimyasal Karakterizasyonu**

**Anahtar
Kelimeler**
Lactobacillus brevis,
Fitaz,
Enzim
saflaştırması

Öz: Son 20 yılda fitaz enzimi çevre koruma, beslenme ve biyoteknoloji alanlarında bilim insanlarının dikkatini çekmiştir. Fosfataz enzim grubunda yer alan miyo-inositol heksafosfat fosfohidrolaz (fitaz), fitatın daha az fosforile edilmiş inorganik fosfatlara ve fitata hidrolizini katalizler. Mikrobiyal kaynaklı fitazlar biyoteknolojik uygulamalarda (kâğıt endüstrisinde, yem sanayinde, gıda endüstrisinde ve toprak iyileştirmede) yaygın bir şekilde kullanılmaktadır. Mevcut çalışmada, taze kaşar peynirinden izole edilen *Lactobacillus brevis* NM-34 suşundan fitaz enzimi kısmi olarak saflaştırıldı ve enzimin optimum aktivite gösterdiği pH ve sıcaklık değerleri belirlendi. *L. brevis* NM-34 amonyum sülfat çöktürmesi sonucunda 243.80 U/mL'lik bir fitaz aktivitesi sergiledi. En yüksek fitaz aktivitesi görülen amonyum sülfat aralığında (%40-60) protein konsantrasyonu 0.989 mg/mL olarak ölçüldü. Fitaz enziminin K_m ve V_{max} değerleri sırasıyla 0.0146 mM ve 1.6 $\mu\text{mol}/\text{min}$ olarak belirlendi. Kısmi olarak saflaştırılan fitazın optimum

aktivite gösterdiği pH ve sıcaklık değerleri sırasıyla pH 5.0 ve 50 °C olarak bulundu. Araştırmamızdan elde edilen bulgulara dayanarak, bu bakteriden saflaştırılan enzimin endüstriyel uygulamalarda kullanılmasını uygun kılan kendine özgü niteliklere sahip olduğu tespit edilmiştir.

1. INTRODUCTION

Recently, there has been increasing interest in lactic acid bacteria (LAB) that can produce lactic acid in the fermentation of carbohydrates and are now widely used in many different industrial fields [1,2]. LAB are catalase negative, non-sporulating, gram positive, acid tolerant, cocci or rod-shaped microorganisms living on carbohydrate-rich substrates [1,3,4,5].

LAB is a large group of bacteria, including genera such as *Lactobacillus*, *Lactococcus*, *Pediococcus*, *Enterococcus* and *Streptococcus*, which are widespread in a variety of environments and have many ecological roles, especially playing an important role in the fermentation processes of food products [6,7]. LAB on the 'Generally Recognized as Safe' list are very useful in many industries as they produce organic acids and other metabolites that prevent spoilage in food, increase flavour development, as a result of fermentation [6,8].

Phytic acid (PA) is an organic form of phosphorus that is present in nature and plays a non-nutritive role, accounting for 60-90% of the total phosphorus content in many seeds and grains during the ripening period [8,9,10]. Phytase enzyme is an important phosphatase that mainly catalyzes phytate into myo-inositol and inorganic phosphate [11,12].

Phytases are isolated from many organisms such as plants, bacteria and fungi [10,13,14]. However, it seems that plants are more preferred than other phytase sources in commercial industrial applications due to the catalytic properties of microbial phytases, their abundance, versatility, easier production, economic stability and environmental friendliness [13,15,16]. The application of microorganisms or enzymes isolated from them in sectors vital to human health is a subject of debate concerning their safety. Phytase enzymes produced by LAB can be used in various industries as they produce safe, cost-effective enzymes with high purity and stability [10,17].

In this study, it was aimed to partially purify phytase from *L. brevis* NM-34 strain isolated from fresh kashar, to determine the optimum pH and temperature values at which the enzyme showed the highest activity, and to determine the protein concentration, K_m and V_{max} values of the enzyme after purification.

2. MATERIAL AND METHOD

2.1. Bacterial Strain

L. brevis NM-34 strain was isolated from fresh kashar cheese and identified. The strain is preserved in the culture collection of N. Dikbas in the Department of Agricultural Biotechnology, Faculty of Agriculture, Atatürk University.

2.2. Phytase Enzyme Production

The strain was inoculated from M17 Agar to M17 Broth and incubated at 35°C for 2 days. The precipitate was then centrifuged at 9000 rpm at 4 °C for 10 min. The supernatant was used to measure enzyme activity [8].

2.3. Partial Purification of Phytase

Partial purification of phytase enzyme was carried out according to Demir et al. [18] *L. brevis* NM-34 strain grown in M17 Broth under appropriate conditions (48 h at 35°C) was centrifuged (10 min at 9000 rpm at 4°C). Phytase was partially purified using ammonium sulfate at a concentration of 0–80%. The partially purified enzyme was dissolved in sodium acetate buffer (0.1 M, pH 6.0) and stored at +4 °C for further studies.

2.4. Measurement of Enzyme Activity

Phytase activity measurement was determined according to Dikbas et al. [8]. Samples containing 0.1 mL of phytase were incubated at 50 °C for 10 min after adding sodium phytate (0.25 mL of 2 mM). After hydrolysis, the reaction was terminated by adding 10% (w/v) trichloroacetic acid. The sample was measured against a blind sample in a spectrophotometer (700 nm).

2.5. Protein Determination

Protein concentration was performed according to Bradford [19] using bovine serum albumin as standard during purification and measured spectrophotometrically at 595 nm.

2.6. Determination of Optimum pH Value of Enzyme

Substrate solutions of the enzyme were prepared by using buffer solutions with different pH values (sodium acetate (pH 2.0-3.0), sodium citrate (pH 4.0-5.0-6.0), Tris-HCl (pH 7.0-8.0-9.0), sodium carbonate (pH 10.0-11.0)) to determine the pH value at which phytase showed optimum activity. The pH value at which the enzyme showed the highest activity was determined by measuring the absorbance values in the spectrophotometer (700 nm) [20].

2.7. Determination of Optimum Temperature of Enzyme

In order to determine the temperature value at which phytase showed the highest activity, the reactions were carried out in the range of 10-90°C with a temperature increase of 10°C. A water bath was used for the determination of temperature measurements. The optimum temperature of the enzyme was determined by measuring absorbance values in a spectrophotometer (700 nm) [21].

2.8. Determination of K_m and V_{max} Values

The activity of phytase enzyme was measured under optimum conditions at different substrate concentrations and K_m and V_{max} values were determined by drawing Lineweaver-Burk graph [22].

3. RESULTS

3.1. Partial Purification Results of Phytase Enzyme

Phytase enzyme from *L. brevis* NM-34 strain was partially purified by ammonium sulfate precipitation in the range of 0-80%, and phytase activity of each range was measured. The purification range with the highest activity was determined to be 40-60% with an activity of 243.80 U/mL (Figure 1). The protein concentration in the range of 40-60% was measured as 0.989 mg/mL.

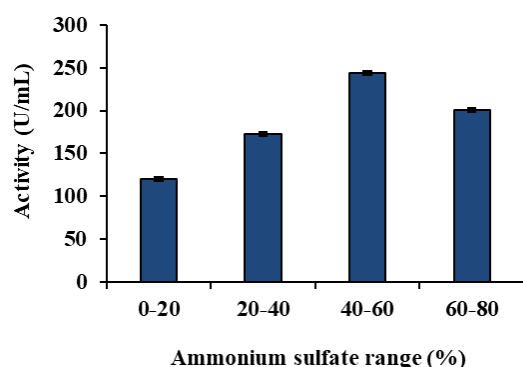


Figure 1. Phytase enzyme activity of ammonium sulfate ranges

3.2. Optimum pH and Temperature Results of Phytase Enzyme

The pH and temperature values at which the phytase enzyme purified from *L. brevis* NM-34 strain showed optimum activity were determined as pH 5.0 and 50 °C, respectively. It was determined that phytase showed an activity of 67.1 U/mL at pH 5.0 and 115.87 U/mL at 50 °C (Figure 2,3).

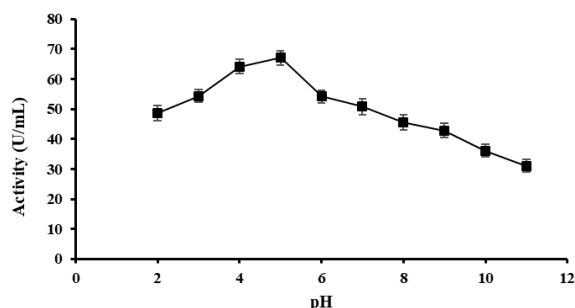


Figure 2. Effect of pH on activity of phytase enzyme

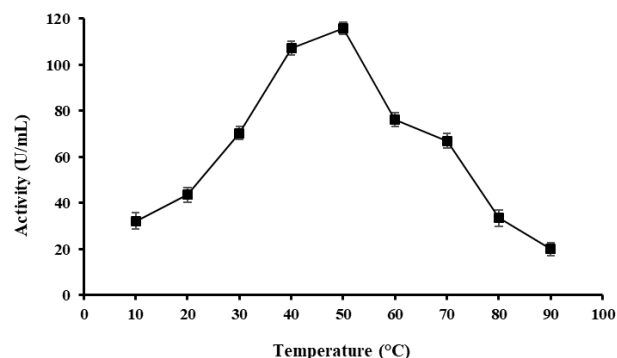


Figure 3. Effect of temperature on activity of phytase enzyme

3.3. K_m and V_{max} Values

As a result of testing the phytase enzyme for *L. brevis* NM-34 strain against sodium phytate, the enzyme showed a K_m value of 0.0146 mM and a V_{max} value of 1.6 $\mu\text{mol}/\text{min}$ (Figure 4).

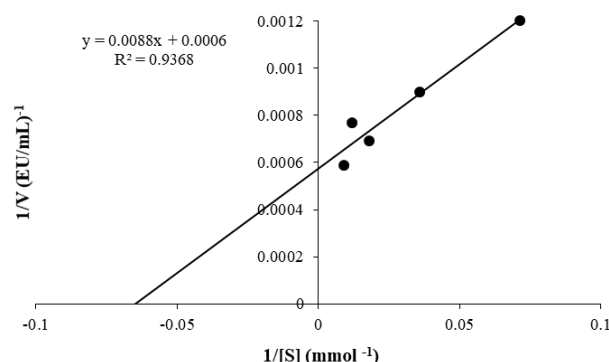


Figure 4. Graph for determining K_m and V_{max} values of phytase enzyme for phytate

4. DISCUSSION AND CONCLUSION

Enzymes are routinely used in many industrial fields. Phytase, one of the industrial enzymes, plays an important role in the field of biotechnology due to its worldwide adoption and being the subject of various studies [9]. Phytases exhibit exceptional versatility in a variety of fields, including human dietary enrichment, animal feed development and industrial processes, driving interest in the discovery of new microorganisms capable of producing phytases [15].

In the present study, the phytase activity of *L. brevis* NM-34 strain was found to be 243.80 U/mL after partial purification. Demir et al. [22] reported the specific activity of phytase of *L. coryniformis* as 202.25 (EU/mg protein). Sharma et al. [23] cloned the phytase gene identified as PhyLf isolated from *L. fermentum* NKN51 and determined the specific activity of phytase as 174.5 U/mg. Bhagat et al. [24] reported that the phytase of *L. paracasei* isolated from Kalarei showed a specific activity of 278 U/mg. Karagöz et al. [11] and Ahire et al. [25]

determined the specific activity of phytase purified from *L. plantarum* as 278.82 EU/mg and 48.59 U/mg, respectively. Dikbaş et al. [8] determined the phytase activity of *L. brevis* isolated from kashar cheese as 212.97 U/mL. Dikbaş et al. [15] reported the specific activity of phytase enzyme purified and isolated from *L. coryniformis* as 188.31 (EU mg⁻¹ protein). The data obtained in our study are consistent with the literature.

In this study, the concentration of the protein was measured as 0.989 mg/mL after partial purification. Dikbaş et al. [8] from *L. brevis* and Dikbaş et al. [15] from *L. coryniformis* determined the protein value of the phytase enzyme they purified as 0.504 mg/mL and 0.16 mg/mL, respectively. Karagöz et al. [11] reported the protein concentration of phytase purified from *L. plantarum* as 0.11 mg/mL. Sandez Penidez et al. [26] reported the protein value of phytase enzyme partially purified from *L. plantarum* as 0.08 mg/mL. Demir et al. [22] determined the protein amount of phytase purified from *L. coryniformis* as 0.12 mg/mL in their study. These findings in the literature support our results.

After partial purification of the enzyme, the phytase enzyme for *L. brevis* NM-34 strain was tested against sodium phytate as substrate and the kinetic parameters of the enzyme were calculated by Lineweaver-Burk plot. K_m and V_{max} values of the enzyme were determined as 0.0146 mM and 1.6 $\mu\text{mol}/\text{min}$, respectively. It can be concluded that the partially purified phytase has a high affinity for sodium phytate with low K_m and V_{max} values compared to phytases purified from different sources. Furthermore, the evaluation of the kinetic parameters of phytase showed that the enzyme could be used in industrial applications. Our results are similar to other studies in the literature [8,22,27,28].

In order to determine the optimum temperature and pH values of the phytase enzyme, activity measurements were made in the range of pH 2.0-11.0 and in the temperature range of 10-90°C. The optimum temperature at which phytase showed optimum activity was 50 °C and the pH value was determined as pH 5.0. In contrast to the results obtained, Sumengen et al. [29] determined the temperature and pH values at which the phytase of *L. plantarum* isolated from turnip showed optimum activity as 120 °C and pH 3.4, respectively. Arif et al. [30] reported that *L. gallinarum* (PDP10), *L. reutri* (PDP24) and *L. fermentum* (FYP38) isolated from fermented milk products showed the highest phytase activity at pH 5 at 35°C. Bhagat et al. [24] reported the optimum temperature and pH of the enzyme purified from *L. paracasei*, a species with the highest phytase activity, as 37 °C and 5.5, respectively. Similar to our results, Demir et al. [22] found that phytase purified from *L. coryniformis* isolated from curd cheese and Sharma et al. [23] found that recombinant PhyLf phytase isolated from *L. fermentum* NKN51 showed optimum activity at pH 5.0 at 60 °C. Dikbaş et al. [8] determined the pH and temperature at which the phytase enzyme partially purified from *L. brevis* showed optimum activity as pH 3.0 and 60 °C, respectively. Sandez Penidez et al. [26] found that *L. plantarum* CRL1964 (PhyLP) phytase exhibited optimum activity at

pH 4.5 and 55°C. Based on the literature studies and the findings obtained, it is seen that the phytase enzyme purified from *Lactobacillus* spp. is generally acidic and shows optimum activity in the range of 35-70 °C.

The results obtained in the present study show that *L. brevis* NM-34 strain can produce phytase with high activity. According to the results obtained, our study confirmed that the phytase enzyme produced by *L. brevis* is an important biotechnological product that can be used in many different industrial fields due to its characteristic properties. Lactic acid bacteria are microorganisms that are important for food safety and preservation and have received limited research. Therefore, further studies are needed to isolate phytase-producing LABs and determine the biochemical properties of the enzymes to further increase their commercial applicability.

REFERENCES

- [1] Mora-Villalobos JA, Montero-Zamora J, Barboza N, Rojas-Garbanzo C, Usaga J, Redondo-Solano M, et al. Multi-product lactic acid bacteria fermentations: A review. *Ferment.* 2020; 6(1):23.
- [2] Wang Y, Wu J, Lv M, Shao Z, Hungwe M, Wang J, et al. Metabolism characteristics of lactic acid bacteria and the expanding applications in food industry. *Front Bioeng Biotechnol.* 2021;9:612285.
- [3] Mbandlwa P. LAB as probiotics and silage inoculants for enteric methane [dissertation]. University College Cork; 2022.
- [4] Pirouzian HR, Pourjafar H, Probiotic Lactic Acid Bacteria 46. *Handbook of Food Bioactive Ingredients*;1473.
- [5] Onoruoiza MA, Ayodele AM, David-Momoh TE, A Review on the Effects of Functional Food on Humans and Microorganisms. *Int J Probiotics and Dietetics.* 2024; 4(1):01-14.
- [6] Ayivi RD, Gyawali R, Krastanov A, Aljaloud SO, Worku M, Tahergorabi R, et al. Lactic acid bacteria: Food safety and human health applications. *Dairy.* 2020;1(3):202-232.
- [7] Mathur H, Beresford TP, Cotter PD, Health benefits of lactic acid bacteria (LAB) fermentates. *Nutrients.* 2020; 12(6):1679.
- [8] Dikbaş N, Uçar S, Alım Ş, Purification of phytase enzyme from *Lactobacillus brevis* and biochemical properties. *Biol.* 2023;1-9.
- [9] Handa V, Sharma D, Kaur A, Arya SK, Biotechnological applications of microbial phytase and phytic acid in food and feed industries. *Biocatal Agric Biotechnol.* 2020; 25:101600.
- [10] Sharma N, Angural S, Rana M, Puri N, Kondepudi KK, Gupta N, Phytase producing lactic acid bacteria: Cell factories for enhancing micronutrient bioavailability of phytate rich foods. *Trends Food Sci Technol.* 2020; 96:1-12.
- [11] Karagöz FP, Demir Y, Kotan MŞ, Dursun A, Beydemir Ş, Dikbaş N, Purification of the phytase enzyme from *Lactobacillus plantarum*: The effect on pansy growth and macro-micro element content. *Biotechnol Appl Biochem.* 2021; 68(5):1067-1075.

- [12] Han R, Chen JY, He SX, Liu CJ, Dai ZH, Liu X, et al. Phytate and arsenic enhance each other's uptake in As-hyperaccumulator *Pteris vittata*: root exudation of phytate and phytase, and plant uptake of phytate-P. *Environ Sci Tech.*2022; 57(1):190-200.
- [13] Rizwanuddin S, Kumar V, Naik B, Singh P, Mishra S, Rustagi S, et al. Microbial phytase: Their sources, production, and role in the enhancement of nutritional aspects of food and feed additives. *J Agric Food Res.*2023;100559.
- [14] Pragma Sharma KK, Kumar S, Manisha Singh D, Kumar V, Singh B, (2023). Enhanced production and immobilization of phytase from *Aspergillus oryzae*: a safe and ideal food supplement for improving nutrition. *Lett Appl Microbiol.* 2023;76(2): ovac077.
- [15] Dikbaş N, Parlakova Karagöz F, Uçar S, Demir Y, Ornamental cabbage (*Brassica oleracea* var. acephala) responses to phytase enzyme purified from *Lactobacillus coryniformis* application. *Biotechnol Appl Biochem.*2023.
- [16] Joudaki H, Aria N, Moravej R, Rezaei Yazdi M, Emami-Karvani Z, Hamblin, MR, Microbial Phytases: Properties and Applications in the Food Industry. *Curr Microbiol.* 2023; 80(12):374.
- [17] Priyodip P, Prakash PY, Balaji S, Phytases of probiotic bacteria: characteristics and beneficial aspects. *Indian J Microbiol.* 2017; 57:148-154.
- [18] Demir Y, Şenol Kotan M, Dikbaş N, Beydemir Ş, Phytase from *Weissella halotolerans*: purification, partial characterisation and the effect of some metals. *Int J Food Prop.* 2017;20(2):2127-2137.
- [19] Bradford MM, A rapid and sensitive method for the quantitation of microgram quantities of protein utilizing the principle of protein-dye binding. *Anal Biochem.* 1976;72(1-2):248-254.
- [20] Caglayan C, Taslimi P, Türk C, Gulcin İ, Kandemir FM, Demir Y, et al. Inhibition effects of some pesticides and heavy metals on carbonic anhydrase enzyme activity purified from horse mackerel (*Trachurus trachurus*) gill tissues. *Environ Sci Pollut Res.* 2020; 27:10607-10616.
- [21] Sanbuga E, Nadaroglu H, Dikbas N, Senol M, Cetin B, Purification, characterization of phytase enzyme from *Lactobacillus plantarum* bacteria and determination of its kinetic properties. *Afr J Biotechnol.* 2014;13(23).
- [22] Demir Y, Dikbaş N, Beydemir Ş, Purification and biochemical characterization of phytase enzyme from *Lactobacillus coryniformis* (MH121153). *Mol Biotechnol.* 2018; 60:783-790.
- [23] Sharma R, Kumar P, Kaushal V, Das R, Navani NK, A novel protein tyrosine phosphatase like phytase from *Lactobacillus fermentum* NKN51: cloning, characterization and application in mineral release for food technology applications. *Bioresour Technol.* 2018; 249:1000-1008.
- [24] Bhagat D, Slathia PS, Raina N, Sharma P, Production of phytase from *Lactobacillus paracasei* strain and its probiotic profile. *Indian J Exp Biol.* 2019; 57:839–851
- [25] Ahire JJ, Jakkamsetty C, Kashikar MS, Lakshmi SG, Madempudi RS, In vitro evaluation of probiotic properties of *Lactobacillus plantarum* UBLP40 isolated from traditional indigenous fermented food. *Probiotics Antimicrob Proteins.* 2021;13(5):1413-1424.
- [26] Sandez Penidez SH, Velasco Manini MA, Gerez CL, Rollán GC, Partial characterization and purification of phytase from *Lactobacillus plantarum* CRL1964 isolated from pseudocereals. *J Basic Microbiol.* 2020;60(9):787-798.
- [27] Georgiev D, Dobrev G, Shilev S, Purification and properties of a phytase from *Candida melibiosica* 2491. *Emir J Food Agric.*2018;927-934.
- [28] Abdolshahi A, Yancheshmeh BS, Arabameri M, Marvdashti LM, Phytase from *Bacillus* sp. Strain LA12: isolation, purification and characterization. *J Microbiol Biotechnol Food Sci.* 2021;10(4):572-576.
- [29] Sumengen M, Dincer S, Kaya A, Production and characterization of phytase from *Lactobacillus plantarum*. *Food Biotechnol.*2013;27(2):105-118.
- [30] Arif A, Nawaz M, Rabbani M, Iqbal S, Mustafa A, Yousuf MR, et al. Screening, characterization and physicochemical optimization of phosphorus solubilization activity of potential probiotic *Lactobacillus* spp. *Pak Vet J.* 2018;38(3):316-320.

Vibration Response of Thermoplastic Veil Interleaved Carbon Fiber Reinforced Epoxy Composites

Yavuz Selim TARİH^{1*}, Volkan ACAR², Ömer GÜNDOĞDU², Adem YAR³

¹ Vocational College of Technical Sciences, Bingöl University, Bingöl/Türkiye

² Department of Mechanical Engineering, Atatürk University, Erzurum/Türkiye

³ Department of Mechanical Engineering, Bingöl University, Bingöl/Türkiye

Yavuz Selim TARİH ORCID No: 0000-0002-8267-7706

Volkan ACAR ORCID No: 0000-0001-7412-301X

Ömer GÜNDOĞDU ORCID No: 0000-0003-2656-4181

Adem YAR ORCID No: 0000-0002-1432-9590

*Corresponding author: ystarih@bingol.edu.tr

(Received: 8.12.2023, Accepted: 17.03.2024, Online Publication: 26.03.2024)

Keywords

Natural
frequency,
Damping,
Thermoplastic
veil,
PEEK,
PA,

Abstract: This study investigated the vibration responses of carbon/epoxy composites interleaved with polyether ether ketone (PEEK) and poliamid (PA) thermoplastic veils. The composite manufacturing was carried out using the vacuum-assisted resin transfer molding (VARTM) technique utilizing veils interleaved carbon fabrics, and the test specimens were prepared according to the ASTM E756-05 standard. The vibration tests showed that the thermoplastic veil reinforcement increased the natural frequencies of the composites but decreased the damping ratios. In this context, approximately a 29% increase was recorded in the natural frequencies of PA interleaved composites, and it was observed that the thermoplastic veil reinforcement significantly affected the dynamic properties.

Termoplastik Keçe İlaveli Karbon Fiber Takviyeli Epoksi Kompozitlerinin Titreşim Cevabı

Anahtar Kelimeler

Doğal frekans,
Sönüm,
Termoplastik
keçe,
PEEK,
PA,

Öz: Bu çalışmada, polieter eter keton (PEEK) ve poliamid (PA) termoplastik keçe ilave edilmiş karbon/epoksi kompozitlerinin titreşim cevapları incelenmiştir. Karbon elyaflar arasına ilave edilen keçeler ile VARTM tekniği kullanılarak kompozit üretimleri gerçekleştirilmiş ve ASTM E756-05 standardı kullanılarak test numuneleri hazırlanmıştır. Yapılan titreşim testleri, termoplastik keçe ilavelerinin, kompozitlerin doğal frekanslarını arttırdığı fakat sönüm oranlarını azalttığı anlaşılmıştır. Bu kapsamda, PA takviyeli kompozitlerin doğal frekanslarında yaklaşık %29'luk artışlar meydana gelmiş ve termoplastik keçe takviyesinin dinamik özellikleri önemli ölçüde etkilediği görülmüştür.

1. INTRODUCTION

Carbon fiber-reinforced polymer composites are widely used in many sectors, such as aviation, wind turbines, energy, etc., because of their superior mechanical properties [1]. However, laminated composite structures are susceptible to delamination damage [2]. Delaminations resulting from micro-cracks, voids formed during manufacturing, and damage occurs under loads reduce the composite's rigidity, strength, and service life [3]. The presence of damages, such as delamination and matrix cracks, cause composites to have low interlaminar properties which negatively affect the mechanical performance of the composite [4]. Various studies, such

as hybridization, stitching, etc., are available to improve interlaminar properties [5]. One of them is nanostructure reinforcement. The primary purpose of this process is to strengthen the fiber/matrix interface or toughening the resin. However, the difficulties of dispersion of nanostructures in the resin stands out as a problem that needs to be overcome [6]. A promising method for improving the interlaminar properties is the interleaving process.

The interleaving process is a method that increases the fracture toughness of the composite interface. Nanofiber veils, short fibers, and thermoplastic films are frequently used in interleaving processes. [6]. In one of these studies,

the interface of the laminated composite consisting of carbon fiber prepregs was reinforced with ultra-thin short aramid fiber veils. A toughened interface was created by strengthening the resin-rich regions between the layers with the veil [7]. In another study, carbon and glass nonwoven veils with different areal densities were interleaved to unidirectional glass fiber-reinforced composites and the mode I and mode II fracture toughness of these composites were determined. In all veil-interleaved composites, fracture toughness increased by 5-25% compared to non-veil-interleaved composites during propagation [8].

The meltability of some veils has also been the topic of study. In a study, meltable/non-meltable hybrid veils were interleaved to carbon composites. It was reported that the meltable veil strengthened the matrix, while the non-meltable veil created a bridging effect and significantly improved the fracture toughness of the composites [9]. Veil interleaving for fatigue-based delaminations has also been the topic of investigation. In a study conducted on this topic, significant increases were recorded in the fatigue life of composite manufacturing by interleaving processes using meltable (PA) and non-meltable polyphenylene-sulphide (PPS) resins [10]. Also, studies on the surface treatment of thermoplastic veils are available to ensure a better bonding with epoxy. For example, by applying the UV-irradiation technique to the PPS veil surface, the veil/epoxy interface improved, and the fracture toughness of the composites increased [11]. In another study in this context, nickel-coated carbon fiber veils were interleaved between carbon prepregs and increased the impact contact force [12].

Another process in the veil interleaving is nanostructure/veil interaction. It was observed that PPS veil reinforcement increases the fracture toughness, and composites interleaved with multi-walled carbon nanotube (MWCNT) reinforced PPS veils exhibit additional advantages with the bridging effect occurring at the interface between the epoxy/veil interface with the presence of MWCNTs [13]. In another study, partially cured, functionalized graphene-reinforced epoxy veils were interleaved to the carbon/epoxy composite, and significant increases were observed in the mode I test compared to control specimens [14].

Studies have also been carried out on the vibration response behavior of composites interleaved with veils. For example, a study utilizing four different thermoplastic-elastomer veil reinforcements exhibited

that the veil reinforcement significantly affected the damping ratios of carbon fiber prepregs [15]. In a study regarding carbon composites interleaved with poly (ethylene-co-acrylic acid) (PEAA), the veil reinforcement significantly increased the damping ratio of the composite [16]. In another study in which the hybridization of basalt fibers between carbon layers can be considered an interleaving process, it was observed that basalt fiber reinforcement improved the damping ratios of hybrid composites [17]. In a previous study conducted by our research group, the vibration responses after the impact of carbon and glass fiber composites interleaved with five different thermoplastic veils were examined, and significant improvements were noted, especially in the natural frequencies of the carbon composites [18].

In this study, the vibration response behaviors of PEEK and PA veil interleaved carbon composites were investigated. In the previous study carried out by our research group [18], the vibration response of specimens prepared for impact testing was discussed. This study investigated the natural frequency and damping ratio performances of vibration specimens prepared per the ASTM E756-05 standard [19].

2. MATERIAL AND METHOD

2.1. Materials

Carbon fabric in plain weaving with a nominal weight of 500 g/m² utilized in the study was supplied from Carbomid Co. (Istanbul/Turkey). Duratek DTE 1120 epoxy and DTS 1151 hardener were used as epoxy system (Duratek Co. Kocaeli/Turkey). Thermoplastic veils (PA and PEEK) with 10 g/m² areal weight were purchased from Technical Fiber Products Ltd. (Cumbria/England).

2.2. Composite Manufacturing

Vacuum-assisted resin transfer molding (VARTM) was used in laminated composite manufacturing [20]. A schematic view of the VARTM technique is given in Figure 1. This technique is based on the principle of vacuuming the release film, fabric, peel ply and flow mesh stacked on the mold with a vacuum bag and the resin infusion. The resin system was prepared by mixing the resin with a mechanical mixer at 500 rpm for five minutes, with an epoxy/hardener ratio of 100/27 by weight according to the recommendation of the resin system's manufacturer [21]. The prepared resin system was subjected to a degassing process in a vacuum chamber.

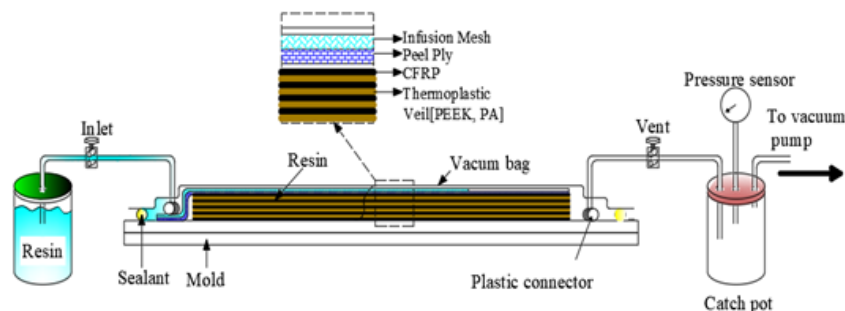


Figure 1. The VARTM technique, adapted from [18, 20]

The interleaving of thermoplastic veils in composite manufacturing is based on the principle of interply hybridization. Accordingly, the manufacturing details given in Table 1 are presented for the interleaving process performed by placing veils between the eight-layer carbon composite layers. Figure 2 shows the schematic of thermoplastic veil-reinforced and unreinforced products.

Table 1. Manufactured composites in the study.

Stacking Sequence	Designation
[C/C/C/C/C/C/C/C]	Carbon-8
[C/PEEK/C/PEEK/C/PEEK/C/PEEK/C/PEEK/C/PEEK/C/PEEK/C]	Carbon-8/7-PEEK
[C/PA/C/PA/C/PA/C/PA/C/PA/C/PA/C/PA/C]	Carbon-8/7-PA

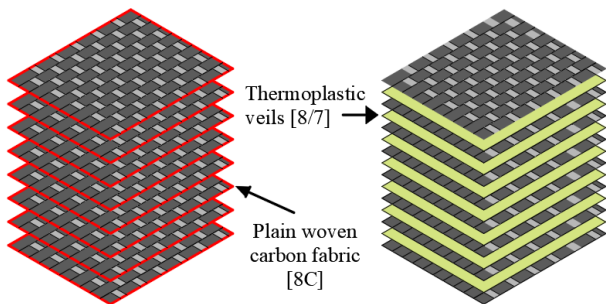


Figure 2. Composites interleaved with/without veils, adapted from [18]

2.3. Vibration Tests

Vibration tests were performed according to the ASTM E756-05 standard [19]. In this context, specimens with a dimension of 25x250 mm² were prepared (Figure 3), and vibration responses were obtained using the PULSE vibration test measurement setup (Brüel & KjærSound & Vibration Measurement A/S, Denmark), (Figure 4). The impact of creating a vibration response in the test specimens was applied using an impact hammer. Vibration responses of the specimens were achieved with a laser vibrometer. Natural frequency and damping data were obtained with the ME'scopeVES software [22-24]. The tests were carried out under clamped-free boundary conditions.

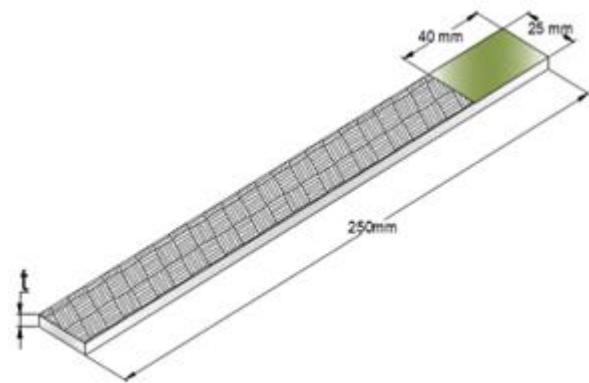


Figure 3. Dimensions of a vibration test specimen [20].

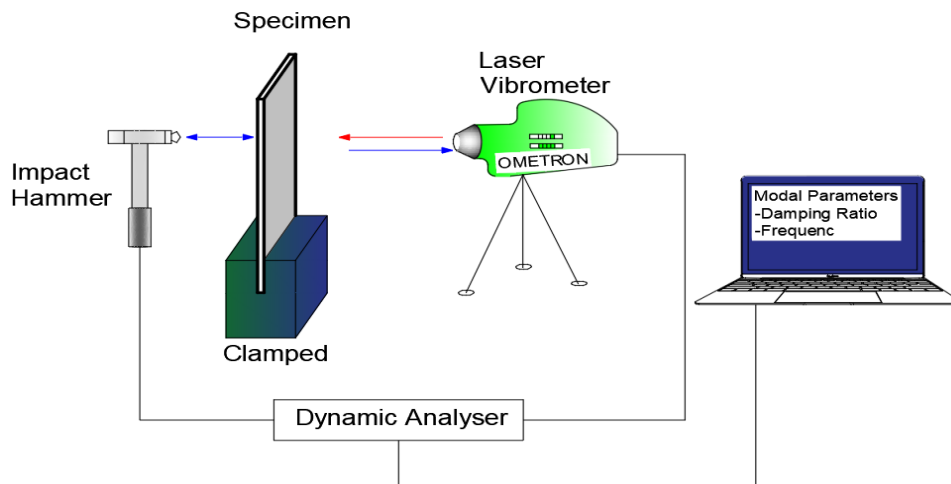


Figure 4. Schematic representation of the vibration measurement system, adapted from [18, 20]

3. RESULTS AND DISCUSSIONS

Six specimens from each composite group were used in the clamped-free condition in the vibration tests. The average of the values obtained with at least three hammer strikes for each specimen was taken. The results were analyzed by calculating the final average values and standard deviations for the average vibration results of the composite group. In this context, the first natural frequency values and damping ratios were determined. Table 2 shows the first natural frequency and damping ratio values obtained. Figure 5 shows the graphs of the vibration test results.

Table 2. First natural frequency and damping ratio values [20].

Designation	Stacking Sequence	1 st Natural Frequency (Hz)	Damping Ratio (%)
Carbon-8	8	54.6 ± 1.71	0.574±0.141
Carbon-8/7-PEEK	8/7	59.7 ± 2.76	0.541±0.166
Carbon-8/7-PA	8/7	70.4 ± 1.05	0.476±0.126

It was understood that thermoplastic veil interleaving increases the first natural frequency of carbon composites. Accordingly, the average natural frequencies of Carbon-8/7-PEEK and Carbon-8/7-PA specimens increased by approximately 9% and 29%, respectively, compared to

the control specimen. On the other hand, decreases in the damping ratios of carbon composites with veil reinforcement were observed. In this context, approximately 6% and 17% decreases occurred in Carbon-8/7-PEEK and Carbon-8/7-PA composites, respectively.

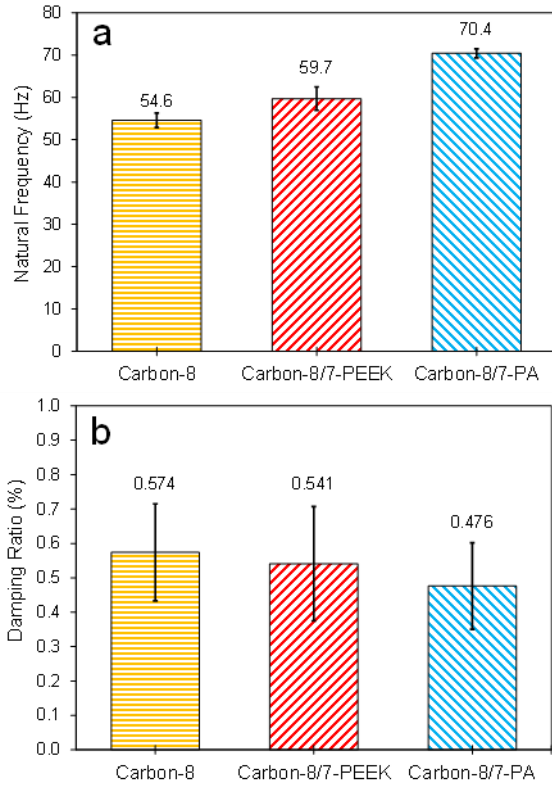


Figure 5. Vibration test results, a) 1st natural frequency, b) damping ratio.

In the study, it is thought that the veils interleaved between the layers provide enhanced adhesion with epoxy. Therefore, it is assumed that veils that create a new interface with epoxy increase the interlaminar toughness, and this improvement increases the rigidity of the composites. As the stiffness of the composites increased, the natural frequency values also increased. On the other hand, increasing stiffness had adverse effects on damping, and decreases in damping ratios were recorded. The inverse relationship between stiffness and damping is a phenomenon. In a study, it was noted that basalt fiber hybridization increased the damping ratios of carbon composites, and this was due to the low stiffness of the basalt fiber composites [17]. A similar trend is observed in our study.

On the other hand, in the study conducted by our research group [18], vibration responses of specimens with similar composites used in this study were investigated according to the condition of pre/post impact testing. In the motioned research [18], natural frequencies of the pre-impact specimens with dimensions of 100x150 mm² were significantly higher than those prepared according to ASTM E756-05 standard in this study. In addition, it was noted that the damping ratio of PEEK interleaving was slightly lower compared to the similar specimen used in this study. However, the damping ratios of other

composites were found to be higher than their equivalents in this study. In this context, it has been understood that dimensional difference is an effective parameter for vibration response. Moreover, it is thought that the mechanical properties of composites with increased natural frequency enhance as their stiffness increases.

4. CONCLUSION

In this study, the effect of two different thermoplastic veils interleaved between the layers of carbon fiber-reinforced composites on the vibration response behavior of the composite was experimentally investigated. The results are summarized below.

- It was observed that both veil interleaving had enhanced adhesion with epoxy and toughened the interface. Therefore, the stiffness and natural frequencies of the modified composites were increased.
- Decreases were observed in damping ratios.
- While PA veil interleaving exhibited high performance in terms of natural frequency, PEEK veil interleaved composites show similar damping behavior with non-interleaved composites.

For future studies, it is necessary to interleave these veils in different stacking sequences within the composite by an interply hybridization and to perform more comprehensive vibration analyses.

Acknowledgement

This study was prepared from the corresponding author's Ph.D. thesis and was supported by Ataturk University (BAP, Project No: FBA-2021-9447) and Bingöl University (BAP, Project No: BAP-MMF.2021.002).

REFERENCES

- [1] Acar V, Sarikanat M, Seki Y, Akbulut H, Seydibeyoğlu MÖ. Graphene oxide modified carbon fiber preregs: A mechanical comparison of the effects of oxidation methods. *eXPRESS Polymer Letters*. 2020;14(12):1106-1115.
- [2] De Morais AB, De Moura MF, Marques AT, De Castro PT. Mode-I interlaminar fracture of carbon/epoxy cross-ply composites. *Composites Science and Technology*. 2002;62:679-686.
- [3] Choi NS, Kinloch AJ, Williams JG. Delamination fracture of multidirectional carbon-fiber/epoxy composites under mode I, mode II and mixed-mode I/II loading. *Journal of Composite Materials*. 1999;33(1):73-100.
- [4] Wicks SS, De Villoria RG, Wardle BL. Interlaminar and intralaminar reinforcement of composite laminates with aligned carbon nanotubes. *Composites Science and Technology*. 2010;70:20-28.
- [5] Ou Y, Gonzalez C, Vilatela JJ. Interlaminar toughening in structural carbon fiber/epoxy composites interleaved with carbon nanotube veils. *Composites Part A*. 2019;124:105477.
- [6] Cheng C, Chen Z, Huang Z, Zhang C, Tusiime R, Zhou J, et al. Simultaneously improving mode I and

- mode II fracture toughness of the carbon fiber/epoxy composite laminates via interleaved with uniformly aligned PES fiber webs. *Composites Part A*. 2020;129:105696.
- [7] Yuan B, Ye M, Hu Y, Cheng F, Hu X. Flexure and flexure-after-impact properties of carbon fibre composites interleaved with ultra-thin non-woven aramid fibre veils. *Composites Part A*. 2020;131:105813.
- [8] Uppin VS, Gouda PSS, Sridhar I, Umarfarooq MA. Effects of carbon/glass nonwoven interleaving veils and their areal density on opening and shearing mode interlaminar fracture toughness of glass epoxy composites. *Theoretical and Applied Fracture Mechanics*. 2024;130:104292.
- [9] Quan D, Alderliesten R, Dransfeld C, Murphy N, Ivankovic A, Benedictus R. Enhancing the fracture toughness of carbon fibre/epoxy composites by interleaving hybrid meltable/non-meltable thermoplastic veils. *Composite Structures*. 2020;252:112699.
- [10] Quan D, Murphy N, Ivankovic A, Zhao G, Alderliesten R. Fatigue delamination behaviour of carbon fibre/epoxy composites interleaved with thermoplastic veils. *Composite Structures*. 2022;281:114903.
- [11] Quan D, Deegan B, Alderliesten R, Dransfeld C, Murphy N, Ivankovic A, et al. The influence of interlayer/epoxy adhesion on the mode-I and mode-II fracture response of carbon fibre/epoxy composites interleaved with thermoplastic veils. *Materials and Design*. 2020;192:108781.
- [12] Liu H, Qu P, Guo Y, Zhou Y, Wan G, Jia Y. Experimental and numerical studies on low-velocity impact damage of composite laminates toughened by nickel-coated carbon fiber veil. *Polymer Composites*. 2022;43:2460-2476.
- [13] Quan D, Mischo C, Binsfeld L, Ivankovic A, Murphy N. Fracture behaviour of carbon fibre/epoxy composites interleaved by MWCNT- and graphene nanoplatelet-doped thermoplastic veils. *Composite Structures*. 2020;235:111767.
- [14] Du X, Zhou H, Sun W, Liu HY, Zhou G, Zhou H, et al. Graphene/epoxy interleaves for delamination toughening and monitoring of crack damage in carbon fibre/epoxy composite laminates. *Composites Science and Technology*. 2017;140:123-133.
- [15] Kishi H, Kuwata M, Matsuda S, Asami T, Murakami A. Damping properties of thermoplastic-elastomer interleaved carbon fiber-reinforced epoxy composites. *Composites Science and Technology*. 2004;64:2517-2523.
- [16] Liao FS, Su AC, Hsu TCJ. Vibration Damping of Interleaved Carbon Fiber-Epoxy Composite Beams. *Journal of Composite Materials*. 1994;28:1840.
- [17] Bozkurt ÖY, Gökdemir ME. Effect of Basalt Fiber Hybridization on the Vibration-Damping Behavior of Carbon Fiber/Epoxy Composites. *Polymer Composites*. 2018;39:2274-2282.
- [18] Tarih YS, Coskun T, Yar A, Gündoğdu Ö, Sahin ÖS. The influences of low-velocity impact loading on the vibration responses of the carbon/glass fiber-reinforced epoxy composites interleaved with various non-woven thermoplastic veils. *Applied Polymer Science*. 2023;140:53728.
- [19] ASTM E756-05 Standard Test Method for Measuring Vibration-damping Properties of Materials, American Society for Testing and Materials (ASTM) Standard, West Conshohocken, PA, 2017.
- [20] Tarih, YS. Termoplastik Keçe Katmanın Karbon Kumaş-Cam Kumaş/ Epoksi Kompozitlerde Mekanik Özelliklerine ve Dinamik Davranışlarına Etkilerinin İncelenmesi. Doktora Tezi, 2022, Fen Bilimleri Enstitüsü, Atatürk Üniversitesi, Erzurum/Türkiye.
- [21] Duratek 1200 Product Data Sheet, Rev. 04-27.04.2016, Duratek Protective Materials Co. Ltd. (2016).
- [22] Aydın MR, Acar V, Cakir F, Gündoğdu Ö, Akbulut H. Experimental investigation of mechanical and modal properties of Al₂O₃ nanoparticle reinforced polyurethane core sandwich structures. *Materials Today Communications*. 2020;24:101233.
- [23] Khan T, Aydın OA, Acar V, Aydın MR, Hülagü B, Bayrakçeken H, et al. Experimental investigation of mechanical and modal properties of Al₂O₃ nanoparticle reinforced polyurethane core sandwich structures. *Materials Today Communications*. 2020;24:1001233.
- [24] Hülagü B, Acar V, Aydın MR, Aydın OA, Gök S, Ünal HY, et al. Experimental modal analysis of graphene nanoparticle-reinforced adhesively bonded double strap joints. *The Journal of Adhesion*. 2020;97(12):1107-1135.

Investigation of Mechanical Properties of Graphene-CNT Reinforced Nickel Metal Matrix Nanocomposite Structure

Ünal DEĞİRMENCI* 

¹ Bingöl University, Department of Machinery and Metal Technologies, Bingöl, Türkiye
Ünal DEĞİRMENCI ORCID No: 0000-0003-1480-2488

*Corresponding author: udegirmenci@bingol.edu.tr

(Received: 16.02.2024, Accepted: 17.03.2024, Online Publication: 26.03.2024)

Keywords

Nickel,
Carbon-based
nanomaterials,
Mechanical
properties,
Molecular
dynamics
simulations

Abstract: Nickel is a metal widely used in many industrial applications, but despite its superior properties, it also has some shortcomings. Carbon-based structures can be important reinforcement elements in improving the properties of metals. By providing a balance between the high corrosion resistance, high electrical conductivity and good magnetic properties of the nickel material and the lightness and high strength of carbon-based structures, a material with advanced properties can be obtained. Therefore, in this study, a new Nickel-Carbon nanostructure supported by a covalently bonded graphene-carbon nanotube (CNT) skeleton structure is presented. Additionally, it was aimed to investigate the mechanical properties and deformation mechanisms in all directions by designing three materials with different geometric dimensions (Ni-G-CNT(5,5), Ni-G-CNT(10,10) and Ni-G-CNT(15,15)). According to the results, it was observed that G-CNT structures increased the tensile and compressive behavior of the Ni structure in the CNT direction. With the addition of G-CNT structures, a 36% increase in the elastic modulus of the nickel structure and a 12% increase in the maximum tensile value were observed. For tensile loading in the CNT direction, as the CNT diameter decreases, the elastic modulus of the hybrid structures increases, while the maximum stress values are independent of the CNT diameter. As the CNT diameter increases, the ductility of the structures increases. In terms of compressive strength, it has been observed that in the linear region, as the CNT diameter increases, the strength generally increases and in the condensation region, it exhibits better compressive strength. With this study, an anisotropic nanostructure that is lighter and can exhibit higher mechanical strength compared to the Nickel structure is presented.

133

Grafen-CNT Takviyeli Nikel Metal Matrisli Nanokompozit Yapının Mekanik Özelliklerinin İncelenmesi

Anahtar Kelimeler

Nikel,
Karbon bazlı
nanomalzemeler,
Mekanik
özellikler,
Moleküler
dinamik
simülasyonları

Öz: Nikel, birçok endüstriyel uygulamada yaygın olarak kullanılan bir metaldir, ancak üstün özelliklerinin yanı sıra bazı eksik yanları da mevcuttur. Metallerin özelliklerini iyileştirmede karbon temelli yapılar önemli takviye elemanı özelliği gösterirler. Nikel malzemesinin yüksek korozyon direnci, elektrik iletkenliği ve iyi manyetik özelliği ile karbon bazlı yapıların hafiflik ve yüksek mukavemeti arasında bir denge sağlayan gelişmiş özelliklere sahip bir malzeme elde edilebilir. Bu nedenle, bu çalışmada, kovalent olarak bağlı grafen-karbon nanotüp (KNT) iskelet yapısı ile desteklenmiş yeni bir nikel-karbon nanoyapısı sunulmaktadır. Ayrıca, farklı geometrik boyutlara sahip üç malzeme tasarımı (Ni-G-CNT(5,5), Ni-G-CNT(10,10) ve Ni-G-CNT(15,15)) yapılarak yapıların tüm doğrultulardaki mekanik özellikleri ve deformasyon mekanizmaları araştırılmıştır. Sonuçlara göre, G-CNT yapılarının Ni yapısının çekme ve basma davranışını KNT doğrultusunda artırdığı görülmüştür. G-CNT yapılarının eklenmesi ile nikel yapısının elastik modülü değerinde %36, maksimum gerilme değerinde ise %12 artış gözlenmiştir. KNT doğrultusunda çekme yüklemeleri için KNT çapı azaldıkça hibrit yapıların elastik modülü artarken maksimum gerilme değerleri KNT çapından bağımsızdır. KNT çapı arttıkça ise yapıların süneklikleri artmaktadır. Basma dayanımı açısından ise lineer bölgede genel olarak KNT çapı arttıkça dayanımın arttığı yoğunlaşma bölgesinde ise daha iyi basma dayanımı sergilediği görülmüştür. Bu çalışma ile Ni yapısına kıyasla daha hafif ve daha yüksek mekanik dayanım sergileyebilen anizotropik bir nanoyapı sunulmuştur.

1. INTRODUCTION

Today, materials science and engineering form the basis of advanced technologies and innovative applications. In this field, improving and optimizing the properties of materials is vital to improving performance in various industries. In this context, hybrid nanocomposites have attracted great attention from researchers in recent years. Metal matrix nanocomposites have an important place in this field [1]. Among metals, nickel is very important due to its rust resistance, high temperature and chemical resistance, improved electrical conductivity and magnetic properties [2, 3]. Due to these properties, it is used in many areas such as automotive, shipbuilding, maritime, chemical industry, electric motors, magnetic sensors and power plants [4, 5]. Despite the many good properties of nickel material, its mechanical strength is not at the desired level [6]. For this reason, there is a need to strengthen it with various reinforcement materials.

Many materials are used as reinforcement materials in metal matrix nanocomposites [7, 8]. Among these, nanoscale materials such as graphene and CNT (Carbon Nanotube) have the potential to provide excellent reinforcement in composite materials because they have unique mechanical, electrical and thermal properties [9-12]. Some studies indicate that there is a potential to form a strong bond between carbon-based structures and some metals such as Ni, Pt, Pd and Ti [13, 14]. When nickel metal is combined with CNTs and graphene, a nickel matrix composite can be obtained, which is important for many applications. For this reason, there are various studies in the literature about carbon-based structures and nickel. For example; Jiang and his team [15], synthesized CNT/Ni hybrid nanostructure arrays using one-step chemical vapor deposition method (CVD). The study has shown that these structures can be used as high-performance capacitor materials thanks to their large area capacitance and superior rate capacitance. In another study, Wang et al. [16] investigated the effects of Ni-MWCNTs with different aspect ratios on the uniaxial tensile behavior of ultra-high strength concrete (UHPC) by experimental and MD analyses. The results obtained showed that the presence of Ni-MWCNTs markedly changed the tensile performances of UHPC.

Producing nanostructures and investigating their properties experimentally is a very expensive and difficult process. For this reason, using the Molecular Dynamics (MD) method provides a great advantage when investigating the properties of these structures [17, 18]. Molecular dynamics simulations are a powerful tool for studying material behavior at the atomic level. This method allows modeling of material behavior, taking into account atomic interactions and material properties. If we look at some studies conducted in this context; Zhou et al. [6] investigated the mechanical properties of nanoporous nickel and carbon nanotube (CNT) reinforced composites using molecular dynamics (MD) simulations at 900K. It was found that out-of-plane mechanical behavior were better than in-plane properties and CNT reinforcement increased the elastic modulus, tensile strength and compressive strength while decreasing the weight of the

composites. Song and Zha [19] examined the behavior of nickel-plated single-wall CNTs and their gold matrix composites under axial loading using MD simulations. As a result, they found that although nickel plating reduced the tensile strength, nickel-CNT reinforcement could increase the Young's modulus of the composite. Yan et al. [20] investigated the mechanical properties of CNTs with different geometric properties embedded in the nickel matrix. They investigated the effects of CNT rotation angle, CNT number and CNT length on the deformation mechanism, ultimate tensile strength (UTS) and Young's modulus. It has been observed that the distribution of long and short CNTs significantly affects the Young's modulus and UTS of CNT/Ni nanocomposites, and the number of CNTs increases these properties.

There are some studies in the literature on composite materials obtained by combining graphene and CNT structures with nickel material. However, although the single effects of graphene and CNT have been mostly studied, there are no studies in which they are used together. For this reason, in this study, the Nickel nanocomposite structure supported by the G-CNT skeleton structure obtained by covalently bonding graphene to the CNT side walls was modeled with MD simulations and its mechanical properties were investigated. This new carbon-metal hybrid nanostructure is called Ni-G-CNT (Nickel-Graphene-CNT). In addition, in this study, three models with different G-CNT skeletons (G-CNT(5, 5), G-CNT(10, 10), and G-CNT(15, 15)) were created by keeping the carbon density constant and their mechanical behaviors such as tensile and compression were compared. It is thought that the results will make a significant contribution to the design and production of more durable, lightweight and high-performance materials. Additionally, this composite has the potential to be used in structural components in the aerospace, automotive and aerospace industries.

2. MATERIAL AND METHOD

2.1. Atomistic Modeling

The Ni-G-CNT hybrid structures proposed in this study consist of a Nickel matrix nanocomposite structure reinforced with graphene-CNT skeleton covalently bonded together along the CNT. Atomic models of the relevant nanostructures were created in three steps. In the first step, the atomic coordinates of graphenes (GNRs) and carbon nanotubes (CNTs) were created separately using Visual Molecular Dynamics (VMD) [21] software. In the second step, a certain number of graphene sheets were placed along the outer surface of the CNTs and a G-CNT skeleton was formed by creating a covalent bond between the graphene and CNT structures with the help of thermal welding process. In the next stage, the G-CNT skeleton structure was embedded in the nickel matrix and the atomic model of the Ni-G-CNT structures was obtained. After the coordinates of the nanostructures are created, they are minimized and stabilized at room temperature (300 K) and their stability is examined. The diagram of the modeling process of hybrid nanostructures is shown in Figure 1.

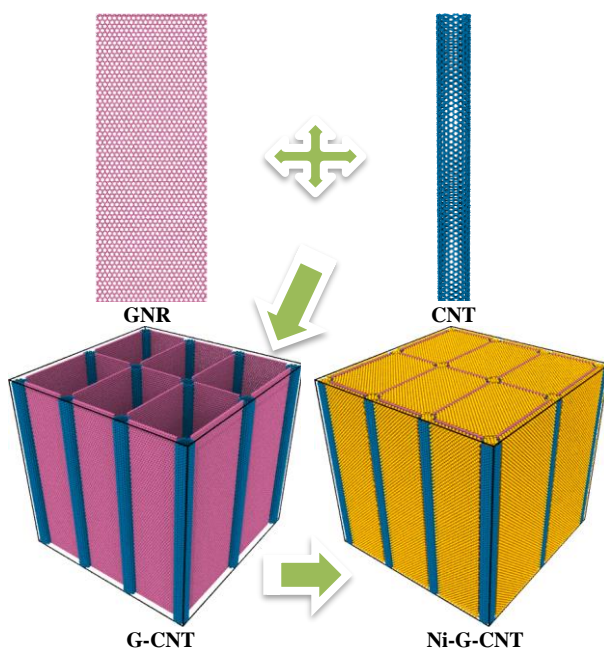


Figure 1. Schematic representation of the modeling process of Ni-G-CNT structures.

In this study, three different Ni-G-CNT structures containing different G-CNT types (G-CNT(5, 5), G-CNT(10, 10), and G-CNT(15, 15)) with equal lengths and CNTs of different diameters containing approximately a fixed number of carbons were created. In order to provide approximately equal carbon atom density, the size of graphene and the number of CNTs vary depending on the models. The dimension and numbers of the carbon nanotubes and graphene used in the structures are given in Table 1.

Table 1. Dimension and atomic numbers of graphene and CNTs in models.

Models	Ni-G-CNT(5,5)	Ni-G-CNT(10,10)	Ni-G-CNT(15,15)
CNT Type	(5,5)	(10,10)	(15,15)
CNT Diameters (nm)	0.6808	1.3560	2.0324
Graphene Dimensions(nm)	Y	5.5x20	7.5x20
	X	5.5x20	4.5x20
CNT Numbers	16	12	12
GNR Numbers	24	17	17

To create G-CNT structures, it is necessary to create covalent bonds between graphene plates and CNTs. This process is carried out by the thermal welding method, which is an annealing process [22, 23]. In this annealing process, graphene sheets are aligned to the CNT side walls. Then, by applying high temperatures to the boundaries of CNT and graphene, bonds break in the structures and new bonds are formed between graphene and CNT. High temperatures are required to ensure bond formation during the thermal welding process. In order to save time and cost by performing this process in a lower

temperature and time range, partial deformations are created in the atoms on the CNT side surfaces corresponding to the side surfaces of the graphene sheets. In this way, it is possible to create new ligaments more easily with the sagging ligaments created. Sample representations of Ni-G-CNT structures can be seen in Figure 2.

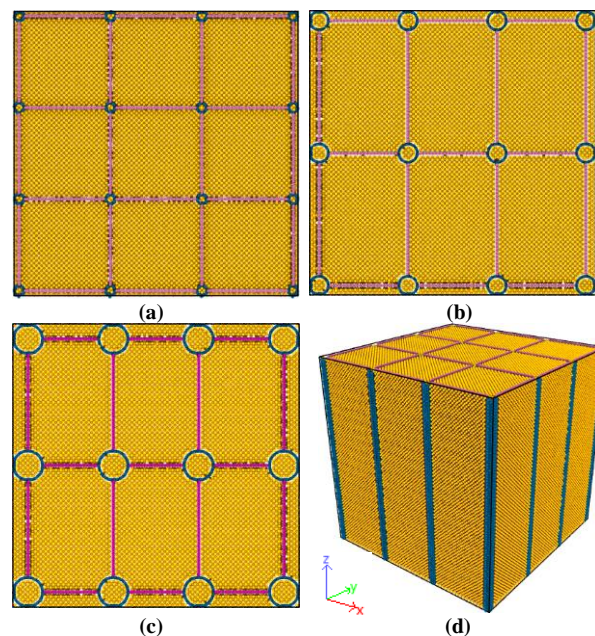


Figure 2. Sample representations of Ni-G-CNT structures; (a) Ni-G-CNT(5,5), (b) Ni-G-CNT(10,10), (c) Ni-G-CNT(15,15), (d) 3D image of Ni-G-CNT(5,5).

2.2. Simulation Details

MD simulations for the thermal welding process and mechanical analysis are performed using the open source Large Scale Atomic/Molecular Massively Parallel Simulator (LAMMPS) [24]. MD simulations provide interactions between atoms using interatomic potentials to calculate material behavior. In this study, hybrid potential was used for the interaction between atoms. In this context, the Adaptive Molecular Reactive Empirical Boundary Series (AIREBO) potential is used for the carbon atom interaction between graphene and CNT[25, 26]. The AIREBO potential is an important potential that can represent a dynamic system as it can accurately predict the formation of new bonds. The Embedded Atom Method (EAM) is used for force calculations between nickel atoms[27, 28]. Lennard jones potential is used for hybrid interactions between nickel and carbon atoms [29-31]. In the thermal welding procedure, the Nosé-Hoover thermostat and the canonical ensemble (NVT) system were used as thermodynamic properties to ensure the thermal balance of the system. The time step of the simulation was determined as 0.001 picoseconds (ps). Periodic boundary conditions are defined in all directions for the system to represent a large material structure. The sintering temperature of nickel metal and the temperature values (1200 K) required to form covalent bonds between graphene and CNTs are very close to each other. For this reason, the thermal welding process is applied simultaneously to graphene and CNT atoms. In the thermal welding process, first the environment is kept

at 300 K for 50 picoseconds (ps) to achieve thermal equilibrium. Then, the temperature of the atoms in the region is gradually increased to the reference temperature of 1200 K with a temperature increase of 300 K. Energy is needed for both the sintering process and the breaking of bonds in CNTs and the formation of bonds with graphene. To provide this energy, the ambient temperature is kept constant at 1200K for 60 ps. Then, fractional cooling is performed to reduce the temperature of the region from 1200 K to 300 K within 50 ps. Finally, it is relaxed for 50 ps at 300 K. Thus, the stability of the bonds in the connection regions is examined [32]. The bonds formed between CNTs and graphene at the end of the thermal welding process are shown in Figure 3.

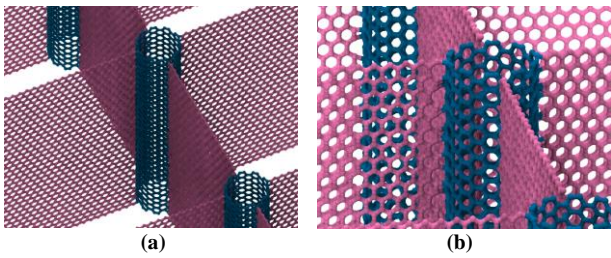


Figure 3. Covalent bonds formed between CNT and graphene layers, a) bond view, b) close bond view.

Once the atomic models are created, the free energy profiles are monitored for 100 ps at room temperature to observe their thermal stability. For this process, it is thermalized at room temperature using the Nose-Hoover thermostat and NPT assembly. Mechanical tensile and compression analyzes were carried out by selecting the loading rate of 0.001 ps^{-1} , which is widely used in the literature, and equilibrated at room temperature with NVT integration. Tensile analyzes were carried out separately in all three directions (X, Y, Z) to calculate the Elastic modulus (E), yield stress (σ_y) and ultimate stress (σ_u) values of the material and compare them with each other. Compression analyzes were carried out only in the CNT direction (Z), which is thought to exhibit the best behavior of the material. The atomistic stresses used to generate the stress-strain curves are calculated using the Virial stress theorem[33].

3. RESULTS AND DISCUSSION

In this study, firstly, the energy profiles were examined at 300 K for a sufficiently long time to examine whether the nanostructures were thermodynamically stable. It is seen that the energy values of the proposed structures remain almost constant. Additionally, there is no significant structural change in the structures compared to the initial design, indicating that they are thermodynamically stable. After it was understood that the structures were stable, mechanical tests were carried out.

3.1. Tensile Behavior

In this study, the tensile strengths of Ni-G-CNT structures supported by nickel and three G-CNT nanoskeleton system with different CNT diameters in each direction were analyzed by MD simulations under uniaxial loading.

Since the structure has an anisotropic structure in terms of model, it exhibits different mechanical properties in each direction. The stress-strain graph of the structures obtained from the analysis results in the z-axis direction is given in Figure 4.

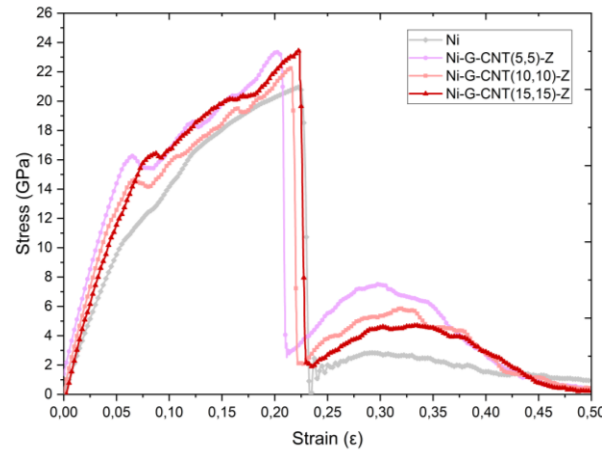


Figure 4. Tensile stress-strain curves of Ni-G-CNT structures in the z direction.

When the stress strain values in the CNT direction of the structures given in Figure 4 are examined, it is seen that with the addition of the G-CNT structure to the Ni structure, the mechanical properties increase with a partial decrease in the ductility of the nickel structure. When the mechanical behaviors of the structures are compared within themselves, the highest value in this direction belongs to the [CNT (5,5)] Ni-G-CNT(5,5) structure containing small diameter CNTs. The addition of carbon structures increased the tensile behavior of the structures in the linear region. It has been observed that as the CNT diameter increases, the elastic modulus and yield stress values of the structures decrease, but they still have high values compared to the Nickel structure. Although there was a regularly decreasing relationship between mechanical properties and increasing CNT diameter in the linear region, no regular relationship was found between CNT size and mechanical behavior after the linear region. Although the elastic modulus values of the Ni-G-CNT (15,15) structure are the lowest, it has the highest maximum stress value and exhibits a behavior similar to nickel in terms of ductility. The mechanical values of the structures in the CNT direction are given in detail in Table 2.

Table 2. Mechanical properties of the structures under tensile stress in the Z direction.

Models	Elastic Module (GPa)	Yield Strain	Yield Strength (GPa)	Ultimate strain	Ultimate Strength (GPa)
Ni	211,02	0,0368	7,33	0,223	20,96
Ni-G-CNT(5,5)	287,48	0,0349	10,95	0,203	23,34
Ni-G-CNT(10,10)	282,42	0,0346	9,94	0,215	22,31
Ni-G-CNT(15,15)	280,91	0,0331	8,20	0,224	23,47

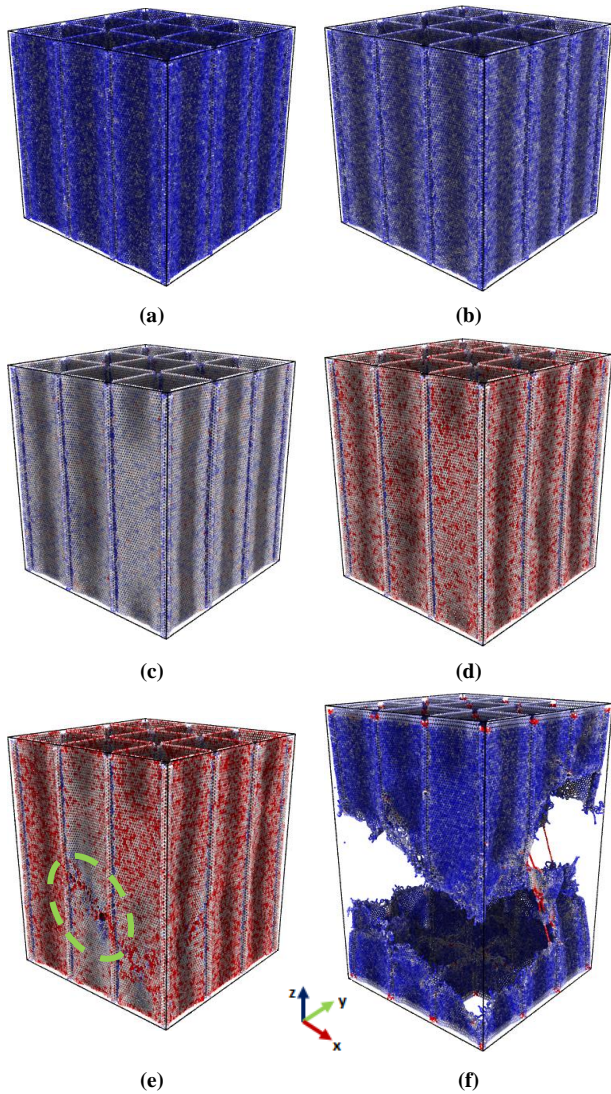


Figure 5. Deformation states of the Ni-G-CNT(5, 5) structure depend on tensile loading perpendicular to the plane, (a) 0.02, (b) 0.06, (c) 0.12, (d) 0.20, (e) 0.22 and (f) 0.44.

In order to better understand the deformation mechanism of Ni-G-CNT structures, the deformation states of an example structure due to tensile loading in the CNT direction are given in Figure 5. When the images are examined, the stresses in the structure gradually increase due to the strain. It has been observed that most of the stresses are concentrated in graphene and CNTs, but nickel material also carries the load. The first rupture deformation occurred at the nickel atoms located at the border between 0.07 and 0.08. For this reason, a decrease in the stress curve is observed. From this point on, stresses accumulate in graphene and CNTs and it is seen that the stresses increase again and reach the maximum value in the 0.20-0.23 strain range. As seen in Figure 5. (e), it was observed that the breaks in this range occurred diagonally from the midpoint of the graphene. Although there was a rapid decrease in stresses after the maximum stress value with the rupture of the ligaments, the stresses continued to increase up to 0.30-0.31 ϵ because the other unruptured graphene and CNT structures continued to carry stress.

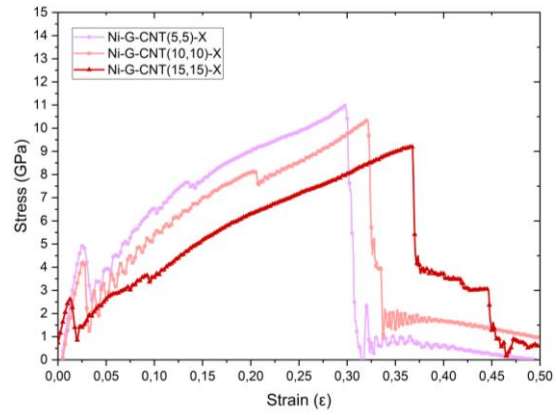


Figure 6. Tensile stress-strain curves of Ni-G-CNT structures in the x direction.

In order to examine the behavior of the structures in the horizontal direction, when the stress strain curves in the transverse direction of CNT of the structures given in Figure 6 are examined, it was observed that the stresses increased linearly, followed by a partial decrease in the stresses and then increased again. It is thought that the reason for the decrease in this first region is due to the flattening of CNTs with circular cross-sections. After the flattening of the CNTs occurred, the stresses increased again and reached the maximum stress value in the range of 0.30-0.37 ϵ and ruptures occurred in the structure. When the mechanical behaviors of different N-G-CNT structures were compared with each other, it was seen that the highest value in this direction belonged to the Ni-G-CNT (5,5) structure and the lowest value belonged to the Ni-G-CNT (15,15) structure. As the CNT diameter increases, the ductility of the material increases, while its elastic modulus, Yield stress and ultimate tensile strength decrease. Table 3 shows the detailed mechanical values of the structures.

Table 3. Mechanical properties of the structures under tensile stress in the X direction.

Models	Elastic Module (GPa)	Yield Strain	Yield Strength (GPa)	Ultimate strain	Ultimate Strength (GPa)
Ni-G-CNT(5,5)	266,73	0,0247	5,14	0,305	11,78
Ni-G-CNT(10,10)	223,74	0,0259	4,74	0,321	11,16
Ni-G-CNT(15,15)	184,69	0,0122	2,59	0,367	9,22

The deformation states obtained for the transverse tensile loading of the Ni-G-CNT(5x5) structure are given in Figure 7. As can be seen from the deformation images, the stresses in the structure increase up to 0.025 ϵ due to the shape change. After this value, it was observed that the stresses decreased and then increased again as flattening occurred in the circular sections of CNTs. The majority of the stresses occur in graphene. After 0.025 ϵ , fluctuating decreases and increases in stress values are observed as the contractions continue in the circular cross-sections of CNTs. The rupture in the structure occurred in the graphene region at values of 0.305, 0.321 and 0.367 ϵ , from small-diameter CNT structures to large ones, respectively. When the tensile strengths of the structures in the transverse direction of CNTs were compared with the nickel structure, it was observed that the tensile strength decreased in this direction but the ductility

increased. It is thought that this decrease is due to two reasons. The first reason may be the fact that CNTs are located in the transverse direction and the flattening of their circular cross-sections. The second reason is that it is thought that nickel atoms exhibit rigid motion and do not contribute to tensile strength due to the division of nickel atoms by the G-CNT cage system.

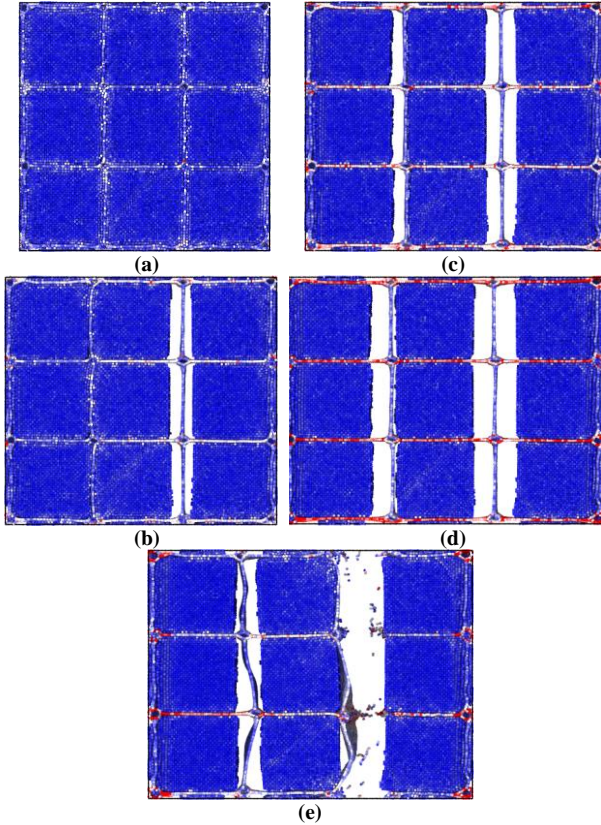


Figure 7. Deformation states of the Ni-G-CNT (5, 5) structure subjected to tensile loading in the transverse direction, (a) 0.00, (b) 0.10, (c) 0.20, (d) 0.30 and (e) 0.31.

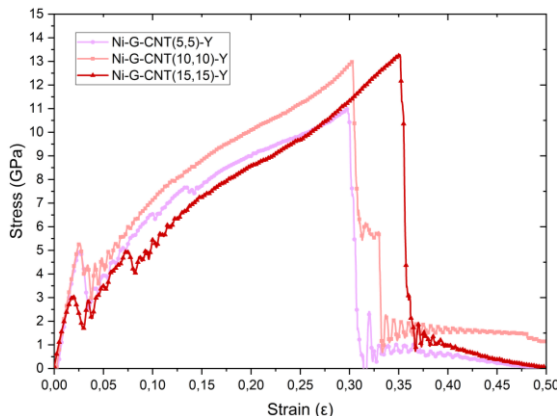


Figure 8. Tensile stress-strain curves of Ni-G-CNT structures in the y direction.

The stress-strain curves of the structures in the y-axis direction are given in Figure 8. When the stress strain curves were examined, it was seen that the behavior was parallel to the x-axis. The stresses increase until the CNT strength is exceeded and then show a partial decrease due to the narrowing in the cross-section. Table 4 gives the mechanical values of the structures in the Y direction.

Table 4. Mechanical properties of the structures under tensile stress in the Y direction.

Models	Elastic Module (GPa)	Yield Strain	Yield Strength (GPa)	Ultimate strain	Ultimate Strength (GPa)
Ni-G-CNT(5,5)	266,73	0,0247	5,14	0,305	11,78
Ni-G-CNT(10,10)	244,75	0,0257	5,29	0,303	13,02
Ni-G-CNT(15,15)	195,46	0,0171	2,81	0,351	13,28

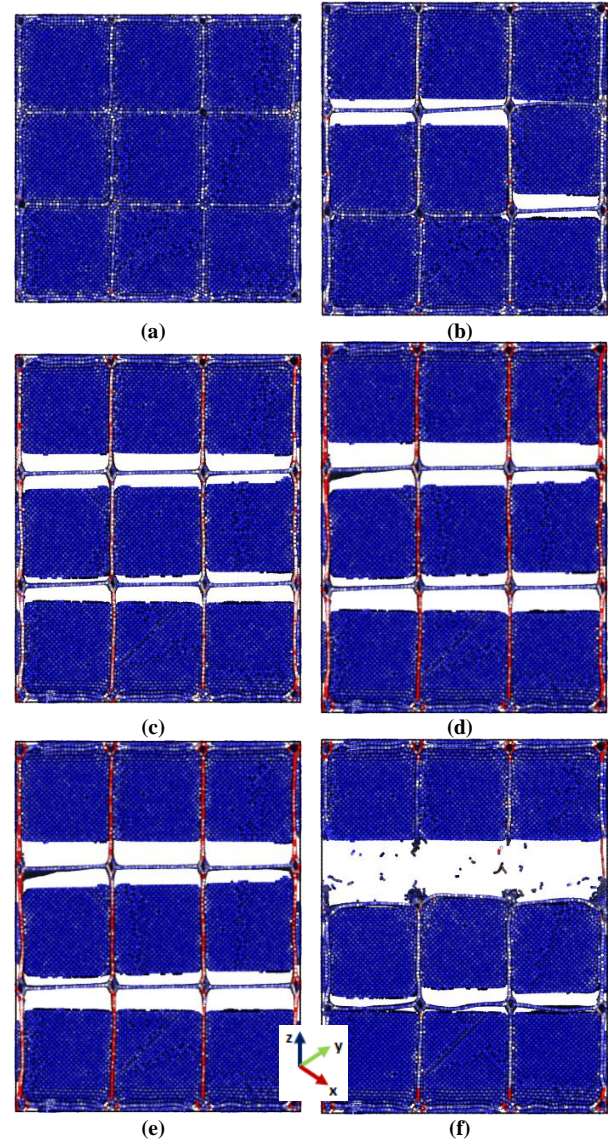


Figure 9. Deformation states of the Ni-G-CNT(5, 5) structure subjected to tensile loading in the Y direction, (a) 0.00, (b) 0.10, (c) 0.16, (d) 0.22, (e) 0.30 and (f) 0.31.

When the values were examined, it was seen that the elastic modulus values decreased as the CNT diameter increased. However, unlike the x direction, the highest maximum stress value and ductility were seen in the Ni-G-CNT (15x15) structure containing CNTs with the largest diameter. It is seen that the tensile strengths of the structures change depending on the number and arrangement of graphene and CNT. Since the Ni-G-CNT(5,5) structure has the same number of graphene and CNTs in both directions, its mechanical strength is the same, while in the other two structures, it is seen that the mechanical strength in the Y direction is higher than in the x direction. This is related to the presence of fewer

CNTs and graphene in the Y direction. In this direction, graphenes is longer and the number of divisions in the nickel structure due to G-CNT connections is less. For this reason, it is thought that the decrease in mechanical values is less. Deformation images of the structures are given in Figure 9. When the deformation images are examined, it is seen that the stresses are mostly concentrated in the graphene, similar to the x direction, and the rupture starts from the graphene in the middle part.

3.1. Compression Behavior

To examine the compression performances of the structure obtained by adding the G-CNT skeleton structure to the Ni structure, the comparative compressive stress-strain curves of different Ni-G-CNT structures are given in Figure 10.

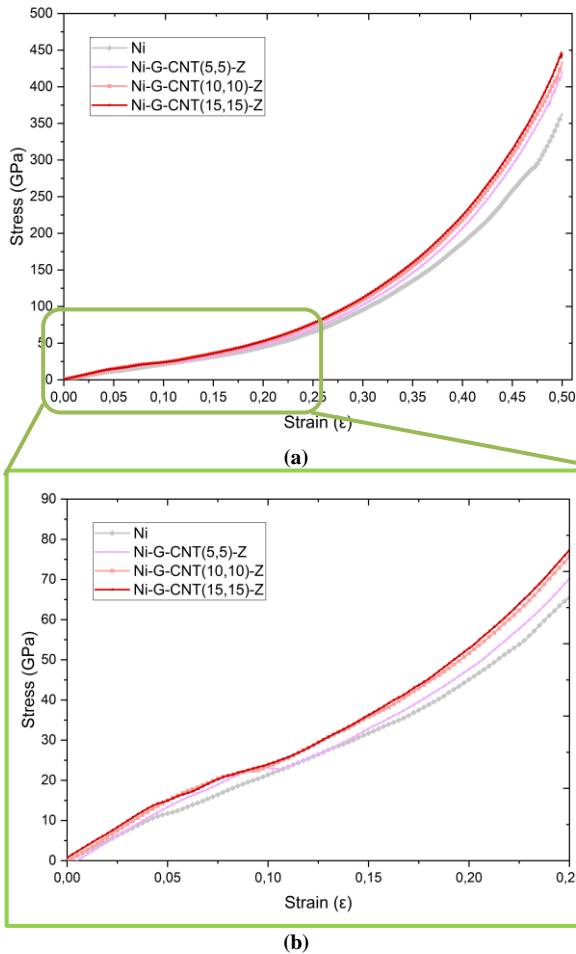


Figure 10. (a) Compressive stress-strain curves of Ni-G-CNT structures in the z direction, (b) zoomed region for 0,00-0,25 strain.

When the behaviors were examined, three different regions were observed. It was observed that in the first region, the stresses in the structure increased linearly up to $\epsilon = 0.035-0.050$. Then, the slope of the stresses decreases to a certain value. It was observed that after this value, a concentration zone was formed where the stresses increased. Adding G-CNT structures to the structure increased the compressive strength of the nickel material. When the structures were evaluated in terms of CNT dimensions, it was seen that as the diameter of the CNTs increased, up to a certain value in the linear region, the stress values and CNT strengths were higher. Although

the increases in this part are low, the stress contribution is more clearly seen in the condensation and hardening region. Detailed mechanical values of the structures are given in table 5.

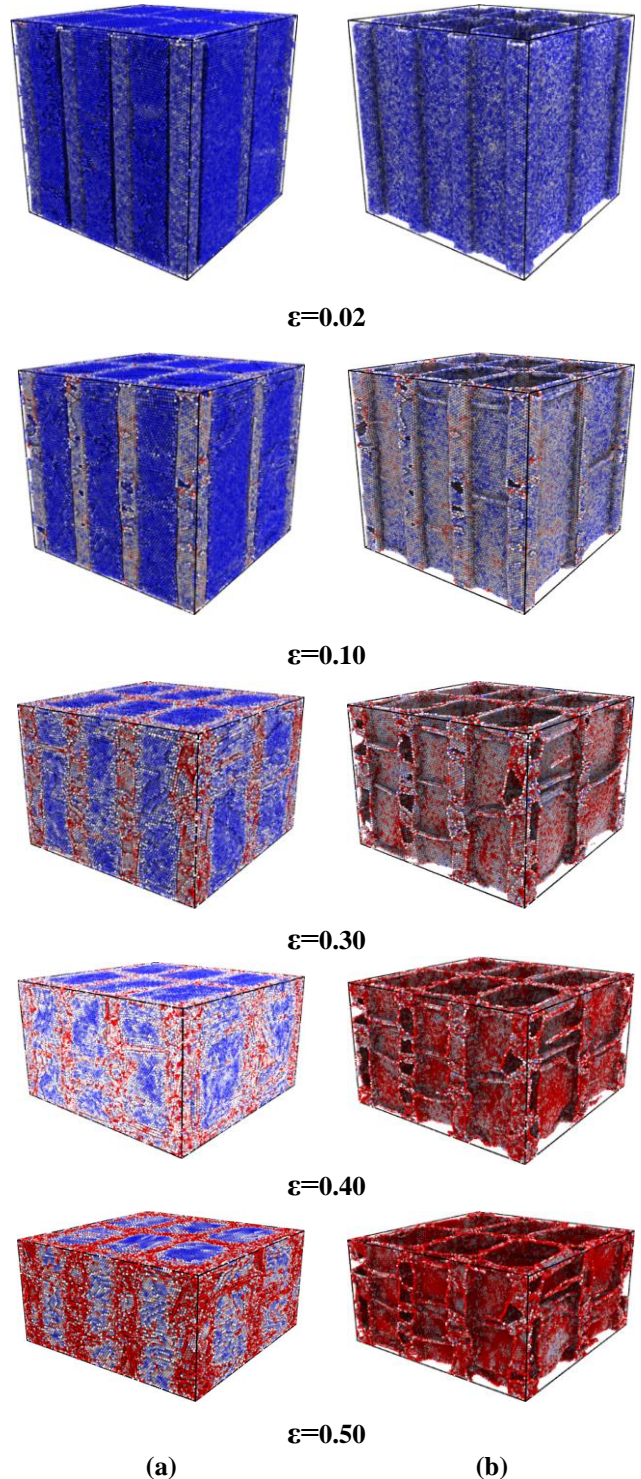


Figure 11. Compressive stress-strain curves in the Z direction of the Ni-G-CNT(15x15) structure, (a) the entire structure, (b) G-CNT skeleton.

Table 5. Mechanical properties of Ni-G-CNT nanomaterials for uniaxial compressive loading.

Model name	Elastic Module (GPa)	Yield strain (%)	Yield Strength (GPa)
Ni	245,67	0,048	11,49
Ni-G-CNT(5,5)	302,33	0,054	14,25
Ni-G-CNT(10,10)	306,15	0,053	16,14
Ni-G-CNT(15,15)	307,65	0,047	14,49

In order to better understand the compression behavior, the stress images of the materials were examined (Figure 11). The first stresses in the structure occurred in graphene and CNTs rather than nickel. It has been observed that as the stresses increase, bending begins in the CNTs and increases up to $\epsilon=0.03-0.05$. After this value, the slope of the increase in stresses decreases due to lateral deformations occurring in CNTs. In this part, the stresses show a low slope. It was observed that the stresses increased again with an increasing slope starting from $\epsilon = 0.10$. When the structures with different CNT diameters were examined, in the structures containing large diameter CNTs, the stress was higher in the first region, while this difference became more evident in the concentration region. The highest compressive strength belongs to the Ni-G-CNT(15,15) structure.

4. CONCLUSION

In summary, in this study, a new nanostructure was presented by embedding the carbon-based skeleton structure created by covalently bonding Graphene and CNT together into nickel metal. After checking the thermodynamic stability of the structures, mechanical analyzes were performed using MD simulations. The results showed that strong covalent bonds were formed between graphene and CNT structures and a structure exhibiting higher elastic modulus, ultimate strength and strain values in the vertical direction was obtained compared to the Ni structure. With the addition of G-CNT structures, a 36% increase in the elastic modulus of the nickel structure and a 12% increase in the maximum tensile value were observed. The structure inherently exhibits an anisotropic behavior. Additionally, when the effects of different CNT diameters on the mechanical strength of the structure were investigated, it was seen that larger diameter CNTs were better in compressive strength in the vertical direction. The situation may differ in tensile strength. With this study, an important G-CNT structure reinforcement has been presented to improve the low mechanical strength of nickel material, which has unique properties such as rust resistance, high temperature, electrical conductivity and chemical resistance.

Declaration of conflicting interests

The authors declared no potential conflicts of interest with respect to the research, authorship, and/or publication of this article.

REFERENCES

- [1] U. Degirmenci, Y.O. Yildiz, Examination of mechanical behaviour of fullerene doped aluminium matrix composite produced by sintering process, *Materials Today Communications* 38 (2024) 107916.
- [2] J. Xu, J. Tao, S. Jiang, Z. Xu, Investigation on corrosion and wear behaviors of nanoparticles reinforced Ni-based composite alloying layer, *Applied Surface Science* 254(13) (2008) 4036-4043.
- [3] L. Zhang, D. Shi, T. Liu, M. Jaroniec, J. Yu, Nickel-based materials for supercapacitors, *Materials Today* 25 (2019) 35-65.
- [4] Y. Li, J. Zhang, Z. Chen, M. Chen, Nickel-based materials: Toward practical application of the aqueous hybrid supercapacitors, *Sustainable Materials and Technologies* 33 (2022) e00479.
- [5] B. Li, M. Zheng, H. Xue, H. Pang, High performance electrochemical capacitor materials focusing on nickel based materials, *Inorganic Chemistry Frontiers* 3(2) (2016) 175-202.
- [6] Y. Zhou, W.-G. Jiang, D.-S. Li, Q.-H. Qin, Study on Lightweight and Strengthening Effect of Carbon Nanotube in Highly Ordered Nanoporous Nickel: A Molecular Dynamics Study, *Applied Sciences*, 2019.
- [7] M. Dadkhah, A. Saboori, P. Fino, An Overview of the Recent Developments in Metal Matrix Nanocomposites Reinforced by Graphene, *Materials*, 2019.
- [8] M. Tabandeh-Khorshid, K. Ajay, E. Omrani, C. Kim, P. Rohatgi, Synthesis, characterization, and properties of graphene reinforced metal-matrix nanocomposites, *Composites Part B: Engineering* 183 (2020) 107664.
- [9] C. Qiu, Y. Su, J. Yang, B. Chen, Q. Ouyang, D. Zhang, Structural modelling and mechanical behaviors of graphene/carbon nanotubes reinforced metal matrix composites via atomic-scale simulations: A review, *Composites Part C: Open Access* 4 (2021) 100120.
- [10] B. Guo, B. Chen, X. Zhang, X. Cen, X. Wang, M. Song, S. Ni, J. Yi, T. Shen, Y. Du, Exploring the size effects of Al₄C₃ on the mechanical properties and thermal behaviors of Al-based composites reinforced by SiC and carbon nanotubes, *Carbon* 135 (2018) 224-235.
- [11] D. Kuang, L. Xu, L. Liu, W. Hu, Y. Wu, Graphene-nickel composites, *Applied Surface Science* 273 (2013) 484-490.
- [12] N. Wang, S. Pandit, L. Ye, M. Edwards, V.R.S.S. Mokkupati, M. Murugesan, V. Kuzmenko, C. Zhao, F. Westerlund, I. Mijakovic, J. Liu, Efficient surface modification of carbon nanotubes for fabricating high performance CNT based hybrid nanostructures, *Carbon* 111 (2017) 402-410.
- [13] S. Inoue, Y. Matsumura, Influence of metal coating on single-walled carbon nanotube: Molecular dynamics approach to determine tensile strength, *Chemical Physics Letters* 469(1) (2009) 125-129.
- [14] S. Inoue, Y. Matsumura, Molecular dynamics simulation of metal coating on single-walled carbon

- nanotube, *Chemical Physics Letters* 464(4) (2008) 160-165.
- [15] J. Jiang, J. Liu, W. Zhou, J. Zhu, X. Huang, X. Qi, H. Zhang, T. Yu, CNT/Ni hybrid nanostructured arrays: synthesis and application as high-performance electrode materials for pseudocapacitors, *Energy & Environmental Science* 4(12) (2011) 5000-5007.
- [16] D. Wang, X. Wang, L. Qiu, H. Ye, N. Maimaitituersun, B. Han, Effect of nickel-coated carbon nanotubes on the tensile behaviors of ultra-high performance concrete (UHPC): insights from experiments and molecular dynamic simulations, *Journal of Materials Science* 58(45) (2023) 17225-17240.
- [17] K. Duan, L. Li, Y. Hu, X. Wang, Enhanced interfacial strength of carbon nanotube/copper nanocomposites via Ni-coating: Molecular-dynamics insights, *Physica E Low Dimens. Syst. Nanostruct.* 88 (2017) 259-264.
- [18] P.K. Singh, K. Sharma, A. Kumar, M. Shukla, Effects of functionalization on the mechanical properties of multiwalled carbon nanotubes: A molecular dynamics approach, *Journal of Composite Materials* 51(5) (2016) 671-680.
- [19] H. Y. Song, X.-W. Zha, Mechanical properties of nickel-coated single-walled carbon nanotubes and their embedded gold matrix composites, *Physics Letters A* 374(8) (2010) 1068-1072.
- [20] Y. Yan, A. Zou, Y. Lei, P. Xu, S. Zhou, Atomic insights into the tensile behavior of carbon nanotube with different geometrical characteristics embedded in nickel matrix, *Diamond and Related Materials* 141 (2024) 110576.
- [21] W. Humphrey, A. Dalke, K. Schulten, VMD: Visual molecular dynamics, *Journal of Molecular Graphics* 14(1) (1996) 33-38.
- [22] F.Y. Meng, S.Q. Shi, D.S. Xu, R. Yang, Size effect of X-shaped carbon nanotube junctions, *Carbon* 44(7) (2006) 1263-1266.
- [23] U. Degirmenci, M. Kirca, Design and mechanical characterization of a novel carbon-based hybrid foam: A molecular dynamics study, *Comput. Mater. Sci.* 154 (2018) 122-131.
- [24] S. Plimpton, Fast Parallel Algorithms for Short-Range Molecular Dynamics, *Journal of Computational Physics* 117(1) (1995) 1-19.
- [25] U. Degirmenci, M. Kirca, Carbon-based nano lattice hybrid structures: Mechanical and thermal properties, *Physica E Low Dimens. Syst. Nanostruct.* 144 (2022) 115392.
- [26] S.K. Deb Nath, S.-G. Kim, Study of the Nanomechanics of CNTs under Tension by Molecular Dynamics Simulation Using Different Potentials, *ISRN Condensed Matter Physics* 2014 (2014) 606017.
- [27] M.S. Daw, M.I. Baskes, Embedded-atom method: Derivation and application to impurities, surfaces, and other defects in metals, *Physical Review B* 29(12) (1984) 6443-6453.
- [28] X.-M. Bai, A.F. Voter, R.G. Hoagland, M. Nastasi, B.P. Uberuaga, Efficient Annealing of Radiation Damage Near Grain Boundaries via Interstitial Emission, *Science* 327(5973) (2010) 1631-1634.
- [29] Y.-H. Lin, T.-C. Chen, P.-F. Yang, S.-R. Jian, Y.-S. Lai, Atomic-level simulations of nanoindentation-induced phase transformation in mono-crystalline silicon, *Applied Surface Science* 254(5) (2007) 1415-1422.
- [30] S.-P. Huang, D.S. Mainardi, P.B. Balbuena, Structure and dynamics of graphite-supported bimetallic nanoclusters, *Surface Science* 545(3) (2003) 163-179.
- [31] Y. Shibuta, S. Maruyama, Bond-order potential for transition metal carbide cluster for the growth simulation of a single-walled carbon nanotube, *Comput. Mater. Sci.* 39(4) (2007) 842-848.
- [32] M. Kirca, X. Yang, A.C. To, A stochastic algorithm for modeling heat welded random carbon nanotube network, *Computer Methods in Applied Mechanics and Engineering* 259 (2013) 1-9.
- [33] A.P. Thompson, S.J. Plimpton, W. Mattson, General formulation of pressure and stress tensor for arbitrary many-body interaction potentials under periodic boundary conditions, *The Journal of Chemical Physics* 131(15) (2009) 154107.

Developing a Regression Model for Predicting the Seismic Input Energy of RC Buildings Using 6 February 2023 Kahramanmaraş Earthquake

Bilal BALUN^{1*} 

¹ Bingöl University, Centre for Energy the Environment and Natural Disasters and Department of Architecture, Bingöl, Türkiye

Bilal BALUN ORCID No: 0000-0003-0906-4484

*Corresponding author: bbalun@bingol.edu.tr

(Received: 18.09.2023, Accepted: 19.03.2024, Online Publication: 26.03.2024)

Keywords

Kahramanmaraş earthquake, Input energy, Multiple regression, Correlation

Abstract: Energy-based seismic analysis and structural design require understanding the seismic input energy response of reinforced concrete buildings subjected to strong ground motions. Thus, calculating and predicting input energies becomes of great importance. The object of this study is to introduce a regression model for predicting the seismic input energies of reinforced concrete buildings using the 6 February 2023 Kahramanmaraş/Pazarcık earthquake which devastating damage occurred. For this purpose, three regular 3, 6 and 9-storey residential reinforced concrete buildings are designed. Input energy response histories of buildings subjected to a set of horizontal acceleration histories of 67 stations of the February 6 Kahramanmaraş/Pazarcık earthquake were obtained. Subsequently, the ground motion parameters were used to estimate the input energies. It was revealed that acceleration-based parameters generally had better consequences than velocity-based parameters in low periods, while the opposite was the case in high periods. In 3, 6 and 9-storey buildings, the highest correlation coefficients were obtained in I_c (0.91), ASI (0.83) and VSI (0.73) parameters, respectively. This study proposed new equations in which multiple ground motion parameters are combined to better reflect input energy from a single parameter. In the multi regression where all parameters were used, correlation values (R^2) of 0.94, 0.85 and 0.77 were determined, respectively, according to the number of floors of the buildings. As the height and period of the buildings increase, the multiple linear regression coefficient decreases and the estimation of input energy becomes difficult with the ground motion parameters.

6 Şubat 2023 Kahramanmaraş Depremi Kullanılarak Betonarme Binaların Sismik Giriş Enerjisinin Tahmin Edilmesine Yönelik Regresyon Modeli Geliştirilmesi

Anahtar

Kelimeler

Kahramanmaraş depremi, Sismik giriş enerjisi, Çoklu regresyon, Korelasyon

Öz: Enerji bazlı sismik analiz ve yapı tasarımı, kuvvetli yer hareketlerine maruz kalan betonarme binaların sismik giriş enerji tepkisinin anlaşılmasını gerektirir. Bu nedenle giriş enerjilerinin hesaplanması ve tahmin edilmesi büyük önem kazanmaktadır. Bu çalışmanın amacı, yıkıcı hasarların meydana geldiği 6 Şubat 2023 Kahramanmaraş/Pazarcık depremini kullanarak betonarme binaların sismik giriş enerjilerini tahmin etmeye yönelik bir regresyon modeli ortaya koymaktır. Bu amaçla 3, 6 ve 9 katlı üç adet düzenli konut betonarme bina tasarlanmıştır. 6 Şubat Kahramanmaraş/Pazarcık depreminin 67 istasyonunun bir dizi yatay ivme geçmişine tabi tutulan binaların giriş enerji tepki geçmişleri elde edildi. Daha sonra giriş enerjilerini tahmin etmek için yer hareketi parametreleri kullanıldı. Düşük periyotlarda ivmeye dayalı parametrelerin genellikle hızla dayalı parametrelere göre daha iyi sonuçlara sahip olduğu, yüksek periyotlarda ise bunun tam tersi olduğu ortaya çıktı. 3, 6 ve 9 katlı binalarda en yüksek korelasyon katsayıları sırasıyla I_c (0,91), ASI (0,83) ve VSI (0,73) parametrelerinde elde edildi. Bu çalışma, tek bir parametreden gelen girdi enerjisini daha iyi yansıtmak için birden fazla yer hareketi parametresinin birleştirildiği yeni denklemler önermiştir. Tüm parametrelerin kullanıldığı çoklu regresyon modelinde binaların kat sayısına göre sırasıyla 0,94, 0,85 ve 0,77 korelasyon değerleri (R^2) belirlendi. Binaların yüksekliği ve periyodu arttıkça çoklu doğrusal regresyon katsayısı azalmakta ve yer hareketi parametreleri ile girdi enerjisinin tahmini zorlaşmaktadır.

1. INTRODUCTION

Türkiye has been affected by many devastating earthquakes throughout its history, as it is a seismically active region. [1]. Türkiye experienced massive destruction during the earthquake couple which occurred, at nine-hour intervals in Pazarcık (M_w 7.7) and Elbistan (M_w 7.6) on February 2023 [2]. On February 6, the accumulated energy of the Eastern Anatolian Fault Zone (EAFZ) was released by a tearing mechanism from north to south, just like a zipper [3]. The successive occurrence of these earthquakes caused property damage and loss of life three times than of the 1999 Marmara earthquake [4]. Balun [5] stated this situation as the seismic energy intensity of the February 6 Kahramanmaraş earthquake was much greater than previous earthquakes in Türkiye after the invention of devices. After these two significant earthquakes, in 11 different provinces more than 50,000 people lost their lives and caused many buildings to collapse or significant structural damage [6]. Previous studies pointed out the damage of the many types of structures. Destructions and damages were observed, especially in reinforced concrete buildings, which constitute the majority of the building stock of the region, and it was stated that poor materials, workmanship quality, inadequate detailing and architectural design errors were the main factors of these damages [1,3,4,7–9]. Furthermore, masonry structures, mosques and minarets were also examined and damages due to structural defects were reported [2,6,10]. It has been understood that earthquake code design criteria and requirements are insufficient in some regions. Considering the very severe earthquake level, it is a striking result that the accelerations obtained from many stations exceed the response spectrum values estimated by Türkiye Building Earthquake Code (TBEC 2018) [4,10]. All these field observations have revealed that construction and design defects cause inevitable loss of life and property. It has also been emphasized that ground motions above the design spectrum values are another important cause of damage. Apart from the structural damage caused by buildings, examining the density distribution after these earthquakes through peak ground acceleration and estimation of actual loss of life and structural damage has contributed to the literature [11,12]. In addition to all the researches and assessments made, it is thought that the interpretation of the February 6 earthquakes through the estimation of the seismic input energies will be valuable in terms of understanding both the design approach and the destructive effects of these earthquakes.

Strong ground motions that have occurred in the world in recent years have caused serious damage to relatively many new buildings designed according to conventional force or displacement-based seismic methods. If the instance exists due to deficiencies in the seismic design code, it is further confirmation that force or displacement-based design does not result in reliable structural seismic design of building systems [13]. This situation has increased the importance of energy-based design. To overcome these problems, an alternative

seismic analysis and design approach that takes into account the duration, frequency content and cumulative damage potential of ground motion, defined as energy-based seismic design, has been introduced by Housner [14].

Although earthquakes are quite irregular ground motions, the input energy passing through the structure is a very stable parameter. Part of the input energy passing through the structure by ground motion is distributed by the damping mechanism, while the other part is distributed by cyclic energy [15–17]. Energy-based methods are achieved by providing sufficient capacity to building elements compared to seismic demand. The basis of energy-based seismic design is that the loading effect of seismic excitation on structures can be interpreted not as separate forces or displacements, but as the product of both in terms of input energy. However, it is accepted by many authors that the loading history affects the cumulative damage in seismic excitations [18–21].

Energy and energy parameters are the most promising parameters for the design of structures exposed to moderate or severe earthquakes. In the energy-based design approach, the primary task is the precise calculation of the input energy. Practical prediction of seismic input energy of multi degree of freedom systems (MDOF) is quite essential, especially in terms of seismic-based design [22]. The damage potential of structures is not only affected by the characteristics of ground motion but is also a function of structural characteristics. With a similar approach, seismic input energy is also affected by both characteristics. The damage potential of structures is generally reflected by ground motion parameters such as peak ground acceleration (PGA), peak ground velocity (PGV) and peak ground displacement (PGD). Although PGA is widely used as a dominant parameter in the assessment of structural performance, some studies have shown that this parameter alone does not have a strong correlation with structural damage [23–25]. Correlations and relationships of ground motion parameters with seismic input energy can eliminate complex calculations. In support of this, many studies in the literature have found relationships between ground motion characteristics and structural damage [26–28]. However, in most studies, it has been difficult to establish strong relationships between damage potential and ground motion characteristics [16,29]. It is thought that evaluating more than one parameter together will provide advantages in seismic input energy estimation.

Unlike the studies conducted for the February 6 Kahramanmaraş earthquake, estimating the input energy that causes structural damage with ground motion parameters in this study is a different perspective in terms of seismic evaluation. For this purpose, this study aims to reveal a strong correlation with seismic input energy by taking into account multiple regression in which ground motion characteristics are considered together. Three regular residential reinforced concrete buildings with 3, 6 and 9 storeys were designed to

determine the relationships between seismic input energy and ground motion parameters. Input energy response histories of 3D-designed buildings subjected to a series of horizontal acceleration histories of 67 stations of the February 6 Pazarçık earthquake were obtained, and their correlations with seismic parameters were evaluated. Ultimately, seismic input energy will be predicted using the multiple regression analysis based on several parameters, such as acceleration, velocity, displacement, frequency and duration.

2. STRONG GROUND MOTION DATASET

The current study consists of 25 ground motion parameters to analyze the relationship with seismic input energy. In structural damage assessment, commonly used peak values alone do not lead to an understanding

of the damage potential of strong ground motions to structures. Many other ground motion parameters can contribute to structural damage [30]. The seismic parameters given in Table 1 are classified according to acceleration, velocity, displacement, frequency and ground motion duration. Additionally, in this study, significant duration was considered to reveal the duration effect. The values of parameters used in the study are determined using the software SeismoSignal (2021) [31]. The relationship between a parameter and other parameters can be examined through correlation analysis. Additionally, multiple regression analysis was performed to reveal the relationship of multiple parameters with seismic input energy and equations were obtained for prediction.

Table 1. Seismic parameters

Type	Parameter	Definition	Formula
Acceleration-based	PGA	Peak ground acceleration	$PGA = \max a(t) $
	a_{RMS}	Root-mean-square of acceleration	$a_{RMS} = \sqrt{\frac{1}{t_{tot}} \int_0^t [a(t)]^2 dt}$
	I_a	Arias intensity	$I_a = \frac{\pi}{2g} \int_0^t a^2(t) dt$
	I_c	Characteristic intensity	$I_c = (a_{RMS})^2 \sqrt{t_{tot}}$
	CAV	Cumulative absolute velocity	$CAV = \int_0^t a(t) dt$
	SMA	Sustained maximum acceleration	3rd largest peak in acceleration time history
	EDA	Effective Design Acceleration	Peak acceleration value above 9 Hz
	A_{95}	A_{95} Parameter	The acc. level below 95% of the total I_a
	SCAV	Standardized Cumulative Absolute Velocity	$SCAV = \sum_{i=1}^n (H(PGA) - 0.025) \int_{t_{i-1}}^i a(t) dt$
	$S_{a,avg}$	Average Spectral Acceleration	$S_{a(T1...TN)} = \left(\prod_{i=1}^n S_a(T_i) \right)^{1/n}$
ASI	Acceleration spectrum intensity	$ASI = \int_{0.1}^{0.5} S_a(\xi = 0.05, T) dT$	
Velocity-based	PGV	Peak ground velocity	$PGV = \max v(t) $
	v_{RMS}	Root-mean-square of velocity	$v_{RMS} = \sqrt{\frac{1}{t_{tot}} \int_0^t [v(t)]^2 dt}$
	SED	Specific energy density	$SED = \int_0^t [v(t)]^2 dt$
	SMV	Sustained maximum velocity	3rd largest peak in velocity time history
	MIV	Maximum Incremental Velocity	Acc. curve between two zero crossings of the accel.
	VSI	Velocity spectrum intensity	$VSI = \int_{0.1}^{2.5} S_v(\xi = 0.05, T) dT$
HI	Housner intensity	$HI = \int_{0.1}^{2.5} PSV(\xi = 0.05, T) dT$	
Disp.-based	PGD	Peak ground displacement	$PGD = \max d(t) $
	d_{RMS}	Root-mean-square of displacement	$d_{RMS} = \sqrt{\frac{1}{t_{tot}} \int_0^t [d(t)]^2 dt}$
v_{max}/a_{max}	Peak velocity to acceleration ratio	v_{max}/a_{max}	
Frequency-based	T_p	Predominant Period	The period at which the maximum spectral acc.
	T_m	Mean Period	$T_m = \frac{\sum C_i^2 / f_i}{\sum C_i^2}$
Duration-based	D_{5-95}	Significant duration (5%-95%)	The time period over which total Arias Intensity is collected from 5% to 95%
	D_{5-75}	Significant duration (5%-75%)	The time period over which total Arias Intensity is collected from 5% to 75%

Analyzes were performed under the ground motion record set listed in Table 2 for the determined building

models. Both horizontal components of the 67 station records of the 2023 Kahramanmaraş earthquake, which

occurred at 04:17 local time and had a magnitude of M_w 7.7, extracted from the AFAD database, were used. Furthermore, the coordinates of the stations, shear wave velocity (V_{s30}) of the soil and distance to epicenter values are also given. The selection criterion for ground motions is that the peak ground acceleration values of the records are greater than 0.1g, where g is the gravitational acceleration. In the analysis, acceleration records were used without spectrum

matching. The aim is to reveal the relationships that are the subject of the article by using real ground motions of the Kahramanmaraş earthquake, which caused a lot of destruction and loss of life. In the intensity map in Figure 1 presented by AFAD [32], it is seen that ground motions greater than 0.1 g mostly occur in Hatay and Kahramanmaraş provinces and their surroundings.

Table 2. The properties of the selected earthquake records (February 6 Kahramanmaraş (M_w 7.7))

No	Station	City	District	Longitude	Latitude	V_{s30} (m/s)	R_{epi} (km)
1	120	Adana	Yumurtalık	35.790	36.770	439	125.25
2	125	Adana	Ceyhan	35.796	37.015	208	114.62
3	131	Adana	Saimbeyli	36.115	37.857	None	103.35
4	201	Adiyaman	Adiyaman	38.267	37.761	391	120.12
5	213	Adiyaman	Tut	37.930	37.797	None	96.48
6	2703	Gaziantep	Şahinbey	37.350	37.058	758	37.34
7	2704	Gaziantep	Nizip	37.802	37.009	721	74.10
8	2708	Gaziantep	İslahiye	36.648	37.099	523	40.77
9	2709	Gaziantep	İslahiye	36.670	37.129	555	37.45
10	2711	Gaziantep	Yavuzeli	37.560	37.317	None	45.88
11	2712	Gaziantep	Nurdağı	36.733	37.184	None	29.79
12	2714	Adiyaman	Besni	37.621	37.492	None	55.92
13	2715	Gaziantep	İslahiye	36.686	36.855	None	57.62
14	2716	Gaziantep	İslahiye	36.688	36.856	None	57.38
15	2717	Gaziantep	İslahiye	36.691	36.855	None	57.34
16	2718	Gaziantep	İslahiye	36.627	37.008	None	48.30
17	3112	Hatay	İskenderun	36.148	36.588	233	111.31
18	3115	Hatay	Belen	36.165	36.546	424	113.7
19	3116	Hatay	İskenderun	36.207	36.616	870	105.38
20	3123	Hatay	Antakya	36.160	36.214	470	143.00
21	3124	Hatay	Antakya	36.172	36.239	283	140.11
22	3125	Hatay	Antakya	36.133	36.238	448	142.15
23	3126	Hatay	Antakya	36.138	36.220	350	143.54
24	3129	Hatay	Defne	36.134	36.191	447	146.39
25	3131	Hatay	Antakya	36.163	36.191	567	144.98
26	3132	Hatay	Antakya	36.172	36.207	377	143.12
27	3133	Hatay	Reyhanlı	36.574	36.243	377	123.47
28	3134	Hatay	Dört Yol	36.205	36.828	374	90.29
29	3135	Hatay	Arsuz	35.883	36.409	460	142.15
30	3136	Hatay	Altınözü	36.247	36.116	344	148.38
31	3137	Hatay	Hassa	36.489	36.693	688	82.48
32	3138	Hatay	Hassa	36.511	36.803	618	71.70
33	3139	Hatay	Kırıkhan	36.414	36.584	272	96.19
34	3140	Hatay	Samandağ	35.950	36.082	210	165.82
35	3141	Hatay	Antakya	36.220	36.373	338	125.42
36	3142	Hatay	Kırıkhan	36.366	36.498	539	106.49
37	3143	Hatay	Hassa	36.557	36.849	444	65.13
38	3144	Hatay	Hassa	36.486	36.757	485	77.04
39	3145	Hatay	Kırıkhan	36.406	36.645	533	91.13
40	3146	Hatay	Belen	36.227	36.491	None	114.57
41	4404	Malatya	Pütürge	38.874	38.196	1380	190.02
42	4406	Malatya	Akçadağ	37.974	38.344	815	143.07
43	4408	Malatya	Doğanşehir	37.887	38.096	654	116.59
44	4611	Kahramanmaraş	Çağlayancerit	37.284	37.747	731	55.32
45	4612	Kahramanmaraş	Göksun	36.482	38.024	246	95.59

46	4613	Kahramanmaraş	Andırın	36.357	37.570	998	68.19
47	4614	Kahramanmaraş	Pazarcık	37.298	37.485	541	31.42
48	4615	Kahramanmaraş	Pazarcık	37.138	37.387	484	13.83
49	4616	Kahramanmaraş	Türkoğlu	36.838	37.375	390	20.54
50	4617	Kahramanmaraş	Onikişubat	36.838	37.375	574	38.04
51	4618	Kahramanmaraş	Onikişubat	36.872	37.600	715	37.84
52	4619	Kahramanmaraş	Onikişubat	36.866	37.587	545	36.73
53	4620	Kahramanmaraş	Onikişubat	36.898	37.586	484	35.48
54	4621	Kahramanmaraş	Dulkadiroğlu	36.929	37.593	714	35.42
55	4624	Kahramanmaraş	Onikişubat	36.918	37.536	280	29.73
56	4625	Kahramanmaraş	Dulkadiroğlu	36.982	37.539	346	28.40
57	4626	Kahramanmaraş	Onikişubat	36.915	37.575	317	33.89
58	4629	Kahramanmaraş	Türkoğlu	36.789	37.287	382	22.05
59	4630	Kahramanmaraş	Türkoğlu	36.789	37.287	347	21.89
60	4632	Kahramanmaraş	Türkoğlu	36.774	37.256	428	24.09
61	6303	Şanlıurfa	Siverek	39.329	37.752	986	208.12
62	6304	Şanlıurfa	Bozova	38.513	37.365	376	130.27
63	6305	Şanlıurfa	Haliliye	38.513	37.365	None	155.06
64	8002	Osmaniye	Bahçe	36.562	37.192	430	43.91
65	8003	Osmaniye	Osmaniye	36.269	37.084	350	72.18
66	8004	Osmaniye	Kadirli	36.098	37.380	426	84.20
67	NAR	Kahramanmaraş	Pazarcık	37.157	37.392	None	15.35

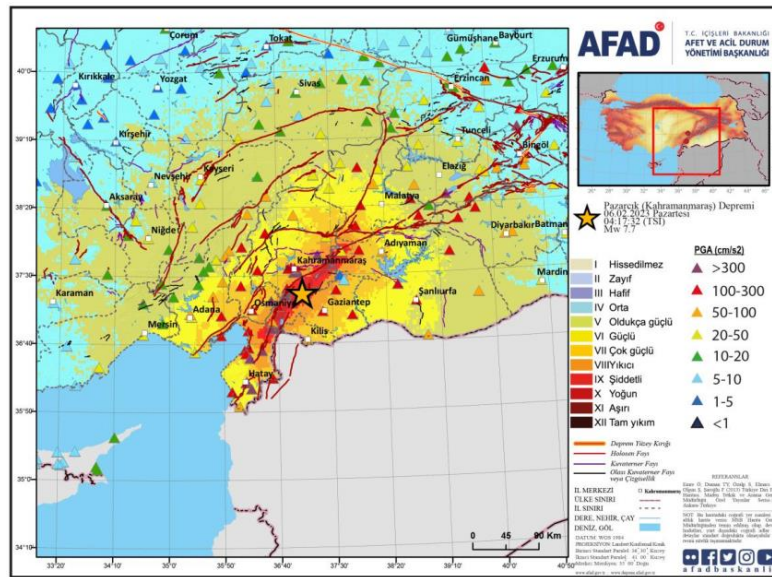


Figure 1. AFAD-RED intensity map of M_w 7.7 magnitude earthquake [32].

3. BUILDING MODEL

Building models with 3, 6 and 9 storeys are designed to represent the building inventory in the earthquake affected region. Even if buildings have different numbers of storey, buildings may have similar mass and period values due to their structural features. In this study, models were designed to provide diversity in terms of mass and period and correlations were examined. The plan and 3D model of the buildings in which nonlinear analyses were performed is given in Figure 2 and 3. The building structural system consists of frames with beams and columns but no shear walls. In the building model with four bays with a fixed width of 5.0 m, the storey height is 3.0 m on all storeys. Structural elements are designed by TBEC 2018 [33]

code. The periods of the models representing low-rise, medium-rise and high-rise buildings are 0.40, 0.67 and 0.96 seconds, respectively. The floor/slab thickness is maintained at 0.15 m. The column dimensions are selected as 0.4x0.4 m, 0.5x0.5 m and 0.6x0.6 m for 3, 6 and 9-storey buildings, respectively. All beam dimensions are considered as 0.25x0.5 m. A rigid diaphragm model is assumed of the lateral response for the beam at each story level. The additional dead and live loads acting on floors are assumed to be 1 kN/m² and 2 kN/m², respectively. In the design and analysis process, the C25 grade concrete (28-day characteristic compressive strength of 25 N/mm²) and the S420 grade of both longitudinal and transverse reinforcement steel (yield strength of 420 N/mm²) are used for structural elements. Nonlinear time history analyses are

performed in ETABS V19 by using 134 different ground motion records of the 2023 Kahramanmaraş earthquake.

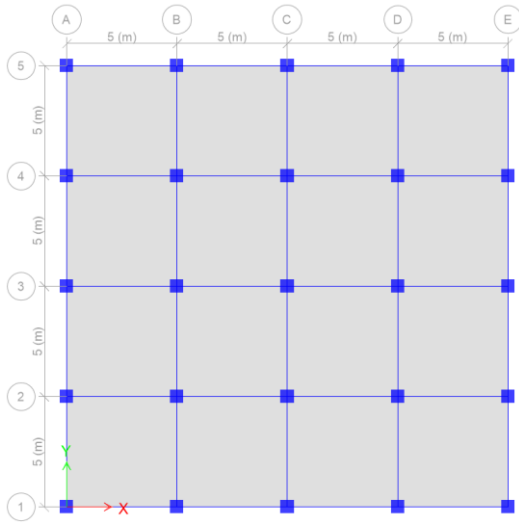


Figure 2. Plan of building models

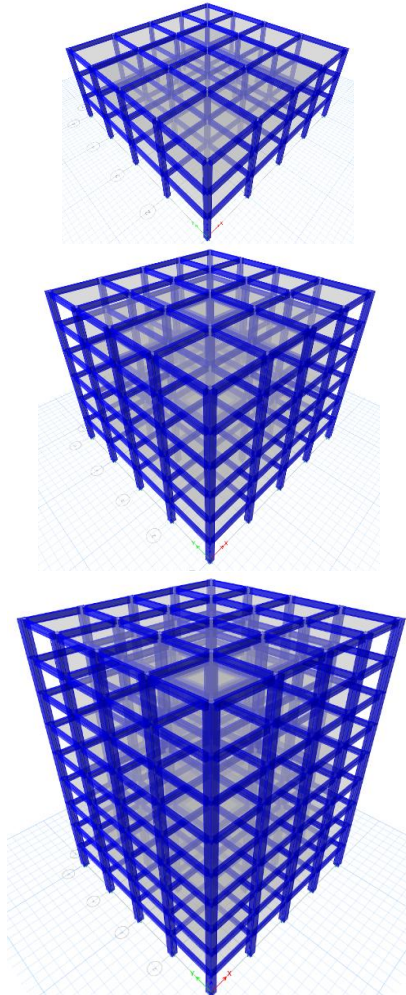


Figure 3. 3D models of buildings (3, 6 and 9-storey)

4. RESULTS AND DISCUSSIONS

Nonlinear time-history analyses were performed with 134 different acceleration records from 67 stations, and

seismic input energies were obtained for each building model. Figure 4 presents the stations where the greatest input energy transmitted to 3, 6 and 9-storey buildings occurs and the graph of this energy change. First of all, the maximum input energies for each building model were calculated with the station data of the 2023 Kahramanmaraş/Pazarcık earthquake. Among 67 stations, the maximum input energies for 3, 6 and 9-storey buildings were obtained in Kahramanmaraş/Pazarcık, Hatay/Defne and Hatay/Antakya, respectively. This result shows that low-period structures in Kahramanmaraş and high-period structures in Hatay were exposed to more input energy during the earthquake. Increasing seismic input energy may also increase the damage potential, depending on the building features.

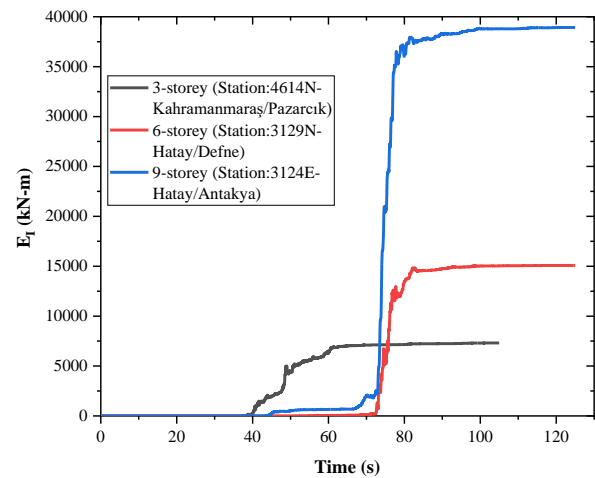


Figure 4. Input energies of 3, 6 and 9-storey RC buildings

In order to make a more accurate assessment, input energy values per unit mass (E_i/m) were obtained and buildings with different storey numbers were compared for 4 stations (Figure 4). These stations are among the stations where the highest acceleration values were obtained in the Pazarcık earthquake. E_i/m values in Kahramanmaraş, where the highest acceleration ground motion occurs (2.43 g), again show that buildings with low periods have to deal with more seismic energy. The same situation was effective in 6-storey buildings in Hatay (station 3129 and 3135) and 9-storey buildings in Gaziantep (station 2708). Hatay and Kahramanmaraş data in Figure 5 supports the results in Figure 4. At station 4614, less input energy was transferred per unit mass in structures with higher periods.

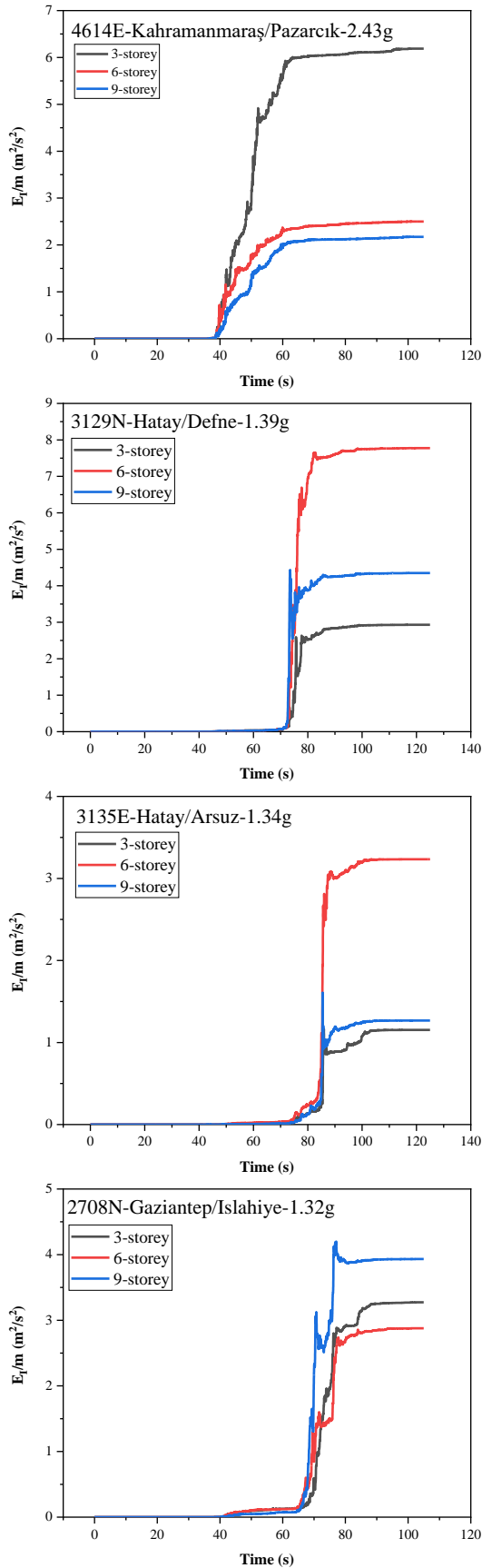


Figure 5. E_i/m values of stations (4614, 3129, 3135, 2708) for 3, 6 and 9-storey buildings

The ground motion parameters given in Table 1 for each station were obtained by SeismoSignal. Correlation analyses of the proposed ground motion parameters were performed with the Pearson

correlation coefficient matrix (Equation 1). In this equation, x_i and y_i indicate the correlation parameters, \bar{x} and \bar{y} indicate the mean values of x_i and y_i , respectively. The correlation coefficient, a dimensionless quantity of variance, is commonly used and ranges from -1 to +1.

$$R = \frac{\sum(x_i - \bar{x})(y_i - \bar{y})}{\sqrt{\sum(x_i - \bar{x})^2(y_i - \bar{y})^2}} \quad (1)$$

The bolded parameters in Table 3 indicate the first 6 highest correlation values in each parameter classification. While ground motion parameters are mostly positively correlated with seismic input energy, significant durations and some frequency-based parameters have a negative correlation. Displacement-based parameters were not among the parameters with the highest correlation. In 3, 6 and 9-storey buildings, the highest coefficients were obtained in I_c (0.91), ASI (0.83) and VSI (0.73) parameters, respectively. It has been determined that displacement-based, frequency-based and duration-based parameters have weaker relationships with input energy. In the correlation assessment, only input energy and one ground motion parameter were taken into account.

Table 3. Correlation coefficients (R) of ground motion parameters with input energy

Type	Parameter	3-storey	6-storey	9-storey
Acceleration-based	PGA	0.86	0.74	0.55
	a_{RMS}	0.90	0.72	0.57
	I_a	0.88	0.56	0.42
	I_c	0.91	0.66	0.51
	CAV	0.87	0.69	0.55
	SMA	0.90	0.73	0.54
	EDA	0.83	0.78	0.58
	A_{95}	0.86	0.74	0.55
	SCAV	0.88	0.68	0.54
	$S_{a,avg}$	0.54	0.78	0.72
Velocity-based	ASI	0.88	0.83	0.57
	PGV	0.46	0.65	0.6
	v_{RMS}	0.41	0.59	0.64
	SED	0.38	0.59	0.7
	SMV	0.51	0.66	0.66
	MIV	0.43	0.69	0.67
	VSI	0.53	0.77	0.73
HI	0.49	0.74	0.72	
Disp.-based	PGD	0.28	0.45	0.47
	d_{RMS}	0.38	0.44	0.47
Freq.-based	v_{max}/a_{max}	-0.27	-0.09	0.00
	T_p	-0.07	0.12	0.35
	T_m	-0.19	0.03	0.20
Dur.-based	D_{5-95}	-0.28	-0.29	-0.26
	D_{5-75}	-0.25	-0.28	-0.27

Figure 6 shows the changes in the correlation of acceleration-based, velocity-based and displacement-

based parameters. Figure 6a indicates that the correlation values in acceleration-based parameters decrease as the number of storey increases. Only the data obtained from the $S_{a,avg}$ parameter are excluded from this situation. Figure 6b explains that velocity-based parameters are generally more effective in buildings with high periods. Velocity-based parameters used in input energy estimation of low-period

structures make their estimation more difficult. When both graphs in Figure 6 are examined, it is determined that acceleration-based parameters have a higher correlation with mean input energies than velocity-based parameters. The highest correlation occurs between the I_c -3-storey building and the lowest correlation between the PGD-3 storey building.

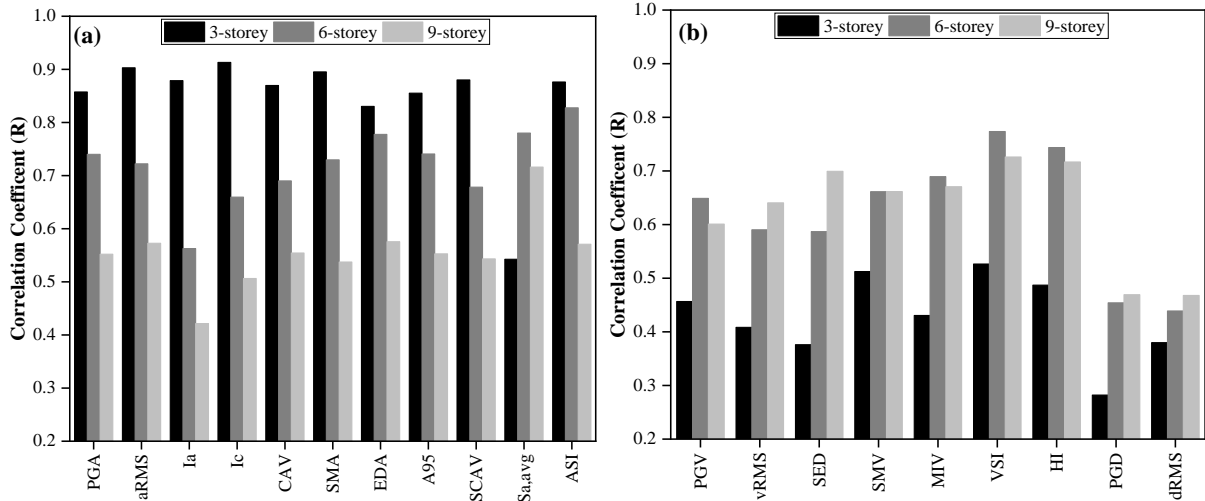


Figure 6. Correlation coefficients (R) of parameters with input energy (a) acceleration-based parameters, (b) velocity and displacement-based parameters

Table 4 contains the parameters with the highest correlation with seismic input energy for 3, 6 and 9-storey buildings. It has been determined that seismic input energy and acceleration-based parameters (a_{RMS} , I_a , I_c , ASI, SCAV, SMA) are in higher correlation in low-period structures. This situation changes as the period of the structure increases and as a result, the correlation relationship shifts towards velocity-based parameters (VSI, HI, SED, SMV, MIV). In many studies, it has been stated that peak ground motion parameters and acceleration-based parameters are in high correlation with demand variables in short-period structures [34–37]. In structures with intermediate periods, the input energy is closely related to both acceleration-based (ASI, A_{95} , SA, EDA) and velocity-based parameters (VSI, HI). a_{RMS} , ASI and VSI parameters reflect the input energy potential as the best single parameter for 3, 6 and 9-storey buildings, respectively.

Table 4. Predominant parameters for 3, 6 and 9-storey buildings

	3-storey	6-storey	9-storey
Predominant Parameters	a_{RMS}	ASI	VSI
	I_a	VSI	HI
	I_c	HI	SED
	ASI	A_{95}	SMV
	SCAV	SA	MIV
	SMA	EDA	SA

The method used to explain the cause-effect relationships between two or more independent variables affecting a variable with a model and to determine the effect levels of these independent

variables is called multiple regression analysis. In this study, parameters used for multiple linear regression analysis define amplitude, frequency, and duration characteristics of ground motion. Predictive relationships are developed with multiple variables. Multiple regression analysis has been executed and performed for 25 ground motion parameters (GMP). The determinant coefficient (R^2), which expresses the degree of closeness to reality of the multiple regression where the dependent variable is input energy, is detailed in Table 5. Two different models were considered in this assessment. The first one expresses the multiple regression developed with the 6 ground motion parameters with the highest correlation value, while the second one covers all (25) ground motion parameters. Higher correlation values were obtained in the approach where all ground motion parameters were taken into account. Additionally, the highest R^2 values emerged for both models in low-period structures. As the building period increases, differences occur between the actual values in the calculation and the estimated values. As a result of linear regression analyses performed, equations 2, 3 and 4 were derived separately for 3, 6 and 9-storey buildings, respectively. The number of variables has been reduced to easily calculate the amount of input energy in the equations with fewer parameters (the first 6 GMPs).

Table 5. Correlation (R) and determinant (R^2) coefficients of GMP's

	6 GMP		All (25) GMP	
	R	R^2	R	R^2
3-storey	0,93	0,87	0,97	0,94
6-storey	0,87	0,76	0,92	0,85
9-storey	0,75	0,56	0,88	0,77

$$E_I(m^2/s^2) = -0.151 - 6.796a_{RMS} - 0.060I_a + 15.154I_c + 1.682ASI - 0.166SCAV - 1.282SMA \quad (2)$$

$$E_I(m^2/s^2) = -0.449 + 3.198ASI + 0.013VSI - 0.015HI + 0.012A_{95} + 3.048S_a - 1.350EDA \quad (3)$$

$$E_I(m^2/s^2) = -0.351 + 0.023VSI - 0.019HI + 7.6E^{-0.5}SED - 0.001SMV - 0.001MIV + 0.184S_a \quad (4)$$

5. CONCLUSION

In this study, input energy estimation for the devastating 6 February 2023 Kahramanmaraş earthquake was carried out and which parameters were highly correlated in which periods were revealed. As a result of the analyses of the structures, it is shown that the low-period structures in Kahramanmaraş and the high-period structures in Hatay are exposed to more input energy during the earthquake. It is worth noting that only structures with limited period values were analyzed. It has been found that acceleration-based parameters generally have better results than velocity-based parameters in low periods, and the opposite occurs in high periods. This study also proposed new regression equations in which multiple ground motion parameters are combined to better reflect input energy from a single parameter. With multiple linear regression analysis, a strong relationship between ground motion parameters and input energy was detected in low-period structures, and it was revealed that it was easier to estimate input energy with ground motion parameters in such structures for this earthquake. There is less difference between the coefficients of the two regression models proposed for low-period structures. However, to provide higher correlations in future studies, the database should be expanded, that is, more earthquake ground motion data should be used. The relationship between seismic parameters and input energies is also affected by the use of regression types. By accurately calculating and/or estimating input energies, damage indices and input energies can be more closely correlated in practice. Additionally, results can be obtained as to which earthquake parameters are more effective for a certain building stock. In subsequent studies, it is suggested that the relationships between strong ground motion parameters and input energy transmitted to the structure should be developed in irregular buildings.

REFERENCES

- [1] Zengin B, Aydın F. The Effect of Material Quality on Buildings Moderately and Heavily Damaged by the Kahramanmaraş Earthquakes. *Appl Sci* 2023;13.
- [2] Işık E. Structural Failures of Adobe Buildings during the February 2023 Kahramanmaraş (Türkiye) Earthquakes. *Appl Sci* 2023;13.
- [3] Avcil F, Işık E, İzol R, Büyüksaraç A, Arkan E, Arslan MH, vd. Effects of the February 6, 2023, Kahramanmaraş earthquake on structures in Kahramanmaraş city. 2023.
- [4] Ozturk M, Arslan MH, Korkmaz HH. Effect on RC buildings of 6 February 2023 Turkey earthquake doublets and new doctrines for seismic design. *Eng Fail Anal* 2023;153:107521.
- [5] Balun B. Assessment of seismic parameters for 6 February 2023 Kahramanmaraş earthquakes. *Struct Eng Mech* 2023;88:117–28.
- [6] Işık E, Avcil F, Büyüksaraç A, İzol R, Hakan Arslan M, Aksoylu C, vd. Structural damages in masonry buildings in Adıyaman during the Kahramanmaraş (Türkiye) earthquakes (Mw 7.7 and Mw 7.6) on 06 February 2023. *Eng Fail Anal* 2023;151.
- [7] Ozkula G, Dowell RK, Baser T, Lin JL, Numanoglu OA, Ilhan O, vd. Field reconnaissance and observations from the February 6, 2023, Turkey earthquake sequence. vol. 119. Springer Netherlands; 2023.
- [8] Ozturk M, Arslan MH, Dogan G, Ecemis AS, Arslan HD. School buildings performance in 7.7 Mw and 7.6 Mw catastrophic earthquakes in southeast of Turkey. *J Build Eng* 2023;79:107810.
- [9] Nemutlu ÖF, Balun B, Sarı A. 06 Şubat 2023 Kahramanmaraş Depremleri Kaynaklı Yapısal Hasarların Adıyaman İli Özelinde İncelenmesi. 3rd Int. Conf. Innov. Acad. Stud., Konya, Turkey: 2023, s. 353–61.
- [10] Işık E, Avcil F, Arkan E, Büyüksaraç A, İzol R, Topalan M. Structural damage evaluation of mosques and minarets in Adıyaman due to the 06 February 2023 Kahramanmaraş earthquakes. *Eng Fail Anal* 2023;151.
- [11] Büyüksaraç A, Işık E, Bektaş Ö, Avcil F. Achieving Intensity Distributions of 6 February 2023 Kahramanmaraş (Türkiye) Earthquakes from Peak Ground Acceleration Records. *Sustain* 2024;16.
- [12] Nemutlu ÖF, Sarı A, Balun B. 06 Şubat 2023 Kahramanmaraş Depremlerinde (Mw 7.7-Mw 7.6) Meydana Gelen Gerçek Can Kayıpları Ve Yapısal Hasar Değerlerinin Tahmin Edilen Değerler İle Karşılaştırılması. *Afyon Kocatepe Univ J Sci Eng* 2023;23:1222–34.
- [13] Shiwua AJ, Rutman Y. Assessment of Seismic Input Energy By Means of New Definition and the Application To Earthquake Resistant Design. *Archit Eng* 2016;1.
- [14] Çalım F, Güllü A, Yüksel E. Evaluation of Seismic Input Energy Distribution in Moment Frames. 14th Int Congr Adv Civ Eng 2021:1–6.
- [15] Manfredi G. Evaluation of seismic energy demand. *Earthq Eng Struct Dyn* 2001;30:485–99.

- [16] Chou C-C, Uang C-M. Establishing absorbed energy spectra-an attenuation approach. *Earthq Eng Struct Dyn* 2000;29:1441–55.
- [17] Hancıoğlu B. Yapıların Deprem Davranışının Enerji Esaslı Analizi. Yıldız Teknik Üniversitesi, 2009.
- [18] Decanini LD, Mollaioli F. An energy-based methodology for the assessment of seismic demand. *Soil Dyn Earthq Eng* 2001;21:113–37.
- [19] Erberik A, Sucuoğlu H. Seismic energy dissipation in deteriorating systems through low-cycle fatigue. *Earthq Eng Struct Dyn* 2004;33:49–67.
- [20] Benavent-Climent A. An energy-based damage model for seismic response of steel structures. *Pacific Conf Earthq Eng* 2007:1–6.
- [21] Chai YH. Incorporating low-cycle fatigue model into duration-dependent inelastic design spectra. *Earthq Eng Struct Dyn* 2005;34:83–96.
- [22] Ucar T. Computing input energy response of MDOF systems to actual ground motions based on modal contributions. *Earthq Struct* 2020;18:263–73.
- [23] Kostinakis K, Fontara IK, Athanatopoulou AM. Scalar Structure-Specific Ground Motion Intensity Measures for Assessing the Seismic Performance of Structures: A Review. *J Earthq Eng* 2018;22:630–65.
- [24] Moustafa A, Takewaki I. Characterization of earthquake ground motion of multiple sequences. *Earthq Struct* 2012;3:629–47.
- [25] Kamal M, Inel M. Correlation between ground motion parameters and displacement demands of mid-rise rc buildings on soft soils considering soil-structure-interaction. *Buildings* 2021;11.
- [26] Cao V Van, Ronagh HR. Correlation between seismic parameters of far-fault motions and damage indices of low-rise reinforced concrete frames. *Soil Dyn Earthq Eng* 2014;66:102–12.
- [27] Ozmen HB, Inel M. Damage potential of earthquake records for RC building stock. *Earthq Struct* 2016;10:1315–30.
- [28] Yang D, Pan J, Li G. Non-structure-specific intensity measure parameters and characteristic period of near-fault ground motions. *Dixiong. Earthq Eng Struct Dyn* 2009;38:1257–80.
- [29] Elenas A, Meskouris K. Correlation study between seismic acceleration parameters and damage indices of structures. *Eng Struct* 2001;23:698–704.
- [30] Poreddy LR, Pathapadu MK, Navyatha C, Vemuri J, Chenna R. Correlation analysis between ground motion parameters and seismic damage of buildings for near-field ground motions. *Nat Hazards Res* 2022;2:202–9.
- [31] SeismoSoft. SeismoSignal-Signal Processing of Strong Motion Data 2021.
- [32] AFAD. 06 Şubat 2023 Pazarcık (Kahramanmaraş) Mw 7.7 Elbistan (Kahramanmaraş) Mw 7.6 Depremlerine İlişkin Ön Değerlendirme Raporu. 2023.
- [33] TEC. Turkish Earthquake Code. Ankara, Turkey: 2018.
- [34] Yang D, Pan J, Li G. Non-structure-specific intensity measure parameters and characteristic period of near-fault ground motions. *Earthq Eng Struct Dyn* 2009;38:1257–80.
- [35] Riddell R, Garcia JE. Hysteretic energy spectrum and damage control. *Earthq Eng Struct Dyn* 2001;30:1791–816.
- [36] Akkar S, Özen Ö. Effect of peak ground velocity on deformation demands for SDOF systems. *Earthq Eng Struct Dyn* 2005;34:1551–71.
- [37] Chen G, Yang J, Liu Y, Kitahara T, Beer M. An energy-frequency parameter for earthquake ground motion intensity measure. *Earthq Eng Struct Dyn* 2023;52:271–84.

Classification of Microscopic Fungi Images Using Vision Transformers for Enhanced Detection of Fungal Infections

Abdurrahman GUMUS^{1*} 

¹ Izmir Institute of Technology, Faculty of Engineering, Electrical-Electronics Engineering, Izmir, Türkiye
Abdurrahman GUMUS ORCID No: 0000-0003-2993-5769

*Corresponding author: abdurrahmangumus@iyte.edu.tr

(Received: 24.02.2024, Accepted: 19.03.2024, Online Publication: 26.03.2024)

Keywords

Vision transformer, Swin transformer, Image classification, Fungal infection, Microscopic images

Abstract: Fungi play a pivotal role in our ecosystem and human health, serving as both essential contributors to environmental sustainability and significant agents of disease. The importance of precise fungi detection cannot be overstated, as it underpins effective disease management, agricultural productivity, and the safeguarding of global food security. This research explores the efficacy of vision transformer-based architectures for the classification of microscopic fungi images of various fungal types to enhance the detection of fungal infections. The study compared the pre-trained base Vision Transformer (ViT) and Swin Transformer models, evaluating their capability in feature extraction and fine-tuning. The incorporation of transfer learning and fine-tuning strategies, particularly with data augmentation, significantly enhances model performance. Utilizing a comprehensive dataset with and without data augmentation, the study reveals that the Swin Transformer, particularly when fine-tuned, exhibits superior accuracy (98.36%) over the ViT model (96.55%). These findings highlight the potential of vision transformer-based models in automating and refining the diagnosis of fungal infections, promising significant advancements in medical imaging analysis.

152

Mantar Enfeksiyonlarının Gelişmiş Tespiti İçin Görüntü Dönüştürücüleri Kullanılarak Mikroskopik Mantar Görüntülerinin Sınıflandırılması

Anahtar Kelimeler

Görüntü dönüştürücüler, Swin dönüştürücü, Görüntü sınıflandırma, Mantar enfeksiyonu, Mikroskopik görseller

Öz: Mantarlar, hem çevresel sürdürülebilirliğe temel katkıda bulunarak, hem de önemli hastalık etmenleri olarak hizmet ederek, ekosistemimizde ve insan sağlığında kritik bir rol oynamaktadırlar. Mantarların hassas olarak tespiti, etkili hastalık yönetimi, tarımsal verimlilik ve küresel gıda güvenliğinin korunması açısından önemlidir. Bu araştırma, çeşitli mantar türlerinin mikroskopik görüntülerinin sınıflandırılmasında görüntü dönüştürücü tabanlı mimarilerin etkinliğini keşfetmekte ve mantar enfeksiyonlarının tespitini geliştirmeyi amaçlamaktadır. Çalışma, önceden eğitilmiş temel görüntü dönüştürücü (ViT) ve Swin dönüştürücü modellerini karşılaştırmış, özellik çıkarma ve ince ayarlanma yeteneklerini değerlendirmiştir. Nakil öğrenme ve ince ayar stratejilerinin, özellikle veri artırımı ile birlikte, model performansını önemli ölçüde artırdığı belirlenmiştir. Veri artırımı yapılmış ve yapılmamış kapsamlı bir veri setini kullanarak yapılan çalışma, ince ayar yapıldığında Swin dönüştürücünün (%98,36), ViT modeline kıyasla (%96,55) üstün doğruluk sergilediğini ortaya koymuştur. Bu bulgular, mantar enfeksiyonlarının tanısını otomatikleştirmede ve iyileştirmede vizyon dönüştürücü tabanlı modellerin potansiyelini vurgulamakta, tıbbi görüntüleme analizinde önemli ilerlemeler vaat etmektedir.

1. INTRODUCTION

Fungi are critical to addressing global challenges, significantly impacting both ecosystems and human health. They exist in diverse forms, from complex multicellular organisms to single-celled entities, thriving mostly on land in soil or plant matter. Fungi's dual nature

is evident in their contributions to medicine, agriculture, and ecological processes through antibiotic production, food fermentation, and nutrient cycling, contrasted with their potential to cause diseases in humans, animals, and plants, leading to significant health and economic concerns [1–3].

Fungal infections pose a substantial challenge to global health, impacting millions of people each year across various demographics and geographic locations. Fungal diseases, ranging from minor infections like athlete's foot to severe systemic conditions, pose threats to humans, animals, and crops, impacting economic stability and food security [2,4–6]. Accurate fungi identification is crucial for enhancing human well-being, promoting effective disease treatment, optimizing agricultural practices, and preventing disease outbreaks. Early and precise diagnosis is key to effective treatment, reducing the risk of severe outcomes and ensuring appropriate care. Particularly, microscopic fungi are major culprits behind superficial infections, making precise identification crucial for successful treatment [7–9].

Traditional diagnostic methods, reliant on microscopy and culture techniques, face challenges in speed and specificity, leading to a demand for more advanced solutions. Automated fungi classification, leveraging deep learning algorithms, offers significant advantages in processing efficiency, diagnostic accuracy, and cost reduction. It enables rapid analysis of large image datasets, facilitating timely and informed decisions in healthcare and agriculture. Automated classification mitigates the risk of human error and supports research by providing consistent, reproducible results, which is critical for understanding disease patterns and contributing to public health efforts [7,8,10,11].

Recent advances in deep learning have shown promise in different fields [12–14], especially in medical image analysis [15–18]. The integration of deep learning techniques for fungal detection, especially through microscopic imaging, has demonstrated the ability to accurately identify various fungal species, highlighting the technology's potential in both medical and agricultural fields [8,9,19]. A multitude of studies have applied convolutional neural networks (CNNs) and, more recently, vision transformers, demonstrating their efficacy in distinguishing fungal species with high accuracy. These advances offer profound implications for understanding the morphological diversity of fungi and their impact on human health and food security [20–22].

For instance, the work of S. S. Gaikwad et al. highlights the application of CNN models to categorize fungi affecting apple plant leaves, achieving an impressive 88.9% accuracy using images from an accessible plant pathology dataset. This study illustrates the potential of deep learning in agricultural disease management by facilitating early detection and treatment of fungal infections in crops [20]. Similarly, L. Picek et al. introduced the Danish Fungi 2020 dataset, a comprehensive collection aiding in the fine-grained classification of fungal species. Their research underscores the challenges posed by highly unbalanced class distributions and complex class hierarchies in fungal identification. By comparing CNN models and vision transformers, they demonstrated the superior performance of vision transformers, with an accuracy of 80.45% and a notable reduction in classification error,

showcasing the potential of these models in handling complex, fine-grained classification tasks [21]. Koo et al. developed a deep learning model with a regional convolutional neural network to detect fungal hyphae in microscopic images, achieving high sensitivity (95.2% for 100× and 99% for 40× magnification models) and specificity (100% for 100× and 86.6% for 40× magnification models), suggesting significant improvements over conventional fungal infection diagnostics [23]. Gao et al. (2021) developed an automated microscope coupled with a deep learning model, primarily ResNet-50, to enhance fungal detection in dermatological samples. The system demonstrated high sensitivity (99.5% for skin, 95.2% for nails) and specificity (91.4% for skin, 100% for nails), showcasing the potential to significantly improve efficiency and accuracy in fungal diagnostics in dermatology [24]. In another vein, M. A. Rahman et al. explored the classification of pathogenic fungi using deep CNN models across several well-known architectures. Their study, which achieved top accuracy of 65.35% with the DenseNet model, underscores the diverse capabilities of CNNs in processing microscopic images to distinguish among 89 different fungal genera, thereby contributing to faster and more accurate diagnostic processes [22].

C. J. P. Sopo, F. Hajati, and S. Gheisari's work further exemplifies the role of deep learning in fungi classification, experimenting with different CNN models and training approaches. Their findings, particularly the high performance of the VGG16 model under transfer learning, highlight the effectiveness of leveraging pre-trained models to enhance classification accuracy in specialized domains such as mycology [25]. Nawarathne et al. explored the classification of fungi images using various CNNs, addressing challenges like class imbalance through data augmentation and employing multiple preprocessing techniques. By testing thirteen pre-trained CNN models across different image resolutions, the research finds the BigTransfer (BiT) model, particularly with a mix of original and high-resolution images, to outperform others with an accuracy of 87.32%, with optimal precision, recall, and F1-score [26]. Cinar et al. investigated the application of deep learning techniques for detecting fungal infections from microscopic images, employing CNNs and transfer learning for accurate classification of various fungal species. Through data augmentation and fine-tuning, the study achieves significant improvements in accuracy as 97.19%, showcasing the potential of deep learning in enhancing diagnostic processes for fungal infections [27]. These studies exemplify the continuous evolution of methodologies in the classification and identification of fungal infections, promising to improve diagnostic processes through increased efficiency and reduced costs, with profound implications for global health, agriculture, and ecological preservation.

Our study delves into the application of deep learning techniques, specifically leveraging vision transformers within a framework that utilizes the DeFungi dataset, transfer learning, and data augmentation to enhance the accuracy of fungal detection from microscopic images.

The aim is to improve the identification and classification of fungal infections, thereby supporting clinical decision-making with rapid, accurate, and scalable diagnostic tools.

The remaining of the paper is organized as follows. In Section 2, the details of the methodology are given, such as dataset, data augmentation, vision transformer architectures, transfer learning, and experimental details. In Section 3, the results of the proposed methods and corresponding discussions are presented. The conclusion of the study is reported in the last section.

2. MATERIAL AND METHOD

In the Methodology section, an approach employing vision transformers for classifying fungi images into five distinct categories is detailed. This section describes the process of dataset selection and preparation, the application of data augmentation techniques to enhance model performance, the experimental setup, and the architecture of the vision transformers utilized. Additionally, the application of transfer learning and fine-tuning processes aimed at enhancing the accuracy of the model is described.

2.1. Dataset

The DeFungi dataset utilized for this study was acquired from the University of California Irvine (UCI) Machine Learning Repository [25]. The images in the dataset were provided by a mycological laboratory in Colombia. The dataset contains images depicting superficial fungal infections attributed to yeasts, molds, and dermatophyte fungi. These images underwent a detailed classification process, being manually sorted into five distinct categories with the assistance of domain experts to ensure the categorization's accuracy and relevance. Subsequently, automated coding procedures were employed to crop and patch these images. The finalized dataset includes a total of 9,114 images, distributed across five categories. The fungi image samples from the dataset are shown in Figure 1.

2.2. Data Augmentation

Data augmentation was implemented to enhance the diversity of the training dataset, especially to increase the representation of underrepresented classes. The augmentation aimed to balance the number of images across all categories, as depicted in Table 1, which illustrates the image counts in each class before and after augmentation. The augmentation procedure involved four specific transformations applied to the images in the dataset such as vertical flip, horizontal flip, and 45-degree rotations.

For each class (H1, H2, H3, H5, and H6), the number of images was augmented to match a target value. The target for classes H2, H3, H5, and H6 was set to approximately match the initial count of H1, which had the most images at 4404.

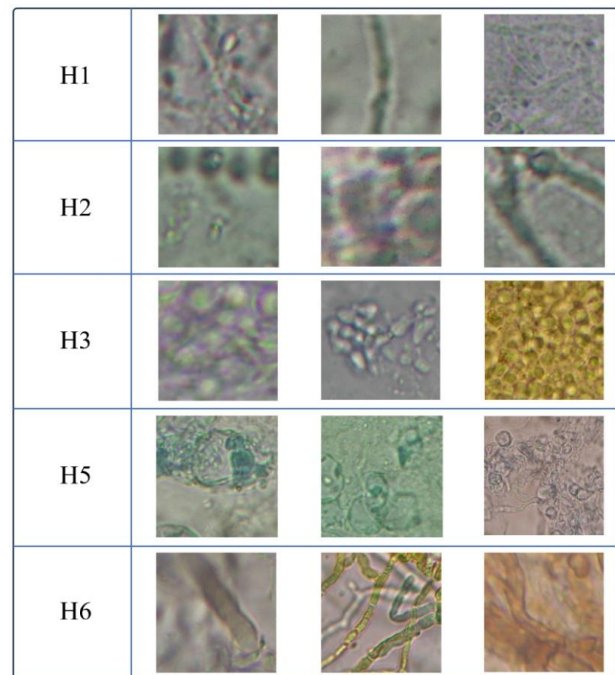


Figure 1. Representative images illustrating five distinct classes within the fungi dataset. H1) Tortuous septate hyaline hyphae (TSH), H2) Beaded arthroconidial septate hyaline hyphae (BASH), H3) Groups or mosaics of arthroconidia (GMA), H5) Septate hyaline hyphae with chlamydoconidia (SHC), and H6) Broad brown hyphae (BBH).

This target was selected to ensure that each class had a similar number of images, thus preventing class imbalance that could bias the model training. The augmentation script dynamically generated the required number of images by applying the aforementioned transformations consecutively to existing images until the target count was reached. The generated images were saved with a unique naming convention indicating the class, the type of transformation, and a sequence number to ensure uniqueness. This data augmentation process allowed the creation of additional training data, which was essential for training robust models capable of generalizing well across different presentations of fungal classes. It increased the total number of images in the dataset from 9,114 to 22,004, significantly enriching the dataset and providing more variability for model training.

Table 1. Number of images for different classes before and after data augmentation.

Classes	Original Data	With Data Augmentation
H1	4404	4404
H2	2334	4400
H3	819	4400
H5	818	4400
H6	739	4400
Total	9114	22004

2.3. Vision Transformer Architectures

In this study, we explore the application of vision transformer models for image classification tasks. Vision transformers represent an adaptation of the transformer architecture, originally designed for natural language processing [28], to the domain of computer vision.

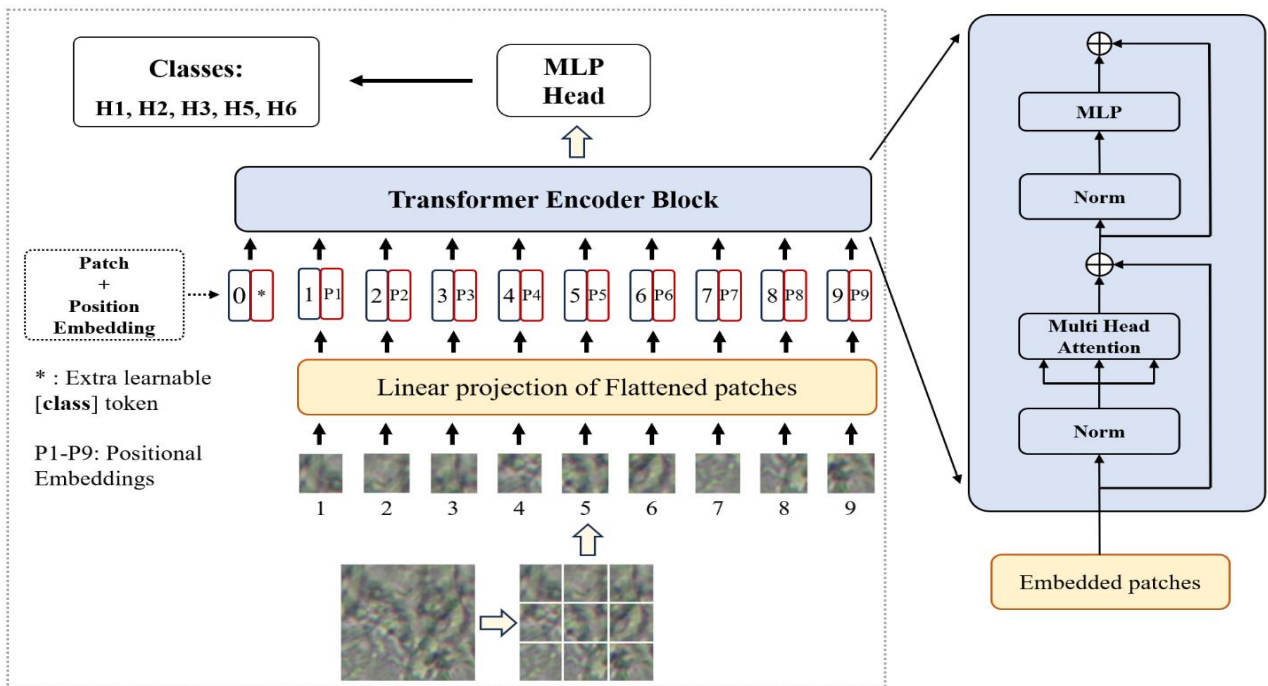


Figure 2. Schematic representation of the Vision Transformer (ViT) model utilized in the study, illustrating the transformer architecture adapted for the task of classifying fungi images into five categories, highlighting the sequence of image patches, positional embeddings, multi-head attention, and the fully connected layers.

Unlike traditional convolutional neural networks (CNNs), vision transformers divide an image into a series of patches and process these patches as a sequence, employing self-attention mechanisms to capture global dependencies within the image [29,30].

In the first model, the base Vision Transformer (ViT) model is utilized [29]. This approach segments an image into fixed-size patches, linearizes these patches, and then processes them through a series of transformer blocks that include multi-headed self-attention and position-wise fully connected layers. The base ViT model treats the image as a sequence of patches to learn representations, relying on the self-attention mechanism to weigh the importance of each patch relative to others in the image. The architecture of the ViT model is shown in Figure 2.

Additionally, the Swin Transformer is employed, which is a variation of the standard ViT that introduces a hierarchical structure through the use of shifted windows [31]. This design allows the Swin Transformer to efficiently manage computational resources by focusing on smaller sections of the image at lower levels of the hierarchy before progressively merging these sections at

higher levels. The Swin Transformer's unique approach to partitioning the image and processing it in stages enables it to adaptively focus on different scales of image features, potentially offering advantages in capturing both local and global image contexts. Figure 3 shows the Swin Transformer architecture.

2.4. Transfer Learning and Fine-Tuning

Transfer learning is a machine learning methodology where a model trained on one task is repurposed for a second related task [32]. This approach is often utilized in image classification, with models pre-trained on large and diverse datasets, such as ImageNet, to leverage learned features and patterns applicable across various visual domains [33]. By starting with models that have already learned a broad representation of images, the training process can be accelerated, higher performance achieved with less labeled data, and model generalization improved.

Fine-tuning represents a specific application of transfer learning, where the pre-trained model is further adjusted to suit the target task more closely. This process involves unfreezing some or all of the layers of the pre-trained

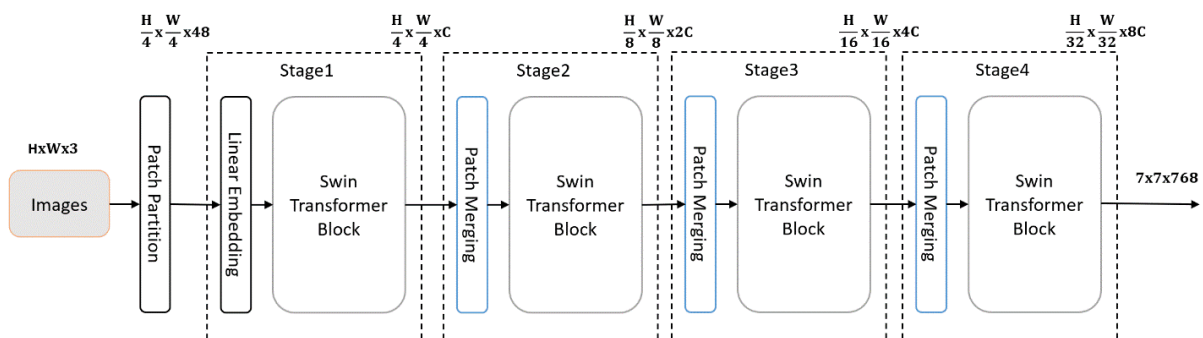


Figure 3. Illustration of the Swin Transformer utilized for image classification, detailing the mechanism of shifted windows and embedded patch processing for feature extraction, as applied to the categorization of complex image data.

model and continuing the training process on the new dataset. The extent of the fine-tuning can vary, from adjusting just the final layers to retraining the entire network. This allows the model to adapt the generic features learned from the initial dataset to the nuances of the new task, enhancing performance on the target domain [32,34].

In this study, both the base ViT and Swin Transformer models were employed, leveraging their pre-training on the ImageNet dataset [35] to harness a rich feature set relevant to the image classification tasks at hand. Two principal approaches were taken: feature extraction and fine-tuning. In feature extraction, the pre-trained models were used as feature extractors. Images were passed through the models to obtain high-level feature representations from the layers preceding the output layer. These features were then used as input to fully connected layers designed for the classification tasks in this study. This method benefited from the deep and complex representations learned by the models without necessitating extensive retraining. The second approach involved fine-tuning the pre-trained models on the specific fungi dataset of this study. This involved making minor adjustments to the model parameters to better align with the specific features and distributions of the task. After fine-tuning, features extracted from these adjusted models were fed into fully connected layers for classification.

2.5. Experimental Details

The Python programming language was used for the preprocessing and training operations. The vision transformer models are implemented in the PyTorch framework. Computational experiments were performed on a workstation with the following properties: Intel i5-12600k CPU, 64 GB RAM, and NVIDIA RTX 3090 Ti 24 GB GPU.

Two distinct approaches for image classification were implemented utilizing the base ViT and Swin Transformer models. The first approach involves fine-tuning, where the pretrained vision transformers are adapted by replacing their classification head with a new fully connected layer tailored to our specific number of output classes. This method allows the entire network to learn and adjust to our dataset during training. The second approach is feature extraction, where vision transformer models are utilized to generate feature representations of the images, effectively freezing the pretrained layers and only training a series of new fully connected layers for classification. This custom network consists of dense layers with ReLU activations, batch normalization, and dropout for regularization, concluding with a softmax layer for output. The training involved optimizing these layers with an Adam optimizer and categorical cross-entropy loss, using the features extracted from vision transformers as input. Hold-out validation is utilized to assess the performance of image classification models. Data is allocated as 70% for training, 15% for validation, and the remaining 15% for testing.

To assess the performance of our image classification models, four metrics are employed: accuracy, precision, recall, and F1-score. Accuracy measures the proportion of correctly identified images across the dataset, providing an overall effectiveness of the model. Precision quantifies the accuracy of positive predictions, indicating the model's ability to minimize false positives. Recall assesses the model's capability to correctly identify all relevant instances, reflecting its sensitivity. F1-score combines precision and recall into a single metric, offering a balanced view of the model's performance by accounting for both the precision's and recall's contributions.

3. RESULTS AND DISCUSSION

The detection of fungi plays a pivotal role in addressing key global challenges, impacting both human health and ecosystems. Fungi, which range from simple single-celled organisms to complex multicellular forms, are significant for their contributions to medicine, agriculture, and ecological balance, but also pose serious health and economic risks through disease [1–3]. Accurate identification of fungi is essential for effective disease management, enhancing agricultural efficiency, and safeguarding food security. Traditional diagnostic methods often fall short in speed and accuracy, underscoring the need for advanced, automated classification techniques. Leveraging deep learning-based algorithms for fungi detection promises greater diagnostic precision, efficiency, and cost-effectiveness, crucial for early and accurate diagnosis, ultimately supporting healthcare, agriculture, and ongoing research efforts [7–9].

In this study, the efficacy of vision transformer models for classifying medical images, specifically for fungi diagnosis, was assessed. The findings suggest that vision transformer models are potentially more adept at capturing detailed and nuanced features from complex medical images than conventional approaches, indicating their capacity to improve diagnostic accuracy. This paper outlines the model's accuracy rates, feature extraction capabilities, and the outcomes of fine-tuning, alongside discussing the progress in fungi image classification facilitated by the use of vision transformer models.

The comparison between Convolutional Neural Networks (CNNs) and vision transformer models reveals unique strengths and challenges for each technology. CNNs excel in identifying spatial features in images due to their strong image analysis capabilities and are more computationally efficient, particularly with smaller datasets or images. However, they face challenges in modeling long-range dependencies, though there are methods to address this issue. Thanks to their localized processing and shared weight architecture, CNNs typically offer better generalization on smaller datasets. Conversely, vision transformers are capable of identifying complex global patterns by analyzing images as a whole, which requires more computational resources, especially for processing larger images.

Table 2. Model performance metrics for feature extraction and fine-tuning. All values are percentages.

Data Augmentation	Method	Model	Accuracy	Precision	Recall	F1-Score
No	Feature Extraction	Swin Transformer	82.32	82.43	82.32	81.40
No	Feature Extraction	ViT	86.70	86.56	86.70	86.48
No	Fine Tuning	Swin Transformer	90.87	90.84	90.87	90.80
No	Fine Tuning	ViT	88.39	88.44	88.39	88.35
Yes	Feature Extraction	Swin Transformer	92.61	92.71	92.61	92.57
Yes	Feature Extraction	ViT	94.34	94.35	94.34	94.33
Yes	Fine Tuning	Swin Transformer	98.36	98.38	98.36	98.36
Yes	Fine Tuning	ViT	96.55	96.55	96.55	96.54

Their use of self-attention mechanisms allows them to effectively handle long-range dependencies. Additionally, vision transformers tend to scale better with larger datasets compared to CNNs [30,36–38].

The architectural distinctions between the models play a pivotal role in their ability to manage the complexities inherent in various classification challenges. The base ViT model, with its straightforward approach to treating images as sequences of patches, demonstrates remarkable efficiency in capturing global image features. However, its performance indicates potential limitations in scenarios requiring a nuanced understanding of local features due to its uniform treatment of image patches. In contrast, the Swin Transformer's hierarchical, shifted window approach introduces a level of adaptability and efficiency not present in the base ViT model. By processing images in stages and allowing for variable-sized representation, the Swin Transformer exhibits a more nuanced capability to balance between local and global feature recognition. This structural difference notably enhances the model's performance on complex image classification tasks, where the interplay of local and global image features is critical. A key advantage of the Swin Transformer is its linear computational complexity, achieved by applying self-attention in a localized manner. On the other hand, the ViT model faces quadratic computational complexity due to its global application of self-attention across all patches.

The comprehensive results presented in Table 2, in conjunction with the visual examples from Figure 1, shed light on the ability of ViT and Swin Transformer models to handle the complexity and variability inherent in microscopic fungi images. The distinct textural and morphological features across the five classes, as depicted in Figure 1, underscore the challenges faced in accurate fungi classification.

When the models were not fine-tuned nor exposed to data augmentation, the ViT model displayed a commendable aptitude for feature extraction with an accuracy of 86.70%. This suggests an innate capability of ViT model to discern proper features even in unaltered datasets. The Swin Transformer lagged slightly behind with an 82.32% accuracy rate. However, once fine-tuned, the Swin Transformer's accuracy improved remarkably to 90.87%, outperforming the fine-tuned ViT model's accuracy of 88.39%.

This improvement hints at the Swin Transformer's ability to adapt its architecture more effectively upon learning from the dataset's specific characteristics.

The introduction of data augmentation substantially increased the number of images across all categories, with the total image count rising from 9,114 to 22,004. This enhancement in dataset volume, particularly for underrepresented classes such as H3, H5, and H6, has contributed to the notable performance gains observed in the models. The feature extraction capacity of the Swin Transformer enhanced to 92.61% accuracy, while the ViT model reached 94.34%, indicating a significant positive impact of data augmentation in preparing the models to recognize and generalize from the diversified visual data. Notably, the fine-tuning of both models with data augmentation yielded the most impressive outcomes, with the Swin Transformer reaching an accuracy of 98.36% and the ViT model an accuracy of 96.55%. These results reflect the models' enhanced ability to classify complex patterns observed in the varied images, achieving high precision, recall, and F1-scores uniformly across classes.

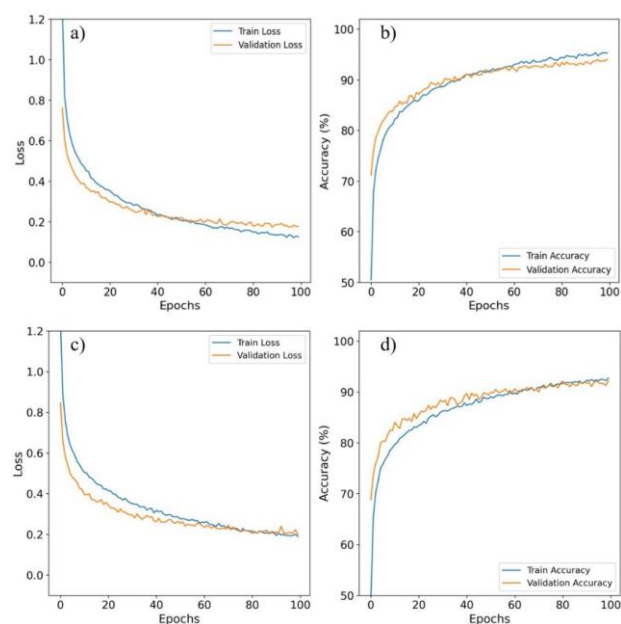


Figure 4. Training performance comparison for the ViT and Swin Transformer models during the feature-extraction approach with augmented data. Subfigures (a) and (b) illustrate the accuracy and loss plots for the ViT model, while subfigures (c) and (d) show the same for the Swin Transformer model.

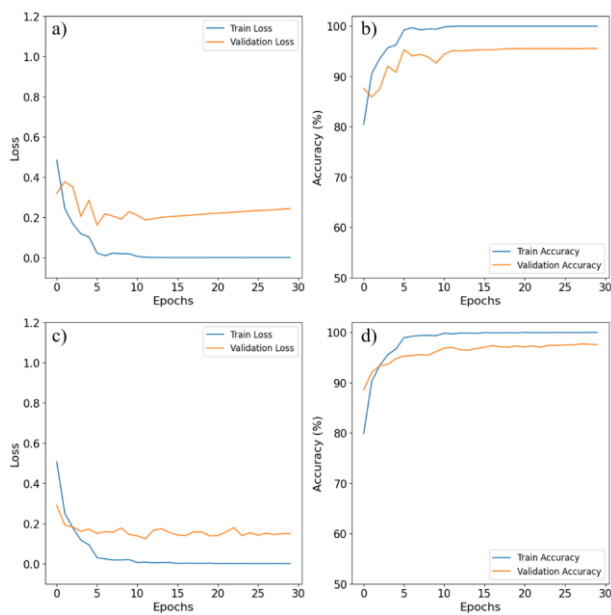


Figure 5. Training performance comparison for the ViT and Swin Transformer models during the fine-tuning approach with augmented data. Subfigures (a) and (b) depict the accuracy and loss plots for the ViT model, whereas subfigures (c) and (d) present these plots for the Swin Transformer model.

The use of transfer learning and fine-tuning in this study is justified by their demonstrated ability to enhance model performance, especially in situations with limited labeled data. By beginning with models that have learned comprehensive visual representations, the need for extensive computational resources and time required to train complex models from scratch is reduced. The nuanced textural differences and class-specific features highlighted in Figure 1 may explain the models' improved performance when fine-tuned with data augmentation, as the process likely aids the models in learning to differentiate subtle variations and complex patterns within and across the classes.

Figures 4 and 5 display the training performance of the ViT and Swin Transformer models with augmented data. In feature extraction (Figure 4), both models exhibit high validation accuracy, with ViT reaching convergence swiftly, indicative of efficient feature transfer. For fine-tuning (Figure 5), the Swin Transformer slightly outperforms ViT in validation accuracy, suggesting a better adaptation to the fungi classification task. Figure 6 depicts confusion matrices for ViT and Swin Transformer models with augmented data. Both models exhibit high classification accuracy across all classes, with improved precision upon fine-tuning, as shown by denser diagonals in Figures 6c and 6d. Fine-tuning particularly enhances the Swin Transformer's ability to distinguish between the more confusable classes.

In conclusion, the exemplary performance of the Swin Transformer and ViT models, especially when fine-tuned with augmented data, demonstrates their robustness and adaptability in classifying high-variability microscopic images. Such findings are promising for the field of automated medical diagnosis, suggesting that with sufficient training and data enhancement, these models can potentially serve as

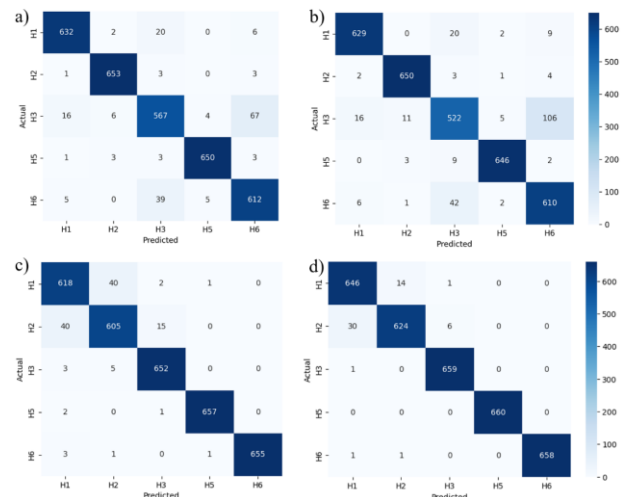


Figure 6. Confusion matrices demonstrating classification accuracy with augmented data for (a, c) the ViT model and (b, d) the Swin Transformer model, with (a, b) illustrating results from feature extraction approach and (c, d) fine-tuning approach, respectively.

reliable tools for accurate fungi classification, ultimately aiding in the prompt and precise diagnosis of fungal diseases.

4. CONCLUSION

Understanding the intricate role of fungi within our ecosystems and their impact on human health emphasizes the need for nuanced approaches to their detection and management. The development of advanced diagnostic tools stands as a critical step towards mitigating the risks fungi pose, while also leveraging their beneficial properties for environmental and medical applications. This research underscores the transformative potential of employing vision transformer-based models in the classification of microscopic fungi images. The Swin Transformer model, especially with fine-tuning and data augmentation, emerges as particularly effective, demonstrating a notable accuracy improvement (98.36%). These results not only advocate for the integration of vision transformer technologies in medical diagnostics but also mark a promising avenue for future research. Further exploration into optimizing these models for broader diagnostic applications and investigating their performance in diverse medical imaging contexts could lead to significant enhancements in automated disease detection, offering a new horizon for precision medicine and healthcare.

REFERENCES

- [1] Lange L. The importance of fungi and mycology for addressing major global challenges. *IMA Fungus* 2014;5:463–71. <https://doi.org/10.5598/imafungus.2014.05.02.10>.
- [2] Almeida F, Rodrigues ML, Coelho C. The still underestimated problem of fungal diseases worldwide. *Front Microbiol* 2019;10:1–5. <https://doi.org/10.3389/fmicb.2019.00214>.
- [3] Ravikant KT, Gupte S, Kaur M. A Review on Emerging Fungal Infections and Their Significance.

- J Bacteriol Mycol Open Access 2015;1:39–41. <https://doi.org/10.15406/jbmoa.2015.01.00009>.
- [4] Brown GD, Denning DW, Gow NAR, Levitz SM, Netea MG, White TC. Hidden killers: Human fungal infections. *Sci Transl Med* 2012;4:1–9. <https://doi.org/10.1126/scitranslmed.3004404>.
- [5] Grosjean P, Weber R. Fungus balls of the paranasal sinuses: A review. *Eur Arch Oto-Rhino-Laryngology* 2007;264:461–70. <https://doi.org/10.1007/s00405-007-0281-5>.
- [6] Hernandez H, Martinez LR. Relationship of environmental disturbances and the infectious potential of fungi. *Microbiol (United Kingdom)* 2018;164:233–41. <https://doi.org/10.1099/mic.0.000620>.
- [7] Kristensen K, Ward LM, Mogensen ML, Cichosz SL. Using image processing and automated classification models to classify microscopic gram stain images. *Comput Methods Programs Biomed Updat* 2023;3:100091. <https://doi.org/10.1016/j.cmpbup.2022.100091>.
- [8] Zhang Y, Jiang H, Ye T, Juhas M. Deep Learning for Imaging and Detection of Microorganisms. *Trends Microbiol* 2021;29:569–72. <https://doi.org/10.1016/j.tim.2021.01.006>.
- [9] Kumar S, Arif T, Alotaibi AS, Malik MB, Manhas J. Advances Towards Automatic Detection and Classification of Parasites Microscopic Images Using Deep Convolutional Neural Network: Methods, Models and Research Directions. *Arch Comput Methods Eng* 2023;30:2013–39. <https://doi.org/10.1007/s11831-022-09858-w>.
- [10] Tahir MW, Zaidi NA, Rao AA, Blank R, Vellekoop MJ, Lang W. A fungus spores dataset and a convolutional neural network based approach for fungus detection. *IEEE Trans Nanobioscience* 2018;17:281–90. <https://doi.org/10.1109/TNB.2018.2839585>.
- [11] Mital ME, Ruzcko Tobias R, Villaruel H, Maningo JM, Kerwin Billones R, Vicerra RR, et al. Transfer learning approach for the classification of conidial fungi (genus aspergillus) thru pre-trained deep learning models. *IEEE Reg 10 Annu Int Conf Proceedings/TENCON* 2020;2020-Novem:1069–74. <https://doi.org/10.1109/TENCON50793.2020.9293803>.
- [12] Mohammad-Rahimi H, Rokhshad R, Bencharit S, Krois J, Schwendicke F. Deep learning: A primer for dentists and dental researchers. *J Dent* 2023;130:104430. <https://doi.org/10.1016/j.jdent.2023.104430>.
- [13] Demir HO, Parlat SZ, Gumus A. Ethereum Blockchain Smart Contract Vulnerability Detection Using Deep Learning. *ISAS 2023 - 7th Int Symp Innov Approaches Smart Technol Proc* 2023:1–5. <https://doi.org/10.1109/ISAS60782.2023.1039179>.
- [14] Kayan CE, Yuksel Aldogan K, Gumus A. Intensity and phase stacked analysis of a Φ -OTDR system using deep transfer learning and recurrent neural networks. *Appl Opt* 2023;62:1753. <https://doi.org/10.1364/ao.481757>.
- [15] Ahmad A, Saraswat D, El Gamal A. A survey on using deep learning techniques for plant disease diagnosis and recommendations for development of appropriate tools. *Smart Agric Technol* 2023;3:100083. <https://doi.org/10.1016/j.atech.2022.100083>.
- [16] Aslani S, Jacob J. Utilisation of deep learning for COVID-19 diagnosis. *Clin Radiol* 2023;78:150–7. <https://doi.org/10.1016/j.crad.2022.11.006>.
- [17] Duzyel O, Catal MS, Kayan CE, Sevinc A, Gumus A. Adaptive resizer-based transfer learning framework for the diagnosis of breast cancer using histopathology images. *Signal, Image Video Process* 2023;17:4561–70. <https://doi.org/10.1007/s11760-023-02692-y>.
- [18] Müjdat Tiryaki V. Mass segmentation and classification from film mammograms using cascaded deep transfer learning. *Biomed Signal Process Control* 2023;84:104819. <https://doi.org/10.1016/j.bspc.2023.104819>.
- [19] Zieliski B, Sroka-Oleksiak A, Rymarczyk D, Piekarczyk A, Brzychczy-Woch M. Deep learning approach to describe and classify fungi microscopic images. *PLoS One* 2020;15:1–16. <https://doi.org/10.1371/journal.pone.0234806>.
- [20] Gaikwad SS, Rumma SS, Hangarge M. Fungi Classification using Convolution Neural Network. *Turkish J Comput Math Educ* 2021;12:4563–9.
- [21] Picek L, Sulc M, Matas J, Jeppesen TS, Heilmann-Clausen J, Lassoe T, et al. Danish Fungi 2020 - Not Just Another Image Recognition Dataset. *Proc - 2022 IEEE/CVF Winter Conf Appl Comput Vision, WACV* 2022 2022:3281–91. <https://doi.org/10.1109/WACV51458.2022.00334>.
- [22] Rahman MA, Clinch M, Reynolds J, Dangott B, Meza Villegas DM, Nassar A, et al. Classification of fungal genera from microscopic images using artificial intelligence. *J Pathol Inform* 2023;14. <https://doi.org/10.1016/j.jpi.2023.100314>.
- [23] Koo T, Kim MH, Jue MS. Automated detection of superficial fungal infections from microscopic images through a regional convolutional neural network. *PLoS One* 2021;16:1–11. <https://doi.org/10.1371/journal.pone.0256290>.
- [24] Gao W, Li M, Wu R, Du W, Zhang S, Yin S, et al. The design and application of an automated microscope developed based on deep learning for fungal detection in dermatology. *Mycoses* 2021;64:245–51. <https://doi.org/10.1111/myc.13209>.
- [25] Sopo C, Hajati F, Gheisari S. Defungi: Direct mycological examination of microscopic fungi images. *Arxiv* 2021. <https://doi.org/10.48550/arXiv.2109.07322>.
- [26] Nawarathne UMMPK, Kumari HMNS. Classification of Fungi Images Using Different Convolutional Neural Networks. *2023 8th Int Conf Inf Technol Res* 2023.
- [27] Cinar I, Taspinar YS. Detection of Fungal Infections from Microscopic Fungal Images Using Deep Learning Techniques. *Proc Int Conf Adv Technol* 2023. <https://doi.org/10.58190/icat.2023.12>.

- [28] Vaswani A, Shazeer N, Parmar N, Uszkoreit J, Jones L, Gomez AN, et al. Attention Is All You Need. *Adv Neural Inf Process Syst* 2017;30.
- [29] Dosovitskiy A, Beyer L, Kolesnikov A, Weissenborn D, Zhai X, Unterthiner T, et al. An image is worth 16x16 words: Transformers for image recognition at scale. *ICLR 2021 - 9th Int. Conf. Learn. Represent.*, 2021.
- [30] Khan S, Naseer M, Hayat M, Zamir SW, Khan FS, Shah M. Transformers in Vision: A Survey. *ACM Comput Surv* 2022;54. <https://doi.org/10.1145/3505244>.
- [31] Liu Z, Lin Y, Cao Y, Hu H, Wei Y, Zhang Z, et al. Swin transformer: Hierarchical vision transformer using shifted windows. *2021 IEEE/CVF Int Conf Comput Vis* 2021.
- [32] Iman M, Arabnia HR, Rasheed K. A Review of Deep Transfer Learning and Recent Advancements. *Technologies* 2023;11:1–14. <https://doi.org/10.3390/technologies11020040>.
- [33] Zhuang F, Qi Z, Duan K, Xi D, Zhu Y, Zhu H, et al. A Comprehensive Survey on Transfer Learning. *Proc IEEE* 2021;109:43–76. <https://doi.org/10.1109/JPROC.2020.3004555>.
- [34] Öztürk C, Taşyürek M, Türkdamar MU. Transfer learning and fine-tuned transfer learning methods' effectiveness analyse in the CNN-based deep learning models. *Concurr Comput Pract Exp* 2023;35:1–26. <https://doi.org/10.1002/cpe.7542>.
- [35] Deng J, Dong W, Socher R, Li L-J, Kai Li, Li Fei-Fei. ImageNet: A large-scale hierarchical image database. *2009 IEEE Conf Comput Vis Pattern Recognit* 2010:248–55. <https://doi.org/10.1109/cvpr.2009.5206848>.
- [36] Mauricio J, Domingues I, Bernardino J. Comparing Vision Transformers and Convolutional Neural Networks for Image Classification: A Literature Review. *Appl Sci* 2023;13. <https://doi.org/10.3390/app13095521>.
- [37] Liu Y, Zhang Y, Wang Y, Hou F, Yuan J, Tian J, et al. A Survey of Visual Transformers. *IEEE Trans Neural Networks Learn Syst* 2023;PP:1–21. <https://doi.org/10.1109/TNNLS.2022.3227717>.
- [38] Jamil S, Jalil Piran M, Kwon OJ. A Comprehensive Survey of Transformers for Computer Vision. *Drones* 2023;7:1–27. <https://doi.org/10.3390/drones7050287>.

Use of New Natural Dyes Extracted from Different Sections of *Salvia urica* in Dye-Sensitized Solar Cells

Fehmi ASLAN^{1*}, Halil İbrahim YAMAÇ²

¹ MTU University, Yeşilyurt MYO, Department of Motor Vehicles and Transportation Technologies, Malatya, Türkiye

² Fırat University, Technologies Faculty, Department of Mechatronics Engineering, Elazığ, Türkiye
Fehmi ASLAN ORCID No: 0000-0002-5304-0503
Halil İbrahim YAMAÇ ORCID No: 0000-0002-4628-0971

*Corresponding author: fehmi.aslan@ozal.edu.tr

(Received: 5.01.2024, Accepted: 21.03.2024, Online Publication: 26.03.2024)

Keywords

Dye-sensitized solar cells, Natural dyes, Photovoltaic performance

Abstract: In this study, natural dyes that were obtained from the branches, flowers and leaves of *Salvia urica* were utilized as sensitizers in TiO₂-based dye-sensitized solar cells (DSSCs). XRD and FE-SEM were used to analyze the crystal structure and morphological properties of the produced TiO₂ nanopowders, respectively. The optical properties of natural dyes extracted from the *Salvia urica* plant were investigated by UV-vis spectroscopy. Functional groups in natural dyes were detected by FTIR spectroscopy, while DSSCs were evaluated for photovoltaic performance and electrochemical impedance. The findings confirmed that the dye obtained from the flower absorbs a wider wavelength of light in the visible region. Among all other natural sensitizers, the highest power conversion efficiency was seen in the flower dye-sensitized cell. This situation was explained by the very strong interaction of the carboxyl/hydroxyl groups and the TiO₂ surface. The efficiencies of DSSCs sensitized with flower, branch and leaf dye of *Salvia urica* were 0.33%, 0.28%, and 0.19%, respectively.

Salvia urica'nın Farklı Kısımlarından Ekstrakte Edilen Boyaların Boya Duyarlı Güneş Pillerinde Kullanımı

Anahtar

Kelimeler

Boya duyarlı güneş pili, Doğal boyalar, Fotovoltaik performans

Öz: Bu çalışmada TiO₂ esaslı boya duyarlı güneş pillerinde hassaslaştırıcı olarak *Salvia urica*'nın yapraklarından, çiçeklerinden ve dallarından faydalanıldı. Sentezlenen TiO₂ nano tozlarının kristal yapısını ve morfolojik özelliklerini analiz etmek için sırasıyla XRD ve FE-SEM kullanıldı. *Salvia urica* bitkisinden ekstrakte edilen doğal boyaların optik özellikleri UV-vis spektroskopisiyle incelendi. Boya duyarlı güneş pilleri fotovoltaik performans ve elektrokimyasal empedans açısından incelenirken doğal boyalardaki fonksiyonel gruplar FTIR spektroskopisiyle tespit edildi. Bulgular, çiçekten elde edilen boyanın görünür bölgede ışığı daha geniş bir dalga boyunda absorbe ettiğini doğruladı. Diğer tüm doğal hassaslaştırıcılar arasında en yüksek güç dönüşüm verimi çiçek boyasıyla duyarlılaştırılmış hücrede görüldü. Bu durum karboksil/hidroksil grupları ile TiO₂ yüzeyinin çok güçlü etkileşimi ile açıklandı. *Salvia urica*'nın çiçek, dal ve yaprak boyası ile duyarlı hale getirilen DSSC'lerin verimliliği sırasıyla % 0,33, % 0,28 ve % 0,19 bulundu.

1. INTRODUCTION

Rapidly increasing industrialization brings energy demands to higher levels [1]. All countries have turned to alternative energy sources for meeting their increasing energy demands [2]. One of the main causes of this is that fossil fuels will run out shortly and pose a risk to the environment [3]. This viewpoint emphasizes how important environmentally friendly and renewable

sources of energy are [4]. Particularly alluring are photovoltaic systems, which directly transform solar energy through electrical power [5]. Due to their high efficiency, solar cells made with silicon achieved an important milestone on the path to commercialization in these circumstances [6]. Many developed and developing countries use these silicon-based photovoltaic modules extensively and produce energy. However, as silicon-based solar cells are costly, studies on eco-friendlier and

more economical solar cell technologies have accelerated [7]. Thanks to their low cost and easy production processes, dye-sensitized solar cells are pivotal to scientific and technological developments within this framework [8]. As a result of intensive studies on DSSCs, power conversion efficiencies of over 15% have been achieved [9]. This is an important step toward the commercialization of DSSCs in a short span time [10]. Researchers are attempting to improve the power conversion performance of DSSCs by focusing on the photonode layer, dye, redox electrolyte, and counter electrode because the efficiency of these devices is still below the level that is desired [11]. The components of a DSSC are a dye molecule, counter electrode, electrolyte solution, and photoanode layer [12]. The mechanism of operation of a typical DSSC seems quite simple, as shown in Fig. 1. Sensitizing molecules of dye absorb the photon flux emitted on the exterior of TiO_2 when light strikes the photoanode layer, exciting the electrons in the sensitizer [13]. The transparent conductive oxide, the electrolyte solution, and the cathode, in that order, receive the generated current. In order to finish the cycle and direct the ions into the dye solution, the counter electrode provides ions into the redox solution.

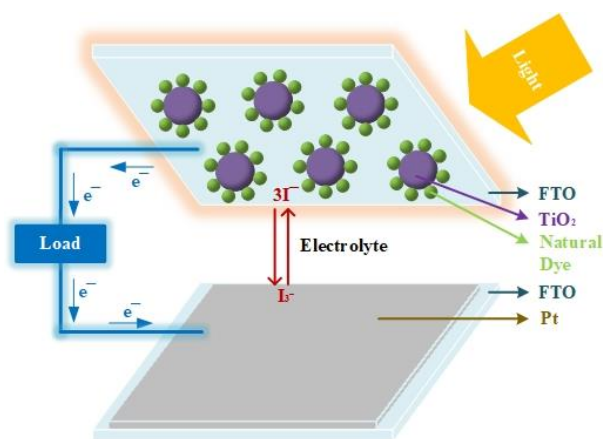


Figure 1. A standard DSSC's operating concept.

There are two types of dyes employed in DSSCs: natural and synthetic. Synthetic dyes are also categorized as metal-free organic dyes and metal complex dyes [14]. The classification of dyes used as sensitizers in DSSCs is given in Fig. 2. The dye used as a sensitizer in DSSCs is important for photovoltaic performance. The properties that the dye used in a DSSC must have are summarized below [15];

- Its visible region must possess a strong absorption quality.
- It must contain carbonyl and/or hydroxyl groups that will create energetic interaction with the TiO_2 surface.
- The lowest conduction band must match the Lowest Unoccupied Molecular Orbital (LUMO) level.
- The redox level of the electrolyte solution must be higher than the Highest Molecular Orbital (HOMO) level.

Metal complex dyes have been utilized in DSSCs to achieve high power conversion efficiencies. In particular, DSSCs with power conversion efficiencies over 15% have been successfully produced using Ruthenium (Ru)

based dyes [16]. On the other hand, these dyes are expensive and pose a great risk to the environment. Additionally, metal complex dyes face stability problems due to recombination events within the cell [17]. This circumstance has brought attention to metal-free organic dyes, which are an excellent substitute because they are less harmful to the environment, affordable, readily accessible, and do not contain metal. Intensive research has been conducted to achieve high power conversion efficiency in DSSCs using metal-free organic dyes [18]. Metal-containing dyes have lower extinction coefficients than metal-free organic-based dyes. Additionally, they enable the use of thinner oxide films that minimize energy losses during charge transfer [19]. However, because of their intense and narrowed absorptions in the visible light spectrum's blue region, they have a low light collection efficiency. In this instance, the metal-free organic dye-sensitized DSSCs' efficiency values stayed below 10% [20].

The high costs of metal complex dyes, difficult synthesis steps and environmental hazards limit the wide range of use of these dyes in DSSCs and encourage the search for alternative sensitizers. This makes the non-toxic, environmentally friendly natural sensitizing dyes prominent [13]. Numerous organic dyes have already been investigated thus far for use as DSSC sensitizers. Among these dyes, the most commonly used are chlorophylls, carotenoids, betalains, anthocyanins and flavonoids [21]. The classification of natural dyes is determined by the chemical structures and photophysical properties of plants. Carbonyl and/or hydroxyl groups in the plant structure have a strong interaction with the TiO_2 surface due to their chemical structure [22]. This kind of interaction lessens the recombination of charge in the contact point and promotes electron transfer to TiO_2 's conduction band [23]. Natural dyes obtained from plants are put to use in areas such as the pharmaceutical industry, textile dyes and food [24]. Among these plants, the genus *Salvia* has an important place in the food, medicine and cosmetic industries. *Salvia urica*, also known as lime tea, grows in the Mediterranean region and is in high demand due to its aromatic properties. Dyes extracted from the above-ground parts of the *Salvia urica* plant have antibacterial, antifungal and dyeing properties [25]. The main pigment found in the structure of this plant is eupatilin and they are organic compounds defined as 6-O-methylated flavonoids. Eupatilin is considered a flavonoid as it represents the methoxy groups of the C6 atom attached to the flavonoid backbone [26]. Nonetheless, DSSCs sensitized with natural dyes do not possess the desired level of power conversion efficiency, so researchers have carried out different studies to increase the stability of the dyes used in DSSCs. Researchers have implemented strategies such as purification by column chromatography [27], the use of different extraction methods [28], and mixing natural dyes [29]. In a study by Zhou et al., catalysts in DSSCs were made from natural dyes that were taken from 20 various plants, and the highest efficiency value (1.17%) was obtained from *Mangosteen* extract [30]. In a study by Kristoffersen et al., cell performance increased significantly after the removal of nonpigmentary organic

components from the anthocyanin dye [31]. In a study reported by Hamadian et al., the cell sensitized with the *Consolida ajacis* plant exhibited the highest cell performance with 0.6% among 10 different plant extracts [32]. In a study by Ramomoorthy et al., cells sensitized with a mixture of betalain and anthocyanin showed the highest efficiency [33]. Nnorom et al., obtained the highest power conversion efficiency (0.58%) by using *Baphia nitida* dye in DSSCs prepared using natural sensitizers [3]. In a study by Calogero et al., cell efficiency was improved by up to 1.6% by using different extraction methods [34]. Ahmadi et al improved the filling factor up to 0.76 in lichen *Collema nigra* dye-sensitized DSSCs [35]. Singh et al. reported 0.72 mA/cm² J_{sc}, 5.55 V V_{oc}, 0.70 FF and 0.28% power conversion efficiency using *Tropaeolum majus* flowers as sensitizers [36]. When the studies conducted with natural dyes are examined, attempts have been made to increase the power conversion efficiency of DSSCs by using techniques such as different dye extraction methods, different solvents, purification processes and mixing natural dyes. The aim of this study is to investigate how dyes extracted from different parts of a plant species that have not previously been used in DSSCs affect cell performance.

Three DSSCs were made for this study using dyes that were extracted from the *Salvia urica* plant's leaves, branches, and flowers. DSSCs sensitized with *Salvia urica* have not been previously reported in the literature. It has also been observed that natural dyes that were gleaned from various sections of the plant have different sensitization performance.

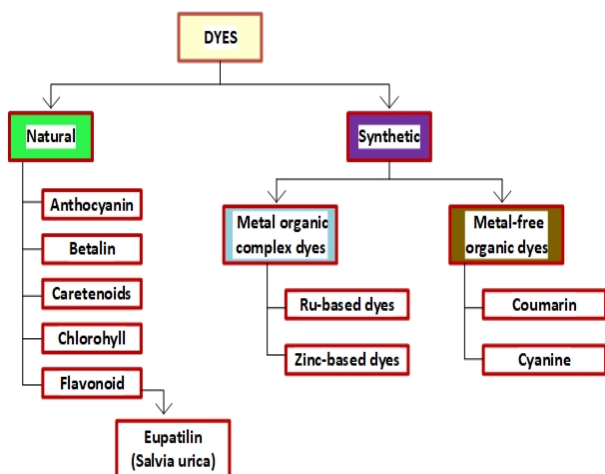


Figure 2. Classification of dyes used as sensitizers in DSSCs.

2. EXPERIMENTAL

2.1. Materials

The *Salvia urica* plant used as a sensitizer in this study was obtained from the city of Elazig in the Eastern Anatolia Region of Turkey. The chemicals were purchased commercially to be used in the experiments and they were not subjected to additional purification. The chemicals used in the study and the companies from which they were purchased are summarized below;

- Tetraisopropyl (TTIP)- $\geq 97.0\%$ purity – Acros Organic
- Ethyl cellulose - Sigma-Aldrich

- α -terpineol - Acros Organic
- FTO glass-TCO30 sodalime/resistivity 10 Ω /sq-Solaronix
- Pt Pastes (Liquit paint:Platisol-T)-Aldrich
- Redox solution (AN-50) - iodide/tri-iodide/Solaronix
- Thermoplastic sealing gasket (Meltonix 20 μ m)/Solaronix
- Absolute ethanol (ethyl alcohol)- Sigma-Aldrich
- Hydrochloric acid (HCl) - Sigma-Aldrich.

2.2. Synthesis of TiO₂ Nanoparticles

In this study, TiO₂ based nanopowders were synthesized by the sol-gel method that was also used previously [37]. 2 ml TTIP and 50 ml absolute ethanol were mixed vigorously at ambient temperature until the color of the mixture turned yellow. While this process was continuing, 0.19 ml HCl was added dropwise to the mixture and stirred for another 24 h. Pure water and alcohol were used several times to wash the precipitate obtained after centrifugation. The cleaned precipitate was kept in an oven at 50 °C to dry for 12 h before it was sintered in a high temperature operate furnace at 400 °C for 1 h. The synthesized TiO₂ particles were pulverized with a mortar and stored in a desiccator in a dark environment.

2.3. Extraction of Natural Dyes

The leaves, branches and flowers of the *Salvia urica* plant were carefully removed from the plant skeleton. Plant parts were cleaned of dust by repeatedly washing leaves and branches in pure water and then drying them in an oven. These plant parts were pulverized with the help of a high-speed grinder. A 10 g portion of each powder was placed into 3 different soxhlet cartridges. Each soxhlet system received ethyl alcohol (150 ml) and the system was siphoned until the dye extraction was finished. In this study, ethyl alcohol was used as a solvent to separate the dye from plants. Many previous studies have shown that eupatilin dye is more soluble in ethyl alcohol [32,38,39]. The extracted dyes were adjusted to the appropriate concentration with the help of a rotary evaporator so that 80% of the alcohol was recovered. Finally, it was passed through a filter paper to remove insoluble residues in the dye and stored in a dark environment at 4 °C. In Fig. 3, the extraction processes of natural dyes are shown.

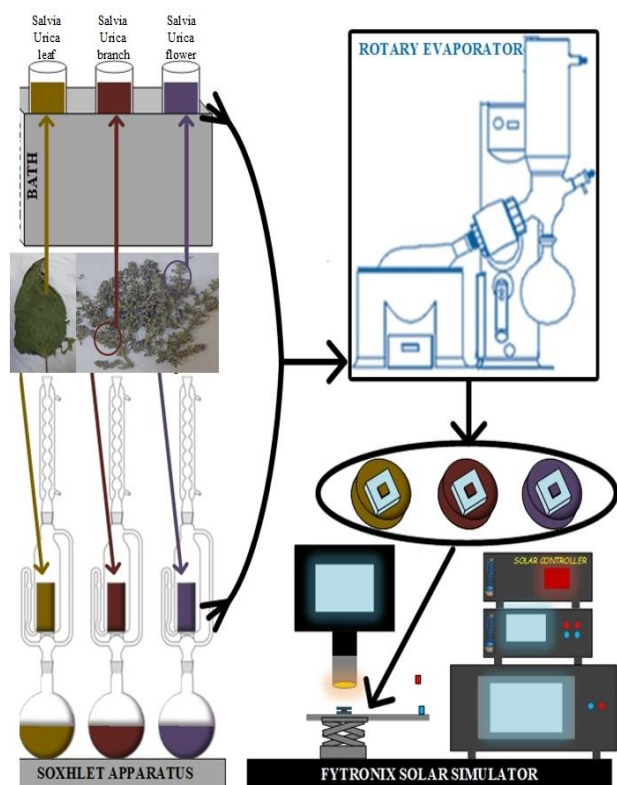


Figure 3. Extraction of dye from flowers, branches and leaves of *Salvia urica*.

2.4. Assembling of DSSC

TiO₂ paste was prepared with the same procedure that was used in previous studies on high-performance DSSCs [40]. For this purpose, 225 mg TiO₂, 100 mg ethyl cellulose and 10 ml absolute ethanol were ultrasonically mixed until the dispersion of TiO₂ particles in the mixture. After the ultrasonic treatment was completed, this mixture was magnetically stirred strongly (1000 rpm) for 24 h in a dark environment at room temperature. Some of the alcohol in the mixture was removed with the help of a rotary evaporator to achieve the appropriate paste consistency. Then, the process of cleaning the FTO was started. Commercially purchased FTO glasses were ultrasonically treated separately in acetone, ethyl alcohol and water. Using the doctor blade method, a synthesized paste was created on the conductive part of the cleaned glasses. The produced photoelectrodes were sintered for 45 min at 450 °C after being dried in an oven for 30 min at 80 °C. The photoelectrodes were left in a vacuum desiccator to cool following the sintering process. The preparation stages of the photoanode layer are given in Fig. 4. When the temperature of the photoelectrodes dropped to an average of 70 °C, they were removed from the desiccator. While the TiO₂ thin film was in the up position, it was dipped into previously prepared natural dyes and left for 24 h. Photoanodes sensitized with natural dyes were immersed in an alcohol solution several times to remove undissolved residues on the TiO₂ surface. These photoanodes, sensitized with natural dyes, were quickly dried in the cold air form of a dryer and stored in a desiccator. After the preparation of the photoanode layer, the production of Platinum (Pt) counter electrodes began. The even distribution of the commercially purchased platisol paste on the conductive part of the pre-

cleaned FTO was handled with an acrylic brush. The Pt paste was spread smoothly on the conductive part of the FTO with a brush and heat treated at 450 °C for 15 min. For the assembly of DSSCs, a thermoplastic seal was placed around the TiO₂ thin films and combined with the counter electrode. To combine the sealing gasket and the counter electrode, the photoanode layer was subjected to heat treatment at 100 °C for 20 s. Redox solution was injected onto the TiO₂ surface through a hole on the upper surface of the Pt electrode, using a special syringe that prevents the formation of air gap.

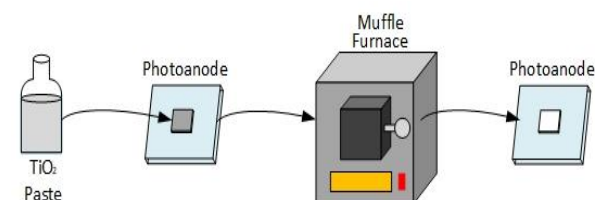


Figure 4. Preparation of the photoanode layer.

The production of DSSCs was completed after a thermoplastic sealing gasket was utilized to close the hole in the Pt electrode. A representative view of a typical DSSC is seen in Fig. 5.

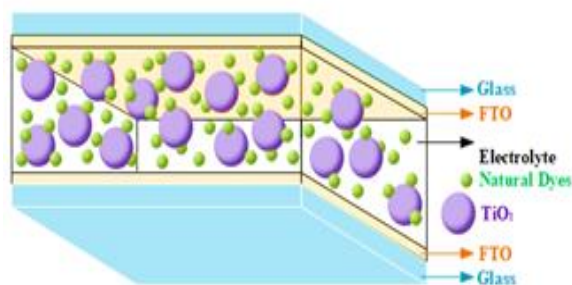


Figure 5. Parts of a consolidated DSSC.

2.5. Characterization

In this study, the crystal structure and morphological properties of TiO₂ thin films produced by the sol-gel method were analyzed with the Rigaku X-ray diffraction (XRD) system and Zeiss Sigma 300 field emission electron microscope (FESEM), respectively. While the measurement of the thickness of TiO₂ films was carried out with KLa Stylus Profiler P7, Brunauer-Emmett-Teller (BET) was used to determine the pore size and specific surface area of the synthesized TiO₂ particles. The absorption properties of the extracted natural dyes were measured with the UV-3600 Shimadzu-Japan device. Fourier transmission infrared (FTIR) spectra were used to detect some functional groups in natural dyes (Thermo Scientific Nicolet Summit device). Electrochemical Impedance Spectra (EIS) and Photovoltaic measurements of DSSCs were recorded by the Fytronix Impedance Analysis System and the LSS 9000 I-V Characterization System (Fytronix Solar Simulator).

3. RESULTS AND DISCUSSION

The method called sol-gel is employed to produce TiO₂ nanoparticles which structures can be seen in Fig. 6. The sharp peaks seen in the Fig. 6 reflect the crystalline nature of TiO₂ nanoparticles. The peak positions (101) (004) (200) (105) (211) (204) (116) (220) (215) correspond to the anatase TiO₂ according to JCPDS card number: 50-00-223. The photoanode layer in high-performance DSSCs is mostly formed with anatase TiO₂ [41].

The average particle size of the metal oxide semiconductor TiO₂ nanopowder was determined using the William-Son-Hall formula and XRD spectra seen in the Eq. 2[42]. β s in this equation reflects the FWHM, which is the full-width value at half the height of the peak. The symbols " ϵ ", " θ ", " D ", and " λ " in the equation correspond to the lattice voltage, reflection angle of the peaks, crystal size, and X-ray wavelength, respectively. The average crystal size of TiO₂ particles synthesized according to this formula is 14.28 nm.

$$\beta \cos \theta = \frac{0.9\lambda}{D} + 4\epsilon \sin \theta \quad (1)$$

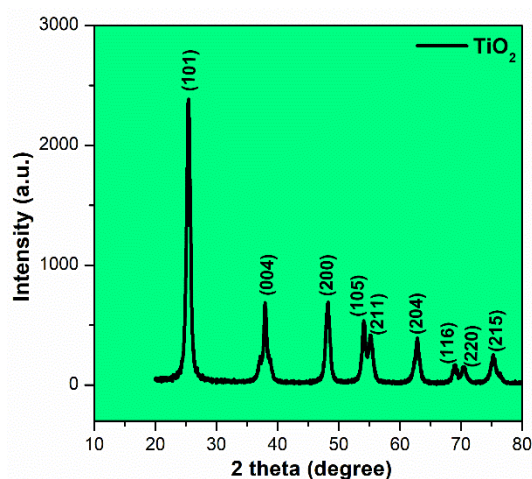


Figure 6. XRD example of the synthesized metal-oxide semiconductor nanopowder.

Fig. 7 shows the surface photographs of the TiO₂ thin film coated on the FTO surface using the doctor blade method at 1 μ m and 100 nm scales. As seen in the Fig.7, almost all TiO₂ nanoparticles have a spherical structure. TiO₂ nanoparticles are tightly bonded to each other. The tight contact of thousands of aggregations improves electron transport. Such a contact provides more pathways for the transport of electrons injected into the thin film and minimizes electron losses [43]. The average size of TiO₂ nanoparticles in the photoanode layer is 15 nm. Nanoparticles have a central function as donors and acceptors in the active layer of DSSCs. The size of TiO₂ nanoparticles in the photoanode layer affects both electron transfer and recombination states of holes. As the size of the particles decreases, the surface/volume ratio and surface area increase. This causes increased dye absorption on the surface [44].

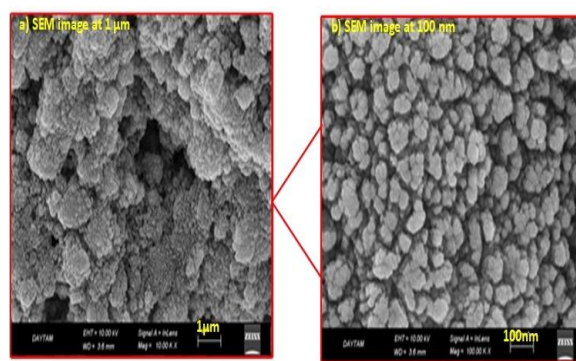


Figure 7. SEM images at different scales of TiO₂ based nanopowder produced with the sol-gel technique.

The specific surface area and pore size of the produced TiO₂ nanopowders were determined by the BET method. The isotherm curve of the produced sample is given in Fig. 8. The adsorption and desorption curves of N₂ gas are associated with the Brunauer Deming Deming Teller (BDDT) classification. According to this classification, the synthesized TiO₂ particles reflect the isotherm type IV and mesoporous structure. Both pore size and specific surface area of TiO₂ in DSSCs play important roles in cell performance. The specific surface area and pore size of the synthesized TiO₂ particles were recorded as 6.28 m²/g and 70.95 nm, respectively. Increasing the specific surface area and pore size of nanoparticles in the photoanode layer improves the dye loading and electron transport pathways of the TiO₂ thin film [45]. Morphological parameters obtained from BET studies showed that the synthesized TiO₂ nanoparticles were suitable for high-performance DSSCs [46].

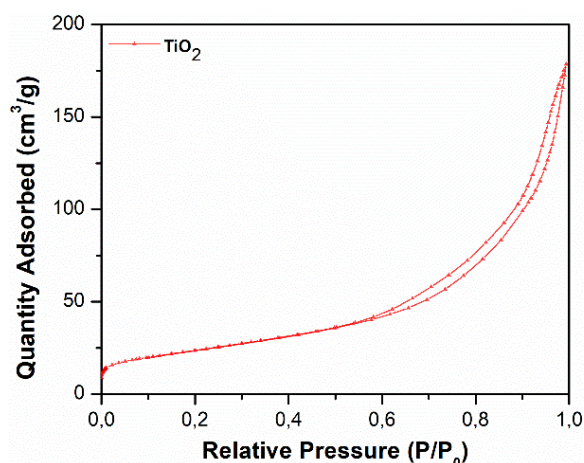


Figure 8. N₂ adsorption/desorption graphs of semiconductor metal-oxide TiO₂ powders.

Fig. 9 shows the UV-vis absorption spectra of dyes obtained via flowers, *Salvia urica* plant' branches and leaves. Such dyes can evidently be used as sensitizers in DSSCs, for light is absorbed by them in the UV-vis. Differences in the absorption behavior of the dyes significantly affected the performance of the synthesized solar devices. This is due to the different pigment structures in natural dyes. The maximum absorbance wavelength of 3 dyes extracted from different sections of the *Salvia urica* plant is 660 nm. Additionally, the dye extracted from the flower has an additional peak at 473 nm. The dye utilized by the plant's flowers exhibits two

distinct peak patterns inside the visible region, indicating that it has the highest absorption. Peaks at 660 nm indicate that the dye is eupatilin, which generally belongs to the flavonoid class [32]. The extra peak exhibited by the flower dye at 473 nm reveals the presence of chlorophyll in the respective dye extract. Chlorophyll is known to strongly absorb light within the observable spectrum, particularly from wavelengths as 400 to 500 nm [47]. Compared to dyes extracted from the branches and leaves, the *Salvia urica* plant's flowers demonstrated absorption at a wider wavelength in the visible spectrum. It is known that the absorption behavior at this wider wavelength increases cell performance [48]. Additionally, absorptions in different energy regions help DSSCs capture more photons [49]. The dye obtained from the flowers of the *Salvia urica* plant absorbs a wider wavelength, resulting in higher cell performance. Furthermore, dyes obtained from various plant parts may have different absorption qualities, according to UV research.

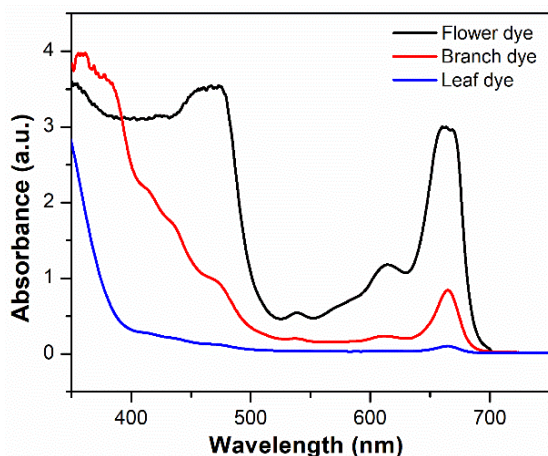


Figure 9. Natural dye absorption spectra obtained from various components of *Salvia urica*.

Fig. 10 shows the FTIR spectra of 3 natural dyes leached from different sections of the *Salvia urica* plant. The chemical structure of eupatilin, the basic pigment of *Salvia urica*, is given in Fig. 11. The functional groups that constitute the basic structure of natural dyes that are put to use as sensitizers in cells were determined thanks to the spectrum which shown at the Fig. 10. For natural dyes to form a strong interaction with the TiO_2 surface, they must contain carbonyl and/or hydroxyl groups in their chemical structure. Natural dyes that are derived from various sections of the plant showed identical spectral properties, and the presence of functional groups in the main pigments is manifested by the peaks observed in the IR spectra of these dyes [14,32,47]. However, the spectrum of the dye derived from the flowers of the *Salvia urica* plant showed stronger characteristic absorption. This is due to the superposition of the two main pigments (chlorophyll, and eupatilin) in the dye [38]. The dyes obtained from this plant's branches and leaves have nearly identical spectra. The hydroxyl group presence in the three natural dye extracts is indicated by the broad peak at 3321 cm^{-1} [50]. The peaks at 2923 and 2851 cm^{-1} are attributed to alkyl C-H of polyphenolic compounds [14,48]. The peaks appearing at 1600 cm^{-1} correspond to aromatic ring vibrations [49]. The peak at 1259 cm^{-1} is assigned to the C-N stretching of amine groups, while the

sharp peak observed at 1046 cm^{-1} corresponds to the C-O-C stretching of carbohydrate or ester groups [3,21]. The bands attributed to 990 and 917 cm^{-1} arise from out-of-plane bendings of the C-H bond [51]. FTIR test results clearly show that, for DSSCs, natural pigments containing carbonyl and/or hydroxyl functional groups are applicable and useful sensitizers.

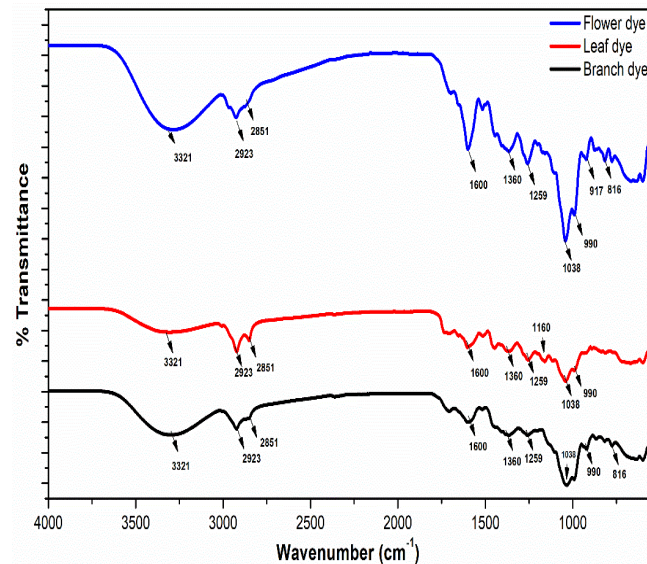


Figure 10. FTIR spectra of dyes leached from flowers, branches and leaves of the *Salvia urica* plant.

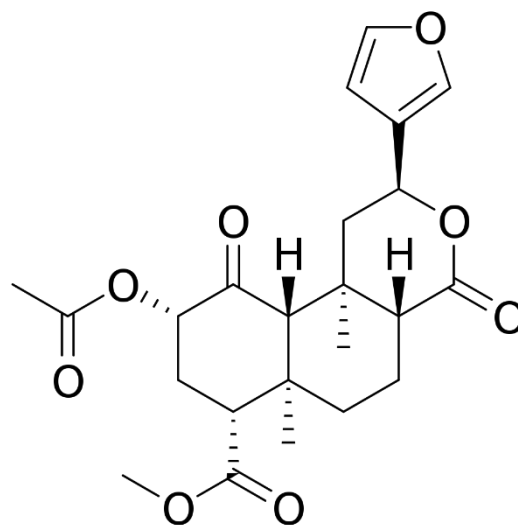


Figure 11. Chemical structure of eupatilin.

The electrochemical impedance spectra (EIS) of DSSCs sensitized with natural dyes are shown in Fig. 12(a). Under 100 mW/cm^2 of enlightenment, EIS analyses were recorded in frequency ranges ranging from 0.1 Hz to 100 kHz . With the aid of the Zview program, resistance parameters were computed from EIS data and are shown in Table 1. DSSC electrochemical spectra are typically shown as three semicircles. There is a correspondence between the first semicircle in the high-frequency region and the charge transfer at the counter electrode. The back reaction at the TiO_2 /electrolyte interface and the transport of injected electrons in the TiO_2 film are mirrored by the second semicircle in the mid-frequency region. The third semicircle in the low-frequency region is attributed to the Warburg diffusion process of I^-/I_3^- in the redox electrolyte

[52]. In the Nyquist diagram shown in Fig. 12(a), semicircles of the high and medium-frequency regions can be seen. The absence of the third semicircle in the low-frequency region may be due to Warburg diffusion of redox couples [53]. The series resistance (R_s) value is associated with the intersection of the high-frequency region with the real axis, while R_{ct1} and R_{ct2} stand for the resistance of the charge transfer at the electrode as Pt and the resistance of electron transfer between TiO_2 -electrolyte, respectively. It can be seen in Table 1 that R_s and R_{ct1} values are very close to each other since the same Pt electrode and iodide/tri-iodide redox solution were used in DSSCs sensitized with natural dyes [54]. Therefore, when examining the interface resistances of cells, the impedance value (R_{ct2}) that originates from the transfer of electron out of the conduction band of TiO_2 to the FTO glass must be taken as the reference. Increasing the diameter of the Nyquist curves representing R_{ct2} leads to lower cell performance. When Table 1 is examined, the R_{ct2} values of DSSCs sensitized with the flower, branch and leaf dye of the plant were calculated as 120.6, 140.1 and 162.7 Ω , respectively. DSSCs sensitized with sensitizers obtained from the branches and leaves of the *Salvia urica* plant have higher R_{ct2} . The higher charge transfer resistances of these cells cause higher distortion and separation and negatively affect their power conversion efficiency [55]. In addition, due to increasing R_{ct2} values, the V_{oc} values of the DSSCs produced decreased from 0.65 to 0.55 V. Because as the R_{ct2} value increases, slower electron transfer occurs at the TiO_2 /electrolyte interface, resulting in lower V_{oc} values [56]. In DSSCs, low R_{ct2} values accelerate the charge transfer between the photoanode layer and the Pt electrode. The lower R_{ct2} value shown by flower dye-sensitized DSSC is consistent with the higher cell performance it exhibits [57].

Table 1. EIS parameters of DSSCs sensitized with flowers, branches and leaves of *Salvia urica*.

Sample	R_s (Ω)	R_{ct1} (Ω)	R_{ct2} (Ω)	C_e (μs)
DSSC sensitized with flowers of <i>Salvia urica</i> plant	15.3	6.4	120.6	1310
DSSC sensitized with branches of <i>Salvia urica</i> plant	17.1	8.1	140.1	834
DSSC sensitized with leaves of <i>Salvia urica</i> plant	19.2	8.9	162.7	752

Electron lifetimes (C_e) of DSSCs obtained via natural dyes acquired from different *Salvia urica* plant sections were calculated with the help of Eq. 2 [58] from the Bode graph given in Fig. 12(b). The f_{max} in Eq. 2 is the maximum peak frequency of the Bode lines. The C_e values of DSSCs sensitized with flower, branch and leaf dye were found to be 1310, 834 and 752 μs , respectively. The higher electron lifetime of flower dye-sensitized DSSC is due to its higher recombination resistance. Increasing electron lifetime in a cell improves cell performance by limiting the recombination of electrons and redox pairs [59]. Conversely, though the f_{max} value of DSSC obtained via dye leached from the leaves of *Salvia urica* has the lowest electron lifetime since it is in the

high-frequency region. This caused the leaf-sensitized cell to have the lowest efficiency value.

$$\tau_e = \frac{1}{2\pi f_{(max)}} \quad (2)$$

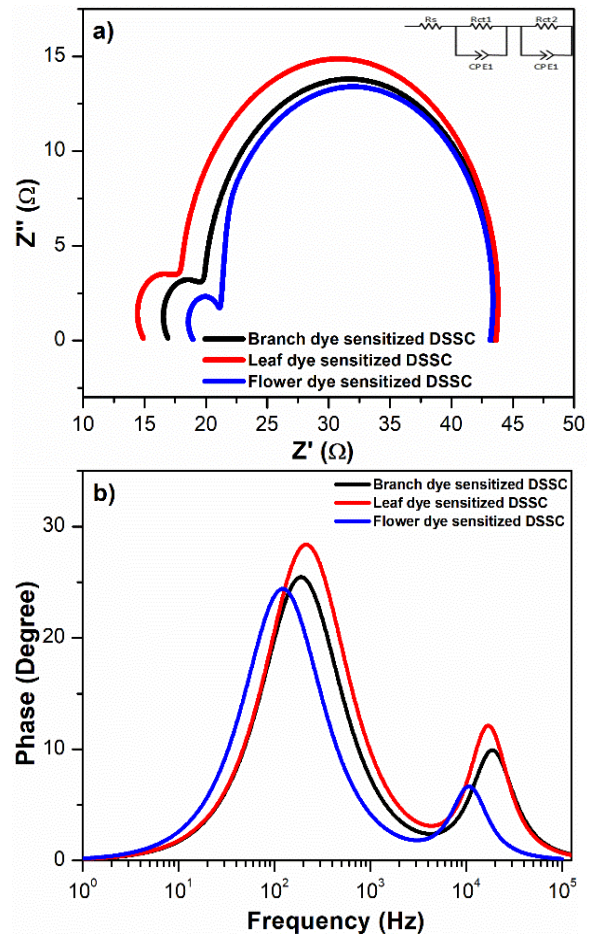


Figure 12. a) Nyquist curves, b) Bode curves of DSSCs using sensitizers extracted from different parts of *Salvia urica*.

Photoelectric properties of DSSCs sensitized with flower, branch and leaf dye of the *Salvia urica* plant were examined using artificial sunlight under 100 mW/cm^2 light intensity (AM 1.5G). J_{sc} -V curves of DSSCs sensitized with natural dyes are seen in Fig. 13. Photovoltaic cell parameters for instance efficiency of cell (η), density of short circuit (J_{sc}) current, open circuit (V_{oc}) voltage and factor of filling (FF) of natural dyes based DSSCs were calculated by Eq. 3, 4 as is shown in Table 2. Compared with other sensitizers, the flower dye-sensitized cell has the best cell efficiency ($\eta=0.33$) with a short-circuit current density of 0.73 mA/cm^2 , an open-circuit voltage of 0.65 V, and a filling factor of 0.71. When DSSCs sensitized with dyes leached from different parts of the *Salvia urica* plant are compared to the performance of cells produced with conventional inorganic Ruthenium complex dyes ($\eta=6.86\%$), the cell efficiency is very low [13]. However, intensive research on organic-based dyes shows that these dyes are promising for DSSCs in the near future [60]. Additionally, in a study reported

by Lohar et al., they reported a cell performance of 0.152 % in cells where *Salvia divinorum*, one of the different species of *Salvia*, was used as a sensitizer. The photoelectric performance of DSSC sensitized with dye obtained from the flowers of the *Salvia urica* plant is higher than cells sensitized with branch and leaf dye. This may be due to the higher presence of some functional groups that show superior performance in DSSCs in the flower-extracted dye. Because the charge transfer transition of flavonoid and chlorophyll pigments from HOMO to LUMO requires less energy. As a result of such behavior, the pigment molecules are energized by visible light, resulting in a wider absorption band in the UV-vis [61]. Two intense absorptions of the flower dye over a wide area in the visible region support this situation. Moreover, the higher V_{oc} value (0.65 V) of DSSC sensitized with flower dye is a result of the strong interaction of alkyl chains with the TiO_2 surface. Such an interaction prevents the leakage of electrons from the photoanode layer into the electrolyte solution [62]. The lower V_{oc} (0.55 V) and J_{sc} (0.52 mA/cm²) values of the leaf dye-sensitized cell can be attributed to the poor electron injection and the low concentration of some pigments that exhibit high performance in DSSCs [63]. As a result, it appears that dyes leached from different parts of natural plants may have different sensitization performances.

$$\eta = \frac{P_{max}}{P_{in}} = \frac{V_{oc} \times J_{sc} \times FF}{P_{in}} \quad (3)$$

$$FF = \frac{J_{max} \times V_{max}}{J_{sc} \times V_{oc}} \times 100 \quad (4)$$

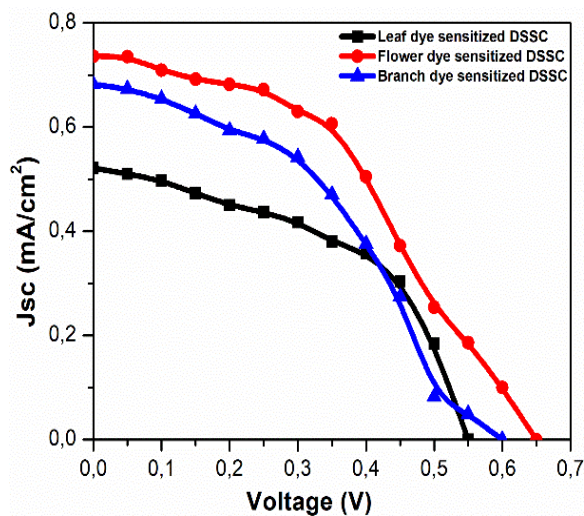


Figure 13. The DSSCs' J_{sc} -V curves sensitized with dyes of the *Salvia urica* plant's flowers, leaves and branches.

Table 2. DSSCs' photovoltaic results sensitized with flowers, branches and leaves of *Salvia urica*.

Sample	J_{sc} (mA/cm ²)	V_{oc} (V)	FF	η (%)
DSSC sensitized with flowers of <i>Salvia urica</i> plant	0.73	0.65	0.71	0.33
DSSC sensitized with branches of <i>Salvia urica</i> plant	0.68	0.60	0.69	0.28
DSSC sensitized with leaves of <i>Salvia urica</i> plant	0.52	0.55	0.68	0.19

4. CONCLUSION

In this study, the performance of dyes extracted from the flowers, branches and leaves of the *Salvia urica* plant on DSSCs was examined. The production of TiO_2 nanoparticles was successfully performed using the sol-gel method and photoelectrodes were prepared by the doctor blade method. XRD studies confirmed that TiO_2 was in the anatase phase. SEM images showed that TiO_2 nanoparticles had a spherical structure in close contact with each other. Fourier spectroscopy testing revealed that dyes containing carbonyl and hydroxyl groups were suitable sensitizers for DSSCs. Dyes extracted from the flowers, branches and leaves of the *Salvia urica* plant showed different absorption behaviors in the visible region. UV-vis studies showed that the flower dye exhibited absorption over a wider wavelength range in the visible region. It was determined from EIS analysis that the longest electron lifetime (1310 ms) was in the flower dye-sensitive DSSC. This was attributed to the high recombination resistance of the flower dye-sensitized cell. The flower dye-sensitized DSSC exhibited the best cell performance (0.33%) with, 0.71 FF, 0.65 V V_{oc} and 0.73 mA/cm² J_{sc} . This behavior was explained by the strong absorption of the flower dye in the visible region and the higher presence of some functional groups in this natural dye. The low V_{oc} (0.55 V) and J_{sc} (0.52 mA/cm²) values of the leaf dye-sensitized cell were attributed to poor electron injection and low concentration of some high-performance pigments. Dyes extracted from different parts of natural plants may exhibit different sensitizing performances in DSSCs. In addition, natural dyes used as sensitizers in DSSCs can offer a sustainable solution to meet energy needs as they are cheaper and eco-friendly. The use of dyes to be leached from different parts of plants with different extraction methods in DSSCs is promising for high-performance DSSCs. Organic-based dyes, especially those obtained with pure critical and high-pressure extraction systems, can be used as high-performance sensitizers in DSSCs.

Acknowledgement

Author Contributions: H.I.Y. and F.A.: Experimental studies, methodology, resources, scientific calculation, edits, research and writing the original draft.

Funding: Not applicable for this study.

Data availability statement: Not applicable for this study.

Ethical approval: Not applicable for this study.

Conflict of interest: It is clearly stated by the author that there is no conflict of interest for the study.

REFERENCES

- [1] Kumar BA, Vetrivelan V, Ramalingam G, Manikandan A, Viswanathan S, Boomi P, Ravi G. Computational studies and experimental fabrication of DSSC device assembly on 2D-layered TiO₂ and MoS₂@TiO₂ nanomaterials. *Physica B: Condensed Matter*. 2022;633: 413770.
- [2] Katta VS, Chappidi VR, Kumar A, Asthana S, Raavi SSK. Enriched visible light absorption by Au-embedded Sm³⁺ doped TiO₂ compact photoanode for enhanced dye-sensitized solar cell performance. *Physica B: Condensed Matter*. 2023;652:414621.
- [3] Nnorom OO, Onuegbu GC, Etus C. Photo-performance characteristics of *Baphia nitida* and *rosella* dye sensitized solar cell. *Results in Optics*. 2022;9:100311.
- [4] Akman E. Enhanced photovoltaic performance and stability of dye-sensitized solar cells by utilizing manganese-doped ZnO photoanode with europium compact layer. *Journal of Molecular Liquids*. 2020;317:14-22.
- [5] Zatirostami A. A dramatic improvement in the efficiency of TiO₂-based DSSCs by simultaneous incorporation of Cu and Se into its lattice. *Optical Materials*. 2021;117:111110.
- [6] Hadi A, Alhabradi M, Chen Q, Liu H, Guo W, Curioni M, Cernik R, Liu Z. Rapid fabrication of mesoporous TiO₂ thin films by pulsed fibre laser for dye sensitized solar cells. *Applied Surface Science*. 2018;428:1089-1097.
- [7] Xu J, Wang G, Fan J, Liu B, Cao S, Yu J. G-C₃N₄ modified TiO₂ nanosheets with enhanced photoelectric conversion efficiency in dye-sensitized solar cells. *Journal of Power Sources*. 2015;274:77-84.
- [8] Wang Z, Fang J, Mi Y, Zhu X, Ren H, Liu X, Yan Y. Enhanced performance of perovskite solar cells by ultraviolet-ozone treatment of mesoporous TiO₂. *Applied Surface Science*. 2018;436:596-602.
- [9] Kakiage K, Aoyama Y, Yano T, Oya K, Fujisawa JI, Hanaya M. Highly-efficient dye-sensitized solar cells with collaborative sensitization by silyl-anchor and carboxy-anchor dyes. *Chemical Communications*. 2015;51:15894-15897.
- [10] Xie Y, Huang N, You S, Liu Y, Sebo B, Liang L, Fang X, Liu W, Guo S, Zhao XZ. Improved performance of dye-sensitized solar cells by trace amount Cr-doped TiO₂ photoelectrodes. *Journal of Power Sources*. 2013;224:168-173.
- [11] Zatirostami A. Electro-deposited SnSe on ITO: A low-cost and high-performance counter electrode for DSSCs. *Journal of Alloys and Compounds*. 2020;844:156151.
- [12] Chu L, Qin Z, Zhang Q, Chen W, Yeng J, Yang J, Li X. Mesoporous anatase TiO₂ microspheres with interconnected nanoparticles delivering enhanced dye-loading and charge transport for efficient dye-sensitized solar cells. *Applied Surface Science*. 2016;360:634-640.
- [13] Akman E, Karapinar HS. Electrochemically stable, cost-effective and facile produced selenium@activated carbon composite counter electrodes for dye-sensitized solar cells. *Solar Energy*. 2022;234:368-376.
- [14] Ammar AM, Mohamed HSH, Yousef MMK, Abdel-Hafez GM, Hassanien AS, Khalil ASG. Dye-Sensitized Solar Cells (DSSCs) based on extracted natural dyes. *Journal of Nanomaterials*. 2019;186:172-186.
- [15] Ludin NA, Al-Alwani A.M, Bakar A, Kadhum AA, Sopian K, Abdul Karim NS. Review on the development of natural dye photosensitizer for dye-sensitized solar cells. *Renewable and Sustainable Energy Reviews*. 2014;31:386-396.
- [16] Al-Alwani MAM, Ludin NA, Mohamad AB, Kadhum AAH, Mukhlus A. Application of dyes extracted from *Alternanthera dentata* leaves and *Musa acuminata* bracts as natural sensitizers for dye-sensitized solar cells. *Spectrochimica Acta - Part A: Molecular and Biomolecular Spectroscopy*. 2018;192:487-498.
- [17] Kumara NT, Petrović M, Peiris DS, Marie YA, Vijila C, Petra MI, Chandrakanth, RL, Lim CM, Hogley J, Ekanayake P. Efficiency enhancement of *Ixora floral* dye sensitized solar cell by diminishing the pigments interactions. *Solar Energy*. 2015;117:36-45.
- [18] Omar A, Ali MS, Rahim N. Electron transport properties analysis of titanium dioxide dye-sensitized solar cells (TiO₂-DSSCs) based natural dyes using electrochemical impedance spectroscopy concept: A review. *Solar Energy*. 2020;207:1088-1121.
- [19] Lee CP, Li CT, Ho KC. Use of organic materials in dye-sensitized solar cells. *Materials Today*. 2017;20:267-283.
- [20] Lee DH, Lee MJ, Song HM, Song BJ, Seo KD, Pastore M, Anselmi C, Fantacci S, Angelis F, Nazeeruddin MK, Gretzel M, Kim HK. Organic dyes incorporating low-band-gap chromophores based on π -extended benzothiadiazole for dye-sensitized solar cells. *Dyes and Pigments*. 2011;91:192-198.
- [21] Safaei-Ghomi J, Masoomi R, Hosseinpour M, Batooli H. Energy Production Using Dye-sensitized Solar Cells by TiO₂ Nanoparticles Fabricated with Several Natural Dyes. *J Nanostruct*. 2020;10:691-701.
- [22] Tabacchi G, Fabbiani M, Mino L, Martra G, Fois E. The Case of Formic Acid on Anatase TiO₂(101): Where is the Acid Proton. *Angewandte Chemie - International Edition*. 2019;58:12431-12434.
- [23] Akila Y, Muthukumarasamy N, Agila S, Mallick TK, Senthilarasu S, Velauthapillai D. Enhanced performance of natural dye sensitised solar cells fabricated using rutile TiO₂ nanorods. *Optical Materials*. 2016;58: 76-83.
- [24] Sen A, Putra MH, Biswas AK, Behera AK, Groß A. Insight on the choice of sensitizers/dyes for dye sensitized solar cells: A review. *Dyes and Pigments*. 2023;213:111087.
- [25] Hayta S, Dogan G, Yuce E, Bageci E. Composition of the essential oil of two *Salvia taxa* (*Salvia sclarea* and *Salvia verticillata* subsp. *verticillata*) from Turkey. *Natural Science and Discovery*. 2015;1:56-

- 62.
- [26] Nageen B, Sarfraz I, Rasul A, Hussain G, Rukhsar F, Irshad S, Riaz A, Selamoglu Z, Ali M. Eupatilin: a natural pharmacologically active flavone compound with its wide range applications. *Journal of Asian Natural Products Research*. 2020;22:1–16.
- [27] Wang XF, Matsuda A, Koyama Y, Nagae H, Sasaki S, Tamiaki H, Wada Y. Effects of plant carotenoid spacers on the performance of a dye-sensitized solar cell using a chlorophyll derivative: Enhancement of photocurrent determined by one electron-oxidation potential of each carotenoid. *Chemical Physics Letters*. 2006;423:470–475.
- [28] Inbarajan K, Sowmya S, Janarthanan B. Direct and Soxhlet extraction of dyes from the peels of *Allium cepa* and its effective application in dye – Sensitized solar cells as sensitizer. *Optical Materials*. 2022;129:112487.
- [29] Enhanced photovoltaic performance and stability Obi K, Frolova L, Fuierer P. Preparation and performance of prickly pear (*Opuntia phaeacantha*) and mulberry (*Morus rubra*) dye-sensitized solar cells. *Solar Energy*. 2020;208:312–320.
- [30] Zhou H, Wu L, Gao Y, Ma T. Dye-sensitized solar cells using 20 natural dyes as sensitizers. *Journal of Photochemistry and Photobiology A: Chemistry*. 2011;219:188–194.
- [31] Kristoffersen AS, Erga, SR, Velauthapillai D. Enhanced photostability of anthocyanin dye for increased efficiency in natural dye sensitized solar cells. *Optik*. 2021;227:166053.
- [32] Hamadani M, Safaei-Ghomi J, Hosseinpour M, Masoomi R, Jabbari V. Uses of new natural dye photosensitizers in fabrication of high potential dye-sensitized solar cells (DSSCs). *Materials Science in Semiconductor Processing*. 2014;27:733–739.
- [33] Ramamoorthy R, Radha N, Maheswari G, Anandan S, Manoharan S, Williams, R. Betalain and anthocyanin dye-sensitized solar cells. *Journal of Applied Electrochemistry*. 2016;46:929–941.
- [34] Calogero G, Barichello J, Citro I, Mariani P, Vesce L, Bartolotta A, Di-Carlo A, Di-Marco G. Photoelectrochemical and spectrophotometric studies on dye-sensitized solar cells (DSCs) and stable modules (DSCMs) based on natural apocarotenoids pigments. *Dyes and Pigments*. 2018;155:75–83.
- [35] Ahmadi N, Yeganeh R, Valizadeh M, Valadbeigi T. Improvement of the fill factor characteristic of TiO₂-based dye-sensitive solar cell using lichen *Collema nigra*. *Optical Materials*. 2022;638:112–131.
- [36] Singh S, Maurya IC, Sharma S, Kushwaha SP, Srivastava P, Bahadur L. Application of new natural dyes extracted from *Nasturtium* flowers (*Tropaeolum majus*) as photosensitizer in dye-sensitized solar cells. *Optik*. 2021;243:167331.
- [37] Aslan F, Esen H, Yakuphanoglu F. Al/P-Si/Coumarin:TiO₂/Al Organic-Inorganic Hybrid Photodiodes: Investigation of Electrical and Structural Properties. *Silicon*. 2019;12:2149–2164.
- [38] Luo P, Niu H, Zheng G, Bai X, Zhang M, Wang W. From salmon pink to blue natural sensitizers for solar cells: *Canna indica* L., *Salvia splendens*, cowberry and *Solanum nigrum* L. *Spectrochimica Acta - Part A: Molecular and Biomolecular Spectroscopy*. 2009;74:936–942.
- [39] Richhariya G, Meikap BC, Kumar A. Review on fabrication methodologies and its impacts on performance of dye-sensitized solar cells. *Environmental Science and Pollution Research*. 2022;29:15233–15251.
- [40] Aslan F. Increasing the photoelectric conversion efficiency of dye-sensitized solar cells by doping SrAl₂O₄:Eu²⁺,Dy³⁺ to TiO₂-based photoanodes. *Physica B: Condensed Matter*. 2023;668:415267.
- [41] Prakash P, Janarthanan B. Review on the progress of light harvesting natural pigments as DSSC sensitizers with high potency. *Inorganic Chemistry Communications*. 2023;152:110638.
- [42] Sethy PP, Pani TK, Rout S. Structural and magnetic properties of Ni / C core – shell nanofibers prepared by one step co-axial electrospinning method. *Journal of Materials Science: Materials in Electronics*. 2023;807:1–15.
- [43] Ge Z, Wan, C, Chen Z, Wang T, Chen T, Shi R, Yu S, Liu J. Investigation of the TiO₂ nanoparticles aggregation with high light harvesting for high-efficiency dye-sensitized solar cells. *Materials Research Bulletin*. 2021;135: 111148.
- [44] Du L, Furube A, Hara K, Katoh R, Tachiya M. Mechanism of particle size effect on electron injection efficiency in ruthenium dye-sensitized TiO₂ nanoparticle films. *Journal of Physical Chemistry C*. 2010;114:8135–8143.
- [45] Wali Q, Bakr ZH, Manshor NA, Fakharuddin A, Jose R. ScienceDirect SnO₂ – TiO₂ hybrid nanofibers for efficient dye-sensitized solar cells. 2016;132:395–404.
- [46] Sayahi H, Aghapoor K, Mohsenzadeh F, Mohebi M, Darabi HR. TiO₂ nanorods integrated with titania nanoparticles: Large specific surface area 1D nanostructures for improved efficiency of dye-sensitized solar cells (DSSCs). *Solar Energy*. 2021;215:311–320.
- [47] Ayalew WA, Ayele DW. Dye-sensitized solar cells using natural dye as light-harvesting materials extracted from *Acanthus sennii* chiovenda flower and *Euphorbia cotinifolia* leaf. *Journal of Science: Advanced Materials and Devices*. 2016;1:488–494.
- [48] Dayang S, Irwanto M, Gomesh N, Ismail B. Natural dyes from roselle flower as a sensitizer in dye-sensitized solar cell (DSSC). *Indonesian Journal of Electrical Engineering and Computer Science*. 2018;9:191–197.
- [49] Güzel E, Arslan BS, Durmaz V, Cesur M, Tutar ÖF, Sari T, Isleyen M, Nebioğlu M, Sisman I. Photovoltaic performance and photostability of anthocyanins, isoquinoline alkaloids and betalains as natural sensitizers for DSSCs. *Solar Energy*. 2018;173:34–41.
- [50] Mozaffari SA, Saedi M, Rahmanian R. Photoelectric characterization of fabricated dye-sensitized solar cell using dye extracted from red *Siahkooti* fruit as natural sensitizer. *Spectrochimica*

Acta - Part A: Molecular and Biomolecular Spectroscopy. 2015;142:226–231.

- [51] Hajji S, Turki T, Boubakri A, Amor M, Mzoughi N. Study of cadmium adsorption onto calcite using full factorial experiment design. *Desalination and Water Treatment*. 2017;83:222–233.
- [52] Subalakshmi K, Senthilselvan J, Kumar KA, Kumar SA, Pandurangan A. Solvothermal synthesis of hexagonal pyramidal and bifrustum shaped ZnO nanocrystals: natural betacyanin dye and organic Eosin Y dye sensitized DSSC efficiency, electron transport, recombination dynamics and solar photodegradation investigations. *Journal of Materials Science: Materials in Electronics*. 2017;20:10854.
- [53] Bella F, Galliano S, Falco M, Viscardi G, Barolo C, Grätzel M, Gerbaldi C. Unveiling iodine-based electrolytes chemistry in aqueous dye-sensitized solar cells. *Chemical Science*. 2016;7:4880–4890.
- [54] Chandra MI, Singh S, Srivastava P, Maiti B, Bahadur L. Natural dye extract from *Cassia fistula* and its application in dye-sensitized solar cell: Experimental and density functional theory studies. *Optical Materials*. 2019;90:273–280.
- [55] Lohrasbi M, Pattanapanishawat P, Isenberg M, Chuang, SS. Degradation study of dye-sensitized solar cells by electrochemical impedance and FTIR spectroscopy. *IEEE Energytech*. 2013;4:1–4.
- [56] Rajan AK, Cindrella L. Studies on new natural dye sensitizers from *Indigofera tinctoria* in dye-sensitized solar cells. *Optical Materials*. 2019;88:39–47.
- [57] Guo J, Cui X, Li S, Mao L, Liu Y, Huang W, Gong T, Wei X, Chen H, Yu B. One-step synthesis of mesoporous TiO₂ film for high photon-to-electron transport efficiency in dye-sensitized solar cells. *Journal of Alloys and Compounds*. 2019;770:662–668.
- [58] Kumar KA, Subalakshmi K, Senthilselvan J. Effect of mixed valence state of titanium on reduced recombination for natural dye-sensitized solar cell applications. *Journal of Solid State Electrochemistry*. 2016;20:1921–1932.
- [59] Lim SP, Pandikumar A, Lim HN, Ramaraj R, Huang NM. Boosting photovoltaic performance of dye-sensitized solar cells using silver nanoparticle-decorated N,S-Co-doped-TiO₂ photoanode. *Scientific Reports*. 2015;5:1–14.
- [60] Aslan F. New natural dyes extracted by ultrasonic and soxhlet method: Effect on dye-sensitized solar cell photovoltaic performance. *Optical and Quantum Electronics*. 2024;56:1–22.
- [61] Shalini S, Balasundara R, Prasanna S, Mallick TK, Senthilarasu S. Review on natural dye sensitized solar cells: Operation, materials and methods. *Renewable and Sustainable Energy Reviews*. 2015;51:1306–1325.
- [62] Hamadani M, Jabbari V, Gravand A, Asad M. Band gap engineering of TiO₂ nanostructure-based dye solar cells (DSCs) fabricated via electrophoresis. *Surface and Coatings Technology*. 2012;206:4531–4538.
- [63] Narayan MR. Review: Dye sensitized solar cells based on natural photosensitizers. *Renewable and Sustainable Energy Reviews*. 2012;16:208–215.

Dyadic Maximal Function Maps the Weighted Hardy Space $H^1(w)$ to the Weighted $L^1(w)$ Space

Sakin DEMİR^{1*} 

¹ Agri Ibrahim Cecen University, Faculty of Education, Department of Basic Education, Ağrı, Türkiye
 Sakin DEMİR ORCID No: 0000-0002-8019-6917

*Corresponding author: sakin.demir@gmail.com

(Received: 09.01.2024, Accepted: 20.03.2024, Online Publication: 26.03.2024)

Keywords

Weighted Hardy space,
 Muckenhoupt weight,
 A_p weight,
 Hardy space,
 Dyadic maximal function

Abstract: Let $f : \mathbb{R} \rightarrow \mathbb{R}$ be a locally integrable function, and define the dyadic maximal function

$$Tf(x) = \sup_j \frac{1}{2^j} \left| \int_0^{2^j} f(x-t) dt \right|.$$

Let $1 < p < \infty$, and $w \in A_p$, i.e.,

$$\sup_I \left(\frac{1}{|I|} \int_I w(x) dx \right) \left(\frac{1}{|I|} \int_I w(x)^{-\frac{1}{p-1}} dx \right) < \infty,$$

where the supremum is taken over all intervals I in \mathbb{R} . In this research we prove that Tf maps the weighted Hardy space $H^1(w)$ to the weighted $L^1(w)$ space. More precisely, we show that there exists a positive constant α such that

$$\|Tf\|_{L^1(w)} \leq \alpha \|f\|_{H^1(w)}$$

for all $f \in H^1(w)$.

172

İkili Maksimal Fonksiyon Ağırlıklı $H^1(w)$ Hardy Uzayını Ağırlıklı $L^1(w)$ Uzayına Dönüştürür

Anahtar Kelimeler

Ağırlıklı Hardy uzayı,
 Muckenhoupt ağırlığı,
 A_p ağırlığı,
 Hardy uzayı,
 İkili maksimal fonksiyon

Öz: Yerel olarak integrallenebilen bir $f : \mathbb{R} \rightarrow \mathbb{R}$ fonksiyonu için Tf ikili maksimal fonksiyonunu

$$Tf(x) = \sup_j \frac{1}{2^j} \left| \int_0^{2^j} f(x-t) dt \right|$$

olarak tanımlayalım. $1 < p < \infty$ ve $w \in A_p$ olsun. Yani supremum \mathbb{R} reel sayılar kümesindeki bütün I aralıkları üzerinden alınmak üzere

$$\sup_I \left(\frac{1}{|I|} \int_I w(x) dx \right) \left(\frac{1}{|I|} \int_I w(x)^{-\frac{1}{p-1}} dx \right) < \infty$$

olsun. Bu araştırmada Tf fonksiyonunun ağırlıklı Hardy uzayı $H^1(w)$ yı ağırlıklı $L^1(w)$ uzayına dönüştürdüğü gösterilmiştir. Yani her $f \in H^1(w)$ için

$$\|Tf\|_{L^1(w)} \leq \alpha \|f\|_{H^1(w)}$$

olacak şekilde bir pozitif α sabitinin varlığı gösterilmiştir.

1. INTRODUCTION

We say that a positive function $w \in L^1_{loc}(\mathbb{R})$ is a Muckenhoupt's A_p weight for some $1 < p < \infty$ if the following condition is satisfied:

$$\sup_I \left(\frac{1}{|I|} \int_I w(x) dx \right) \left(\frac{1}{|I|} \int_I w(x)^{-\frac{1}{p-1}} dx \right) < \infty,$$

where the supremum is taken over all intervals I in \mathbb{R} . We say that $w \in A_1$ if given any interval I in \mathbb{R} there exists a constant $C > 0$ such that

$$\frac{1}{|I|} \int_I w(y) dy \leq Cw(x)$$

for a.e. $x \in I$.

We say that $w \in A_\infty$ if there exist $\delta > 0$ and $\varepsilon > 0$ such that given an interval I in \mathbb{R} , for any measurable set $E \subset I$,

$$|E| < \delta \cdot |I| \Rightarrow w(E)(1-\varepsilon) \cdot w(I)$$

where

$$w(E) = \int_E w.$$

One can find an extensive study of weighted Hardy spaces $H^p(w)$ in Garcia-Cuerva, J. (1979), where w is a Muckenhoupt's A_p weight. The atomic characterization of $H^p(w)$ has also been given in Garcia-Cuerva, J. (1979). Given a weight function w on \mathbb{R} , as usual we denote by $L^p(w)$ the space of all functions satisfying

$$\|f\|_{L^p(w)}^p = \int_{\mathbb{R}} |f(x)|^p w(x) dx < \infty.$$

When $p = \infty$, $L^\infty(w)$ is equal to the space L^∞ and

$$\|f\|_{L^\infty(w)} = \|f\|_{L^\infty}.$$

Let ϕ be a function in $S(\mathbb{R}^n)$, the Schwartz space of rapidly decreasing smooth functions, satisfying

$$\int_{\mathbb{R}} \phi(x) dx = 1.$$

Define

$$\phi_t(x) = t^{-n} \phi(x/t), \quad t > 0, x \in \mathbb{R},$$

and the maximal function f^* by

$$f^*(x) = \sup_{t>0} |f * \phi_t(x)|.$$

Then $H^p(w)$ consists of those tempered distributions $S'(\mathbb{R}^n)$ for which $f^* \in L^p(w)$ with

$$\|f\|_{H^p(w)} = \|f^*\|_{L^p(w)}.$$

These weighted Hardy spaces $H^p(w)$ can also be characterized in terms of these atoms in

the following way:

Definition 1. Let $0 < p \leq 1 \leq q \leq \infty$ and $p \neq q$ such that $w \in A_q$ with critical index q_w . Set $[\cdot]$ the integer function. For $s \in \mathbb{Z}$ satisfying $s \geq [n(q_w / p - 1)]$, a real-valued function a defined on \mathbb{R} is called a (p, q, s) -atom with respect to w if

- (i) $a \in L^p(w)$ and is supported on an interval I ,
- (ii) $\|a\|_{L^q(w)} \leq w(I)^{1/q-1/p}$,
- (iii) $\int_{\mathbb{R}} a(x) x^\alpha dx = 0$ for every multi-index α with $|\alpha| \leq s$.

The real-valued atom defined above is called a (p, q, s) -atom centered at x_0 with respect to w ($w-(p, q, s)$ -atom centered at x_0), where x_0 is the center of the interval I .

Remark. Let a be any real-valued $w-(p, q, s)$ -atom supported in an interval I . Then we have

$$\int_I |a(x)|^p w(x) dx \leq 1.$$

Proof. Let a be any B -valued $w-(p, q, s)$ -atom. It is clear that $a \in L^p_B(w)$ and $\|a\|_{L^p_B(w)} \leq 1$, since by Hölder's inequality

$$\begin{aligned} \int_I |a(x)|^p w(x) dx &\leq \|a^p\|_{L^{r'}(w)} \left(\int_I w(x) dx \right)^{1/r'} \\ &= \|a\|_{L^p(w)}^p \cdot w(I)^{1-p/q} \\ &\leq 1, \end{aligned}$$

where $r = q/p$ and $1/r' = 1 - 1/r = 1 - p/q$.

Note that analog to the classical case any function in $H^p(w)$ admits a decomposition

$f = \sum \lambda_i a_i$, where a_i 's are $w-(p, q, s)$ -atoms and $\sum |\lambda_i|^p < \infty$. For a fixed weight function w and $f \in H^p(w)$ it is well known (see Garcia-Cuerva, J. (1979)) that

$$\|f\|_{H^p(w)} = \inf \left(\sum_i |\lambda_i|^p \right)^{1/p}.$$

2. RESULTS

Let $f : \mathbb{R} \rightarrow \mathbb{R}$ be a locally integrable function, and define the dyadic maximal function

$$Tf(x) = \sup_k \frac{1}{2^k} \left| \int_0^{2^k} f(x-t) dt \right|.$$

It is clear that $Tf(x) = \sup_k |K * f(x)|$, where

$$K(x) = \frac{1}{2^k} \chi_{[0, 2^k]}(x).$$

Our first result is the following lemma that will be used when proving our main result:

Lemma 1. There exists a positive constant C independent of $y \in \mathbb{R}$ such that

$$\int_{|x|>2|y|} \sup_k |K(x-y) - K(x)| dx \leq C.$$

Proof. Let

$$\begin{aligned} \Phi_k(x, y) &= \frac{1}{2^k} \chi_{[0, 2^k]}(x-y) - \frac{1}{2^k} \chi_{[0, 2^k]}(x) \\ &= \frac{1}{2^k} \chi_{[y, y+2^k]}(x) - \frac{1}{2^k} \chi_{[0, 2^k]}(x). \end{aligned}$$

First consider the case $x \geq 0, y \geq 0$. Since $x > 2y$, we obviously have $\Phi_k(x, y) = \frac{1}{2^k} \chi_{[y, y+2^k]}(x)$. If for some $k \in \mathbb{Z}^+$ we have $x > y + 2^k$, it is then clear that $\Phi_k(x, y) = 0$. So we only need to consider the case $\Phi_k(x, y) = \frac{1}{2^k} \chi_{[y, y+2^k]}(x)$ when evaluating the integral.

Now assume that $x < 0, y < 0$. Since $|x| > 2|y|$, we have $y > x$, and thus we obtain $\Phi_k(x, y) = 0$. Also, same is true if $x \leq 0, y \geq 0$ since this implies $x < y$. If $x \geq 0, y \leq 0$, we have the same situation as in the first case.

We conclude that we only need to evaluate

$$\Phi_k(x, y) = \frac{1}{2^k} \chi_{[y, y+2^k]}(x),$$

and we have

$$\begin{aligned} &\int_{|x|>2|y|} \sup_k |K(x-y) - K(x)| dx \\ &= \int_{|x|>2|y|} \sup_k \frac{1}{2^k} \chi_{[y, y+2^k]}(x) dx \\ &= \int_y^{y+2^k} \sup_k \frac{1}{2^k} dx \\ &= 1 \end{aligned}$$

and thus, our proof is complete.

Lemma 2. There exists a constant $C > 0$ such that

$$\int_{\mathbb{R}} |Tf(x)|^p w(x) dx \leq C \int_{\mathbb{R}} |f(x)|^p w(x) dx$$

for all $f \in L^p(w), 1 < p < \infty$, where

$$L^p(w) = \left\{ f : \mathbb{R} \rightarrow \mathbb{R} : \int_{\mathbb{R}} |f(x)|^p w(x) dx < \infty \right\}.$$

Proof. Recall the Hardy-Littlewood maximal function

$$Mf(x) = \sup_I \frac{1}{|I|} \int_I f(x-t) dt,$$

where the supremum is taken over all intervals I in \mathbb{R} . It is clear that for any $x \in \mathbb{R}$ we have $Tf(x) \leq Mf(x)$ and it is also well known (see Muckenhoupt, B. (1972)) that there exists a constant $C > 0$ such that

$$\int_{\mathbb{R}} |Mf(x)|^p w(x) dx \leq C \int_{\mathbb{R}} |f(x)|^p w(x) dx$$

for all $f \in L^p(w), 1 < p < \infty$. We thus obtain

$$\begin{aligned} \int_{\mathbb{R}} |Tf(x)|^p w(x) dx &\leq \int_{\mathbb{R}} |Mf(x)|^p w(x) dx \\ &\leq C \int_{\mathbb{R}} |f(x)|^p w(x) dx \end{aligned}$$

and this completes our proof.

We can now state and prove our main result:

Theorem 1. Let $1 < p < \infty$, and $w \in A_p$. Then there exists a constant $C > 0$ such that

$$\|Tf\|_{L^p(w)} \leq C \|f\|_{H^1(w)}$$

for all $f \in H^1(w)$.

Proof. Given an interval $I = I(x_0; R)$ in \mathbb{R} with center x_0 and length $2R$, and denoting by \tilde{I} the double interval, $\tilde{I} = I(x_0; 2R)$, we first claim that

$$\int_{\mathbb{R}-\tilde{I}} |T(f)| w(x) dx \leq C \|f\|_{L^1(w)}$$

for every $f \in L^1(w)$ supported in I such that

$$\int f(x) dx = 0.$$

But for such a function f ,

$$Tf(x) = \int_I \{K(x-y) - K(x-x_0)\} \cdot f(y) dy$$

$$(x \in \tilde{I})$$

and therefore

$$\int_{\mathbb{R}-\tilde{I}} |Tf(x)| w(x) dx$$

$$\leq \int_{|x-x_0| \geq 2R > 2|y-x_0|} \sup_k |\{K(x-y) - K(x-x_0)\} \cdot f(y)| dy w(x) dx$$

$$\leq C \int_{|y-x_0| < R} |f(y)| w(y) dy,$$

which proves our claim.

Let now $a(x)$ be an atom with supporting interval J , and let I be the smallest interval containing J , and \tilde{I} as before. Then there exists a positive constant C_1 such that

$$\int_{\mathbb{R}-\tilde{I}} |Ta(x)| w(x) dx \leq C_1.$$

On the other hand, since by Lemma 2

$$\int_{\mathbb{R}} |Ta(x)|^q w(x) dx \leq C_2 \int_{\mathbb{R}} |a(x)|^q w(x) dx$$

we have by Hölder's inequality,

$$\int_{\tilde{I}} |Ta(x)| w(x) dx \leq C_3 \|a(x)\|_{L^q(w)} (Cw(J))^{1/q'}$$

$$\leq \text{Constant}.$$

REFERENCES

- [1] Coifman, R, Fefferman, C. Weighted norm inequalities for maximal functions and singular integrals. *Studia Math.* 1974; 51, 241-250.
- [2] Demir, S. H^p spaces and inequalities in ergodic theory. Ph.D Thesis, University of Illinois at Urbana-Champaign, Urbana, IL, USA, 1999.
- [3] Garcia-Cuerva, J. Weighted H^p spaces. *Dissertations Math.* 1979; 162, 1-63.
- [4] Garcia-Cuerva, J, Rubio de Francia, JL. Weighted norm inequalities and related topics. *Mathematics Studies* 116, North-Holland, Amsterdam, 1985.
- [5] Muckenhoupt, B. Weighted norm inequalities for the Hardy maximal function. *Trans. Amer. Math. Soc.* 1972; 165, 207-226.

Possible Health Problems Caused by Bee Products and Uncontrolled Use

Gıyasettin BAYDAŞ^{1*}, F. Tutku AKSOY², Zeynep GÜNGÖRDÜ DALAR³, Merve Nur AKSAKAL⁴,
İpek ÇORUHLU⁵, Sara ÇIBİK², Elif Sena ÖZCAN⁶, Öykü TOPTAŞ³, Zümra KUL¹

¹Altınbaş University, Faculty of Medicine, Department of Medical Physiology, İstanbul, Türkiye

²Altınbaş University, Faculty of Medicine, Department of Medical Biochemistry, İstanbul, Türkiye

³Altınbaş University, Faculty of Medicine, Department of Medical Microbiology, İstanbul, Türkiye

⁴Altınbaş University, Faculty of Medicine, Department of Medical Biology, İstanbul, Türkiye

⁵Altınbaş University, Faculty of Medicine, Department of Histology&Embryology, İstanbul, Türkiye

⁶Altınbaş University, Faculty of Medicine, Department of Anatomy, İstanbul, Türkiye

Gıyasettin BAYDAŞ ORCID No: 0000-0002-9206-3177

F. Tutku AKSOY ORCID No: 0000-0001-6402-0666

Zeynep GÜNGÖRDÜ DALAR ORCID No: 0000-0003-2177-4235

Merve Nur AKSAKAL ORCID No: 0000-0001-5624-0140

İpek ÇORUHLU ORCID No: 0000-0003-3925-0413

Sara ÇIBİK ORCID No: 0000-0003-0100-3409

Elif Sena ÖZCAN ORCID NO: 0000-0002-4410-7622

Öykü TOPTAŞ ORCID NO: 0000-0002-0342-535X

Zümra KUL ORCID NO: 0000-0002-6317-5639

*Corresponding author; baydas@hotmail.com

(Received: 1.02.2024, Accepted: 11.03.2024, Online Publication: 26.03.2024)

Keywords
Apitherapy,
Honey,
Bee pollen,
Propolis,
Apilarnil,
Bee venom,

Abstract: Traditional and alternative medicine practices are used in Turkey, as well as around the World, to protect health and treat various diseases. Among these applications, Apitherapy has come to the fore particularly in recent years. As the use of medicines causes serious side effects, especially on human health, people are increasingly turning to alternative medical treatments. Apitherapy is a treatment method involving bee products such as honey, pollen, Royal Jel, propolis, and bee venom. It is primarily used for the purpose of promoting a healthier lifestyle. While these products have been traditionally used in various treatments for many years, their systematic use has gained prominence in recent years. Studies have shown that these products strengthen the immune system, provide protection against various types of cancer, and exhibit antimicrobial and antioxidant properties. In addition, the high protein, vitamin, mineral and amino acid content in these products increases the treatment potential. However, in addition to the benefits of these supportive and therapeutic substances, there is also the possibility of various toxic effects when used irregularly and without medical supervision. Sometimes these conditions can lead to various organ failures. This review aims to reveal the adverse effects encountered in the use of bee products and apitherapy applications and emphasizes that all natural products, especially bee products, should not be used uncontrolled.

Arı Ürünleri ve Kontrolsüz Kullanımlarından Kaynaklanabilen Sağlık Sorunları

Anahtar Kelimeler
Apiterapi,
Bal,
Arı poleni,
Propolis,
Apilarnil
Arı zehri

Özet: Tüm Dünya'da olduğu gibi Türkiye'de de sağlığın korunması ve çeşitli hastalıkların tedavisinde geleneksel ve alternatif tıp uygulamaları kullanılmaktadır. Apiterapi bu uygulamalar arasında özellikle son yıllarda dikkat çekmektedir. İlaç kullanımının özellikle insan sağlığı açısından ciddi yan etkilere sebep olmasından dolayı insanlar yan etkileri az veya hiç olmayan alternatif tıbbi tedavi yöntemlerine yönelmektedir. Apiterapi, bal, polen, arı sütü, propolis, arı zehiri gibi arı ürünleriyle yapılan bir tedavi yöntemi olup daha çok sağlıklı yaşam amacıyla da kullanılmaktadır. Arı ürünleri her ne kadar uzun yıllardır geleneksel olarak çeşitli tedavilerde kullanılıyor ise de özellikle son yıllarda daha sistematik olarak kullanılmaya başlandı. Bu ürünlerin, immun sistemi

güçlendirdiği, çeşitli kanser türlerine karşı koruyucu olduğu, antimikrobiyal, antioksidan özellik gösterdiği yapılan çalışmalarda anlaşılmıştır. Ayrıca bu ürünlerin yüksek oranda protein, vitamin, mineral, aminoasitler içermesi de bu tedavi potansiyellerini yükseltmektedir. Bununla beraber, her destekleyici ve tedavi edici maddenin yararlarının yanında, düzenli ve doktor kontrolünde kullanılmadıklarında çeşitli toksik etki gösterme ihtimali vardır ve bazen bu durumlar çeşitli organ yetmezliğine de neden olabilmektedir. Bu derleme, arı ürünlerinin kullanımı ve apiterapi uygulamalarında karşılaşılan olumsuz etkileri ortaya koymayı amaçlamakta ve başta arı ürünleri olmak üzere tüm doğal ürünlerin kontrolsüz kullanılmaması gerektiğini vurgulamaktadır.

1. INTRODUCTION

Apitherapy has been increasingly utilized in recent years. However, as with any supportive or complementary product, the use of supplementary foods may have beneficial effects, they may also have harmful consequences for health. Therefore, the application of apitherapy under the medical supervision has gained importance. In this review, the benefits and potential risks of bee products will be discussed based on recent studies.

1.1. Honey

Honey is divided into two primary groups, flower honey and secretory honey, based on the origin of the collected nectar by bees. Flower honey originates from the nectar of various plant flowers, and notable varieties include lime, clover, citrus, cotton, thyme, and acacia honey. Secretory honey is sourced from plant secretions such as pine, oak, and leaf honey [1]. It is prohibited by law and regulation to add any external substance or to remove any substance from the natural structure of honey that contains many bioactive substances beneficial to health. According to the *Turkish Food Codex Honey Regulation* [2], honey should have a distinctive taste and odor, should be free of any additives, should not contain pollen and honey-specific substances that have not been removed, and should not contain pathogens, parasites and their eggs that are harmful to health such as *Clostridium botulinum*.

Honey contains on average 80% carbohydrate, 17% water and various minor compounds including organic acids, mineral salts, vitamins, proteins, phenolic compounds, fats, and free amino acids [3]. The colour of honey can vary from a light yellow to a dark brown or even black colour. The colour of honey is determined by compounds such as the phenolic compounds of the pollen, carotene and anthocyanidins. Dark honey has higher mineral content and antioxidant properties than light honey [4].

Honeybees generally prefer flowers as a source of nectar and sometimes use secretions left by trees (oak honey) or secretions left by insects in trees (pine honey) [5]. Depending on the source of honey and the substances it contains, honey has antimicrobial, antitumour, antiparasitic, immunomodulatory, anti-inflammatory, antioxidant, gastroprotective (antiulcerative), cardioprotective, hepatoprotective, antianemic, prebiotic, antiosteoporotic, and wound healing properties [6].

Honey has been recognized for its effectiveness against both gram-negative and gram-positive bacteria [6]. In a study [3], a 10% concentration of honey applied to the *Echinococcus granulosus* parasite, which causes hydatid cyst (echinococcosis), exhibited a lethal effect from the third minute onwards. Aksoy et al. [7] evaluated the antimicrobial activity of honey samples collected from Bingöl region and reported that 0.1 mL honey inhibited the growth of bacterial species such as *Escherichia coli*, *Staphylococcus aureus*, *Klebsiella pneumoniae*, *Bacillus brevis*, *Pseudomonas aeruginosa*, as well as fungal species like *Candida albicans* and *Rhodotorula rubra*. The antibacterial properties of honey are due to its osmotic structure and H₂O₂ formed by the glucose oxidase enzyme in its structure, in addition to phenolic compounds [8].

Viuda-Martos et al. [6] reported that flavonoids such as pinocembrin, galangin and caffeic acid phenethyl ester (CAPE) inhibit bacterial RNA polymerase. In addition, they reported that quercetin inhibited ATP synthesis of the bacterium by increasing the permeability of the cell membrane, leading to the loss of the ability to transport substances through the cell membrane and mobility.

The anti-cancer effects of honey has been noted across a range of tumour cells, including those associated with breast cancer, cervical cancer, leukaemia, renal cell cancer, bladder cancer, colon cancer, prostate cancer, oral cancer, bone cancer, and brain cancer [9]. Apart from honey's antimicrobial, antioxidant, and anticancer effects, researches indicate that the metabolites within its composition also exhibit positive influences on wound healing, as well as on the diseases of digestive system and cardiovascular system [9]. Ajibola et al. [10] reported that honey reduces the effect of gastritis and ulcer by inhibiting the development of *Helicobacter pylori* bacteria, the main causative agent of gastric ulcer. In addition to the many beneficial health effects of honey, it is emphasized that there are also some adverse effects. One of these situations is mad honey poisoning. Mad honey poisoning occurs when consuming honey produced from *Rhododendron* flowers containing grayanotoxin. *Rhododendron* is commonly found in the eastern Black Sea region and cities bordering the Black Sea in Türkiye. The flowers, particularly in spring, provide a rich source of nectar for honeybees. Grayanotoxins bind to sodium channels, resulting in their effects. The heart is the organ most rapidly affected by this toxin. Death with severe bradycardia can occur with consumption of this honey. Symptoms of poisoning in humans depend on the amount of honey consumed and may include increased salivary secretion, vomiting,

and paraesthesia around the mouth and extremities. The clinical signs are typical of grayanotoxin poisoning, as indicated by the patient's history of eating honey and clinical findings [11].

The consumption of honey is not recommended for infants under one year of age due to the possible presence of *Clostridium botulinum* bacteria spores. These spores can open in the stomach and intestines, producing toxins that cause poisoning. Symptoms typically include nervous system issues, weakness, decreased sucking, weak crying, constipation, and diminished muscle strength. If the symptoms untreated, respiratory muscle involvement can lead to death [12].

1.2. Propolis

Propolis is a collective term referring to a resinous substance that honeybees gather from various plants, along with pollens and waxes. Additionally, its quality is enhanced by incorporating assorted saliva and enzyme-containing secretions. Resin, primarily sourced from trees, is collected by bees, who enhance it with substances from their salivary glands and further process the mixture using their mandibles. Bees use propolis to disinfect honeycombs, as a building material and for mummification. The word, propolis, Pro"; front, entrance, and "police"; is Greek in origin, it means city and was used in relation to honeybees defending their hives [13].

The colour of propolis varies, appearing in shades of yellow, brown, or green, influenced by the region of collection and the diversity of the local plant flora. Structurally, it has a sticky and resinous form. It is known as bee glue due to its gummy feature. Propolis turns rigid and fragile when the temperature drops below 10 degrees, and it becomes smooth and resin-like at temperatures between 15 and 25 degrees. At 30-40 degrees, it becomes softer and has a pronounced sticky structure. It turns into the structure known as liquid propolis at temperatures above 40 degrees [14].

Propolis comes from several continents, locations, and plant species, which contribute to its unique composition. The composition and structure of propolis vary based on the diversity of plants accessible to bees. Propolis activities could consist of enhancing the stability of the structure and lowering vibration, enhancing the hive's thermal insulation, and minimizing water loss and offering defence against infections through antifungal and antibacterial qualities [15,16].

Propolis is primarily created by plants, compounds released by the metabolism of honeybees, and elements that arise during propolis synthesis (17). Propolis typically consists of approximately 50% plant resin, 30% wax, 10% essential oils, and 5% pollen. Its composition also contains small quantities of other chemicals (5%) including benzoic acid, lactones, quinones, steroids, sugars, vitamins (B1, B2, B3, and B6) and natural pigments (carotenoids and chlorophyll). Among the most significant chemical components of propolis are

flavonoids, responsible for its antibacterial, antiviral, anti-fungal, and anti-inflammatory properties, along with aromatic acids, terpenoids (including diterpenoid acids and triterpenoids), fatty acids, esters, phenols, aldehydes, and ketones. [15, 18].

According to the researches propolis and its extracts in particular, have been shown to possess antibacterial, antiviral, antifungal, antioxidant anti-inflammatory, anti-allergic, anticarcinogenic, anti-diabetic, cytostatic, hepatoprotective, photoprotective, immunogenic, and because of its wide range of biological actions, including anaesthetic, it has been used for a very long time for both illness prevention and therapy [19, 20, 21, 22, 23]. Propolis is beneficial in treatments of tumours, some types of cancer, some neurological diseases, mouth sores, wound, burn and respiratory system diseases (flu, pneumonia, bronchitis), some digestive system diseases, and infections affecting the urinary tract. [17, 24, 25]

Propolis and its constituents play a crucial role in promoting good health and preventing and treating minor illnesses. It has many positive qualities, however researches have shown that in those who are allergic to any of its constituents, it can trigger allergic reactions. The following adverse reactions were observed: dyspnea, oral pain, perioral dermatitis, labial edema, peeling of the lips, and contact cheilitis [26, 27]. Propolis has been found to contain a few allergens, including phenylethyl caffeate, ferulic acid, benzyl caffeate, 3-methyl-2-butenyl caffeate, geranyl caffeate, methyl cinnamate, benzyl alcohol, and tectochrysin. Propolis should also be routinely tested in children and adolescents prior to prescription, as it appears to be one of the most common allergens [26].

Moreover, heavy metals and other environmental contaminants may be present in propolis as a natural product. According to the analysis, six harmful metals were detected in 106 samples of raw propolis from Brazil [20], Harmful metals, as they do not break down naturally, can build up in organisms throughout the food chain and ultimately reach humans primarily through food (up to 90%). It's noteworthy to note that heavy metal concentrations are decreased by 24.24% to 100.00% during the filtration and separation of crude propolis [26].

A study assessing the effects of propolis extracts on health revealed that propylene glycol extract led to blood vessel dilation and neuron apoptosis in brain tissue. Furthermore, it was observed that propylene glycol extracts of propolis exhibited higher toxicity levels compared to olive oil and water extracts. Consequently, olive oil and water extracts of propolis are regarded as safer alternatives for pregnant and infant rats in comparison to propylene glycol extract [28].

Propolis and products derived from it have the potential to become contaminated with in-hive acaricides such as coumaphos and tau-fluvalinate. Moreover, since honeybees utilize propolis in the hive as a protective substance and building material, they are consistently

exposed to pesticide residues present in the product [29]. The available data suggests that various pesticide residues, particularly acaricides, may accumulate in perge, propolis, and beeswax, reaching concentration levels exceeding a thousand $\mu\text{g}/\text{kg}$ [30].

Diagnosing medication-induced liver injury can pose a challenge for many potential causes, including both prescription and over-the-counter medications, as well as herbs and other medicines. Propolis is not currently listed as a cause, and there is no recommended dosage as the product is considered safe. But a case report describes a young man who experienced elevated liver enzymes because of chronic consumption of high doses of propolis [31].

Propolis finds extensive use in traditional medicine, so more research in this area is necessary. Additional data collection is needed to assess the potential harmful impact of this bee product when consumed in large amounts over an extended period. Despite the numerous advantages, widespread accessibility, and economic viability, it is crucial to reconsider the potential applications of propolis and its flavonoids as medicinal treatments.

1.3. Bee Pollens

Basically, Pollen, the reproductive cell of flowering plants, is a microscopic structure resembling grains that is discovered in the anthers of stamen within closed-seeded plants. Honeybees collect and process this pollen into bee pollen.

Thanks to its high protein content, it plays a crucial role in sustaining the nutrition of bees royal jell production, the development of the muscular and digestive systems of young bees, the development of offspring, in short, in ensuring the continuity of the colony [32].

Different plant sources are the reason to produce different colours, such as red, yellow, green, purple and orange. The size (6-300 μm), colour and shape of pollen grains varies according to its plant origin [32; 33].

The physical, biological, or chemical properties of pollen may vary depending on the geographical location of the region from which it is collected, climatic characteristics, storage and packaging [33]. Typically, bee pollen constitutes a multicomponent colloidal system consisting of biopolymers and diverse particles, including oil droplets, gas bubbles, lipid crystals, and more.

According to plant sources, pollen has approximately 200 components. Although the carbohydrate ratio of bee pollen varies between 13-55%, it is around 30.8% on average. Of the total 30.8%, 25.7% comprises glucose and fructose sugars, while the protein content of bee pollen ranges from 10% to 40% depending on the plant source, with an average of 22.7%. [34]

Recently, there has been significant interest in refining snacks using honey-making irritant, as it serves as an

excellent model for healthy minerals [35]). It holds lipids, proteins and micronutrients essential principally for honeybees, while presenting nutraceutical potential for human countering many afflictions [36].

Bee pollen has a wide range of therapeutic properties, including antioxidant, antimicrobial, fungicidal, anti-radiation, hepatoprotective, chemoprotective, and/or chemotherapeutic. It has preventive, anti-inflammatory and intestinal function regulating activities. Additionally, it improves cardiovascular health and acts as an antibiotic, anticancer, and anti-diarrheal agent. It also strengthens the digestive and immune systems, consequently delaying aging, and improving issues such as gastroenteritis, arteriosclerosis, respiratory diseases, and prostate problems [37]. In addition to the therapeutic effects of pollen, many side effects including allergic reactions such as anaphylactic shock have been reported.

1.3.1. Pollen Allergy

In addition to the therapeutic effects of pollen, anti-therapeutic properties have also been revealed by various studies. Pollen allergy, anaphylactic shock and many side effects are examples. Pollen allergy is the result of a distinguishing reaction invulnerable structure to an irritant. Antigen-presenting cells (APCs) introduce the invulnerable response by communicating incidental signals to added containers. T cells are triggered by aeroallergens [38]

1.3.2. Bee Pollen-Induced Anaphylaxis:

There are various reports of acute susceptible reactions induced by honey-making pollen, containing anaphylaxis [39, 40, 41]. The literature reports cases of anaphylaxis linked to bee pollen consumption, yet many individuals are unaware of this potential danger. Evidence supporting this association mainly stems from case reports and a single small case-control study. For example, Cohen and others reported three cases of allergic rhinitis, one of them developed severe allergic reactions after consuming honey containing dandelion pollen, indicating cross-allergenicity between wind-pollinated ragweed and insect-pollinated dandelion [40, 42].

They have also documented hypersensitive reactions triggered by honey-making pollen [42]. In 50% of these cases, individuals sensitized to wind-pollinated irritant pollen experienced intrinsic allergic responses after consuming honey-made pollen containing bug-pollinated Compositae family appendages like dandelion and goldenrod. Common syndromes observed include facial edema, urticaria, and transient allergic rhinitis.

1.3.3. Other Side Effects of Bee Pollen

Despite honey-making irritant appearing to be generally safe and effective, approvals for using honey-making pollen for hypersensitivity, immunological, and other conditions, as well as emphasizing the healthful compounds it contains, it is essential to consult a

physician before utilizing any unrefined product for any medical condition. Some irritant contains poisonous wealth such as mannose sugars, miscellaneous alkaloids, heavy metals, pesticides, herbicides, mycotoxins, microorganisms, medicines and polyphenolic compounds [42, 43]

Due to the aforementioned anti-therapeutic effects, pollen and pollen products need to be thoroughly characterized for allergens and other components with potentially harmful effects.

In conclusion, there are many mechanisms and much to be investigated on the anti-therapeutic effects of pollen.

1.4. Royal Jelly

Royal Jelly (RJ) which is also known as Apilak has creamy composition and displays colour range between white to yellow. This substance is produced by worker honeybees locally in their hypopharyngeal and mandibular glands. In their life circle, specifically, during the beginning of their larvae stages, bees are fed by this unique food for first three days. Subsequently, the worker bees' diet substitutes to different food choice which is named as perge that includes dominantly honey and pollen while the bees that is selected as the future queen bee proceed to consume RJ for rest of its lifetime [44].

RJ has traditionally been favored in alternative medicine, particularly since ancient times in Egypt, and throughout Asian apitherapy practices, it has been utilized extensively. Today, RJ is favored in the pharmaceutical and alimentary industries and is available over-the-counter as a dietary supplement [45].

RJ contains approximately 67% water, 16% carbohydrates, 12.5% protein and amino acids, and 5% lipids, with notable variations observed among different sources [46]. The distinct and abundant nutritional content of carbohydrates, proteins, lipids, vitamins, minerals, polyphenols, flavonoids, and several biologically active substances is attributed to the many pharmacological properties of RJ [47]. The primary constituent of RJ is protein, accounting for 50% of its dry matter [48]. Sugars, mainly glucose and fructose, comprise 90% of the overall carbohydrates content of RJ, while sucrose 0.8-3.6%. [49]. Minor components of RJ are enzymes, minerals, vitamins and phenolics [46].

RJ contains royalisin peptides and antimicrobial jelleins, MRJPs, 10-hydroxy-2-decenoic acid (10-HDA), which have anti-inflammatory, immunomodulatory, antimicrobial, metabolic syndrome-protecting, neuromodulatory and anti-aging properties [45].

Several research have documented antimicrobial effects of RJ on bacterial, fungal and viral pathogens, while hypotensive, antihypercholesterolemic, antitumor, and anti-inflammatory effects have been reported in model animals [50].

Furthermore, clinical studies have demonstrated antidiabetic effects, benefits for non-malignant prostatic hyperplasia, and assistance in wound repair for diabetic foot ulcers [51].

RJ is considered a significant contributor to healthy aging and longevity. This is because it promotes the overall health and reproductive capabilities of queen bees. Queen bees, which can produce up to 3,000 eggs in a day and live for up to five years, owe their longevity to RJ, while sterile worker bees typically survive for only 45 days [52]. The beneficial effects of RJ in humans extend beyond physical health improvements to encompass enhancements in general mental health, including reductions in anxiety levels and improvements in mood and mild cognitive decline among the elderly (>60 years) [53, 54].

The neurological psychological benefits of RJ are shown by changes in biomarkers of physical health; cholesterol and apolipoproteins can be given as examples. Hypercholesterolaemia has been shown to favour the accumulation of β -amyloid, leading to neuronal loss - a signature finding of Alzheimer's disease. On the other hand, the decrease in plasma lipids caused by RJ has been related with an increase in antioxidant effect, a decline in β -amyloid accumulation and the protection against neuronal damage [55].

In terms of appropriate RJ usage dose, research has shown that 100 mg/kg is typically the most efficient dose, and greater doses are rarely needed. 0.5g/day is suggested and can be continued for 2 to 12 months for infants. For adults, doses ranging from 1 to 5 grams per day can be taken based on the underlying medical condition. To achieve more potent and rapid results, a higher dosage of 10 grams per day can be administered for a shorter duration, such as 3 months with 10 days per month [56].

Ensuring the effectiveness of RJ is essential for its successful application in promoting health. Exposure to heat and certain handling methods can compromise the constituents and efficacy of RJ. Most of RJ's biological properties diminish after being exposed to 40°C for 30 days [57].

Royal jelly is utilized in various products globally, including dietary supplements, beverages, beauty items, and numerous other goods. While it is regarded as relatively harmless and non-toxic adverse reactions of RJ have been reported, the most common of which are allergic reactions, with symptoms ranging from slight to serious [58]. These reactions range from mild to serious, mild gastrointestinal upset, haemorrhagic colitis, and typically include rash, allergic rhinitis, contact dermatitis eczema, conjunctivitis acute asthma, anaphylactic shock, bronchospasm and in a few cases fatality [58, 59].

As with honey, environmental pollutants may exist in RJ. The most prevalent are organochlorine, organophosphorus and carbamate pesticides, which are generally under the minimum hazard grade.

Nevertheless, there have been instances where the highly toxic chloramphenicol has been detected [60].

Bee products like pollen, honey, and venom may lead to allergic reactions that are less severe when compared to those caused by royal jelly. People allergic to these products should not take RJ orally. In addition, caution should be taken when advising RJ to pregnant or breastfeeding women, children [59] and patients with a medical background of allergic conditions such as asthma, rhinitis or atopic dermatitis. If allergic reactions occur following the initial consumption of RJ, this could be attributed to the presence of allergens that cross-react with RJ. [58]. Intake of RJ can incidentally cause contact dermatitis, anaphylaxis, and asthma while MRJP-1 and MRJP-2 are reported as potent allergens [61].

In conclusion, to ensure the efficient and harmless use of RJ as a dietary supplement allergy test should be carried out prior to RJ consumption [58, 59].

1.5. Bee Venom

Bee venom, also known as apitoxin, has a significant role in the defence of the bee colony and is produced in the venom glands located in the abdominal cavity of the bee and stored in the venom sac. The amount of this venom collected in the sac is approximately 0.3 mg. Bee venom is a clear and acidic (pH 4.5-5.5), odorless and watery liquid with a bitter and pungent taste and yellowish-white crystalline structure when dried [62].

The arrangement of bee venom changes depending on many factors to a degree the race of the bee, feeding environments, collection time, and the encircling flora. In general, bee venom consists of various bioactive molecules such as peptides such as melittin, apamin, mast cell degranulation peptide (MCD peptide); minerals such as P, Ca and Mg; enzymes such as phospholipase A2, hyaluronidase, lysophospholipase; biological amines such as dopamine and histamine; and phospholipids [63, 64].

The therapeutic effect of bee venom has been examined by in vivo and in vitro studies, such as its anti-inflammatory, analgesic, anti-hepatotoxic, cytoprotective, antioxidant, antimicrobial, antiviral, radioprotective, antimutagenic, anti-arthritis and anticancer effects [19, 45, 65, 66]. Furthermore, it has been shown that bee venom halts the progression of Alzheimer's disease by protecting the nervous system [67].

The various and complex arrangements of bee venom and the synergistic effects between these components have been stated to aggravate multiple organ damage. Therefore, the mechanisms of toxic reactions caused by bee stings should be thoroughly investigated before treatment with bee venom [68]. The components of bee venom that cause these effects are mainly melittin and phospholipase A2. Melittin has been stated to have analgesic, anticancer, and anti-inflammatory effects. However, it has inflammatory, cytolytic, and hemolytic

effects at high doses. Phospholipase A triggers inflammation is a strong allergen and is the most harmful bee venom component. In the body, it can cause hemolysis and damage the lipid structure of the cell membrane, leading to cell damage and lysis [69]. Hyaluronidase has an allergic effect, while apamin has a neurotoxic effect at high doses. Histamine is another component of bee venom with allergic effects [70].

Bee venom injection, like many different alternative medicine approaches, has been used for thousands of years to relieve pain and various symptoms of inflammatory and painful diseases. Bee venom may be applied in various ways, such as direct bee sting, bee venom injection, or bee venom acupuncture [71]. Clinically, injection of bee venom into acupuncture points has been reported to be successful in the treatment of diseases such as arthritis, Parkinson's disease, multiple sclerosis neuropathic pain, and Alzheimer's disease. In the treatment of rheumatoid arthritis, bee venom treatment in combination with other medications has been reported to be more efficient than treatment with medication alone. In addition, the relapse rate was significantly reduced in patients treated with bee venom [72]. Bee venom has also been reported to have many beneficial effects in vivo and in vitro in Amyotrophic Lateral Sclerosis (ALS), a central nervous system disease defined by degeneration of upper and lower large motor neurons resulting in muscle weakness, including anti-neuroinflammation, reduced neuronal mortality, and decreased glutamate toxicity. A recent study proved that treatment with bee venom showed bright results as a safe adjunctive treatment for Parkinson's disease, providing significant clinical improvement compared to conventional treatment. In Parkinson's Disease in vivo and in vitro, bee venom improved motor symptoms through anti-neurodegenerative effects [71].

Studies have been conducted to examine the anti-cancer activity of bee venom in lung cancer, colon cancer, prostate cancer, melanoma, pancreatic cancer, and many different cancer cell lines. The mechanism of anti-cancer action of bee venom depends on the inhibition of cell proliferation, induction of cell death and apoptosis, inhibition of metastasis, and cytotoxicity. It has been reported that beekeepers have a lower incidence of cancer compared to others, especially a significantly lower incidence of lung cancer [73].

Treatment with bee venom can be therapeutically beneficial or harmful in some patients. Although bee venom therapy is studied as a hopeful therapeutic alternative for the treatment of chronic pain and various diseases, it has not been accepted by food and drug authorities globally. The first reason is that bee venom can cause various allergic reactions in susceptible individuals, which include systemic and anaphylactic reactions. Allergy to bee venom is hazardous and can be lethal [74]. In the study investigating the organismal response following injection of melittin and phospholipase A2, rats were injected with the potential stressors melittin and phospholipase A2. As a result, it was reported that these compounds are extremely potent

stress factors, toxic at the doses tested, and cause degenerative changes in various cell compartments, especially mitochondria [75].

Systemic allergic bee sting reactions have been notified in 3,4% of children and 7,5% of adults. These allergic responses can be mild with skin symptoms such as flushing and angioedema, or categorized as moderate to severe with the risk of lethal anaphylaxis. For this reason, allergy testing should be performed before bee venom treatment [76].

Besides all this, bee venom is a neurotoxin, and apamin in its composition has been shown to trigger depression and drowsiness in rats by blocking Ca²⁺-dependent K⁺ channels (Ludman and Boyle, 2015). Additionally, histamine, acetylcholine, and norepinephrine, which also exist in bee venom, have been shown to affect neuronal responses in rats [77].

Bee venom increased ion permeability and haemoglobin release in human erythrocytes and had a significant lysis activity on human erythrocytes [78].

Several research studies have shown that the therapeutic use of bee venom is contraindicated in children under 5 years of age, pregnant and lactating women, Type 1 diabetes, infections, kidney and liver failure, hepatitis, heart and lung problems, and chronic tuberculosis [79].

In conclusion, despite the therapeutic effects of bee venom therapy that have been concluded in many diseases, its safety is still a limitation and an obstacle to its use as the main treatment. In a systematic review and meta-analysis, 58 out of 145 studies reported mild to severe adverse outcomes following administration [80]. Therefore, more studies are needed to evaluate the safe use and efficacy of bee venom therapy.

1.6. Apilarnil

Apilarnil, which is obtained by collecting and homogenizing Drone larvae in 3-7 days, contains a small amount of RJ, perge, honey and propolis. Although it is not usually used, the honeycomb with apilarnil is cut by beekeepers and thrown away. Apilarnil is a highly concentrated nutritious bee product which ingredients are known to have antiviral, immune-boosting, regenerative power and vitality of the body [81]. It is contained proteins, carbohydrates, fats, polyphenols, amino acids, vitamins (vitamin A, betacarotene, B1, B6, and choline), minerals (calcium, phosphorus, sodium, zinc, manganese, iron, copper, and potassium), hormones, unsaturated compounds (desenoic acids and sulfhydryl compounds), antiviral substances [82]. Apilarnil contains all the essential amino acids of the basic building block of bee larvae so that it is considered a complete food and is widely used in human and animal diets [14].

It has been established by studies that apilarnil stimulates spermatogenesis in men, since it comes mainly from the structure of the male bee larva and is very rich in androgenic hormones. Therefore, both the androgenic

and anabolic effect of apilarnil is considered a natural alternative to medicines and chemicals to stimulate sexual development [83, 84]. Bee larvae in honeycomb cells are consumed as food in many countries [85]. Most of the economically important and edible insects are obtained through production in existing agricultural systems. Apilarnil was first used in Romania in 1980. It was applied by Nicola Iliescu for the treatment of the elderly with neurodegenerative, psychotic or sexual disorders [84].

Male bee larvae are mostly considered a byproduct of beekeeping but have recently been advocated as a high-protein food source. There are some cases related to their allergenic potential [86]. An instance involves a 29-year-old beekeeper who encountered an anaphylactic reaction after consuming a freshly prepared beverage made from male bee larvae. Larval specific susceptibility has been tested and confirmed by basophil activation tests [87]. It has been established that there is an IgE-mediated allergy to drone larvae. There are not enough case reports to develop a specific awareness of the allergenicity of bee larvae, but allergen awareness against the use of apilarnil may be recommended if cases of allergy to other bee products are considered.

It has been described that in some cases of overdose, gastric pain, nausea, diarrhoea. In addition, toxicity, hyperandrogenism, hyperspermatogenesis and a strong antibacterial effect against gram-positive bacteria (*Bacillus aureus*) may occur if the dosage exceed normal usage [88].

The primary function of Apilarnil is to contribute to the battle against disease progression and potentially offer remedies. The diseases that Apilarnil may alleviate include; hypoproteinemia, metabolic diseases, decrease in muscle body weight, chronic fatigue syndrome, physical fatigue, convalescence, premature aging, depression in the elderly, diseases of the nervous system (mental disorders, neuro-psychomotivational diseases), respiratory apparatus diseases, skin deficiencies [89].

Especially, owing to its sexual development properties, Apilarnil offers notable benefits in treating conditions originating from the genital areas, deficiencies in hormones, vitamins, and minerals essential for the optimal development and function of these organs. It is particularly effective against sexual impotence, including issues like low spermatogenesis, erectile dysfunction, and shortened sexual activity duration in men. Moreover, it proves beneficial in addressing endocrine system disorders such as weakened pituitary and adrenal glands, along with alleviating premenstrual syndrome [83, 89].

Several factors may diminish the efficacy of Apilarnil. In cases of diathesis, the body may struggle to digest or absorb Apilarnil efficiently, leading to inadequate processing of its components. Another factor relates to genetic issues; when the "target" organs, such as the endocrine glands, exhibit significant structural or genetic problems, they may not effectively utilize the active compounds present in Apilarnil. It can be inferred that Apilarnil, like other bee products, cannot cure every

disease or bodily issue in instances of diathesis or genetic problems [89].

Performing apitherapy applications by unqualified people, using products that are not medical products, uncontrolled use of products that do not have dose studies, or epigenetic problems specific to the person to whom the application is made may cause negative results in treatment with bee products.

The use of bee products both as food and for apitherapy purposes is very important. However, some allergic reactions may occur in users after the consumption of bee products, incorrect apitherapy applications may be made by non-experts, or some undesirable effects may occur after apitherapy applications in patients.

Although the right applications have been made, the fact that the product used is exposed to environmental contaminants and heavy metals such as pesticide-derived organochlorines, organophosphates, carbamates, and chloramphenicol during the production phase causes the production of unhealthy raw materials [90]. Synthetic acaricides are mostly fat-soluble and persistent in wax [91]. These drug residues accumulated in apitherapy products adversely affect human health and are not suitable for apitherapy. In nature, toxic substances absorbed and stored by plants, as well as pesticides, poison honeybees and their products. All kinds of fat-soluble toxins can be absorbed, and even after a long time, when consumed as food or used in cosmetics, it shows its harmful effect. However, bee products are preferred over drugs due to resistance to antibiotics. Therefore, these products must be natural, antibiotic residue-free products with known quality standards.

1.7. Beeswax

Beeswax is a natural product synthesized from eight wax glands located in the abdomen of the female worker bee and used in the construction of honeycombs [92]. It is mostly produced by *Apis mellifera* and *Apis cerena*, the two most commonly bred species by human.

The amount of beeswax secreted is mostly determined by the needs of the colony. *A. mellifera* can produce approximately half of its body weight in beeswax throughout its life [93]. Beeswax is secreted in liquid form by 12-18 days old young worker bees, and solidifies into flakes as a result of contact with air [94]. The secreted beeswax appears thin and almost white, but later, when it comes in contact with honey and pollen, it becomes intensely yellowish and solidifies due to the effect of the carotenoid pigment passing through the pollen. After four years, its color turns brown because it includes a cocoon [94, 95].

Bees consume 6-10 kg of honey to secrete one kilogram of beeswax and produce the beeswax by forming clusters from their wax glands [96]. The content of the beeswax varies depending on the location of production, the type of honeybee and the age of the beeswax. However, unhydrolyzed beeswax generally contains 71% of esters,

15% of hydrocarbons, 8% of free acids and 6% of the other compounds.

Beeswax is resistant to acids and also gastric juices of honeybees. Water and cold alcohol can not dissolve them, but they are partially soluble in boiling alcohol and completely soluble in chloroform, carbon disulfide and hot turpentine essence. The density of beeswax at 15°C varies between approximately 0.960-0.970 kg/m³ and it melts in the temperature range 63.5-64.5°C [94].

Beeswax has a much larger range of uses compared to other bee products. In the past, beeswax candles were valued more because they had a higher melting point temperature value than other candles and could stay upright in hot weather [93]. In ancient Rome, a cream containing beeswax, olive oil and rose water, known as cold cream, was used to treat burns, cuts, bruises and fractures. Beeswax is included in the first cosmetic cream, together with olive oil and water/rose water emulsion, obtained by the Greek physician Galen in 150 B.C.

Beeswax has also been used in modeling and casting processes, there are sculptures made of beeswax [93, 97]. According to researches beeswax and various combinations of beeswax show antimicrobial properties [97]. Kačániová et al. [98], collected propolis, bee pollen and beeswax samples from two different places in Slovakia and evaluated their antimicrobial activity against various bacteria, molds and yeasts. Beeswax extracts showed antimicrobial effects.

The approach to treatment of non-alcoholic fatty liver disease, which is a disease that can progress to liver fibrosis and cirrhosis, is nutritional change and weight loss. There is no completely successful pharmacological approach, but alternative treatments are being tried to be applied. Studies have shown that a mixture of beeswax alcohols with antioxidant effects, called D-002, help protect the liver [99]. In this research the effectiveness of D-002 was investigated and has been determined that 100 mg D-002 per day improves ultrasonographic findings and insulin resistance indicators in patients, but it has been reported that further studies are needed for confirmation.

Puente et al. [100] determined that administration of D-002, a mixture of beeswax alcohols, administered at 50-100 mg/day for 6 weeks positively affected osteoarthritis symptoms. There was amelioration in pain and stiffness and improvement in physical functionality were observed.

In the study of Perugini et al. [101], 178 beeswax samples collected from Italian hives between 2013 and 2018 were tested for 247 pesticides and the existence of one or more pesticides was determined in 73.6% of the samples. On average, each beeswax sample was reported to contain an average of three different pesticides, each containing up to 14 compounds, some of which are banned in Europe or not permitted in Italy.

It has been determined that more lipophilic pesticides are predominantly found in beeswax. While chromium and zinc were at the highest average concentration values in honey samples, lead and molybdenum were detected only in beeswax. It has been reported that the results obtained show that daily consumption of honey and beeswax may endanger the health of children [102].

1.8. Api-Air

Api-air is an area where the air from beehives is used. The hive contains many flavonoids, including RJ, propolis, honey and pollen. The api-air system was introduced by the German beekeeper Hans Munsch. The basic principle of the api-air system is based on the inhalation of the volatile active components in the bee products in the hive [96].

Heinrich Huttner developed a technique that uses beehive air for treating respiratory diseases. The method involves a hole in the top of the hive equipped with a ventilator and air, a hose through which the patient breathes, and a mask [103]. This therapy is used to treat asthma, bronchitis, pulmonary fibrosis, and respiratory infections [104].

A study identified 56 volatile components in beehive air originating from honey, propolis, perge, RJ, and beeswax. These components include fatty acids, alcohols, aldehydes, esters, ethers, hydrocarbons, phenol, ketones, nitrogenous compounds, and terpenes [105]. In terms of antibacterial activity, beehive air has only been shown to be effective against *S. aureus*. However, individuals using beehive air have reported experiencing relaxation, uninterrupted and restful sleep, increased lung capacity, and improved breathing comfort. Beehive air has also been claimed to be effective in treating various diseases, including bronchitis, asthma, allergies, chronic obstructive pulmonary disease (COPD), emphysema, immune system deficiencies, migraines, and depression. The patients underwent several medical evaluations, including observation of attacks, lung capacity tests, blood tests, and isotope measurements, which showed a rapid and effective recovery process. A beehive air condensation device has been developed for Hiveair in Ukraine.

Currently, in some European countries, such as Germany and Slovenia, this treatment is administered to humans by inhalation of beehive air in well-structured rooms. The aroma produced and inhaled in beehives has been suggested to be beneficial to human health. Air saturated with essential odours treats people with respiratory diseases. This alternative medicine is still a new field of study.

Some cases encountered after the use of other bee products or during their application are not known because they have not been written up. Api-air is one of the popular applications today. Although this application seems to be an innocent application, there are oral reports that the patient died during api-air application due to mycoplasma formation in the hive [106].

2. CONCLUSION

Bee products exhibit numerous pharmacological activities. It is a well-known fact that bee products are used in the treatment of many diseases. However, it is also known that this usage area lacks any control mechanism and is not subject to regulation. Therefore, as observed in many instances, it has been noted that bee products exhibit side effects ranging from mild to potentially fatal levels. To prevent unexpected side effects and potential harms, it is essential that the products obtained after production undergo quality tests and are prepared according to appropriate standards through various processes. Furthermore, routine monitoring of the quality and residue of these products should be conducted through analyses. Based on the detailed information provided, we strongly advise that apitherapy should be carried out under the supervision of a medical professional, considering the potential health issues it may pose.

REFERENCES

- [1] Karabagias IK, Badeka AV, Kontakos S, Karabournioti S, Kontominas MG. Botanical discrimination of Greek unifloral honeys with physico-chemical and chemometric analyses. *Food Chem.* 2014; 165: 181-190.
- [2] Türk Gıda Kodeksi Bal Tebliği. T.C. Resmi Gazete, Sayı: 31107, 22 Nisan 2020.
- [3] Karadal F, Yıldırım Y. Balın kalite nitelikleri, beslenme ve sağlık açısından önemi. *Erciyes Üniv Vet Fak Derg.* 2012; 9(3):197-209.
- [4] Bogdanov S. Honey composition. *The Honey Book.* 2009; p. 1-9.
- [5] Özkök A, D'arcy B, Sorkun K. Total phenolic acid and total flavonoid content of Turkish pine honeydew honey. *JAAS.* 2010; 2(2): 65-71.
- [6] Viuda-Martos M, Ruiz-Navajas Y, Fernández-López J, Pérez-Álvarez JA. Functional properties of honey, propolis, and royal jelly. *J Food Sci.* 2008; 73(9): R117-R124.
- [7] Aksoy Z, Dıġrak M. Bingöl yöresinde toplanan bal ve propolisin antimikrobiyal etkisi üzerinde in vitro arařtırmalar. *Fırat Üniv Fen Müh Bilim Derg.* 2006; 18(4): 471-8.
- [8] White JW, Subers MH, Schepartz AI. The identification of inhibine the antibacterial factor in honey, as hydrogen peroxide and its origin in a honey glucose-oxidase system. *Biochem Biophys Acta.* 1963; 73(1): 57-70.
- [9] Alvarez-Suarez JM, Giampieri F, Battino M. Honey as a source of dietary antioxidants: Structures, bioavailability, and evidence of protective effects against human chronic diseases. *Curr Med Chem.* 2013; 20(5): 621-38.
- [10] Ajibola A, Chamunorwa JP, Erlwanger KH. Nutraceutical values of natural honey and its contribution to human health and wealth. *Nutr Metab.* 2012; 9(61): 1-13.

- [11] Koca I, Koca AF. Poisoning by mad honey: a brief review. *Food Chem Toxicol.* 2007; 45(8): 1315-1318.
- [12] Aureli P, Franciosa G, Fencia L. Infant botulism and honey in Europe: a commentary. *Pediatr Infect Dis J.* 2002; 21(9): 866-868
- [13] Sforcin JM, Bankova V. Propolis: is there a potential for the development of new drugs? *J Ethnopharmacol.* 2011; 133(2): 253-260.
- [14] Krell R. Value-Added Products from Beekeeping, *Fao Agricultural Services Bulletin No. 124*, Chapter 3, Pollen;1996.
- [15] Bankova VS, de Castro SL, Marcucci MC. Propolis: recent advances in chemistry and plant origin. *Apidologie.* 2000; 31(1): 3-15.
- [16] Bogdanov S. Propolis: biological properties and medical applications. *The propolis book.* Chapter 2. 2012; p. 1-42.
- [17] Marcucci MC. Propolis: Chemical composition, biological properties and therapeutic activity. *Apidologie.* 1995; 26: 83-99.
- [18] Yang H, Huang Z, Huang Y, Dong W, Pan Z, Wang L. Characterization of Chinese crude propolis by pyrolysis-gas chromatography/mass spectrometry. *JAAP.* 2015; 113: 158-164.
- [19] Piccinelli AL, Mencherini T, Celano R, Mouhoubi Z, Tamendjari A, Aquino RP et al. Chemical composition and antioxidant activity of Algerian propolis. *J. Agric. Food Chem* 2013; 61(21): 5080-5088.
- [20] Moura, SALD, Negri G, Salatino A, Lima LDDC, Dourado LPA, Mendes JB, et al. Aqueous extract of Brazilian green propolis: primary components, evaluation of inflammation and wound healing by using subcutaneous implanted sponges. *Evidence-Based Complementary and Alternative Medicine.* 2011; 8:1-9.
- [21] Franchin M, Colon DF, Castanheira FV, daCunha MG, Bueno-Silva, B, Alencar SM, Rosalen, PL. Vestitol isolated from Brazilian red propolis inhibits neutrophils migration in the inflammatory process: elucidation of the mechanism of action. *J. Nat. Prod.* 2016; 79(4): 954-960.
- [22] Kang LJ, Lee HB, Bae HJ, Lee SG. Antidiabetic effect of propolis: reduction of expression of glucose-6-phosphatase through inhibition of Y279 and Y216 autophosphorylation of GSK-3 α/β in HepG2 cells. *Phytother Res.* 2010; 24(10): 1554-1561.
- [23] Darendelioglu E, Aykutoglu G, Tartik M, Baydas G. Turkish propolis protects human endothelial cells in vitro from homocysteine-induced apoptosis. *Acta Histochem.* 2016; 118, (4), 369-376,
- [24] De Castro PA, Savoldi M, Bonatto D, Malavazi I, Goldman MHS, Berretta AA, et al. Transcriptional profiling of *Saccharomyces cerevisiae* exposed to propolis. *BMC Complement Altern Med.* 2012; 12: 1-14.
- [25] Tartik M, Darendelioglu E, Aykutoglu G, Baydas G. Turkish propolis suppresses MCF-7 cell death induced by homocysteine. *Biomed Pharmacother.* 2016; 82: 704-712
- [26] Basavaiah ND, Suryakanth DB. Propolis and allergic reactions. *J Pharm Bioallied Sci.* 2012; 4(4): 345.
- [27] de Groot AC. Propolis: a review of properties, applications, chemical composition, contact allergy, and other adverse effects. *Dermatitis,* 2013; 24(6): 263-82.
- [28] Silici S, Okan A, Köklü B, Demiray S, Doğanyigit Z. Toxicity of Propylene Glycol Extract of Propolis on Central Nervous System and Liver in Pregnant and Neonatal Rats. *Z Geburtshilfe Neonatol.* 2023; 227(4): 261-268.
- [29] Wang X, Wang Z, Di S, Xue X, Jin Y, Qi P, et al. Determination of 14 lipophilic pesticide residues in raw propolis by selective sample preparation and gas chromatography-tandem mass spectrometry. *Food Anal. Methods.* 2020; 13: 1726-1735.
- [30] Végh R, Csóka M, Mednyánszky Z, Sipos L. Pesticide residues in bee bread, propolis, beeswax and royal jelly- A review of the literature and dietary risk assessment. *Food Chem Toxicol.* 2023; 176: 113806.
- [31] D'Ercole MC. Prolonged use of propolis can increase liver enzymes. *J Gastrointestin Liver Dis.* 2020; 29(3): 468-469.
- [32] Pasupuleti V.R. Sammugam L. Ramesh N. Gan S.H. Honey, Propolis, and Royal Jelly: A Comprehensive Review of Their Biological Actions and Health Benefits. *Oxid Med Cell Longev,* 2017, 1259510.
- [33] Silici S. Honeybee Products and Apitherapy. *Turk J Food Agric Sci.* 2019; 7(9): 1249-1262.
- [34] Tabatabaei, P. Türkiyenin farklı coğrafi bölgelerinden toplanan arı polenin fenolik bileşikleri ve antioksidan kapasitelerinin araştırılması. Yüksek Lisans Tezi; Ondokuz Mayıs Üniversitesi Fen Bilimleri Enstitüsü. 2017
- [35] Thakur M, Nanda V. Assessment of physico-chemical properties, fatty acid, amino acid and mineral profile of bee pollen from India with a multivariate perspective. *J. Food Nutr. Res.* 2018; 57(4): 328-340.
- [36] Komosinska-Vassev K, Olczyk P, Kafmierczak J. Mencner L, Olczyk K. Bee pollen: Chemical composition and therapeutic application. *Evid Based Complement Altern.* 2015; 1(1): 1-6.
- [37] Kędzia B and Holderna-Kędzia E. Biological properties and therapeutic action of bee pollen, *Postępy Fitoterapii,* 2005; 3-4: 103-108
- [38] Trautmann A, Schmid-Grendelmeier P, Krüger K, Cramer R, Akdis M, Akkaya A, et al. T cells and eosinophils cooperate in the induction of bronchial epithelial cell apoptosis in asthma. *J Allergy Clin Immunol.* 2002; 109(2): 329-337.
- [39] Geyman JP. Anaphylactic reaction after ingestion of bee pollen. *J Am Board Fam Pract,* 1994; 7: 250-252.
- [40] Chivato T, Juan F, Montoro A, Laguna R. Anaphylaxis induced by ingestion of a pollen compound. *J Investig Allergol Clin Immunol.* 1996; 6: 208-209.
- [41] Park HJ, Hur GY, Kim HA, Ye YM, Suh CH, Nahm DH, et al. Anaphylactic reaction after the ingestion

- of bee pollen. *Korean J Asthma Allergy Clin Immunol.* 2007; 27: 57–60.
- [42] Cohen SH, Yunginger JW, Rosenberg N, Fink JN. Acute allergic reaction after composite pollen ingestion. *J Allergy Clin Immunol.* 1979; 64: 270–274.
- [43] Shahali Y. Allergy after ingestion of bee-gathered pollen: influence of botanical origins. *Ann Allergy Asthma Immunol.* 2015; 114(3): 250-1
- [44] Guo J, Wang Z, Chen Y, Cao J, Tian W, Ma B, Dong Y. Active components, and biological functions of royal jelly. *J. Funct. Foods.* 2021; 82: 104514.
- [45] Cornara L, Biagi M, Xiao J, Burlando B. Therapeutic Properties of Bioactive Compounds from Different Honeybee Products. *Front Pharmacol.* 2017; 28(8): 412-433.
- [46] Melliou E, Chinou I. Chemistry and bioactivity of royal jelly from Greece. *J. Agric. Food Chem.* 2005; 53(23): 8987–8992.
- [47] Ramanathan ANKG, Nair AJ, Sugunan VSA. Review on royal jelly proteins and peptides. *J. Funct. Foods.* 2018; 44: 255–264.
- [48] Xin X, Chen Y, Chen D, Xiao F, Parnell LD, Zhao J, et al. Supplementation with Major Royal-Jelly Proteins Increases Lifespan, Feeding, and Fecundity in *Drosophila*. *J. Agric. Food Chem.* 2016; 64: 5803–5812.
- [49] Kunugi H, Mohammed Ali A. Royal jelly and its components promote healthy aging and longevity: From Animal Models to Humans. *Int J Mol Sci.* 2019; 20(19): 4662.
- [50] Ramadan MF, Al-Ghamdi A. Bioactive compounds and health-promoting properties of royal jelly: a review. *J. Funct. Foods.* 2012; 4: 39–52.
- [51] Khoshpey B, Djazayeri S, Amiri F, Malek M, Hosseini A F, Hosseini S, et al. Effect of royal jelly intake on serum glucose, Apolipoprotein A-I (ApoA-I), Apolipoprotein B (ApoB) and ApoB/ApoA-I ratios in patients with type 2 Diabetes: a randomized, double-blind clinical trial study. *Can. J. Diabetes.* 2016; 40: 324–328.
- [52] Silvia C. Remolina & Kimberly A. Hughes. Evolution and mechanisms of long life and high fertility in queen honey bees. *AGE.* 2008; 30: 177–185
- [53] Morita H, Ikeda T, Kajita K, Fujioka K, Mori I, Okada H, Uno Y, Ishizuka T. Effect of royal jelly ingestion for six months on healthy volunteers. *Nutr. J.* 2012; 11(77): 1-7.
- [54] Yakoot M, Salem A, Helmy S. Effect of Memo, a natural formula combination, on Mini-Mental State Examination scores in patients with mild cognitive impairment. *Clin. Interv. Aging.* 2013; 8: 975–981.
- [55] Pan Y, Xu J, Chen C, Chen F, Jin P, Zhu K, et al. Royal jelly reduces cholesterol levels, ameliorates A β pathology and enhances neuronal metabolic activities in a rabbit model of Alzheimer's disease. *Front. Aging Neurosci.* 2018; 10: 50-65.
- [56] Botezan S, Baci GM, Bagameri L, Paşca C, Dezmirean DS. Current status of the bioactive properties of royal jelly: A Comprehensive Review with a Focus on Its Anticancer, Anti-Inflammatory, and Antioxidant Effects. *Molecules.* 2023; 28(3): 1510-1535.
- [57] Kamakura M. Royalactin induces queen differentiation in honeybees. *Nature.* 2011; 473: 478–483.
- [58] Hata T, Furusawa-Horie T, Arai Y, Takahashi T, Seishima M, Ichihara K. Studies of royal jelly and associated cross-reactive allergens in atopic dermatitis patients. *PLoS ONE.* 2020; 15(6): 1-14.
- [59] Maghsoudlou A, Mahoonak AS, Mohebodini H, Toldra F. Royal jelly: chemistry, storage and bioactivities. *J. Apic. Sci.* 2019; 63:17–40.
- [60] Bogdanov S. Contaminants of bee products. *Apidologie.* 2006; 37: 1–18.
- [61] Rosmilah M, Shahnaz M, Patel G, Lock J, Rahman D, Masita A, et al. Characterization of major allergens of royal jelly *Apis mellifera*. *Trop. Biomed.* 2008; 25: 243-251.
- [62] Kolayli S, Keskin M. Natural bee products and their apitherapeutic applications. *Stud. Nat. Prod. Chem.* 2020; 66: 175–196.
- [63] Park D, Jung JW, Lee MO, Lee SY, Kim B, Jin HJ, et al. Functional characterization of naturally occurring melittin peptide isoforms in two honeybee species, *Apis mellifera* and *Apis cerana*. *Peptides.* 2014; 53: 185-93.
- [64] Bogdanov S. Biological and Therapeutic Properties of Bee Venom. In *The Bee Venom Book*; 2016. Bee Product Science: Bern, Switzerland. p. 1–23
- [65] Ahmed O, Fahim H, Mahmoud A, Eman Ahmed EA. Bee venom and hesperidin effectively mitigate complete Freund's adjuvant-induced arthritis via immunomodulation and enhancement of antioxidant defense system. *Arch. Rheumatol.* 2017; 33:198–212.
- [66] Oršolić, N. Bee venom in cancer therapy. *Cancer Metastasis Rev.* 2012; 31: 173–194.
- [67] Ye M, Chung H-S, Lee C, Yoon MS, Yu AR, Kim JS, et al. Neuroprotective effects of bee venom phospholipase A2 in the 3xTg AD mouse model of Alzheimer's disease. *J Neuroinflammation.* 2016; 13(1): 1-12.
- [68] Wehbe R, Frangieh J, Rima M, El Obeid D, Sabatier JM, Fajloun Z. Bee venom: Overview of main compounds and bioactivities for therapeutic interests. *Molecules.* 2019; 24(16): 2997.
- [69] Lewin M, Samuel S, Merkel J, Bickler P. Varespladib (LY315920) appears to be a potent, broad-spectrum, inhibitor of snake venom phospholipase A2 and a possible pre-referral treatment for envenomation. *Toxins.* 2016; 8(9): 248.
- [70] Bogdanov S. Bee venom: composition, health, medicine: a review. *Peptides.* 2015; 1:1-20.
- [71] Zhang S, Liu Y, Ye Y, Wang XR, Lin LT, Xiao LY, et al. Bee venom therapy: Potential mechanisms and therapeutic applications. *Toxicon.* 2018; 148: 64–73.
- [72] Liu S, Yu M, He Y, Xiao L, Wang F, Song C, et al. Melittin prevents liver cancer cell metastasis through inhibition of the Rac1-dependent pathway. *Hepatology.* 2008; 47: 1964–1973

- [73] McDonald J, Li F, Mehta C. Cancer mortality among beekeepers. *Journal of Occupational Medicine*. 1980; 21(12): 811–813.
- [74] Simons FER, Frew AJ, Ansotegui IJ, Bochner BS, Golden DBK, Finkelman FD, et al. Practical allergy (PRACTALL) report: risk assessment in anaphylaxis. *Allergy*. 2008; 63(1): 35-37.
- [75] Harfmann D, Florea A. Experimental envenomation with honeybee venom melittin and phospholipase A2 induced multiple ultrastructural changes in adrenocortical mitochondria. *Toxicon*. 2023; 229: 1-15.
- [76] Sturm GJ, Varga EM, Roberts G, Mosbech H, Bilò MB, Akdis CA, et al. EAACI guidelines on allergen immunotherapy: Hymenoptera venom allergy. *Allergy*. 2018; 73:744–764.
- [77] Han SM, Lee GG, Park KK. Acute dermal toxicity study of bee venom (*Apis mellifera* L.) in rats, *Tox Research*. 2012; 28:99-102.
- [78] Ramirez L, Shekhtman A, Pande, J. Nuclear magnetic resonance-based structural characterization and backbone dynamics of recombinant bee venom melittin. *Biochemistry*. 2018; 57(19): 2775-2785.
- [79] Kim CMH. Apitherapy—Bee Venom Therapy. In *Biotherapy-History, Principles and Practice. A Practical Guide to the Diagnosis and Treatment of Disease using Living Organisms*; Springer: Heidelberg, Germany. 2013. p. 77–112.
- [80] Park JH, Yim BK, Lee JH, Lee S, Kim TH. Risk associated with bee venom therapy: a systematic review and meta-analysis. *PloS one*. 2015; 10(5): 01-26
- [81] Colomar AA. Apilarnil Therapy: The Healing Power of Bee Larvae. *J Apitherapy*. 2023; 10 (09): 1-2
- [82] Ram SKM, Jayapal N, Nanaiah P, Aswal GS, Ramnarayan B, Taher SM. The therapeutic benefits of bee venom. *Int J Curr Microbiol App Sci*. 2014; 3: 377-381.
- [83] İnci H, İlkaya M. And İzol E. Apilarnil (Drone Larvae) Chemical Content, Bioactive Properties and Supporting Potential in Medical Treatment of Some Diseases in Terms of Human Health. *Ulus Gıda Tar Hayv Derg*, 2021; 1 (1): 1-7
- [84] Tunca RI, Taşkın A. ve Karadavut U. Determination of bee products consumption habits and awareness level in some provinces in Turkey. *Turk J Food Agric Sci*. 2015; 3(7): 556-561.
- [85] Aoşan C. Apitherapy in the daily practice clinical applications. In *Apimedita and Apiquality Forum*, Rome, 2016. p. 22-24.
- [86] Lee BW, Shek LPC, Gerez IFA, Soh SE, Van Bever HP. Food Allergy--Lessons from Asia. *World Allergy Organ J*, 2008; 1(7): 129-133.
- [87] Cifuentes, L. Allergy to honeybee... not only stings. *Curr Opin Allergy Clin Immunol*. 2015; 15(4): 364-368.
- [88] Eshraghi S and Seifollahi F. Antibacterial Effects of Royal Jelly on Different Strains of Bacteria. *Iranian J Publ Health*, 2003; 32 (1):25-30
- [89] Stangaciu S. Bee products and their medicinal uses. *Honeybee Science*. 2002; 23(3): 97–104.
- [90] Jayaraj R, Megha P, Sreedev P. Organochlorine pesticides, their toxic effects on living organisms and their fate in the environment. *Interdiscip toxicol*. 2016; 9(3-4): 90–100.
- [91] Johnson RM, Dahlgren L, Siegfried BD, Ellis MD. Acaricide, Fungicide and Drug Interactions in Honeybees (*Apis mellifera*). *PLoS ONE*. 2013; 8(1): 1-11.
- [92] Hepburn HR, Pirk CWW, Duangphakdee O. Synthesis of Beeswax. *Honeybee Nests*. 2014, pp 341–365
- [93] Crane E. Bee Products. *Encyclopedia of Insects*. 2009. p. 71–75.
- [94] Fratini F, Cilia G, Turchi B, Felicioli A. Beeswax: A minireview of its antimicrobial activity and its application in medicine. *Asian Pac J Trop Med*. 2016; 9(9): 839-843.
- [95] Apan MA, Zorba M, Kayaboynu Ü. Honey bee and honey bee products. *Sinop Uni J Nat Sci*. 2021; 6(2): 202-223.
- [96] Sorucu A. Bee products and apitherapy. *Bulletin of Veterinary Pharmacology and Toxicology Association*. 2019; 10(1): 1-15.
- [97] Topal E, Ceylan Ö, Kösoğlu M, Märgäoan R, Cipcigan Mc. Bal Mumunun Yapisi, Kullanım Alanlari ve Bazi Temel Sorunlari. *U Arı D*. 2020; 20(2): 209-220.
- [98] Kačániová M, Vukovic N, Chlebo R, Hascik P, Rovna K, Cubon J, et al. The antimicrobial activity of honey, bee pollen loads and beeswax from Slovakia. *Arch Biol Sci*. 2012; 64(3): 927-934.
- [99] Illnait J, Rodríguez I, Mendoza S, Fernández Y, Mas R, Miranda M, et al. Effects of D-002, a mixture of high molecular weight beeswax alcohols, on patients with nonalcoholic fatty liver disease. *Korean J Intern Med*. 2013; 28(4): 439-448.
- [100] Puente R, Illnait J, Mas R, Carbajal D, Mendoza S, Fernández JC, et al. Evaluation of the effect of D-002, a mixture of beeswax alcohols, on osteoarthritis symptoms. *Korean J Intern Med*. 2014; 29(2): 191-202.
- [101] Perugini M, Tulini SMR, Zezza D, Fenucci S, Conte A, Amorena M. Occurrence of agrochemical residues in beeswax samples collected in Italy during 2013–2015. *Sci Total Environ*. 2018; 625: 470-476.
- [102] Bommuraj V, Chen Y, Klein H, Sperling R, Barel S, Shimshoni JA. Pesticide and trace element residues in honey and beeswax combs from Israel in association with human risk assessment and honey adulteration. *Food Chem*. 2019; 299:1-10.
- [103] Gokulakrishna RK, Thirunavukkarasu S. Apitherapy: A valuable gift from honey bee. *J Entomol Zool Stud*. 2020; 8(5): 2317–2323.
- [104] Alvarez-Suarez JM. Bee products-chemical and biological properties. Springer. 2017.
- [105] Abd El-Wahed AA, Farag MA, Eraqi WA, Mersal GA, Zhao C, Khalifa SA, et al. Unravelling the beehive air volatiles profile as analysed via solid-phase microextraction (SPME) and chemometrics. *J King Saud Univ Sci*. 2021; 33(5): 1-8.

- [106]Kekeçođlu M, Bellici AE, Yıldırım İ, Kınalıkaya A, aprazlı T, Yüksel B. The Use of Bee Products and Undesirable Effects Related to Apitherapy Applications: A Systematic Review. Journal Of Traditional Medical Complementary Therapies. 2023; 6(2): 169-183